Remote Sensing of Surface Currents in The Fraser River Plume with the SeaSonde HF Radar

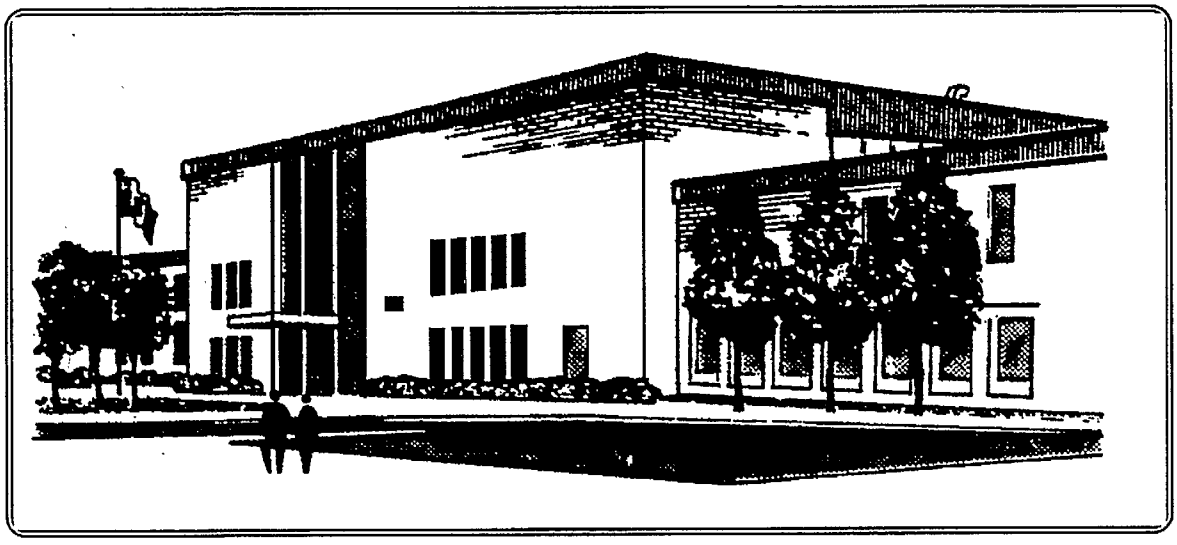

REPORT SERIES NO. **EE-151**

ENVIRONMENTAL TECHNOLOGY CENTRE
EMERGENCIES SCIENCE DIVISION

Environment Canada | Environnement Canada

Canada

Remote Sensing of Surface Currents in the Fraser River Plume With theSeaSonde HF Radar

by

Donald O. Hodgins, John S. Hardy, Sally E. Tinis
Seaconsult Marine Research Ltd.
8805 Osler Street
Vancouver, B.C.
V6P 4G1

Funding for this study was provided by the Canadian Coast Guard, Imperial Oil Resources Limited, Canada Centre for Remote Sensing and the Emergencies Science Division of Environment Canada.

EE-151 **September, 1994**

EXECUTIVE SUMMARY

The shore-based SeaSonde HF radar was deployed for three weeks in the summer of 1993 to measure surface currents in the Strait of Georgia, British Columbia. Experimental objectives included documenting the complex flow regime generated by large tides and the brackish plume of the Fraser River, and determining the radar performance under low-wind, low-salinity conditions. The radar data showed that surface flows are dominated by the plume jet formed by the Fraser River outflow, giving rise to recurring, energetic eddies with scales of 8-12 km, strong flow meanders and convergent fronts. These features were continuously modulated by the along-channel tidal flows. Comparisons with a detailed numerical model hindcast gave good correlation between observed and predicted flow fields, especially at tidal and low frequencies, providing confidence in both the new data and modelling capabilities. Radar return was found to be correlated with local winds, with the poorest data recovery obtained under calm conditions. Radar performance was found to be independent of salinity variations (18-28 ppt) in the plume.

Synthetic aperture radar (SAR) provides a map of the radar scattering characteristics of the ocean surface on a capillary wave scale. Changes in the centimetre-scale roughness can be induced by winds, fronts, ship wakes, surface waves, and current shears, as well as convergent and divergent zones often associated with internal waves. SAR data have been used to detect oil slicks, and the wide-swath images offered by present and future radar satellite sensors suggest that radar imagery will be a useful monitoring tool. ERS-1 and airborne SAR images for July 28, 1993, were obtained and surface features were examined in the context of the HF radar current fields. Results of the study indicate that the SAR images alone cannot reliably provide the dynamical data required in this region by oil spill models. Under certain conditions, however, the radar imagery offers valuable physical information on phenomena affecting oil slick development. It was concluded that interpretation of SAR imagery in conjunction with information from other remote-sensing instruments would offer more quantitative prediction data, and could form the basis for assimilating imagery into numerical models in conjunction with surface current maps from the ground wave radar.

RÉSUMÉ

Le radar HF SeaSonde installé sur la côte a été déployé pendant trois semaines au cours de l'été de 1993 afin de mesurer les courants de surface dans le détroit de Georgie, en Colombie Britannique. Les objectifs expérimentaux comprenaient la documentation du régime d'écoulement complexe généré par les grandes marées et le panache saumâtre du fleuve Fraser, ainsi que la détermination des performances du radar dans des conditions de faible vent et de basse salinité. Les données radar ont montré que les écoulements de surface sont dominés par le jet de panache formé par le déversement du fleuve Fraser, qui donne naissance à des remous récurrents et puissants sur des échelles de 8 à 12 km, à des méandres à écoulement élevé ainsi qu'à des fronts convergents. Ces caractéristiques étaient constamment modulées par l'écoulement des marées le long du cours d'eau. Des comparaisons avec la rétrospection d'un modèle numérique détaillé ont donné une bonne corrélation entre les champs d'écoulement observés et prévus, particulièrement aux fréquences des marées et aux basses fréquences, et ont suscité de la confiance quant aux données nouvelles et aux possibilités de modélisation. Les échos radar étaient en corrélation avec les vents locaux, la plus mauvaise récupération des données étant obtenue dans des conditions calmes. La performance radar s'est avérée indépendante des variations de salinité (18-28 ppt) dans le panache.

Le radar à synthèse d'ouverture (RSO) fournit une carte des caractéristiques de diffusion radar de la surface océanique sur une échelle d'ondes capillaires. Des variations de rugosité sur l'échelle centimétrique peuvent être induites par des vents, des fronts, le sillage des navires, des vagues de surface et le cisaillement des courants, ainsi que par les zones convergentes et divergentes souvent associées aux vagues internes. Les données du RSO servent à détecter les nappes de pétrole, et les images à balayage large offertes par les actuels et futurs détecteurs radar de satellite laissent supposer que l'imagerie radar constituera un outil de surveillance puissant. Les images du 28 juillet 1993 ont été obtenues au moyen d'ERS-1 et d'un RSO aéroporté, et les caractéristiques de surface ont été examinées dans le contexte des champs de courants radar HF. Les résultats de l'étude indiquent que les images de RSO seules ne peuvent pas fournir de façon fiable les données dynamiques qu'exigent dans cette région les modèles de déversement de pétrole. Toutefois, pour certaines conditions, l'imagerie radar offre de l'information physique précieuse quant aux phénomènes qui influent sur la formation des nappes de pétrole. On a conclu que l'interprétation de l'imagerie RSO ainsi que l'information provenant d'autres instruments de détection à distance offrirait plus de données de prévision quantitatives et pourrait constituer la base d'assimilation de l'imagerie à des modèles numériques, avec des cartes de courants de surface provenant d'un radar à onde de sol.

TABLE OF CONTENTS

LIST OF TABLES

LIST OF FIGURES

LIST OF FIGURES

1.0 INTRODUCTION

Surface current mapping with high-frequency, shore-based radars is an effective method for obtaining ocean currents for input to oil spill models. A feasibility study in Queen Charlotte Sound demonstrated consistent data acquisition at ranges exceeding 50 km from each radar under open ocean conditions (Hodgins and Hardy, 1992). In July 1992 the 12.5-MHz SeaSonde radar was deployed on Juan de Fuca Strait (Hodgins et al., 1993a) to examine its performance under low wave and light wind conditions that are typical of more sheltered coastal waterways. While data acquisition did vary with the local wind conditions, current map coverage over the width of the strait was generally good and the data revealed for the first time complex, turbulent flow features generated by the interaction of tidal currents with bathymetry. Analysis of these features led to parameterization of the slowly-varying, predictable flow, and the large-eddy turbulence properties in terms of eddy viscosity (Hodgins et al., 1993b), both of which are essential for spill modelling.

A third study was undertaken in the Strait of Georgia during July 1993, specifically aimed at mapping currents in the Fraser River plume. The plume is comprised of brackish, low salinity water whose position is strongly modulated by the tide, and it is characterized by strong flows, fronts and intense current shear across the plume interface at a depth of about 3-4 m. Since the salinity determines the conductivity of the surface water, and the ground-wave radar reception is to some degree dependent on conductivity, one objective of the study was to examine the radar performance in an area where the fresh water jet might affect radar range. A second objective was to acquire data coincident with SAR imagery (ERS-1 and Convair CV580 airborne imagery) for analysis of large-scale surface flow features.

2.0 RADAR SITING

The radar system was deployed for 3 weeks at the end of July and the first week of August 1993. Both sites were located on Galiano Island with a baseline separation of 21.8 km, yielding a coverage area encompassing the entire mouth of the main arm of the Fraser River (Fig. 2.1). Surface current data were collected without problem for the entire deployment period.

The northern radar unit, at Dionisio Point, was located in a provincial park and manned full-time by a radar technician. The camp was mobilized on July 18-19, and the radar unit went on-line in the morning of July 20 (local time). Data recovery was virtually continuous up until the radar was shut down and demobilized on August 5. There were no support facilities at Dionisio Point and the radar was housed, together with the technician, in a 15-foot Trillium trailer (Fig. 2.2). Power for both trailer and radar was supplied from a 2,500 watt portable generator equipped with a continuous fuel supply lead connected to a 45-gal gasoline tank. Transmit and receive antennas were mounted approximately 5 m above the high tide line (Fig. 2.3).

The radar at Salamanca Point was unmanned and located on private property, with access to 110 VAC line power and a telephone connection. The site was mobilized on July 20-21 and went on-line late on the 21st. Data recovery was almost continuous up until demobilization on August 5, with the exception of an extended period on August 4 when the system was shut down for communications testing. Transmit and receive antennas were located roughly 10 m above the high tide line on the rocky shore (Fig. 2.4). Key radar characteristics are summarized in Table 2.1.

Table 2.1

Characteristics of the SeaSonde Radars Deployed in the Strait of Georgia

	Dionisio Point	Salamanca Point
Latitude	49°00.63'N	48°54.32'N
Longitude	123°34.12'W	123°20.80'W
Sampling interval	1 h	1 h
Transmit frequency	12.421875 MHz	12.656250 MHz
Transmit power	< 100 W	< 100 W
Theoretical range	79.24 km	79.24 km
Range resolution	2.556 km	2.556 km
Radial velocity azimuth resolution	5°	5°

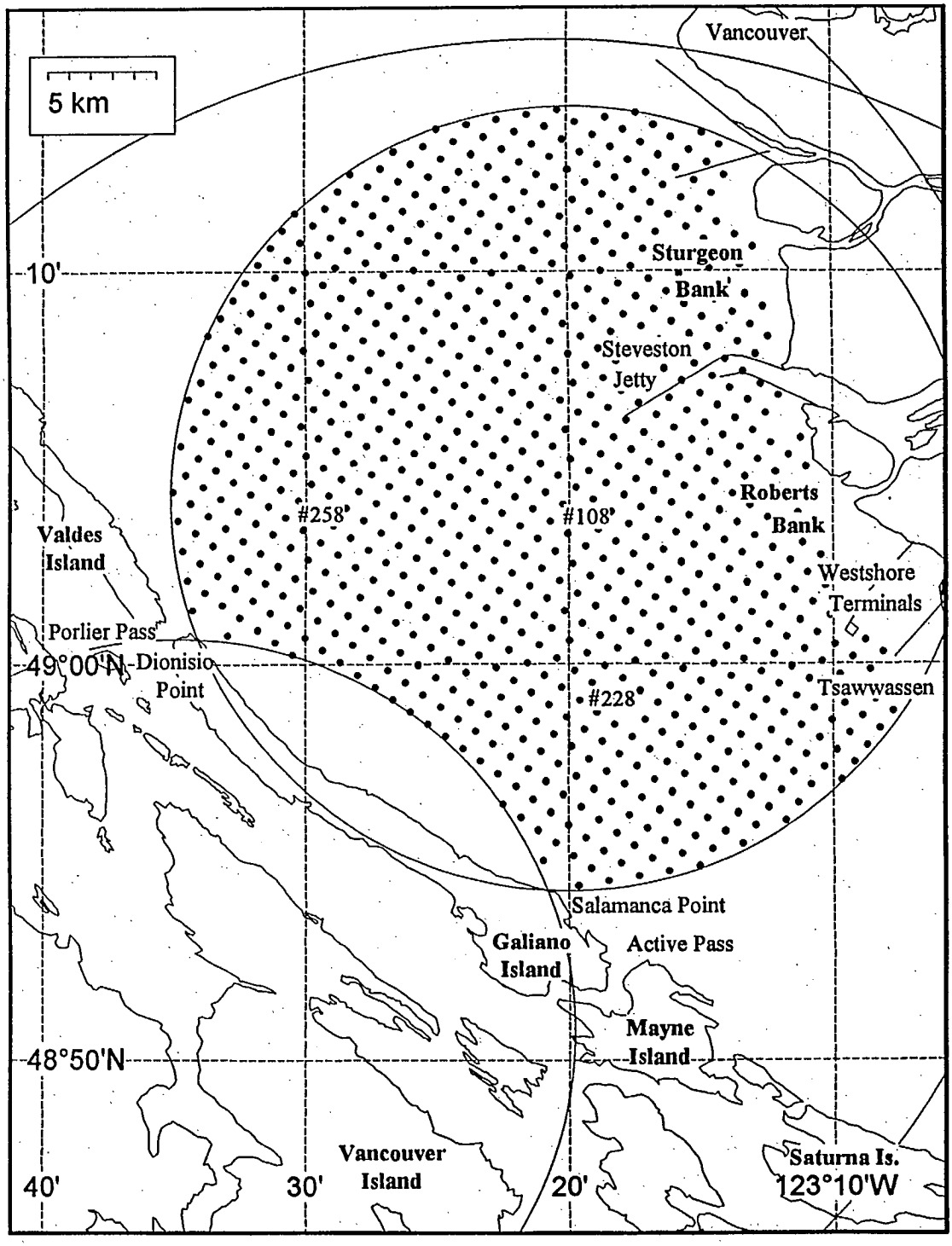

Figure 2.1 Map of the Strait of Georgia showing the Gulf Islands and the Lower Mainland. The SeaSonde coverage area is indicated by the dots.

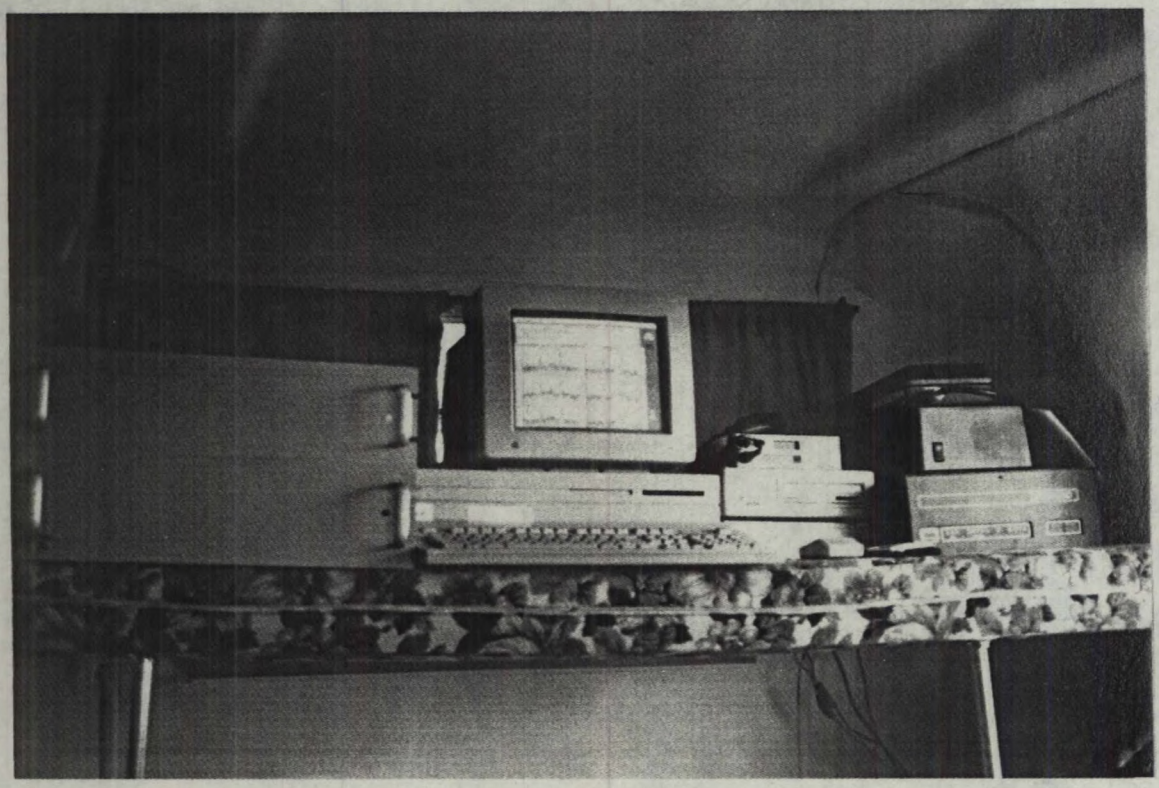

Figure 2.2 The Dionisio Point site showing the 15-foot trailer (upper panel) and the radar hardware housed in the trailer (lower panel).

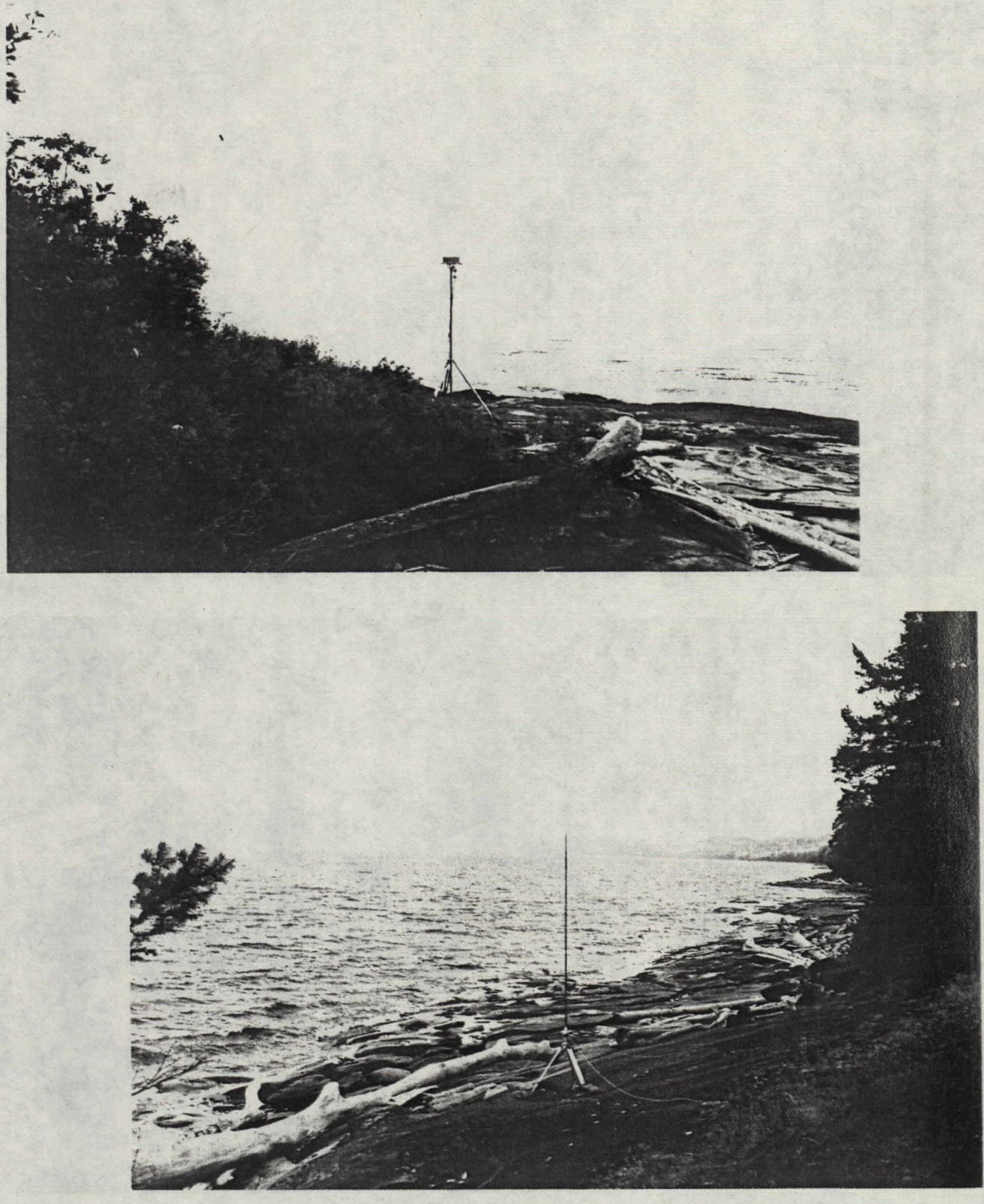

Figure 2.3 Receive (upper panel) and transmit (lower panel) antennas at Dionisio Point.

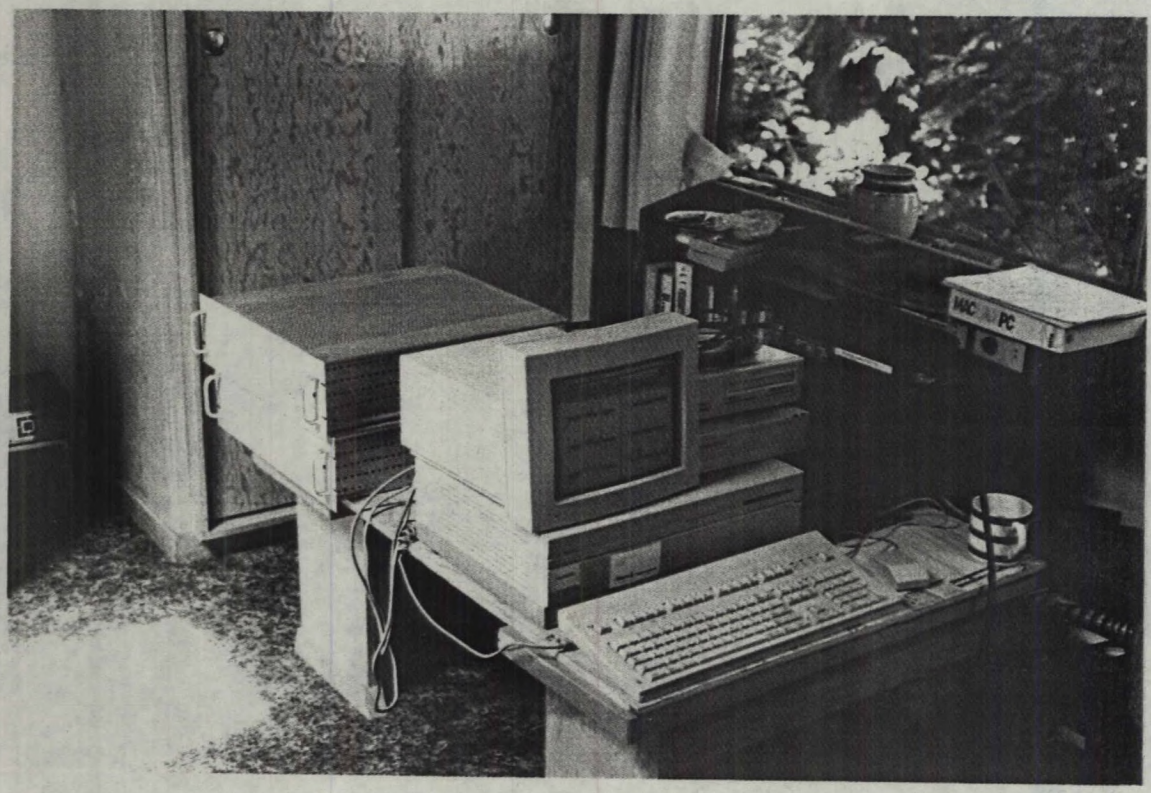

Figure 2.4 Receive antenna (upper panel) and radar hardware (lower panel) at Salamanca Point.

3.0 DATA RECOVERY

The period from July 22 to August 5 provided good, two-site data. A gross measure of data recovery is given by the number of radial velocities measured with each radar. In principle, given equally good siting and total aperture, both radar units should measure about equivalently in terms of range and density of derived radial current information. However, in this deployment, the Salamanca radar had a smaller effective over-water view width for part of its range. As a result, the total radial current return at Salamanca Point was slightly less than at Dionisio Point. This measure of data return is summarized in Fig. 3.1 in which the time-series of radial counts at each radar site are plotted. The figure shows that the return was variable but similar at both sites, indicating that factors external to the radars account for the variations rather than a characteristic of one radar site.

3.1 Wind

Wind data were obtained from various stations around the strait; however, the most representative winds for the coverage are were those observed at Sand Heads. The count data are correlated with variations in the wind speed at this station (Fig. 3.1), which is logical, and reflects increased sea echo strength as resonant wind waves build with stronger winds. In particular, the data return was worst during a period in and around July 31st, coinciding with a significant prolonged dip in wind speed. In addition, the count data are correlated with changes in the wind direction, although this effect is smaller than changes due to wind speed variations. This result is also logical, since cross-channel winds (e.g., 45° or 225°) have a smaller effective fetch from the leeward shore than winds aligned with the main axis of the strait.

The variability in the data return for the Strait of Georgia is greater than has been experienced over the open ocean. This observation may be explained by the lower prevalence of resonant 11-m long waves in the strait compared with the open ocean. A higher operating frequency would decrease the observed variability in radial returns because of the increased occurrence of shorter wind waves producing the required sea echo return signals.

3.2 Tide

As found in the Juan de Fuca experiment (Hodgins et al., 1993a) there was no apparent correlation of the radial returns with tidal phase, although tidal currents are strong and highly modulated in this region. This outcome is expected, since tidal currents do not modify the wave field and consequently are not expected to significantly affect the sea echo return. The intertidal bank at the mouth of the Fraser River was not expected to have a noticeable impact because the area of shelf that dries out is a small part of the total coverage area, and then only for a portion of the tidal cycle.

These results show that the 12.5 MHz radar is effective with moderate winds of 5 to 10 knots and stronger, but will suffer some loss in performance as winds abate completely and the sea becomes flat. Under calm conditions the radars continue to function although range is decreased, and as a result so is the dual-radar coverage area over which total currents can be derived.

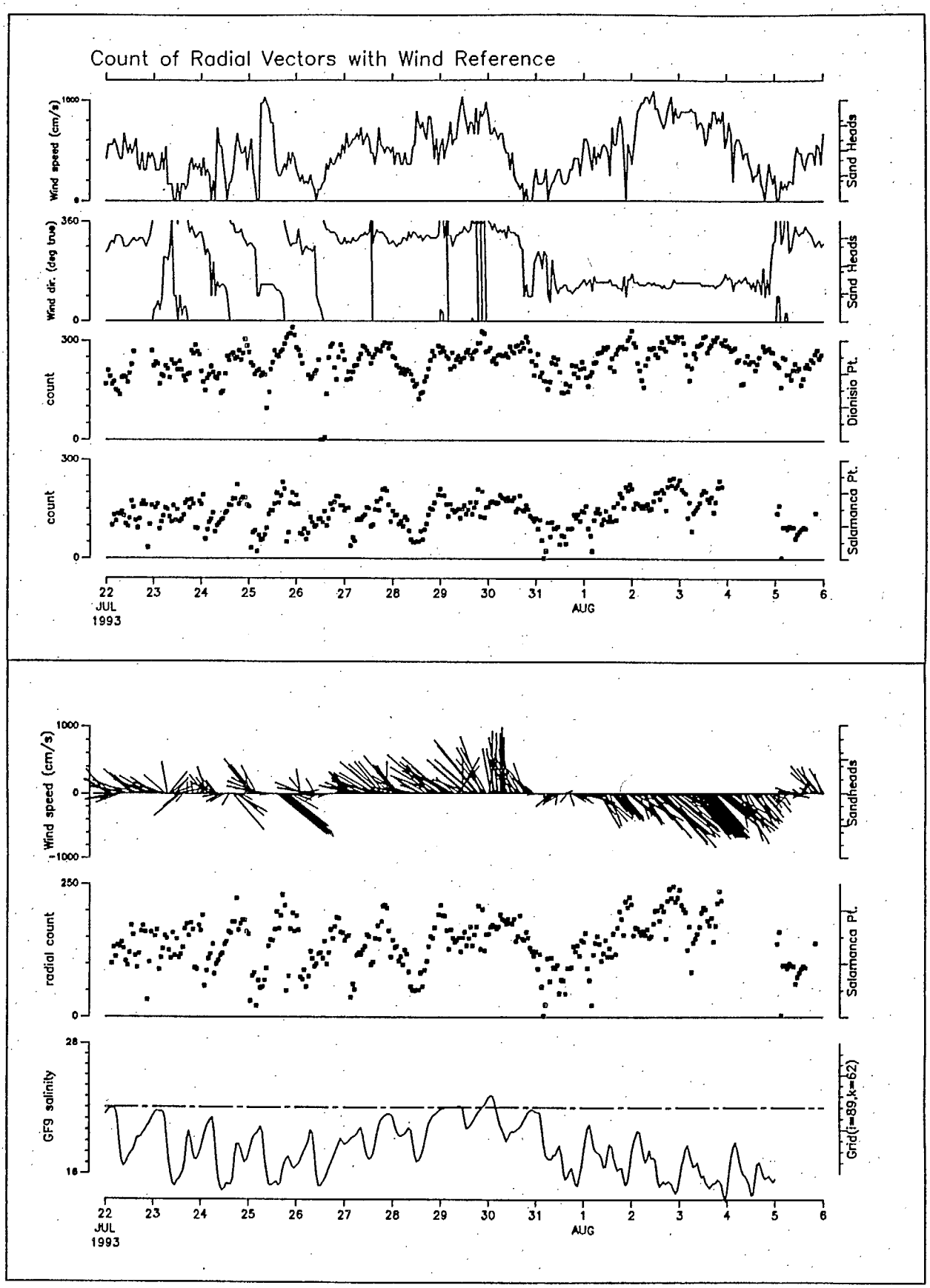

Figure 3.1 Time-series of radar return measured by radial vector count compared with wind speed and direction (upper panel) and with surface salinity (lower panel).

3.3 Salinity

Information on the salinity of the surface layer was derived from the GF9 hydrodynamic model (Stronach et al., 1993). Typically, salinity values ranged from less than 20 ppt near the mouth of the Fraser River up to about 28 ppt at high tide in the extreme south of the study area. Figure 3.2 shows an example of the salinity distribution at high tide, illustrating the spread of the Fraser River plume into the Strait of Georgia. (The corresponding surface current field is shown in Fig. 5.2a.) The radial count data display no apparent correlation with observed variations in the salinity field (Fig. 3.1), consistent with our earlier findings in Juan de Fuca Strait.

The salinity time-series shown is centrally located in the coverage area and is therefore broadly representative of the salinity in the region where the radar signal is strongest. Variations in the salinity are driven primarily by the tidal cycle, and to a lesser extent by changes in wind speed and direction. An example of the wind influence is evident in the salinity time-series during the period of strong northwesterly winds from August 1-4. The salinity shows a mean decrease over this period but the radial count rises, demonstrating that wind-related effects are much more important than changes in salinity in the range of 17-27 ppt.

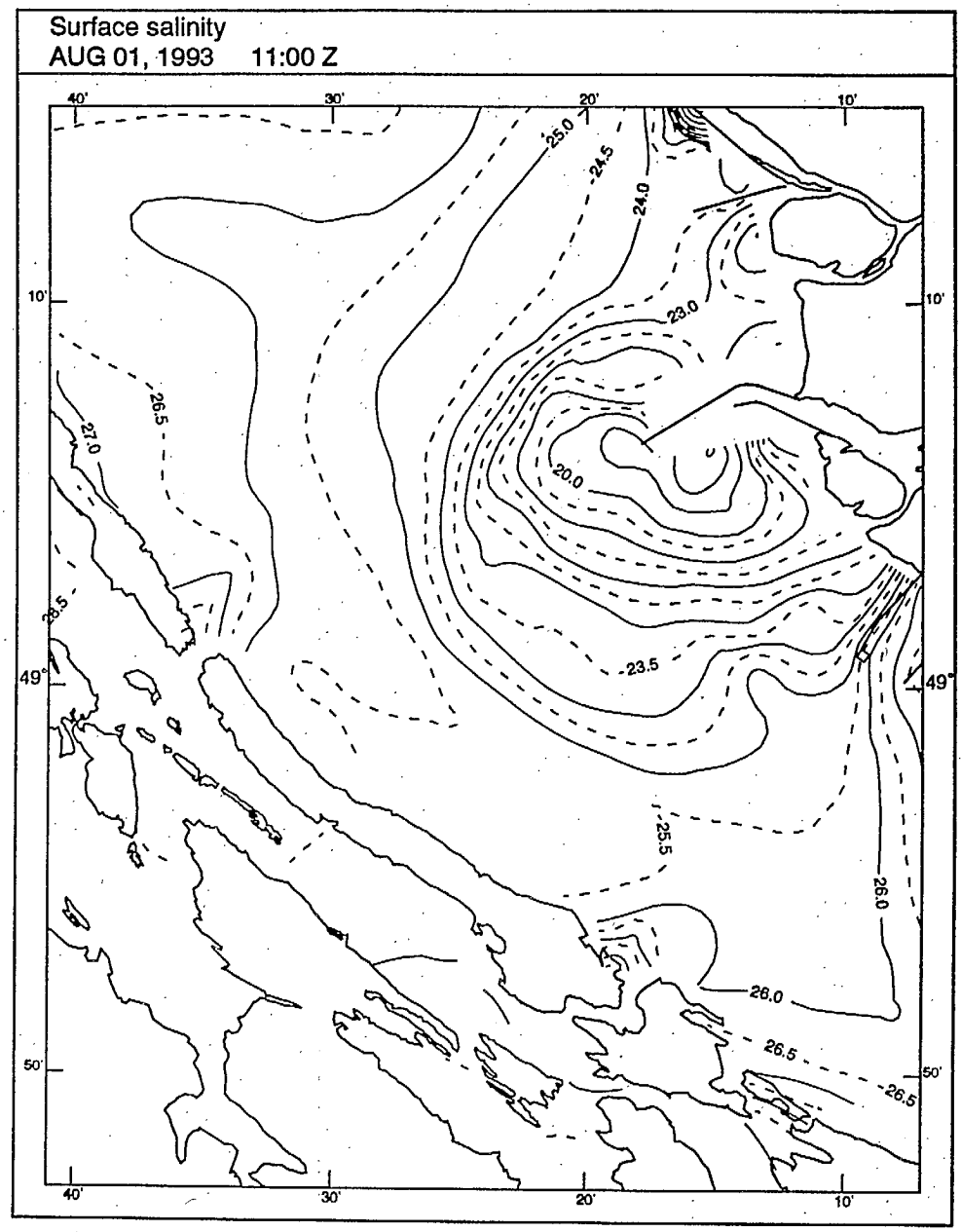

Figure 3.2 Typical surface salinity field (plotted as σ_t) predicted with the GF9 hydrodynamic model.

4.0 SURFACE CURRENT CALCULATION

Radial velocities were extracted hourly from the sea echo spectra using the least-squares method described by Lipa and Barrick (1983). This standard SeaSonde procedure statistically tests the single and dual-angle models for radial currents and selects the one having the best fit to the data. The resulting hourly radial velocity fields consisted of a variable number of range cells, each separated by 2.557 km. Within each range cell, the data records were comprised of the speed, v, and corresponding direction indicated by the sign of the speed; a parameter, δv, expressing the uncertainty associated with the speed (see Lipa and Barrick, 1983); and an angular position, given at 5° intervals. Two thresholds were applied to the radials to remove questionable and bad data points: (1) $\delta v > 80$ cm/s was used as the primary threshold to reject spurious radial estimates (representing about 1% of the radial dataset), and (2) $v \geq 250$ cm/s, which exceeds the 1-hour averaged maximum current velocity that was expected anywhere within the coverage area of each radar.

Gaps in the radial fields were filled by interpolation, using a one-dimensional spline under tension fitted to data within each view sector of the range ring. No extrapolation beyond the range of data points was attempted. The interpolated radial velocities were assigned an uncertainty equal to the average δv for the data used to calculate the interpolating spline function.

Synchronous radial data files were combined to yield total surface current on a Cartesian grid with a spacing of 1 km. The two-site coverage area was constrained by placing an upper bound on the triangulation angle between vectors from the two radar sites. This bound was defined by an error factor of $\epsilon=2.5$ (Leise, 1984) which limits the angles between radials to less than 147.1° and greater than 32.9°.

The radial information from each radar map required to form the total current at each grid point was found by linear interpolation using the four nearest neighbours. This procedure gives better accuracy for the total current near the radar units, and becomes nearly equivalent to the blending radius method (Hodgins and Hardy, 1992) when the Cartesian grid points are further than 5 range rings from both radar sites. The uncertainty of the final current vector was calculated by propagation of error from the speed and δv values of the radial data that enter the interpolation procedure.

The current maps are presented in Appendix 1.

5.0 SURFACE FLOW FEATURES IN THE STRAIT OF GEORGIA

The current map in Fig. 5.1 is typical of many in the dataset and illustrates several oceanographically significant features. At this time, the tide is late on a rising flood, one hour before high water. The surface flow is characterized by two spatially coherent closed eddies: a clockwise one off the southern tip of Valdes Island, with a diameter of approximately 9 to 13 km, and a counterclockwise one near Galiano Island, southeast of the first eddy, with a diameter of about 8 km. Between these two eddies, the tidal flow converges with the Fraser River plume to form a pronounced cross-channel line of convergence. This convergent zone is a manifestation of a strong cross-channel jet towards the western shore of the strait. The jet structure, in conjunction with the two eddies, appears to be a stable feature of the flow field near Galiano Island, apparently produced by the interaction of the tidal currents with the flow out of the Fraser River. Two maps for high tide are shown in Fig. 5.2, each at approximately the same tidal phase as Fig. 5.1. It can be seen that all three maps share an overall pattern similarity, providing confidence in the radar measurements.

The jet structure appears consistently when the tide is near slack water (low or high), although the eddies are generally stronger when the tide is high. As the tide ebbs or floods, the cross-channel component weakens and the eddies are washed out into the stronger flow aligned with the main axis of the strait (as illustrated in Fig. 5.3). In general, the eddies do not disappear at the same time; the Valdes eddy appears to be the more persistent of the two.

The direction of the wind at Sand Heads is most often aligned with the central axis of the strait and acts either with the tidal flow or against it to increase or decrease the net surface current along the main axis. Wind can affect the timing and duration of slack water at the top or bottom of the tidal cycle, and hence either hinders the development of a significant cross-channel flow (increased axial flow) or assists it (reduced axial flow). This observation was confirmed by studying the repeated formation and dissipation of the two eddies throughout the dataset.

Another recurring feature of the flow field is convergence near Roberts Bank, which can take the form of an eddy (Fig. 5.2—upper panel) or a convergent front. When present, an eddy in this area can rotate in either direction, and a front can be parallel to the bank or oriented at an angle into the strait. The convergence is likely the result of the Fraser River plume crossing Roberts Bank and meeting the axial tidal flow in the strait. (As expected, this feature was never seen at or near low water when the cross-bank flow dropped to near zero.)

This type of convergence feature and its orientation depend strongly on the direction of the flow and on the wind. For instance, a weak front seaward of the bank often forms in an ebb tide (southeast flow), although an eddy can also result if the wind acts to turn part of the flow back across Roberts Bank. Figure 5.4 shows a front perpendicular to the bank that formed when a strong river outflow (here assisted by a wind to the southwest) met a flood tide (northwest flow).

These maps show the complex, small-scale, yet spatially-coherent, patterns that develop, drawing their energy from non-linear interactions in the tidal flows. In waterways such as the Strait of Georgia, the energy associated with these sub-mesoscale features, such as fronts and eddies, is large.

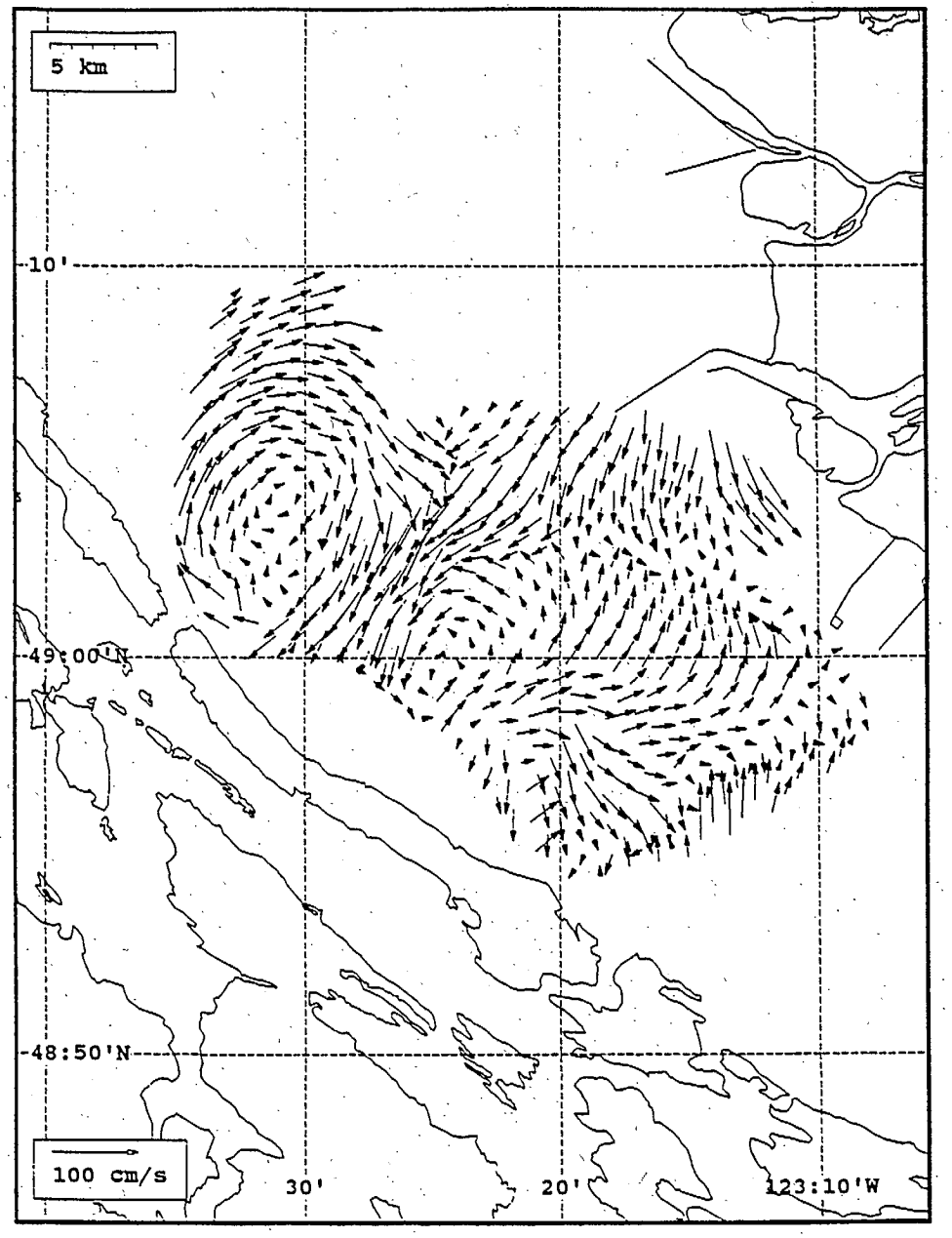

Figure 5.1 Typical surface current map showing the river jet and two eddies.

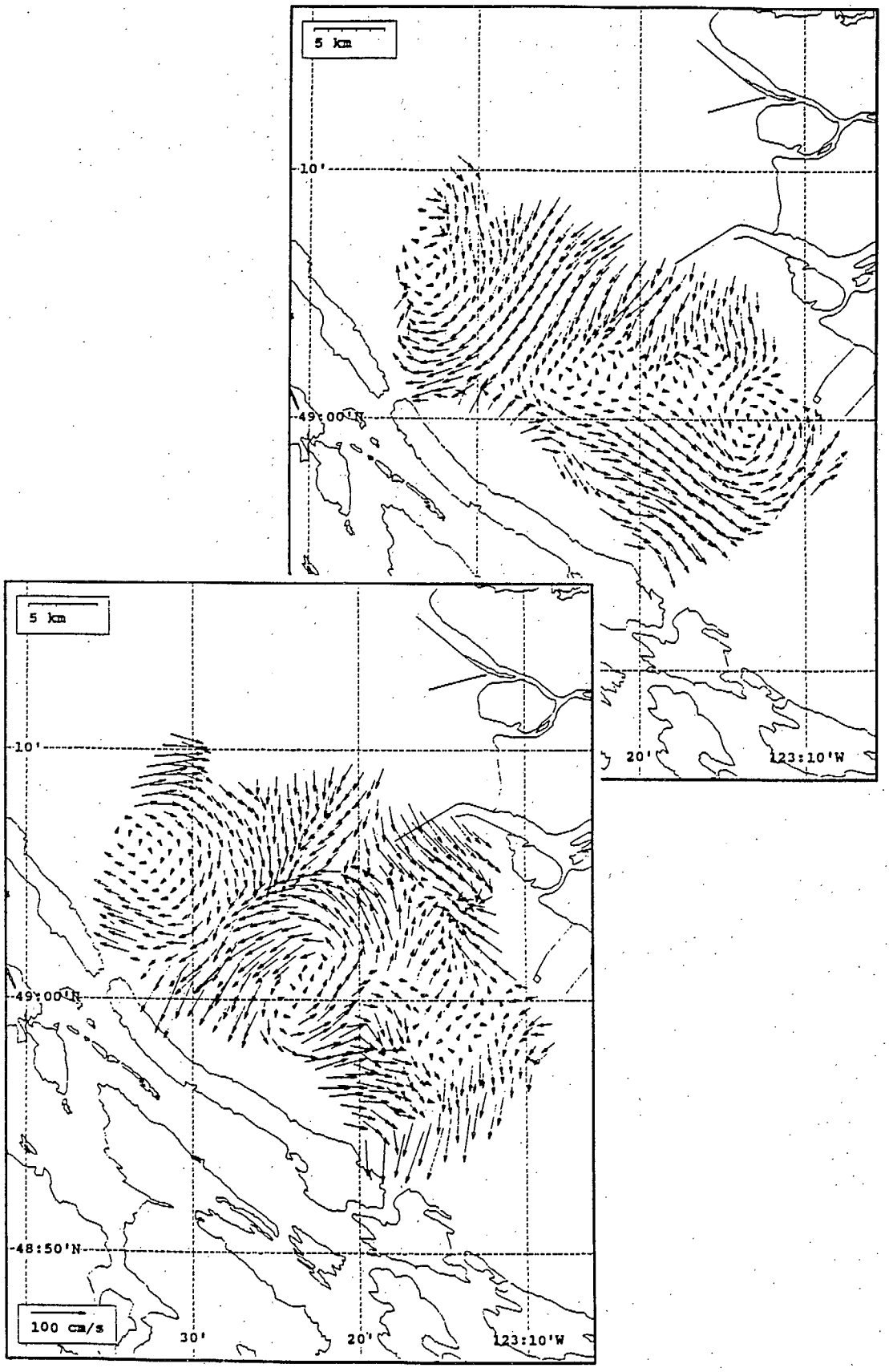

Figure 5.2 Surface current maps at similar tide phase showing the recurring eddy patterns in mid-strait.

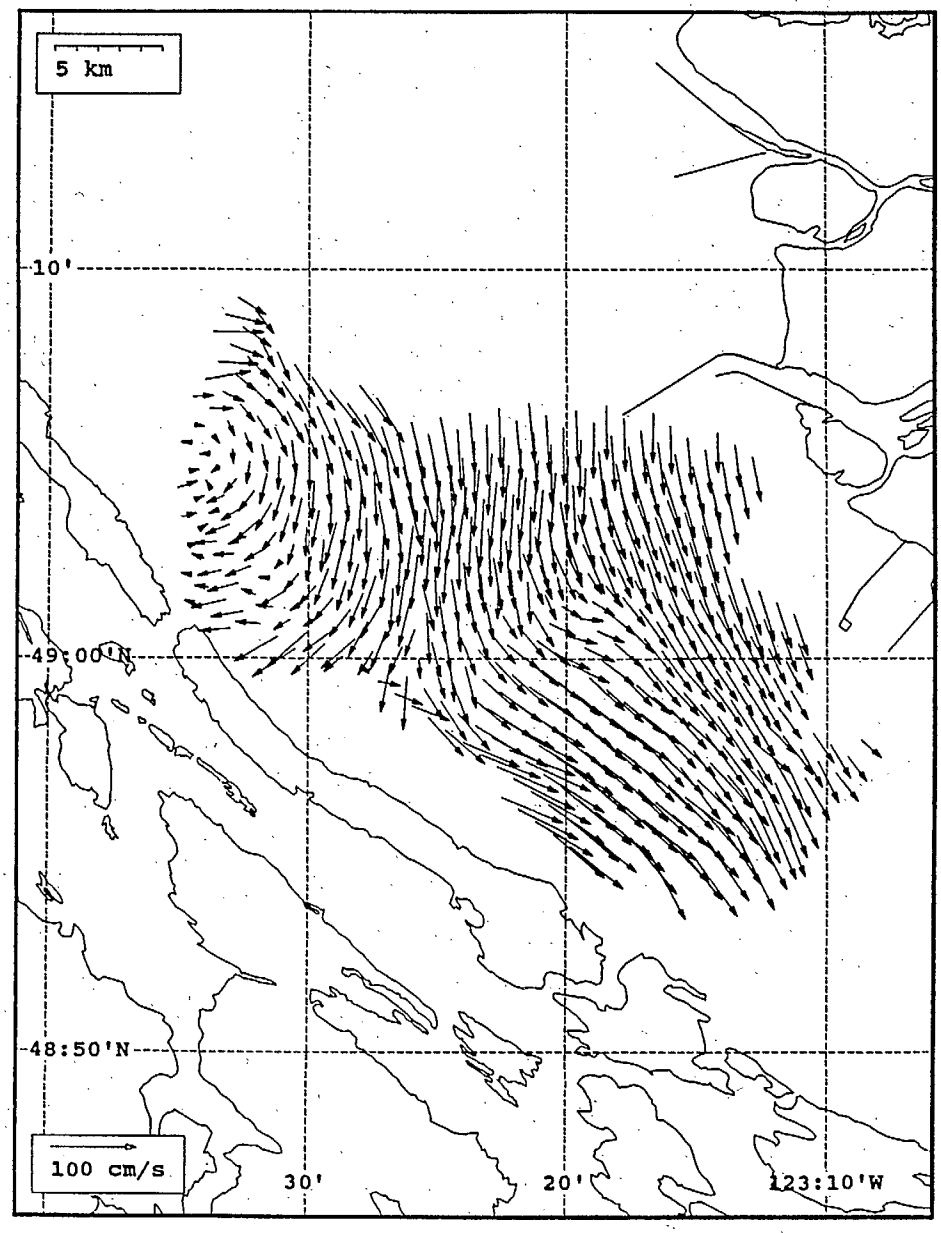

Figure 5.3 Ebb tide flow pattern.

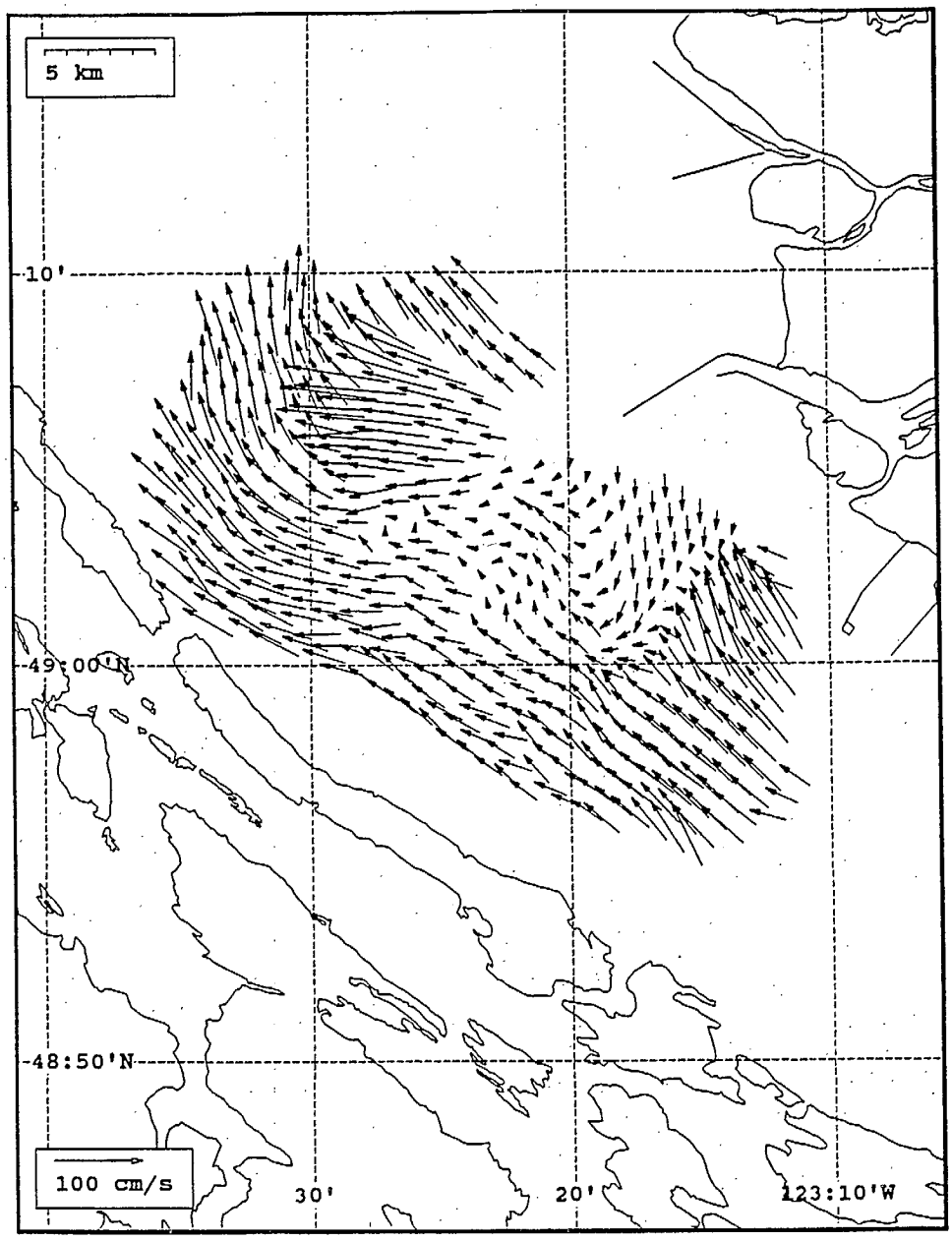

Figure 5.4 Front produced by river flow and wind on a flood tide.

6.0 MODEL COMPARISONS

The observed flow features in the plume are very complex and highly dynamic. No current meter or drifter observations were collected in this experiment to verify the HF radar measurements. Rather, data for comparison was generated by hindcasting the measurement period using the three-dimensional numerical hydrodynamic model GF9 (Stronach et al., 1993). Observed river flows, tides and winds were used for input to this hindcast. GF9 features a dynamic surface layer to simulate the physics controlling the Fraser River plume. Thus, the hindcast results are expected to model some of the features of the interaction between tide and river jet. The model was implemented on a 2-km × 2-km grid. This grid spacing is adequate to resolve the smoothly-varying large-scale flow features of the strait, but may be slightly too coarse to resolve details of the plume close to the river mouth.

Figure 6.1 compares two surface current maps from the SeaSonde dataset, one showing the total measured current and the other containing only the astronomical tidal components, derived by filtering the total current map. The coverage area of the tidal map is larger than the measured total current map because the tidal filter is capable of bridging temporal gaps in the dataset. These maps show clearly that the tide is dominating the surface flows, including the formation of the eddies remarked on earlier. Non-tidal influences are manifested in the strength of the convergent flow into the eastern side of the Valdes eddy and the difference in flow speeds along the southern edge of the coverage area.

The modelled current field is compared with the observed tidal map in Fig. 6.2. The overall flow patterns are similar: the outflowing Fraser River jet, turning south and merging with southward flowing water along the Valdes-Galiano Island shoreline. Both maps exhibit the stagnation point due west of Sand Heads and the shoreward flows in the northeast corner of the map. This degree of correspondence shows that both model and radar are describing the same general circulation; however, there is a considerable difference in detail between the modelled field and either the measured or filtered fields. This difference is seen mainly in the absence of the eddy structures in the model output.

Three points for time-series comparison (Fig. 2.1) were extracted from the observed and modelled data sets (labelled 108, 258 and 228). Site 108 is centrally located in the coverage area. The time-series are compared in Fig. 6.3 and 6.4 using site 108 as a reference. The u,v components represent the E-W and N-S flows, respectively.

There is an obvious close correspondence between the time-series which shows that the dominant tidal oscillation is in reasonable agreement. However, there are substantial differences between the signals at times, and the observed data is more energetic and exhibits greater high-frequency motion. The nature of these differences can be examined by comparing the power spectra of the two signals (Fig. 6.5). The energy at tidal and lower frequencies is in good agreement; however, the spectra diverge at the high-frequency tail. This result indicates that the higher energy in the observed data arises from eddying and meandering motions that have short time scales (1-3 h) and correspondingly smaller characteristic length scales. These findings are similar to the results derived in Juan de Fuca Strait (Hodgins et al., 1993b).

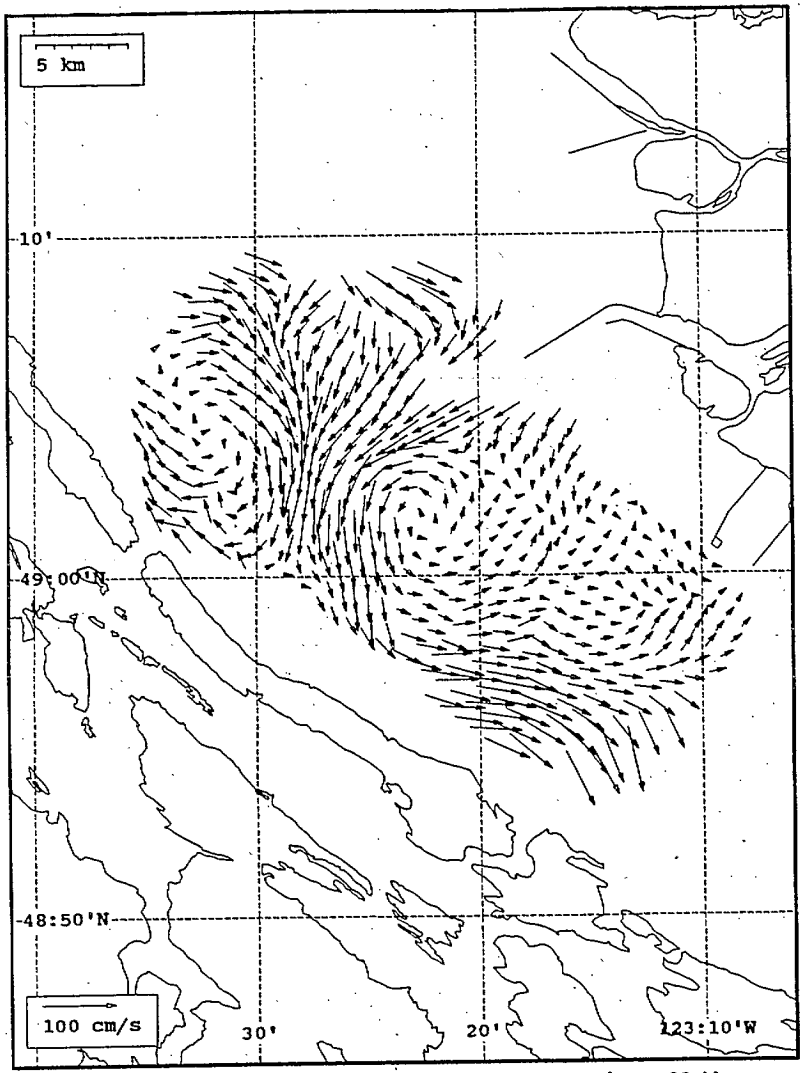

SeaSonde current field from the Strait of Georgia, off the mouth of the Fraser River, for 10:00 Z, August 2, 1993.

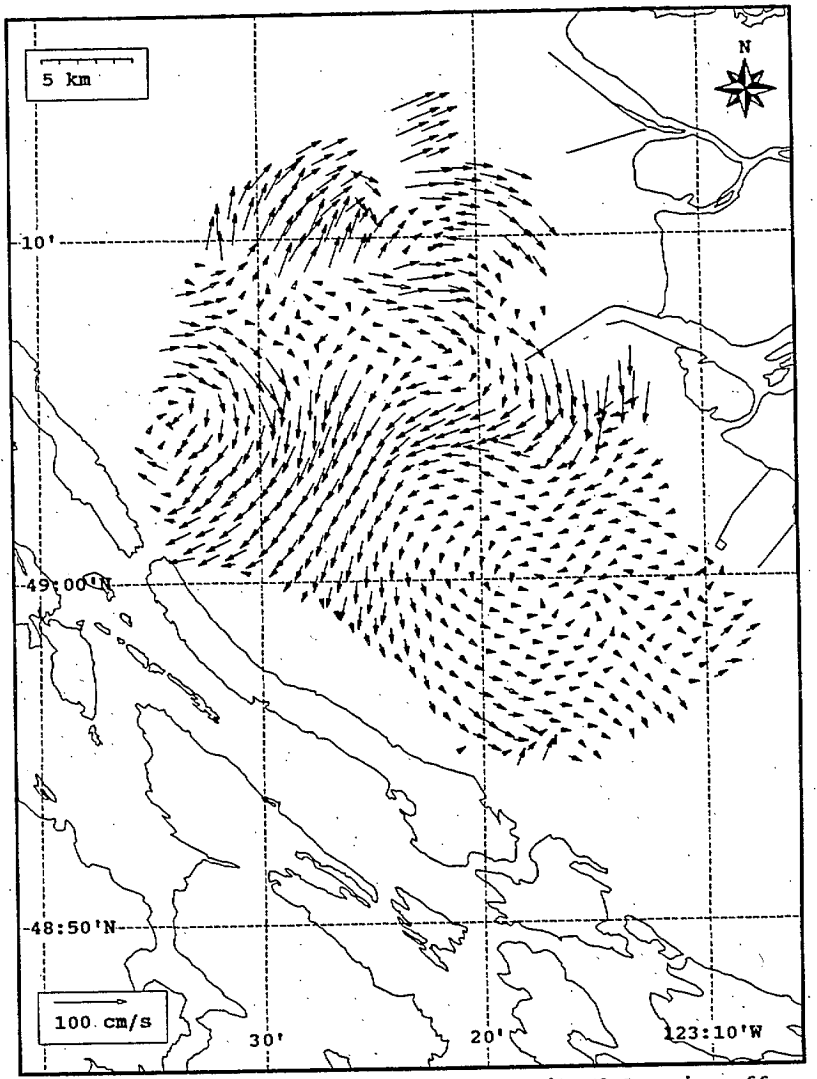

SeaSonde tidal current field from the Strait of Georgia, off the mouth of the Fraser River, for 10:00 Z, August 2, 1993

Figure 6.1 Comparison of the total measured current field (left) and the tidal field (right) showing that the mid-strait eddies are predominantly tidal in origin.

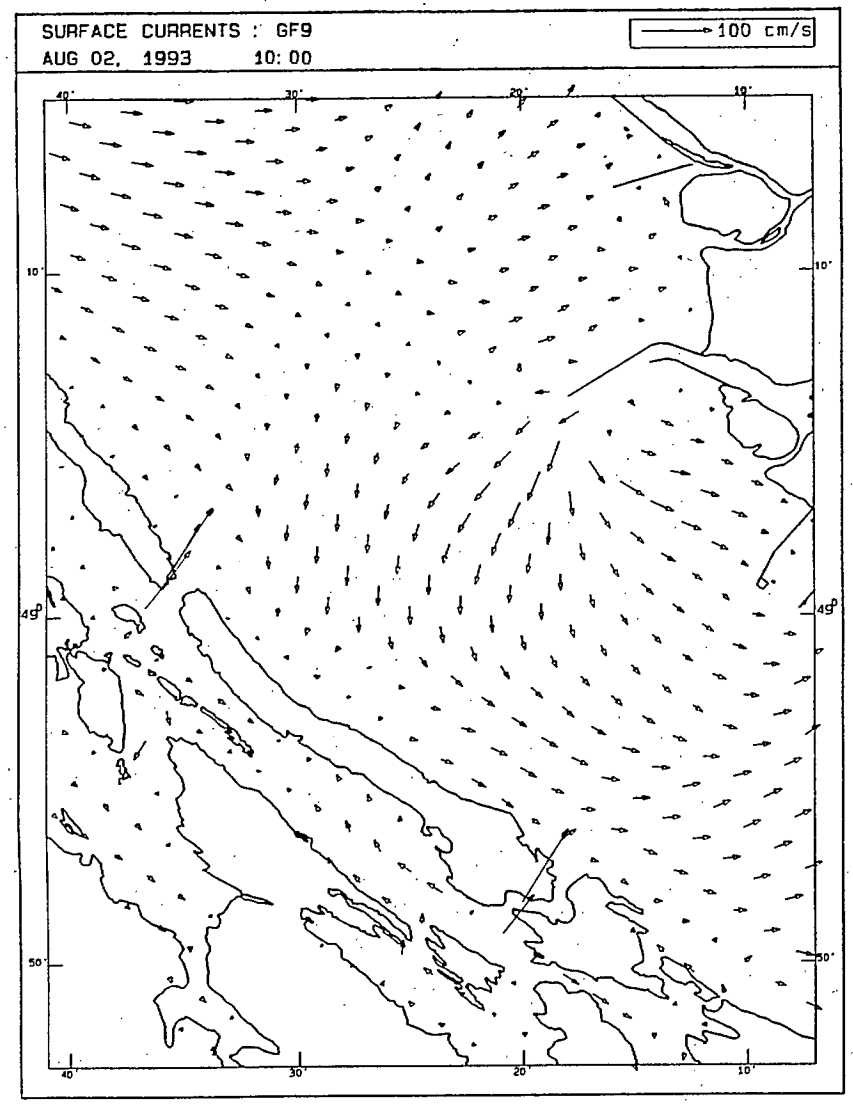

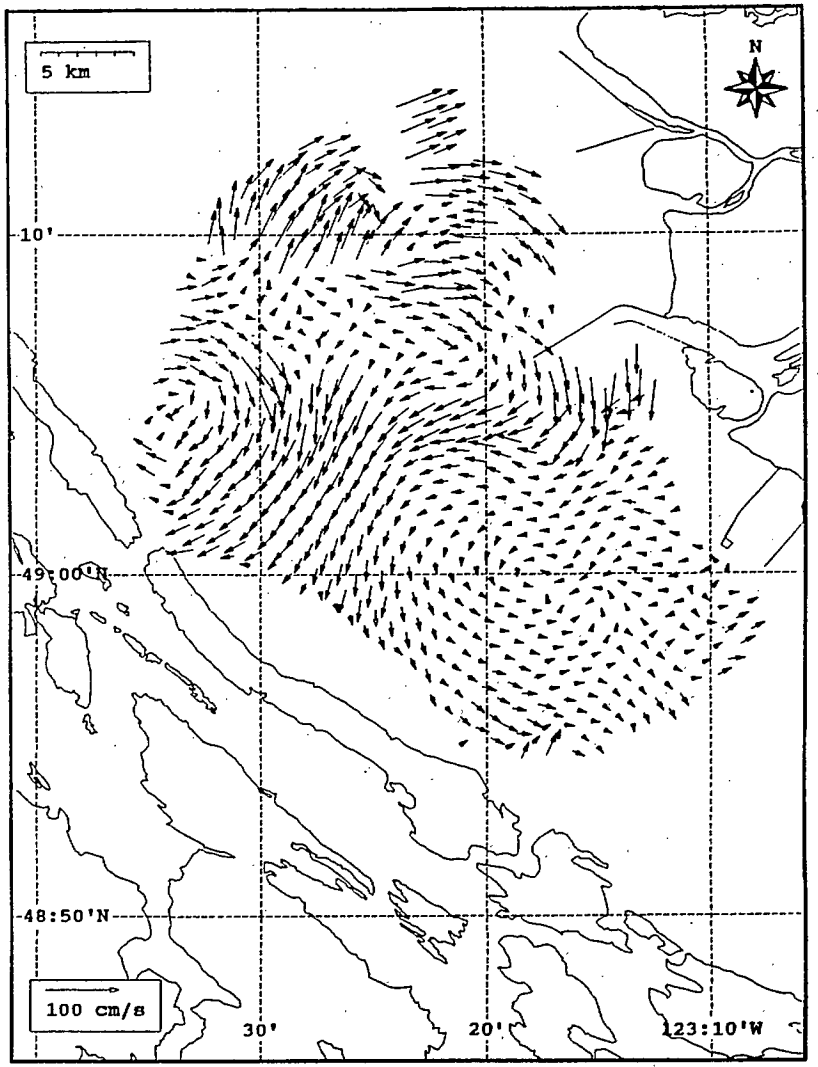

SeaSonde tidal current field from the Strait of Georgia, off the mouth of the Fraser River, for 10:00 Z, August 2, 1993

Figure 6.2 Comparison of modelled (left) and observed (right) flow fields.

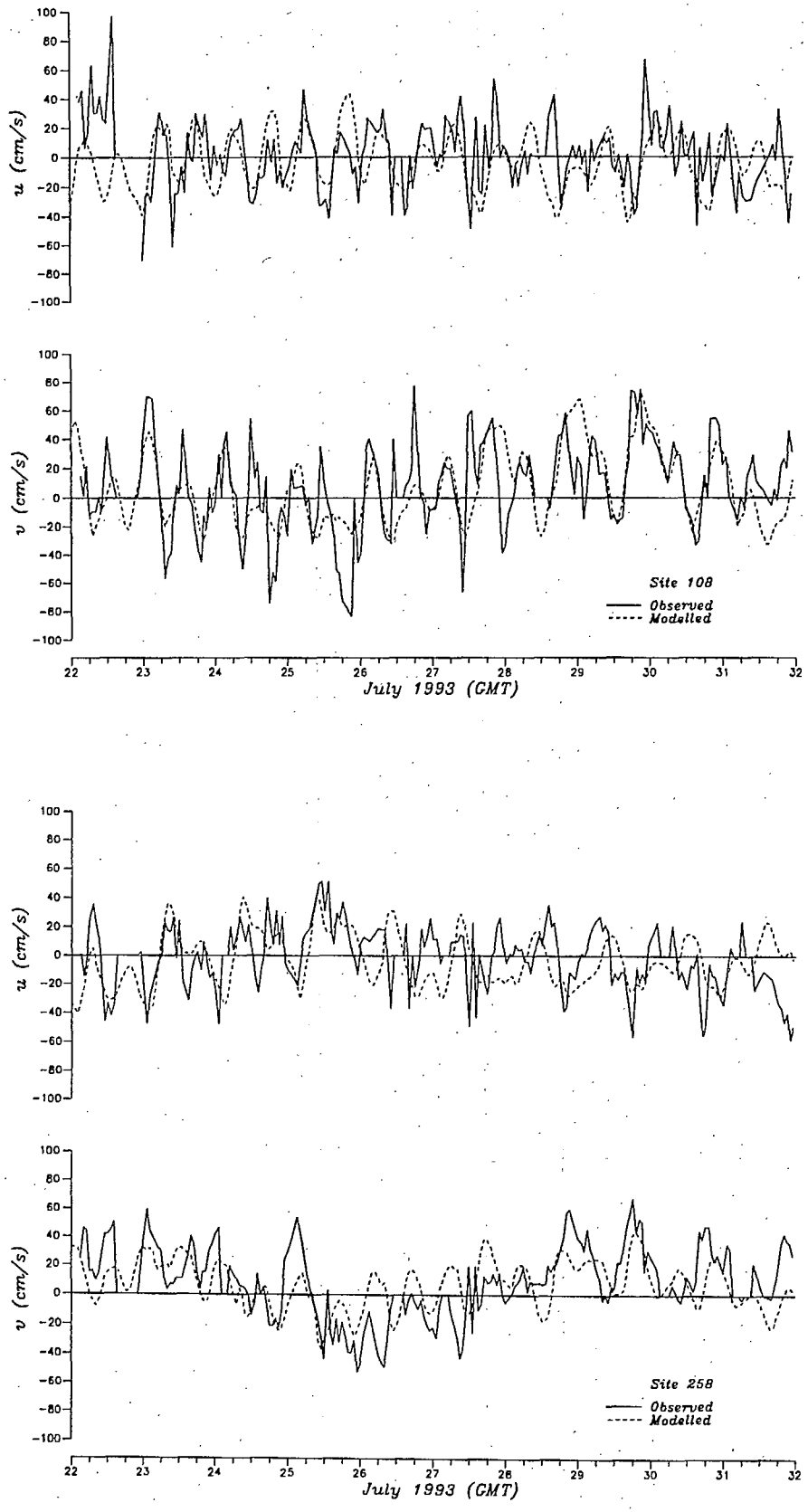

Figure 6.3 Comparison of modelled and observed current time-series at sites 108 and 258. Site locations are shown in Fig. 2.1.

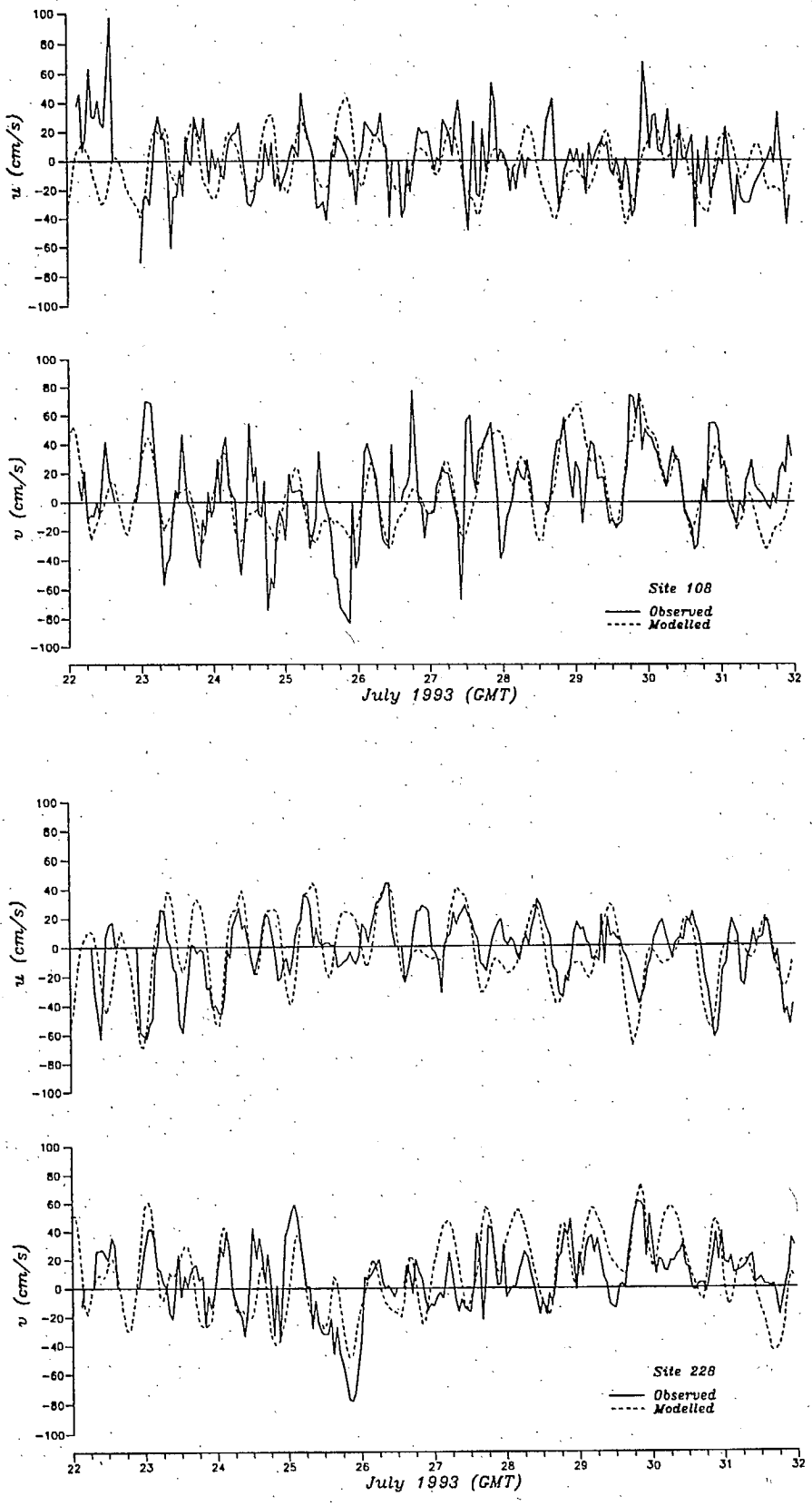

Figure 6.4 Comparison of modelled and observed current time-series at sites 108 and 228. Site locations are shown in Fig. 2.1.

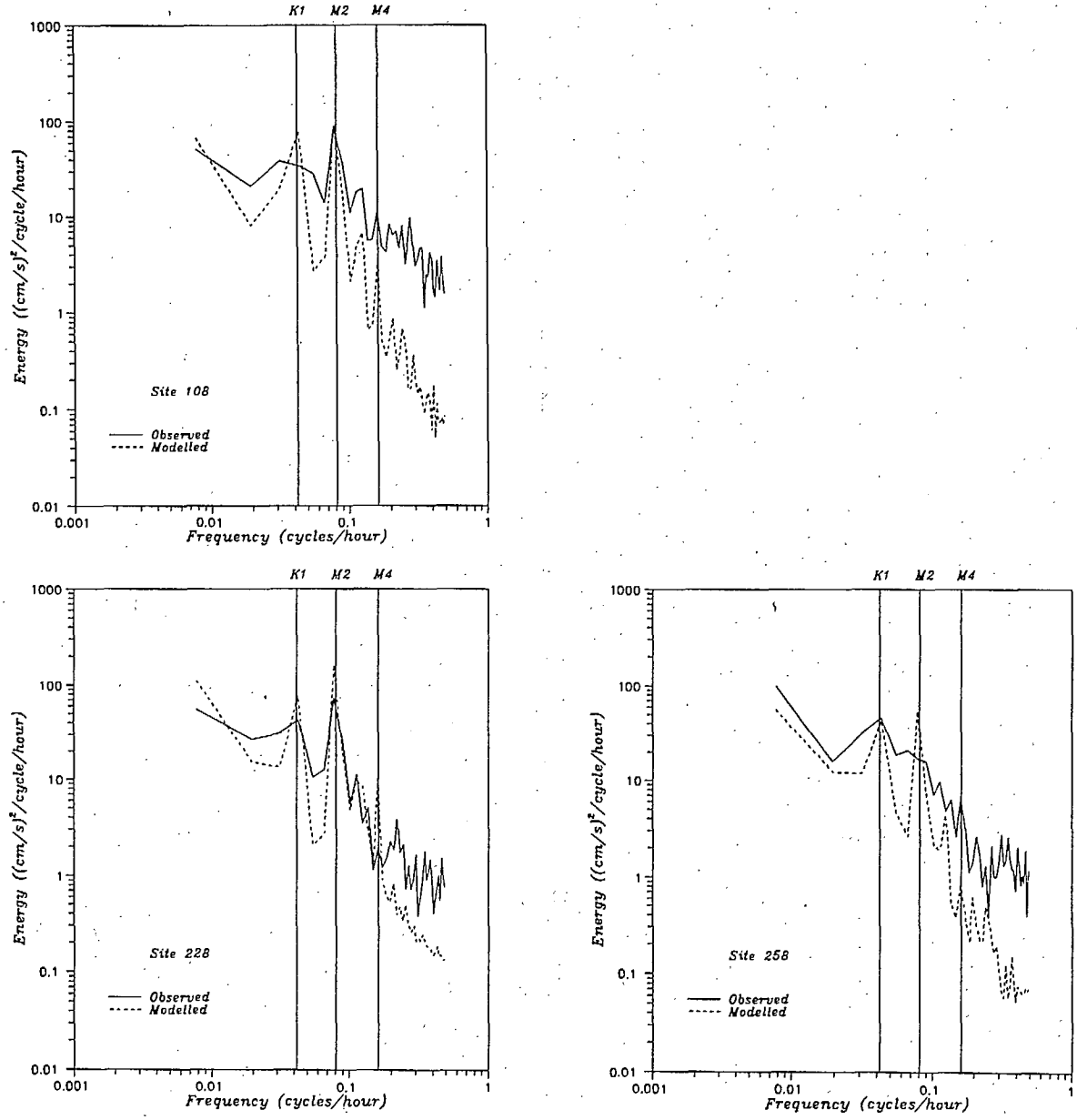

Figure 6.5 Comparison of modelled and observed current power spectra at three sites. Site locations are shown in Fig. 2.1.

7.0 INTERPRETATION OF SAR IMAGERY

7.1 Data Sources

On July 28, 1993, the ERS-1 satellite made a descending pass over the Strait of Georgia region at 19:10 Z, and acquired an image 100 by 100 kilometres in size, centered on the coverage area of the HF radar experiment. At the same time, the Convair 580 aircraft, operated by the Canada Centre for Remote Sensing, made three passes along the strait. The recording time during each pass was approximately twenty minutes. The two narrow swath images (width 16 km) were acquired starting at 20:27 Z and 20:56 Z, and the wide swath (61 km) was taken at 21:26 Z.

Tide conditions at the time of image acquisition are shown in Fig. 7.1. The weather was unsettled, with southeasterly winds and heavy overcast early in the morning. The cloud cover meant that AVHRR satellite images of the water surface temperature were not available. Winds at the time of the overflight were from the southeast, ranging from 6 m/s to 8.5 m/s at most wind stations in the area, and were somewhat lower at Saturna, approximately 15 km south of the Salamanca Point radar.

On August 11, after the conclusion of the HF radar project, one further SAR image was acquired during the ERS-1 ascending pass at 06:20 Z. The tide at this time was beginning to ebb. The heights of the tides immediately preceding and during this time were as follows: at 20:05 Z, high of 3.5 m; at 00:10 Z, low of 3.2 m; at 04:55 Z, high of 4.1 m; and at 13:45 Z, low of 1.6 m. Winds were variable over the image area and on the whole lighter than on July 28. The significant winds at the time of the overpass were from the northwest. No AVHRR data were available for August 11 as a result of an error at the receiving station.

7.2 Ocean Surface Phenomena Seen in SAR Images

In remote sensing studies of large-scale oceanic features, imagery at a range of electromagnetic wavelengths has been used. Optical and infrared bands can be severely affected by the presence of clouds in the target area. The radar employed by SAR sensors, however, is of sufficiently long wavelength that it is not affected by cloud cover. Although heavy rain can degrade SAR image quality, data may be obtained for a target region regardless of weather or time of day.

The configuration of SAR data acquisition is shown in Fig. 7.2. The radar scattering mechanism is a Bragg resonance process. Since there is no topography to complicate the measured backscatter, it is effectively the degree of sea surface roughness on the scale of the radar wavelength that is observed in the image. For a radar with wavelength λ and an angle of incidence θ, waves of length $D = n\lambda/2\sin\theta$ cause Bragg resonance, where n is an integer. Figure 7.3 illustrates the scattering process. The C-band radar employed in this experiment has a wavelength of 5.6 cm, and responds to capillary and short gravity waves of length about 7 to 14 cm for the ERS-1 images (θ=23°).

The key to the interpretation of SAR images of the ocean is to identify the oceanic and atmospheric processes affecting the nature and the roughness of the sea surface. Successful interpretations of ocean SAR images, linked to ground truth data obtained by ships and from moored instruments, have been made in the past. Two recent investigations of this type are

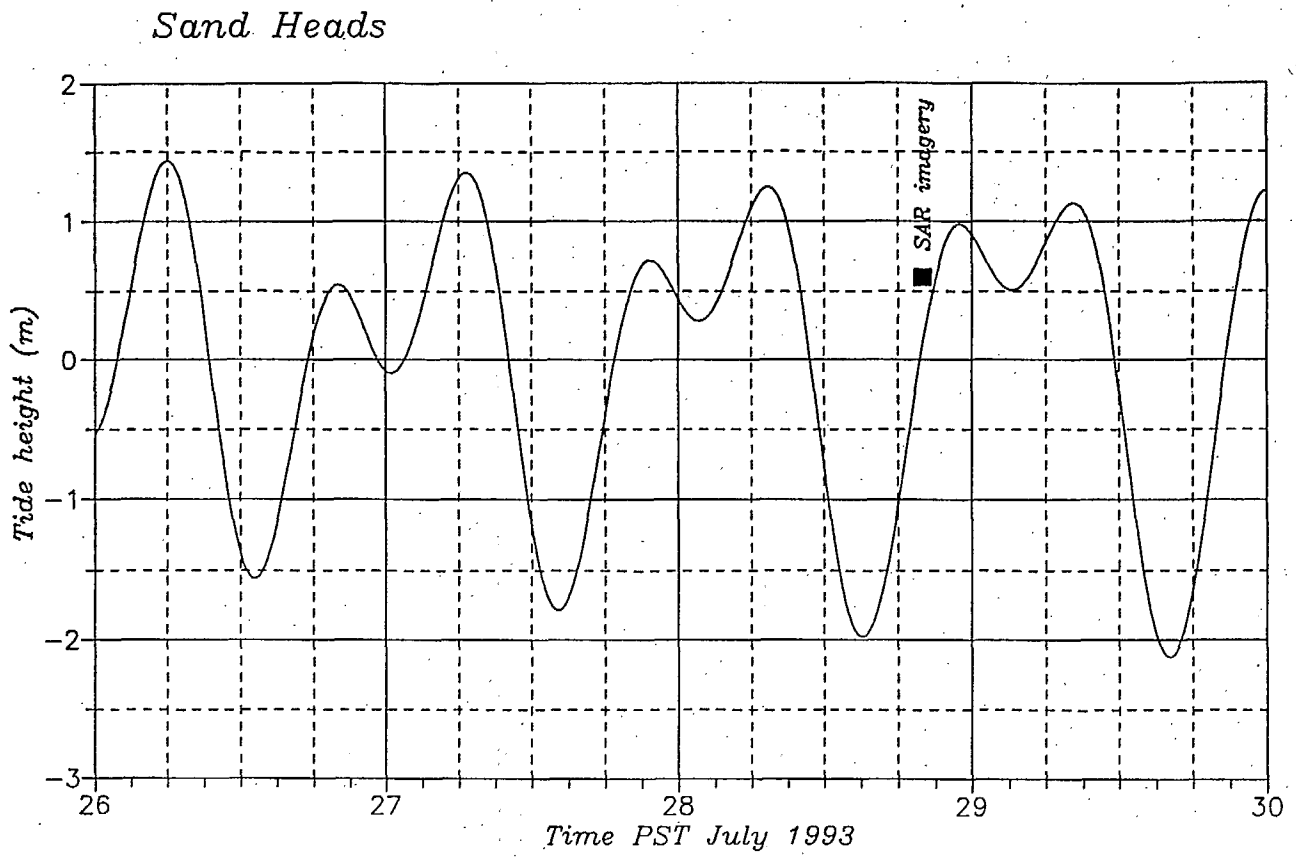

Figure 7.1 Tide conditions at the time of SAR imaging.

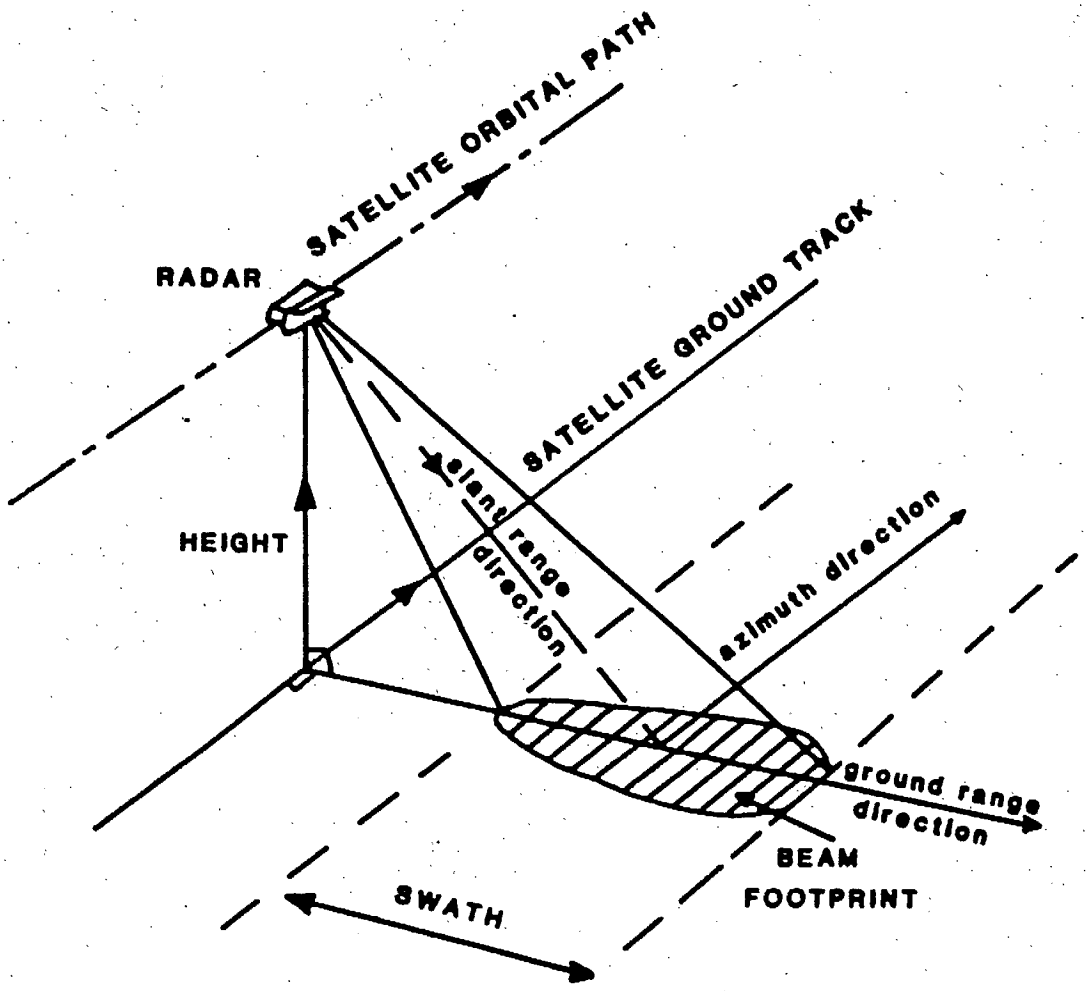

Figure 7.2 SAR configuration diagram.

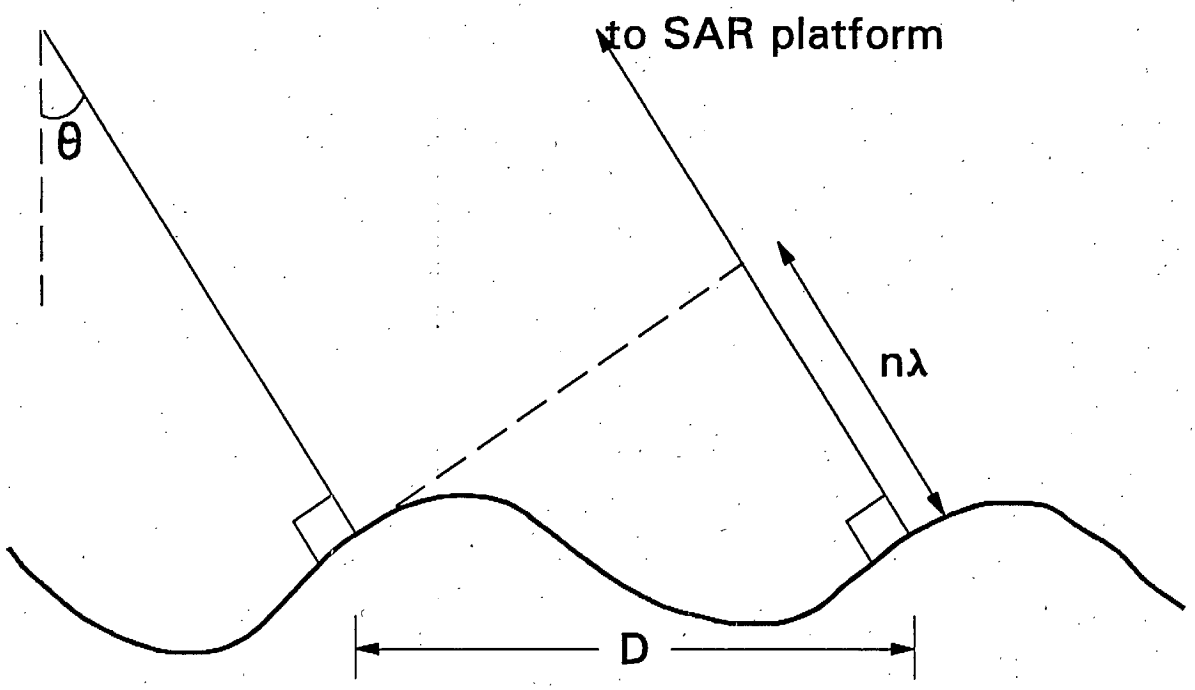

Figure 7.3 Bragg resonant scattering from capillary waves at the ocean surface.

reported by Vachon et al. (1992) for the west coast of Vancouver Island and by Johannessen et al. (1991), and others, for the shelf region off the coast of Norway. These groups observed features which they interpreted as wind speed tracers and wind fronts, ocean thermal fronts, internal waves, current shears, shelf break currents, atmospheric gravity waves, and interactions between currents, waves, and winds. The remainder of this section will review the major influences on SAR backscatter intensity which allow such features to be recognized in the imagery.

7.2.1 Wind and Wind Fronts

The capillary and short gravity waves observed by C-band radar are first formed as ripples on a flat ocean surface by pressure fluctuations in the wind field above the surface. Subsequent growth and development of the ripples is affected by wind, wave, and atmospheric boundary layer properties.

The time-scale over which wave energy density grows by a factor e, in the absence of dissipation, is approximately $3(c/u^*)^2$ wave periods (Vesecky and Stewart, 1982; Phillips, 1981). Here, c is the wave speed and u* is the frictional velocity, given by

$$u^* \approx C_D^{0.5} U_{10} \tag{7.1}$$

where C_D is the drag coefficient of order 10^{-3} (Phillips, 1977) and
U_{10} the wind velocity at altitude ten metres.

The frictional velocity may also be expressed as

$$u^* = (\tau/\rho_a)^{0.5} \tag{7.2}$$

where τ is the surface wind stress and
ρ_a the air density.

Clearly, the energy density grows faster for higher frictional velocity, corresponding to higher wind speed, as intuition would lead one to expect. Processes affecting the surface stress will also be expressed as a change in the energy growth time-scale and hence in the wave energy density. At radar scales, an increase in energy density is perceived as an increase in backscatter intensity.

As the wind speed increases, so does the ocean surface roughness at the radar wavelength scale, and a correlation between radar backscatter and wind speed is observed. One study by the Nansen Environmental and Remote Sensing Centre (NERSC, 1993) found such a relationship to exist over a wind speed range of 4 to 21 m/s. The backscatter value σ_o is linked also to the angle, α, between wind direction and radar look direction, since the greatest degree of backscatter is observed from Bragg waves propagating in the range direction (where $\alpha=0$). The dependence of backscatter level on α and on wind speed U_{10} is described by the model of Jones et al. (1981) for normalized radar cross section. Vesecky and Stewart (1982) review the model and give its form as

$$\sigma_o = K_w U_{10}^m (1 + a \cos\alpha) \tag{7.3}$$

where K_w, m, and a are parameters that are estimated empirically from the data. Deduction of wind speed from radar backscatter intensity is thus an involved process, complicated not only by uncertainty in the wind direction, but by such factors as the air-sea temperature difference and the presence of surface films, which affect the shape and energy of the Bragg-resonant waves.

In the presence of an atmospheric front, changes occur in wind speed and direction. Such a change is easily visible in SAR imagery as a step-like increase in radar backscatter corresponding to the roughening of the ocean surface. Johannessen et al. (1991) claim that the wind speed change across a front can be determined under certain conditions: (1) that the wind direction on one side of the front is known, from the presence of streaks in the image or from the wave spectra and (2) that the wind components normal to the front are equal on both sides, with no turbulence or mixing at the boundary.

7.2.2 Ocean Fronts

An ocean temperature front is also visible as a step-like change in backscatter level. The increased water temperature causes unstable stratification in the atmospheric boundary. This unstable layer has the effect of increasing the surface stress and the frictional velocity u*, and thus the energy density in the waves. Warm water rings associated with the Gulf Stream have been observed and tracked in SAR images in this way (Lichy et al., 1981), and the Gulf Stream itself is often seen to have a SAR backscatter signature brighter than that of the cooler surrounding water (Vesecky and Stewart, 1982).

7.2.3 Waves

Large-scale gravity waves, and particularly swell, may be imaged as a result of their effect on the capillary waves. The most significant modulations of the radar backscatter by gravity waves are categorized as electromagnetic or hydrodynamic.

The slope of the surface gravity waves changes the orientation of the superimposed Bragg-scattering waves with respect to the radar, controlling the fraction of the radar energy which is actually scattered back toward the receiver. This electromagnetic (or tilt) modulation results in higher levels of backscatter from waves travelling in the range direction than from those in the azimuth direction. The level of backscatter is also affected to some degree by the angle of incidence of the radar, since that and the angle of the wave slope determine the wavelength of the Bragg-resonant ripples observed.

A true modification in the surface roughness, known as hydrodynamic modulation, is induced by the interaction of the short waves with long waves or swell. The fluid orbital velocity during the passage of a swell wave creates convergent velocity patterns at the leading edge of the wave, and the interaction of the small-scale current with the short waves results in an increase in short wave amplitude near the swell crest. Similarly the amplitude is reduced in the swell trough region, corresponding to a region of low backscatter. The windward face of the swell also receives a further contribution to the energy in the short waves from the wind.

A less significant modulation in the backscatter than either electromagnetic or hydrodynamic modulation is caused by "velocity bunching," seen only in azimuth-travelling trains of gravity waves. It is observed, for example, in the displacement of ship images from their wakes

where the motion of the scattering target in the range direction causes a shift of its image in azimuth. The vertical motion of the surface in the presence of large gravity waves has a significant component in the range direction, particularly for a radar look direction that is near the vertical. When waves propagating in the azimuth direction are imaged by the SAR, the image of the scattering surface at the position of the rising edge of the wave is displaced in one direction, and the image of the falling edge is displaced in the other; hence, if the azimuth shift is of optimum size, the backscatter is concentrated periodically and a clear image of the wave train is formed. Capillary-scale roughness will enhance such imaging, while it will be weakened or distorted by smaller or larger azimuth shifts than the optimal.

7.2.4 Internal Waves

The effect of internal waves is seen clearly, and is one of most easily recognized features. The current field at the surface is strongly affected by the internal waves, and the resulting convergent and divergent zones are marked by obvious changes in the surface conditions. If a natural slick is present at the surface, it will tend to accumulate at the convergent zones and dampen out the small-scale waves. In the absence of such surfactants, the opposing surface currents at the convergent zones will interact to increase the energy and amplitude of the capillary and short gravity waves, enhancing the surface roughness.

7.2.5 Wave-Current Interaction

A train of gravity waves encountering a current is refracted. Liu et al. (1989) modelled the refraction across a meandering current front, and found that regions of enhanced and diminished energy were created. These regions would be made visible in SAR images through tilt modulation of the refracted waves. An inversion technique was applied to SAR images from the Shuttle Imaging Radar (SIR-B) by Barnett et al. (1989), who found that realistic surface current fields could be obtained if the geometry of swell and current were favourable.

Phillips' (1981) discussion of the interaction between waves and currents was reviewed by Vesecky and Stewart (1982) who reached the following conclusions. In the case of a resonant wave train travelling with a velocity component in the current direction, the wavelength increases, the energy density decreases, and the wave paths turn away from the current. For wave trains with a velocity component opposite to the current, the wavelength decreases, the energy in the waves increases, and the waves tend to turn in toward the current.

A shearing current will also refract a wave train. Waves meeting an adverse shearing current turn normal to the current direction and decrease in energy density. On the other hand, waves with a component of their velocity in the direction of the current increase in wavelength and in wave velocity. As the wave train moves into the current, it turns into the current direction and the energy density increases, reaching a peak at the point of maximum penetration before the train turns back out of the current. This maximum energy density could be linked to the bright filaments seen in regions of current shear by Johannessen et al. (1991) and earlier by Vesecky and Stewart (1982), and others, along the edges of the Gulf Stream.

A region of current shear may also be marked by the accumulation of natural slicks at the shear. The slick, if present, damps out small waves and reduces the SAR backscatter (NERSC, 1993).

7.2.6 Wind-Current Interaction

Johannessen et al. (1991) discuss the effect of interaction between wind and current on the radar backscatter level as it relates to a current jet perceived in their data. They suggest that a change in atmospheric boundary layer stress may be induced by a change in the wind vector velocity $\mathbf{u}_w$ with respect to the current $\mathbf{u}_c$ (or vice versa). If the backscatter due to all effects except wind and current is σ^*, then the estimate of the total backscatter is

$$\sigma = \sigma^*(|\mathbf{u}_w - \mathbf{u}_c|)^{1.5} \qquad (7.4)$$

Their observations under moderate wind conditions support this form of the relation. If the wind and the current have a component opposing one another, the vector difference in the above equation is large and backscatter is increased.

7.2.7 Surface Slicks

The dark filamentary structures observed in SAR images are often related to the presence of surface slicks, which may be of biological origin, or from an oil spill or natural petroleum leak (see, for example, Bern et al., 1992; 1993). Both organic films and petroleum or pollutant layers have a dramatic effect on the small-scale waves, causing them to be damped much more rapidly than in plain seawater. The decreased surface roughness is translated into a region of low backscatter in the SAR images. Slicks can be seen in winds up to about 6 m/s (Scott, 1986; Bern et al., 1992 or 1993). Their SAR signature under higher wind conditions is degraded by a combination of wave breaking and dispersion of the slick material, and depends on the properties of the particular surfactant present.

The organic slicks are thought to be formed in general by convection in turbulent areas, by which means biological material is brought to the surface. The slicks thus track both larger-scale turbulent motions, and surface currents. The images of ship wakes obtained by Ochadlick et al. (1992), for example, show the effects of currents as traced by ship wakes in an offshore region containing large filamentary slicks. The data were acquired in a time-series form, allowing calculation of the speed with which the currents adjacent to a slick displaced the surface wake. The results led Ochadlick and collaborators to propose that the production mechanism for both the slicks themselves and the current shear distorting the wakes was a surface convergence occurring normal to the current.

Flat water in a SAR image may not always indicate the presence of a slick: calm water without a surface film, or smooth water in an upwelling zone, can also produce regions of low backscatter.

7.2.8 Non-surface Phenomena

The ocean surface can carry the physical signatures of processes occurring at locations remote from the atmospheric boundary layer. Thomson et al. (1992) observed periodic backscatter variations off the west coast of Vancouver Island with wavelengths from 1.3 to 2.3 km and propagation speeds on the order of 5 m/s. They interpret these features as resulting from short atmospheric gravity waves formed in a region of temperature inversion, at an altitude of about a kilometre. The perturbations in wind and pressure at the inversion are transmitted rapidly

downward to the ocean surface where they act on the friction velocity and thus on the energy of the capillary wave field.

In addition, it is well known that shallowing underwater topography can increase the energy in the wave field, causing radar backscatter levels to rise in the vicinity of banks and shoals.

7.3 Filtering SAR Images

While the average backscatter in a region of a SAR image represents the true radar reflectivity of the target, the backscatter on a pixel-to-pixel level is contaminated by speckle noise, which arises as a result of the coherent processing of the radar signals (Lee, 1983). Processing the data to multiple looks, which is like averaging a number of simultaneously acquired images, reduces the random backscatter variations and speckle noise to some extent, but further improvement of the image quality is achieved by applying filters to the image. Speckle has the characteristics of a multiplicative random noise, and this fact has been used to design filters to reduce its appearance in SAR images.

7.3.1 Filters for Speckle Reduction

The simplest, and most common, speckle-smoothing filter is the averaging or box filter. The new value of each pixel in the image is computed by taking an average of the pixel values in the surrounding region, and additional smoothing is achieved by applying the filter repeatedly. The advantage of the box filter is that it is computationally simple and time-efficient. It is effective at smoothing random noise in areas where the underlying backscatter signal is relatively smooth. However, fine details in the image are degraded by the averaging process. Contrast edges are softened and blurred, and subtle ones may disappear under successive applications of the filter.

In a median filter the central pixel value is replaced by the median of the pixels in a local window. This filter is best applied using a small window, to reduce blurring of the image. Frost et al. (1982) found that, after several applications, the median-filtered image was less blurry than one filtered using a 3×3 or 5×5 box, but the sharp targets in the median-filtered image were more severely degraded.

Lee (1983) proposed the sigma filter as yet another computationally-efficient means of reducing speckle. A number of windows containing relatively flat data are selected throughout the image, and the mean and variance of the pixel values are computed for each window. A standard deviation for the image is then defined as the average root variance over the average window mean pixel value. The new value of each pixel in the image is computed to be the mean of all those pixel values in a local window which lie within two standard deviations of the original central value. Provision may be made for dealing with spikes which have no surrounding pixel values within 2σ. Lee found that this filter was more effective at reducing speckle and preserving fine features than either the box or the median filter. (In 1981, Lee also proposed an entirely different adaptive filter for which a brief description follows. References to the Lee filter in the SAR literature usually refer to this adaptive filter, rather than to the sigma filter.)

Sometimes it is desirable to emphasize sharp details in an image; this may be accomplished by applying a filter with a sharp profile, such as a Gaussian. However, since the purpose of such

a filter is to enhance spiky features, the speckle in a SAR image is amplified rather than smoothed. Such a filter is damaging to a region with a relatively homogeneous or smoothly varying signature underlying the speckle.

Adaptive filtering is used to deal with such problems. The operation involves computing a new filter to calculate the modified value of each pixel in the image. The shape of the filter is determined by the local pixel statistics calculated in a region centred on the pixel being filtered. If there is high variability, then the area is assumed to contain some underlying structure which should be preserved, and a relatively sharp filter is applied. On the other hand, if the variability is low, the underlying image is thought to be fairly homogeneous, and more averaging is applied. The process of computing and applying a separate filter for each pixel involves heavier consumption of processing time than simple averaging or fixed-template filtering.

The adaptive filter proposed by Frost et al. (1982) uses an MMSE (minimum mean square error) filter to estimate the true radar reflectivity R(t) at a position t=(x,y) in the image, under a simple model for the recorded image I(t) of the form

$$I(t) = [R(t)\cdot u(t)]_{*}h(t) \qquad (7.5)$$

where u(t) is multiplicative noise, usually taken to have a chi-squared probability distribution,
h(t) is the system impulse response, and
* represents convolution.

The impulse response of the filter constructed for the pixel at t_o therefore has the form

$$m(t) = K_1 \exp[\, -KC_A^2(t_o)|t|\,] \qquad (7.6)$$

where K_1 is a normalizing constant,
K specifies the sharpness of the filter (generally in the range 1 to 10), and
$C_A(t_o) = \sigma_A / \langle A \rangle$ is the ratio of the standard deviation to the mean pixel value in the local window centred on t_o. The parameter $C_A(t_o)$ is referred to as the local coefficient of variation.

For the multiplicative speckle noise present in SAR images, both the Lee (1981) and the Kuan et al. (1985) adaptive filters perform in a similar way. The general form of the Kuan filter is based on an assumption of additive noise, and generalized to deal with multiplicative radar noise. Lee's treatment of the additive noise is slightly different, but both filters act as a weighted sum of the mean, $\langle I(t_o) \rangle$, and observed pixel values, $I(t_o)$, where the weighting function is specified by the value of $C_A(t_o)$ computed locally. Quantitatively, the filtered value of the pixel at t_o is

$$R(t_o) = I(t_o)\cdot W(t_o) + \langle I(t_o) \rangle \cdot (1-W(t_o)) \qquad (7.7)$$

where the Lee filter uses the weighting function

$$W(t_o) = 1-C_u^2/C_A^2(t_o) \qquad (7.8)$$

and the Kuan filter employs

$$W(t_o) = W_{Lee}(t_o)/(1+C_u^2) \qquad (7.9)$$

In these equations, C_u represents the coefficient of variation of the speckle noise, calculated as the ratio of the standard deviation to the mean pixel value in a region known to be very homogeneous.

Lopes et al. (1990) proposed alterations to improve the performance of the Frost, Lee, and Kuan filters. They remarked that, of the unmodified filters, the Frost (with K=10) smooths speckle better than either the Lee or the Kuan, particularly in homogeneous areas. Still better smoothing is obtained using a Frost (with K=1) or a box filter, but these blur fine details. The modifications proposed for the three adaptive filters all take the form of specifying the action of the filters in three separate classes of heterogeneity, distinguished by the value of the local coefficient of variation $C_A(t_o)$. For $C_A(t_o)$ less than C_u, the coefficient of variation of the speckle noise, an averaging filter is applied. If $C_A(t_o)$ is greater than some specified C_{max}, as is true of point targets, then the value of the pixel is retained and no averaging is applied. For $C_A(t_o)$ between C_u and C_{max}, the more heterogeneous the area and the higher the value of $C_A(t_o)$, the less smoothing is applied.

The conclusion of Lopes et al. is that all three modified filters are superior to the unmodified versions in enhancing sharpness of edges and linear features while smoothing well in homogeneous areas. They noted that in 5×5-pixel windows, the effectiveness of the new versions of the Lee and Frost filters is equivalent, although the former is much quicker; however, for larger windows, they found the modified Frost filter more efficient.

A significantly different approach to speckle reduction was taken by the group at Nansen (NERSC, 1993), who chose to employ the geometric smoothing technique proposed by Crimmins (1985). The Crimmins filter operates on each row, column, and diagonal line across the image in turn, and the action of the filter may be thought of as follows. If the image were projected into the three dimensions x, y, and pixel value, where all the units below or on the image surface had value 1 and those above had value 0, it would be possible to produce a binary image by taking a slice along a row of the image, for example. The interface between the 1s and the 0s in this binary image is compared with a set of geometric forms or hulls, shown in Fig. 7.4(a). If the pattern surrounding a pixel is found to match one of the geometric hulls, the value of the central pixel is changed. The complement of the binary image slice is then taken, and the same procedure applied.

The effect of the filtering, demonstrated in Fig. 7.4(b), is to reduce the sharpness of curvature of features at the 1-0 interface, by respectively filling in and breaking down narrow valleys and towers. Crimmins (1985) asserts that the geometric filter is particularly suited to the nature of speckle in SAR images. Wider features are left undisturbed except for some reduction in sharpness at the edges. The Nansen group's objective was to smooth a SAR ocean image enough that application of an edge-detecting filter would allow an automated procedure to detect and classify strong contrast features. As such, they were not concerned about the loss of subtle or fine-scale features under the geometrical filtering, since strong features are unlikely to be degraded by this process.

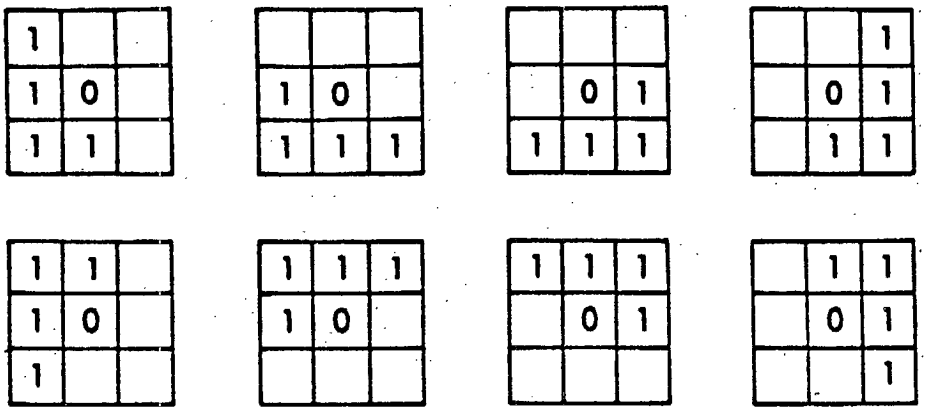

(a) binary hulls

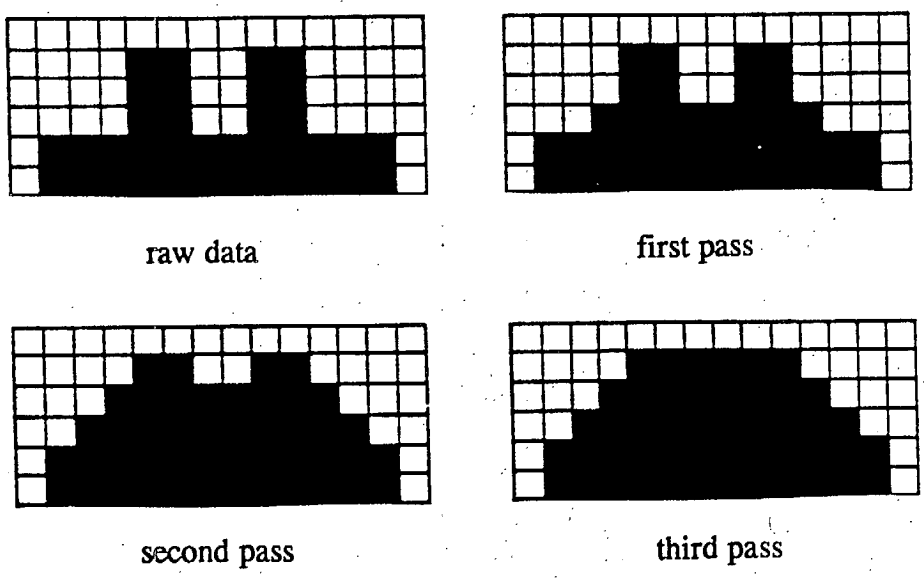

(b)

Figure 7.4 (a) Eight geometric hulls with which pixels are compared in a Crimmins filter. (b) Schematic example of three applications of a Crimmins filter to a binary image.

7.3.2 Image Processing for the Present Study

In order to examine the correspondence between HF radar current maps and contrast features in SAR imagery, fixed filters were applied for speckle reduction over the water surface. Box filters of size from 3×3 to 9×9 pixels were tested under several applications. These filters, as expected, were effective at smoothing speckle, but degraded fine structure seen in the unsmoothed image. The larger averaging filter lost fine resolution in the image particularly quickly.

Figure 7.5 is a 512×512-pixel section extracted from the ERS-1 image of August 11, 1993, shown prior to filtering. The pixel size is 12.5 m. This scene contains a relatively homogeneous region, a dark filamentary slick running from top to bottom through the centre of the image, and a set of fine-scale linear features which may be internal waves. In Fig. 7.6, the effect of applying averaging filters twice in succession is illustrated. The box filters used were of size 5×5 and 9×9 pixels. The larger filter reduces speckle successfully in homogeneous areas, but causes some fine structure seen in the unsmoothed image to be averaged beyond recognition.

A compromise was reached between fixed-average and adaptive filters by computing a single fixed Frost filter which was applied to the whole image. The filter profile was calculated based on the average pixel statistics of regions chosen throughout the observed ocean surface, in the same way that a local Frost filter profile would be constructed for a single pixel based on the statistics of the surrounding values.

The sharpness of the Frost filter is controlled by the value of C_A, the ratio of standard deviation to mean pixel value, and also by the size of the parameter K. The ocean surface level in our images is relatively homogeneous over a large scale, so the average sigma-to-mean ratio was found to have a value of about 0.25. For this value, choosing K=1 produced a slightly tapered filter and K=10 gave a sharper filter. Both filters, computed on a 5×5-pixel template, were applied to a subsection of the image containing a smooth speckled area and some fine-scale features. The results are presented for two and four applications of the K=10 filter (Fig. 7.7) and of the K=1 filter (Fig. 7.8).

The difference between the resulting images only becomes apparent after two or more applications of the filter; although it is subtle, the less tapered version of the filter reduces the effects of the speckle better, while both preserve the fine details equally well. Based on these observations, the images were smoothed with a K=1 non-adaptive Frost filter.

Following smoothing, several edge-detecting filters were tested, including Laplacian and directional Sobel and Prewitt filters. These filters did not effectively enhance the subtle contrast features we sought in the image, as they amplified the remaining speckle noise to a high degree. Edge detectors have been successfully used to locate frontal features of strong contrast in a geometrically-smoothed ocean image (NERSC, 1993), but the degree of smoothing required would significantly degrade features of interest in our images.

The filtered image of the experimental region is presented in Fig. 7.9. This subsection of the full-scene ERS-1 image is approximately 51 km on a side, and has been filtered four times with a 5×5-pixel tapered filter based on the Frost filter with K=1.

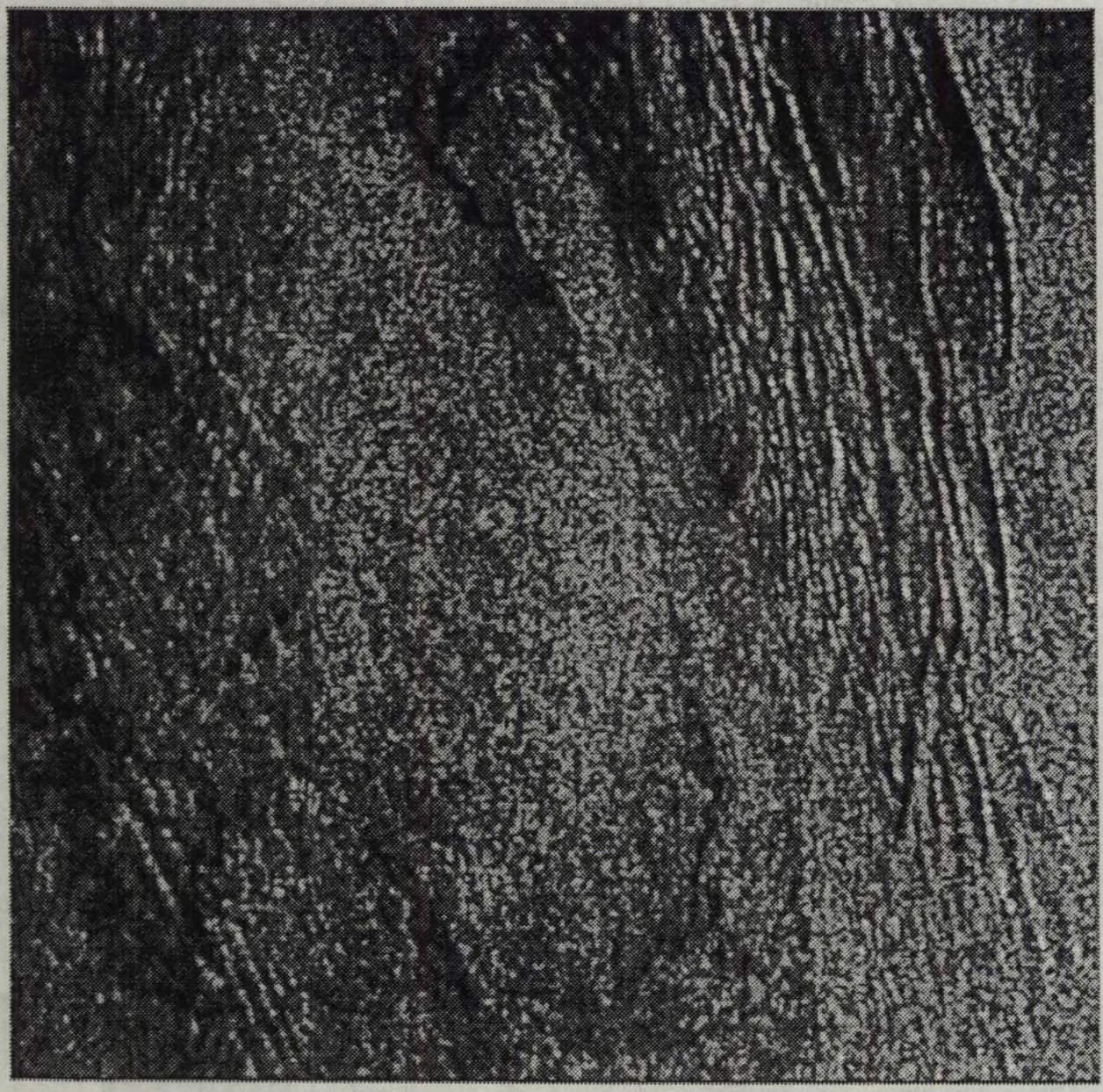

Figure 7.5 A 512×512 pixel subscene of the ERS-1 SAR image on August 11, 1993.

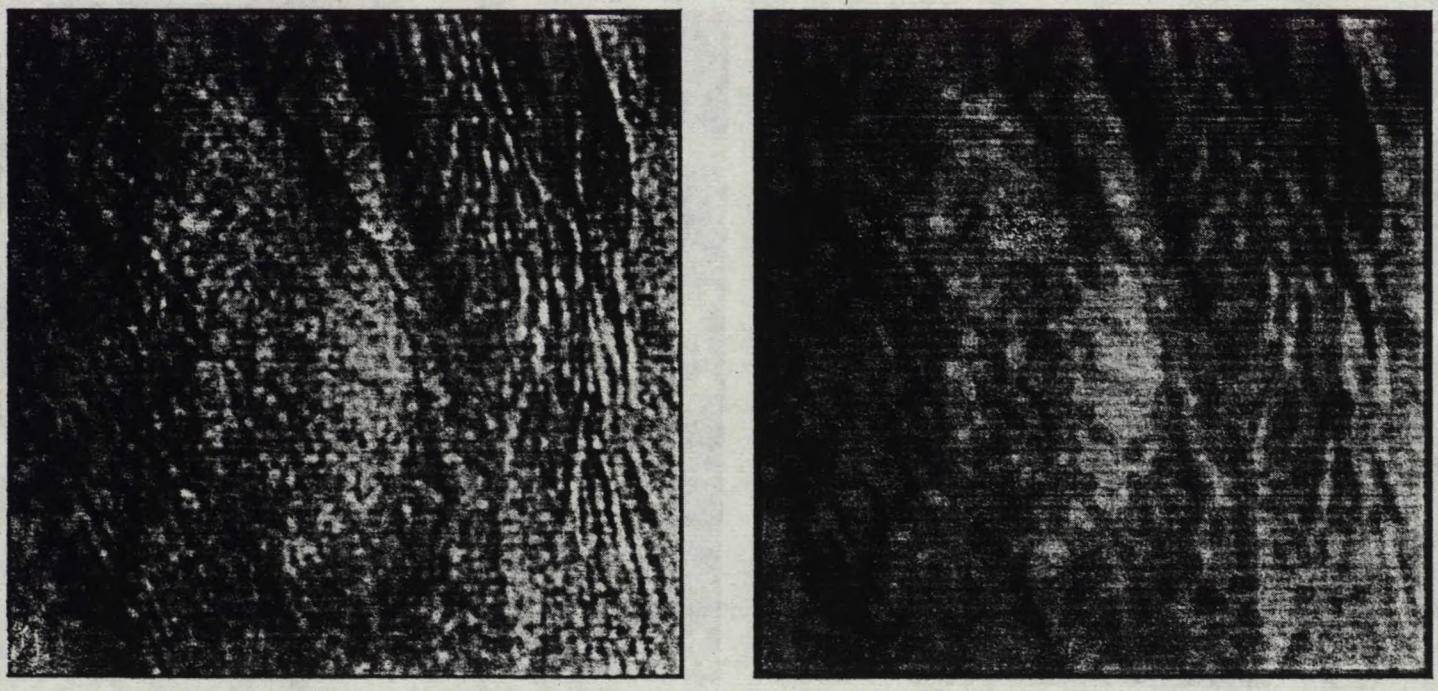

Figure 7.6 The image of Fig. 7.5 smoothed by straight-averaging filters. The left-hand image has been smoothed twice by a 5×5 box filter. The right-hand image has been smoothed by two passes of a 9×9 box filter.

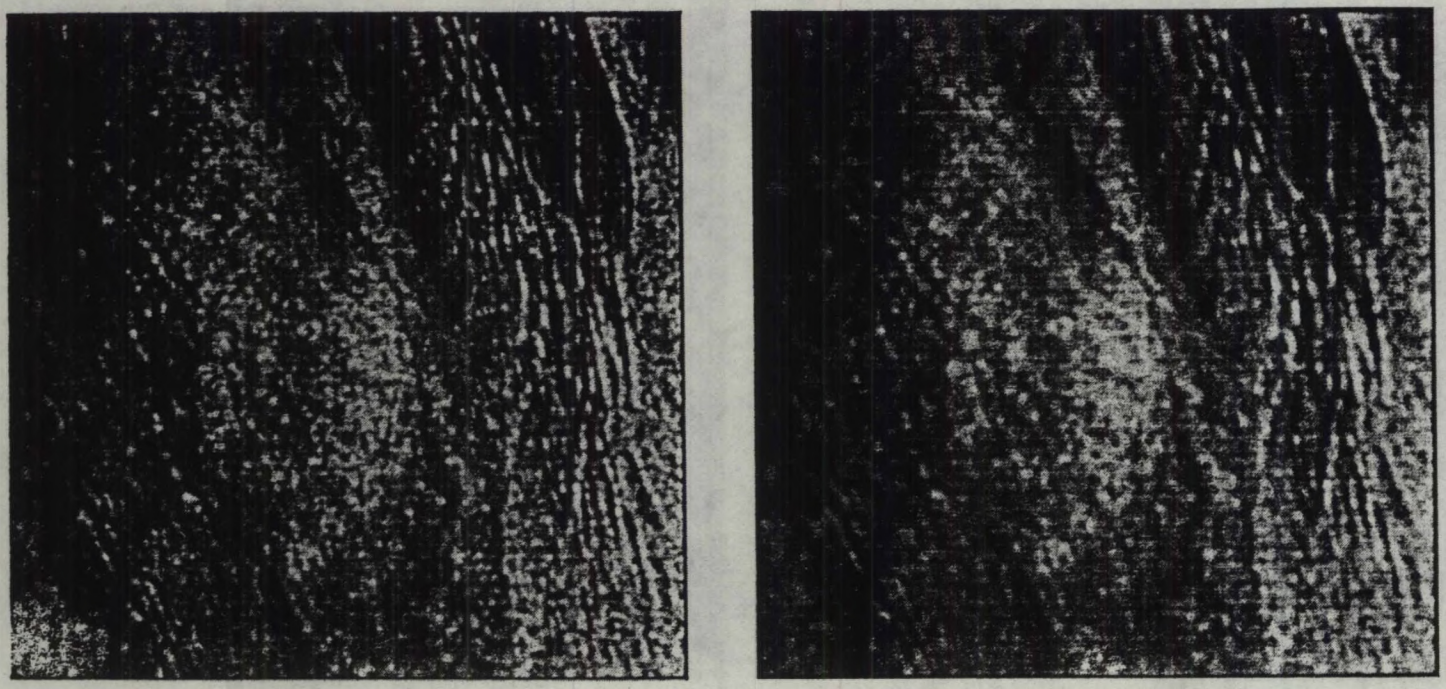

Figure 7.7 The image of Fig. 7.5 smoothed by a non-adaptive filter (similar to the Frost filter) with K=10. The left-hand image has been filtered twice, and the right-hand image has been filtered four times.

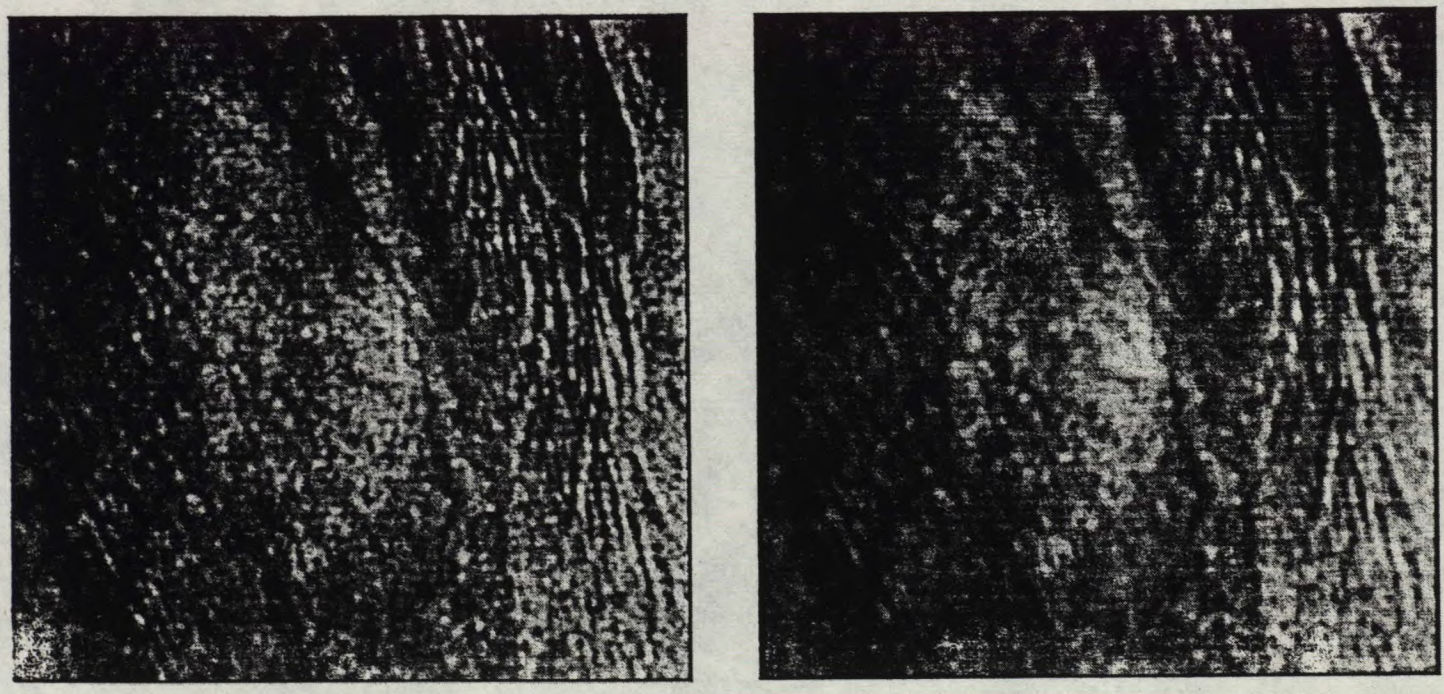

Figure 7.8 The image of Fig. 7.5 smoothed by a non-adaptive filter (similar to the Frost filter) with K=1. The left-hand image has been filtered twice, and the right-hand image has been filtered four times.

Figure 7.9 ERS-1 SAR image of the central Strait of Georgia (July 28, 1993, at 19:10 Z).

7.3.3 Low-Resolution Images

A full scene ERS-1 image has 8000 pixels on a side. For sixteen-bit data, the file size of the image is approximately 130 megabytes. The present study of the surface contrast features did not require full data value precision, nor did it require the full scene; however, the reduced file size was still substantial. We therefore investigated the degree to which the resolution of the image could be reduced without loss of features of interest.

Low-resolution images, or LRIs, were produced by running an averaging filter over the image and then subsampling by row and column. This has the same effect as replacing a group of pixels by a single pixel with the average value of the group. The advantage of LRIs is that they can be quickly transferred over a communications channel. Bern et al. (1992) noted that LRIs produced from ERS-1 images have sufficient spatial resolution to allow successful delineation of oil slicks. The compact size of the LRI files permits rapid distribution to users and therefore a faster response under spill emergency conditions.

Our interest in the quality of LRIs produced from the ERS-1 images has to do with the scale on which features relevant to this study can be seen in the imagery. The original pixels in an ERS-1 image have size 12.5 m. If an increase in the size of the pixels does not affect the visibility of any contrast features associated with surface currents, then it is advantageous, from a data transfer, storage, and processing point of view, to deal with an LRI in this type of study.

Figure 7.10 presents a comparison of four LRIs made from a 510×570-pixel section of the original smoothed ERS-1 image. Each pixel represents the average of a box of original pixels. From top left to bottom right, these boxes have sizes 3×3, 5×5, 7×7, and 9×9. Inspection of an image with resolution reduced by a factor of 3 in both rows and columns reveals little difference from the original image in terms of the contrast features of interest here. Even a 5×5 LRI is acceptable for the study of features at the scale of the internal waves pictured in this subscene. However, with further decreases in resolution, the loss of accuracy in the shape and distinction of the features visible becomes more pronounced.

7.4 Discussion of the SAR Images

7.4.1 The July 28 ERS-1 Image

The ERS-1 SAR image of July 28, 1993, (Fig. 7.9) is dominated by regions of nearly uniform backscatter, which can be attributed to the action of wind on the capillary wave field. A number of striking contrasts in backscatter level are present, but on the whole little information regarding the surface current field can be extracted from the image. Based on knowledge of the physical processes occurring in the strait, and on comparison with published interpretations of SAR ocean data, several mechanisms are discussed in relation to observed signatures in the image. Place names are shown on the map in Fig 2.1.

The most distinct class of features is certainly associated with several sets of internal waves. Off Roberts Bank, a southwesterly-propagating wave train with separation between backscatter maxima of about 200 to 300 m is superimposed over a strongly curved (radius of curvature about 5 km) northwest-propagating train with peak separations ranging from 250 to 800 m. The region of intersection of these two wave trains extends over half the width of the strait.

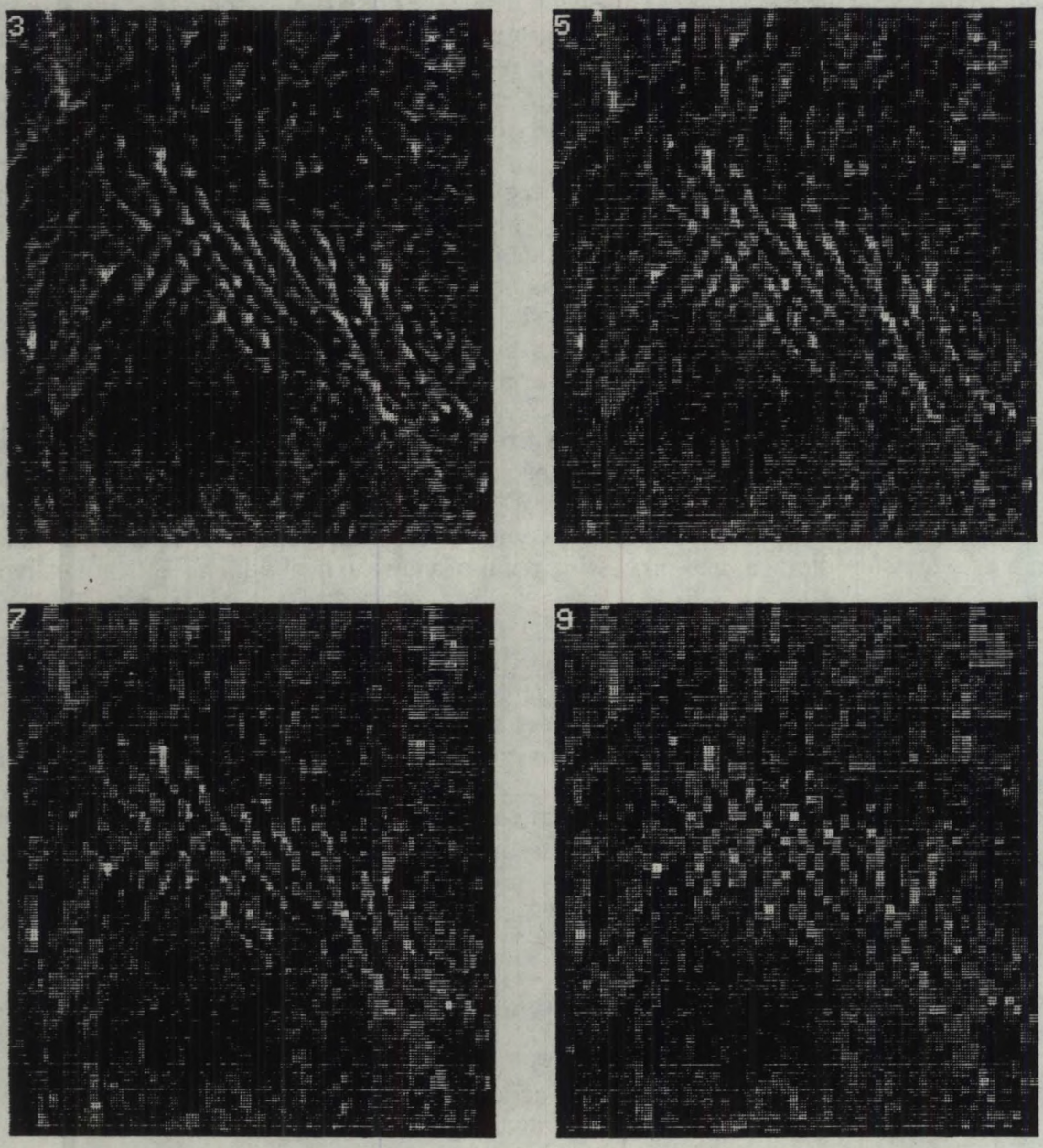

Figure 7.10 Comparison of four LRIs: top left 3×3, top right 5×5, bottom left 7×7, bottom right 9×9.

Just north of this region, several more internal wave signatures can be traced completely across the strait, and further trains of closely-spaced maxima are visible near Active Pass and along the northern shore of Galiano Island.

Internal waves are common in the strait, occurring at the boundary between the brackish surface water from the Fraser River outflow and the underlying seawater. They are generally formed when tidal water floods through Haro Strait and other passes, and flows over relief features on the floor of the basin. Their speed of propagation in the region tends to be on the order of 1 m/s. The internal waves seen in the region of Tsawwassen and Roberts Bank, and across to the northeast coast of Galiano Island, are therefore a surprising distance from the potential generating area at the mouth of Haro Strait, given that the tide was at flood when the image was acquired. However, "fossil" internal waves dating from previous tidal cycles are known to sometimes remain present in the strait (P. LeBlond, UBC, pers. comm., 1994), which can explain not only the extent of the features, but also perhaps the number of separate wave sets visible.

The varying directions of propagation of the wave groups, and in particular the strong curvature of one set just southwest of the Tsawwassen causeway, are less simple to explain. However, past studies of the strait have observed multiple sets of internal waves, some with the curvature observed in this image (P. LeBlond, UBC, pers. comm., 1994), so there is no reason to suspect that these SAR features represent anything other than ordinary internal waves for the region.

The motion of ships produces not only surface waves but also internal waves, under the right conditions. The study of ship wakes in SAR images is an active subfield of SAR ocean research. Several examples are present in this scene, most notably the strong wake of a southbound vessel in the middle of the image and, at upper left, the wake of what is probably a ferry bound for Horseshoe Bay (north of Vancouver). The first wake, and also some of the internal waves discussed above, seem to demonstrate a relationship between orientation of the feature and the radar look direction; that is, internal waves propagating in the range direction appear to have a higher backscatter.

South of Tsawwassen, and extending across the strait to Saturna Island, is a line of strong change in backscatter level. This line has the appearance of a front, and judging by the structure of the interface, it most likely represents an ocean temperature front. The high-backscatter side of a temperature front has been observed to signify warmer water in the context of the Gulf Stream (e.g., Vesecky and Stewart, 1982), and sharp gradients in water temperature are often observed in this region (G. Staples, RSI, pers. comm., 1994). The front is likely associated with the edge of the Fraser River plume, which can extend to this location.

The lack of ground truth data precludes an explanation for some of the strong features in the image, such as wide curving dark bands lying across most of the width of the strait, or the bright linear feature off the coast of Galiano Island. This relatively sharp feature is less than 1 km wide and extends for about 20 km with very little curvature. It could be related to the local wind field, or even to an atmospheric gravity wave if such a phenomenon were present at the time of image acquisition, but without further information such interpretations are conjecture.

Surface slicks are observed in Georgia Strait under light wind conditions, and their filamentary structure may provide some information concerning the recent history of local surface currents. The winds over most of the experimental area on July 28, however, were too strong to permit the effects of any surfactants to be seen in the SAR image. Filamentary slicks were observed in the ERS-1 image of August 11, 1993, but no surface current information was available for comparison with the slick structures.

The surface current vectors mapped by the SeaSonde for the hour of the satellite pass are shown in Fig. 7.11. There is no clear correlation between the flow pattern and SAR backscatter level. In part the lack of correlation may result from the fairly uniform flow field observed at that stage of the tide, and in part from masking of features in the SAR image by the wind.

7.4.2 The CV580 Wide-swath SAR Image

The SAR images acquired from the Convair 580 aircraft differ in several significant ways from the ERS-1 satellite data. The airborne sensor was at an altitude of approximately 6 km during data acquisition for this experiment. The primary effect on the images is the variation of incidence angle across the scene. The ERS-1 satellite platform is sufficiently distant from the earth's surface that the angle between the radar beam direction and the nadir line remains fairly consistent at about 23°. However, in the airborne data, this angle varies from 45° at near range to 76° in the far range for the narrow swath images and 85° for the wide swath.

The effect of the shallow radar incidence on the SAR image depends on the type of surface roughness being illuminated. Intuitively, the highest backscatter from a radar beam with incidence angle 85° should be received from fairly steep-sided or breaking waves, travelling nearly parallel to the radar look direction. Depending on the height of the waves in the target area, the amount of backscattered energy could also be reduced due to potential scattering targets lying in the radar shadow of other waves. Shadowing is not likely of concern for this experiment because surface conditions were relatively calm during the overpasses. However, under normal conditions, less backscatter is received from the far range, and detailed features are thus more difficult to image. The physical scale of the roughness to which the radar responds increases slightly in the far range (since the condition for Bragg resonance is a wave spacing of $n\lambda/2\sin\theta$), but still remains in the capillary and short gravity wave domain.

The second difference between the CV580 and the satellite images is in the dynamic range of the sea surface backscatter signal. The ERS-1 images are provided in 16-bit format, which allows a significant number of discrete pixel values to be assigned to the brightness levels of the ocean surface. The airborne data, on the other hand, are recorded in 8-bit format because of the large size of the images. The highest available pixel value (255) is set to correspond with the strong radar return from the city, and since the sea surface backscatter is much lower, the sea signal occupies only a fraction of the dynamic range of the image. In the wide swath image, 95% of the ocean pixels have values between 12 and 40.

Following slant-to-ground-range correction and the removal of the antenna pattern, the sea-surface contrast features were emphasized by histogram-clipping and contrast stretching, enhancing variation in the pixel values across the ocean surface. Bleeding along rows and columns adjacent to bright pixels is caused by the processing of the radar signals to produce the raw image. This bleeding effect is strengthened in the contrast-stretched image, which

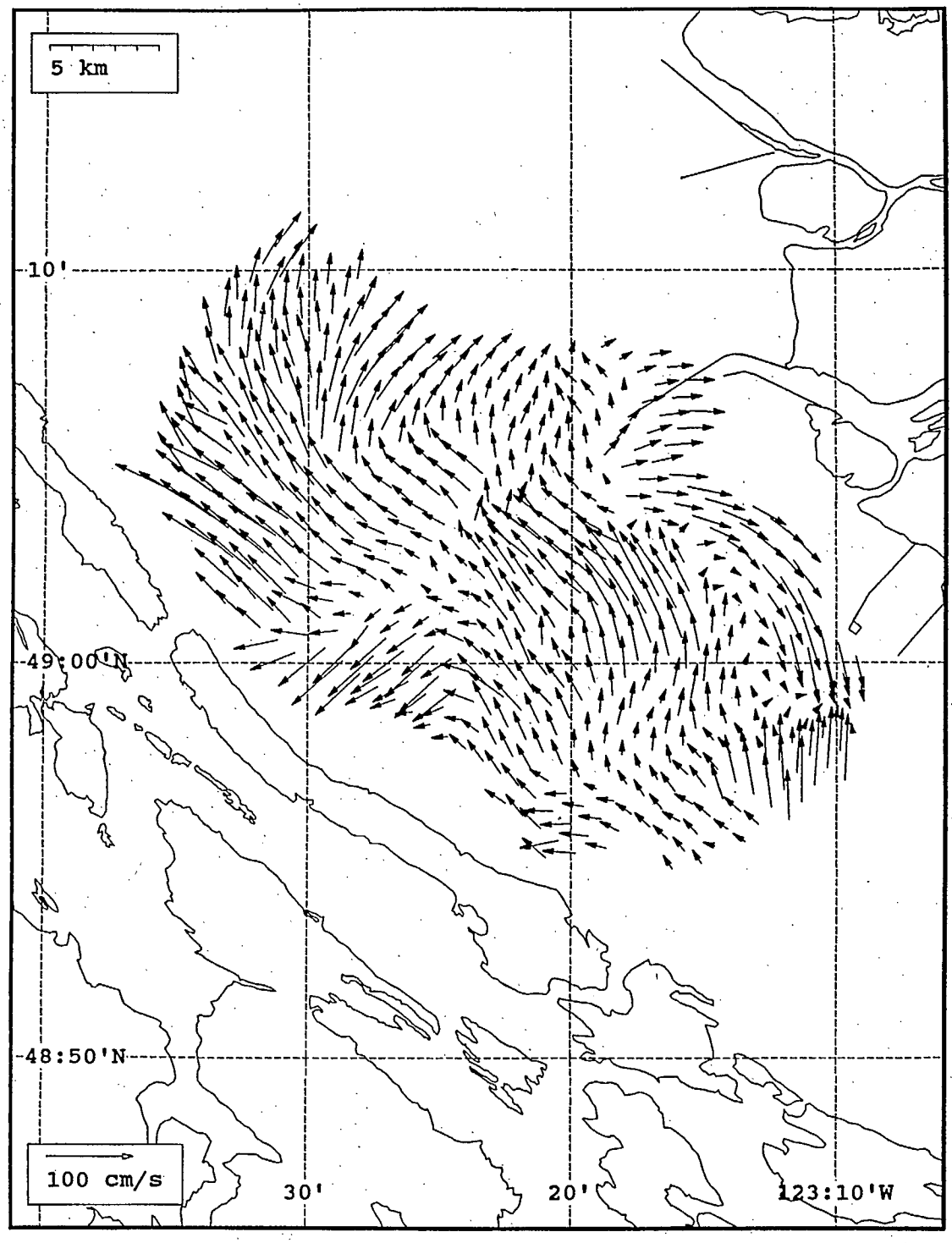

Figure 7.11 Surface current map from July 28, 1993, at 19:00 Z.

explains the fuzzy appearance of the saturated coastline and the linear or cross-shaped features marking strong ship reflections (evident in the narrow-swath images).

Differences between the airborne and satellite images may be due not only to differences in acquisition geometry but also to the fact that all images were not obtained simultaneously. Ocean surface features evolve between the time of the ERS-1 overpass at 19:10 Z, and the acquisition of the wide swath image between 21:26 and 21:46 Z, although the HF radar data indicate that the overall structure of the current field did not change dramatically. The average winds decreased at some stations and remained steady at others during the entire image acquisition period. Therefore, current-related surface roughness changes, and the signatures of the fossil internal waves which are presumed to persist throughout one or more tidal cycles, are expected to be present in the scene during all overpasses. Whether they are actually visible in the image may depend on the geometrical considerations discussed above.

The wide swath image revealed, overall, fewer bright surface roughness returns in the far range, as anticipated from the viewing geometry. It also lacked any obvious correspondence with the surface current maps and is not reproduced here. A fairly strong set of internal waves was evident a few kilometres off Mayne Island. Other signatures which appear to be associated with internal waves were seen throughout the image. The strongly curved crossing trains off Tsawwassen, which are so apparent in the satellite image, were not found in this image. It is not clear from the quality of the image whether the wave train is absent, or is present and was not imaged by the radar. Some curving internal waves are present in approximately the same location, but they are probably associated with the wake of the southeast-travelling ship or barge responsible for the adjacent bright radar reflection.

Most of the internal-wave-like signatures are roughly parallel to the flight path along the mainland side of the image. This observation suggests that surface roughness with a particular orientation relative to the look direction is preferentially imaged. A similar effect, although less dramatic, was observed in the ERS-1 image, where sections of internal wave features aligned in a certain direction were enhanced with respect to the other segments of the same features. The lack of evidence of distinctive features from the ERS-1 image suggests that the combination of look direction and incidence angle strongly affects the visibility of features in the CV580 wide-swath image.

7.4.3 CV580 Narrow-swath Images

The images returned by the Convair 580 SAR in narrow swath mode have a width of 16 km and a pixel size of 4 m. The combined effect of higher resolution and steeper incidence angles in the far range than are employed in the wide-swath mode produces a wealth of surface feature data, including the signatures of numerous trains of internal waves with wavelengths as small as 50 m. Because of the large image sizes, lower-resolution versions of the images with 12-m pixels were produced for analysis. Little or no information on ocean surface characteristics was lost in the process, and the resulting images still display more detailed features than the satellite image. Figure 7.12 shows both images, trimmed of an overlapping region and registered to a map of the coastline. The comparative lack of features in the satellite image may be due in part to higher wind-induced roughness as suggested by wind station measurements.

Figure 7.12 Convair 580 narrow-swath SAR images co-registered with the coastline (July 28,1993, 20:27-21:14 Z).

The effects of varying incidence angle are still visible in both narrow-swath images. The centre of the strait is the near range for both passes, and features are visibly better defined there. In some cases, the signature of a continuous physical phenomenon extending across the image is observed to become less distinct in the far range. The effect of feature orientation is also observed in the pair of narrow-swath images. For example, the wake of a ship heading into Active Pass, travelling parallel to the radar look direction, appears subtle and dark in the west image; yet a ship travelling obliquely with respect to the look direction, in the north end of the eastern image, leaves a distinct wake visible for many kilometres.

These airborne images were obtained between 20:27 Z and 20:45 Z (southwest pass) and 20:56 Z and 21:14 Z (northeast pass), and therefore direct comparison with the ERS-1 image must allow for some change in features. However, despite the time difference, we could reasonably expect to see some features common to both satellite and airborne images, and in fact this is the case.

Water enters the strait during flood tide by both Active and Porlier Passes. Bright streaks observed near both entrances at the time of the ERS-1 overpass are likely associated with roughness caused by strong current shear as tidal jets encounter the generally northward-moving water of the strait. Similar streaks are observed in the west narrow-swath airborne image near Active Pass; their absence at Porlier Pass is consistent with strong flooding ending earlier there than at more southerly entrances.

The thermal front which is clearly visible in the southern portion of the ERS-1 image is not so strongly apparent in the airborne images. Without ground truth measurements it cannot be determined whether the front itself weakened in the intervening time or whether the angle of incidence severely affects visibility of such features. However, a weaker frontal edge is observed southeast of Active Pass in the airborne data. The edge is further north than in the satellite image, but appears to have been pushed away from the shore by the tidal jet from the pass.

Patches of enhanced brightness just off Roberts Bank may be the surface signatures of internal waves breaking on the edge of the bank. These features are observed in both the ERS-1 and the eastern narrow-swath CV580 images, but the strongly curved internal wave train from the satellite image is no longer visible. Since internal waves in this area propagate at a speed of about 1 m/s, then the disappearance of this train is consistent with its travelling northward and breaking on the bank by the time of the aircraft overpass. It is conceivable, though unlikely, that look direction and inclination angle effects could combine to obscure the signature of the wave train.

Some internal waves and other features can be seen to have moved during the time between the first and second narrow-swath overpasses. The straight streak of enhanced backscatter extending across the northern end of the image nearly to the shore of Valdes Island is visible in all three airborne images, and comparison of its imaged location shows its general northwest motion up the strait. Estimation of the times at which the aircraft passed over the feature gives it an approximate northwest speed of 0.5 m/s, consistent with the northwest component of the HF current vectors shown in Fig. 7.11. The feature has a front-like appearance, and may have formed along the edge of the ebb plume from the Fraser River.

The distinct curving backscatter level change just north of Steveston jetty is well aligned with modelled salinity contours (see Fig. 7.13), and is likely associated with the plume. The physical explanation for the well-defined boundary, between low backscatter from the region of fresher water and the higher backscatter from the more saline water to the north, may be related to changes in short waves on the shearing currents along the front. The curved, strong-contrast feature about 6 km from Porlier Pass may also be associated with the plume edge.

The large V-shaped region of low backscatter in the north end of the eastern image appears so geometrically regular that it is more likely to be a processing-induced effect than a real surface feature. Although the wide swath image also shows a dark patch in the same general area, the fact that neither HF currents, surface phenomena, nor internal waves display any marked change at the boundary of the region argues against its being a real feature.

Although current information from the HF radar is not available at the northern end of Valdes Island, evidence of the flooding tide is seen in the roughened lee wakes created by tidal flow over the Gabriola reefs. The wake orientation is consistent with the current direction extrapolated from the HF vectors. South of the reefs is a region of reduced backscatter which may be associated with slick material produced by seaweed in the nearby shallows; however, no clear evidence of surface slicks is observed in the airborne images.

To the south, Roberts Bank is quite accurately delineated by a roughening of the water at the bank edge, as is part of Sturgeon Bank to the north. Immediately south of the end of Steveston jetty, a bright narrow streak and an adjacent low-backscatter patch curve over the shallows. The orientation of both features is well aligned with the currents measured in the region by the HF radar. At this stage of the flooding tide, river runoff meets a strong opposing tidal flow; the streak of high backscatter marks this boundary.

The vector map in Fig. 7.14 shows that the currents at this phase of the tide tend to form spatially-coherent patches separated from one another by lines marking changes in direction and speed. The shear across these lines is smoothed by the range resolution of the HF radar (2.556 km) and the interpolation methods for computing the total current vectors from the measured radial currents (see Hodgins et al., 1994). Nevertheless the changes in flow pattern between patches are quite visible. These flow patterns are often observed in the HF radar maps, and given the implied divergences and convergences between patches, one might expect to see frontal features associated with the shear zones. Such features would likely be much sharper than the 1000-2000 m scale of the shear zone in the HF current maps, and should be visible in the SAR imagery if there are changes to surface roughness from wave-current interactions, upwelling, or the accumulation of debris or surfactants along the front.

The current map suggests the presence of two water masses, one moving northwest on a path parallel to the islands with relatively uniform speed and direction, and the other travelling obliquely across the strait to the south of the first, also with fairly uniform flows. Between them lies a shear zone of reduced speeds (for example, off the northern end of Galiano Island). This zone is well correlated with a patch of enhanced brightness in the SAR image, suggesting a linkage between the surface flow properties and the bright lineal frontal features detected with the SAR.

Without on-water observations it is not possible to form definitive interpretations of the SAR features described here; however, the coincidence in position, extent, and orientation of the

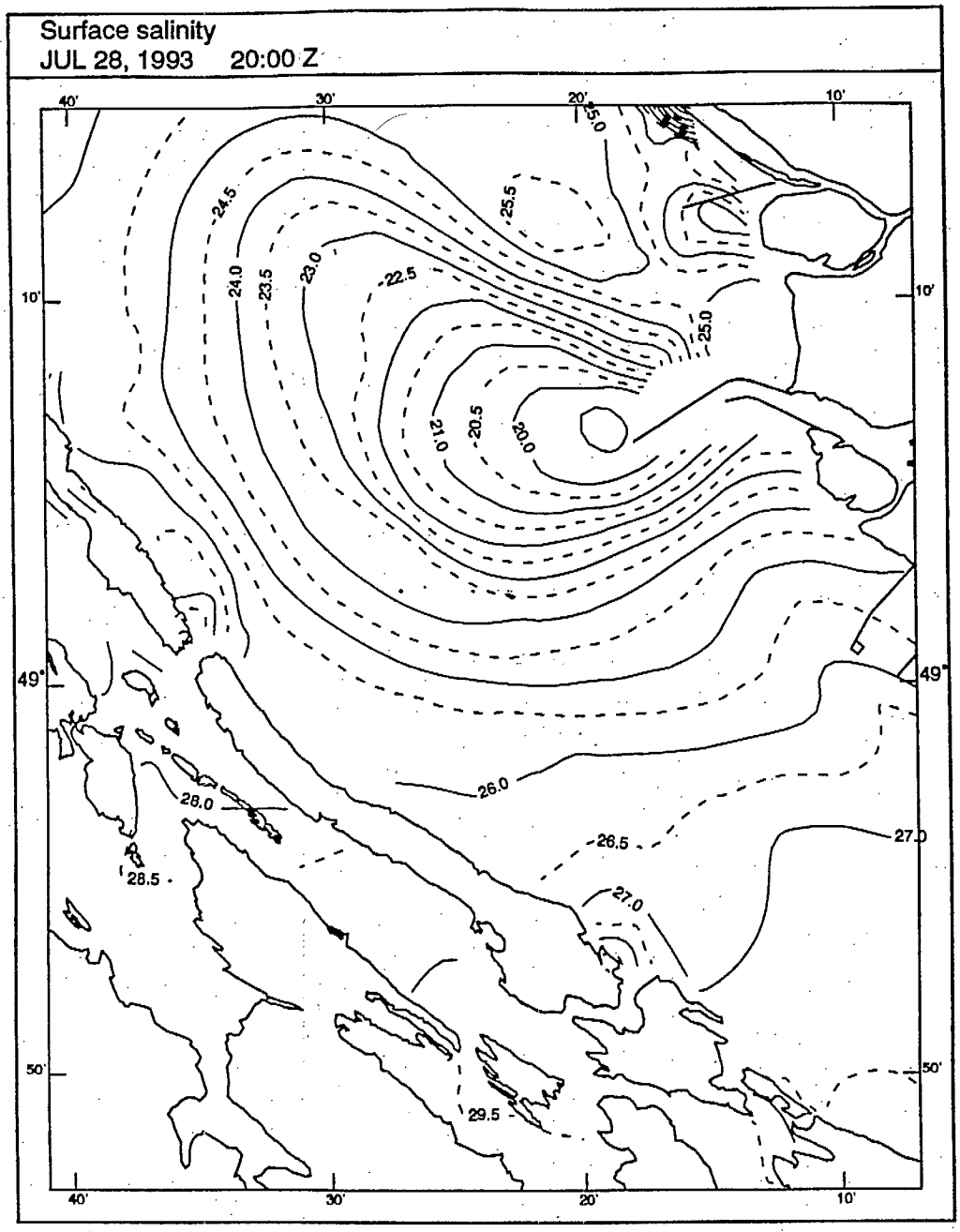

Figure 7.13 Modelled salinity field (plotted as σ_t) for July 28, 1993, at 21:00 Z.

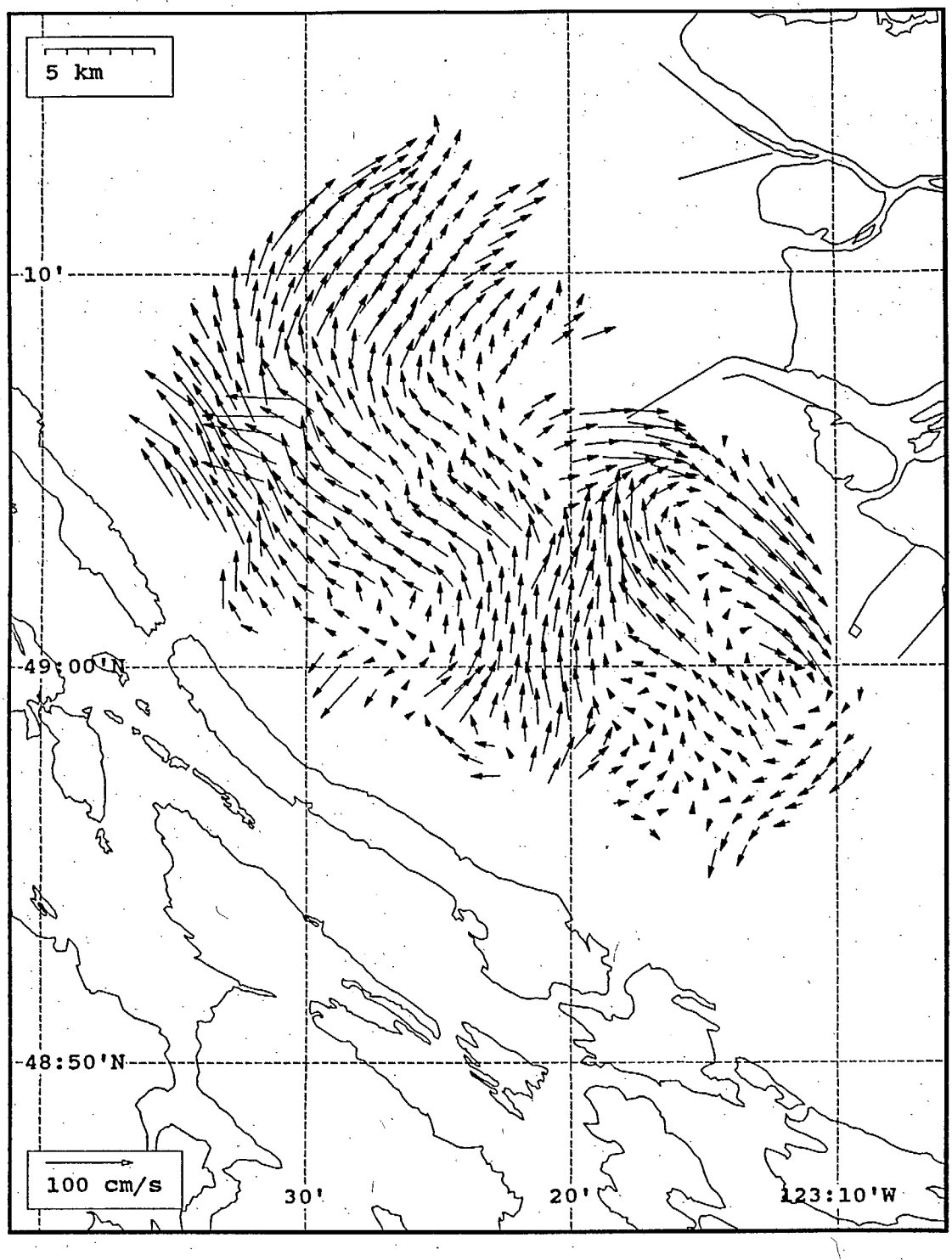

Figure 7.14 Surface current map from July 28, 1993, at 21:00 Z.

lineal frontal features, the brightness contrast patterns and flows at the mouth of the river, and the outline of the edge of the submerged bank all suggest plausible connections with the mapped flow field, or the behaviour of internal waves.

8.0 CONCLUSIONS

8.1 Current Mapping

The SeaSonde radars worked reliably throughout the deployment period and returned current maps showing the complex flow patterns characteristic of the Fraser River plume in the Strait of Georgia. Comparison of the observed currents with a detailed hindcast using a three-dimensional model showed good agreement at tidal frequencies. Differences noted at higher frequencies were associated with eddies and meanders in the flow. This observation is consistent with the previous current mapping study in Juan de Fuca Strait.

The Strait of Georgia is sheltered from ocean swell, and waves which occur there are generated strictly by the local wind. Under calm wind conditions the 11-m Bragg scattering waves required for the SeaSonde can be virtually absent. At these times the return from the radar is poor with range sometimes decreasing to 4-5 range rings ($\approx$10 km) which results in poor current map coverage. During the 15-day deployment such conditions occurred approximately 10% of the time, and the Salamanca radar was more susceptible to range loss than the unit at Dionisio Point. Once some wind flow was re-established, the scattering waves built quickly and range was restored. A change to higher frequency would be appropriate for sheltered coastal waters like the Strait of Georgia to give better Bragg scattering under light wind conditions. No correlation between the radar return and the brackishness of the surface layer was observed.

Experience with the SeaSonde HF radar, and with other ground-wave radars, indicates that coverage will always be variable. Several factors produce fluctuations in range and radial vector return. Variations in wind and sea state (too calm), external RF interference, and antenna pattern distortion are amongst the most important. Consequently HF radar data should be combined with some form of assimilation model for use in oil spill response. The objectives of the modelling include interpolating data spatially to fill gaps, extrapolating data spatially to extend the coverage area, interpolating data temporally to bridge periods of poor coverage, and predicting future flow conditions. Previous work has considered the prediction problem (Hodgins et al., 1993b); however, the spatial modelling problem must now be tackled in order to improve the utility of HF radar data for spill model input. The types of models to be considered include interpolation through some form of objective analysis, kinematic flow modelling (e.g., continuity equation), and dynamic flow modelling (e.g., satisfying both continuity and conservation of momentum).

8.2 SAR Imaging

The SAR component of this study included both ERS-1 satellite imagery and data from the Convair 580 aircraft operated by the Canada Centre for Remote Sensing. The richest image, in terms of ocean features, was obtained with the narrow-swath airborne SAR. Similar features may have existed at the time of the July 28 ERS-1 image but have been masked by local winds. The wide-swath Convair 580 image provided no useful information.

Contrast features in the backscatter from the ocean surface can be enhanced by reducing the speckle noise in the image. The scale of real features to be preserved in the image determines the type of filter and degree of averaging to be applied, and adaptive filters may be used to compute the appropriate degree of averaging for each pixel based on the statistics of the

surrounding area. For this study, a compromise was made between efficiency of the filtering process and preservation of features by adopting a fixed tapered filter, the shape of which was determined by combining pixel statistics throughout the ocean surface image with the specifications for the Frost et al. (1982) adaptive filter.

The pixel size of the filter template was chosen according to both the physical size (in metres) of the pixels, and the scale of the features of interest in the image. The feature scale was large enough (of the order of 50 m for internal waves) that low-resolution images were found to be satisfactory for interpretation of both ERS-1 and Convair 580 data. The feature scale resolved by the HF radar current maps was no better than 1 km; thus, there was a significant difference between the two types of data. The comparison of the SAR image with the current maps sought first an indication of large-scale (>1 km) surface signatures related to the gross flow features, and second, an inference of features detectable by SAR from the flow properties (e.g., a front).

All three types of SAR were successful in imaging internal waves. The ERS-1 SAR also detected frontal features, although there was some ambiguity in distinguishing these features from internal wave signatures. The ERS-1 image suffered some degradation by winds of 6-8 m/s. The wide-swath CV580 image provided no useful data. On the other hand, the narrow-swath CV580 image was rich in surface signatures, dominated by internal waves, fronts and features related to flow over shallow bathymetry. Some correlation between the HF current map and the SAR image was apparent in terms of frontal features separating patches of spatially-uniform flow. The overall impression, however, is that many features found in the SAR image are being advected by the mean flow measured with the HF radar, and that no significant changes in the flow field occur at the spatial scales of the frontal and wave features seen in the imagery.

The principal advantage of the SAR imagery may be as an interpretive aid to spill modelling using current maps as input. For example, fronts tend to trap oil and distribute it along the front, rather than allow the material to cross the discontinuity. Where spill models predict cross-frontal motion, the knowledge of their existence from SAR imaging can be used to modify the computer prediction to better agree with small-scale, unresolved features in the flow.

The SAR images are also difficult to interpret for flow-related phenomena; features vary between different sensors and are often ambiguous (open to different interpretations). For circulation properties multi-sensor imaging (surface roughness by SAR, temperature using AVHRR, and ocean colour with SeaWIFS) would offer more potential than SAR alone. Because each sensor has different resolution and sees the area of interest at different times, assimilation of imaged properties into a model would be required in order to improve current prediction.

9.0 REFERENCES

Barnett, T.P., F. Kelley, and B. Holt, 1989. Estimation of the Two-dimensional Ocean Current Shear Field with a Synthetic Aperture Radar. *J. Geophys. Res.*, **94**, 16087-16096.

Bern, T.-I., S. Barstow, and S. Moen, 1992. Oil Spill Detection Using Satellite-Based SAR, Executive Summary Report. Preport N. OCN R-92096, prepared by Oceanor, Trondheim, Norway.

Bern, T.-I., T. Wahl, T. Anderssen, and R. Olsen, 1993. Oil Spill Detection Using Satellite Based SAR: Experience from a Field Experiment. *Photogr. Eng. & Rem. Sens.*, **59**(3), 423-428.

Crimmins, T.R., 1985. Geometric Filter for Speckle Reduction. *Applied Optics*, **24**(10), 1438-1443.

Frost, V.S., J.A. Stiles, K.S. Shanmugan, and J.C. Holtzman, 1982. A Model for Radar Images and Its Application to Adaptive Digital Filtering of Multiplicative Noise. IEEE *Trans. Pattern Anal. Machine Intell.*, PAMI-4(2), 157-165.

Hodgins, D.O., and J.S. Hardy, 1992. Performance of the SeaSonde High-frequency Radar System for Surface Current Measurements. Proc. 15th AMOP Technical Seminar, June 10-12, 1992, Edmonton, Canada.

Hodgins, D.O., R.H. Goodman, M.F. Fingas and R. Overstreet, 1993a. Surface Current Measurements in Juan de Fuca Strait Using the SeaSonde HF Radar. Proc. Arctic and Marine Oilspill Program (AMOP) Technical Seminar, June 1993, Calgary.

Hodgins, D.O., R.H. Goodman, and M.F. Fingas, 1993b. Forecasting Surface Currents Measured with HF Radar. Proc. 16th AMOP Technical Seminar, June 6-9, 1993, Calgary, Canada.

Hodgins, D.O., R.H. Goodman, and M.F. Fingas, 1994. Remote Sensing of Surface Currents in the Fraser Plume. Proc. Arctic and Marine Oilspill Program (AMOP) Technical Seminar, June 1994, Vancouver.

Johannessen, J.A., R.A. Shuchman, O.M. Johannessen, K.L. Davidson, and D.R. Lyzenga, 1991. Synthetic Aperture Radar Imaging of Upper Ocean Circulation Features and Wind Fronts. *J. Geophys. Res.*, **96**, 10411-10422.

Jones, W.L., V.E. Delnore, and E.M. Bracalente, 1981. The Study of Mesoscale Ocean Winds Using the SAR. In *Spaceborne Synthetic Aperture Radar for Oceanography*, ed. R.C. Beal, P. DeLeonibus, and I. Katz, Johns Hopkins Press, Baltimore, 87-94.

Kuan, D.T., A.A. Sawchuk, T.C. Strand, and P. Chavel, 1985. Adaptive Noise Smoothing Filter for Images with Signal-dependent Noise. IEEE *Trans. Pattern Anal. Machine Intell.*, PAMI-7(2), 165-177.

Lee, J.-S., 1981. Speckle Analysis and Smoothing of Synthetic Aperture Radar Images. *Comput. Graph. and Image Processing*, **17**, 24-32.

Lee, J.-S., 1983. A Simple Speckle Smoothing Algorithm for Synthetic Aperture Radar Images. IEEE *Trans. Syst., Man, Cybern.*, SMC-**13**(1), 85-89.

Leise, J.A., 1984. The Analysis and Digital Signal Processing of NOAA's Surface Current Mapping System. IEEE *J. Ocean. Eng.*, **OE-9**(2), 106-113.

Lichy, D.E., M.G. Mattie, and L.J. Mancini, 1981. Tracking of a Warm Water Ring. In *Spaceborne Synthetic Aperture Radar for Oceanography*, ed R.C. Beal, P. DeLeonibus, and I. Katz, Johns Hopkins Press, Baltimore, 171-182.

Lipa, B.J., and D.E. Barrick, 1983. Least-Squares Methods for the Extraction of Surface Currents From CODAR Crossed-Loop Data: Application at ARSLOE. IEEE *J. Oceanic Eng.*, OE-8(4), 226-253.

Liu, A.K., F.C. Jackson, E.J. Walsh, and C.Y. Peng, 1989. A Case Study of Wave-Current Interaction Near an Oceanic Front. *J. Geophys. Res.*, **94**(C11), 16189-16200.

Lopes, A., R. Touzi, and E. Nezry, 1990. Adaptive Speckle Filters and Scene Heterogeneity. IEEE *Trans. Geosci. Remote Sensing*, GE-**28**(6), 992-1000.

NERSC, 1993. Detection and Classification of Oceanic Current Fronts and Wind Shifts with the Use of ERS-1 SAR: Final Report (Document ii). Technical Report No. 70 prepared by Nansen Environmental and Remote Sensing Centre for the European Space Agency.

Ochadlick, A.R., P. Cho, and J. Evans-Morris, 1992. SAR Observations of Currents Colocated with Slicks. *J. Geophys. Res.*, **97**, 5325-5330.

Phillips, O.M., 1977. *The Dynamics of the Upper Ocean.* Cambridge University Press, New York.

Phillips, O.M., 1981. The Structure of Short Gravity Waves on the Ocean Surface. In *Spaceborne Synthetic Aperture Radar for Oceanography*, ed R.C. Beal, P. DeLeonibus, and I. Katz, Johns Hopkins Press, Baltimore, 87-94.

Scott, J.C., 1986. Surface Films in Oceanography. Proc. ONR Workshop, Role of Surfactant Films on the Interfacial Properties of the Sea Surface, ed. F.L. Herr and J. L Williams, ONR Rep. C-11-86, pp. 19-40, Off. of Nav. Res., Arlington, VA.

Stronach, J.A., J.O. Backhaus, and T.S. Murty, 1993. An Update on the Numerical Simulation of Oceanographic Processes in the Waters Between Vancouver Island and the Mainland: The GF8 Model. *Oceanogr. Mar. Biol. Ann. Rev.*, **31**, 1-86.

Thomson, R.E., P.W. Vachon, and G.A. Borstad, 1992. Airborne Synthetic Aperture Radar Imagery of Atmospheric Gravity Waves. *J. Geophys. Res.*, **97**, 14249-14257.

Vachon, P.W., G.A. Borstad, and R.E. Thomson, 1992. Airborne SAR Observations of Mesoscale Ocean Features. *Can. J. Rem. Sens.*, **18**(3), 152-165.

Vesecky, J.F., and R.H. Stewart, 1982. The Observation of Ocean Surface Phenomena Using Imagery from the SEASAT Synthetic Aperture Radar: An Assessment. *J. Geophys. Res.*, **87**, 3397-3430.

Appendix 1

Surface Current Maps
Strait of Georgia

July 22, 1993, 03:00 Z to
August 5, 1993, 20:00Z

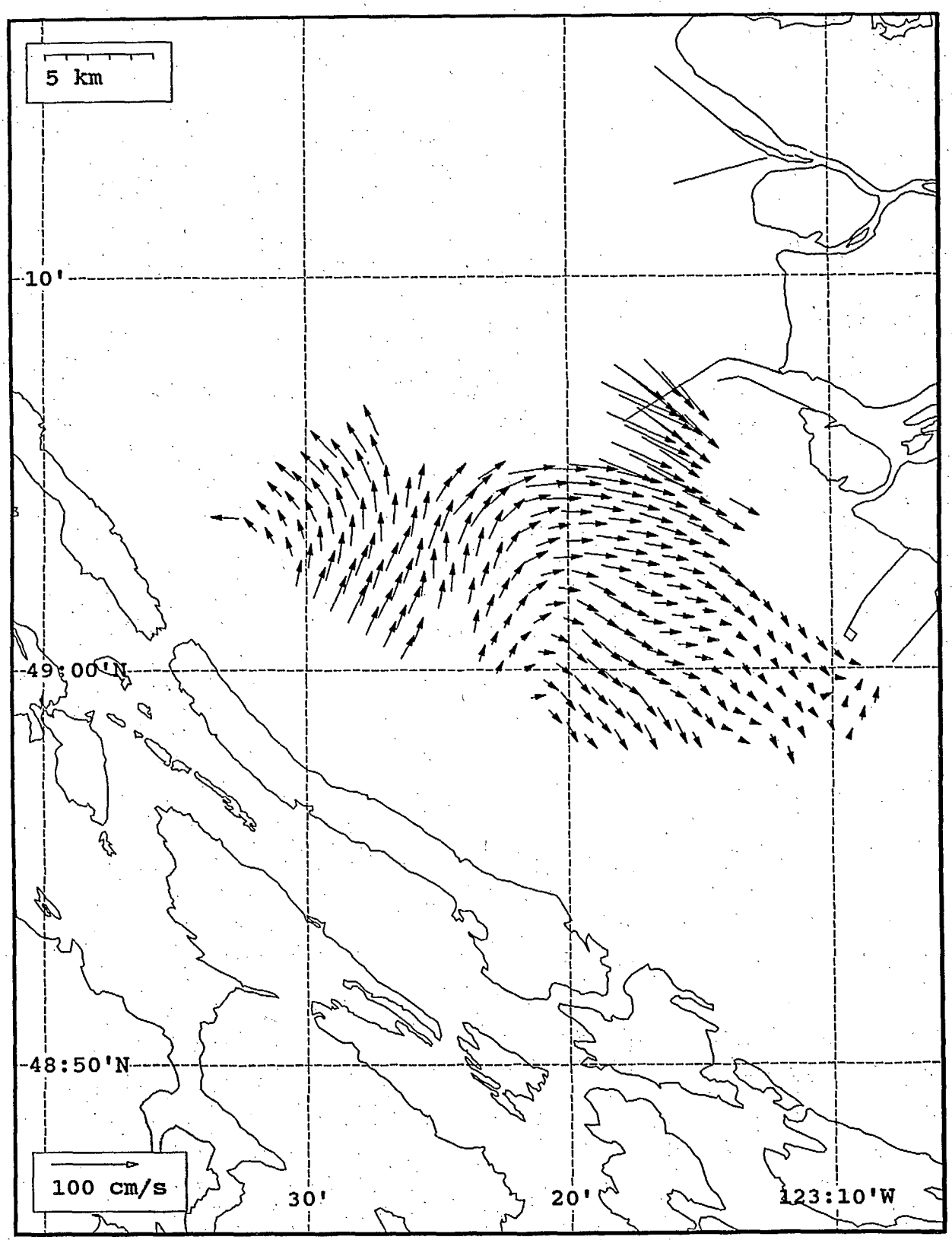

SeaSonde current field from the Strait of Georgia, off the mouth of the Fraser River, for 03:00 Z, July 22, 1993.

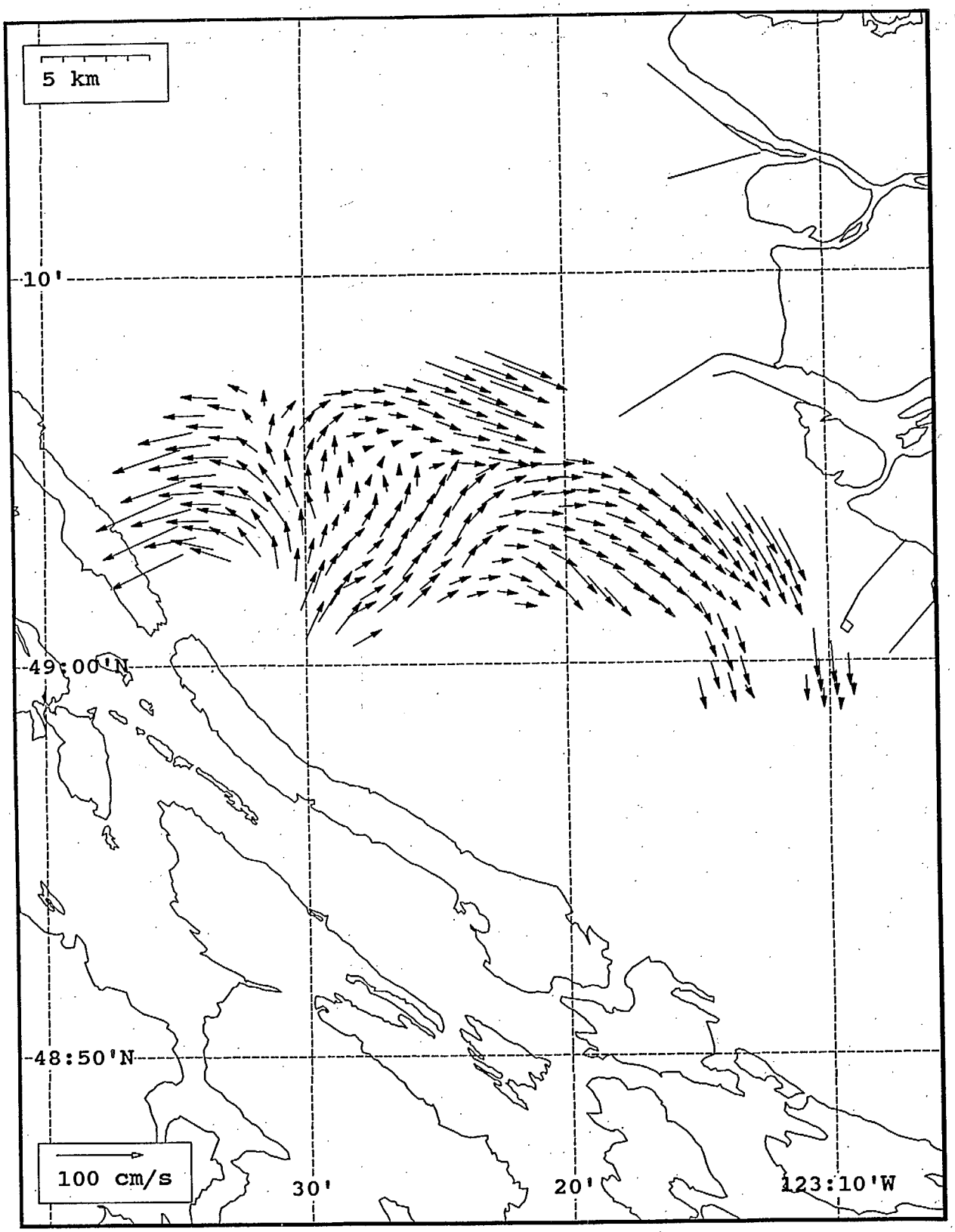

SeaSonde current field from the Strait of Georgia, off the mouth of the Fraser River, for 04:00 Z, July 22, 1993.

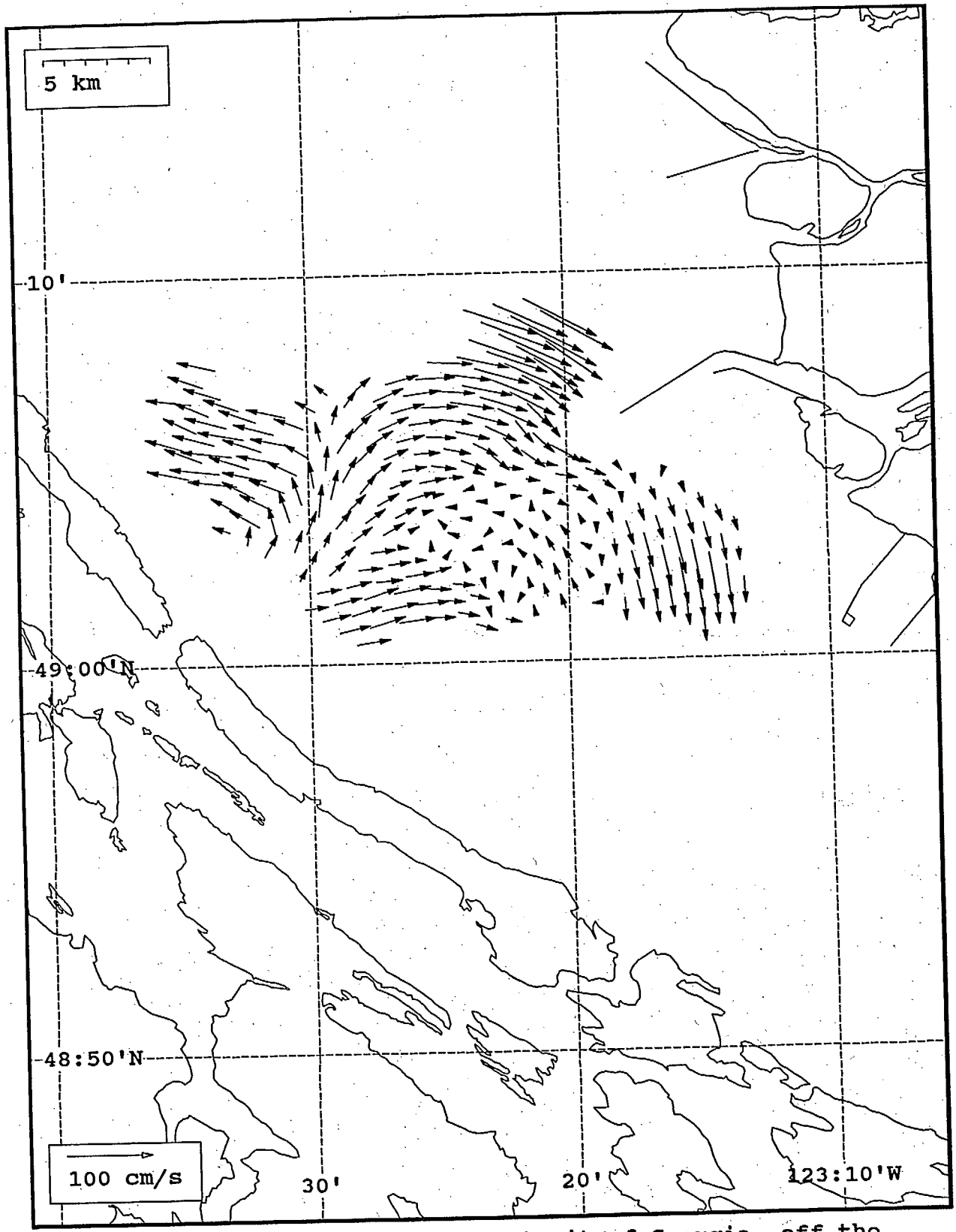

SeaSonde current field from the Strait of Georgia, off the mouth of the Fraser River, for 05:00 Z, July 22, 1993.

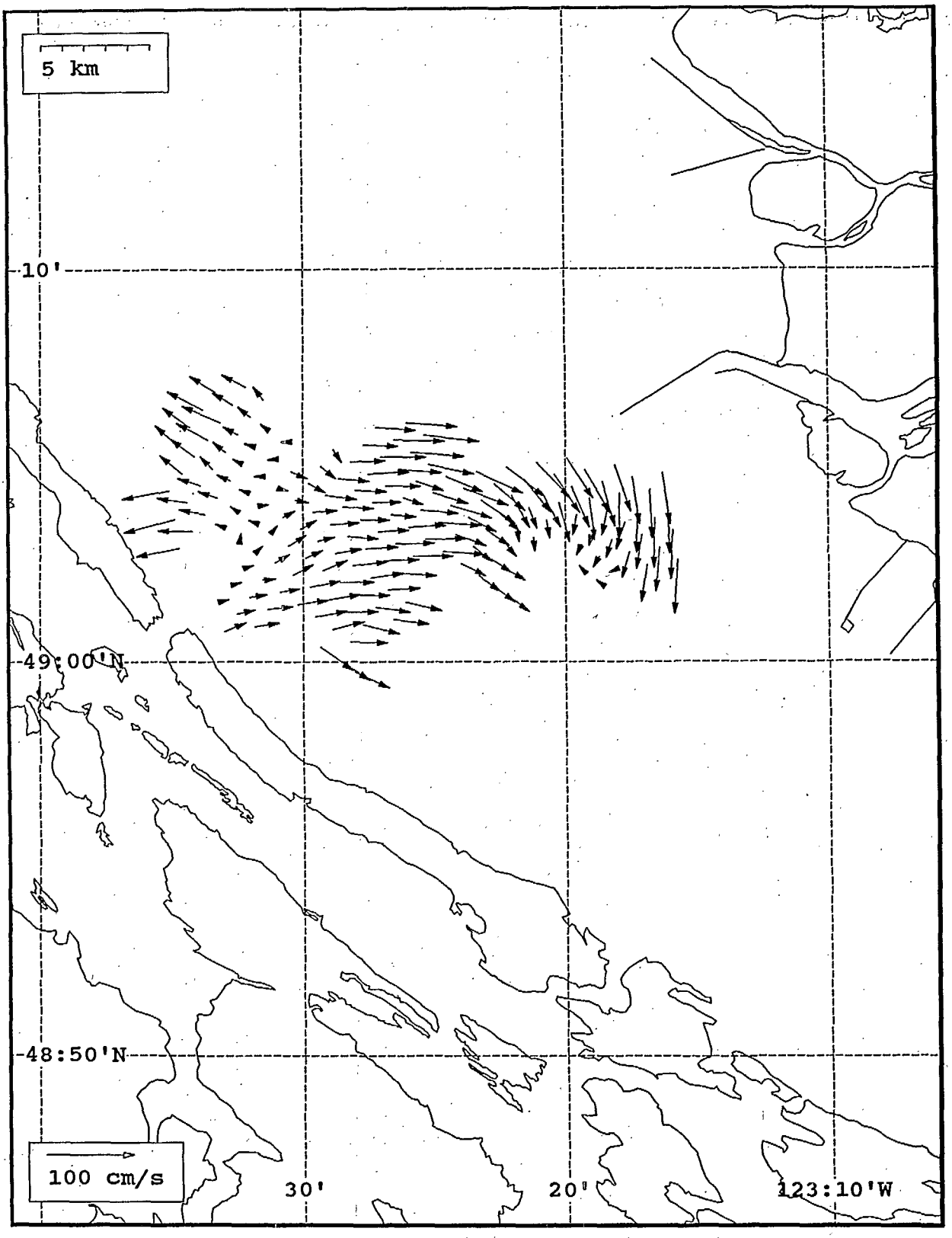

SeaSonde current field from the Strait of Georgia, off the mouth of the Fraser River, for 06:00 Z, July 22, 1993.

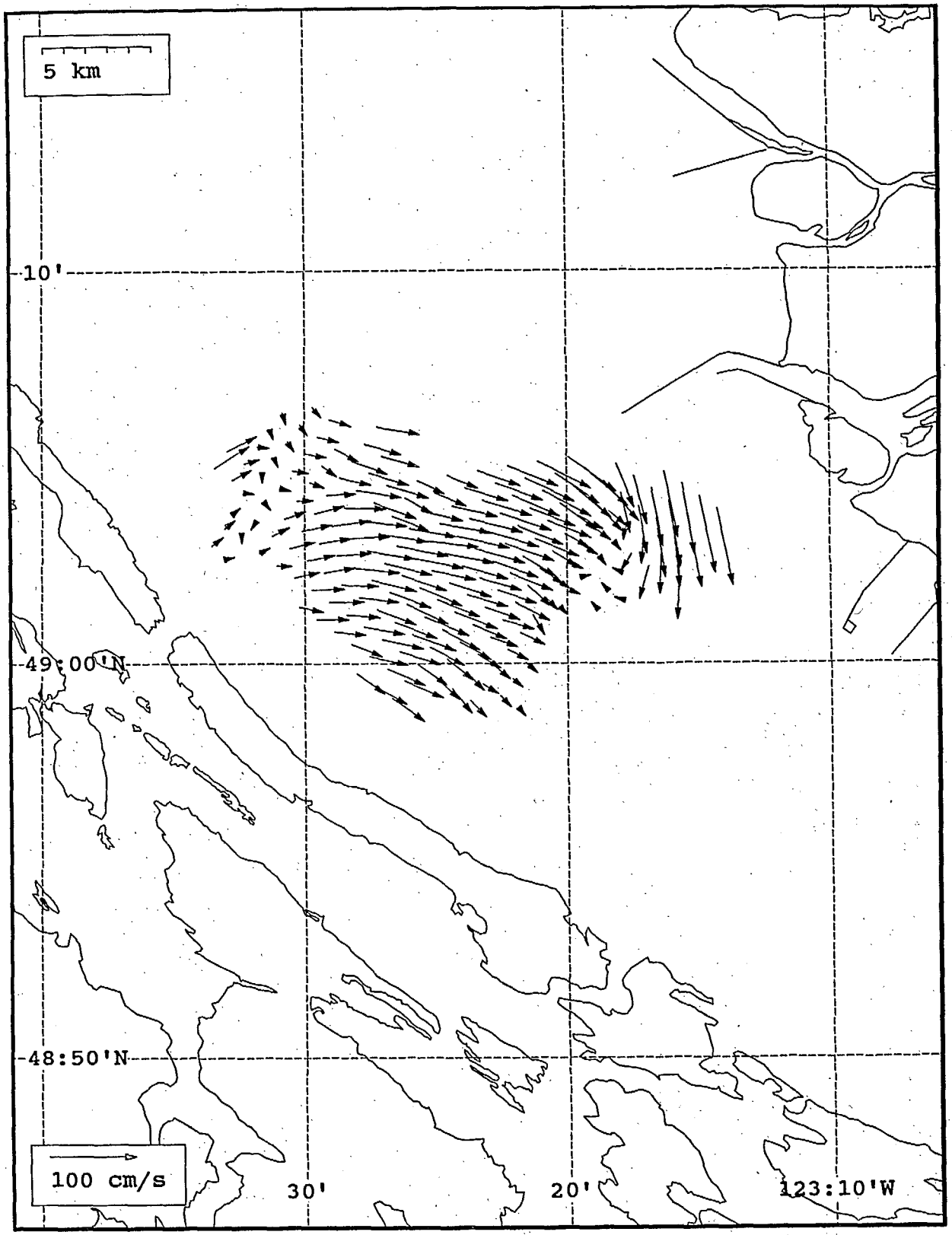

SeaSonde current field from the Strait of Georgia, off the mouth of the Fraser River, for 07:00 Z, July 22, 1993.

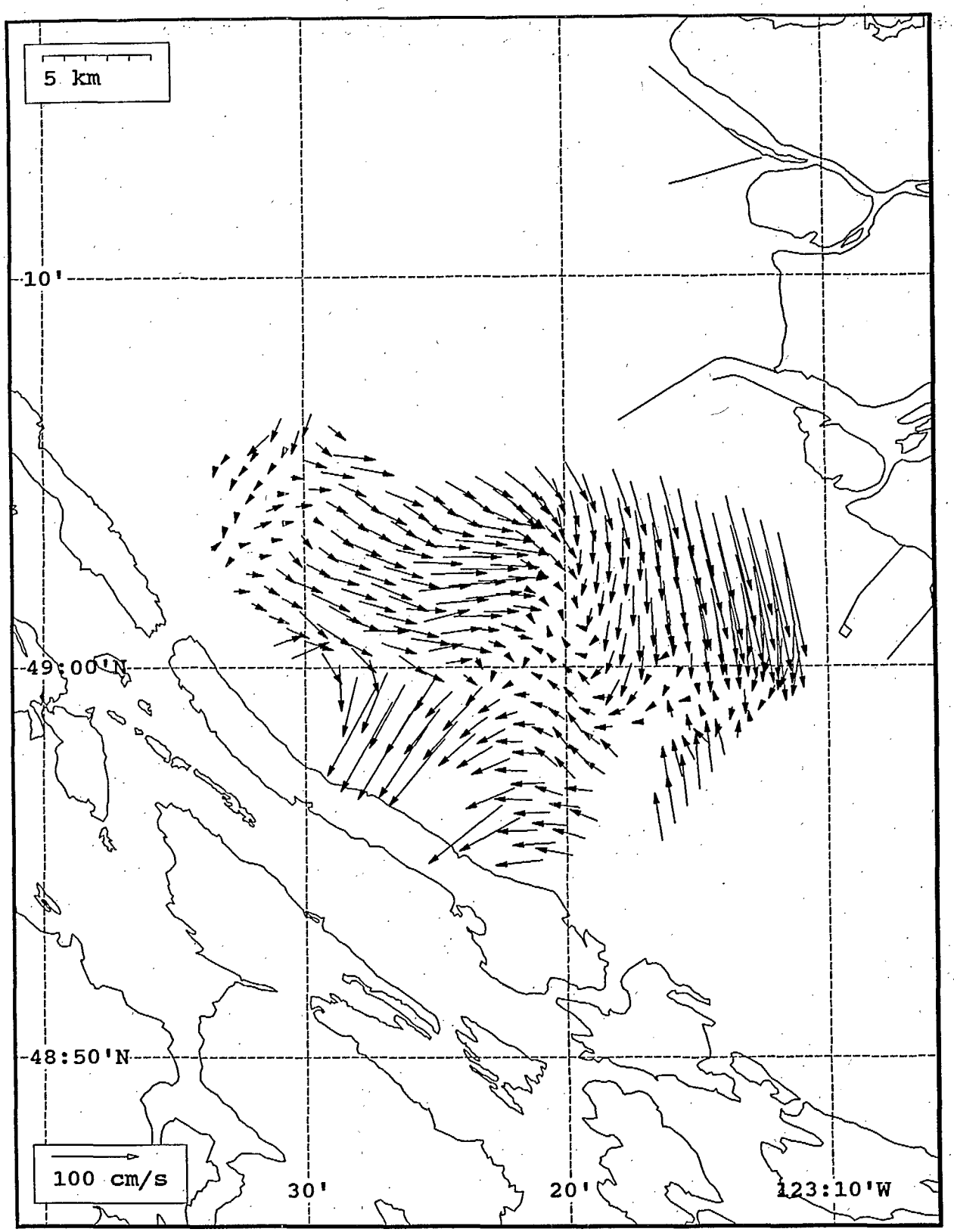

SeaSonde current field from the Strait of Georgia, off the mouth of the Fraser River, for 08:00 Z, July 22, 1993.

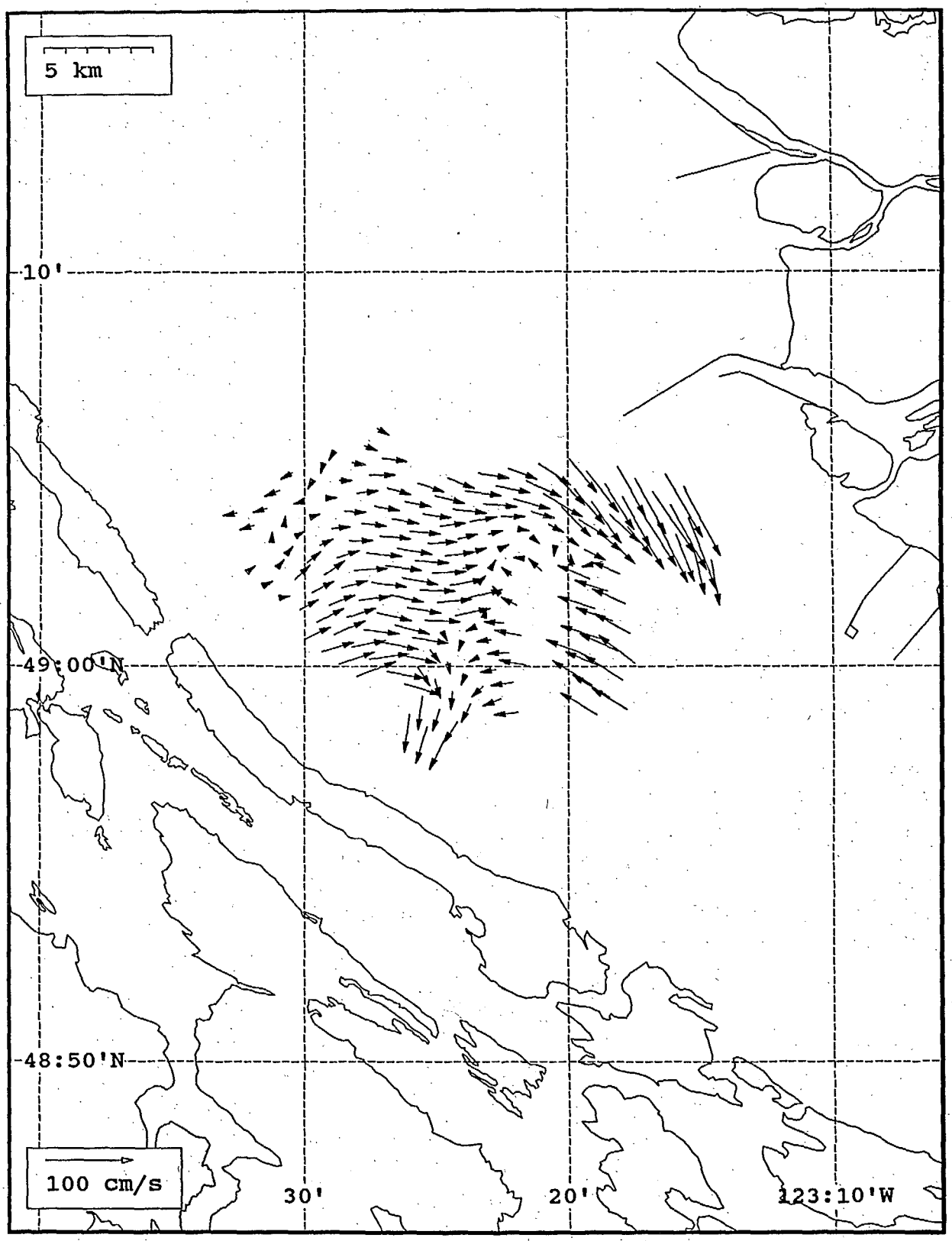

SeaSonde current field from the Strait of Georgia, off the mouth of the Fraser River, for 09:00 Z, July 22, 1993.

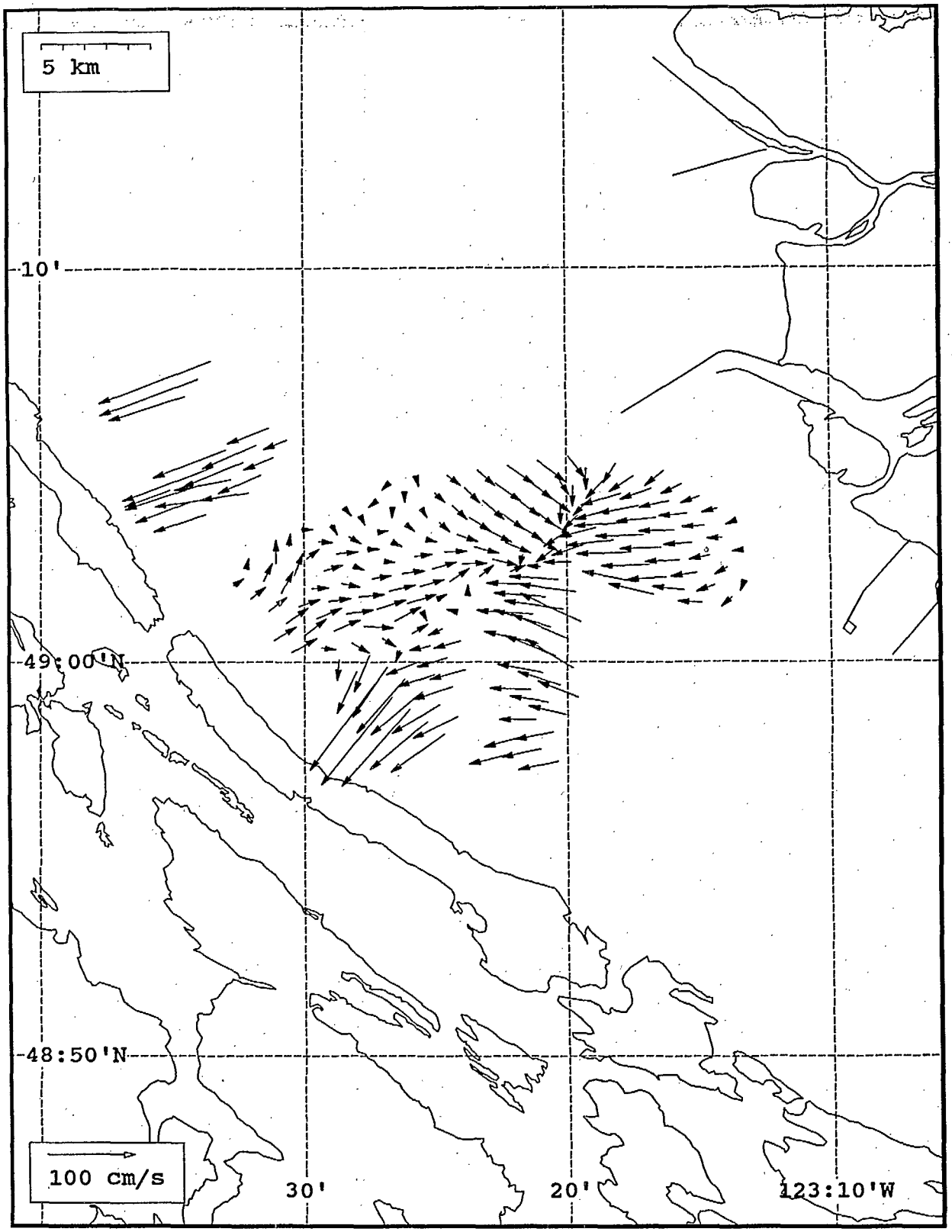

SeaSonde current field from the Strait of Georgia, off the mouth of the Fraser River, for 10:00 Z, July 22, 1993.

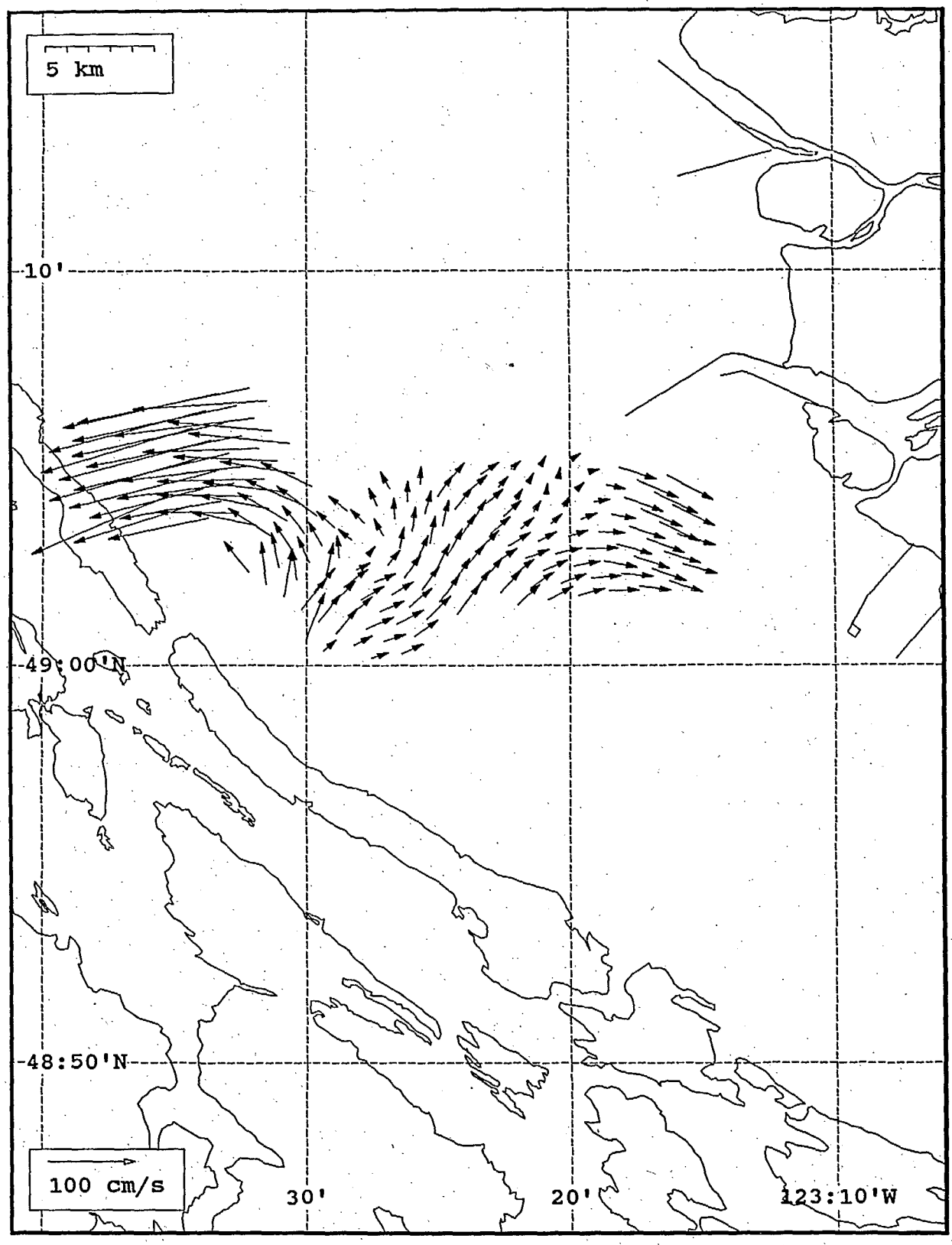

SeaSonde current field from the Strait of Georgia, off the mouth of the Fraser River, for 11:00 Z, July 22, 1993.

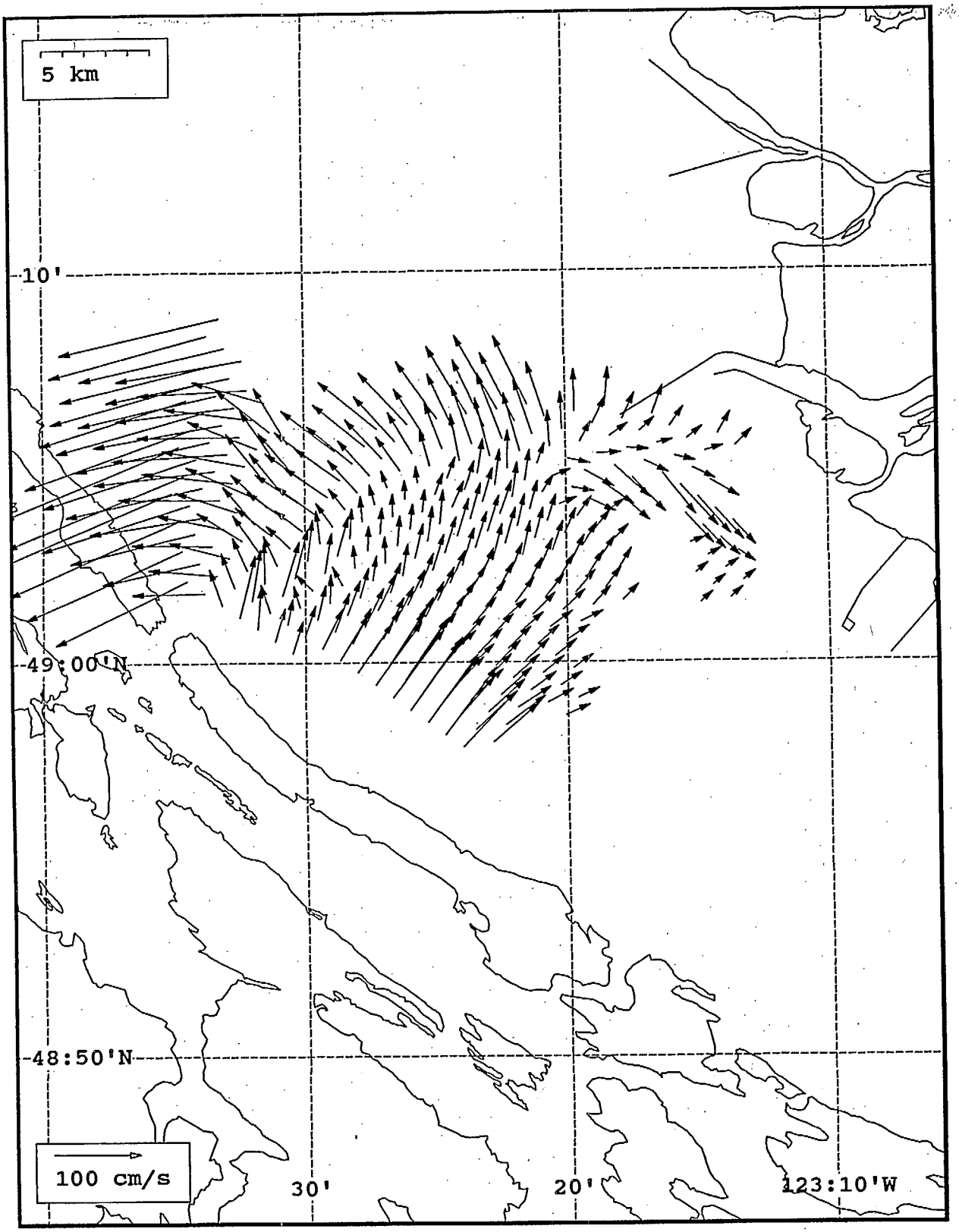

SeaSonde current field from the Strait of Georgia, off the mouth of the Fraser River, for 12:00 Z, July 22, 1993.

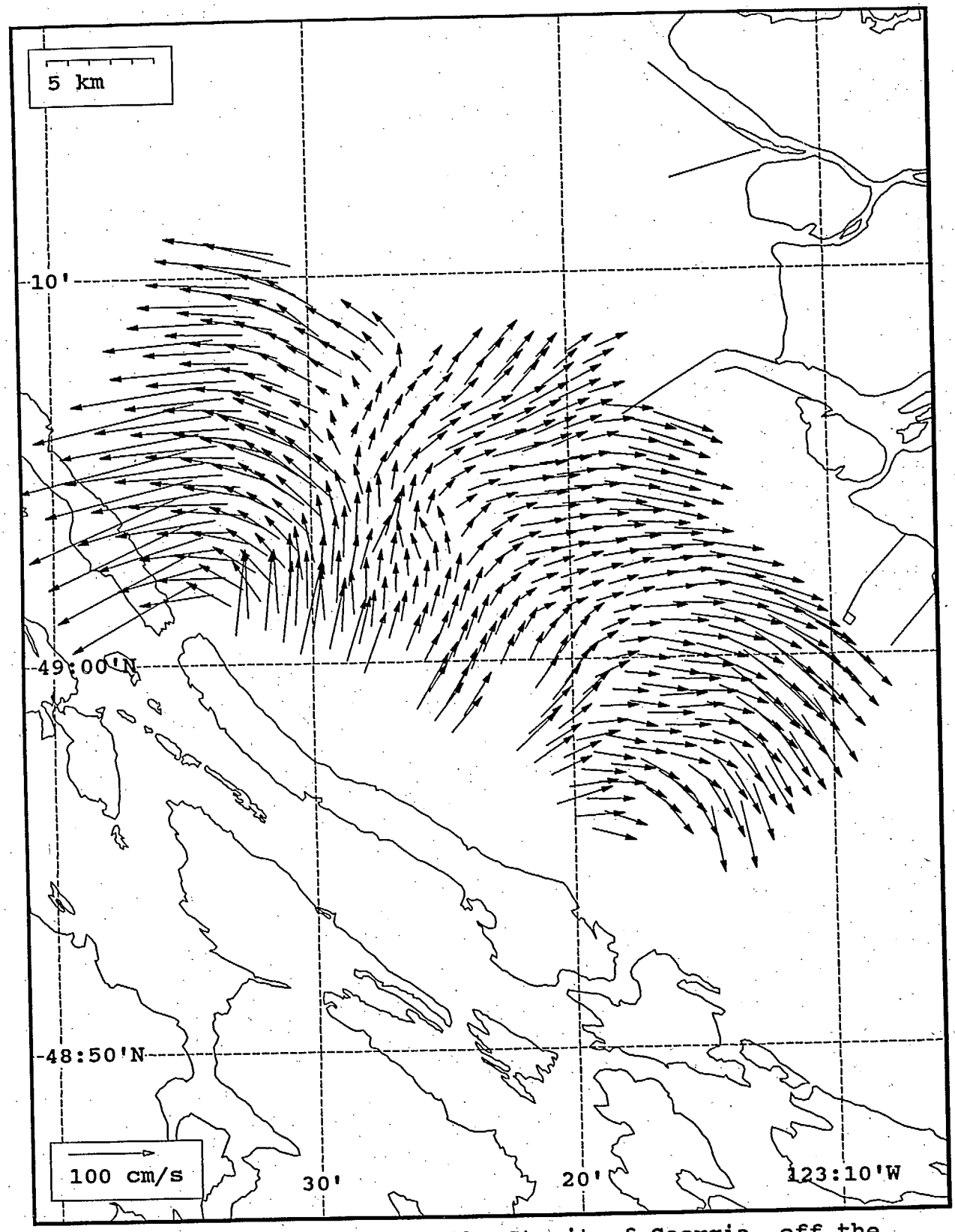

SeaSonde current field from the Strait of Georgia, off the mouth of the Fraser River, for 13:00 Z, July 22, 1993.

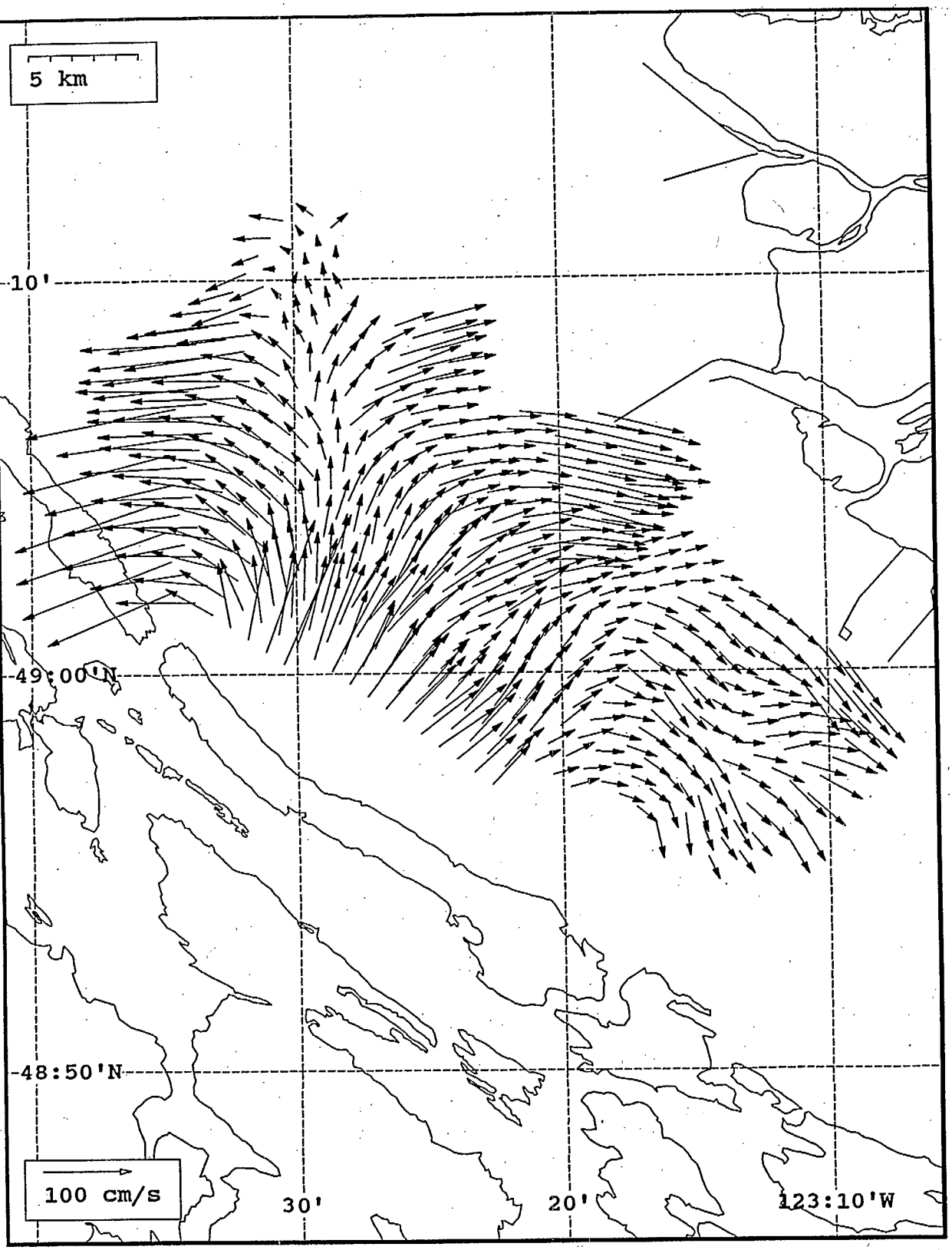

SeaSonde current field from the Strait of Georgia, off the mouth of the Fraser River, for 14:00 Z, July 22, 1993.

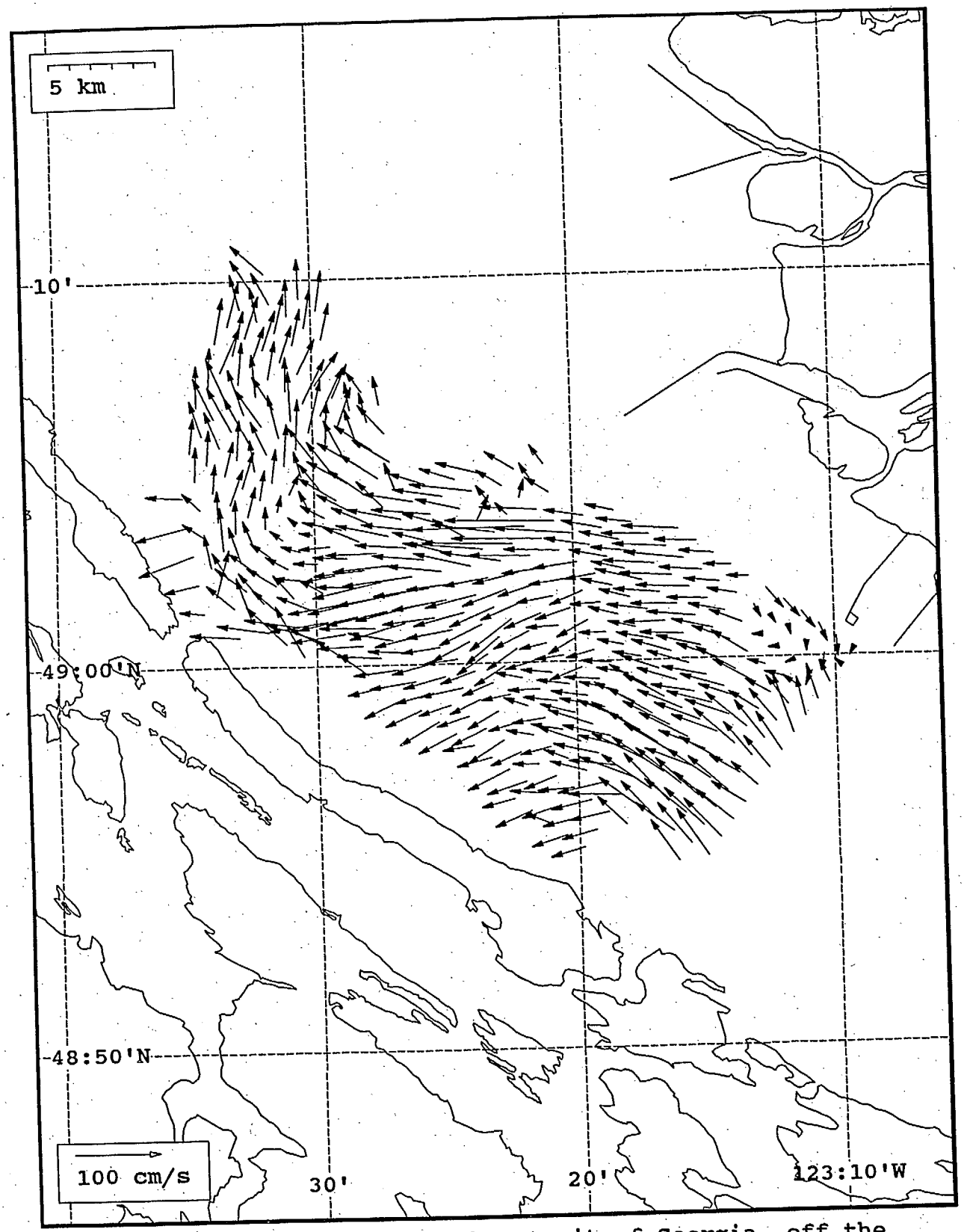

SeaSonde current field from the Strait of Georgia, off the mouth of the Fraser River, for 23:00 Z, July 22, 1993.

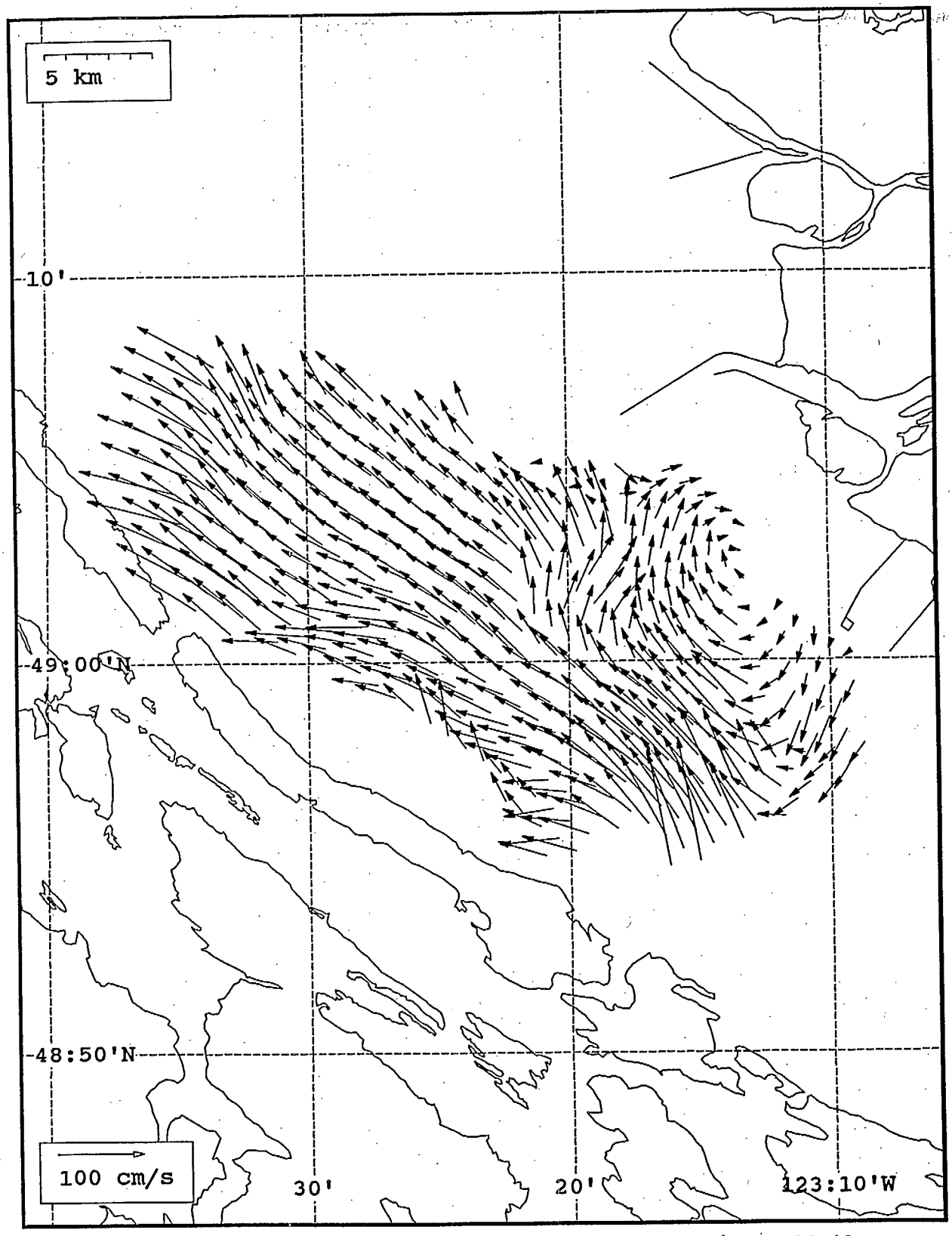

SeaSonde current field from the Strait of Georgia, off the mouth of the Fraser River, for 01:00 Z, July 23, 1993.

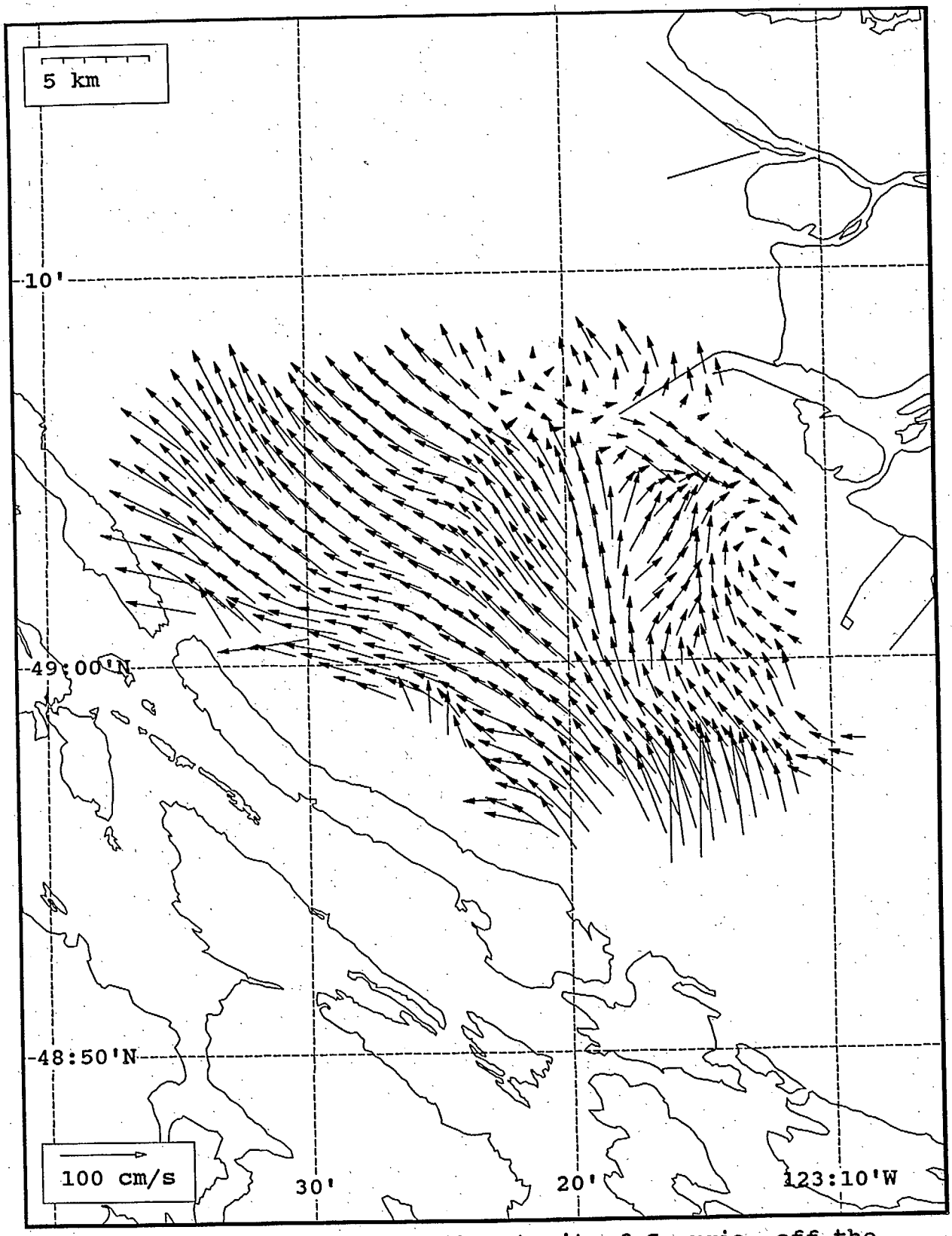

SeaSonde current field from the Strait of Georgia, off the mouth of the Fraser River, for 02:00 Z, July 23, 1993.

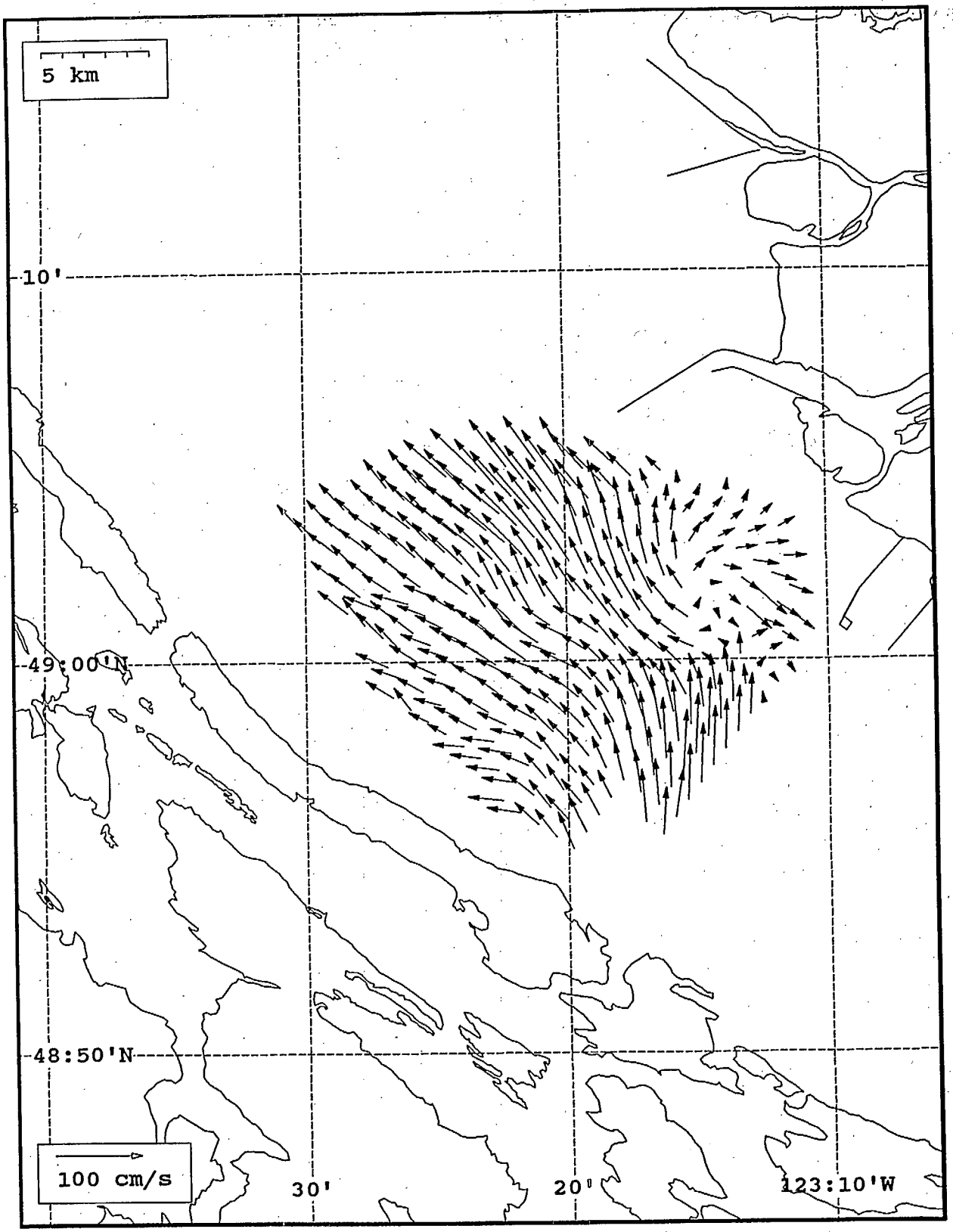

SeaSonde current field from the Strait of Georgia, off the mouth of the Fraser River, for 03:00 Z, July 23, 1993.

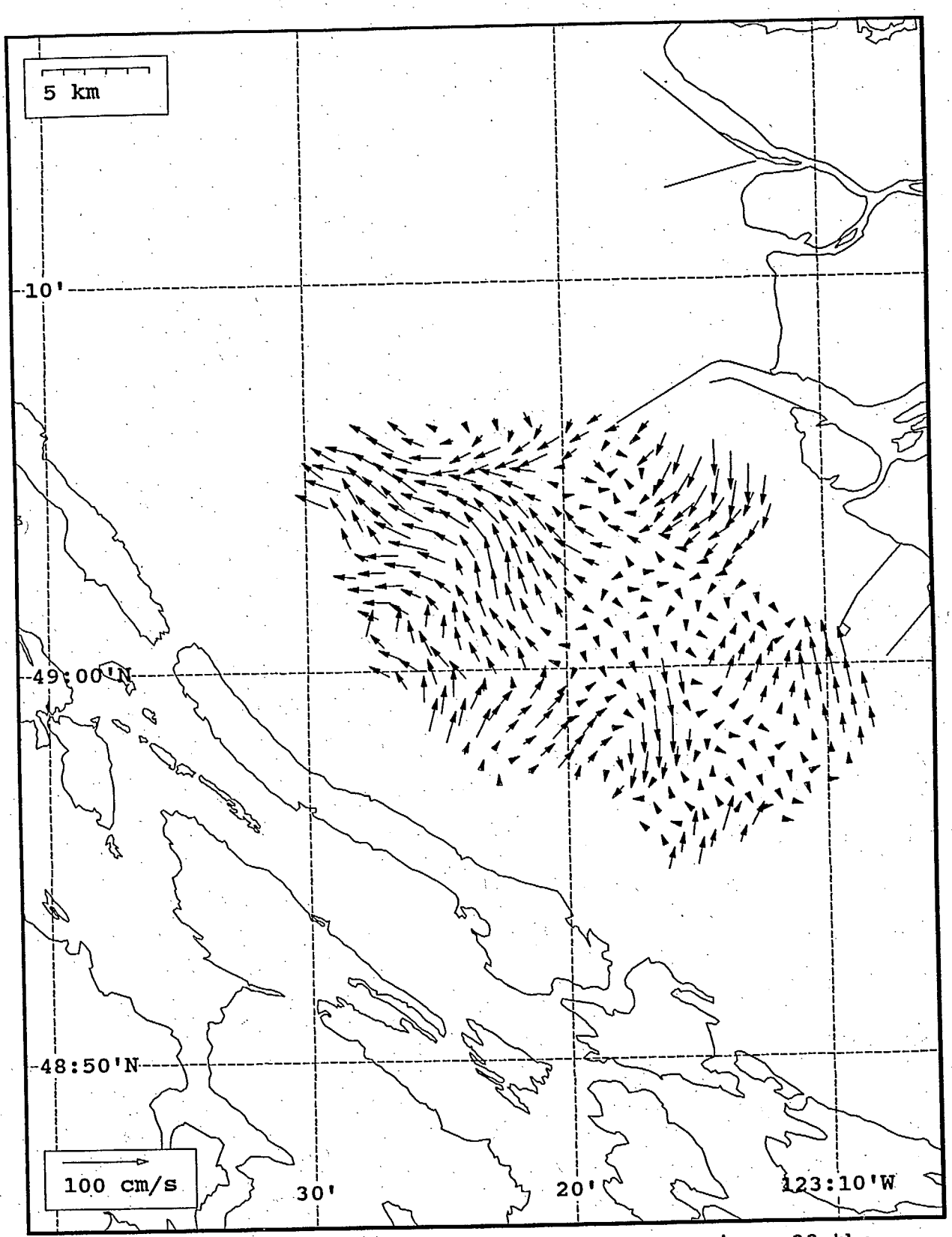

SeaSonde current field from the Strait of Georgia, off the mouth of the Fraser River, for 04:00 Z, July 23, 1993.

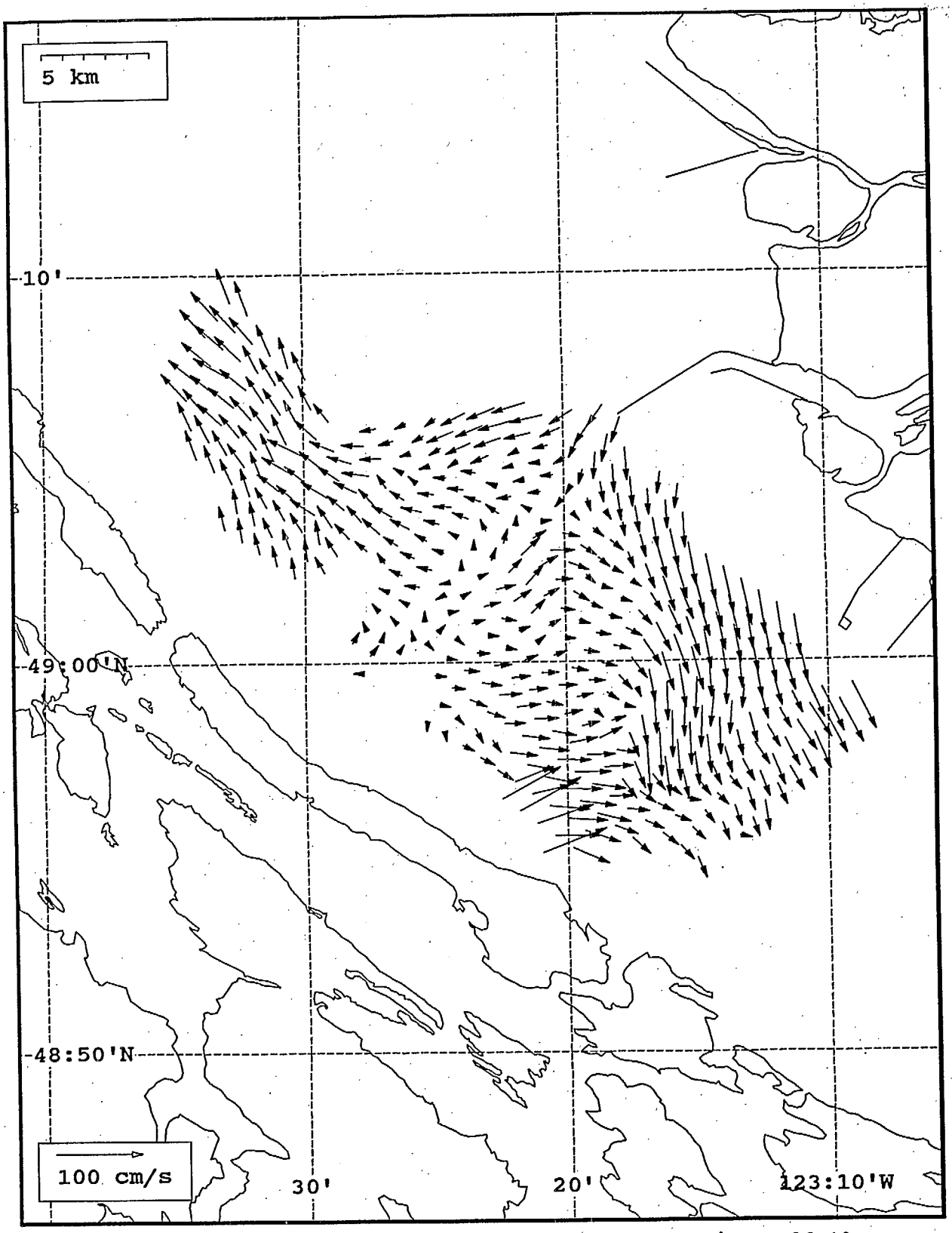

SeaSonde current field from the Strait of Georgia, off the mouth of the Fraser River, for 05:00 Z, July 23, 1993.

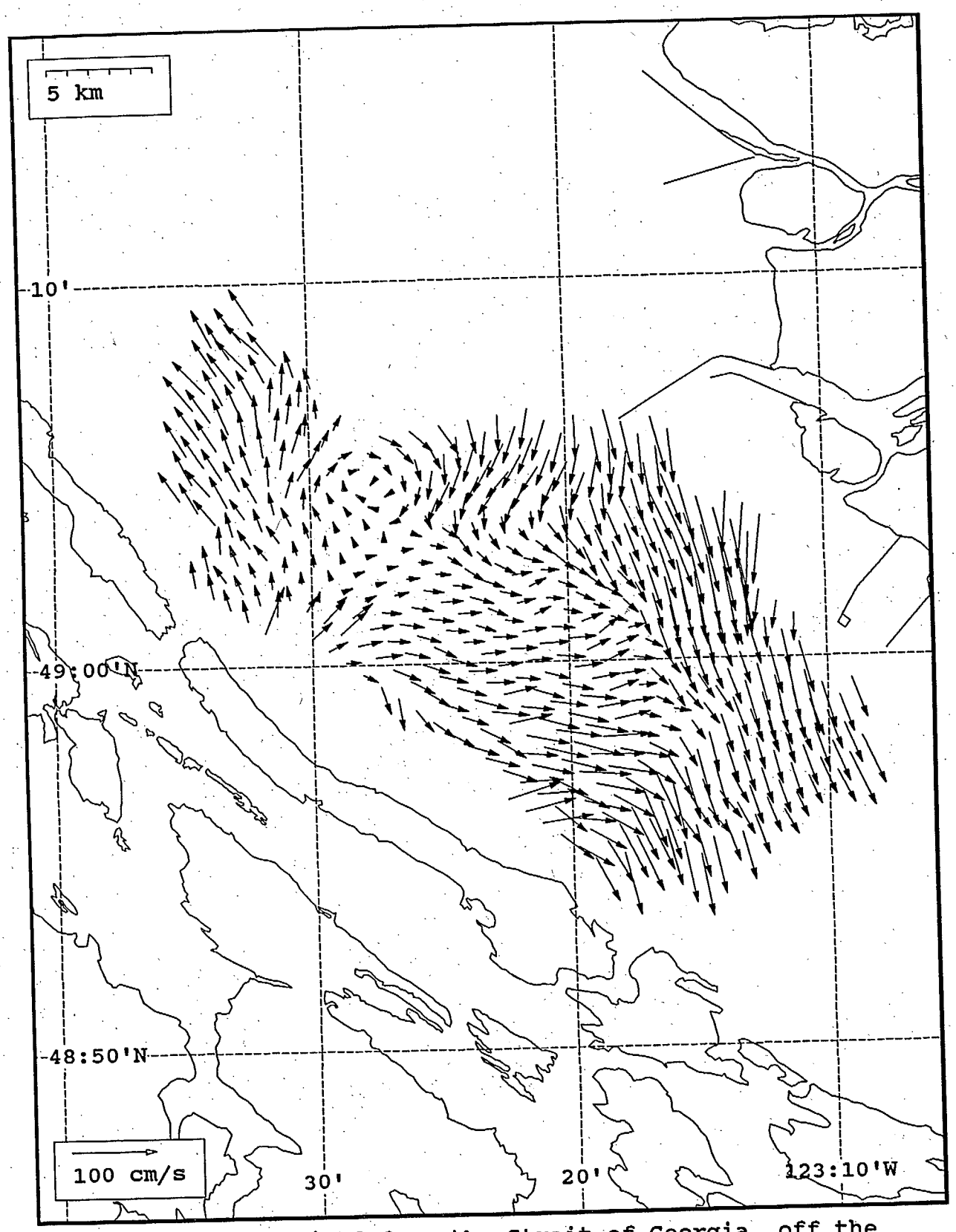

SeaSonde current field from the Strait of Georgia, off the mouth of the Fraser River, for 06:00 Z, July 23, 1993.

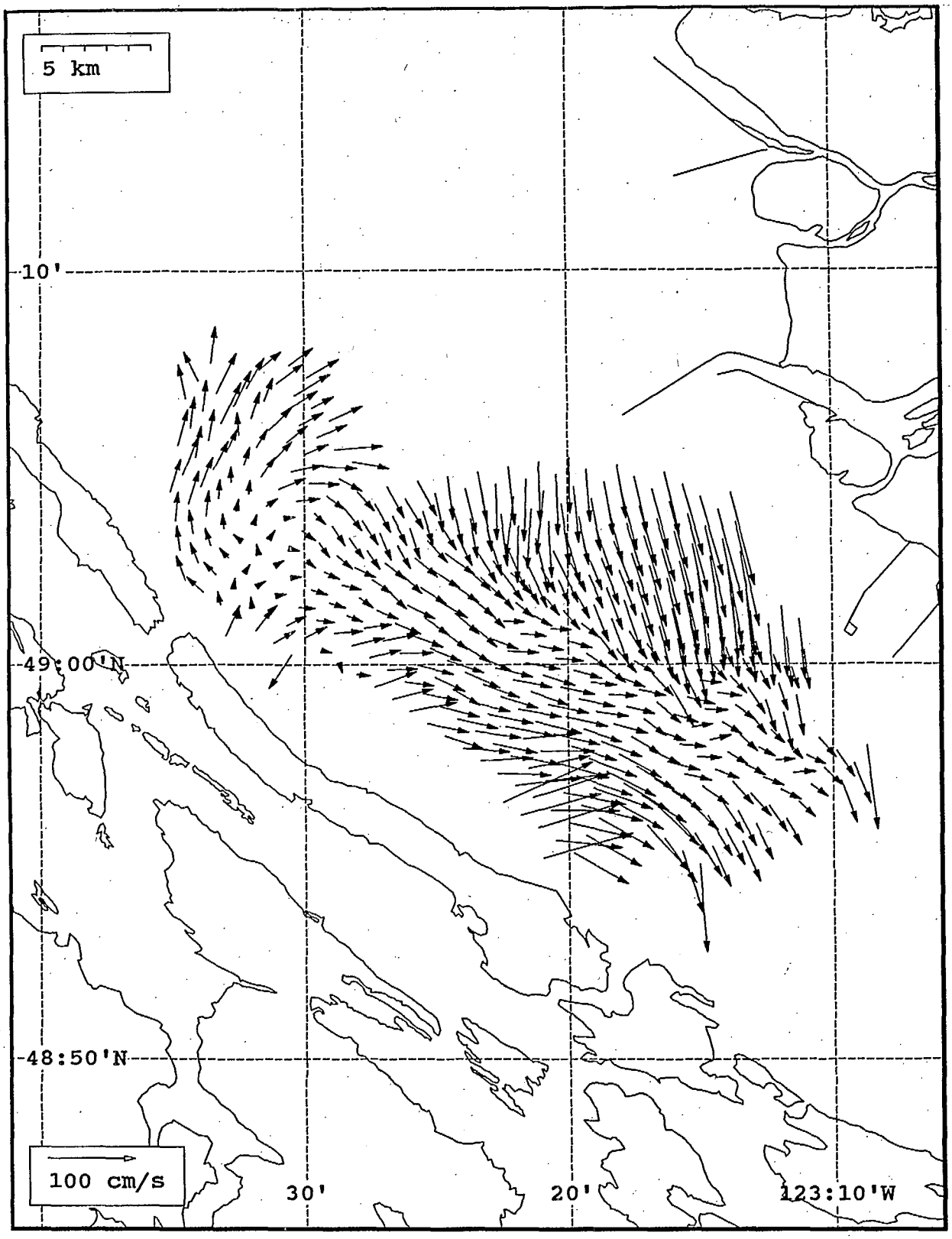

SeaSonde current field from the Strait of Georgia, off the mouth of the Fraser River, for 07:00 Z, July 23, 1993.

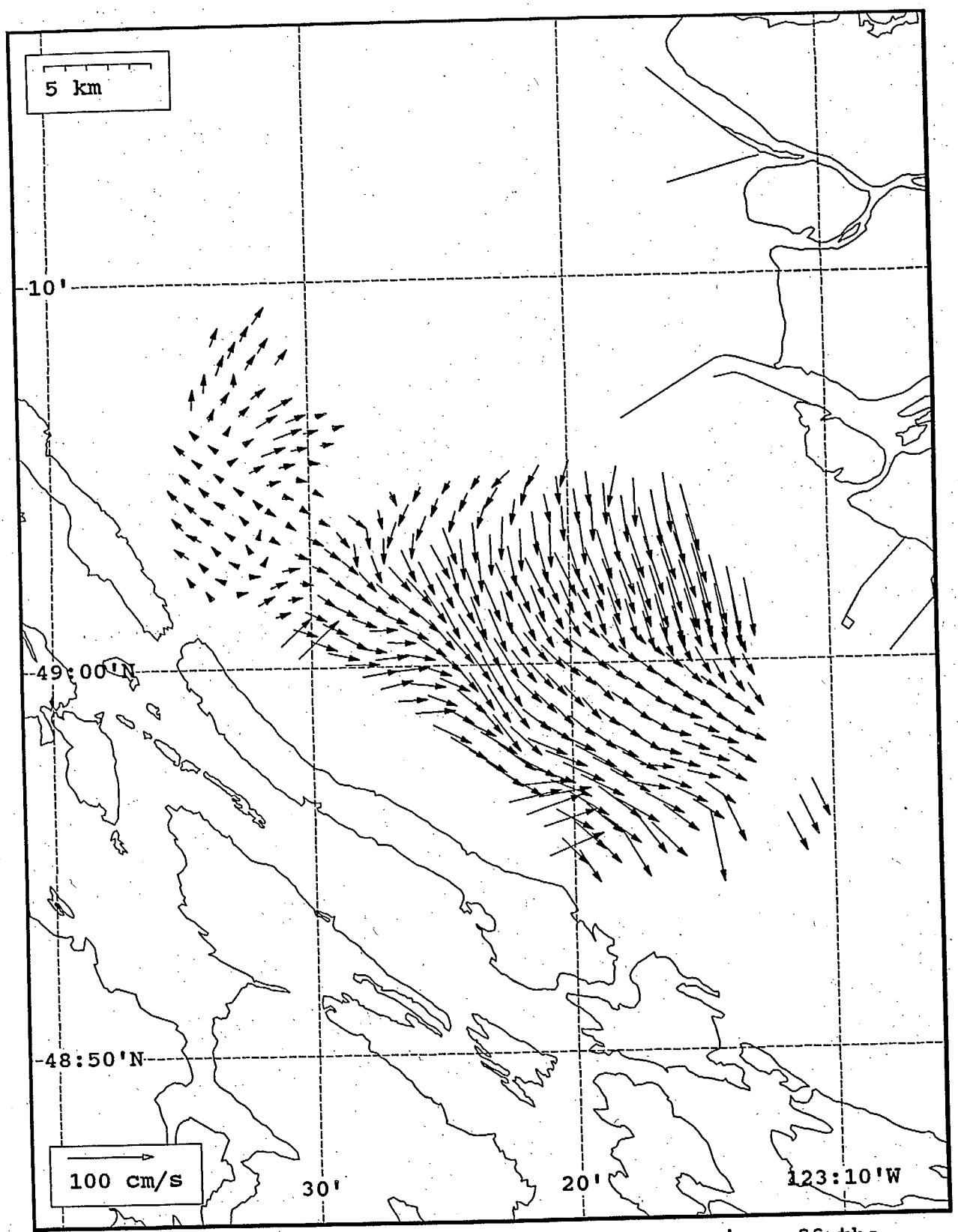

SeaSonde current field from the Strait of Georgia, off the mouth of the Fraser River, for 08:00 Z, July 23, 1993.

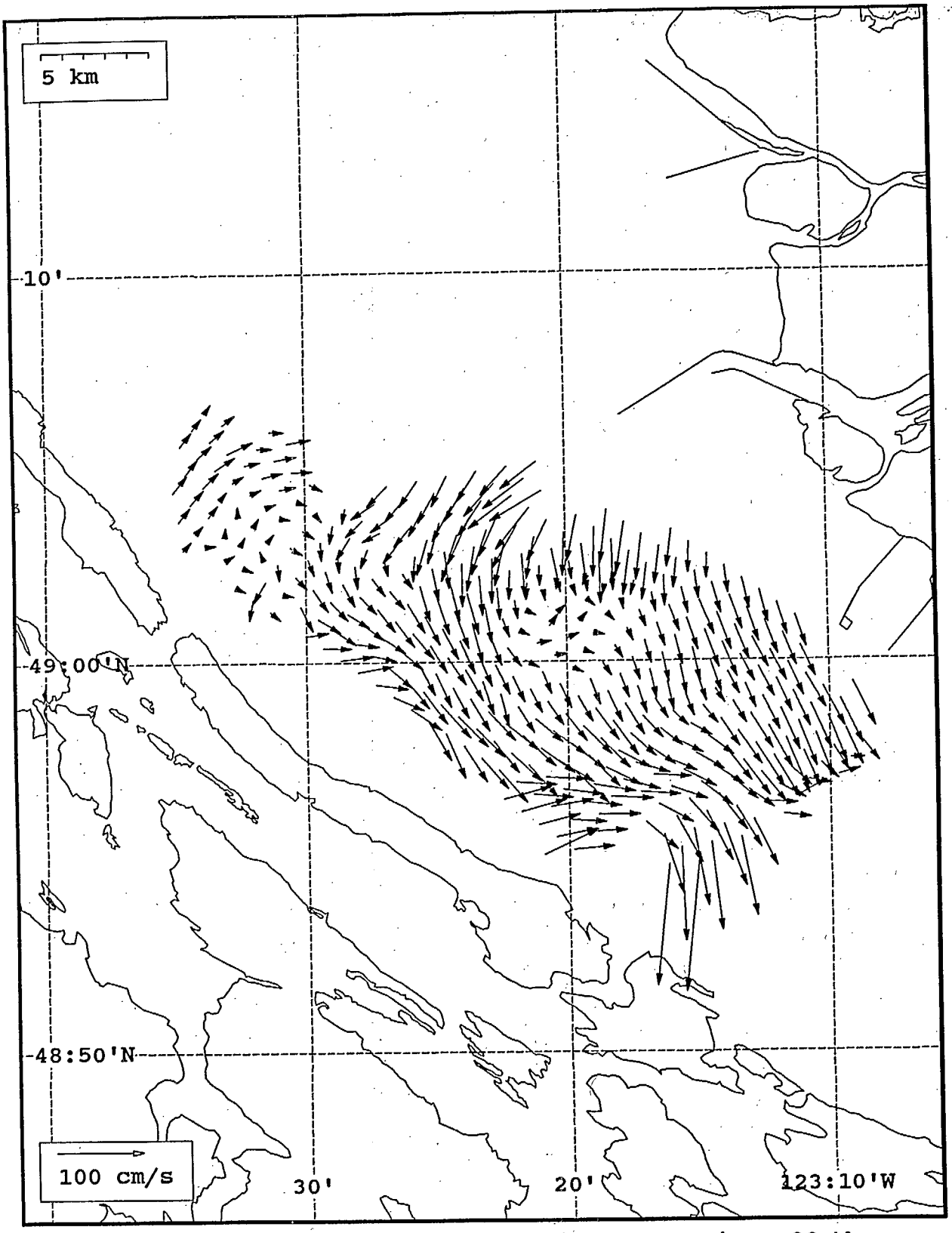

SeaSonde current field from the Strait of Georgia, off the mouth of the Fraser River, for 09:00 Z, July 23, 1993.

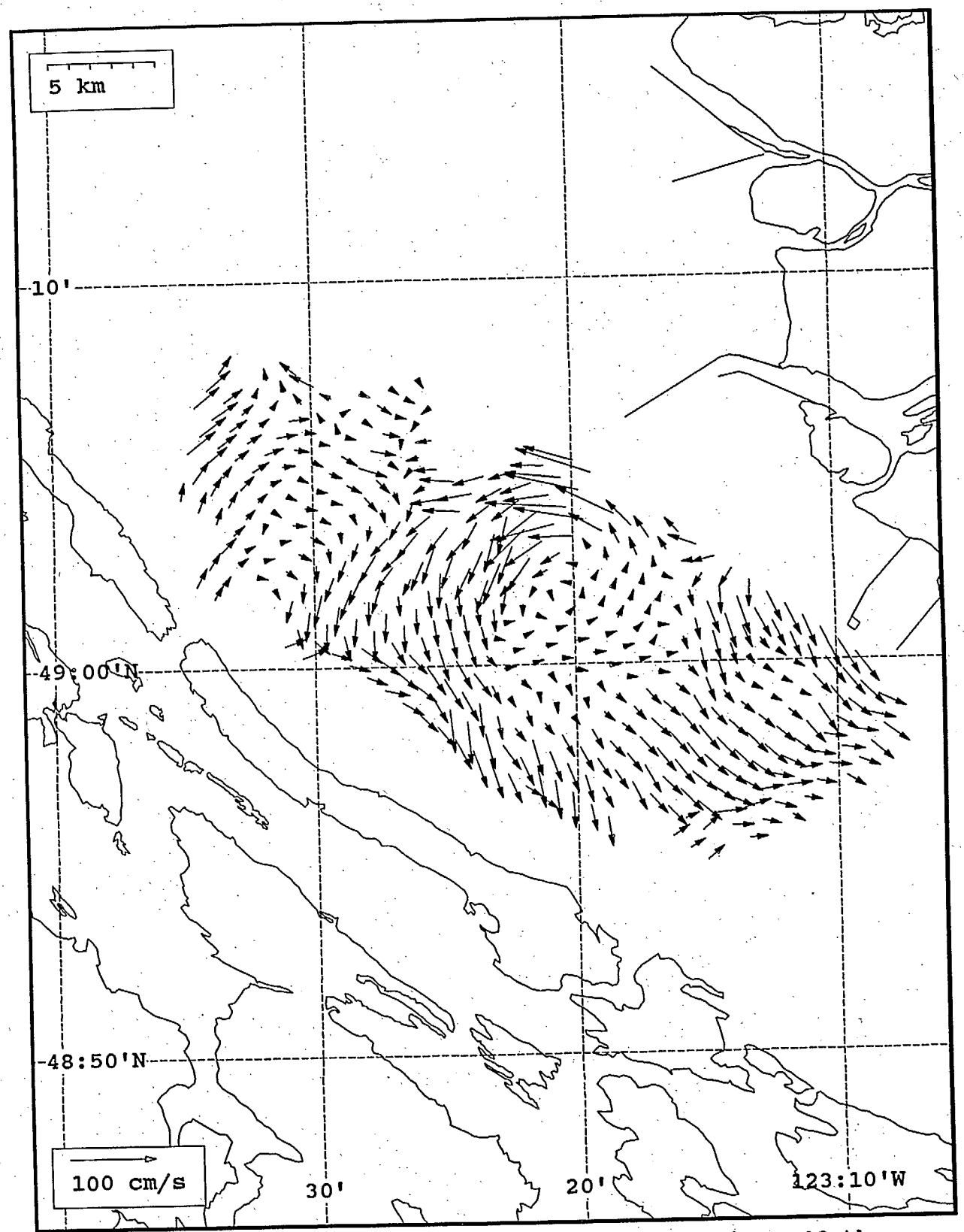

SeaSonde current field from the Strait of Georgia, off the mouth of the Fraser River, for 10:00 Z, July 23, 1993.

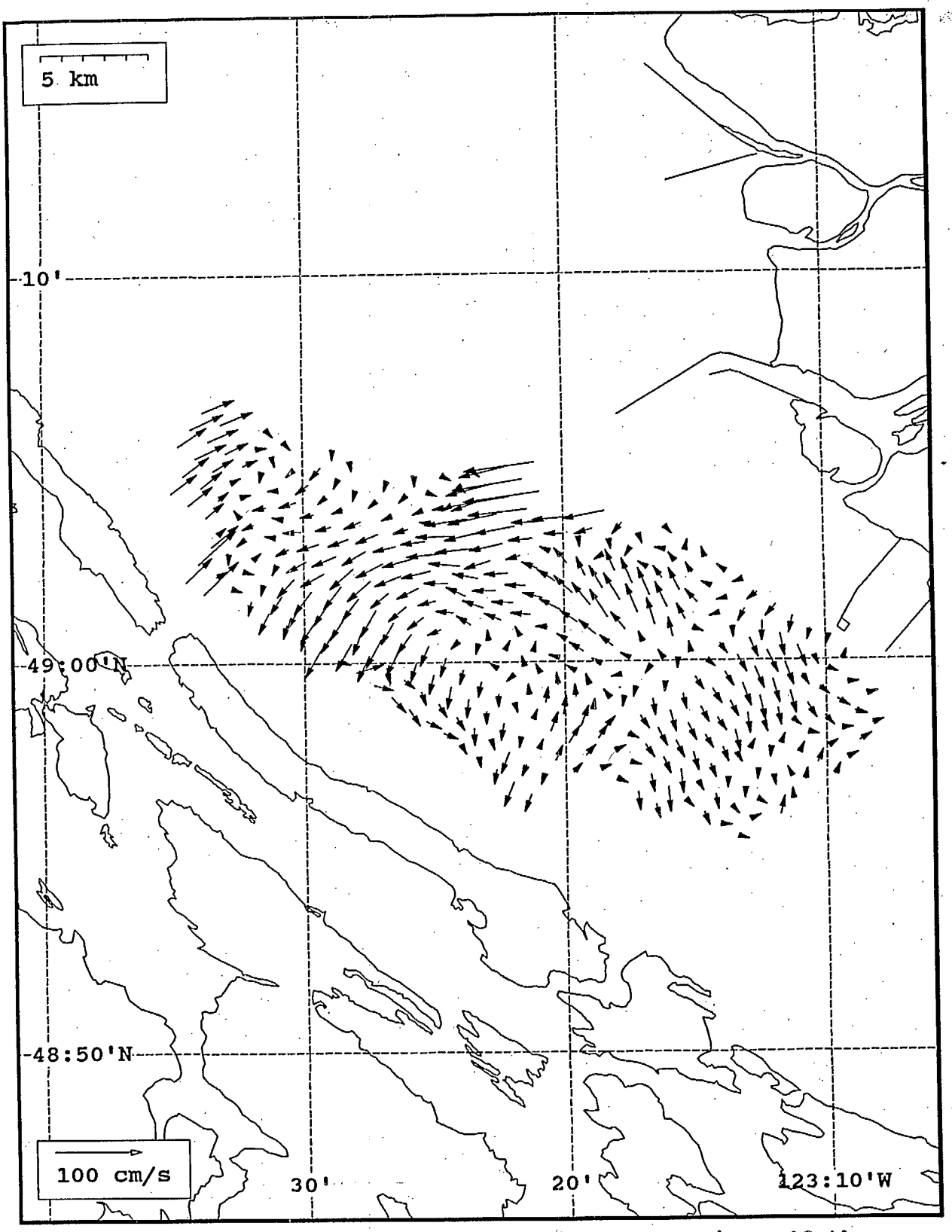

SeaSonde current field from the Strait of Georgia, off the mouth of the Fraser River, for 11:00 Z, July 23, 1993.

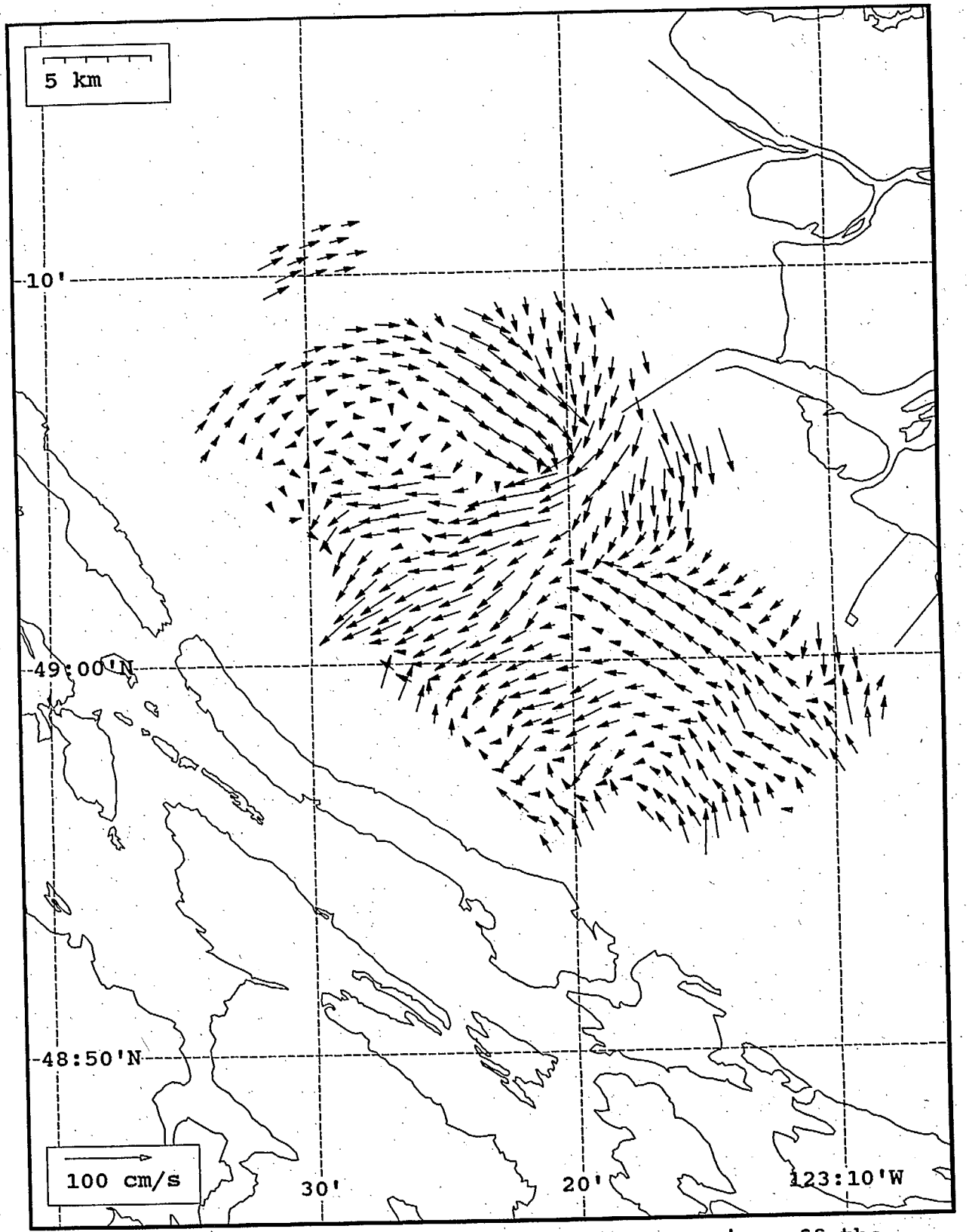

SeaSonde current field from the Strait of Georgia, off the mouth of the Fraser River, for 12:00 Z, July 23, 1993.

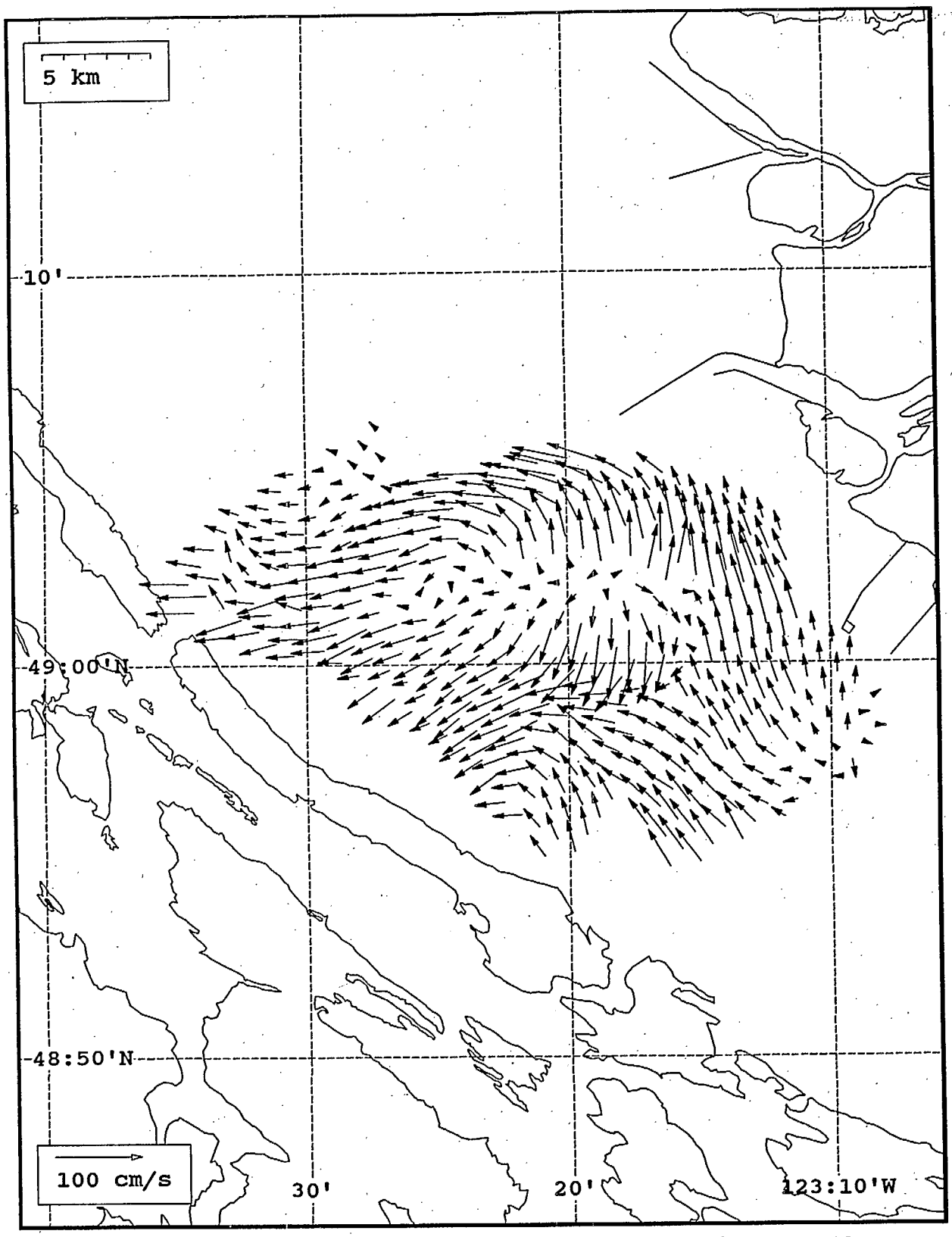

SeaSonde current field from the Strait of Georgia, off the mouth of the Fraser River, for 13:00 Z, July 23, 1993.

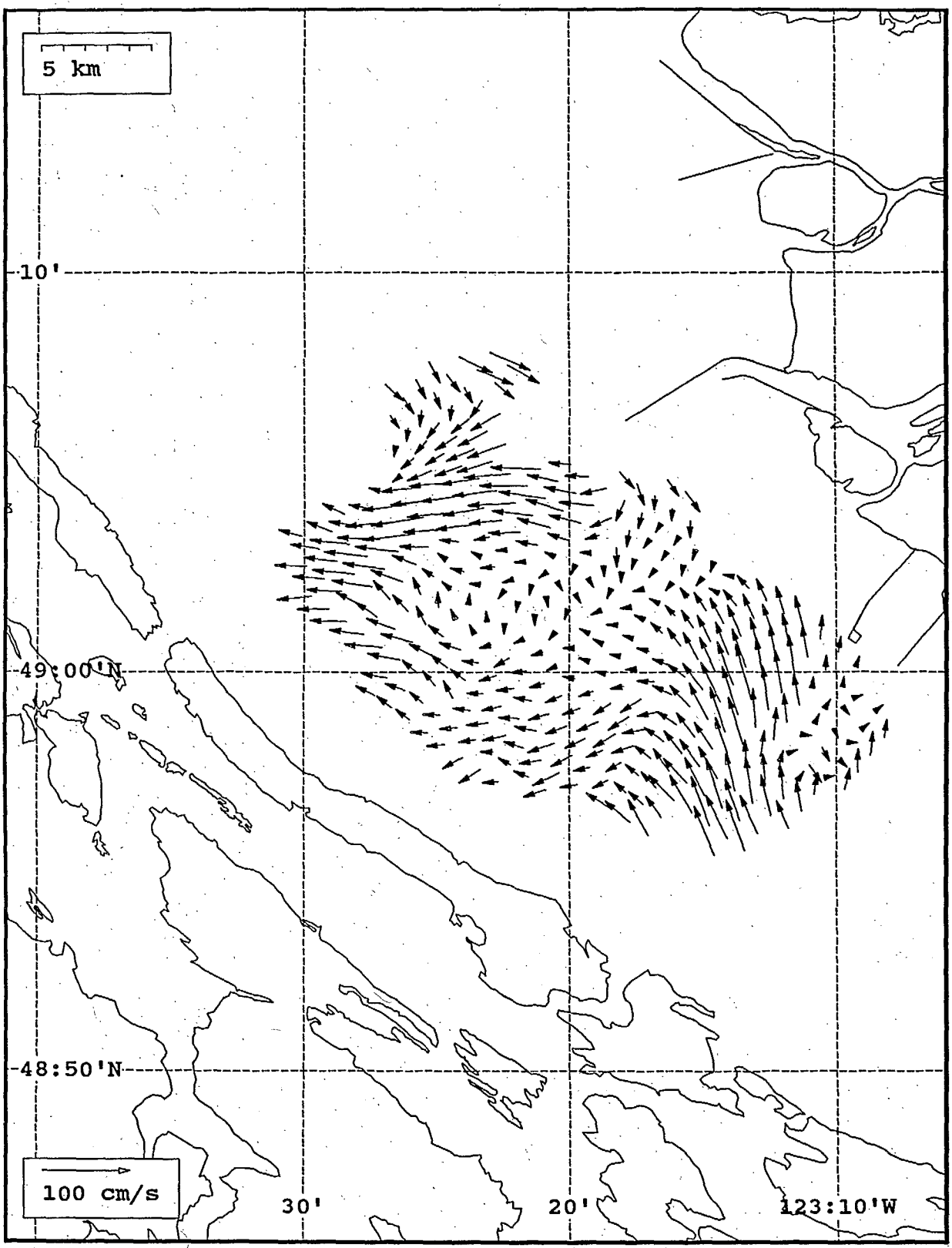

SeaSonde current field from the Strait of Georgia, off the mouth of the Fraser River, for 14:00 Z, July 23, 1993.

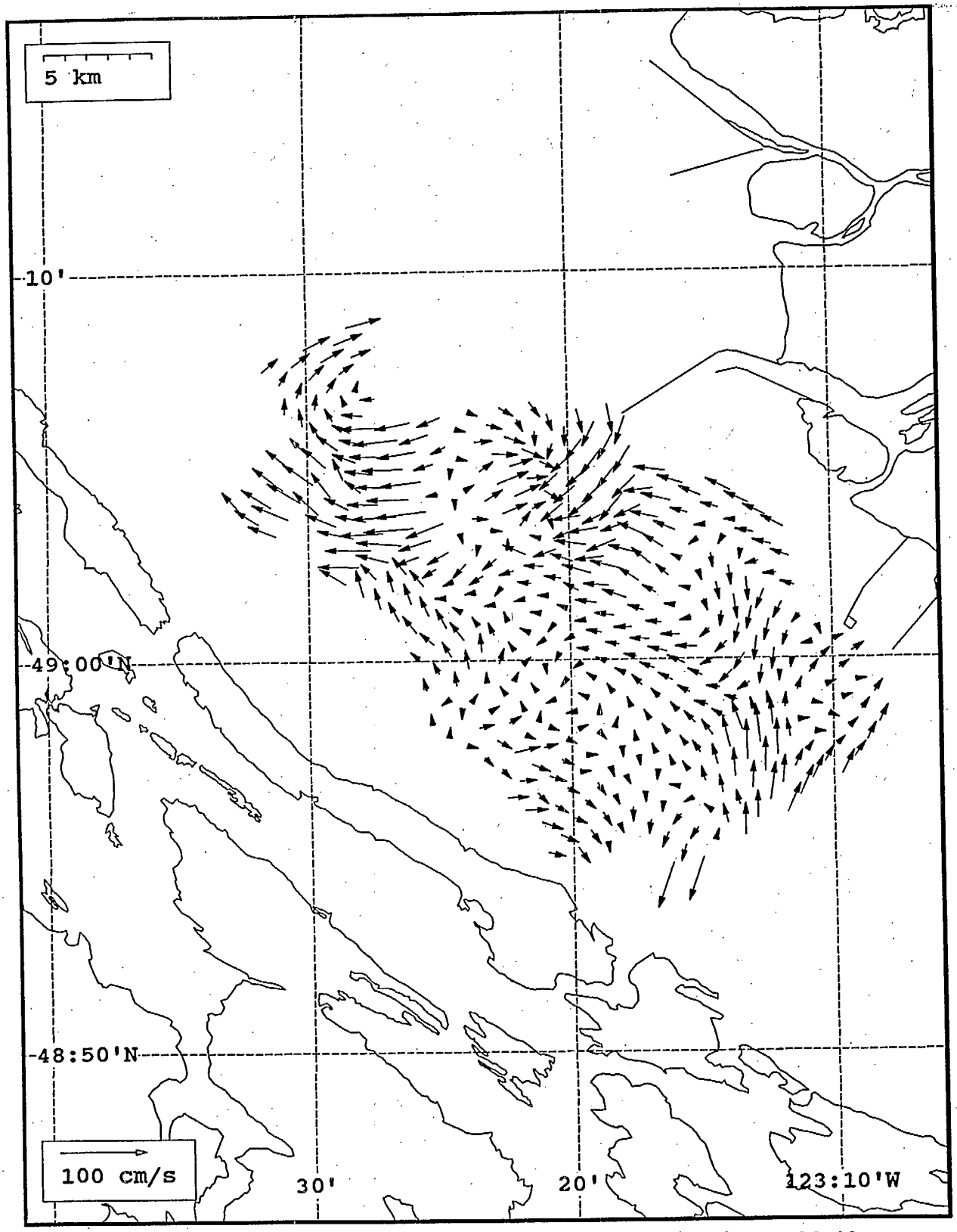

SeaSonde current field from the Strait of Georgia, off the mouth of the Fraser River, for 15:00 Z, July 23, 1993.

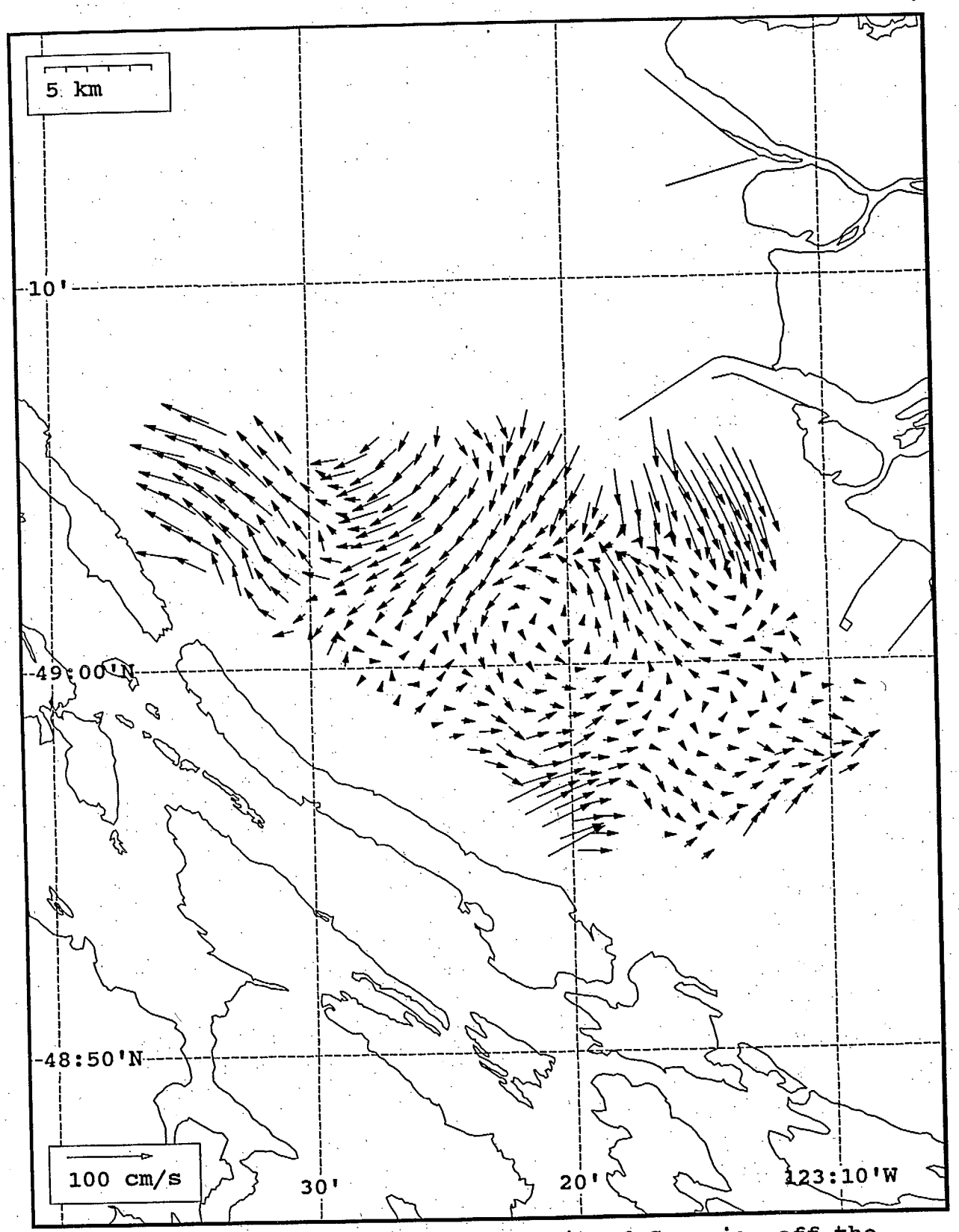

SeaSonde current field from the Strait of Georgia, off the mouth of the Fraser River, for 16:00 Z, July 23, 1993.

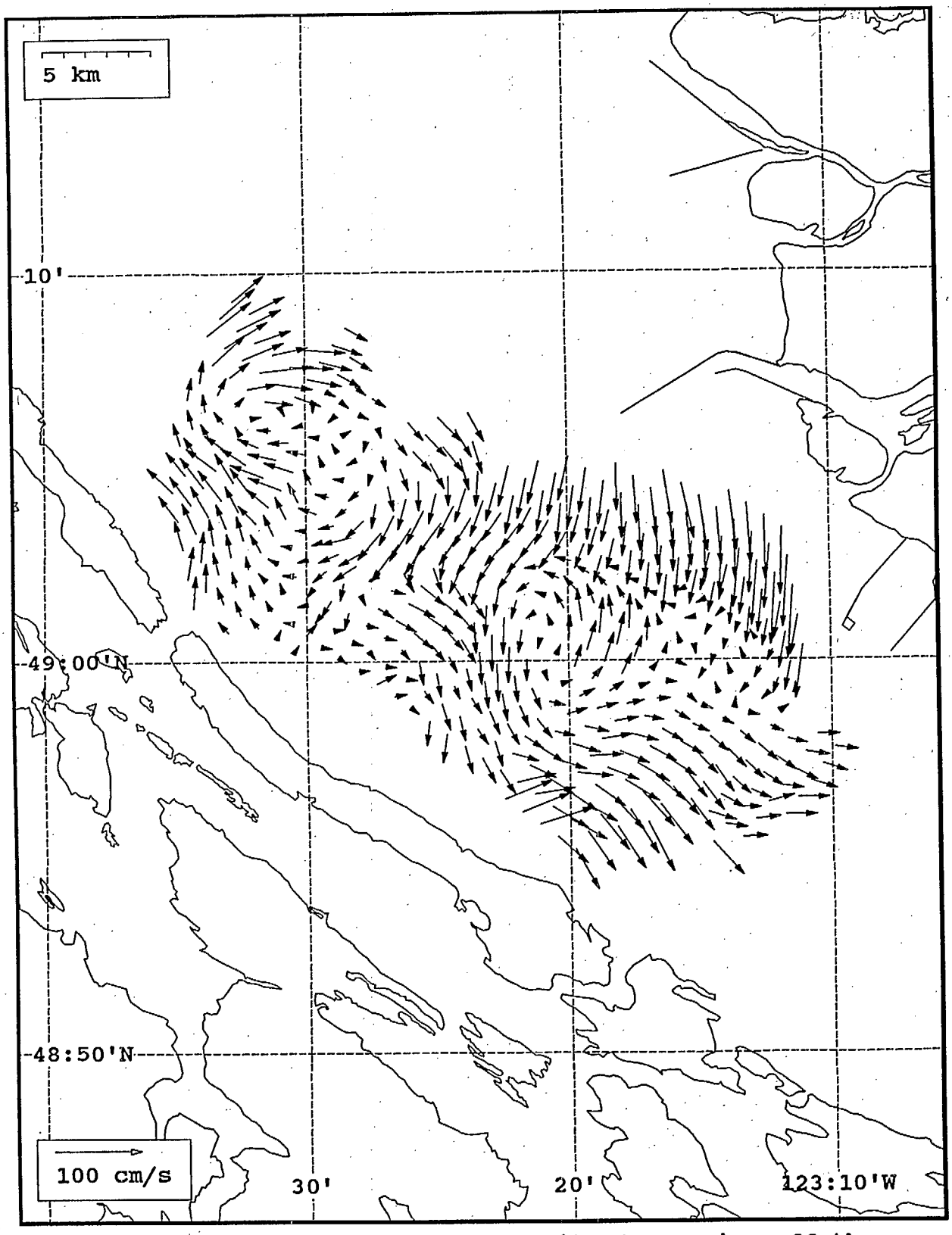

SeaSonde current field from the Strait of Georgia, off the mouth of the Fraser River, for 17:00 Z, July 23, 1993.

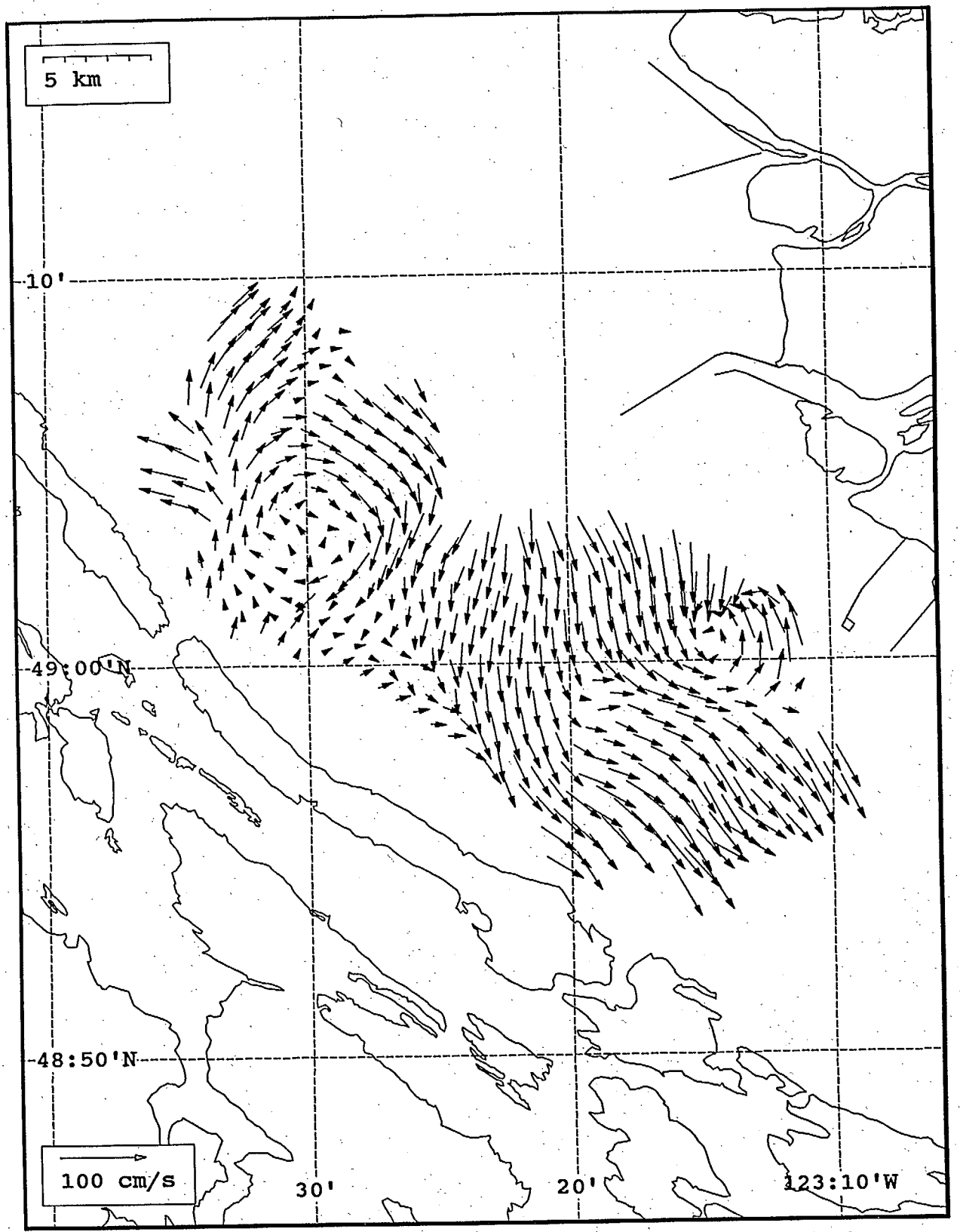

SeaSonde current field from the Strait of Georgia, off the mouth of the Fraser River, for 18:00 Z, July 23, 1993.

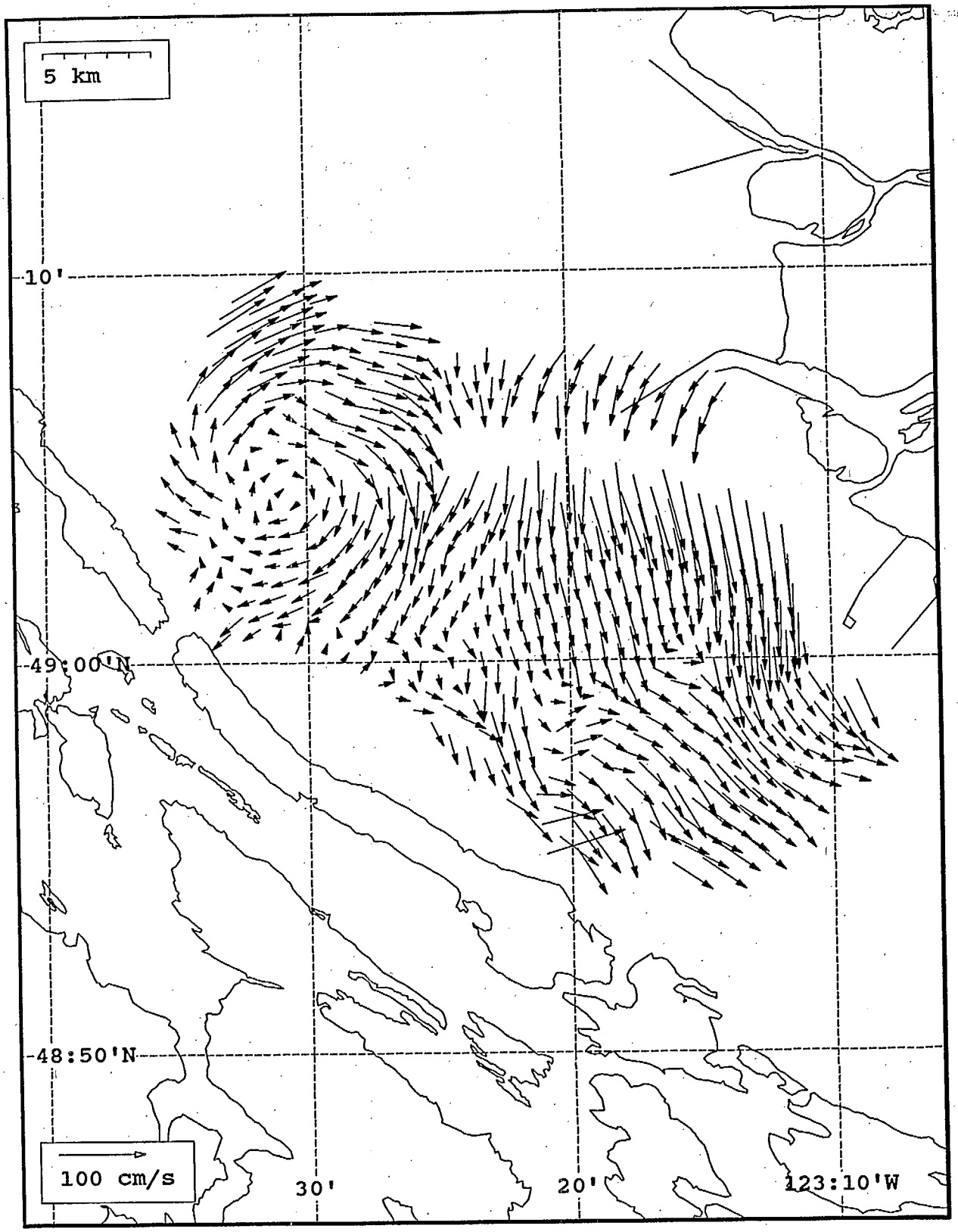

SeaSonde current field from the Strait of Georgia, off the mouth of the Fraser River, for 19:00 Z, July 23, 1993.

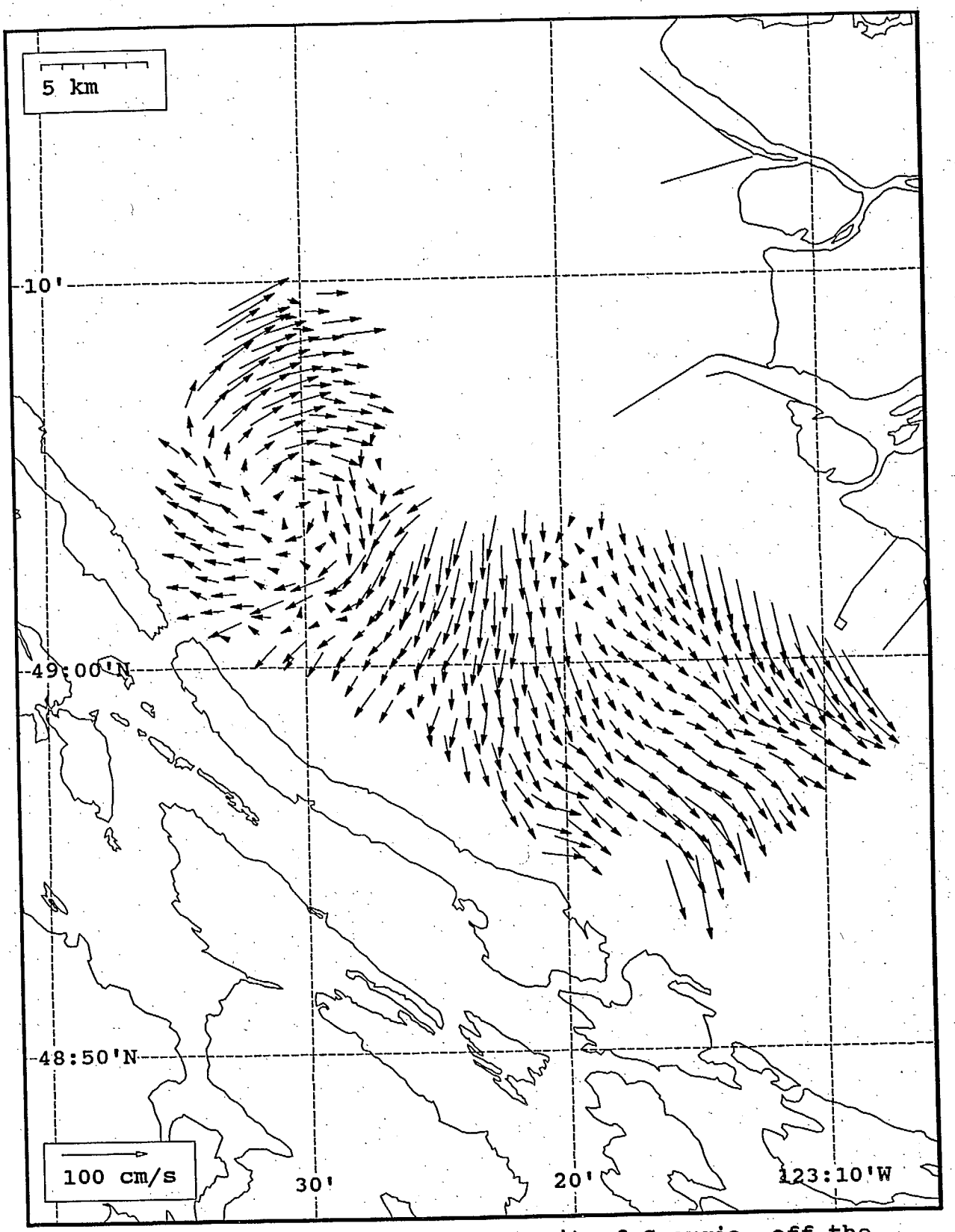

SeaSonde current field from the Strait of Georgia, off the mouth of the Fraser River, for 20:00 Z, July 23, 1993.

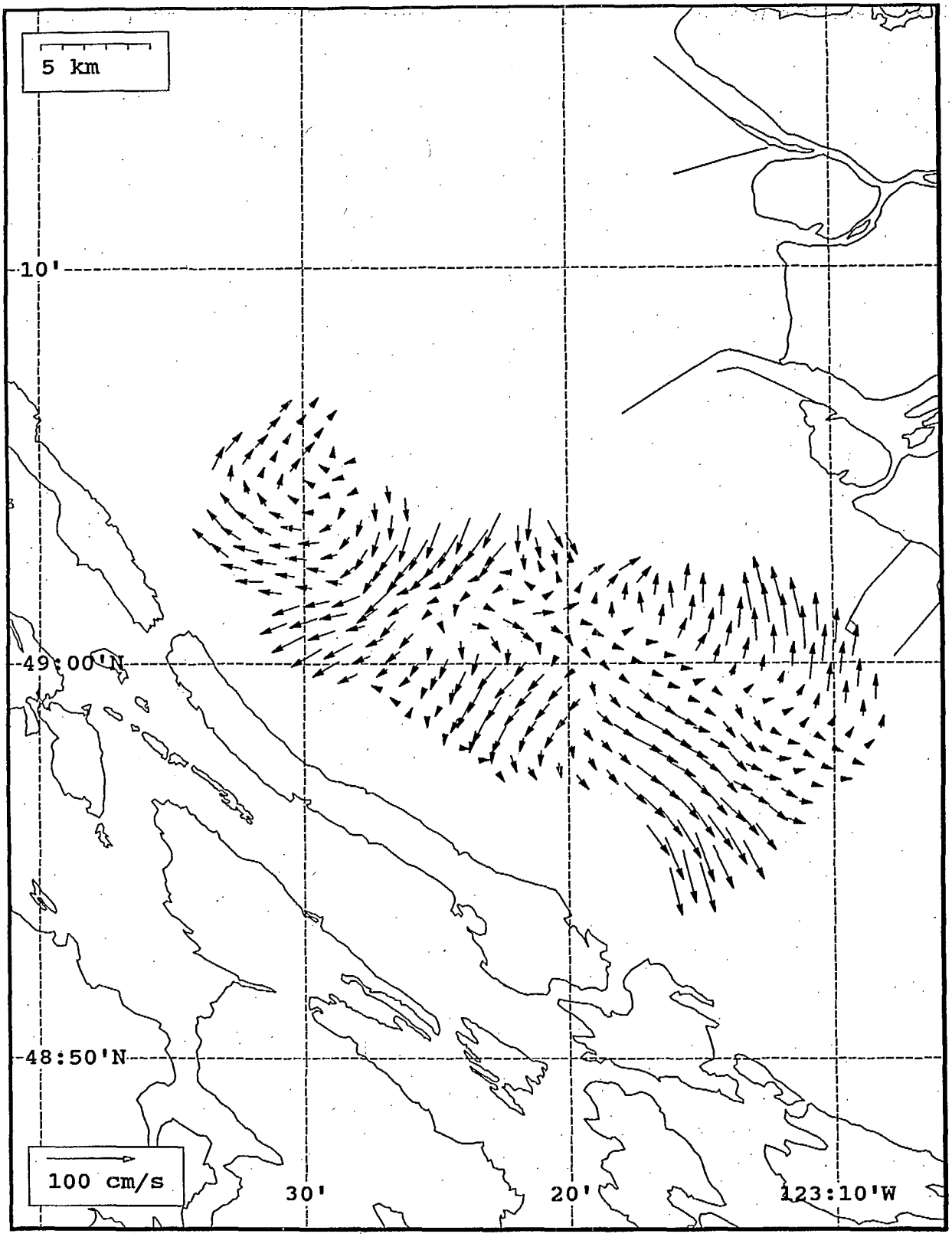

SeaSonde current field from the Strait of Georgia, off the mouth of the Fraser River, for 21:00 Z, July 23, 1993.

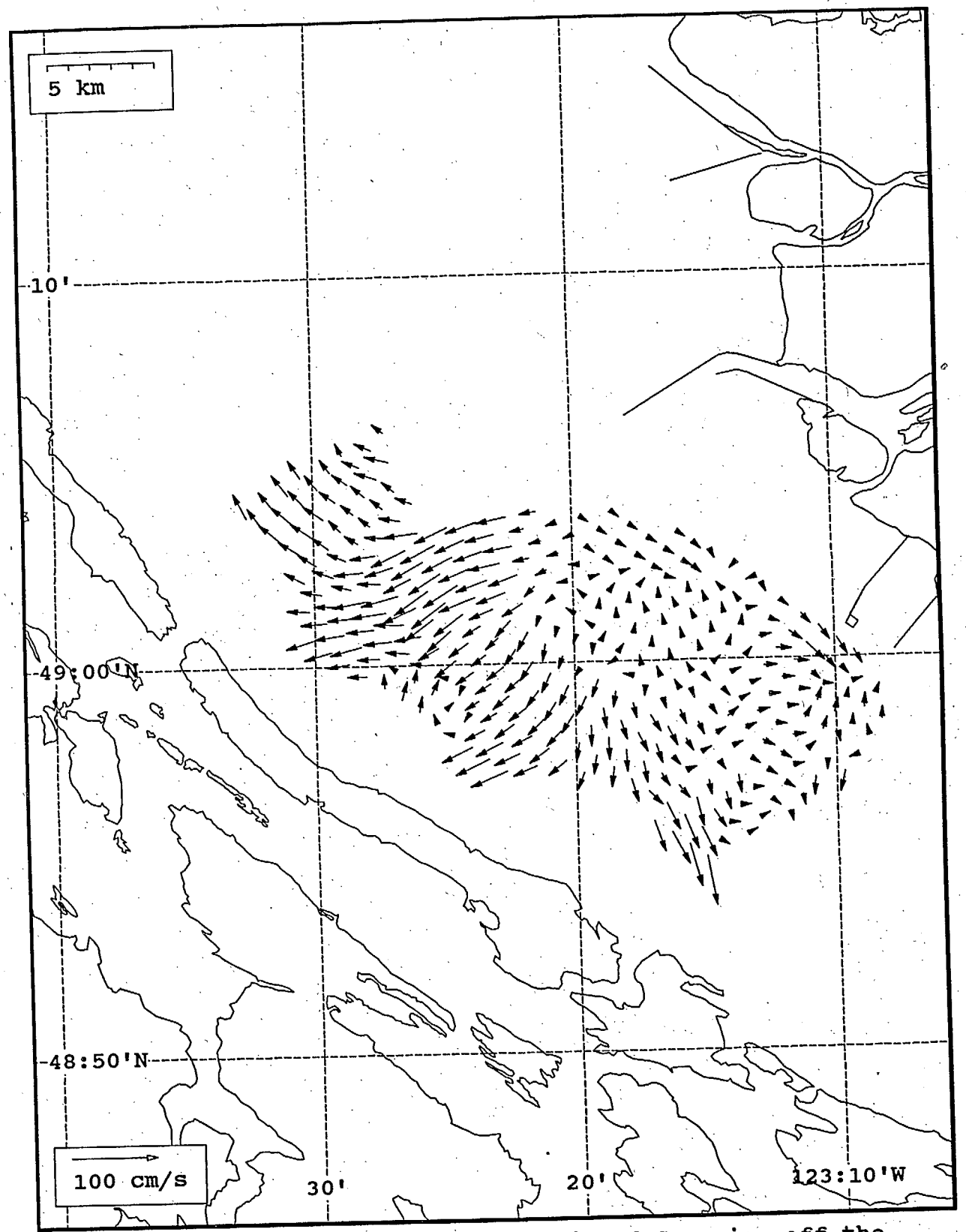

SeaSonde current field from the Strait of Georgia, off the mouth of the Fraser River, for 22:00 Z, July 23, 1993.

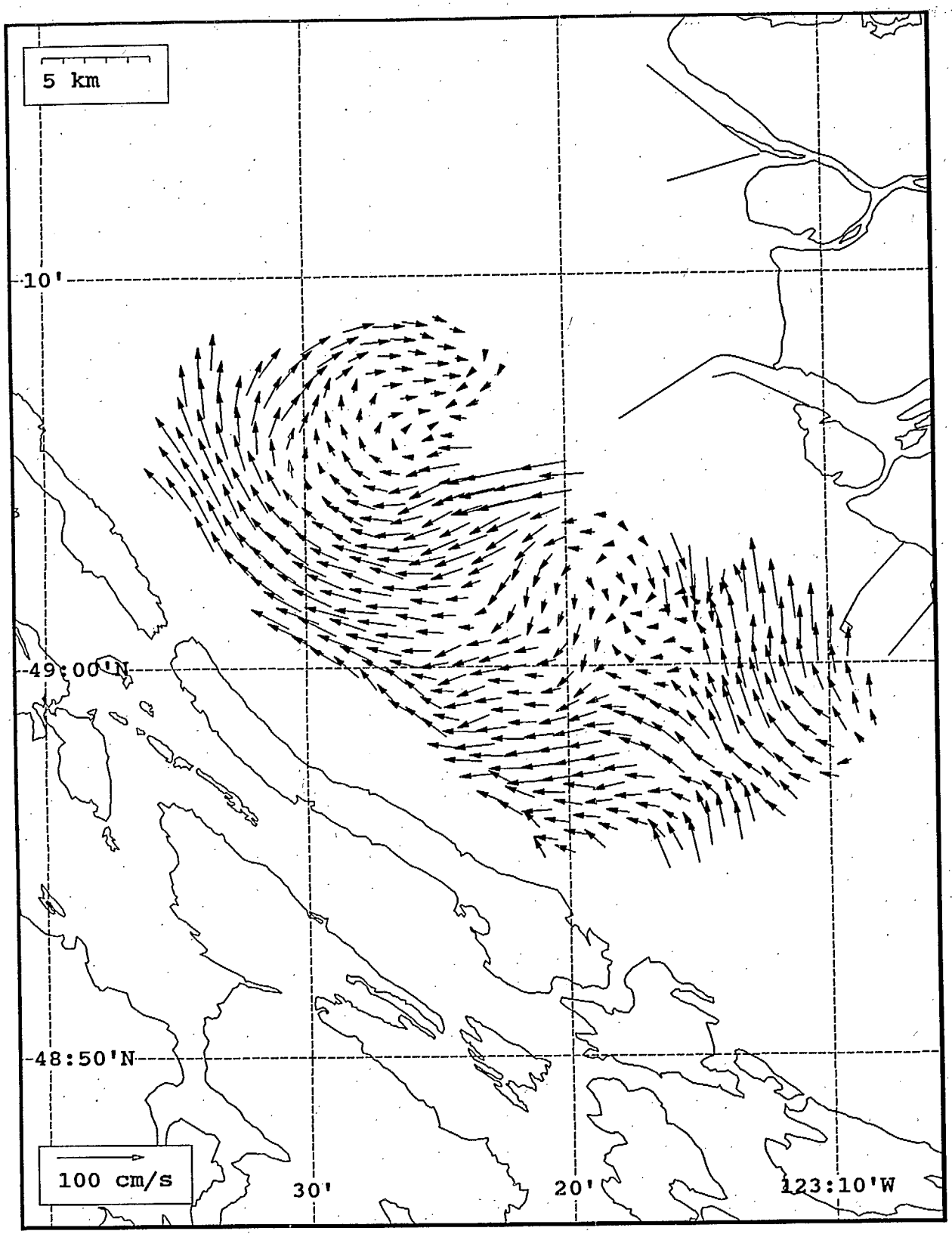

SeaSonde current field from the Strait of Georgia, off the mouth of the Fraser River, for 23:00 Z, July 23, 1993.

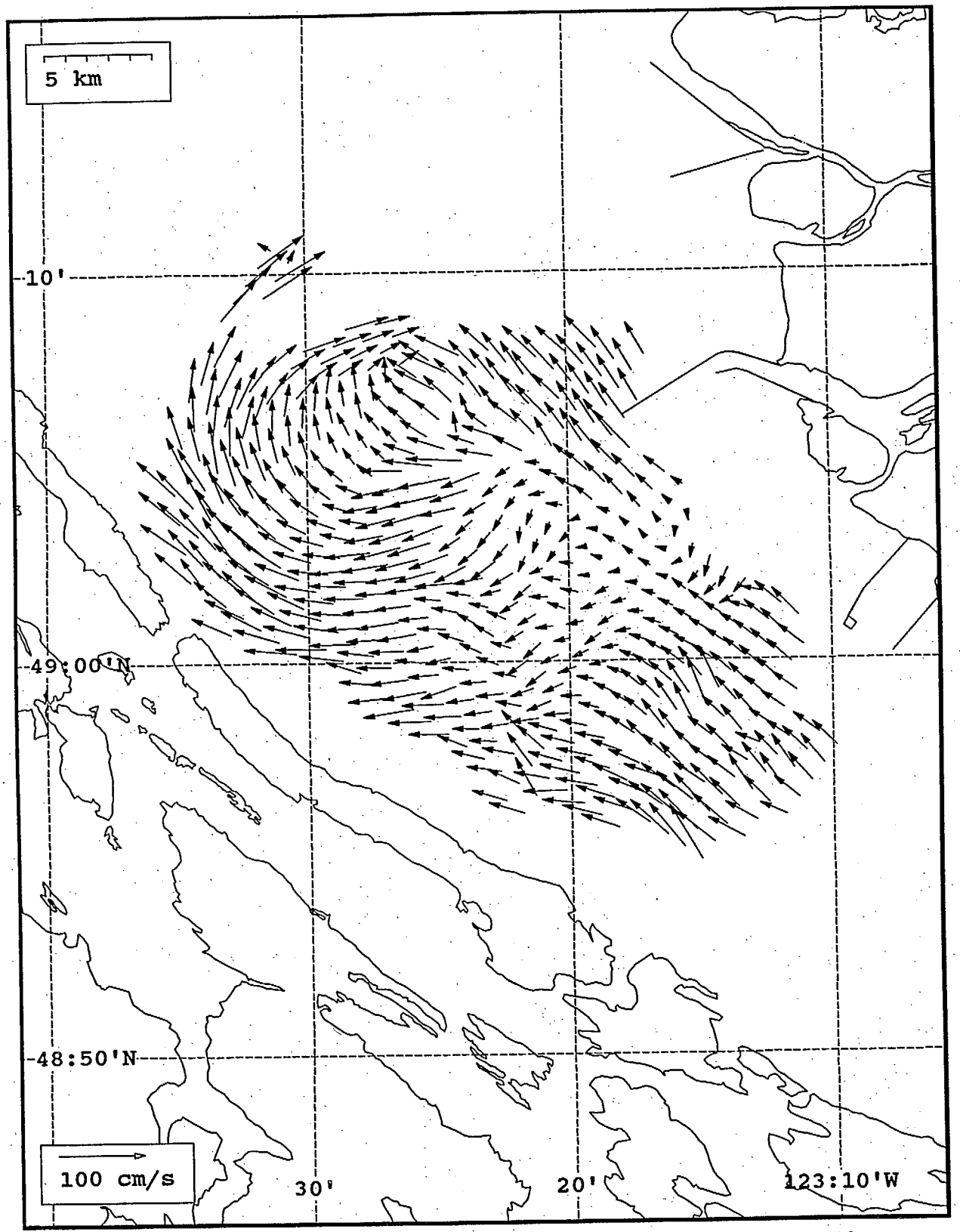

SeaSonde current field from the Strait of Georgia, off the mouth of the Fraser River, for 00:00 Z, July 24, 1993.

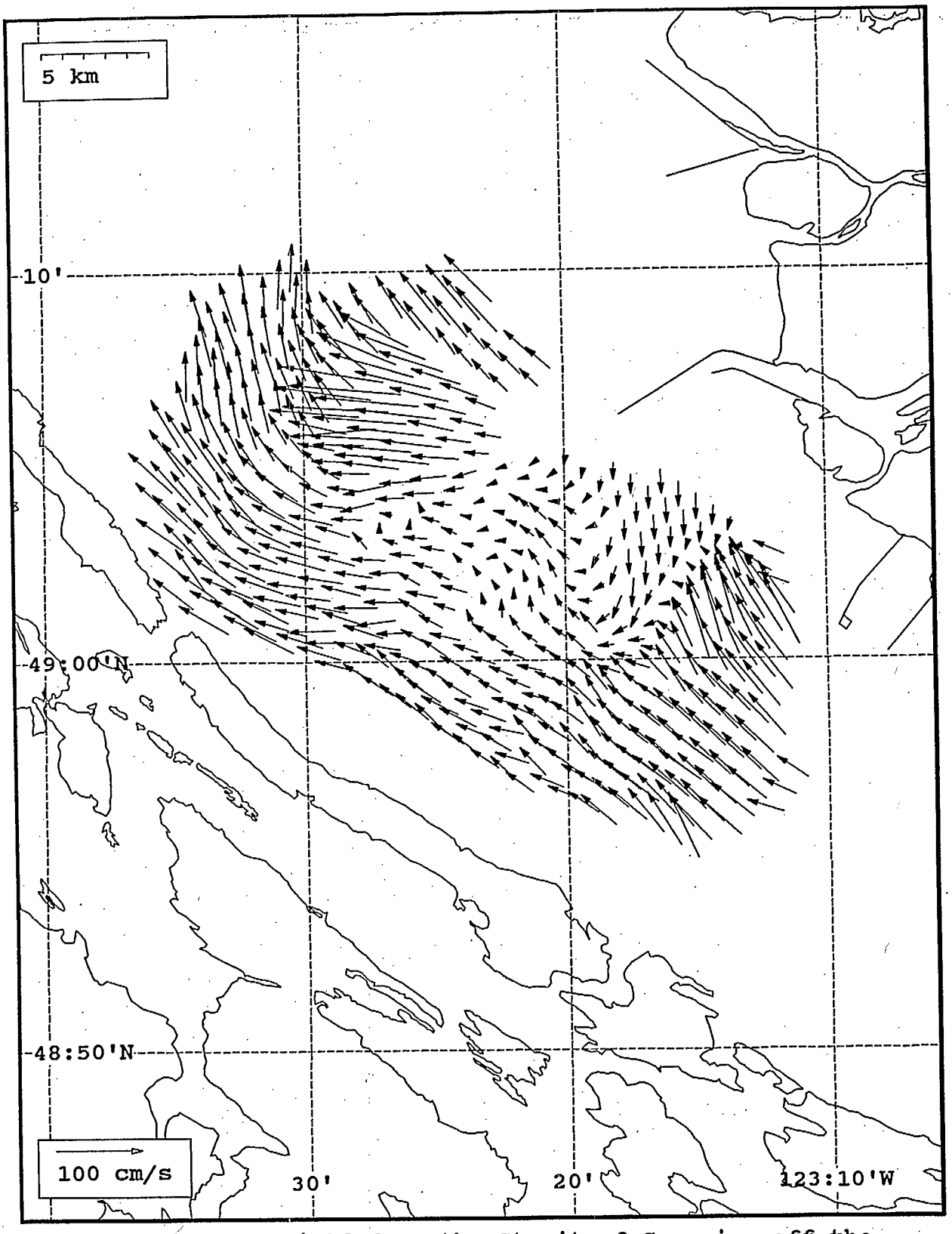

SeaSonde current field from the Strait of Georgia, off the mouth of the Fraser River, for 01:00 Z, July 24, 1993.

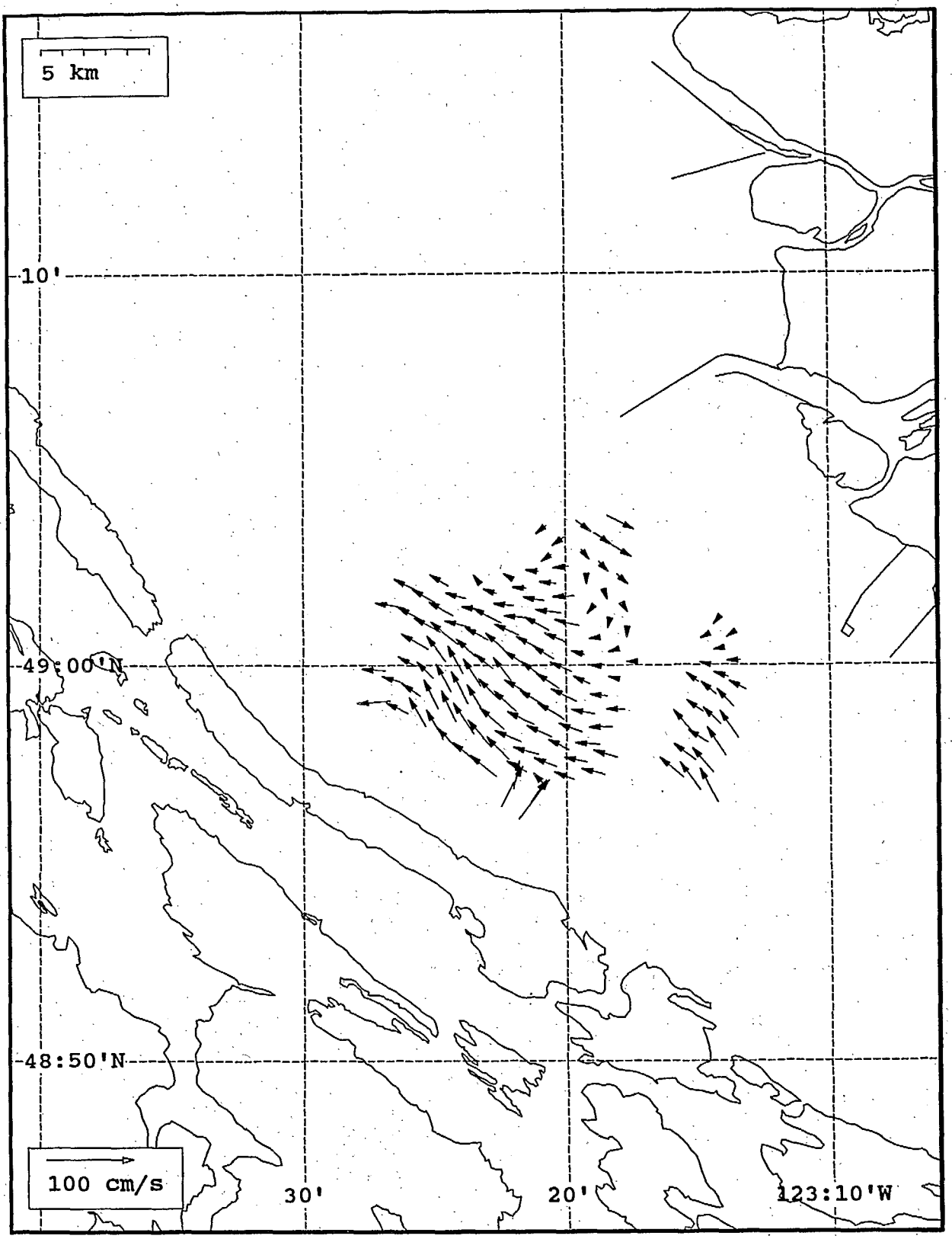

SeaSonde current field from the Strait of Georgia, off the mouth of the Fraser River, for 02:00 Z, July 24, 1993.

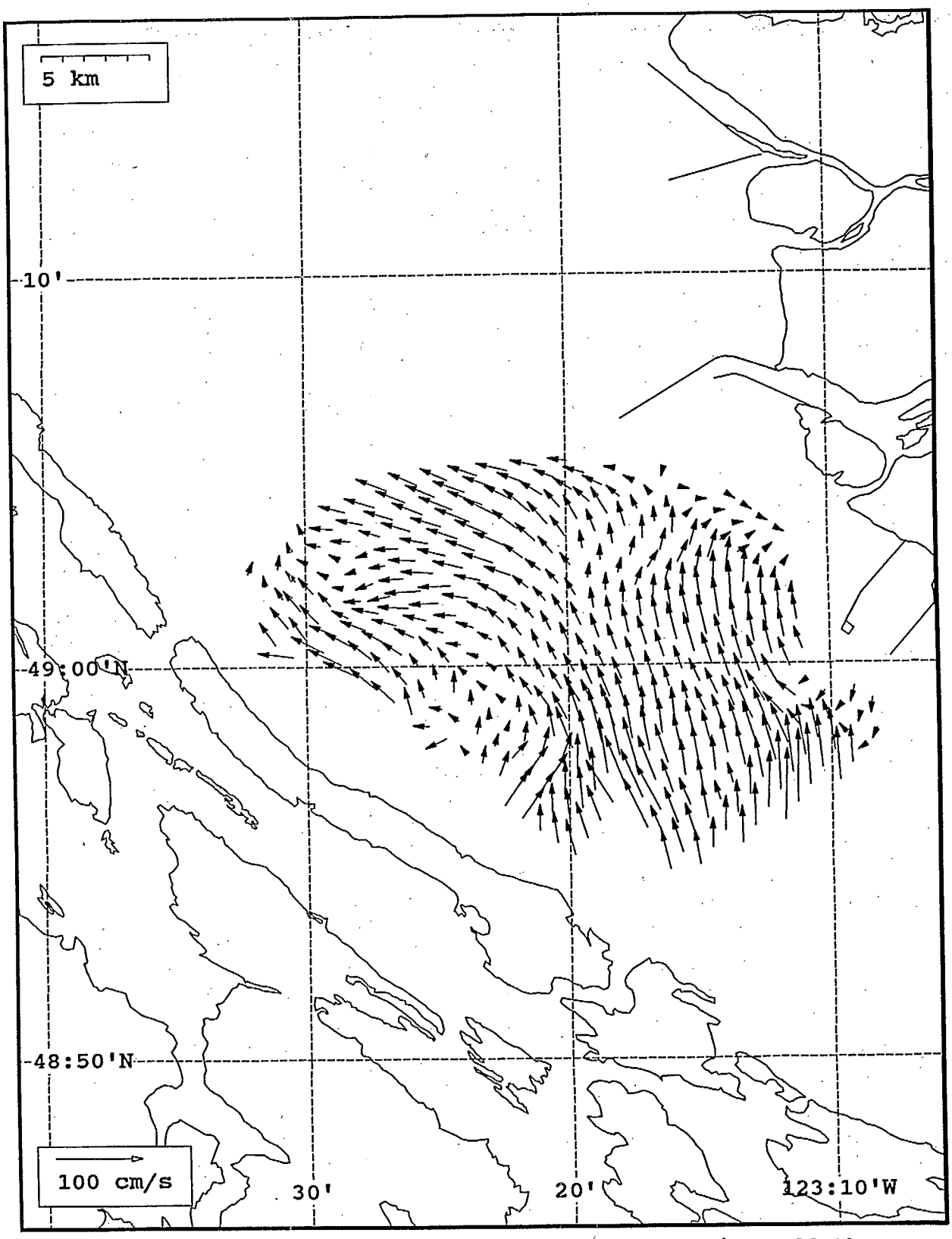

SeaSonde current field from the Strait of Georgia, off the mouth of the Fraser River, for 03:00 Z, July 24, 1993.

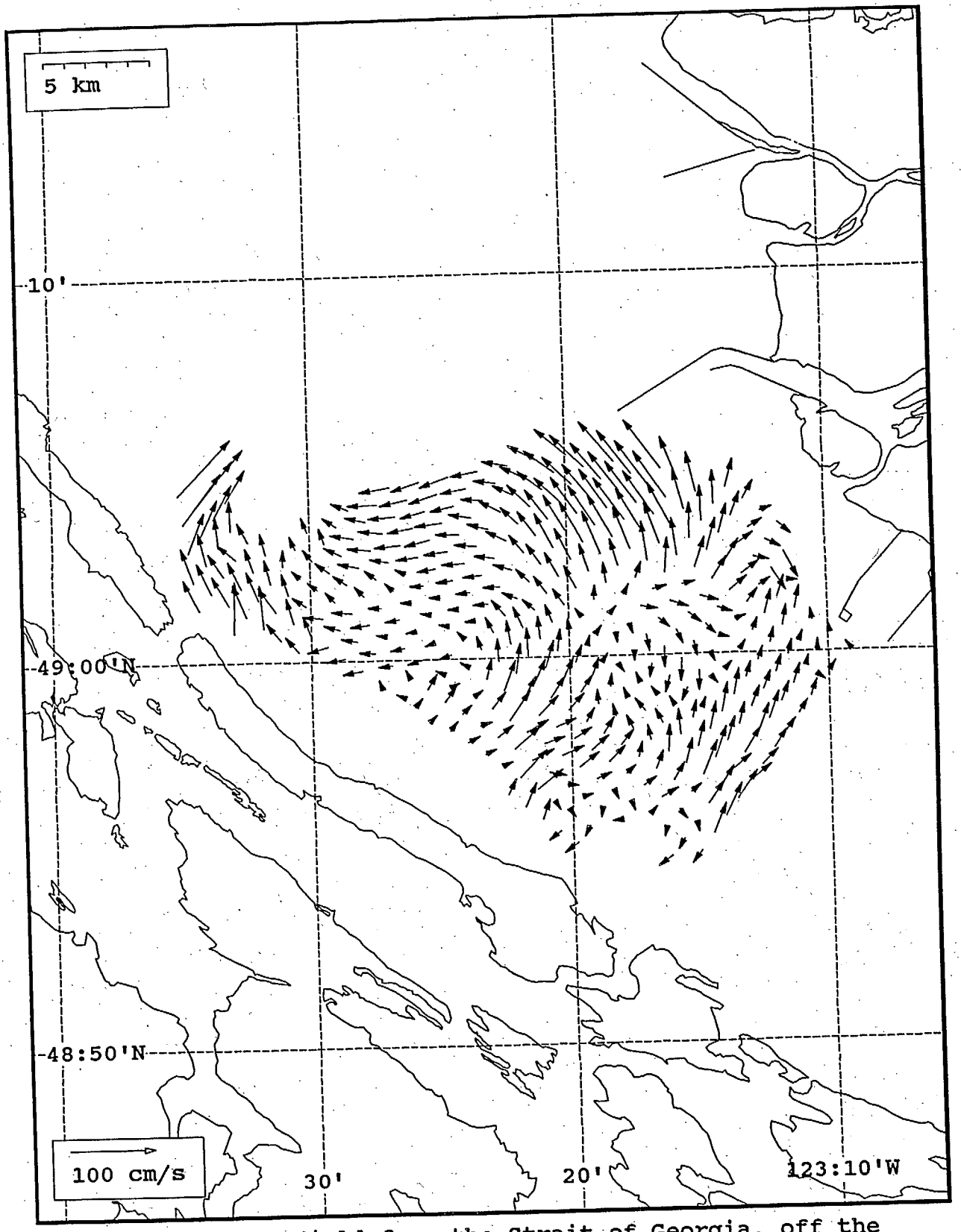

SeaSonde current field from the Strait of Georgia, off the mouth of the Fraser River, for 04:00 Z, July 24, 1993.

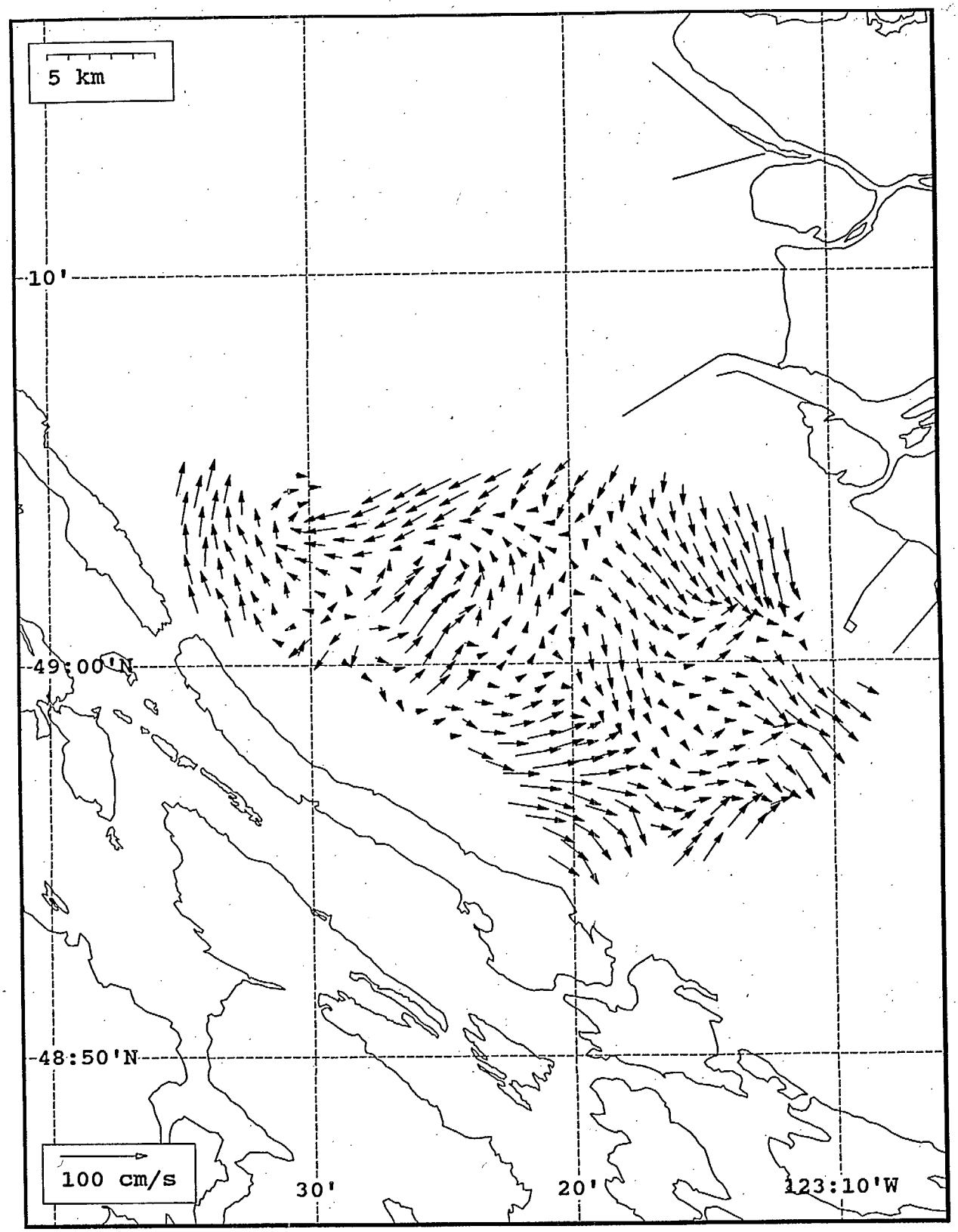

SeaSonde current field from the Strait of Georgia, off the mouth of the Fraser River, for 05:00 Z, July 24, 1993.

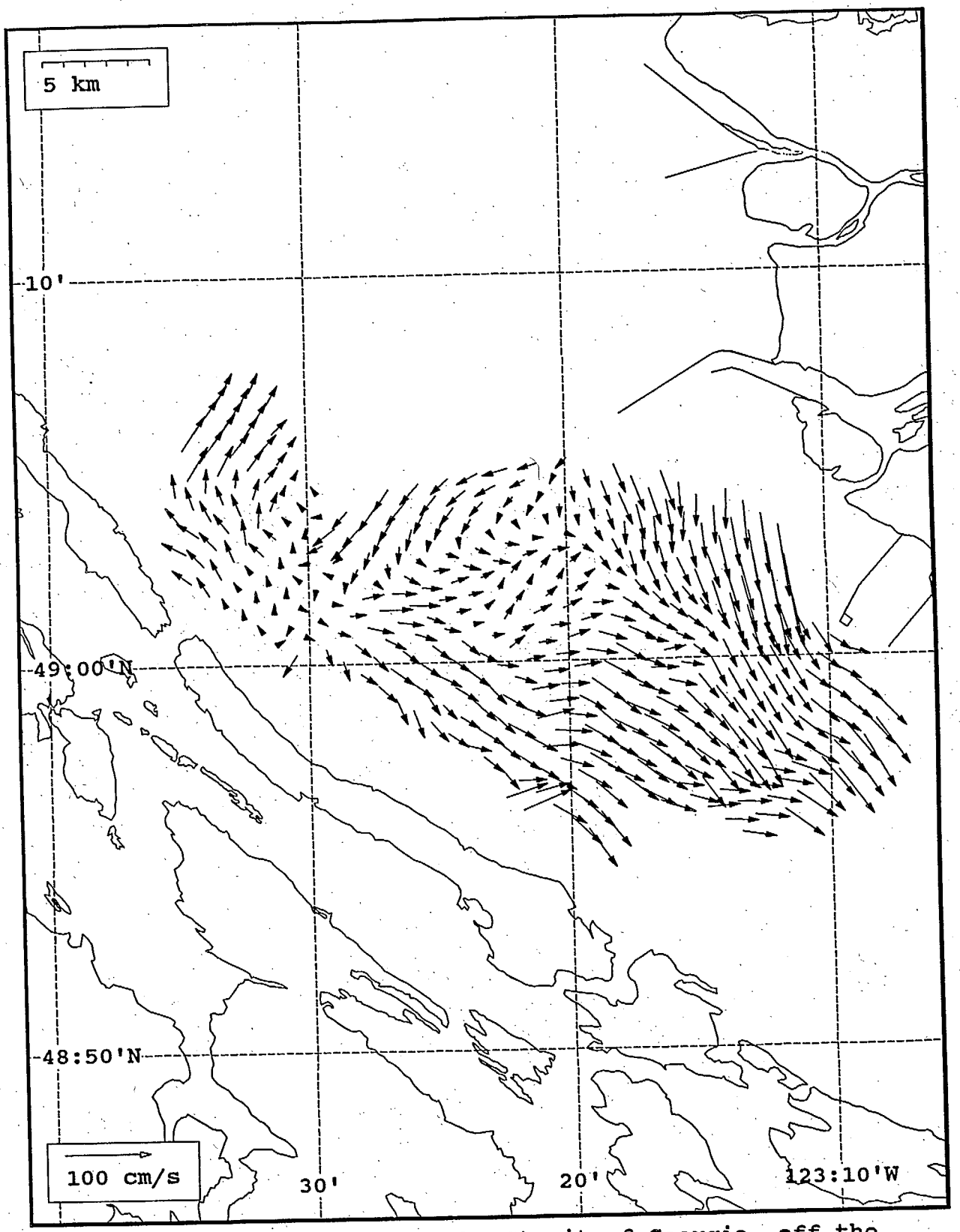

SeaSonde current field from the Strait of Georgia, off the mouth of the Fraser River, for 06:00 Z, July 24, 1993.

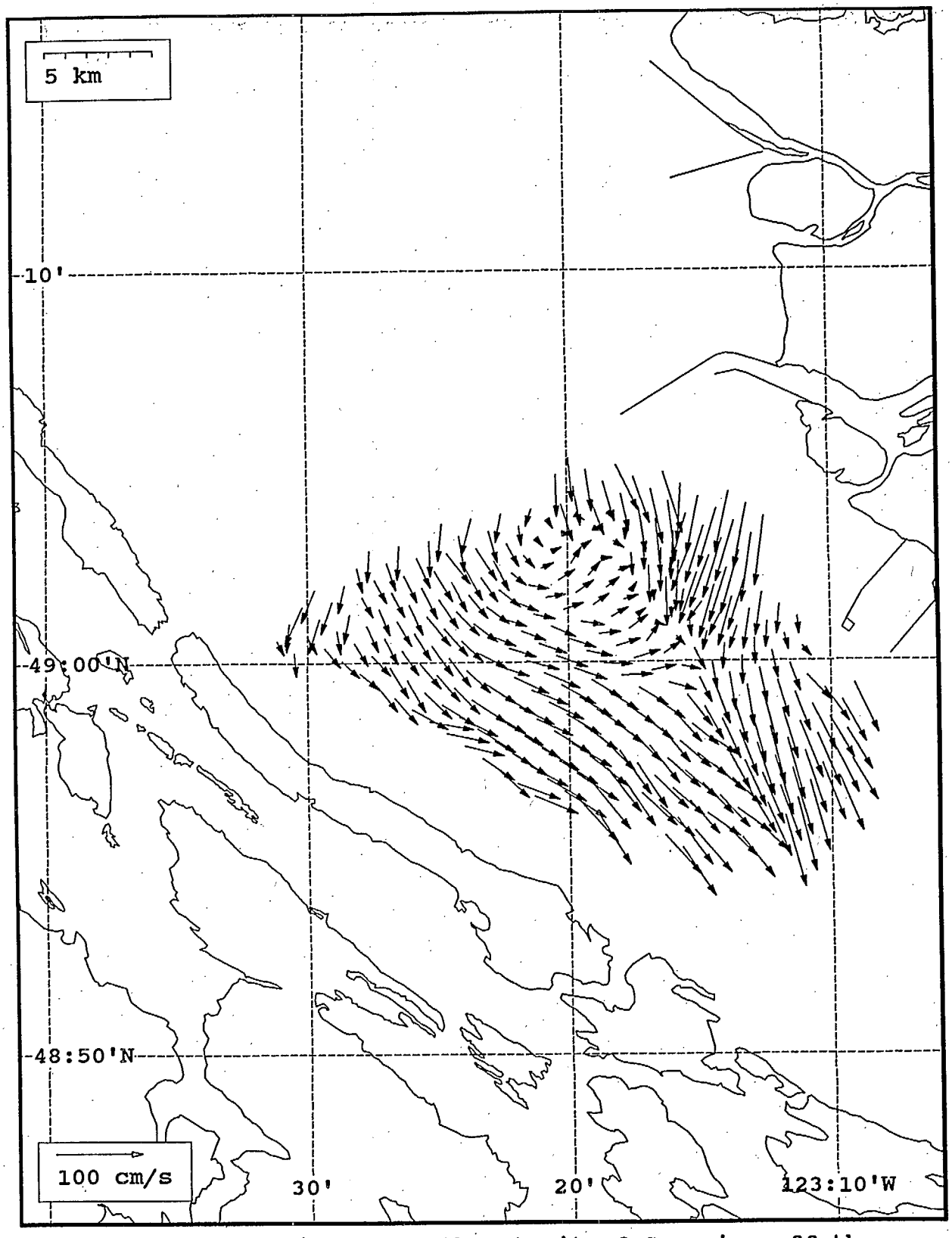

SeaSonde current field from the Strait of Georgia, off the mouth of the Fraser River, for 07:00 Z, July 24, 1993.

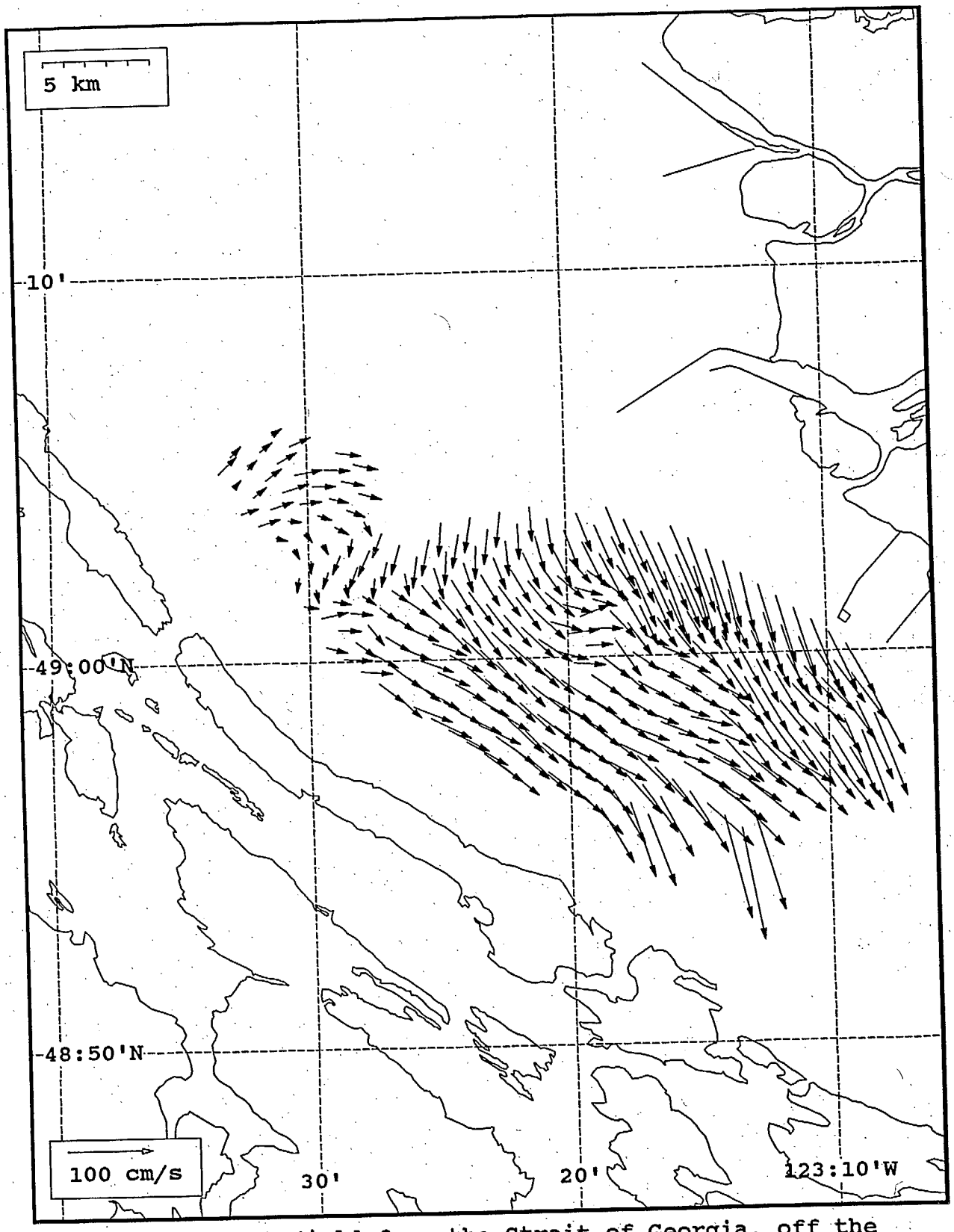

SeaSonde current field from the Strait of Georgia, off the mouth of the Fraser River, for 08:00 Z, July 24, 1993.

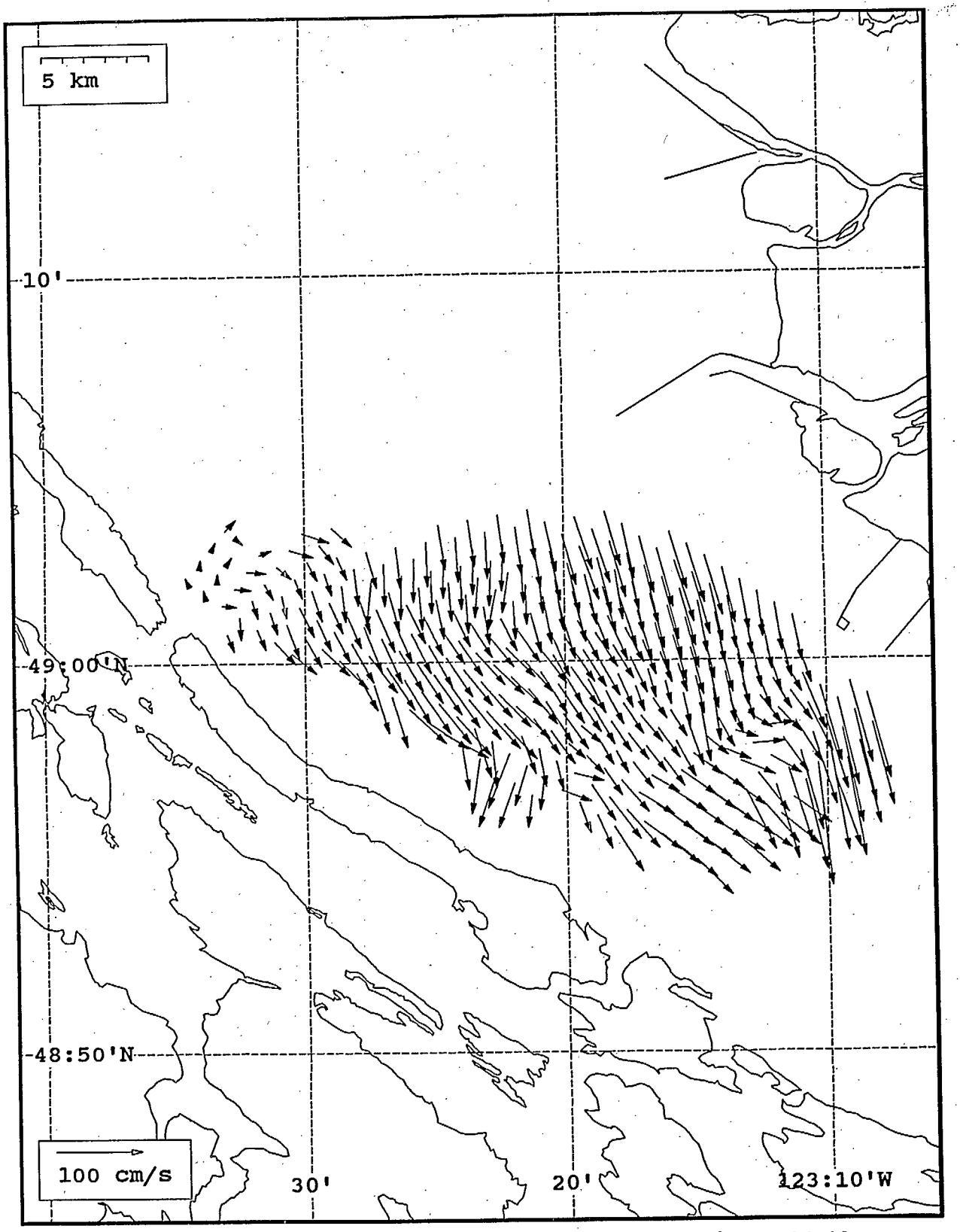

SeaSonde current field from the Strait of Georgia, off the mouth of the Fraser River, for 09:00 Z, July 24, 1993.

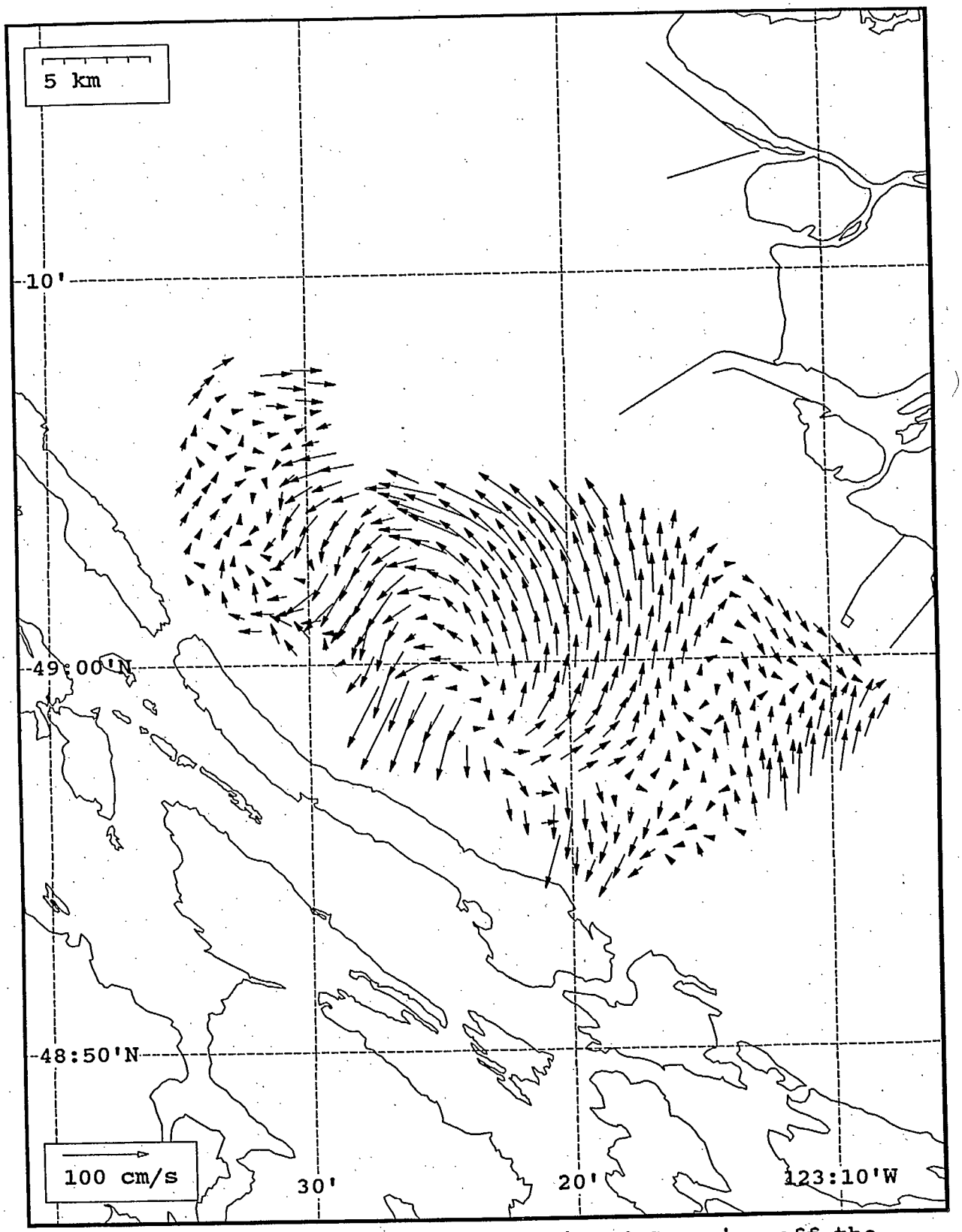

SeaSonde current field from the Strait of Georgia, off the mouth of the Fraser River, for 12:00 Z, July 24, 1993.

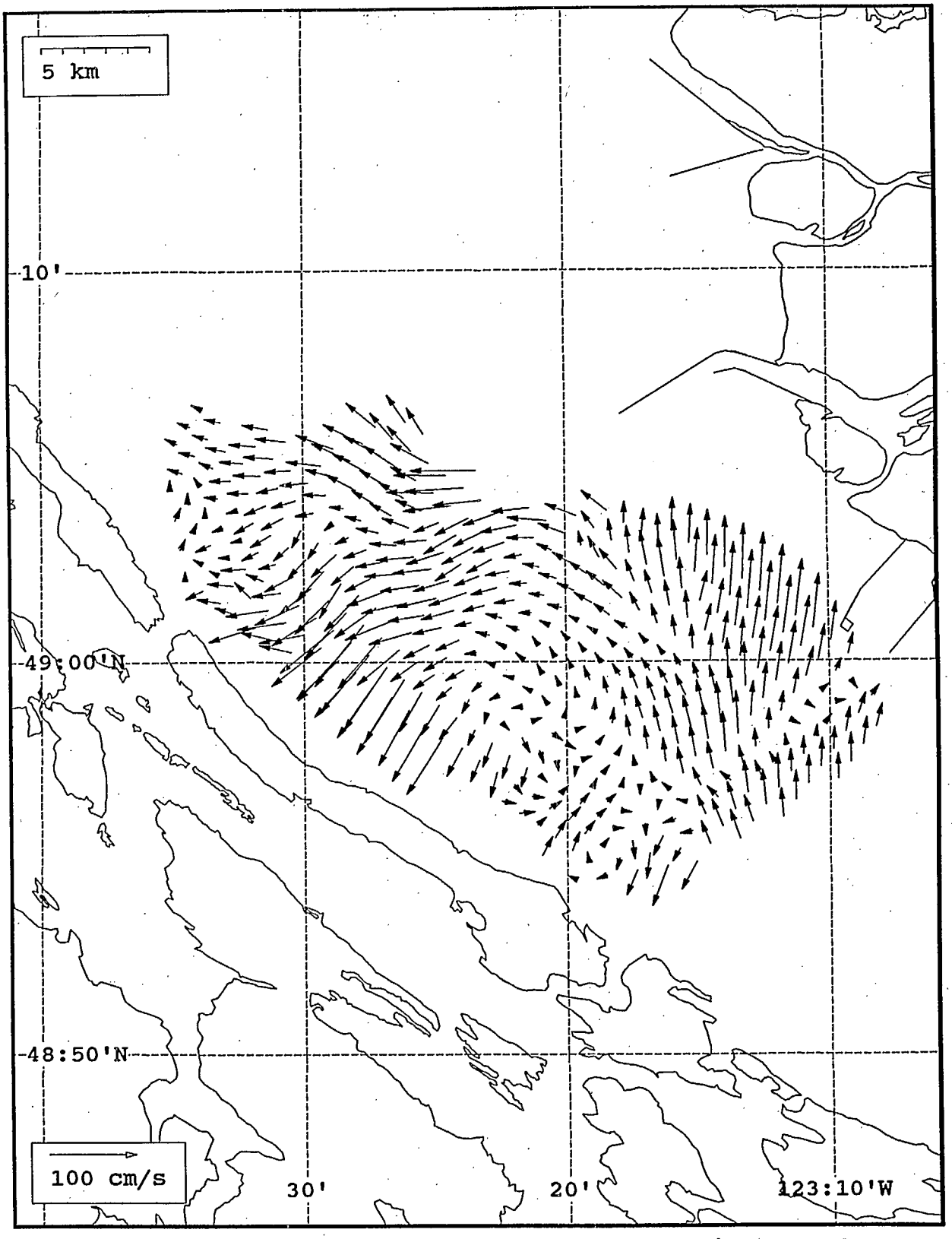

SeaSonde current field from the Strait of Georgia, off the mouth of the Fraser River, for 13:00 Z, July 24, 1993.

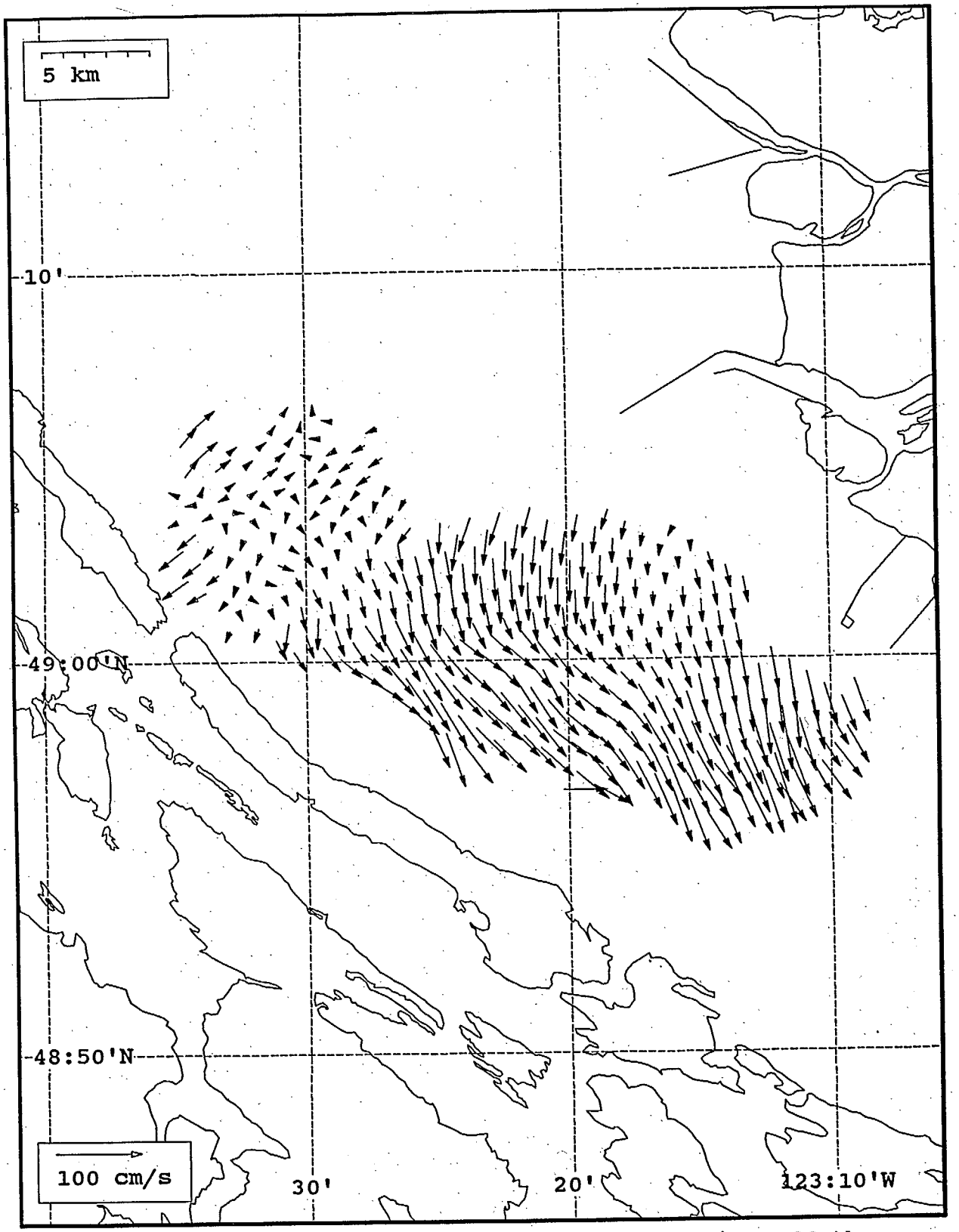

SeaSonde current field from the Strait of Georgia, off the mouth of the Fraser River, for 10:00 Z, July 24, 1993.

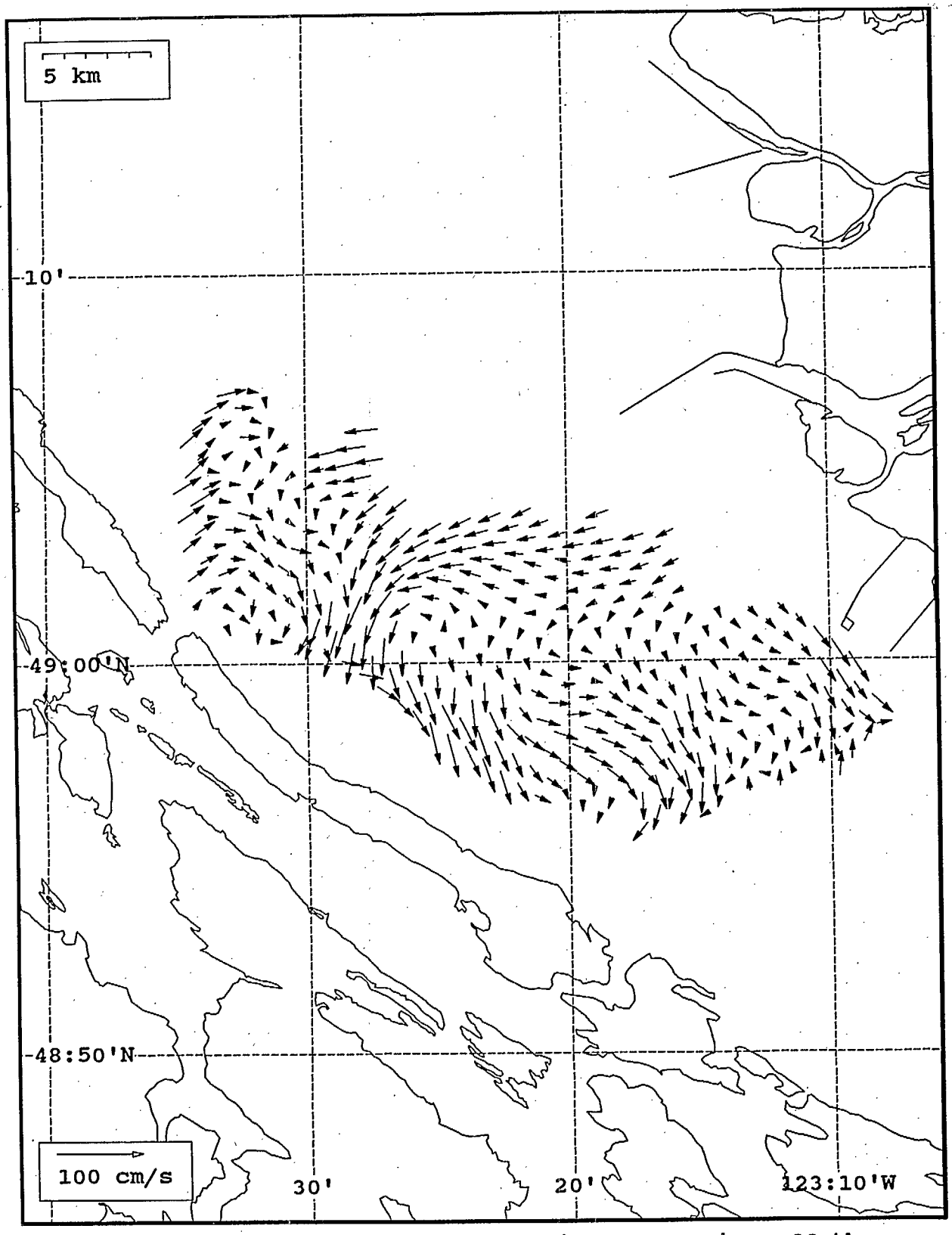

SeaSonde current field from the Strait of Georgia, off the mouth of the Fraser River, for 11:00 Z, July 24, 1993.

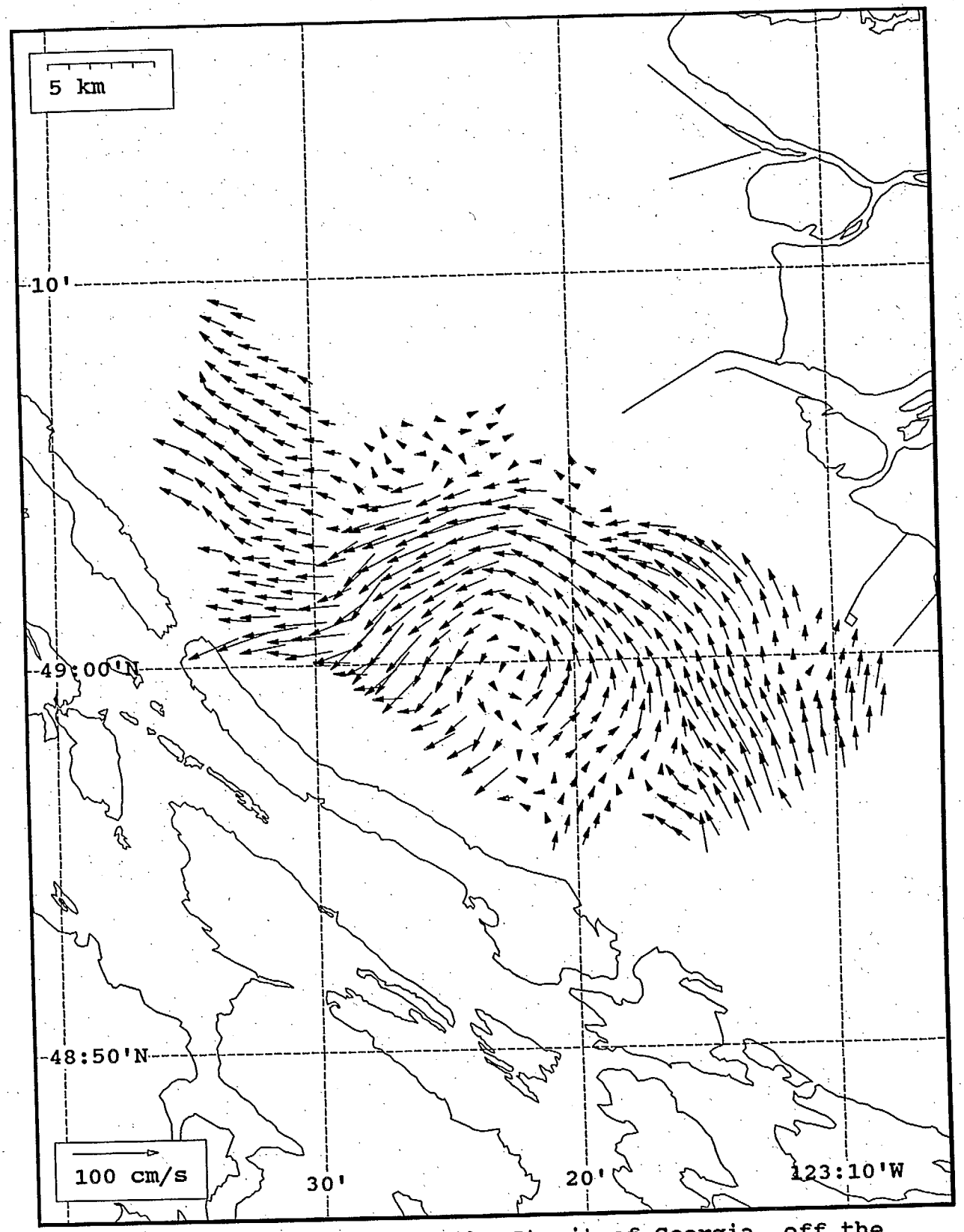

SeaSonde current field from the Strait of Georgia, off the mouth of the Fraser River, for 14:00 Z, July 24, 1993.

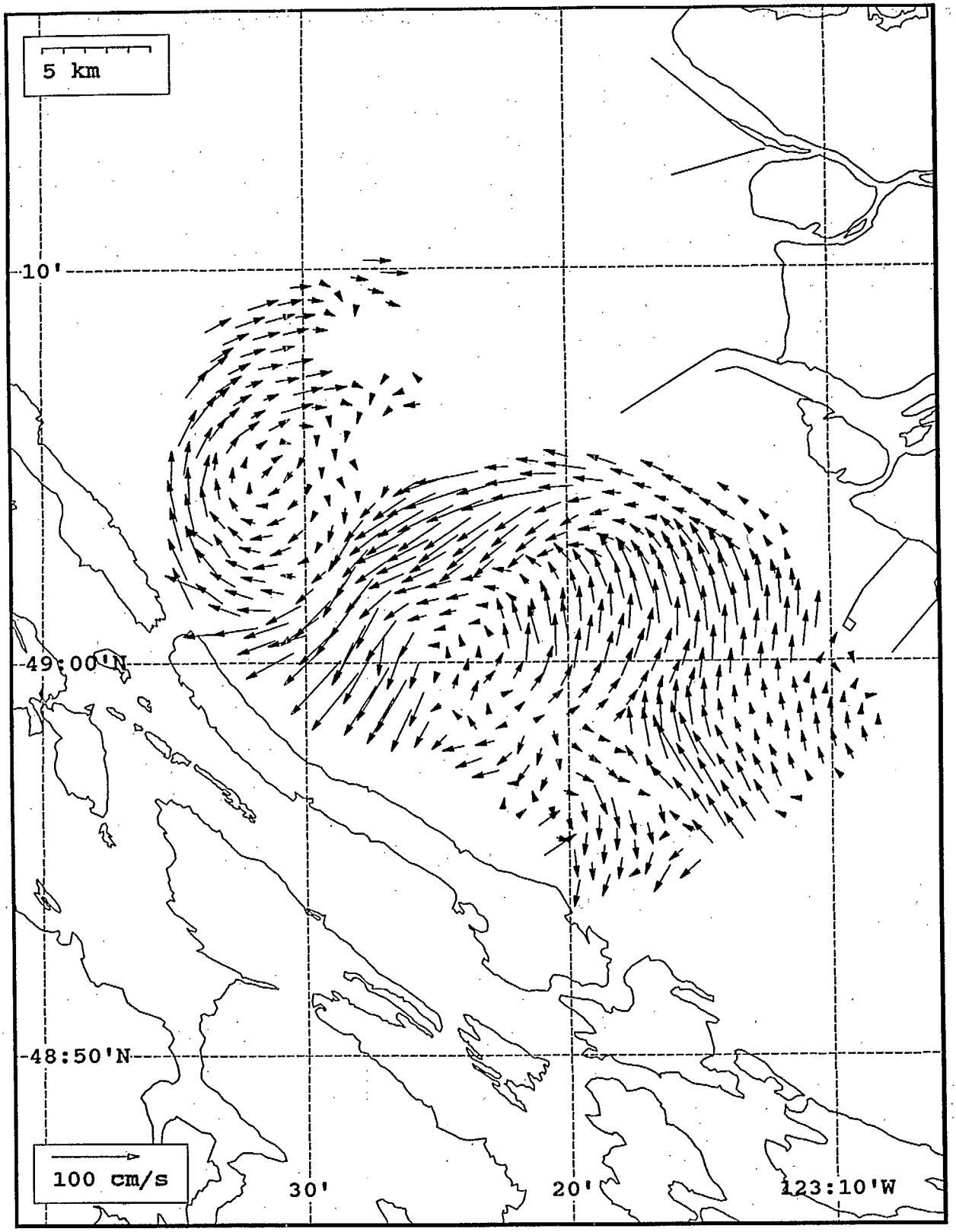

SeaSonde current field from the Strait of Georgia, off the mouth of the Fraser River, for 15:00 Z, July 24, 1993.

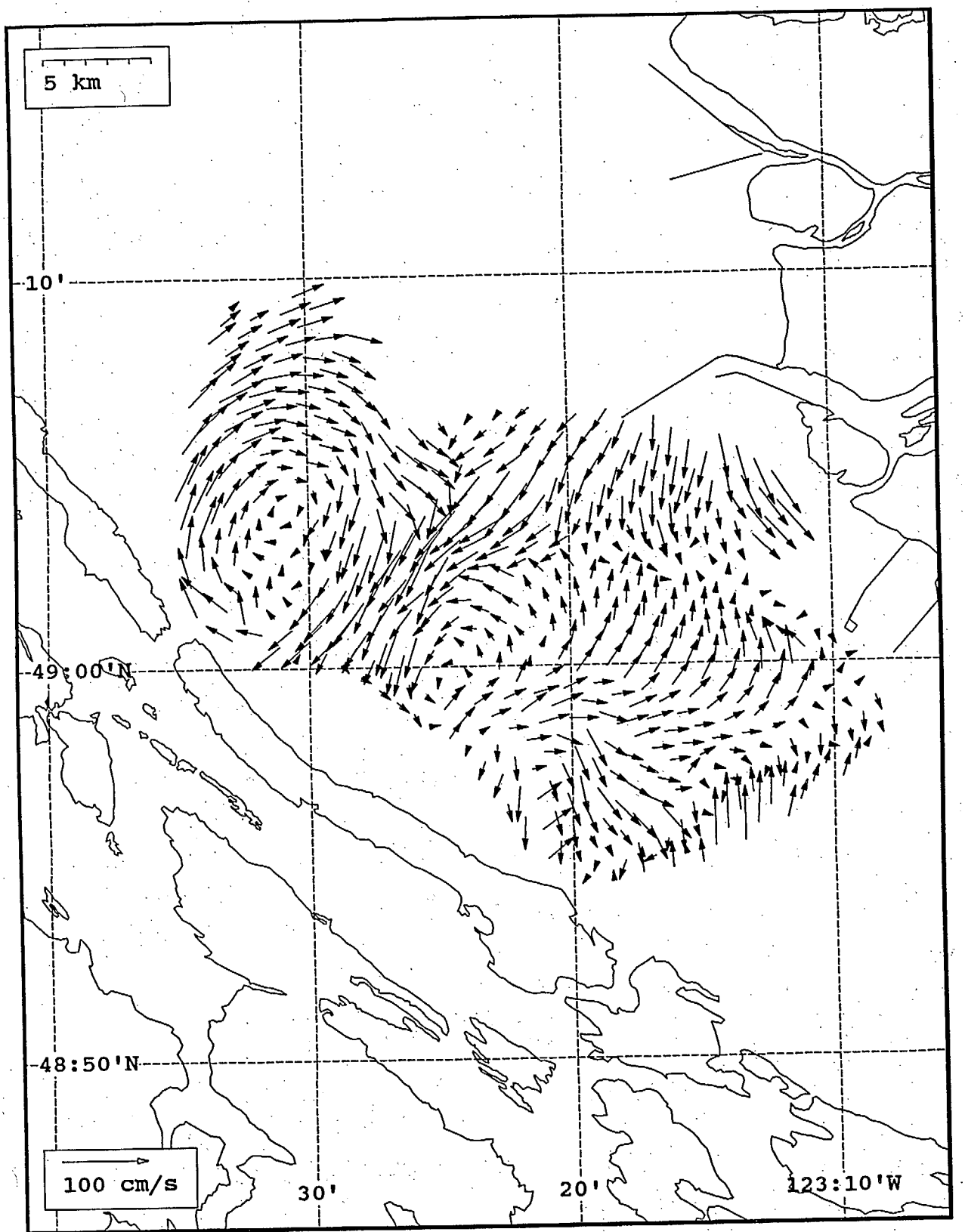

SeaSonde current field from the Strait of Georgia, off the mouth of the Fraser River, for 16:00 Z, July 24, 1993.

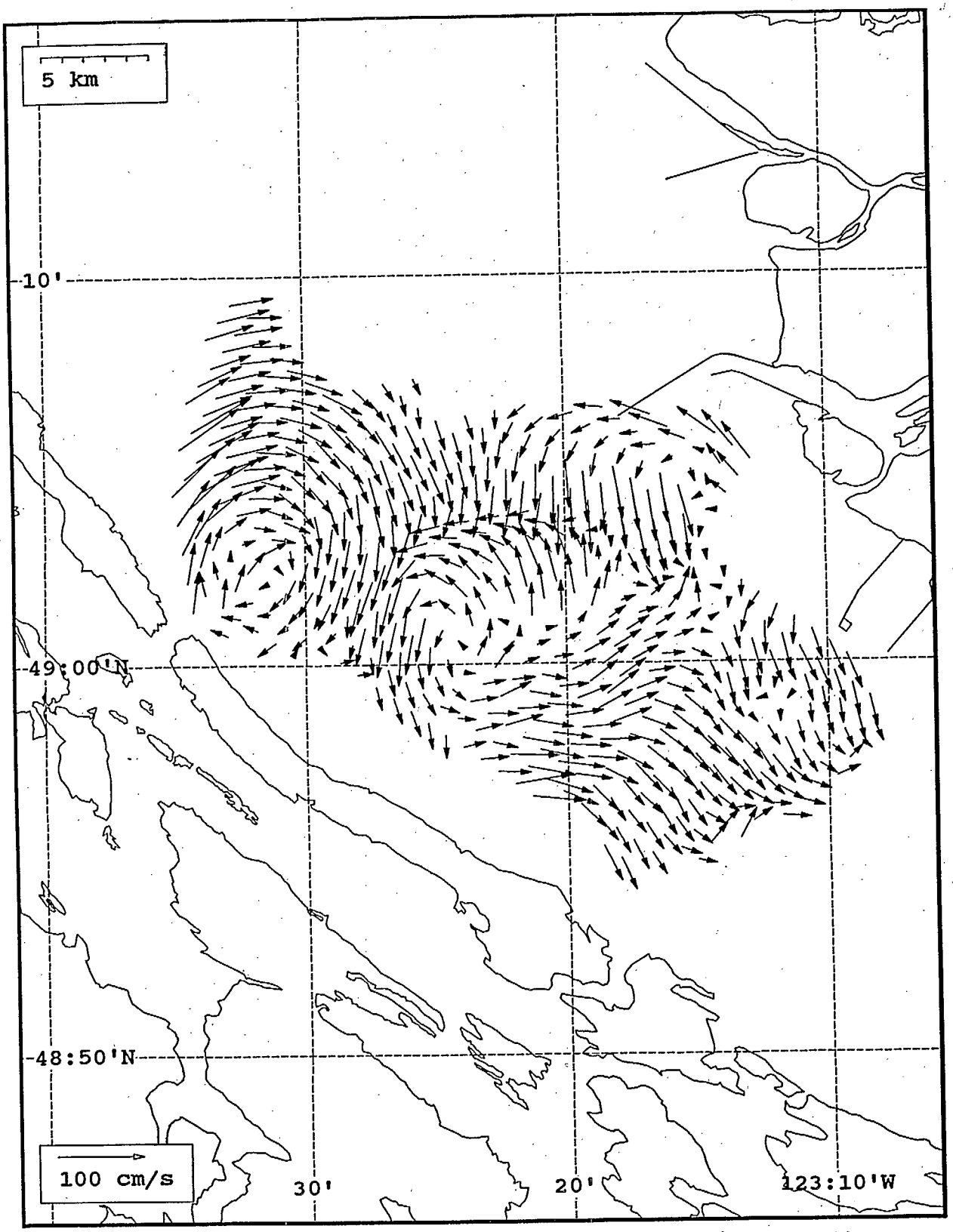

SeaSonde current field from the Strait of Georgia, off the mouth of the Fraser River, for 17:00 Z, July 24, 1993.

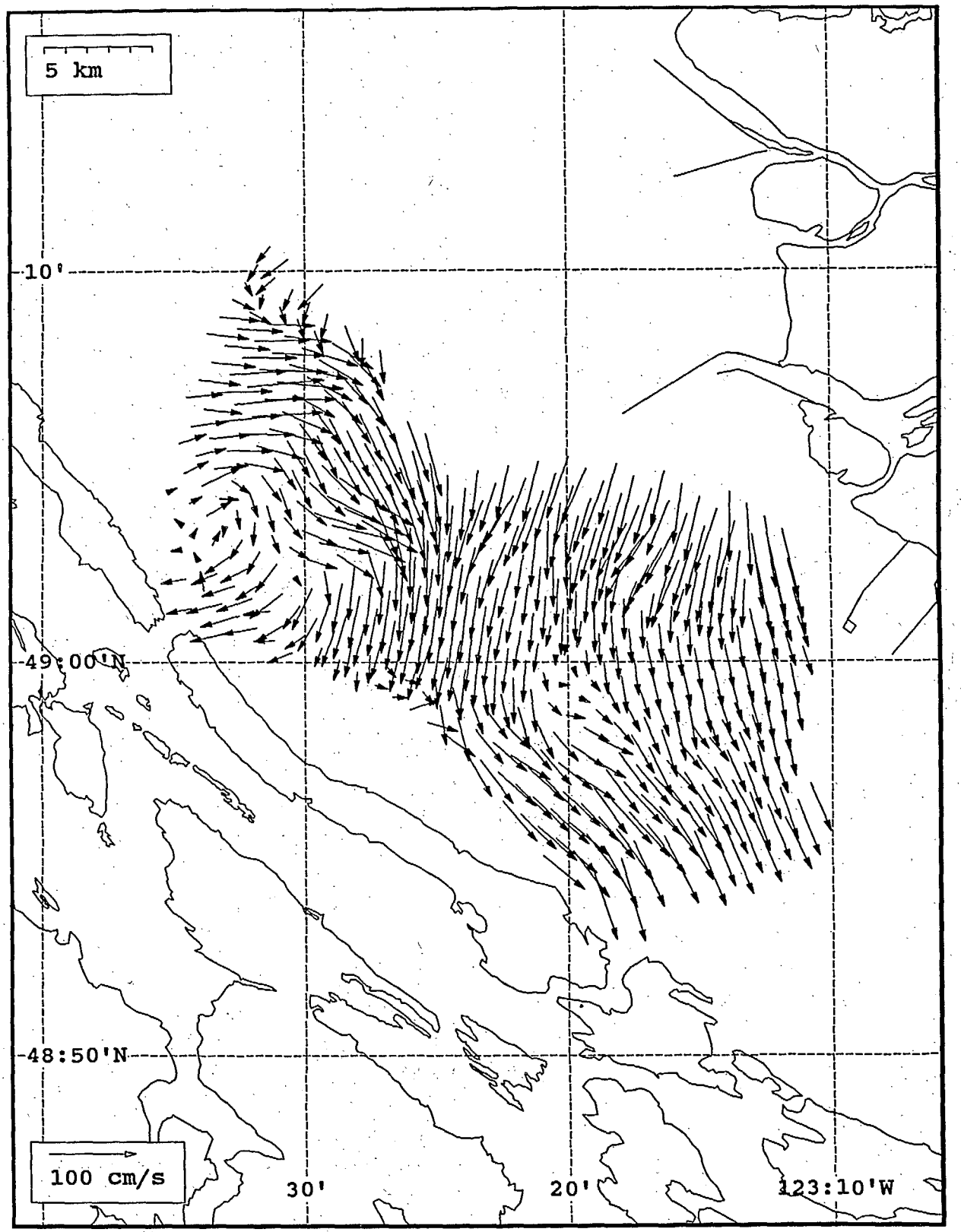

SeaSonde current field from the Strait of Georgia, off the mouth of the Fraser River, for 20:00 Z, July 24, 1993.

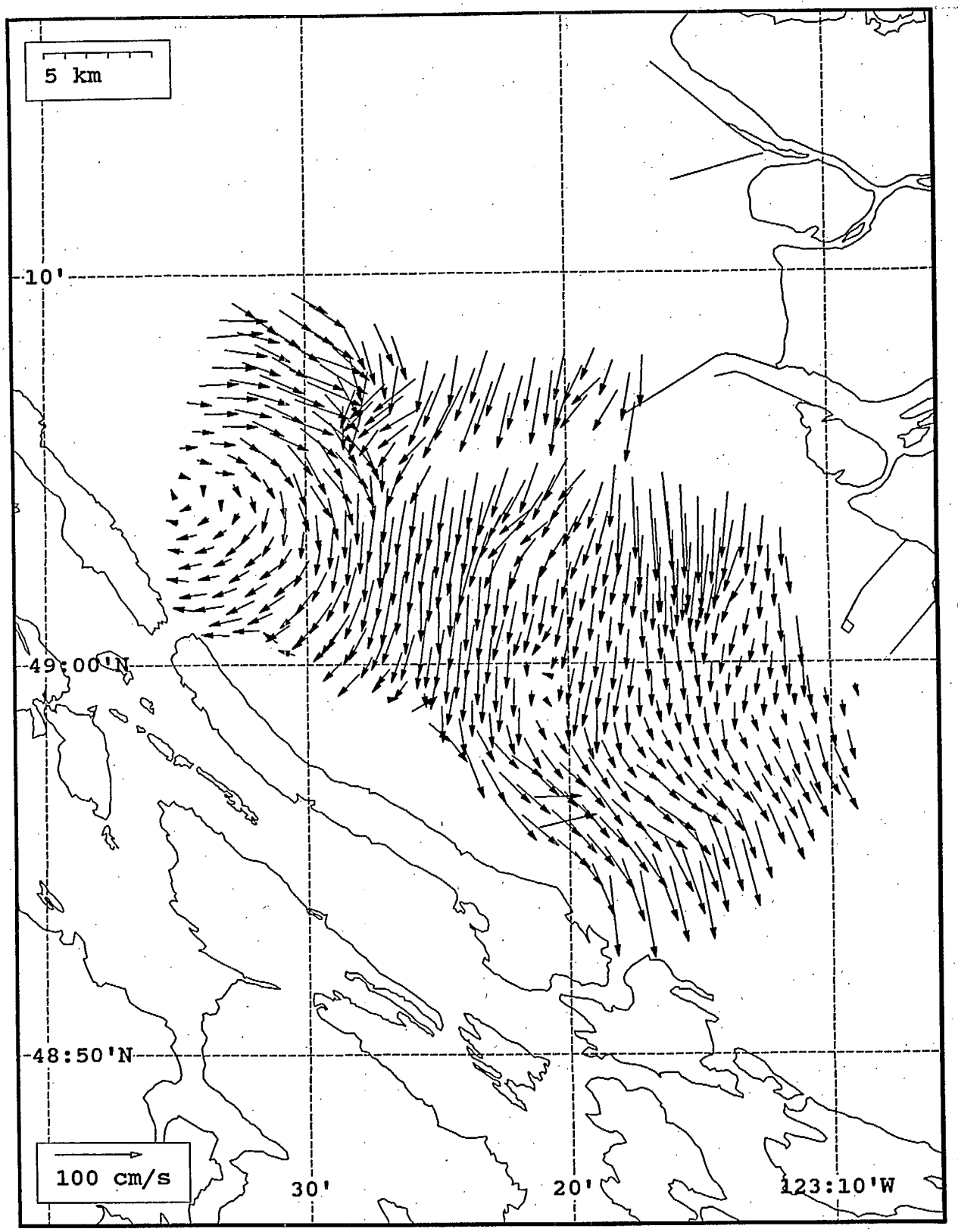

SeaSonde current field from the Strait of Georgia, off the mouth of the Fraser River, for 21:00 Z, July 24, 1993.

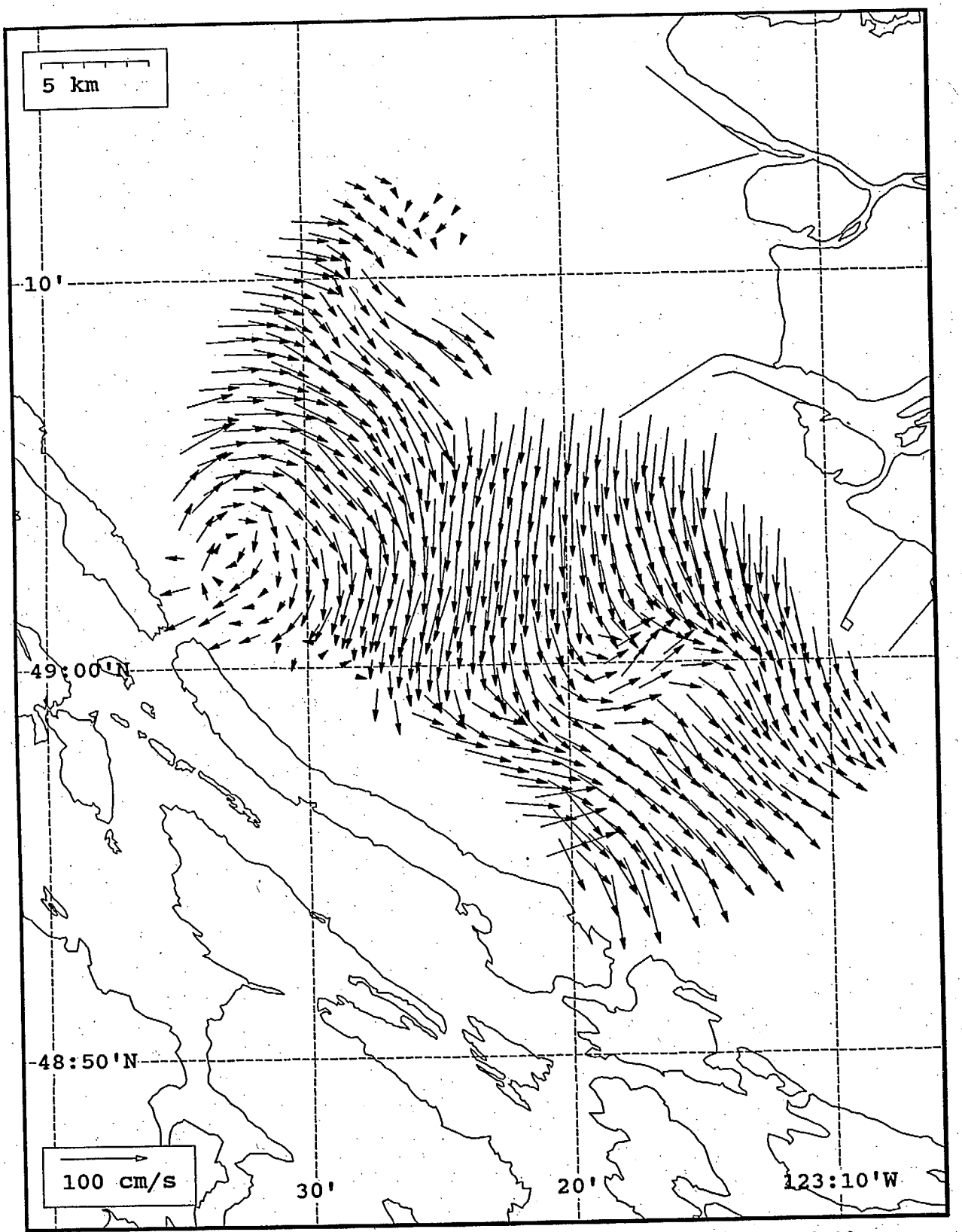

SeaSonde current field from the Strait of Georgia, off the mouth of the Fraser River, for 18:00 Z, July 24, 1993.

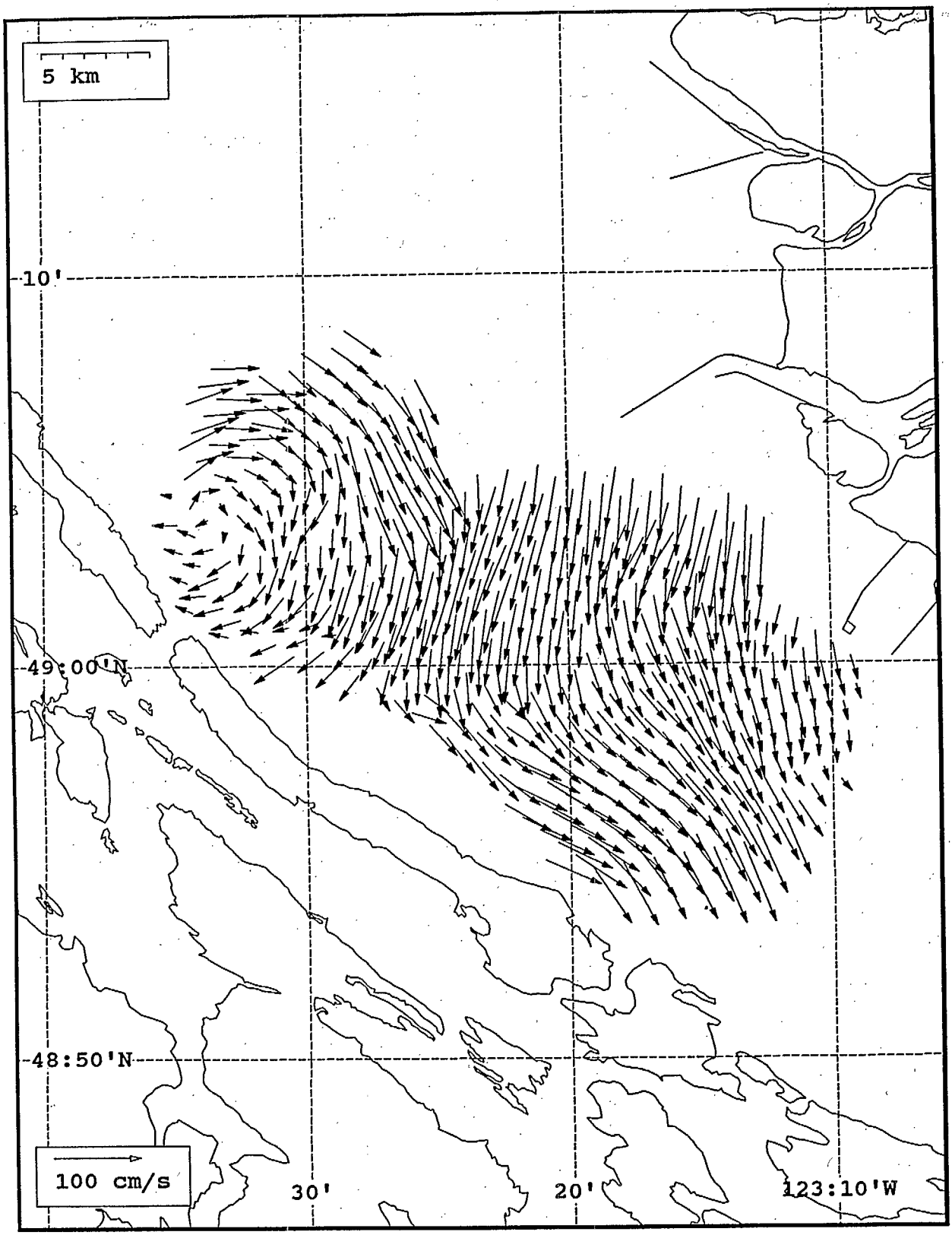

SeaSonde current field from the Strait of Georgia, off the mouth of the Fraser River, for 19:00 Z, July 24, 1993.

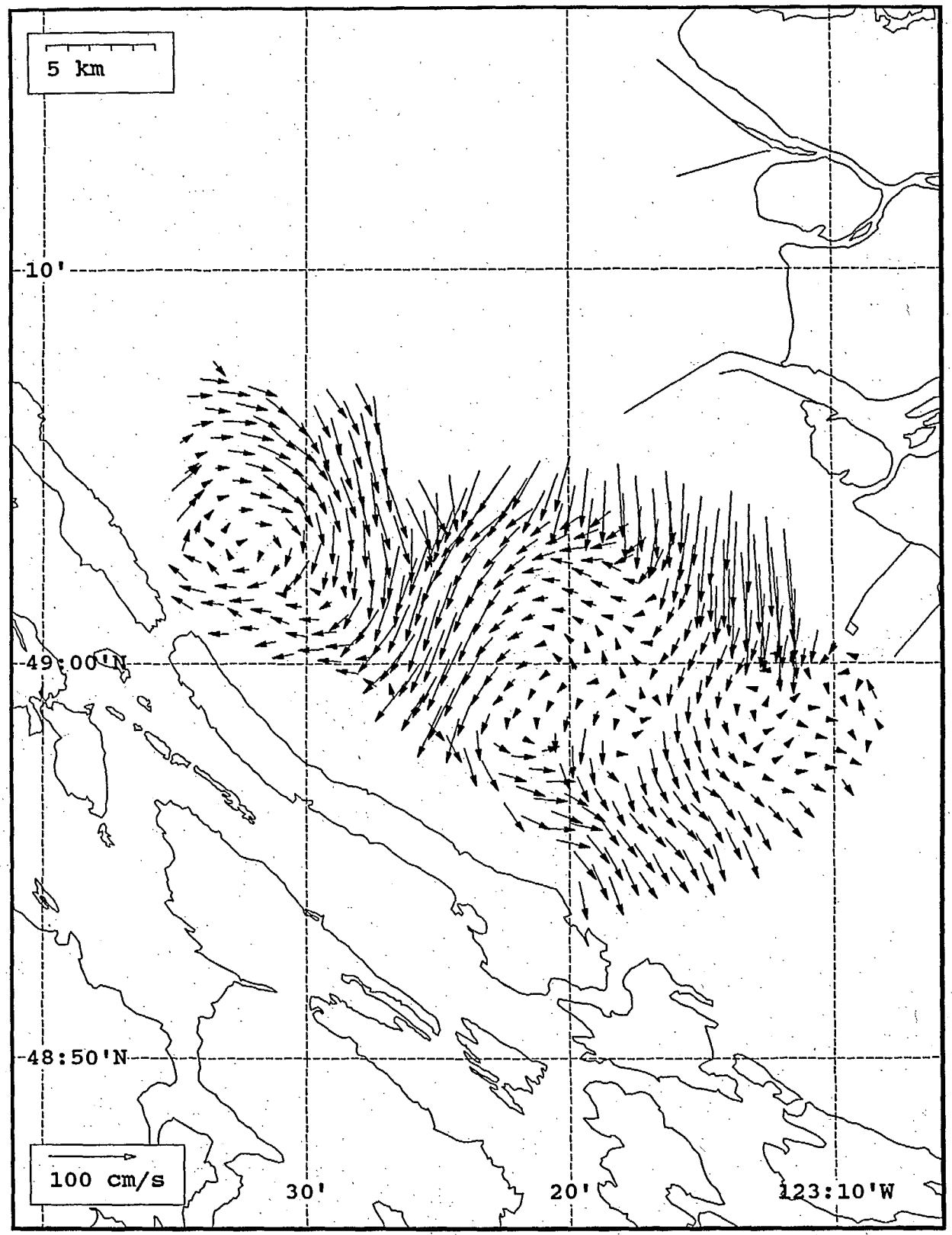

SeaSonde current field from the Strait of Georgia, off the mouth of the Fraser River, for 22:00 Z, July 24, 1993.

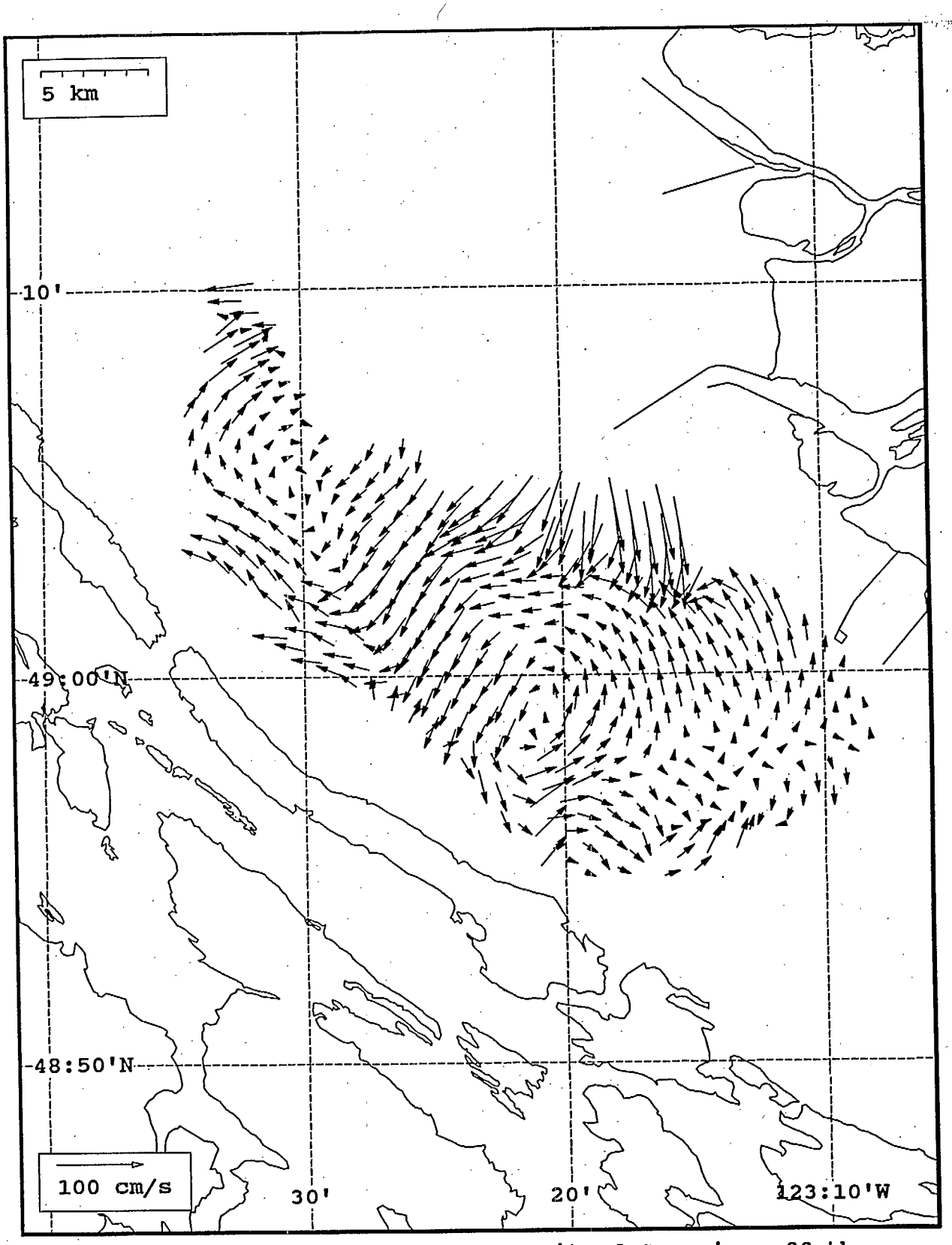

SeaSonde current field from the Strait of Georgia, off the mouth of the Fraser River, for 23:00 Z, July 24, 1993.

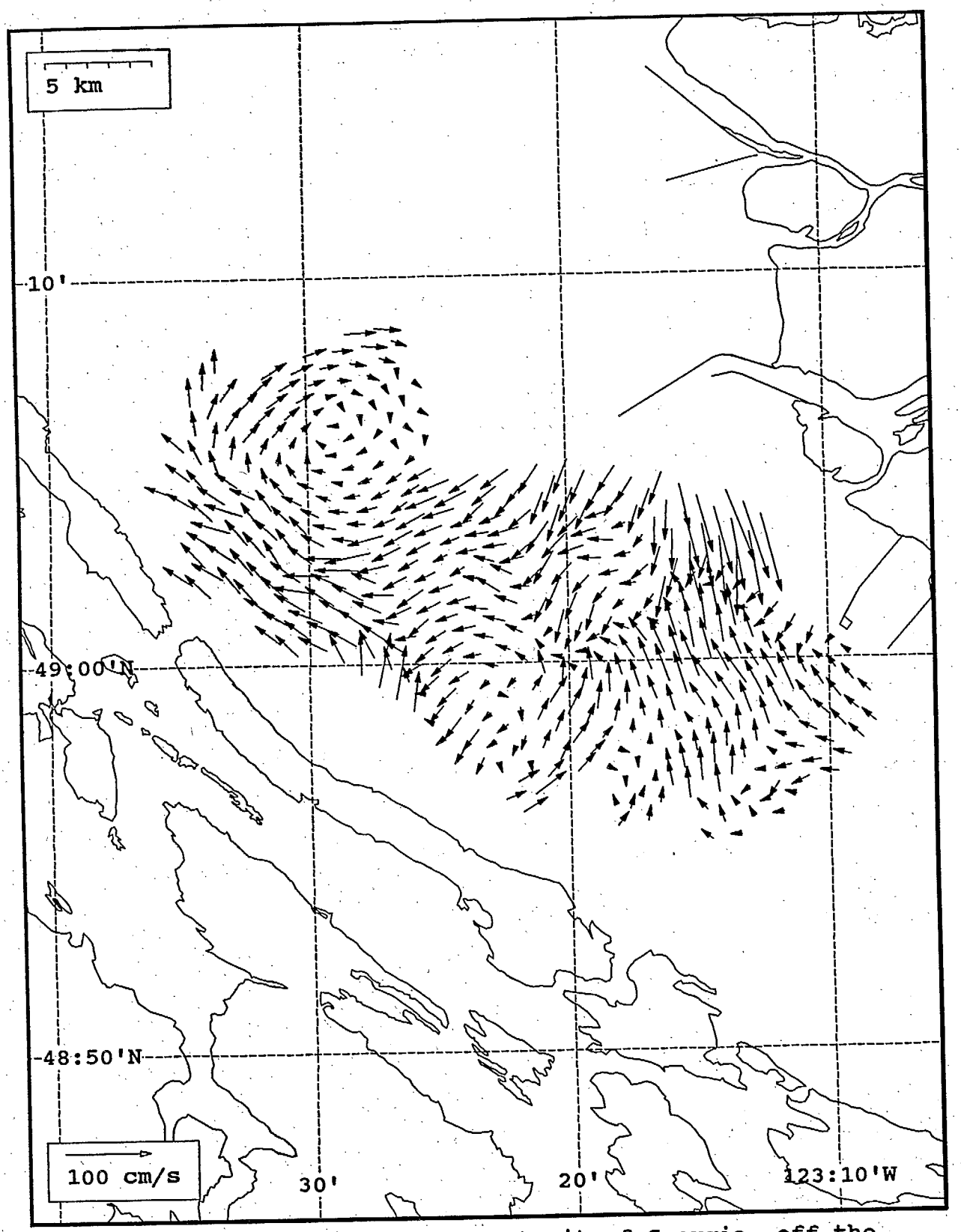

SeaSonde current field from the Strait of Georgia, off the mouth of the Fraser River, for 00:00 Z, July 25, 1993.

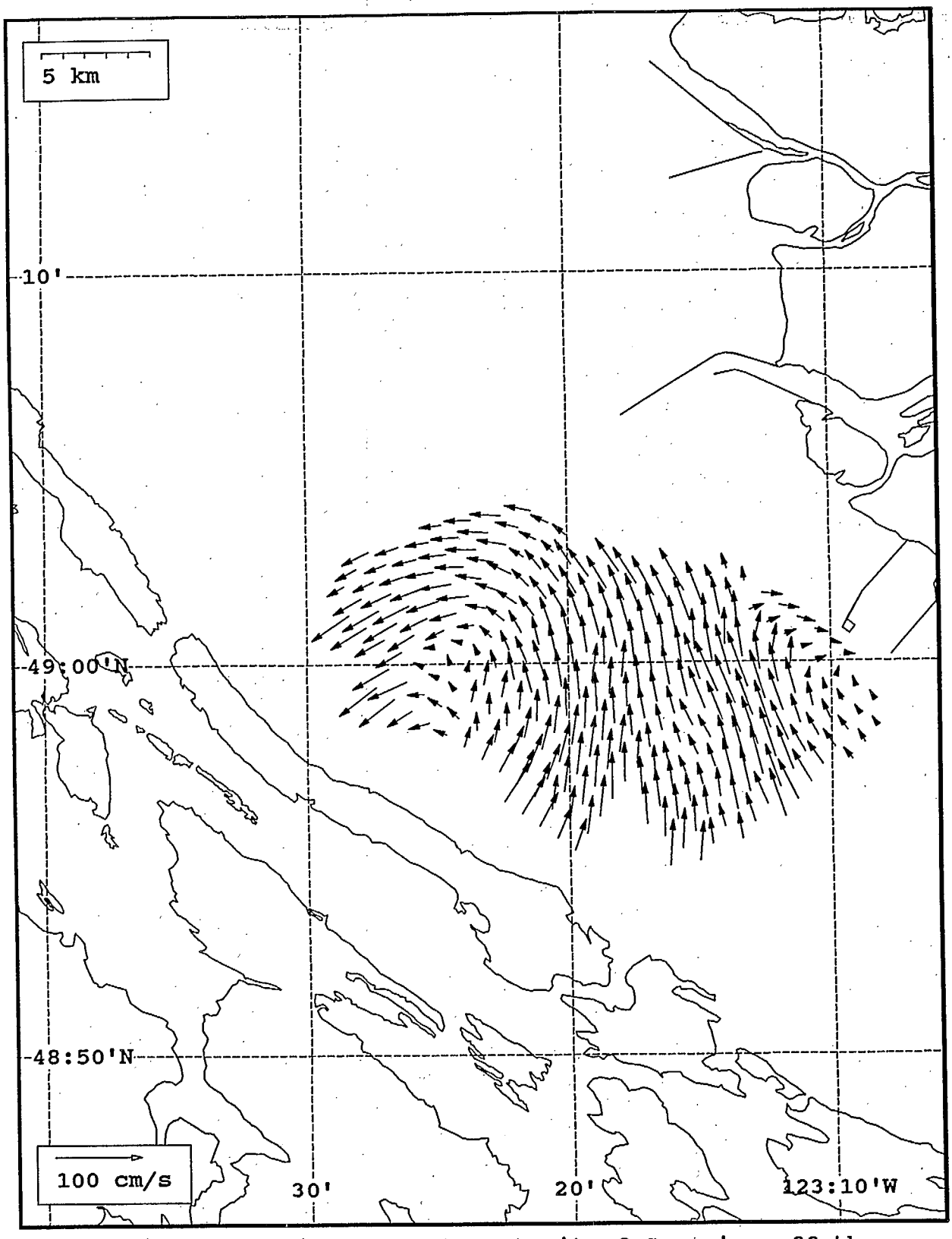

SeaSonde current field from the Strait of Georgia, off the mouth of the Fraser River, for 01:00 Z, July 25, 1993.

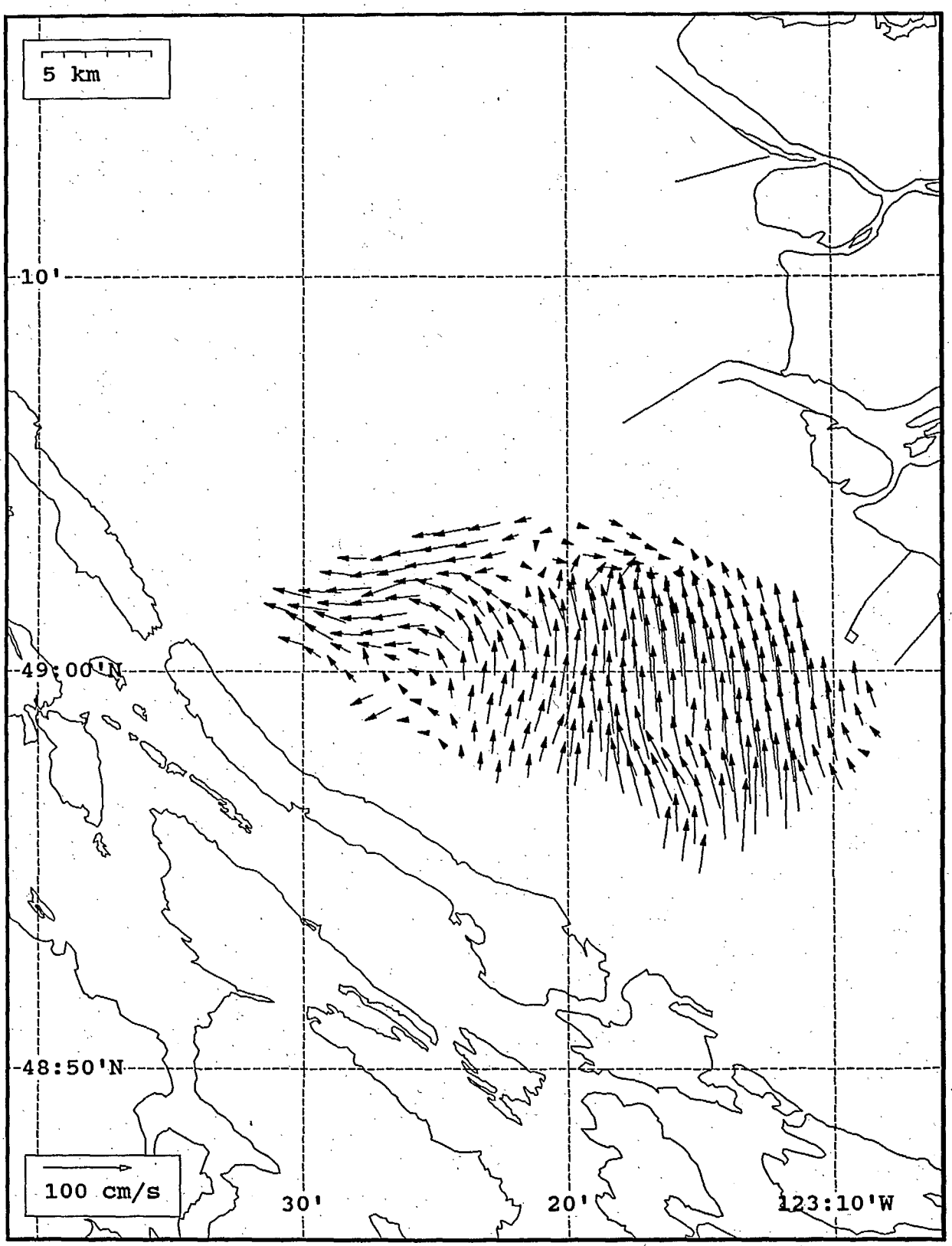

SeaSonde current field from the Strait of Georgia, off the mouth of the Fraser River, for 02:00 Z, July 25, 1993.

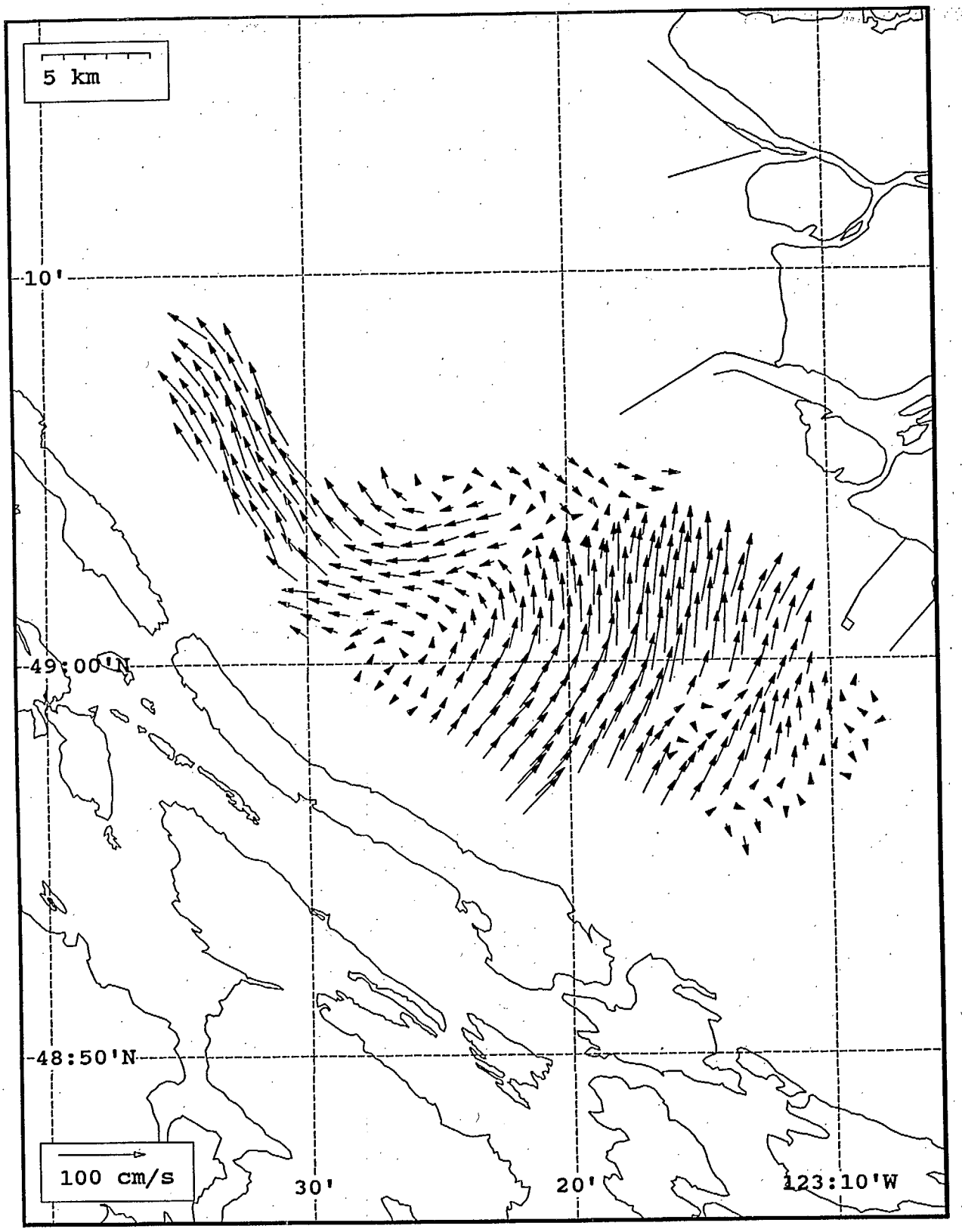

SeaSonde current field from the Strait of Georgia, off the mouth of the Fraser River, for 03:00 Z, July 25, 1993.

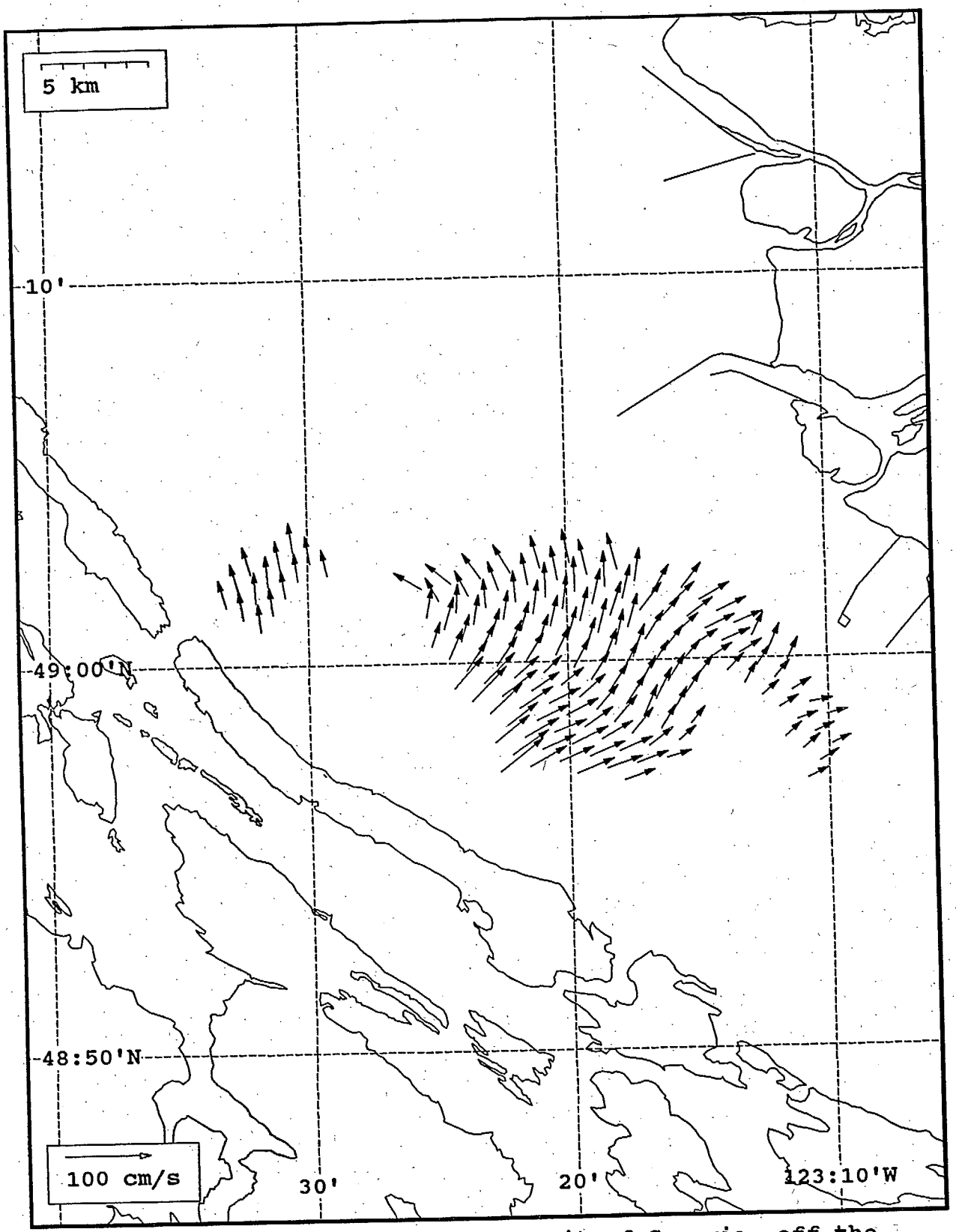

SeaSonde current field from the Strait of Georgia, off the mouth of the Fraser River, for 04:00 Z, July 25, 1993.

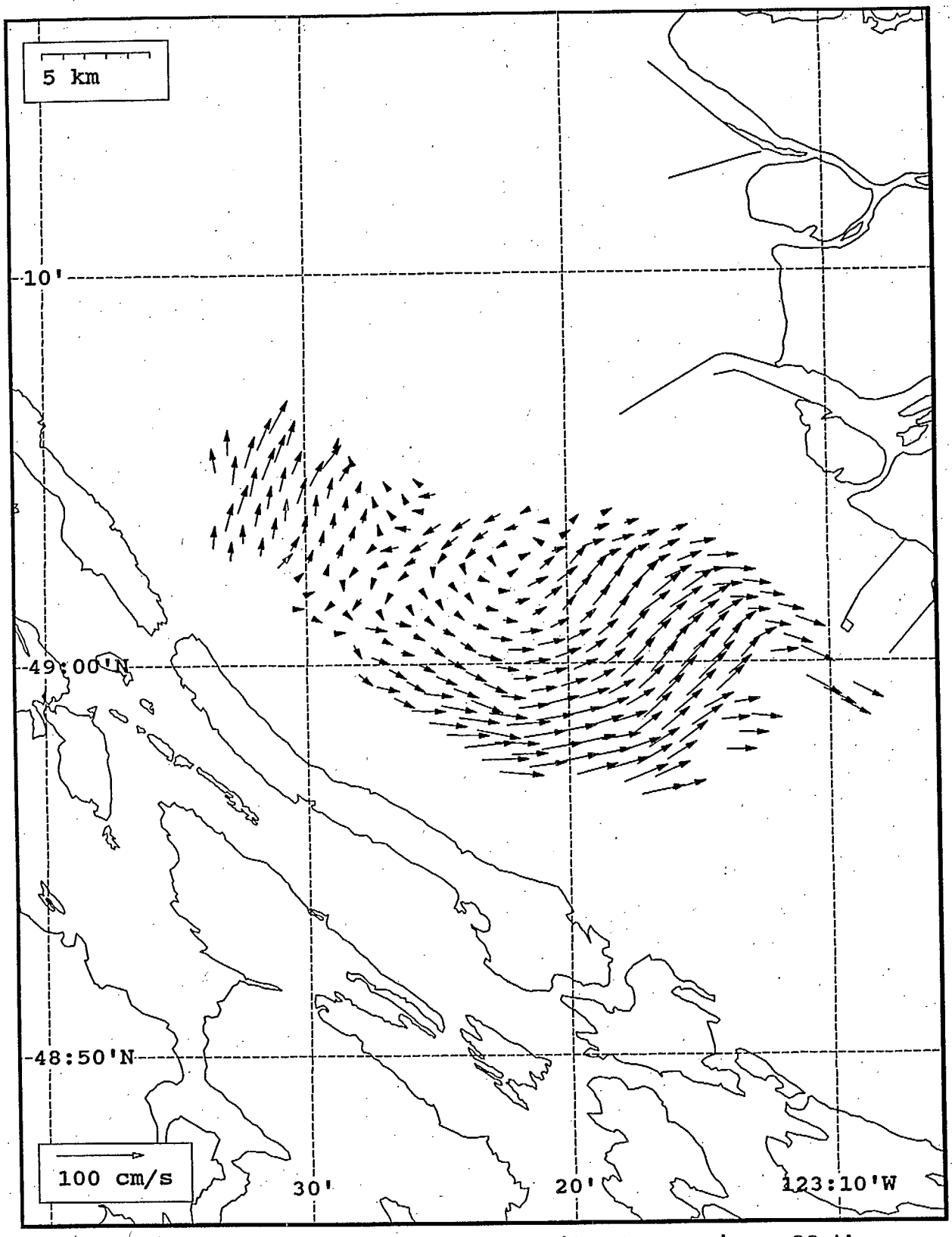

SeaSonde current field from the Strait of Georgia, off the mouth of the Fraser River, for 05:00 Z, July 25, 1993.

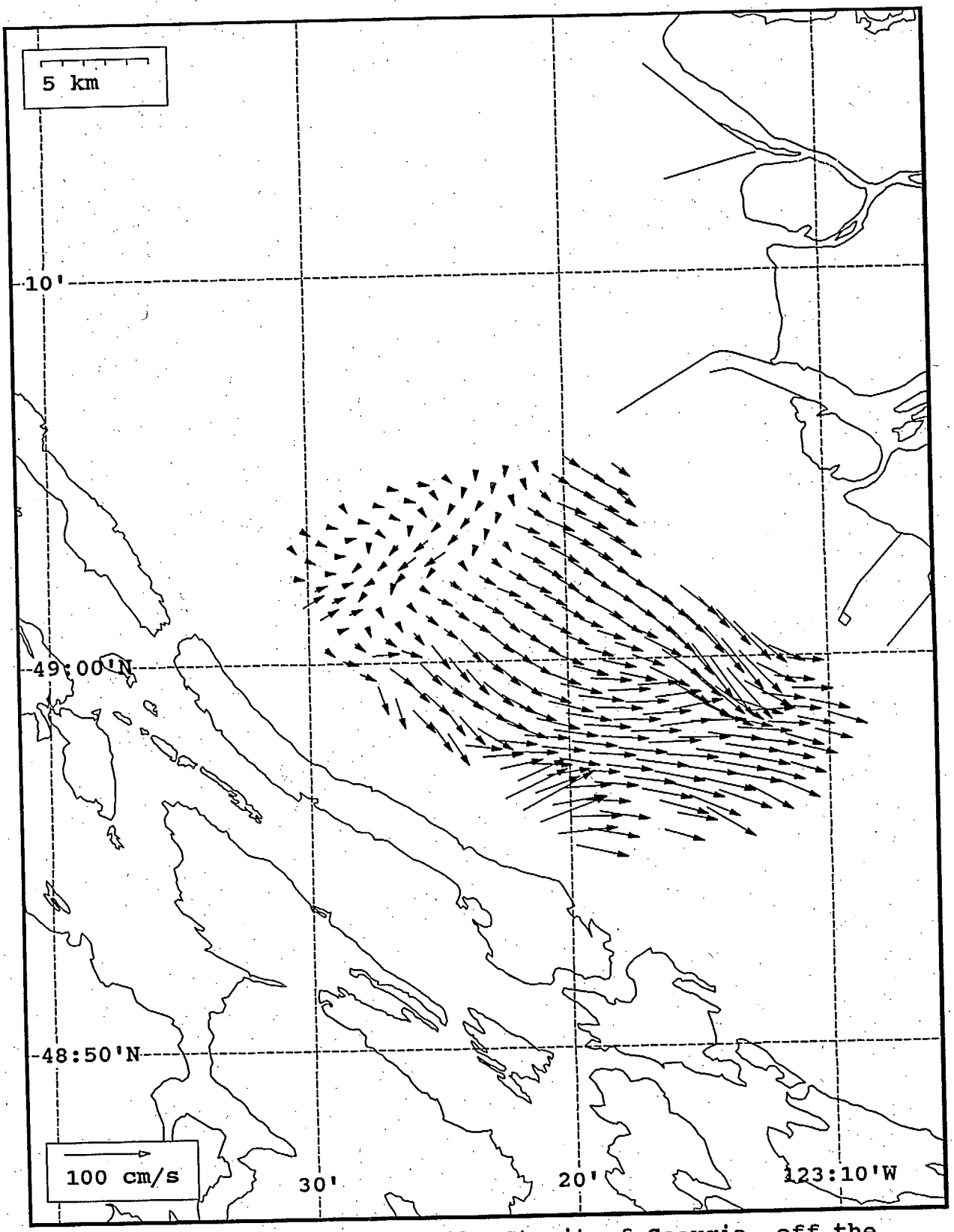

SeaSonde current field from the Strait of Georgia, off the mouth of the Fraser River, for 06:00 Z, July 25, 1993.

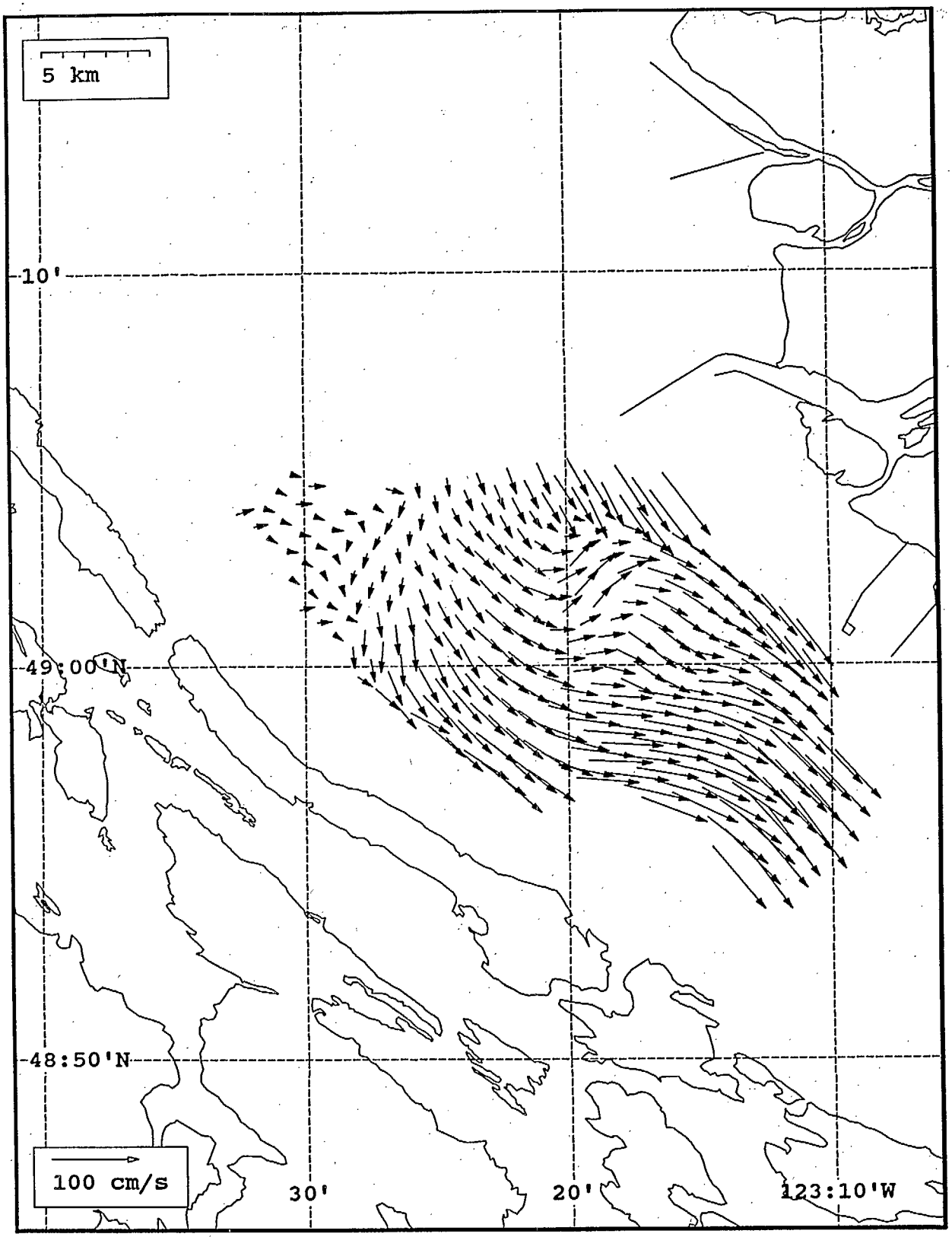

SeaSonde current field from the Strait of Georgia, off the mouth of the Fraser River, for 07:00 Z, July 25, 1993.

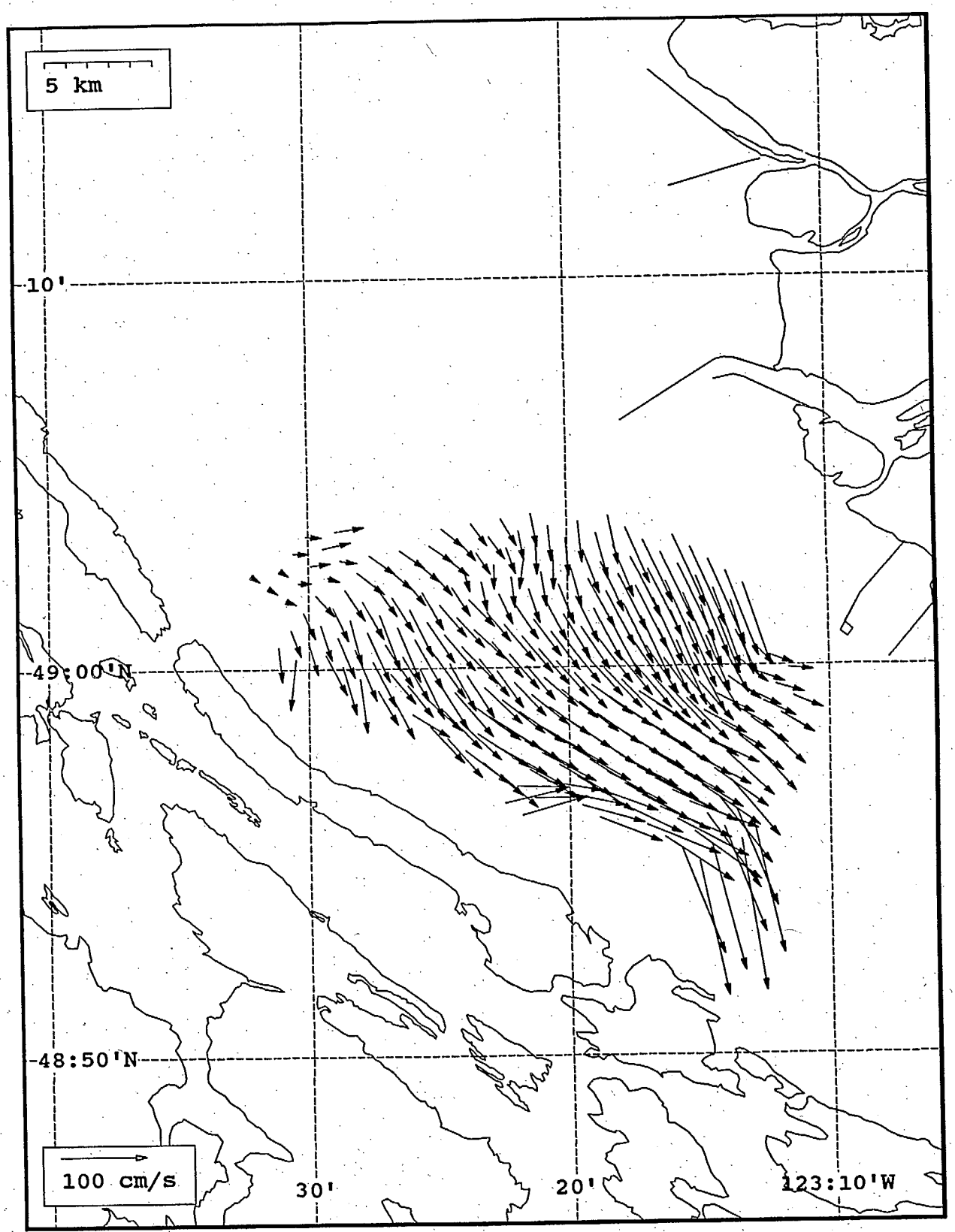

SeaSonde current field from the Strait of Georgia, off the mouth of the Fraser River, for 08:00 Z, July 25, 1993.

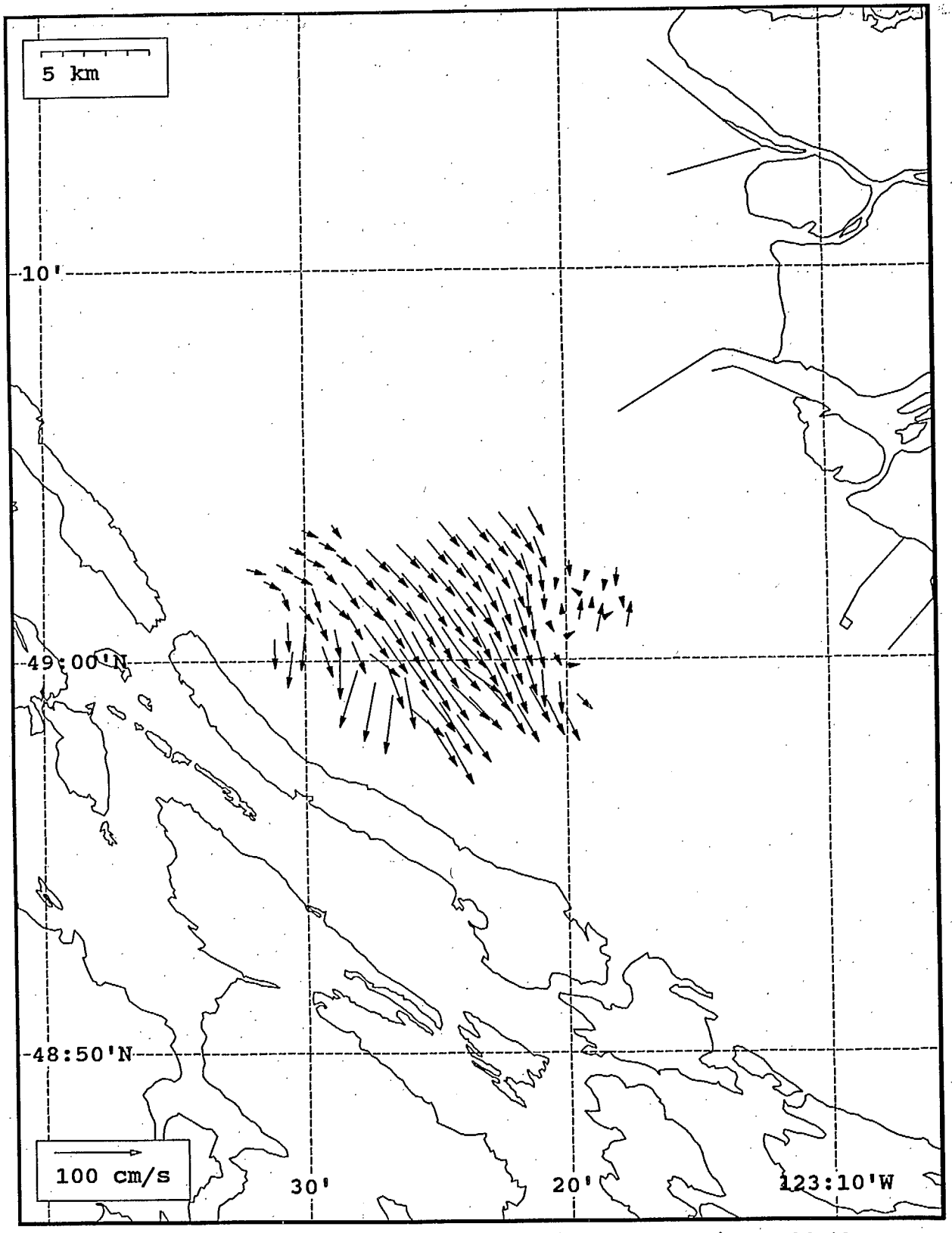

SeaSonde current field from the Strait of Georgia, off the mouth of the Fraser River, for 09:00 Z, July 25, 1993.

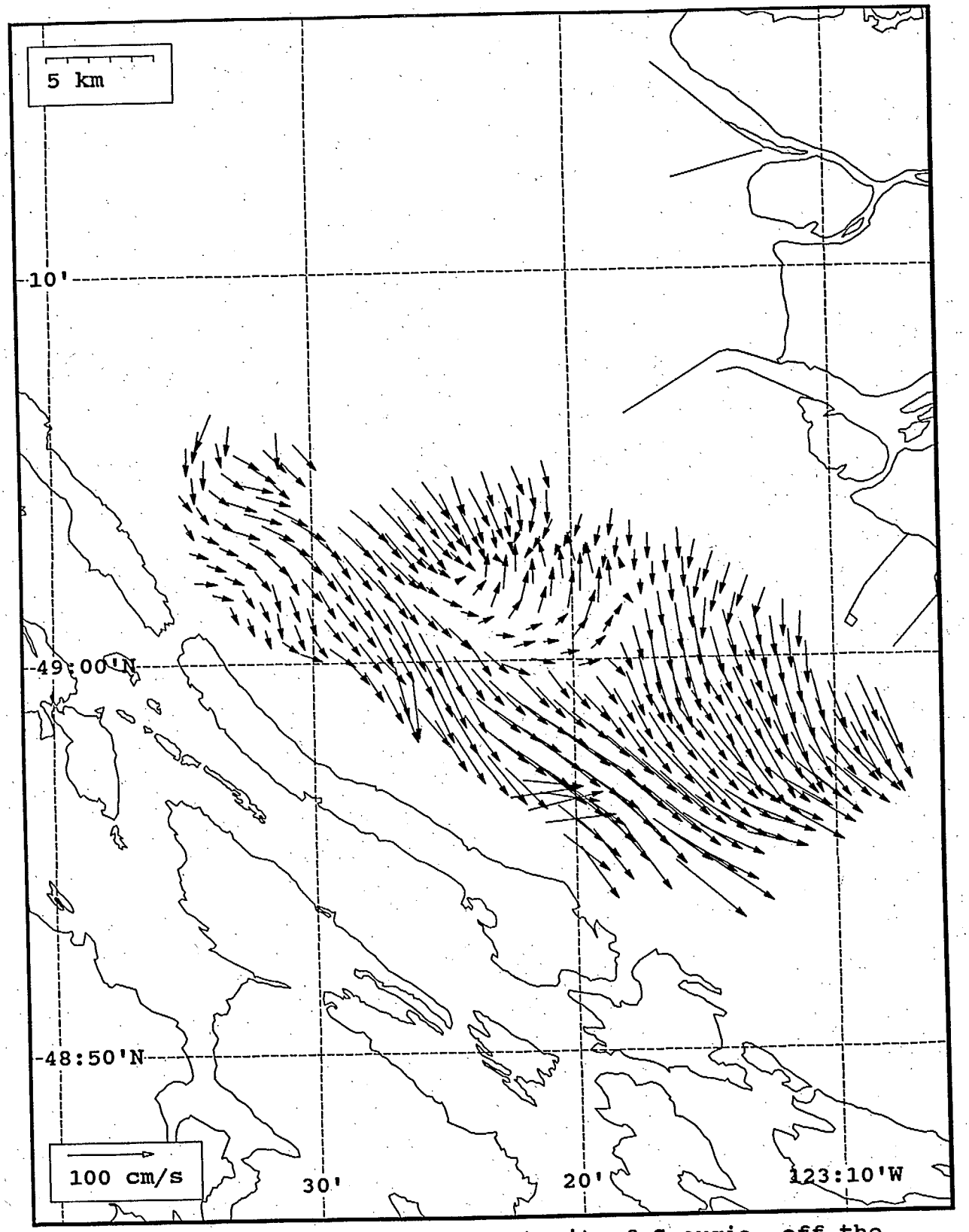

SeaSonde current field from the Strait of Georgia, off the mouth of the Fraser River, for 10:00 Z, July 25, 1993.

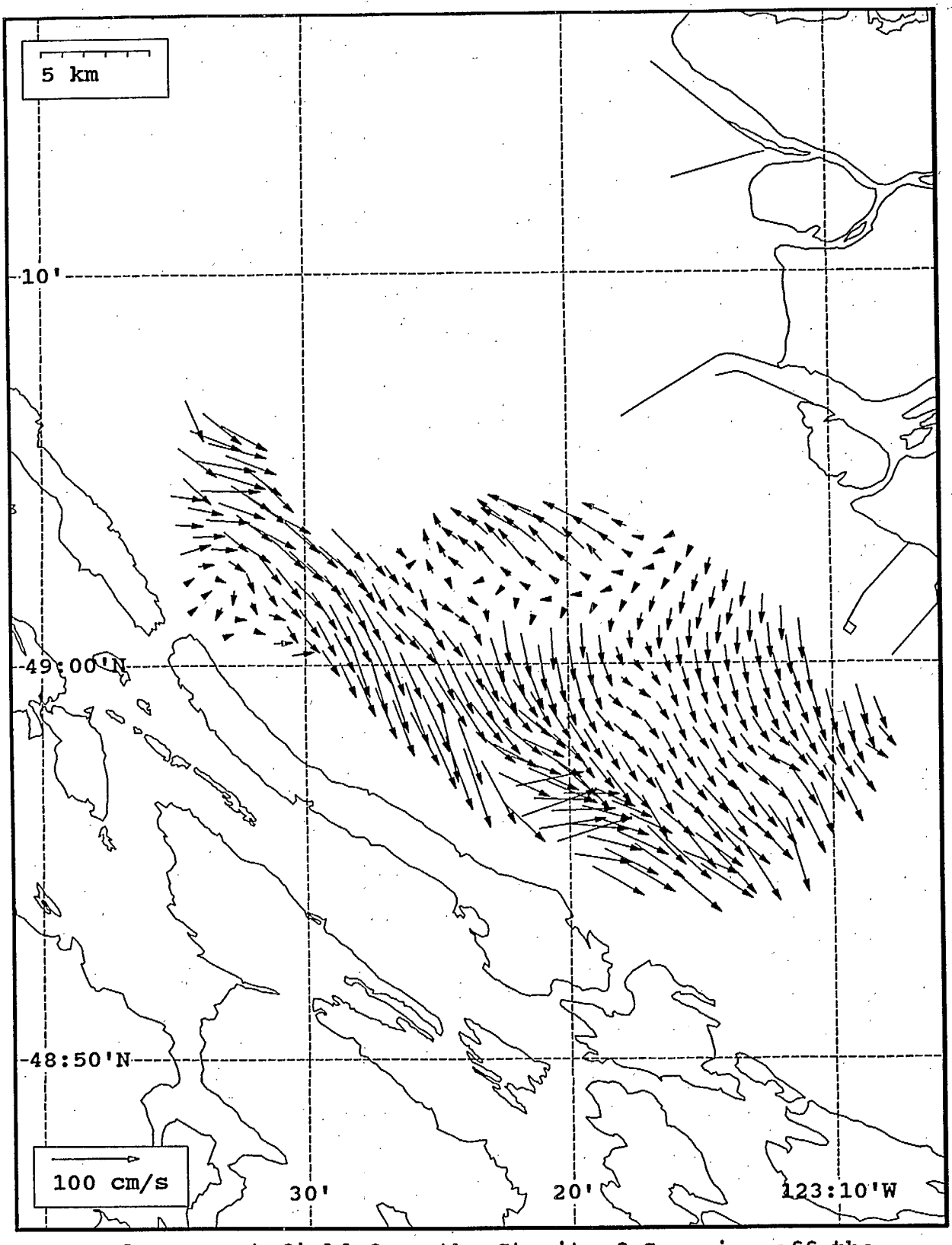

SeaSonde current field from the Strait of Georgia, off the mouth of the Fraser River, for 11:00 Z, July 25, 1993.

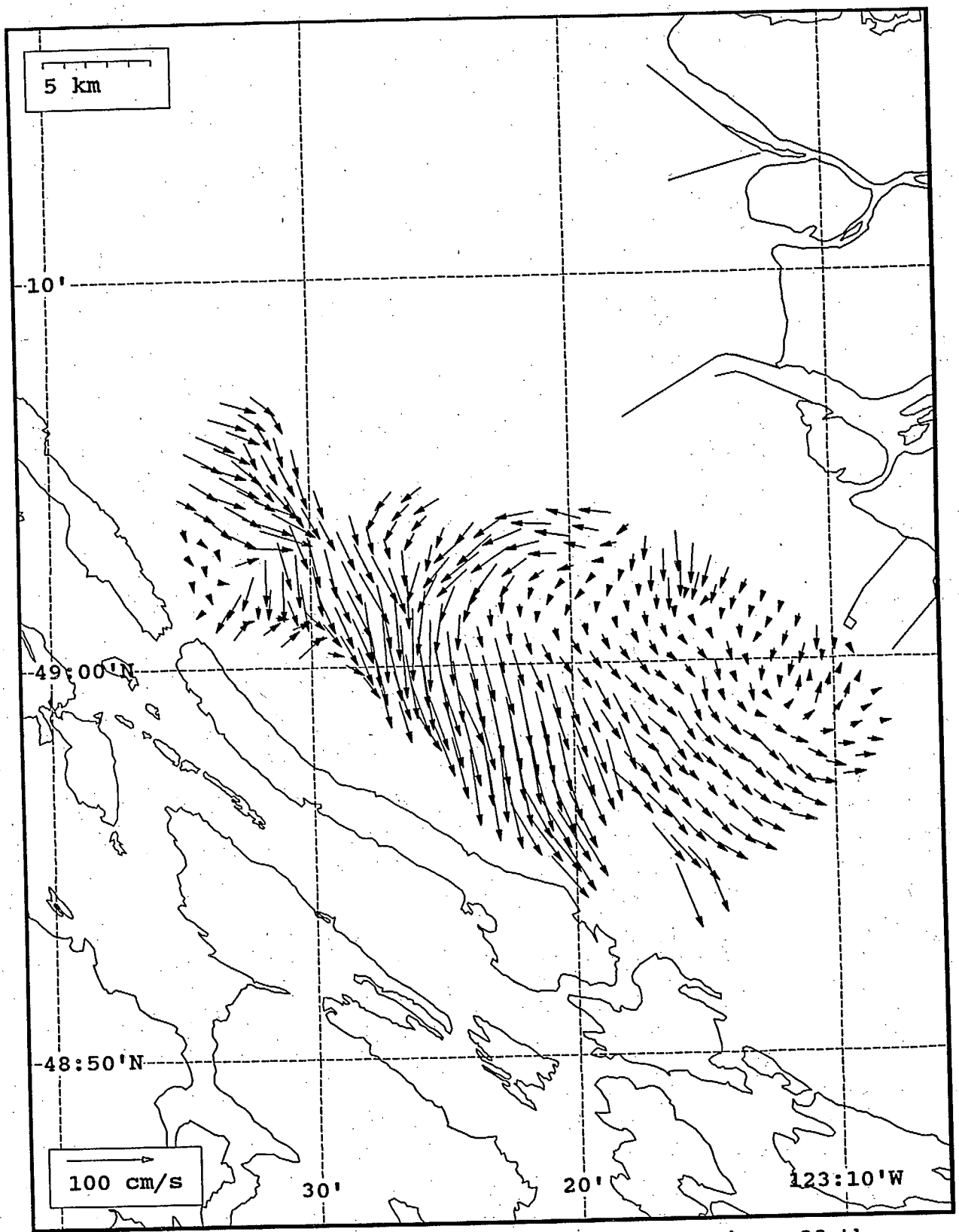

SeaSonde current field from the Strait of Georgia, off the mouth of the Fraser River, for 12:00 Z, July 25, 1993.

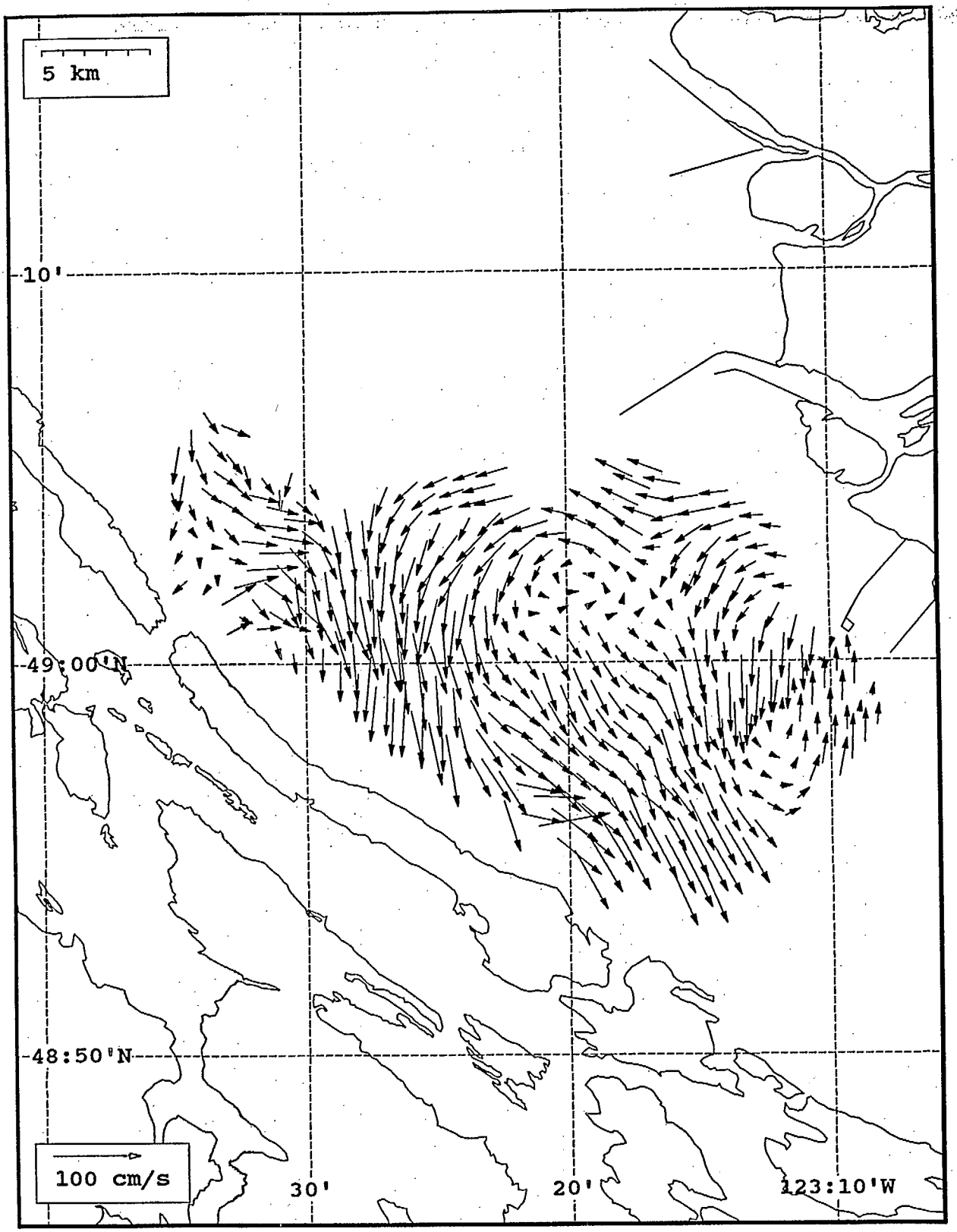

SeaSonde current field from the Strait of Georgia, off the mouth of the Fraser River, for 13:00 Z, July 25, 1993.

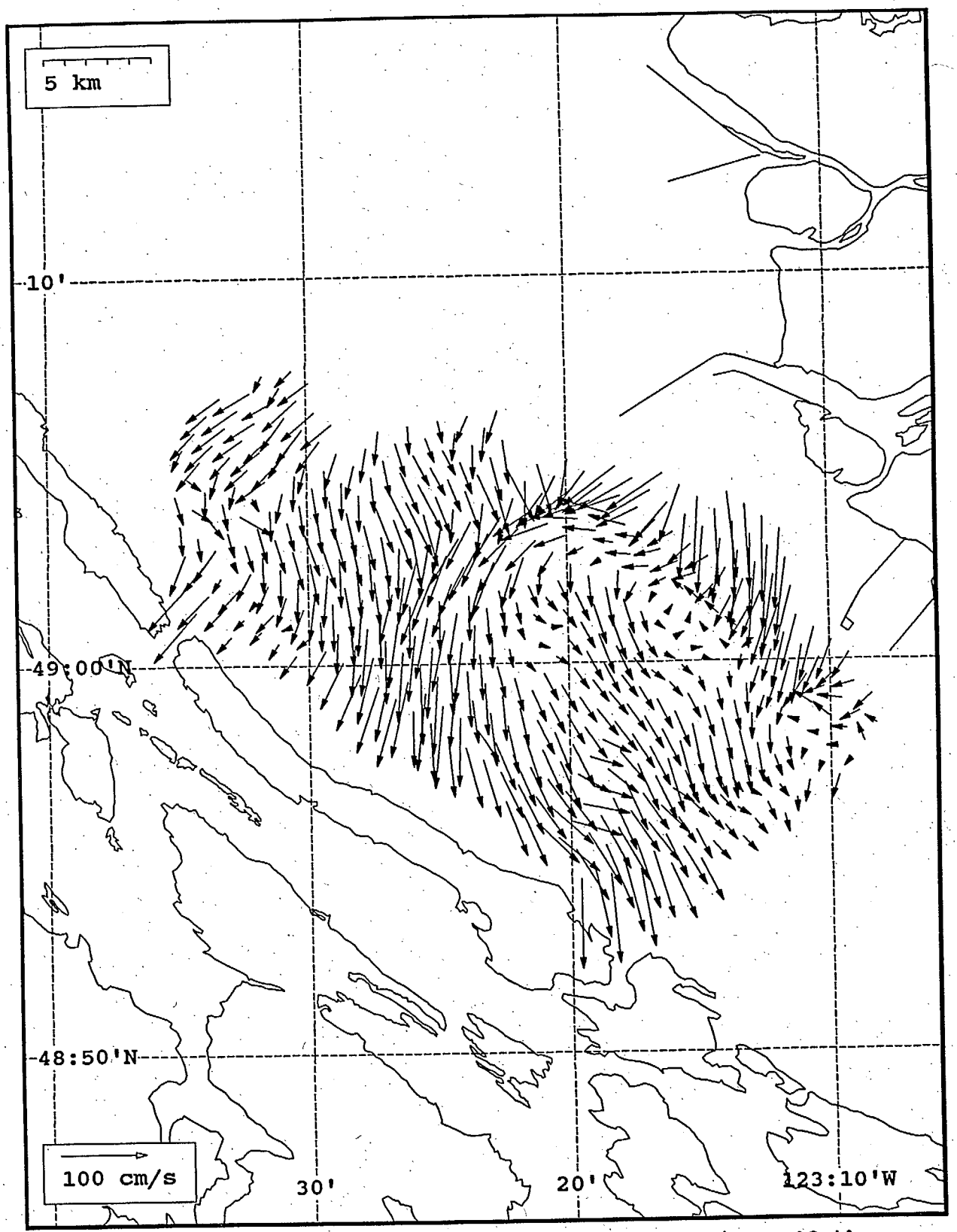

SeaSonde current field from the Strait of Georgia, off the mouth of the Fraser River, for 14:00 Z, July 25, 1993.

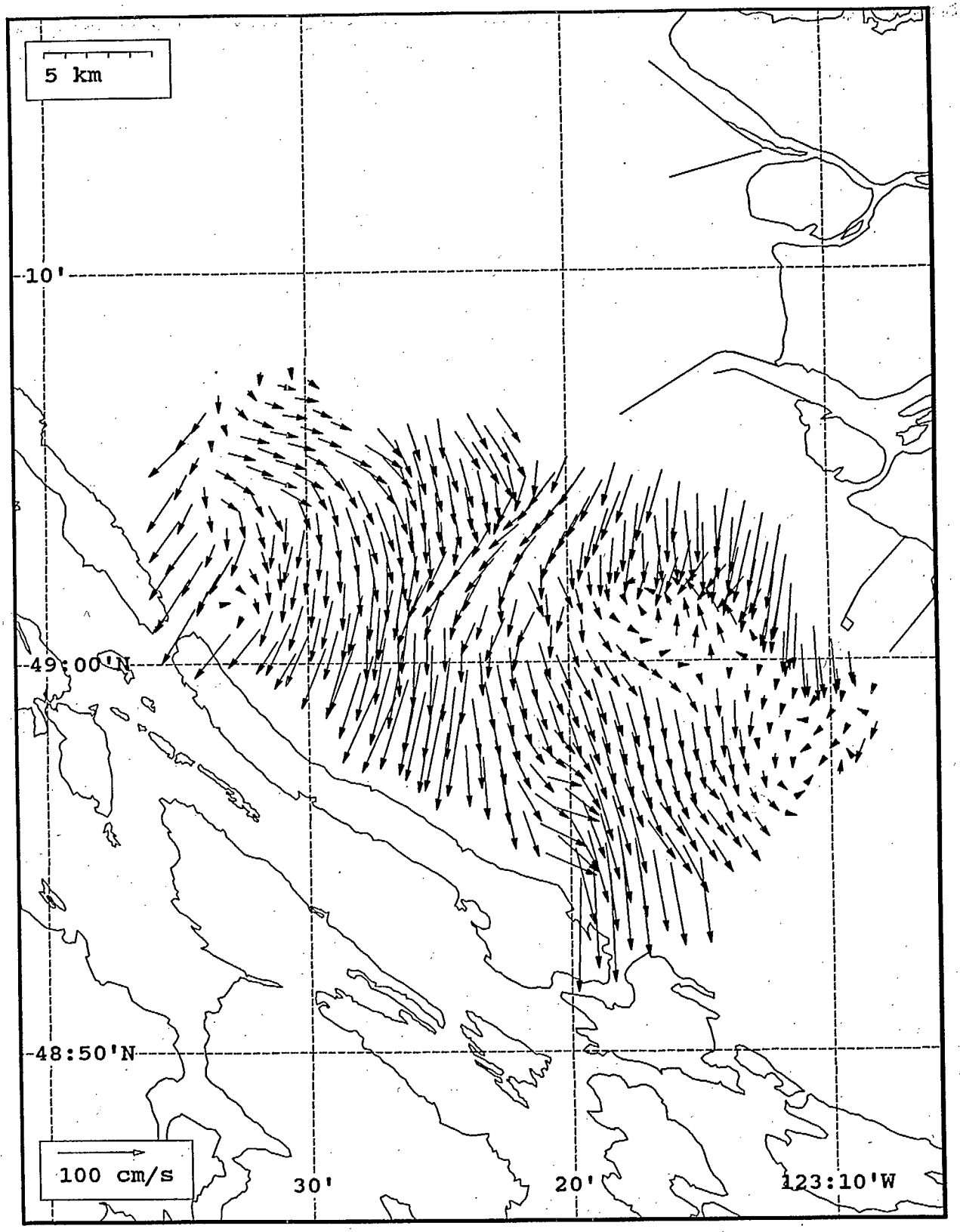

SeaSonde current field from the Strait of Georgia, off the mouth of the Fraser River, for 15:00 Z, July 25, 1993.

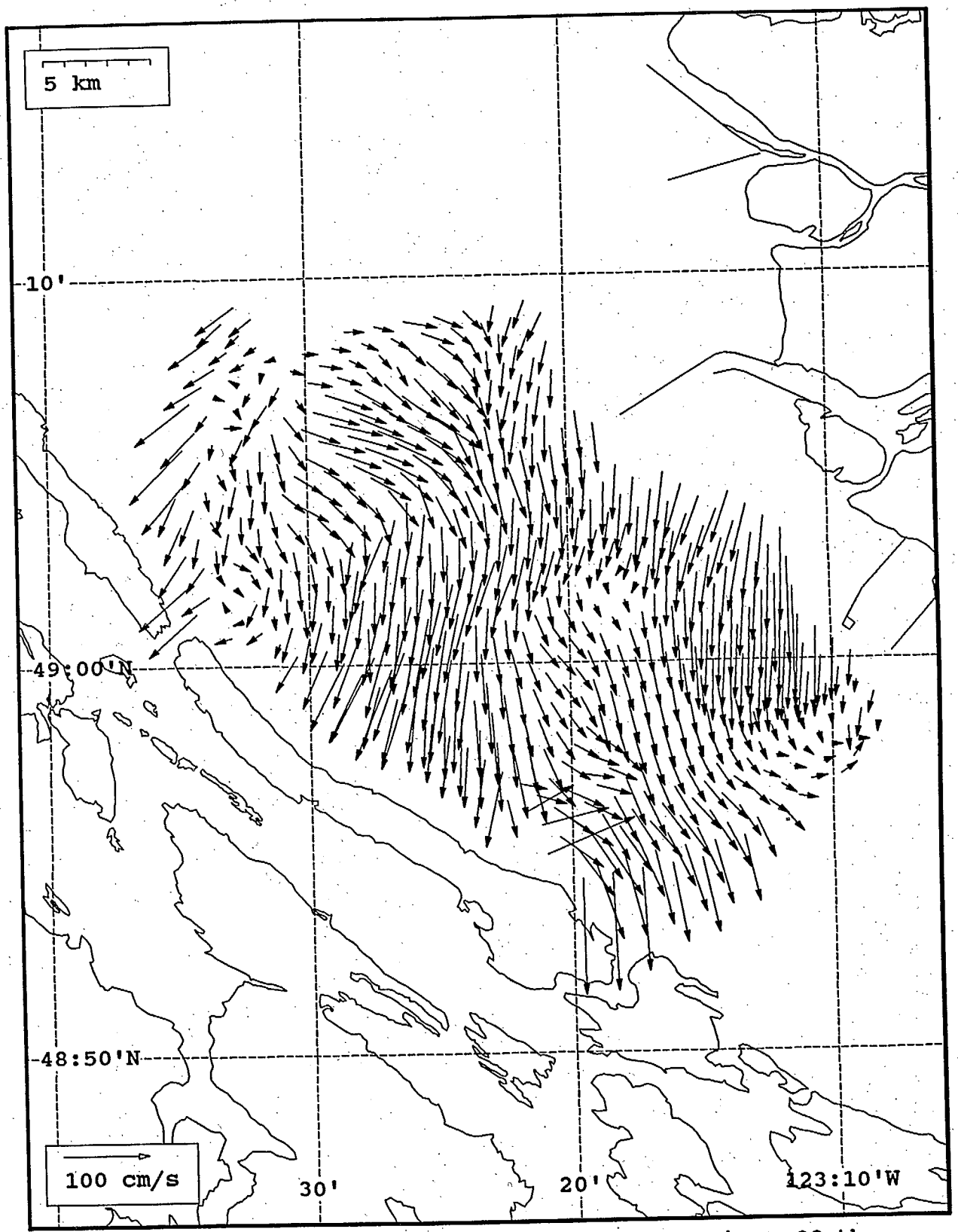

SeaSonde current field from the Strait of Georgia, off the mouth of the Fraser River, for 16:00 Z, July 25, 1993.

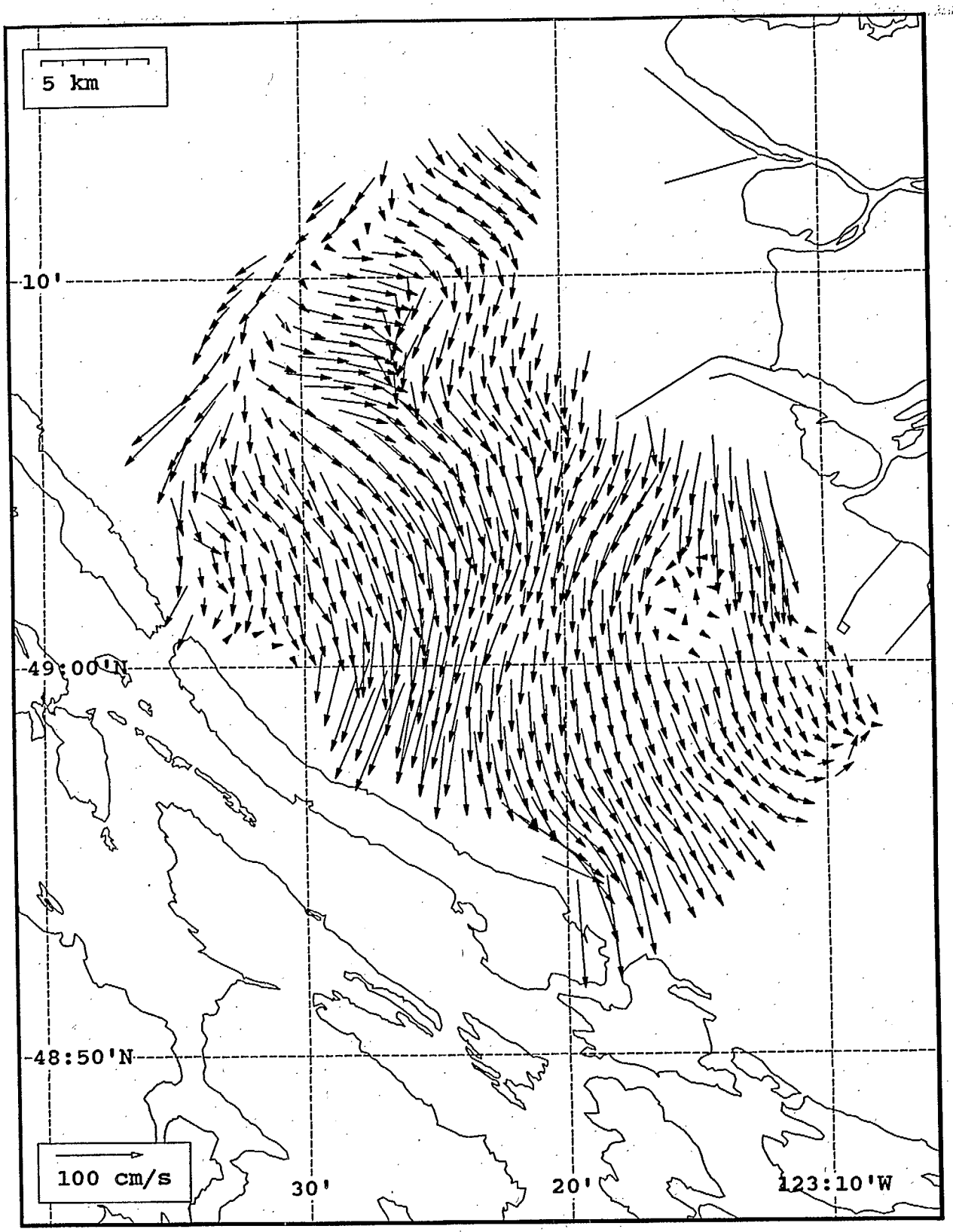

SeaSonde current field from the Strait of Georgia, off the mouth of the Fraser River, for 17:00 Z, July 25, 1993.

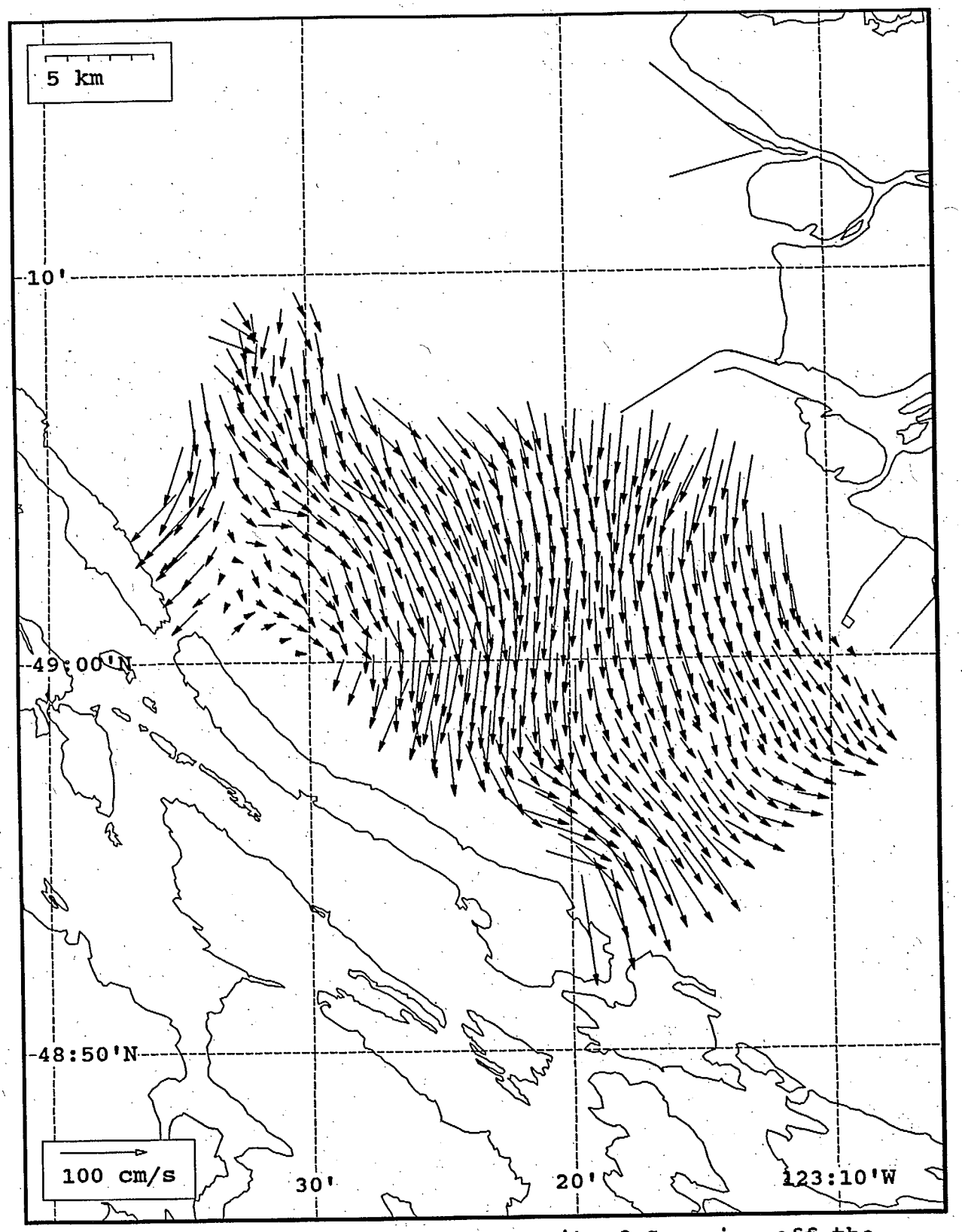

SeaSonde current field from the Strait of Georgia, off the mouth of the Fraser River, for 18:00 Z, July 25, 1993.

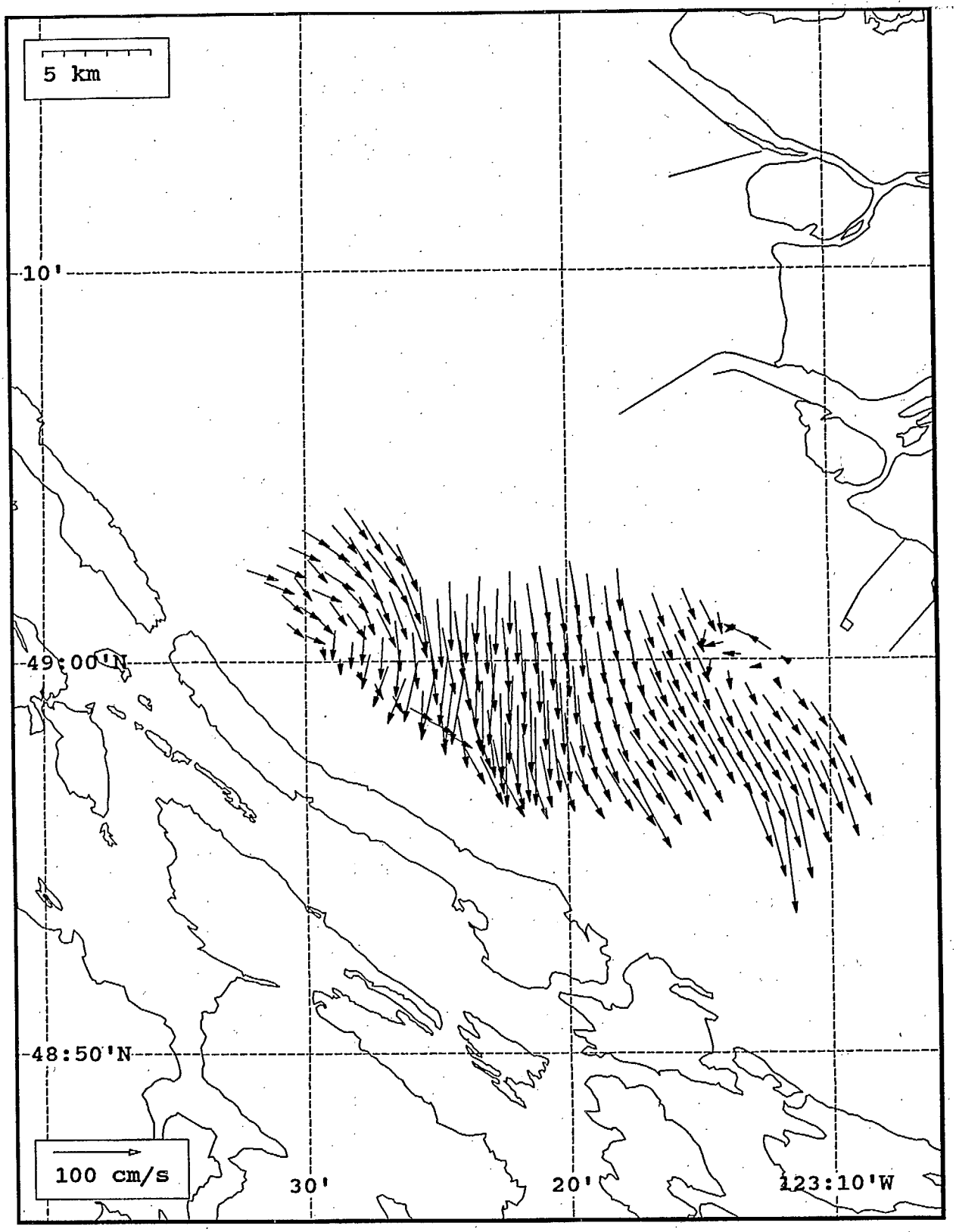

SeaSonde current field from the Strait of Georgia, off the mouth of the Fraser River, for 19:00 Z, July 25, 1993.

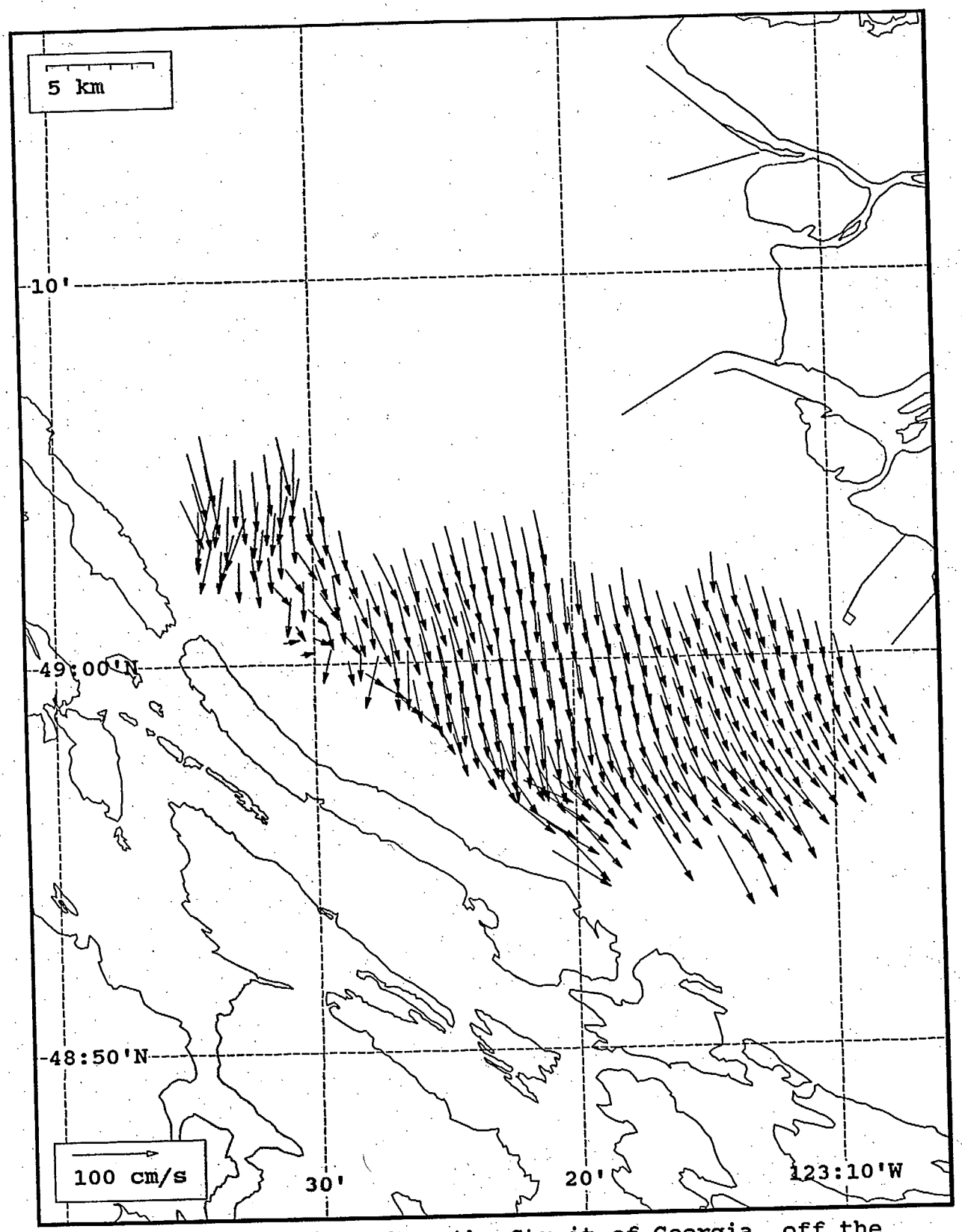

SeaSonde current field from the Strait of Georgia, off the mouth of the Fraser River, for 20:00 Z, July 25, 1993.

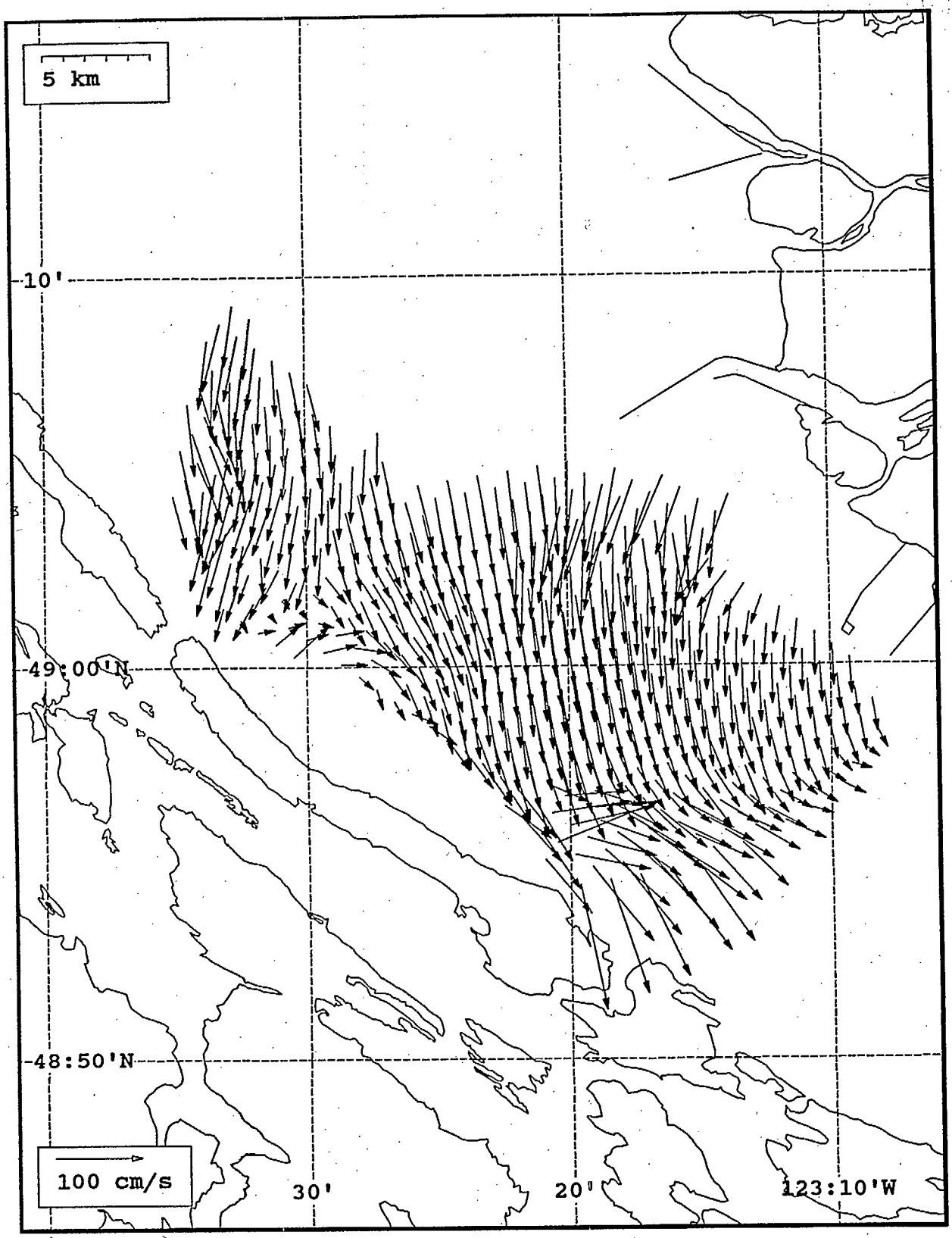

SeaSonde current field from the Strait of Georgia, off the mouth of the Fraser River, for 21:00 Z, July 25, 1993.

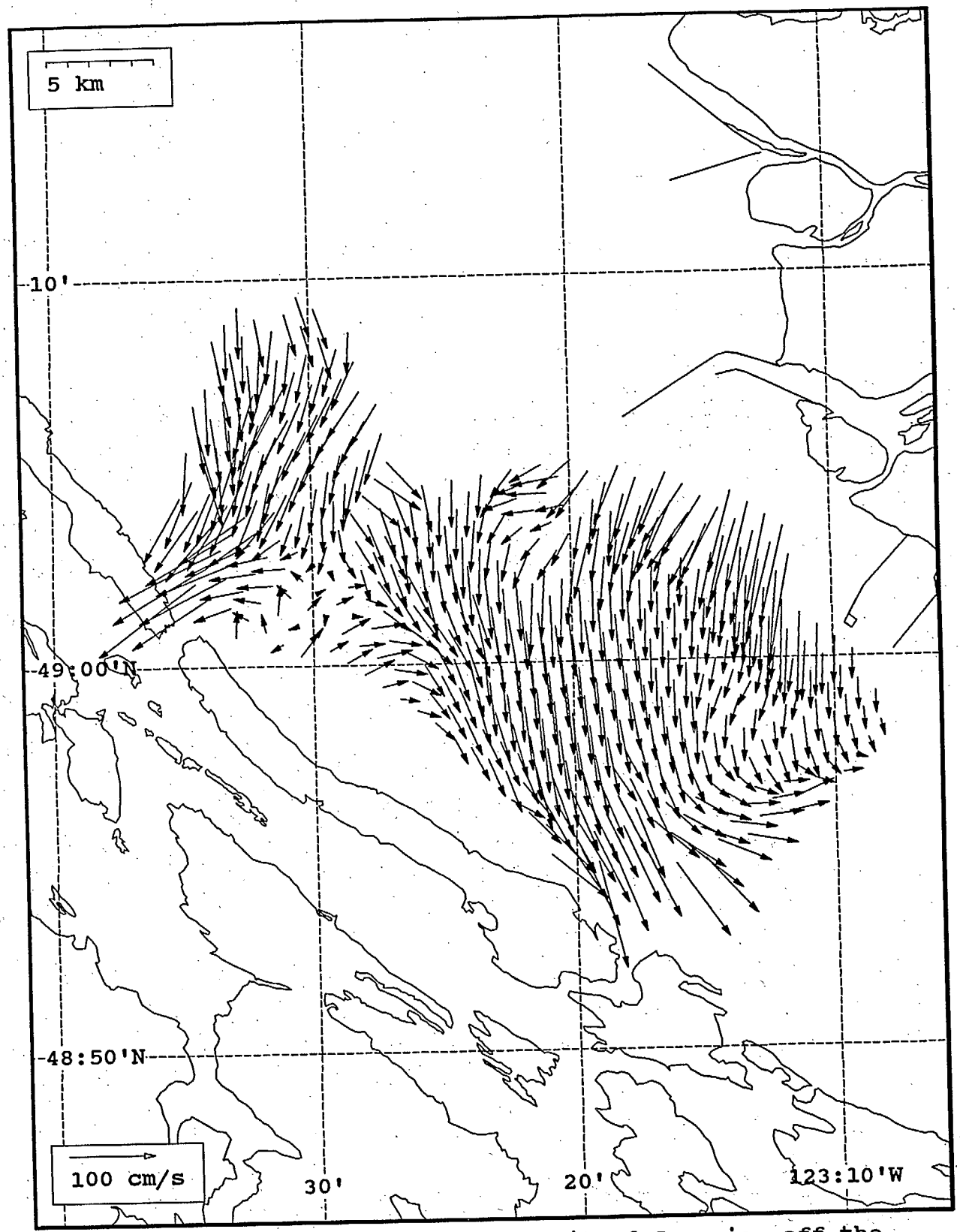

SeaSonde current field from the Strait of Georgia, off the mouth of the Fraser River, for 22:00 Z, July 25, 1993.

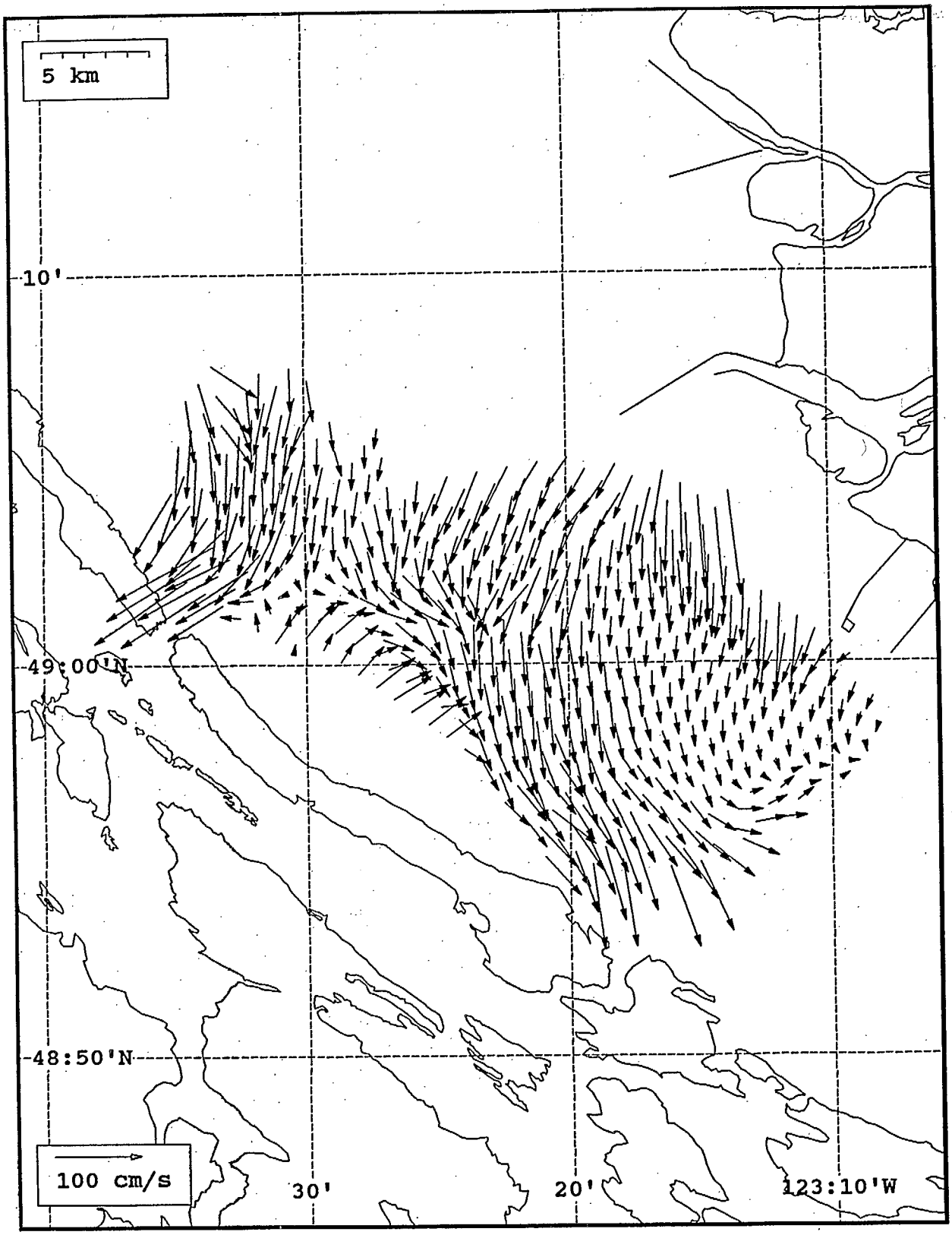

SeaSonde current field from the Strait of Georgia, off the mouth of the Fraser River, for 23:00 Z, July 25, 1993.

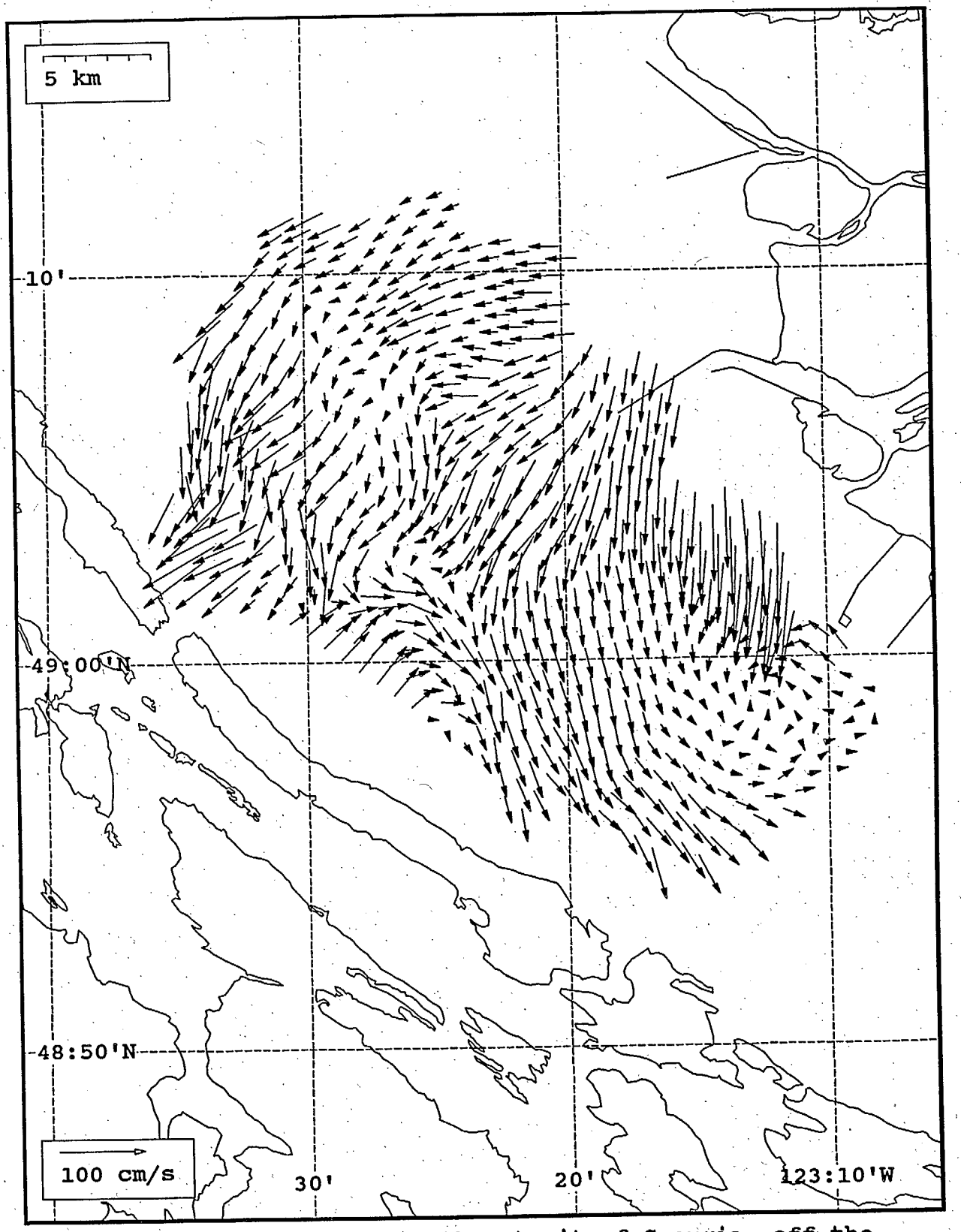

SeaSonde current field from the Strait of Georgia, off the mouth of the Fraser River, for 00:00 Z, July 26, 1993.

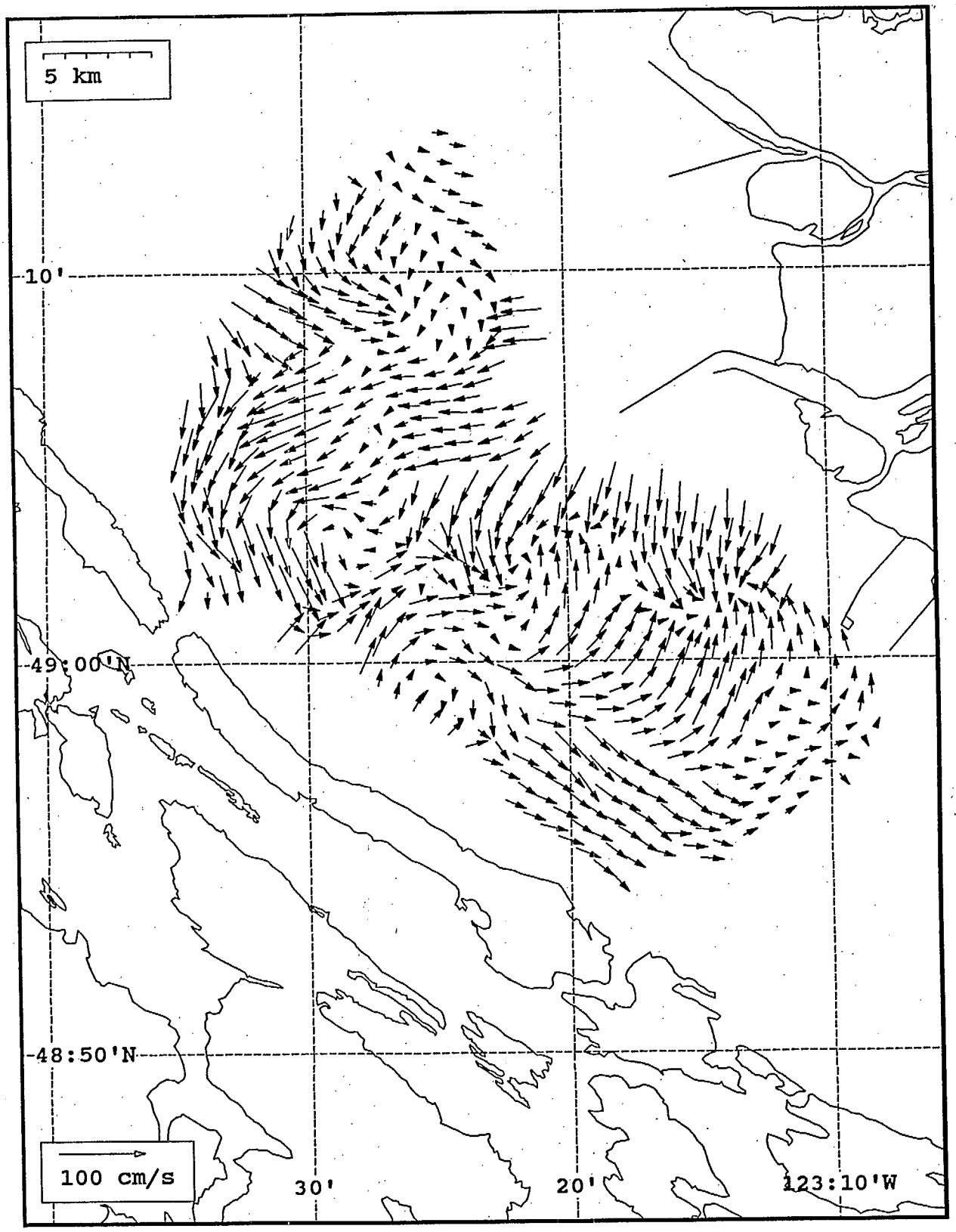

SeaSonde current field from the Strait of Georgia, off the mouth of the Fraser River, for 01:00 Z, July 26, 1993.

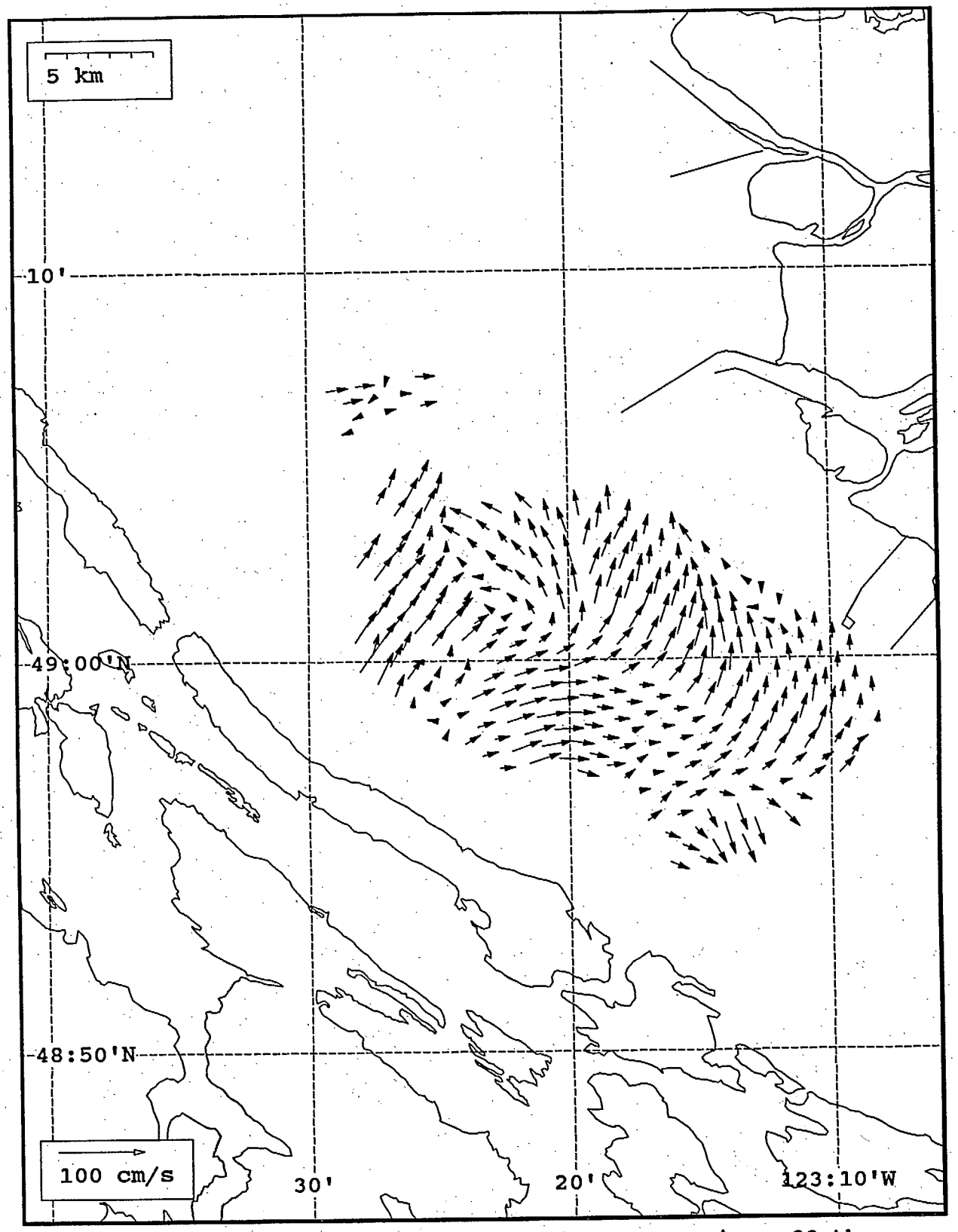

SeaSonde current field from the Strait of Georgia, off the mouth of the Fraser River, for 02:00 Z, July 26, 1993.

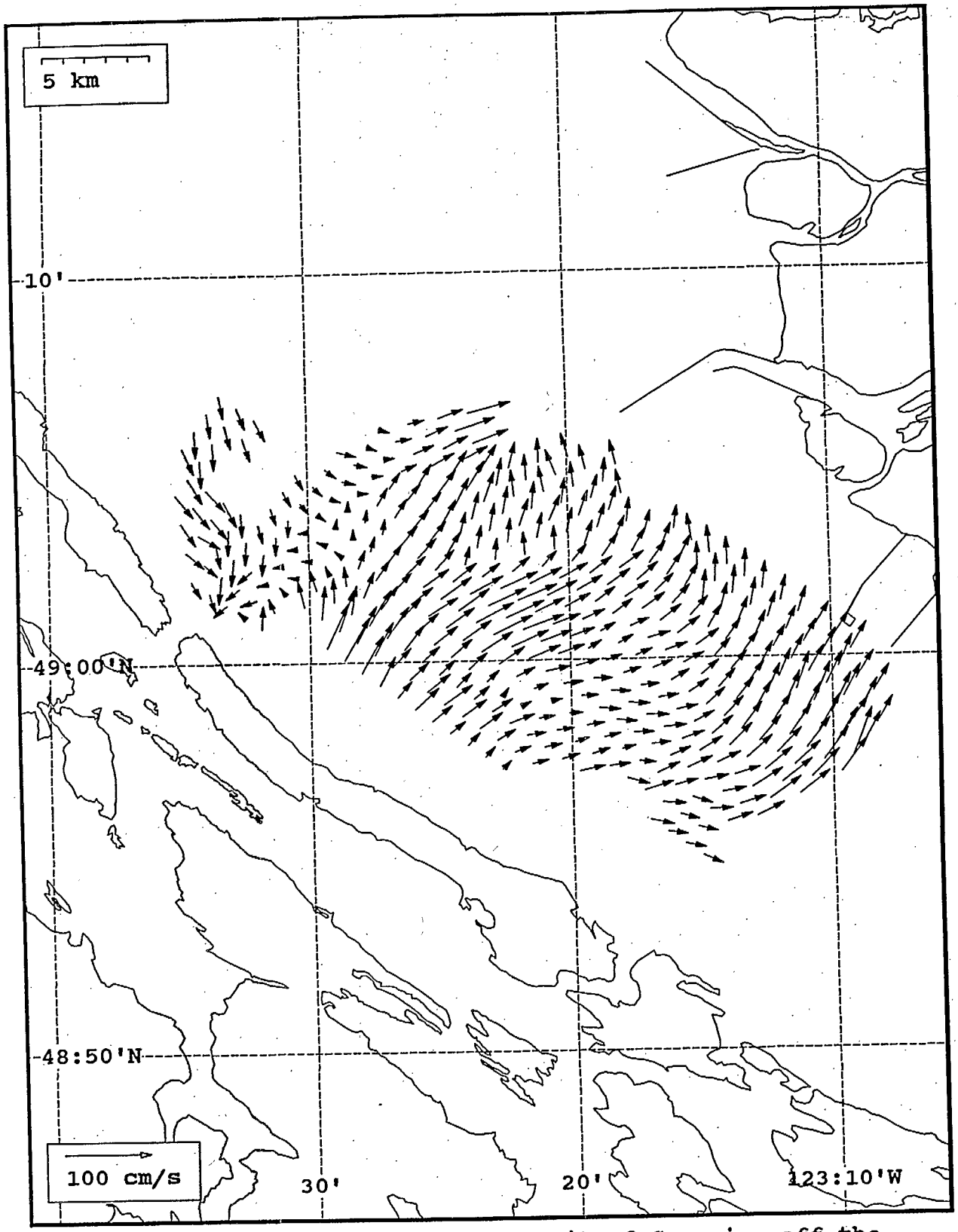

SeaSonde current field from the Strait of Georgia, off the mouth of the Fraser River, for 03:00 Z, July 26, 1993.

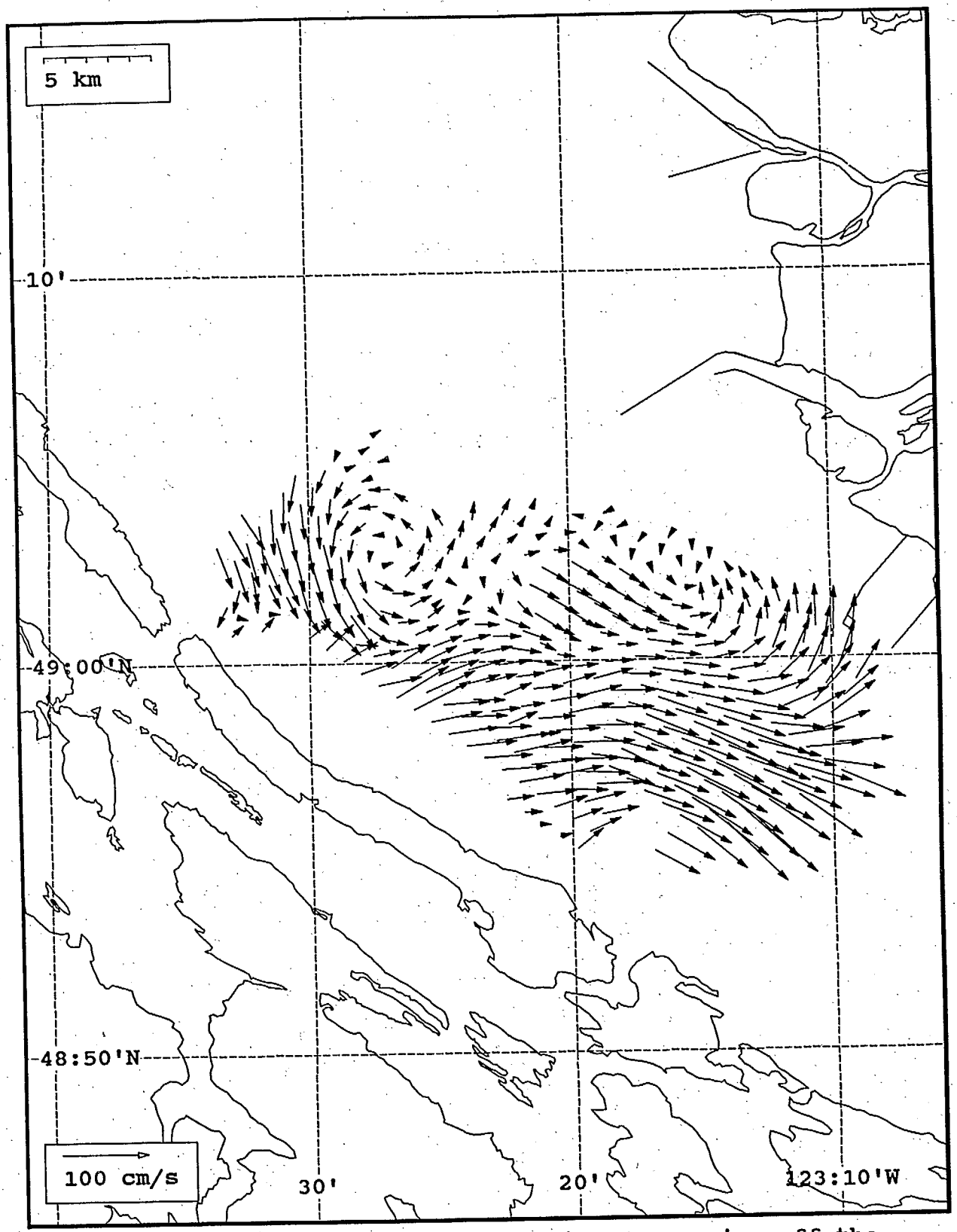

SeaSonde current field from the Strait of Georgia, off the mouth of the Fraser River, for 06:00 Z, July 26, 1993.

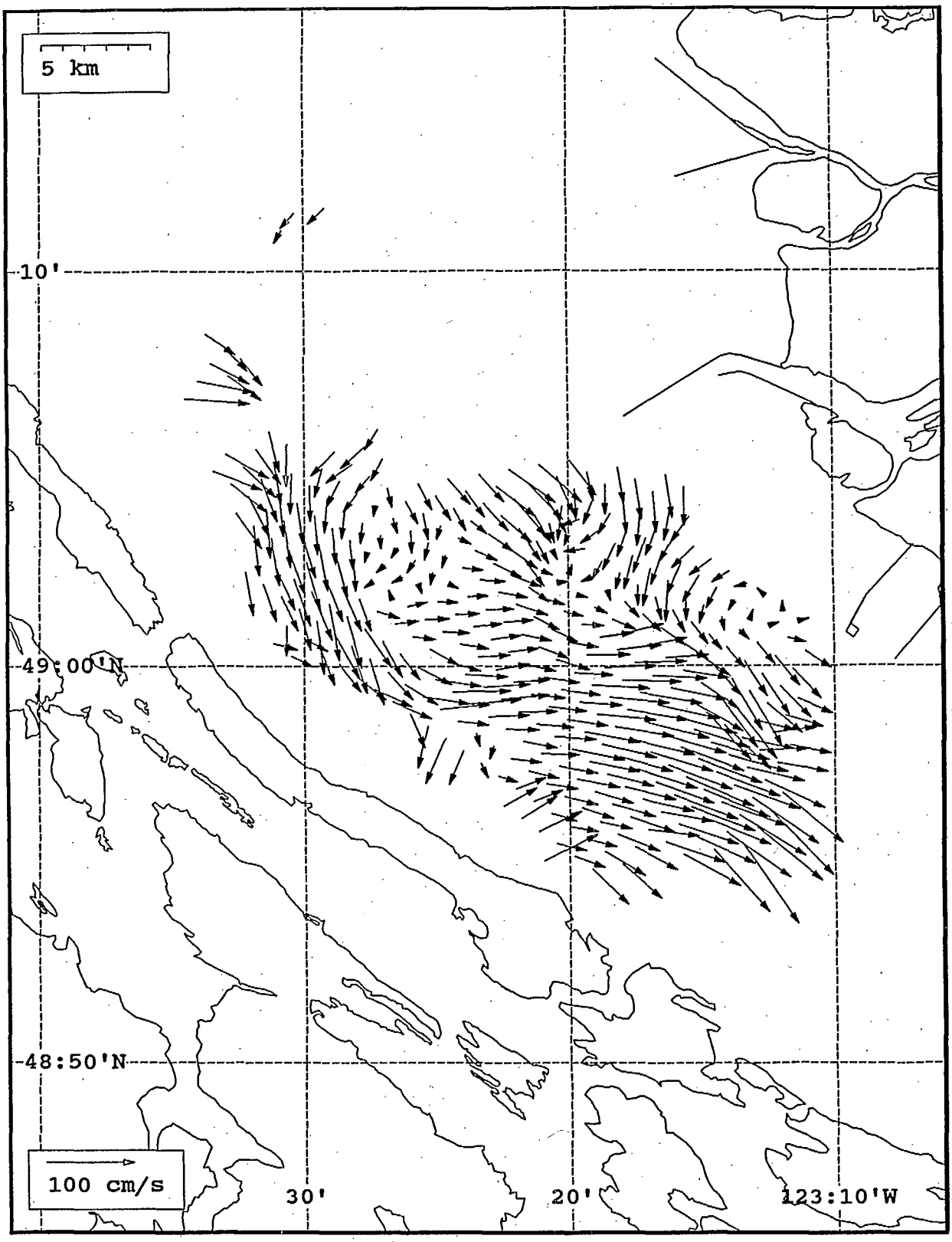

SeaSonde current field from the Strait of Georgia, off the mouth of the Fraser River, for 07:00 Z, July 26, 1993.

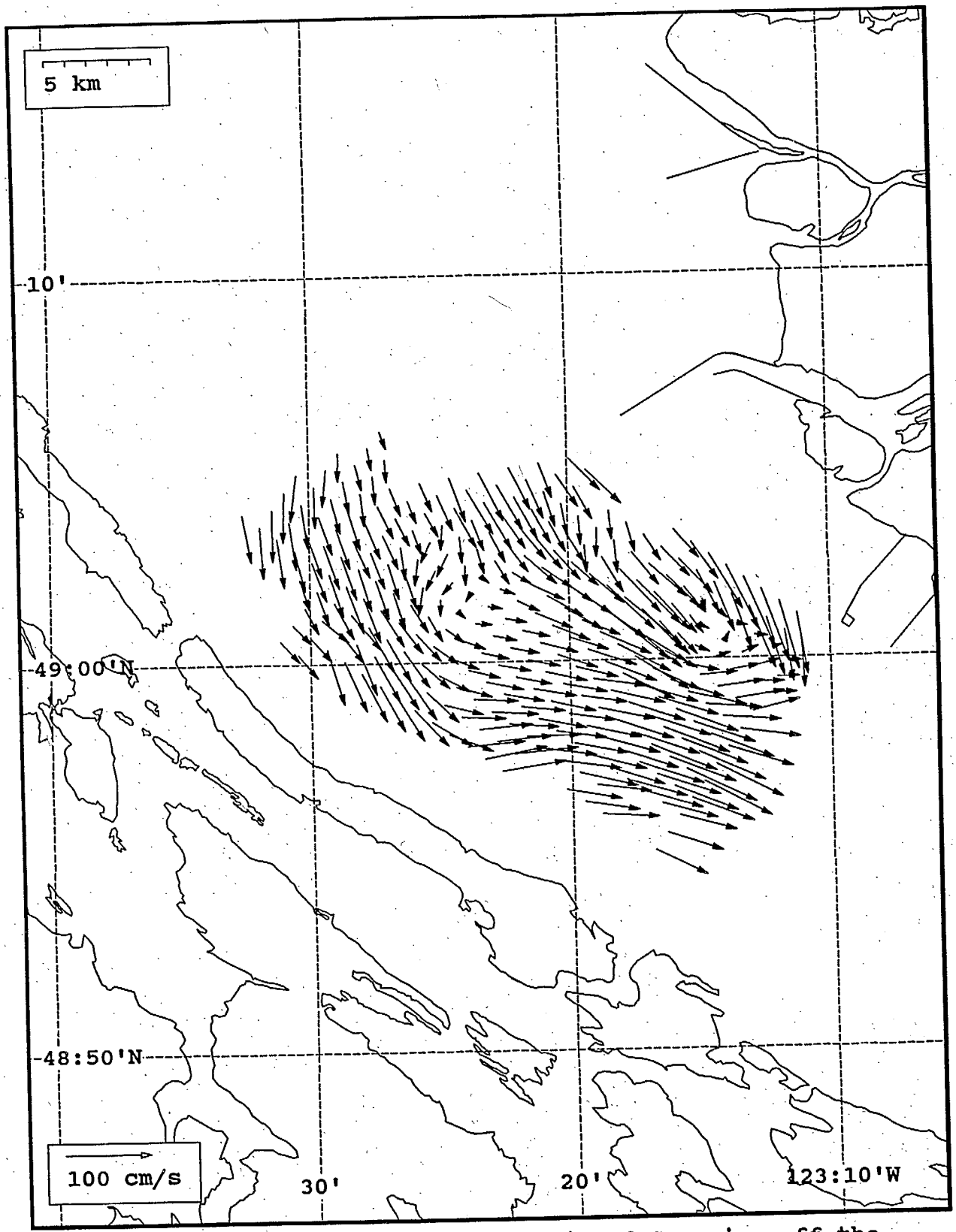

SeaSonde current field from the Strait of Georgia, off the mouth of the Fraser River, for 08:00 Z, July 26, 1993.

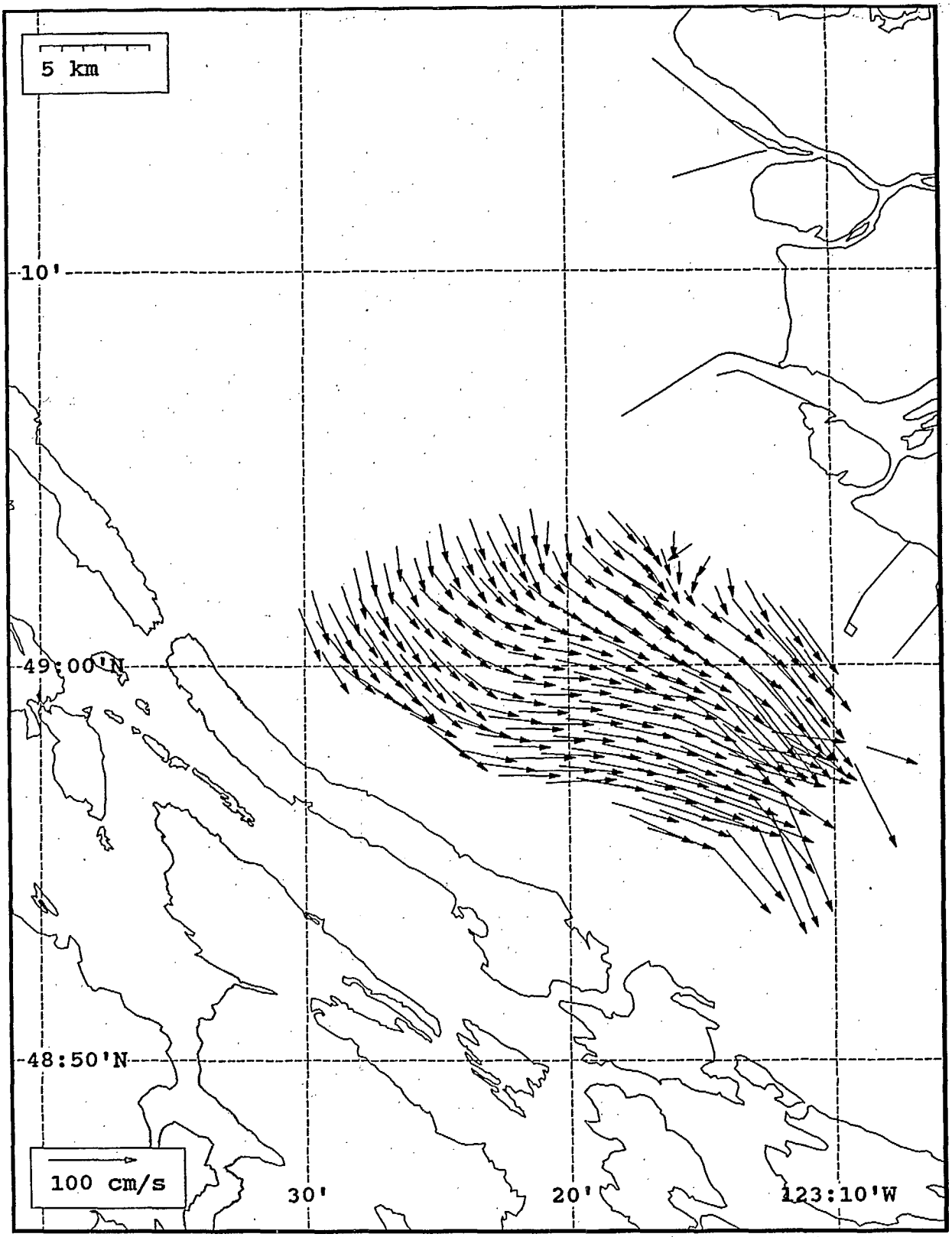

SeaSonde current field from the Strait of Georgia, off the mouth of the Fraser River, for 09:00 Z, July 26, 1993.

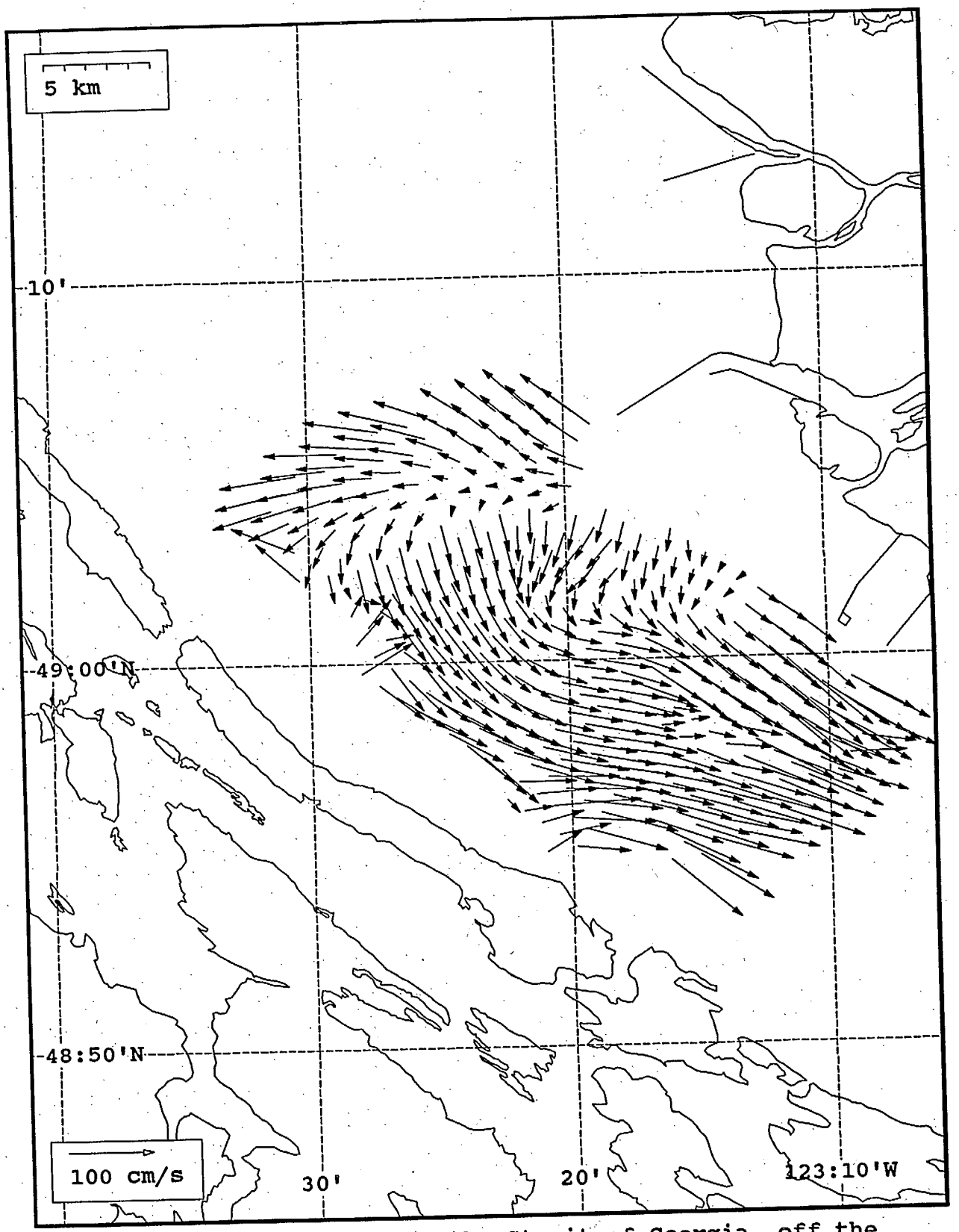

SeaSonde current field from the Strait of Georgia, off the mouth of the Fraser River, for 10:00 Z, July 26, 1993.

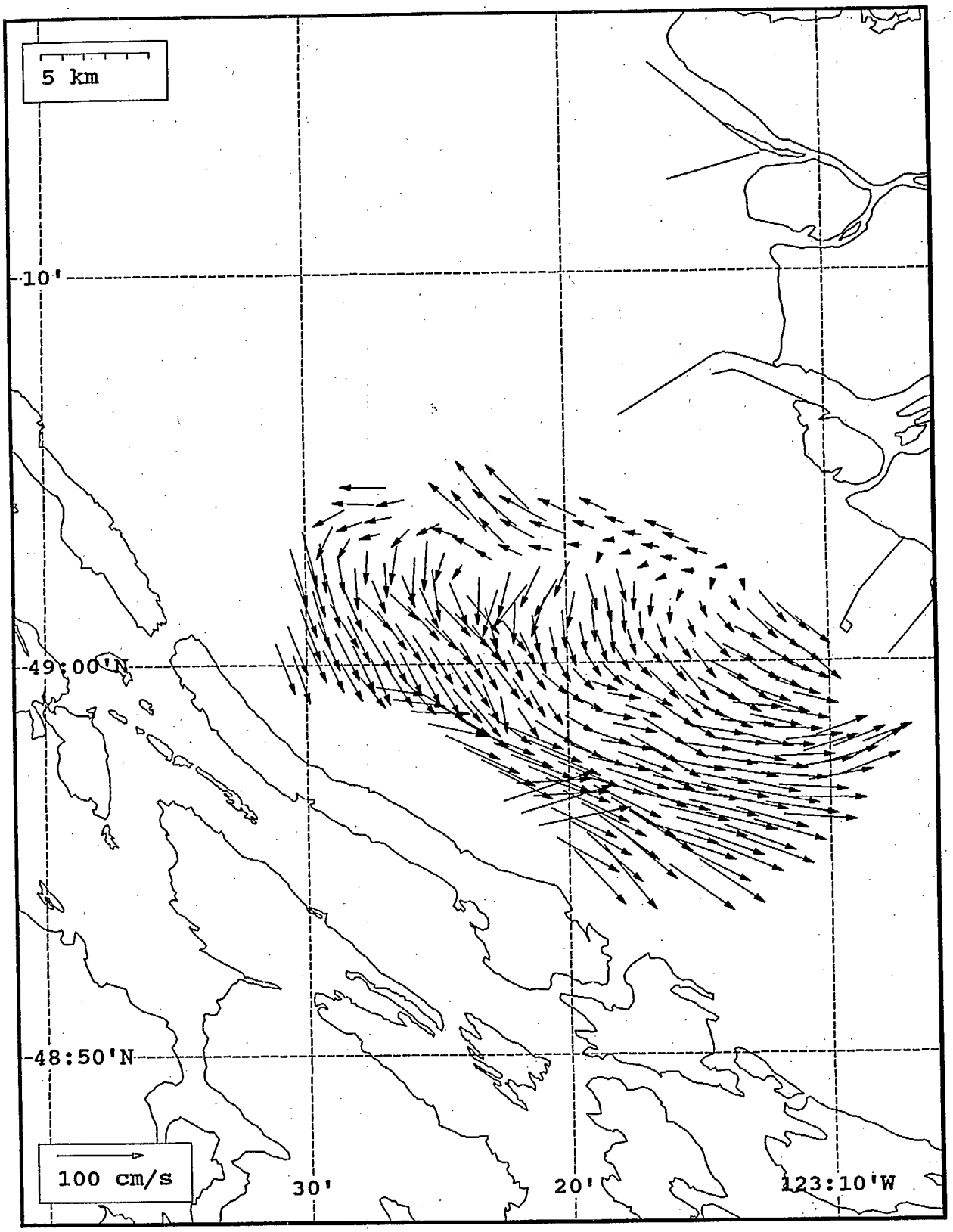

SeaSonde current field from the Strait of Georgia, off the mouth of the Fraser River, for 11:00 Z, July 26, 1993.

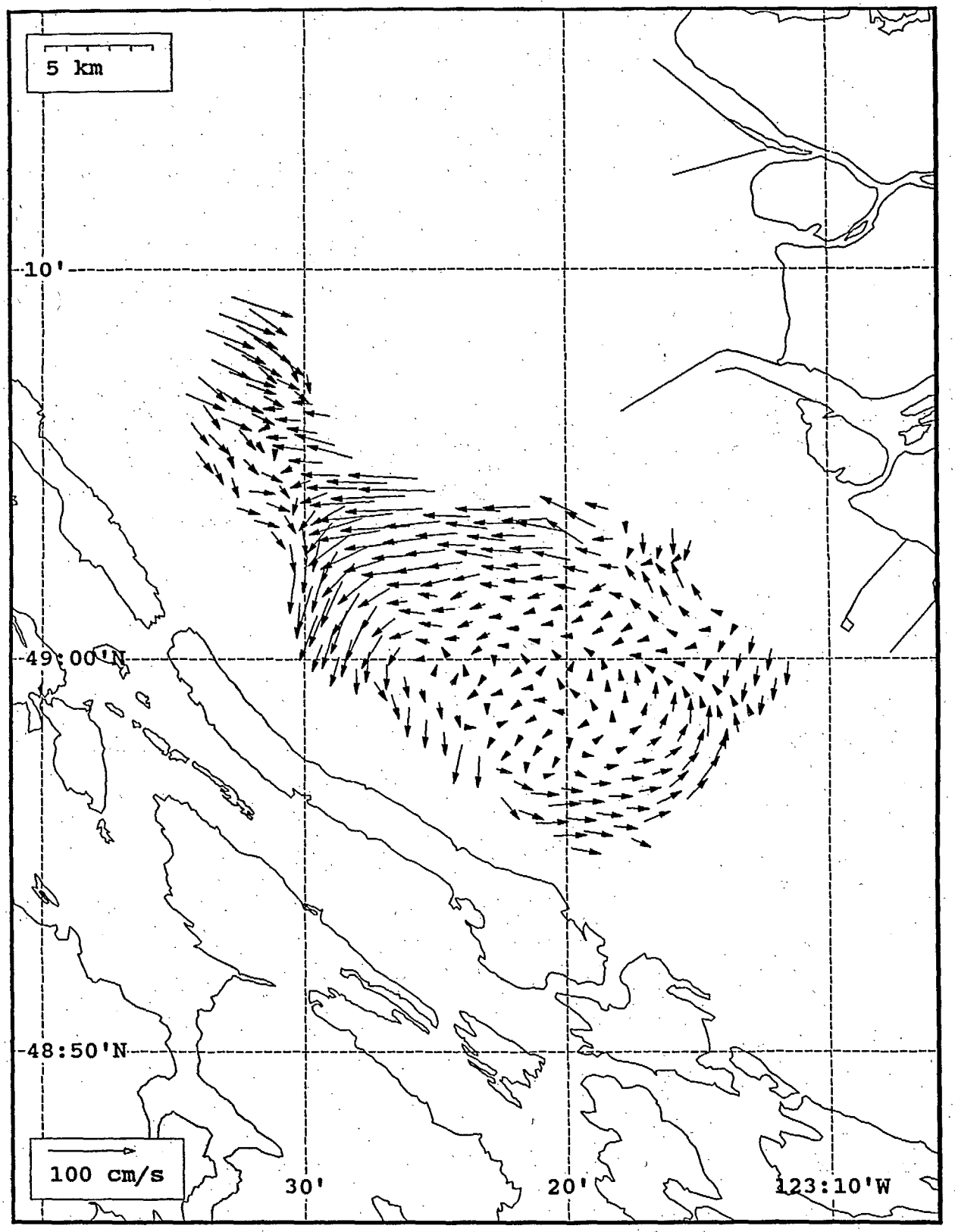

SeaSonde current field from the Strait of Georgia, off the mouth of the Fraser River, for 15:00 Z, July 26, 1993.

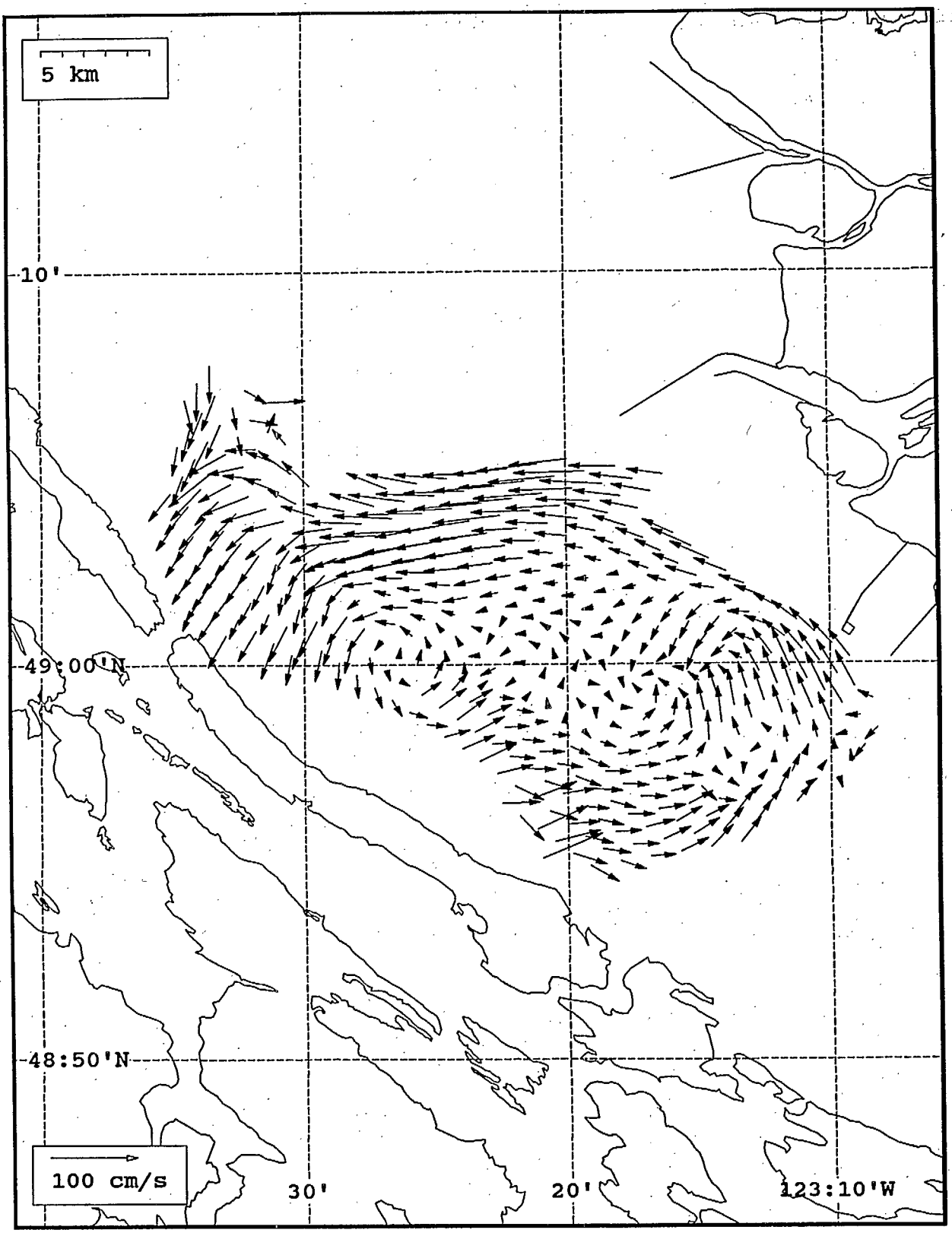

SeaSonde current field from the Strait of Georgia, off the mouth of the Fraser River, for 16:00 Z, July 26, 1993.

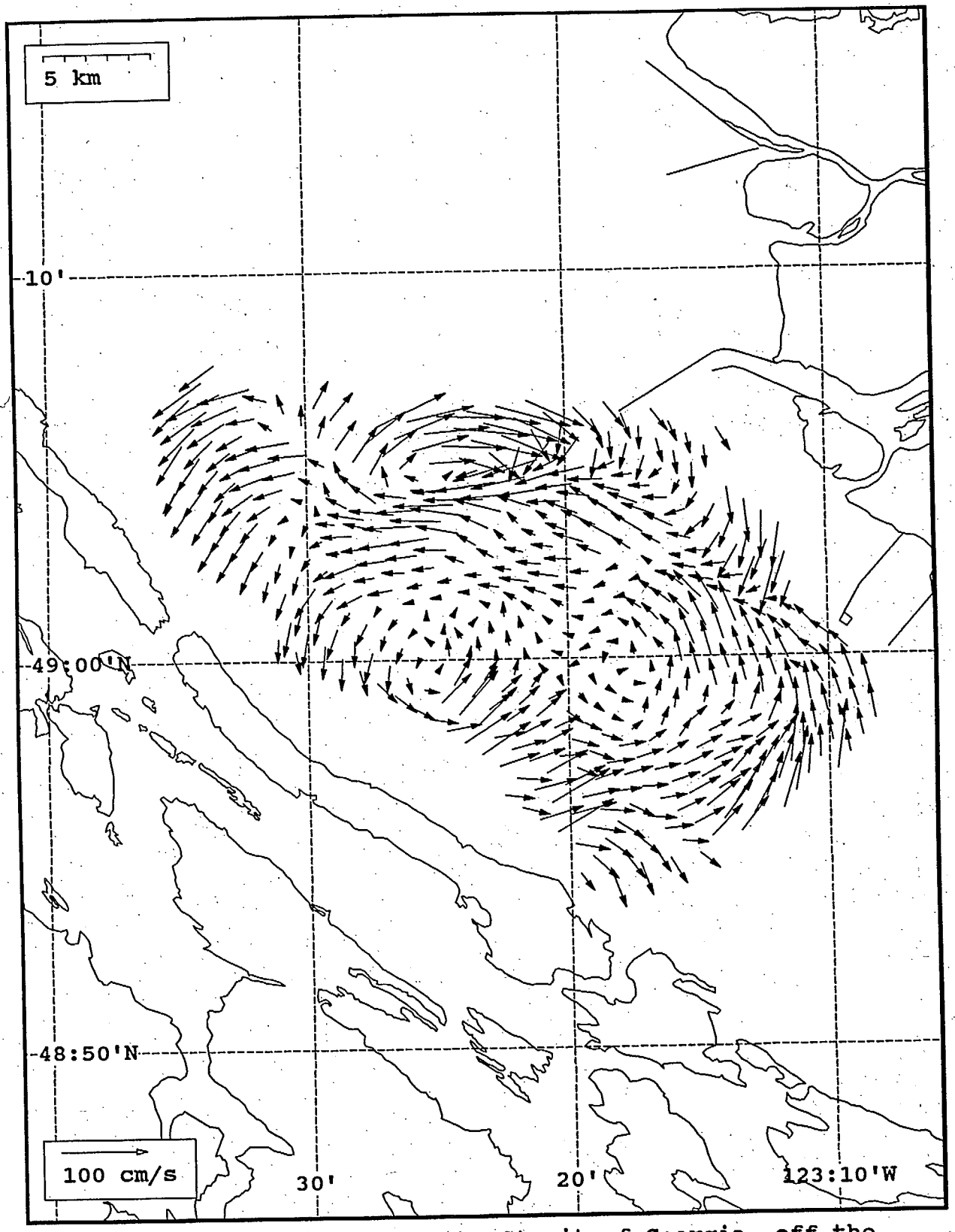

SeaSonde current field from the Strait of Georgia, off the mouth of the Fraser River, for 17:00 Z, July 26, 1993.

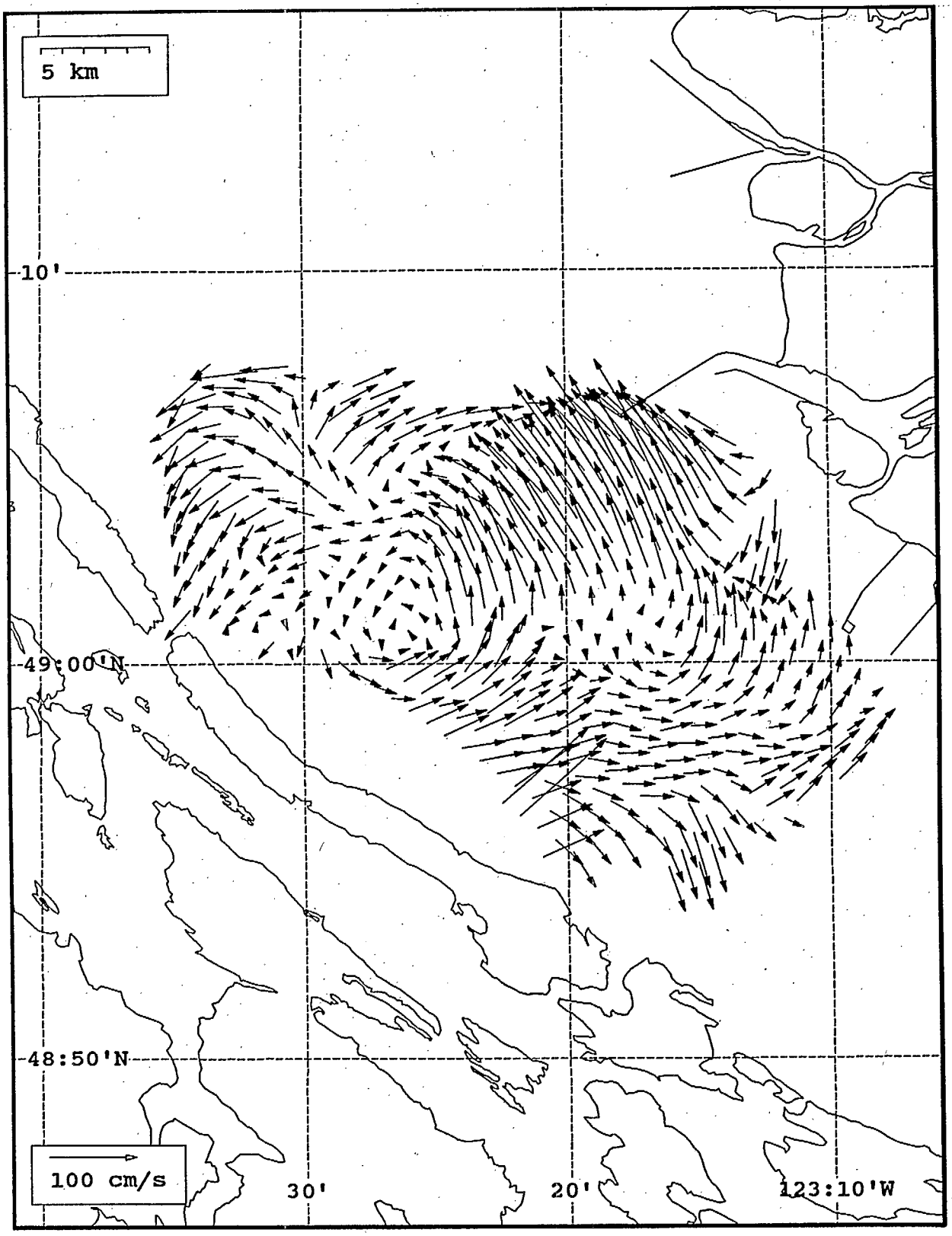

SeaSonde current field from the Strait of Georgia, off the mouth of the Fraser River, for 18:00 Z, July 26, 1993.

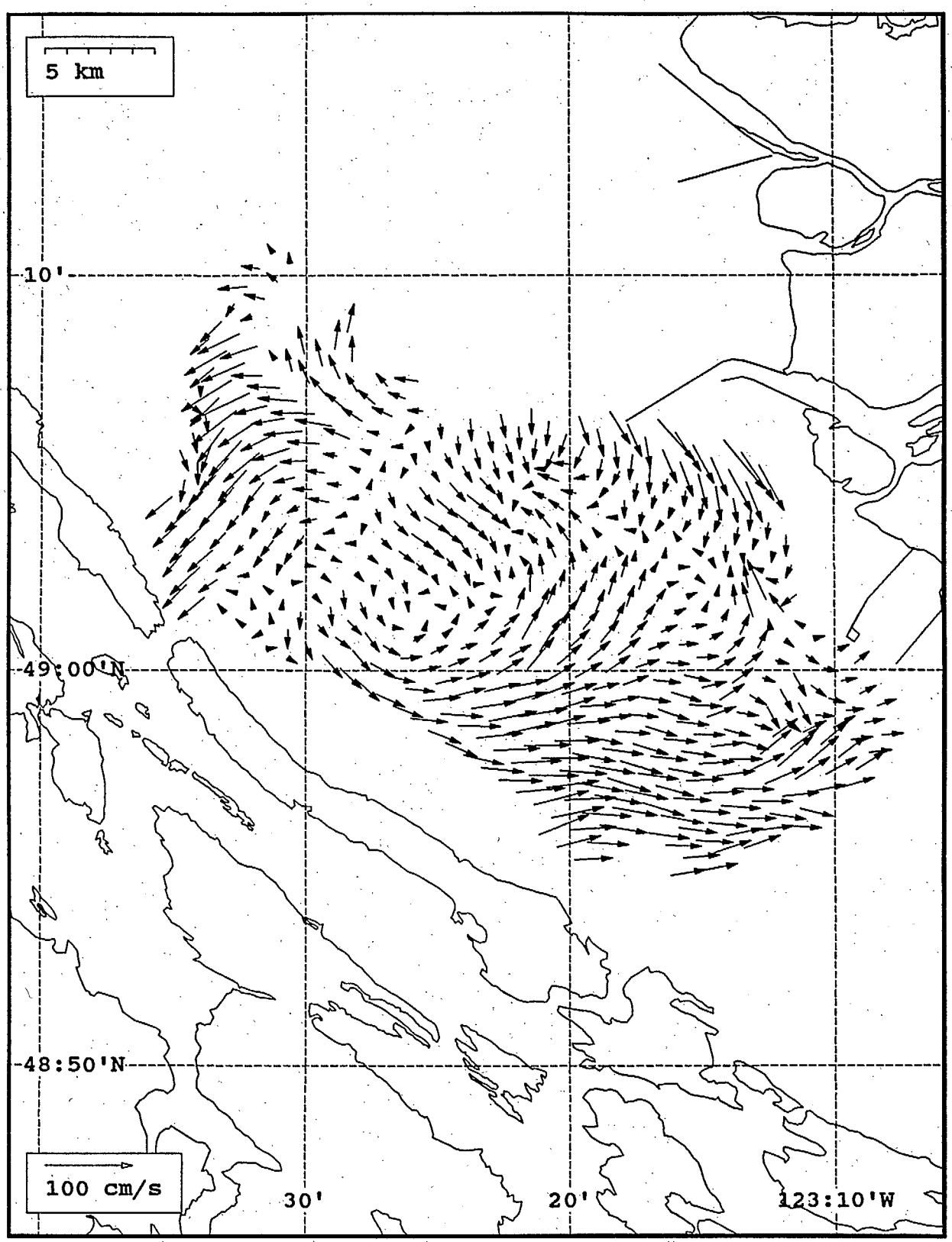

SeaSonde current field from the Strait of Georgia, off the mouth of the Fraser River, for 19:00 Z, July 26, 1993.

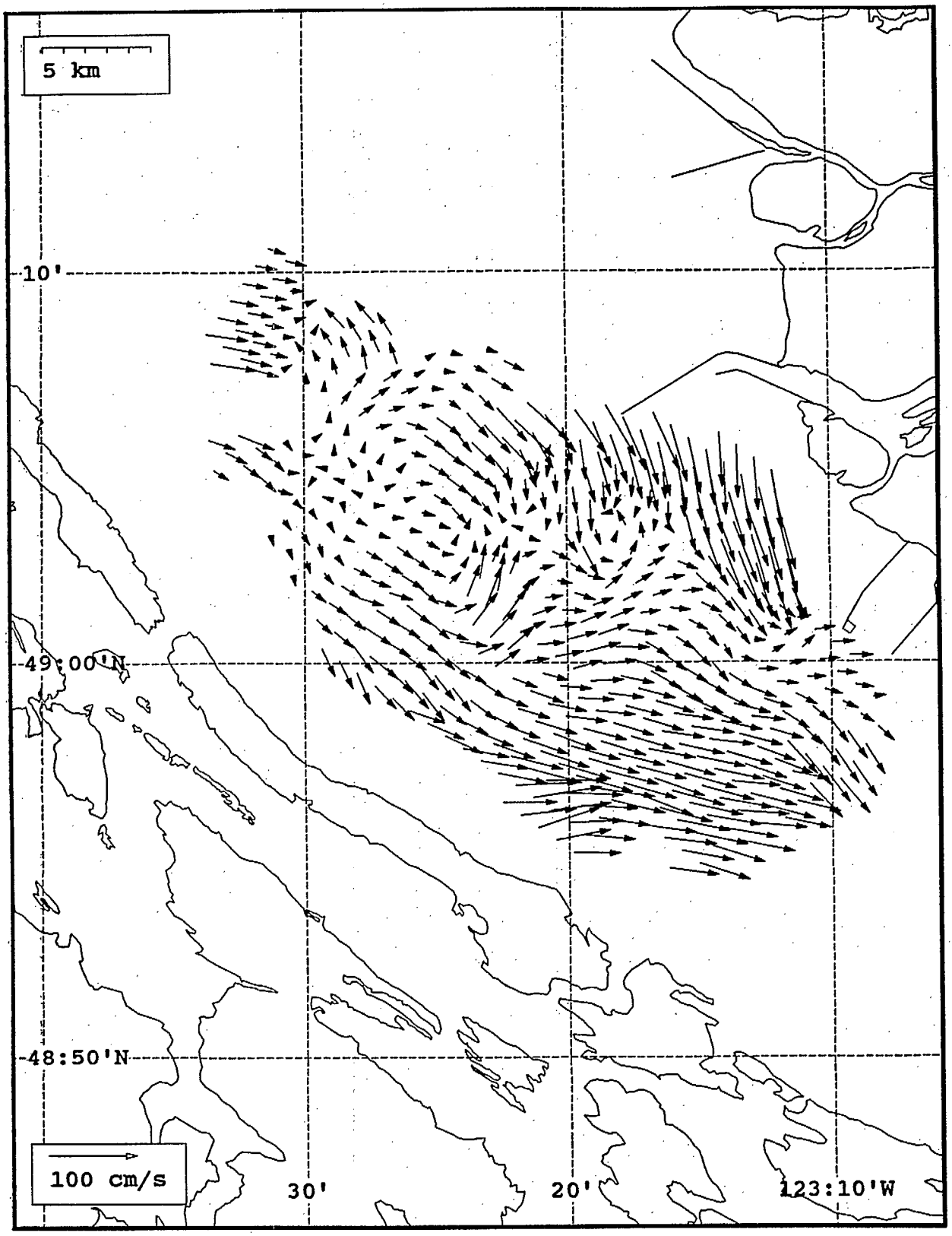

SeaSonde current field from the Strait of Georgia, off the mouth of the Fraser River, for 20:00 Z, July 26, 1993.

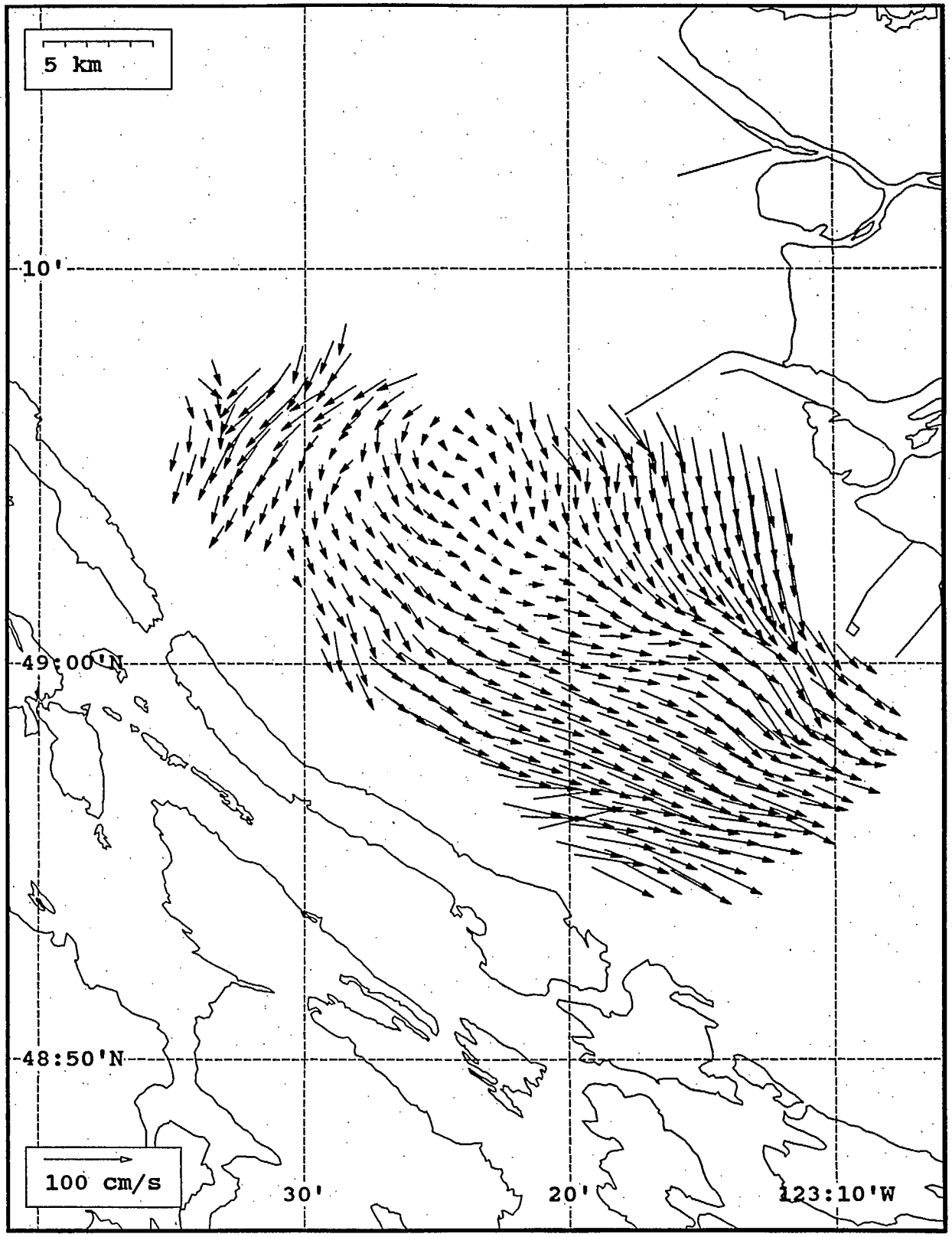

SeaSonde current field from the Strait of Georgia, off the mouth of the Fraser River, for 21:00 Z, July 26, 1993.

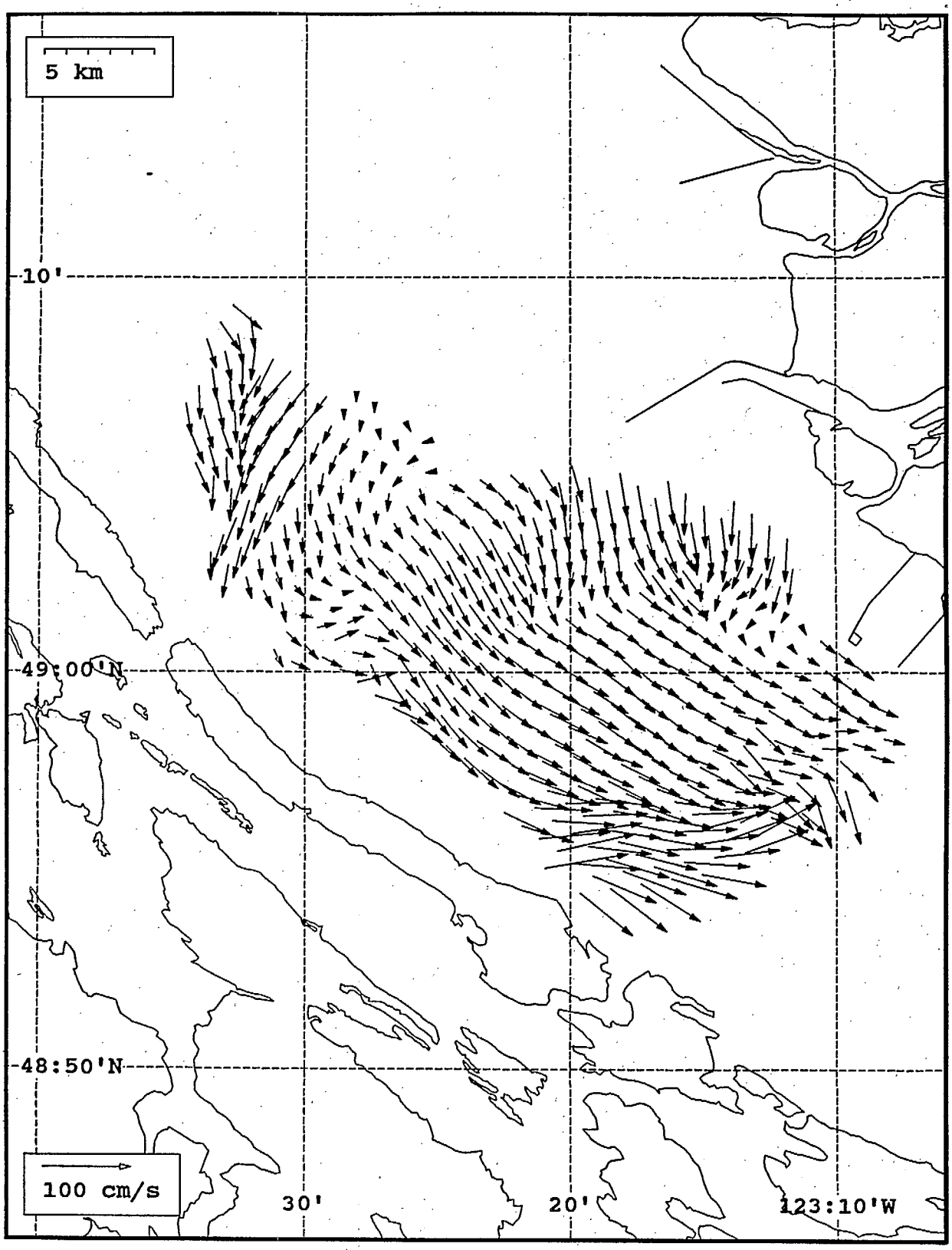

SeaSonde current field from the Strait of Georgia, off the mouth of the Fraser River, for 22:00 Z, July 26, 1993.

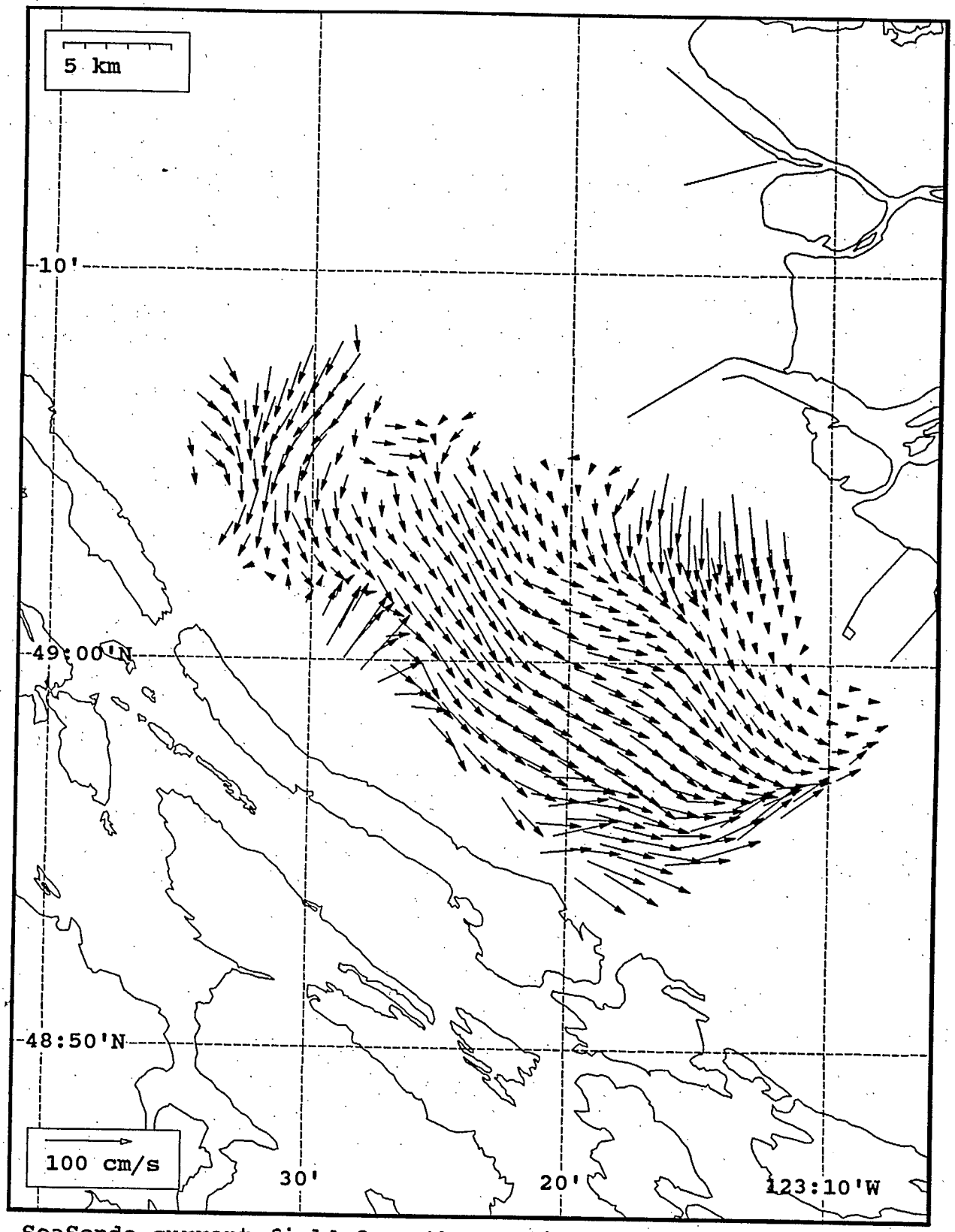

SeaSonde current field from the Strait of Georgia, off the mouth of the Fraser River, for 23:00 Z, July 26, 1993.

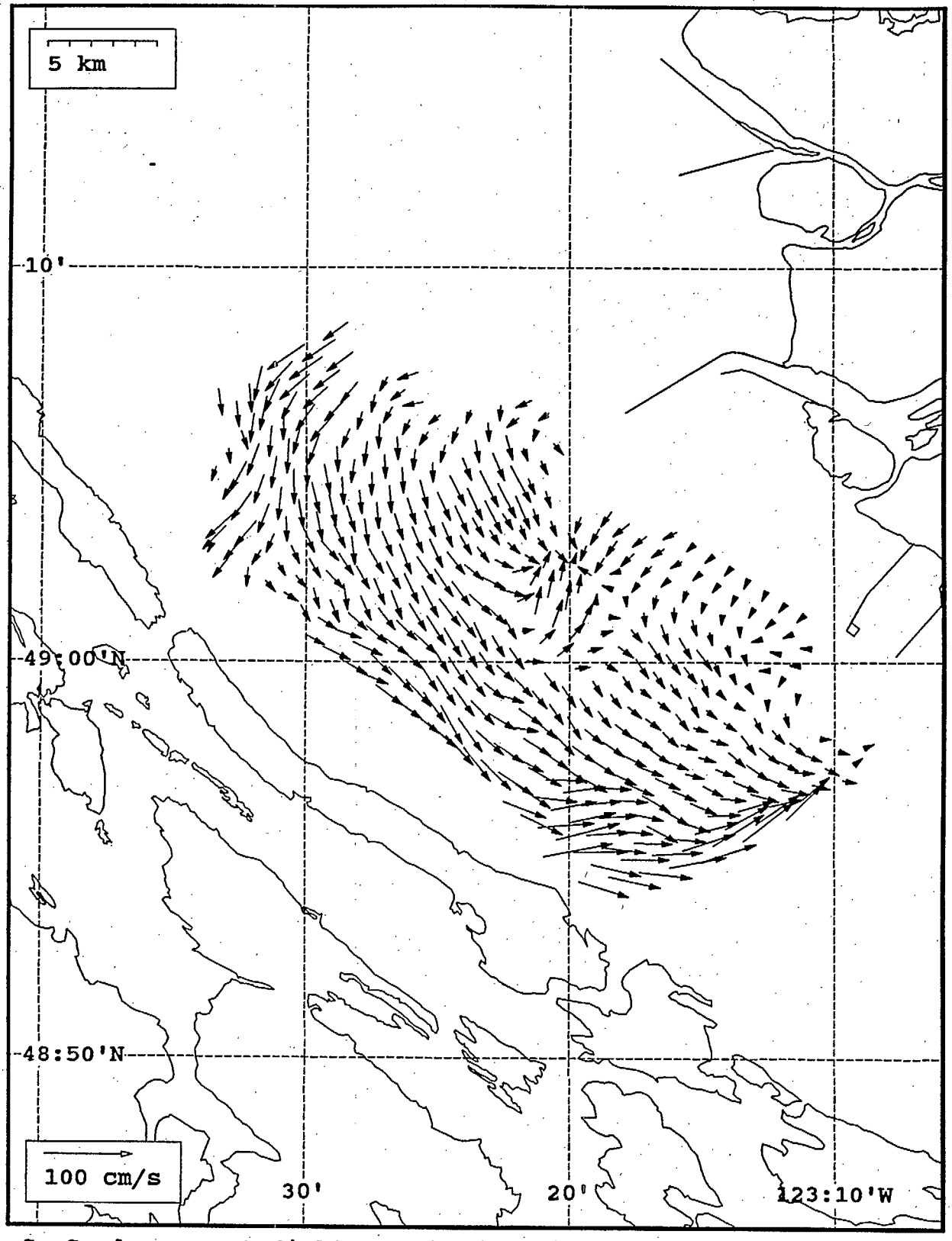

SeaSonde current field from the Strait of Georgia, off the mouth of the Fraser River, for 00:00 Z, July 27, 1993.

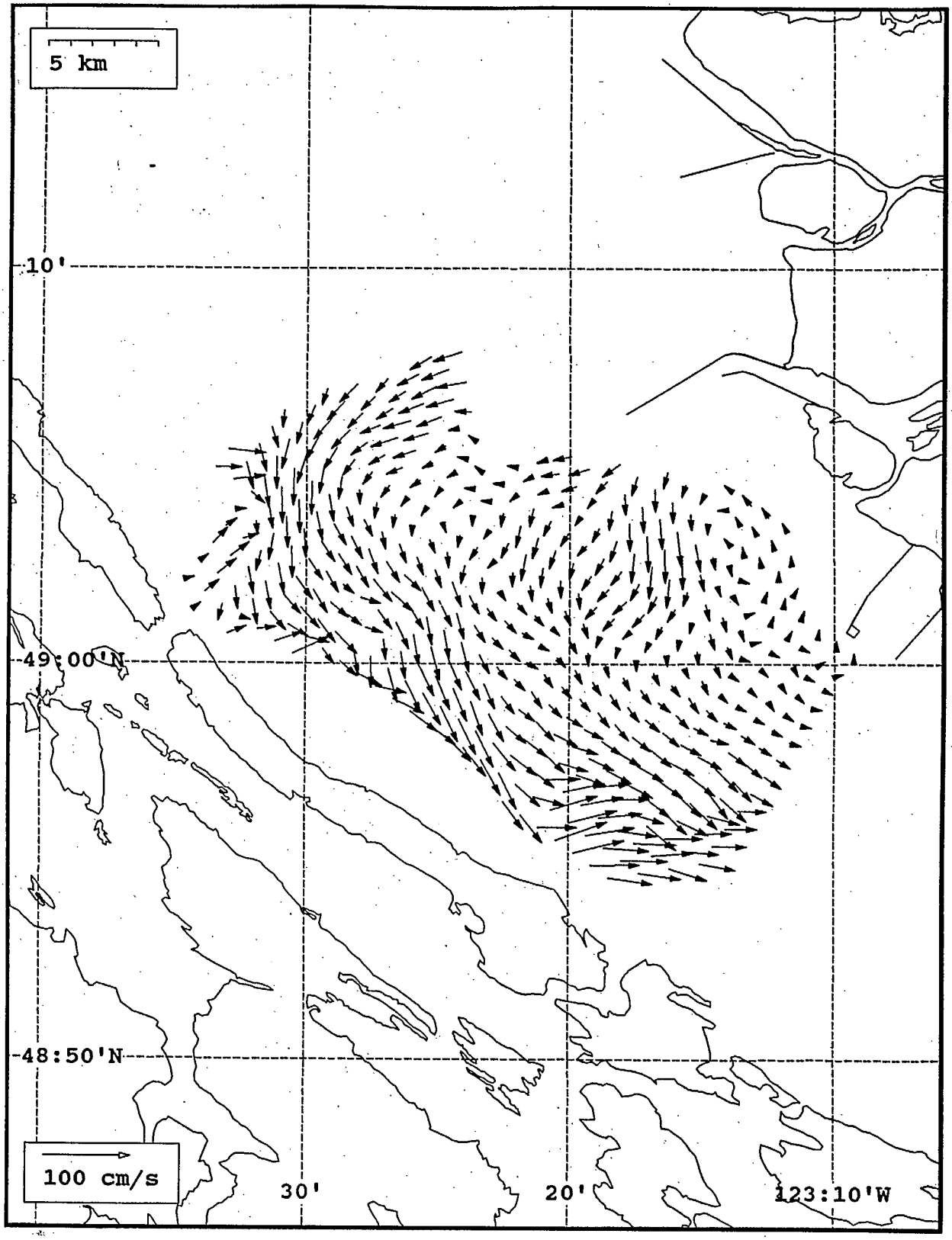

SeaSonde current field from the Strait of Georgia, off the mouth of the Fraser River, for 01:00 Z, July 27, 1993.

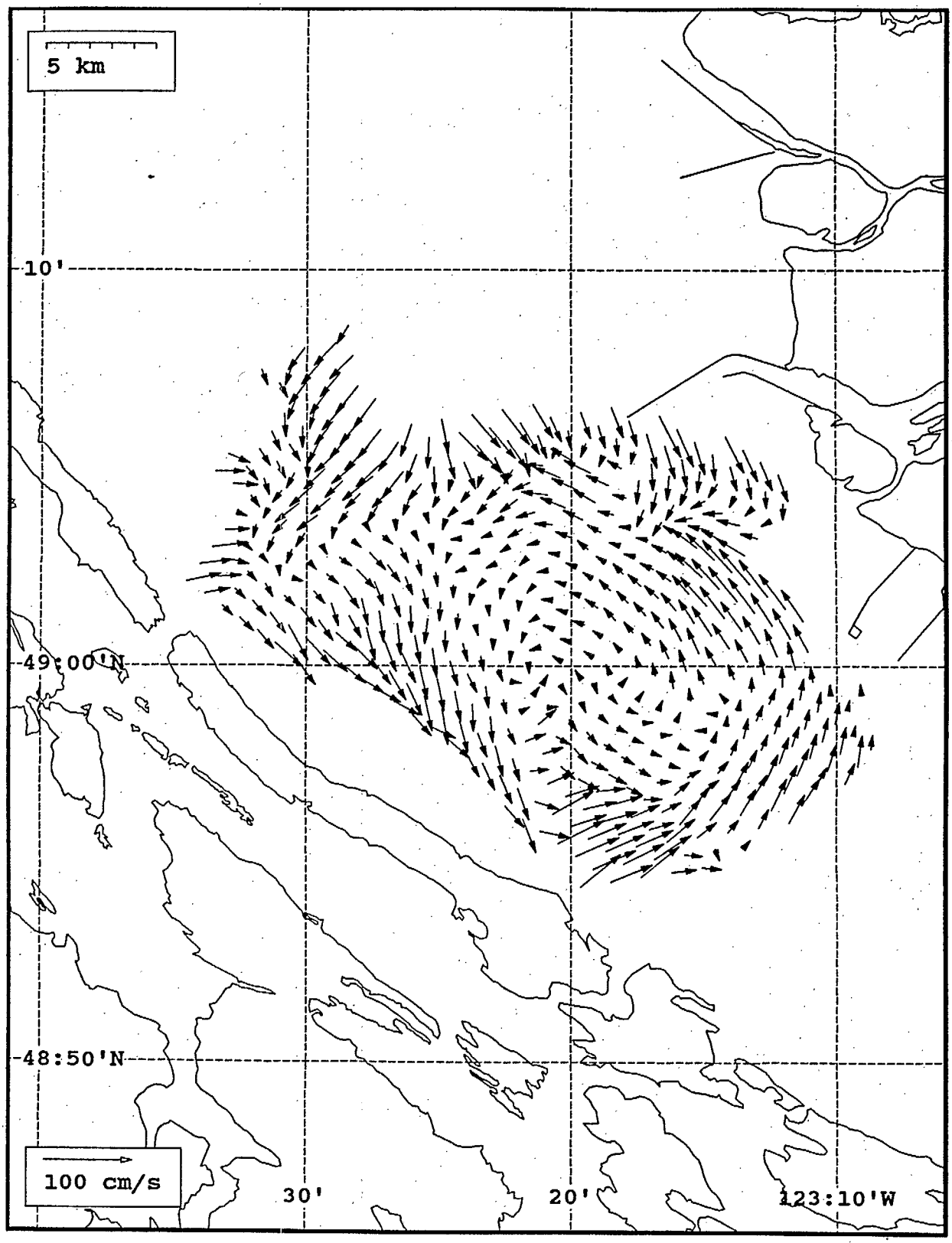

SeaSonde current field from the Strait of Georgia, off the mouth of the Fraser River, for 02:00 Z, July 27, 1993.

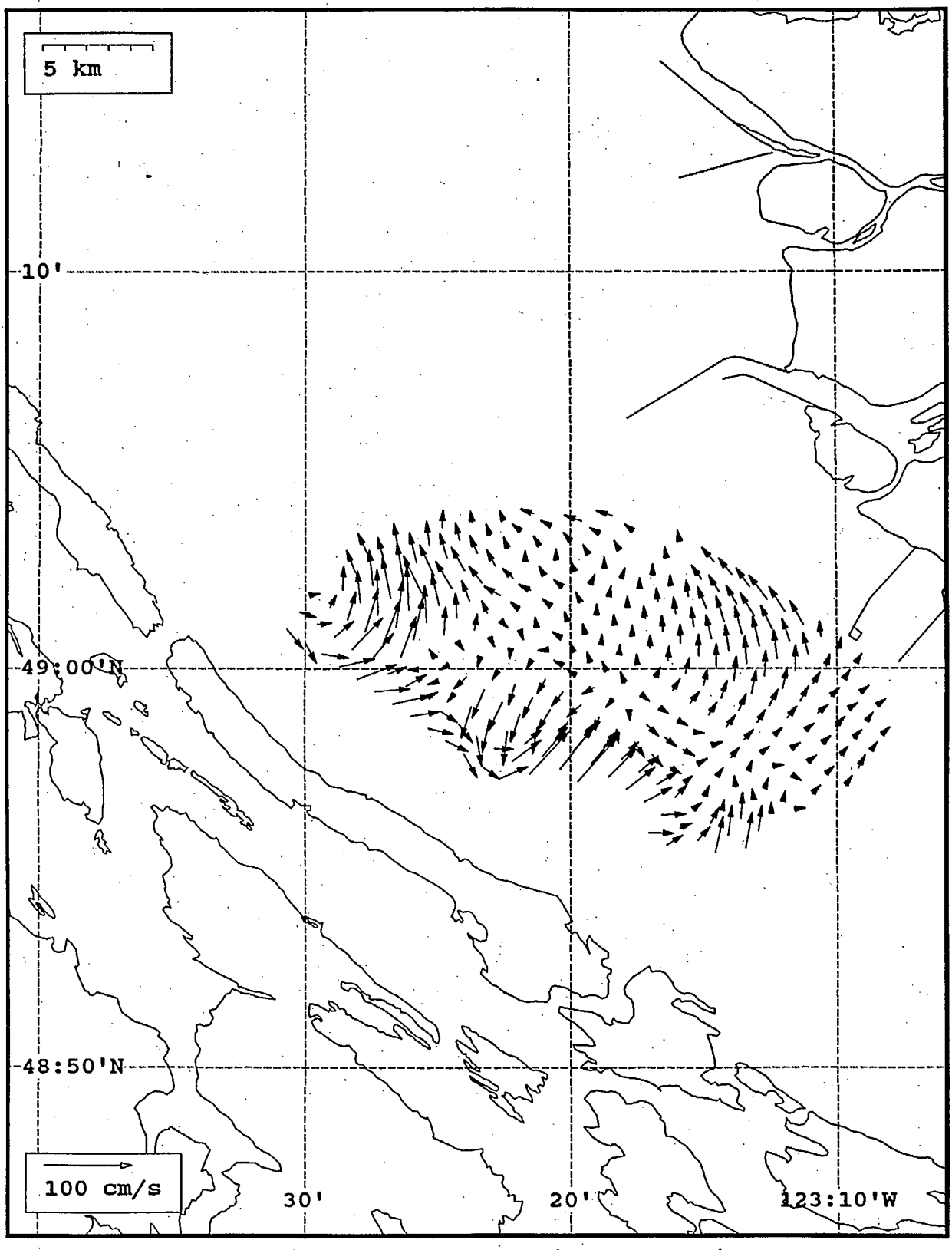

SeaSonde current field from the Strait of Georgia, off the mouth of the Fraser River, for 03:00 Z, July 27, 1993.

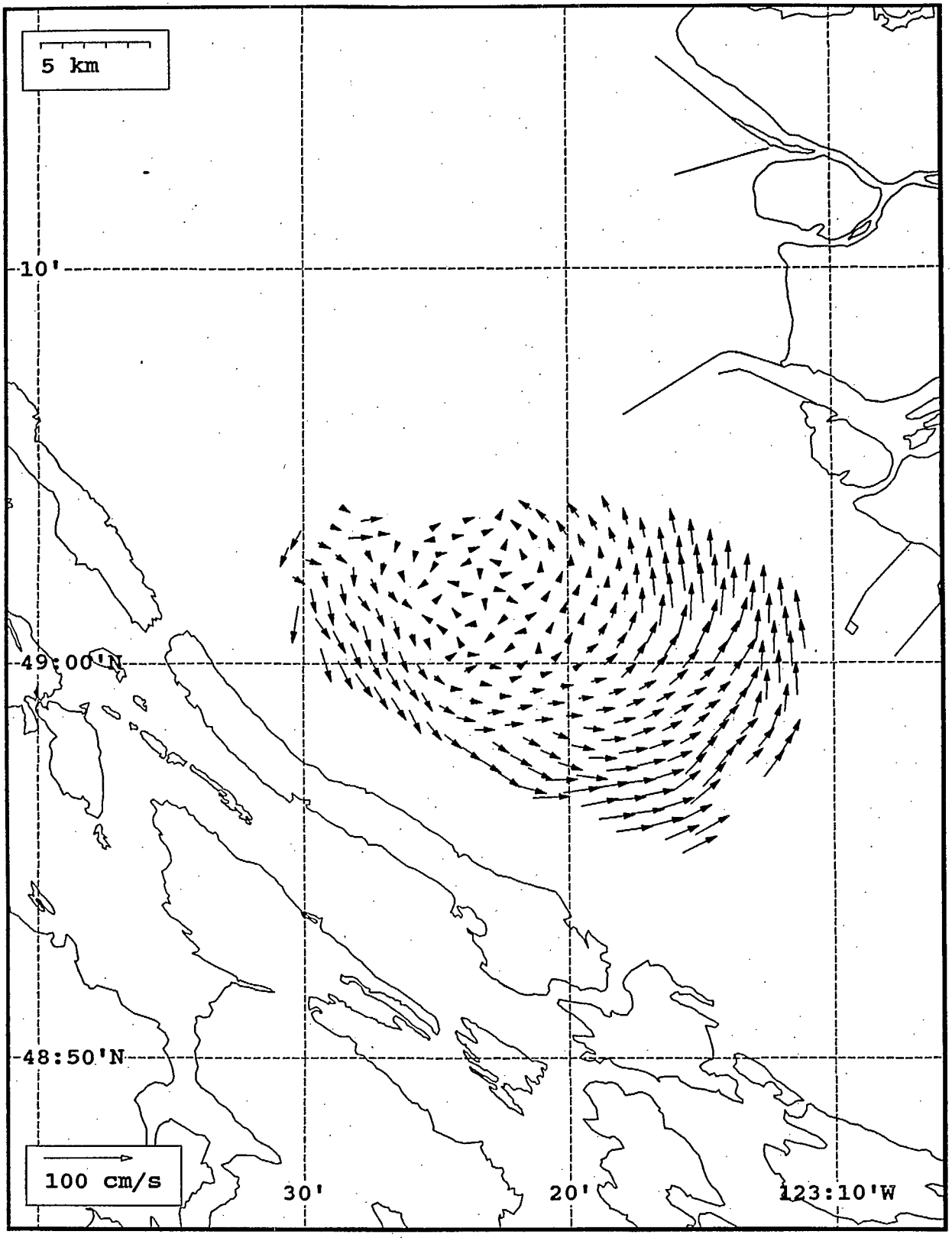

SeaSonde current field from the Strait of Georgia, off the mouth of the Fraser River, for 04:00 Z, July 27, 1993.

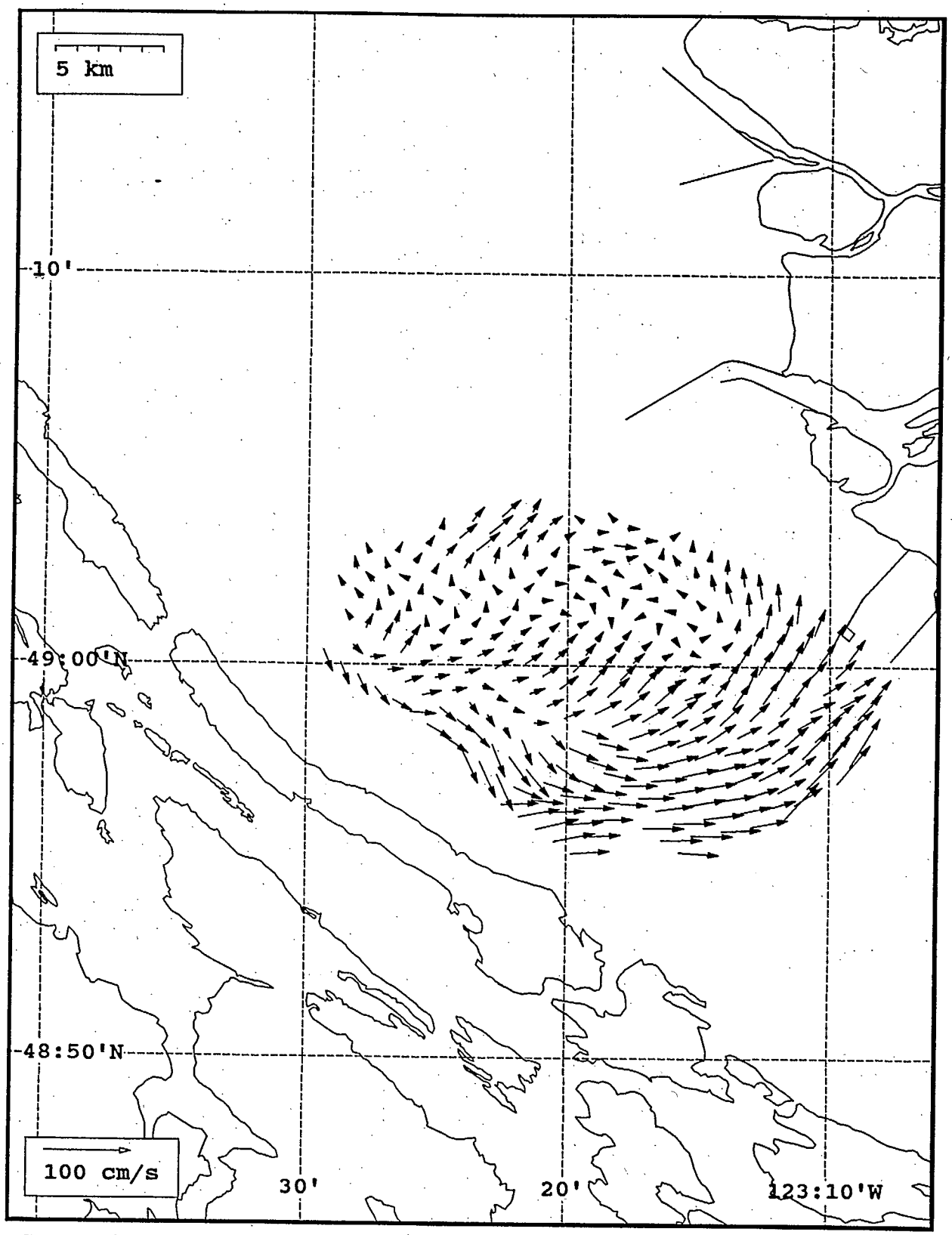

SeaSonde current field from the Strait of Georgia, off the mouth of the Fraser River, for 05:00 Z, July 27, 1993.

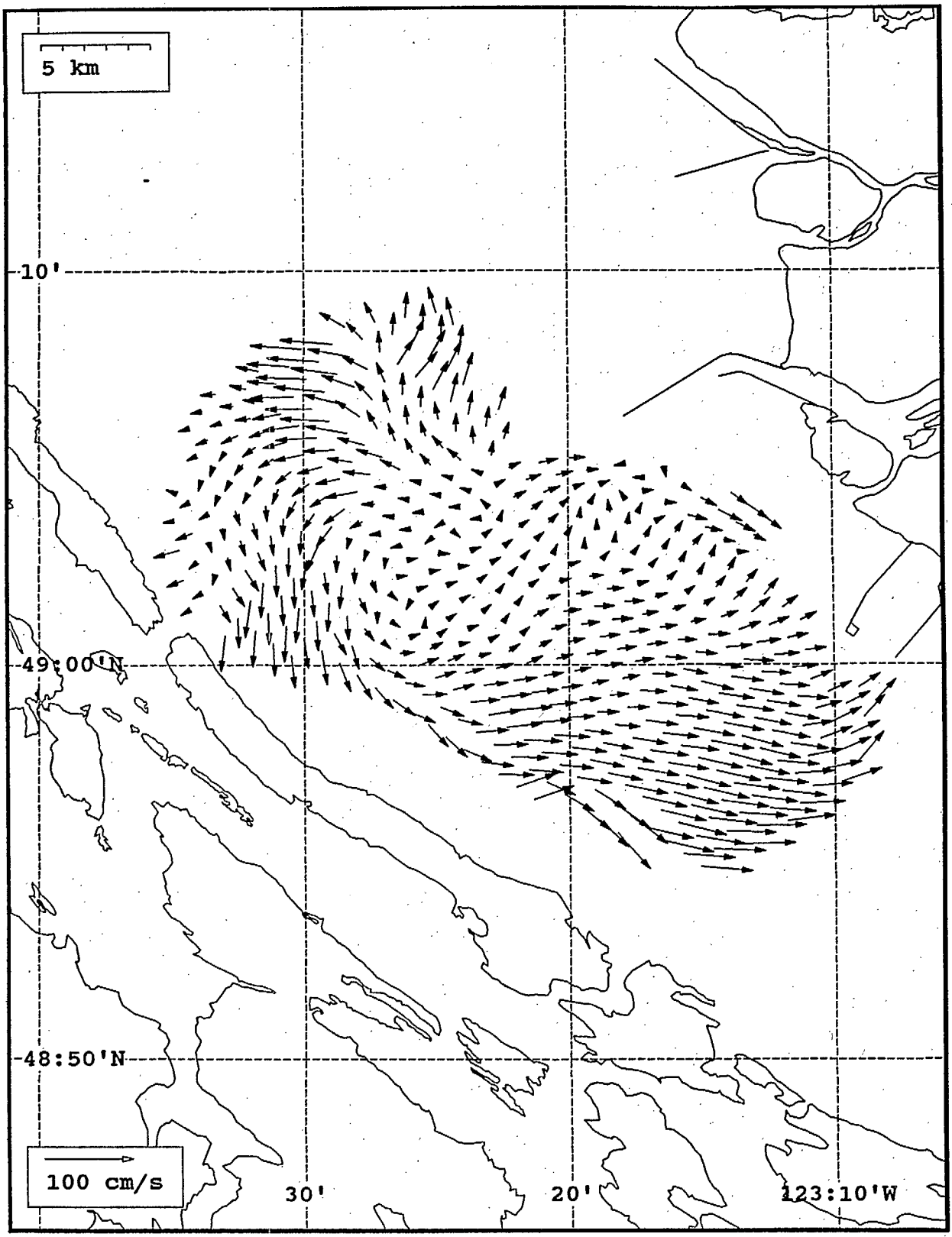

SeaSonde current field from the Strait of Georgia, off the mouth of the Fraser River, for 06:00 Z, July 27, 1993.

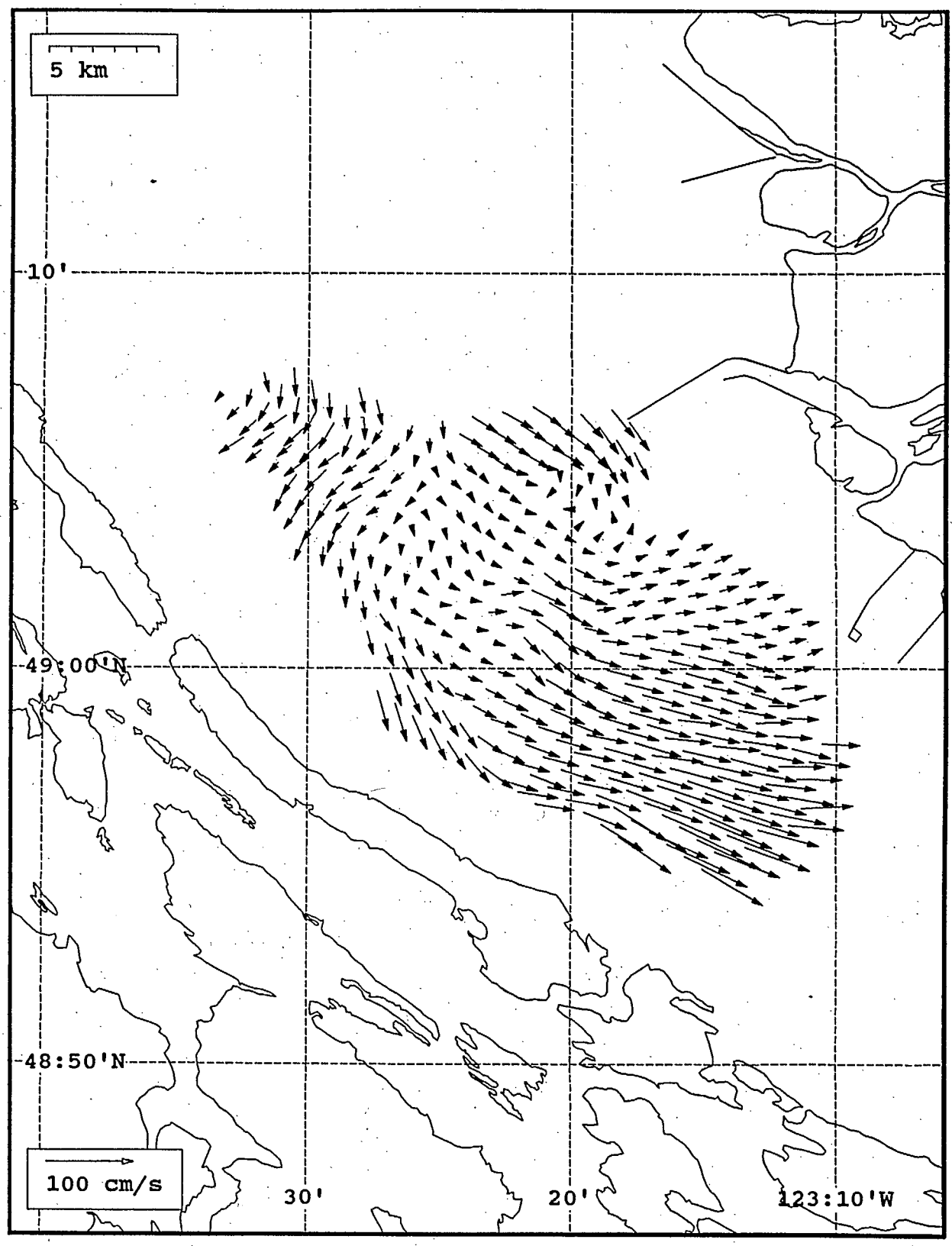

SeaSonde current field from the Strait of Georgia, off the mouth of the Fraser River, for 07:00 Z, July 27, 1993.

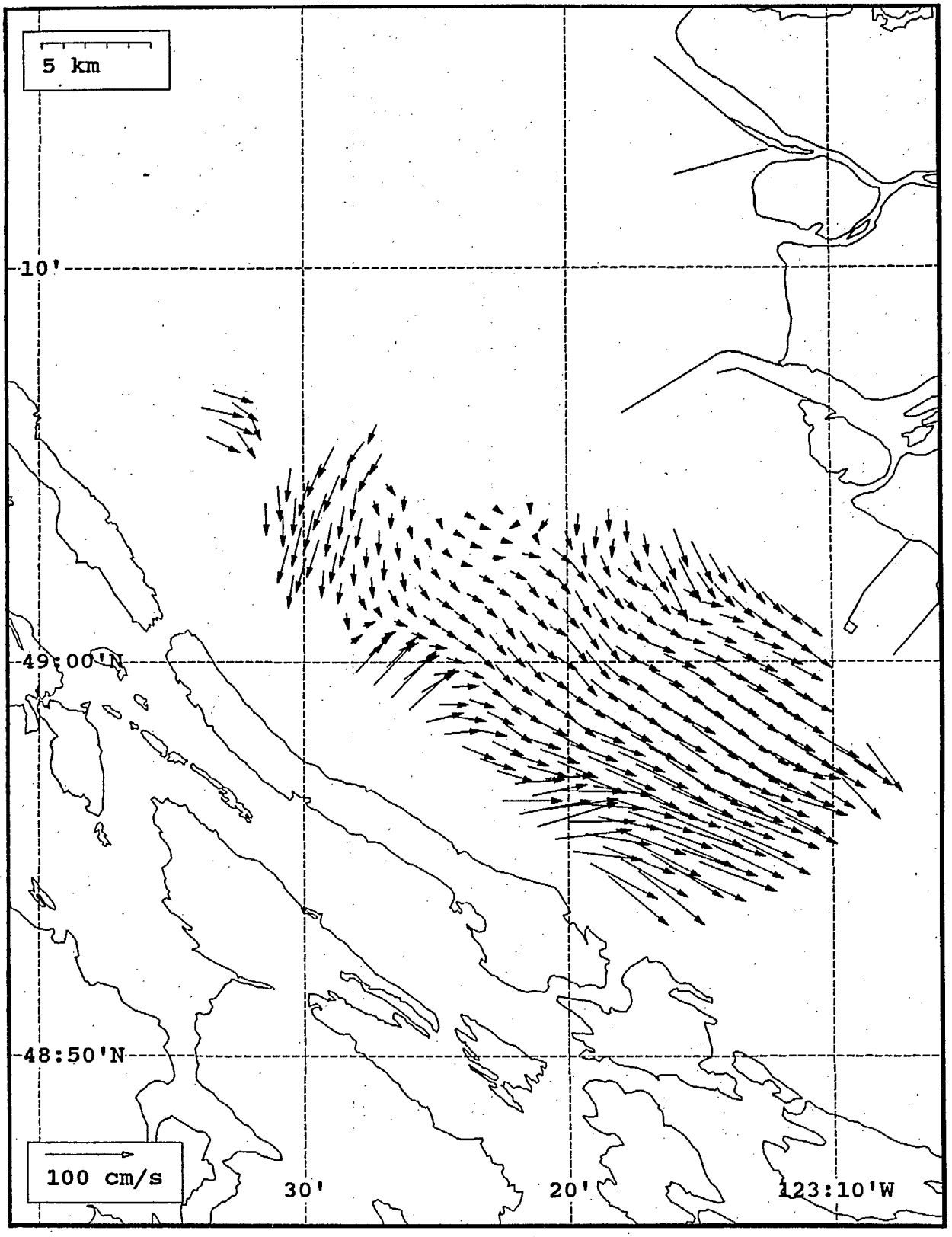

SeaSonde current field from the Strait of Georgia, off the mouth of the Fraser River, for 08:00 Z, July 27, 1993.

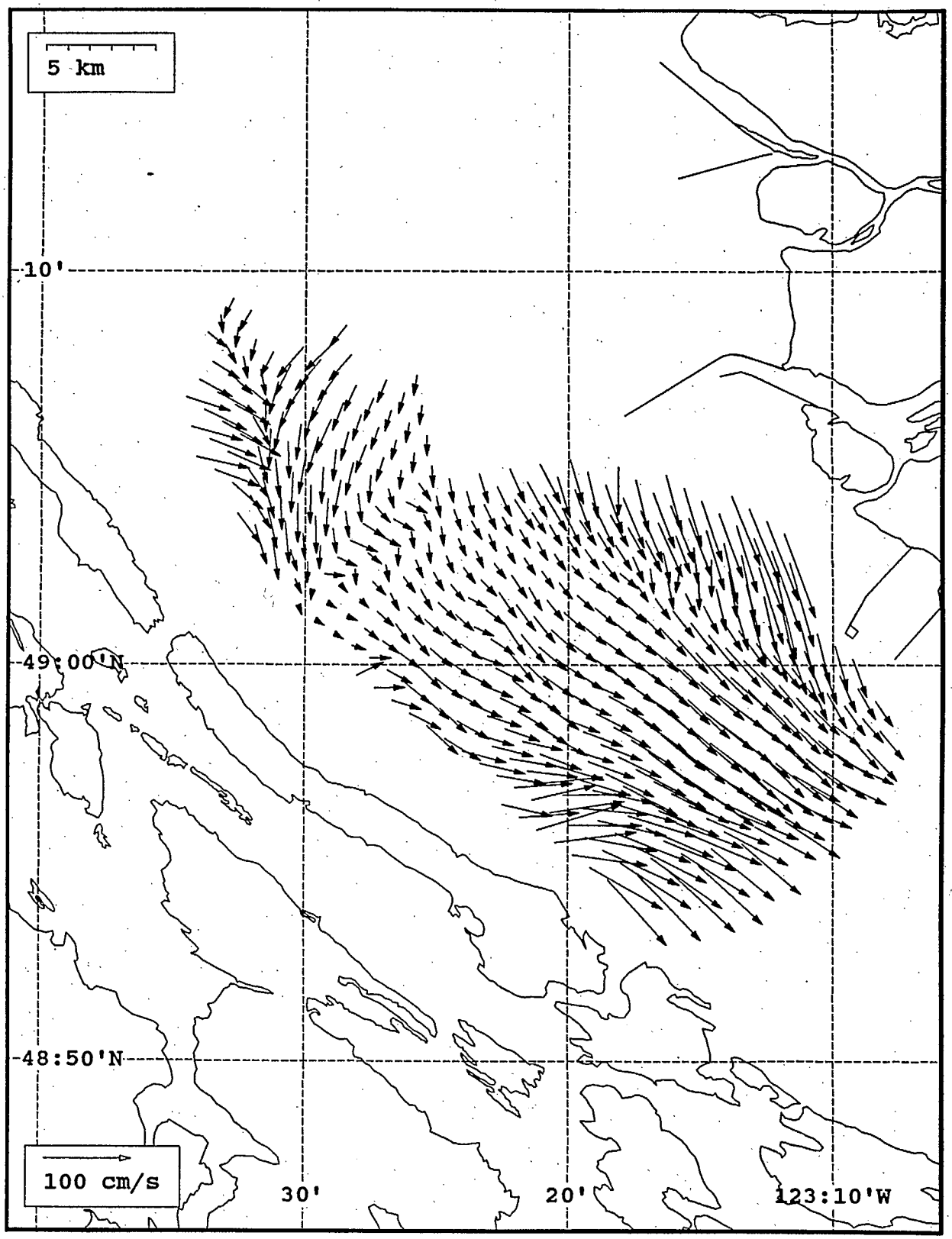

SeaSonde current field from the Strait of Georgia, off the mouth of the Fraser River, for 09:00 Z, July 27, 1993.

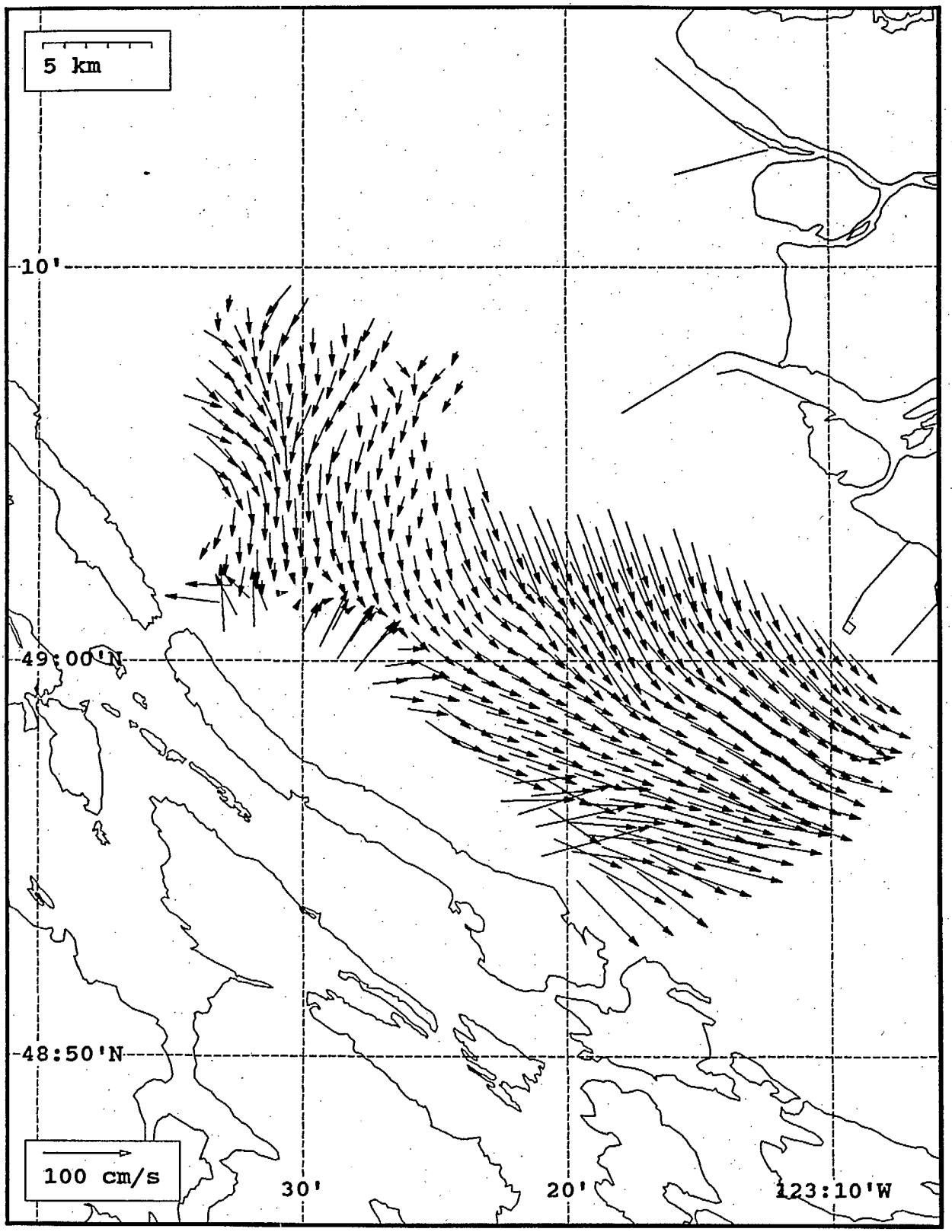

SeaSonde current field from the Strait of Georgia, off the mouth of the Fraser River, for 10:00 Z, July 27, 1993.

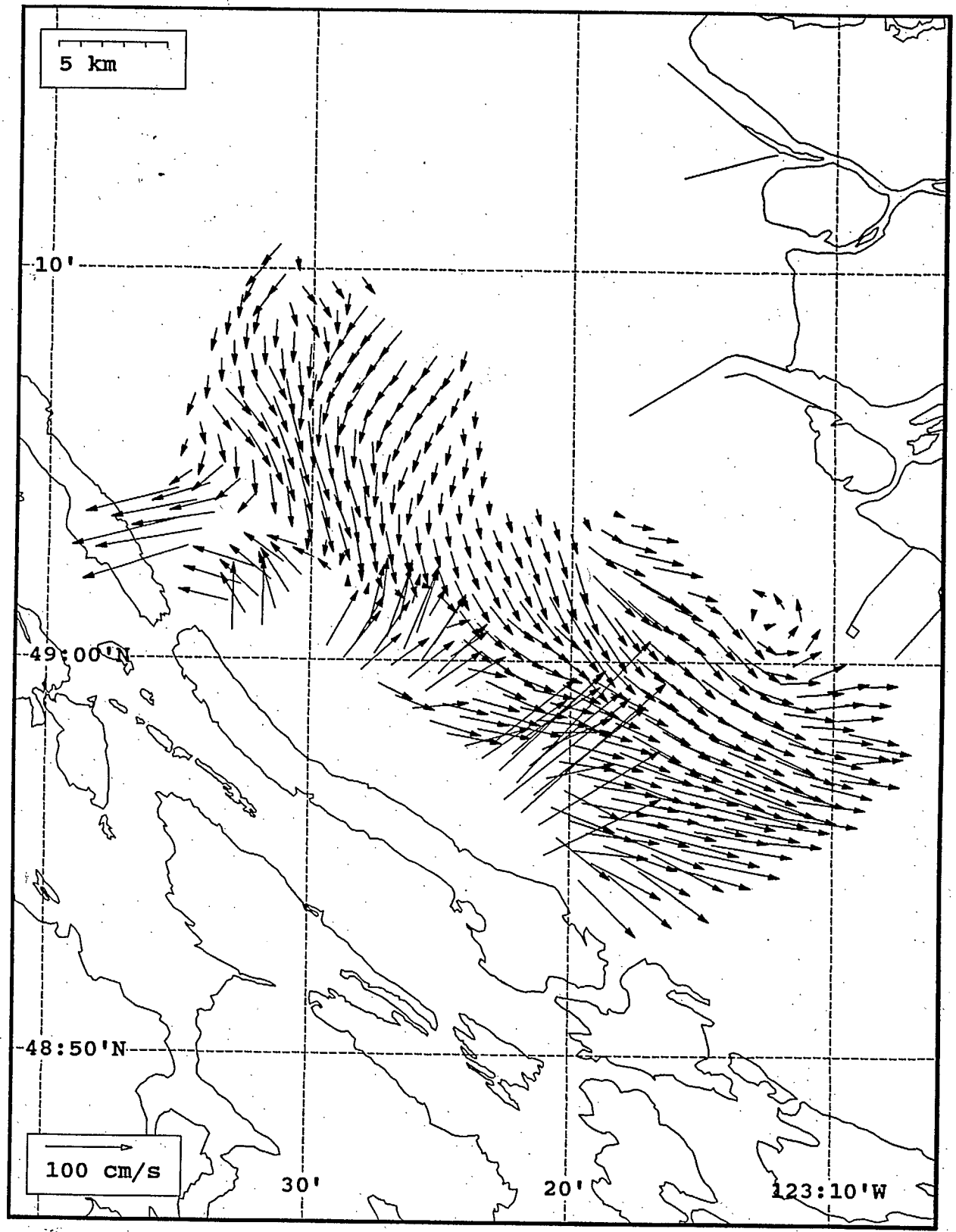

SeaSonde current field from the Strait of Georgia, off the mouth of the Fraser River, for 11:00 Z, July 27, 1993.

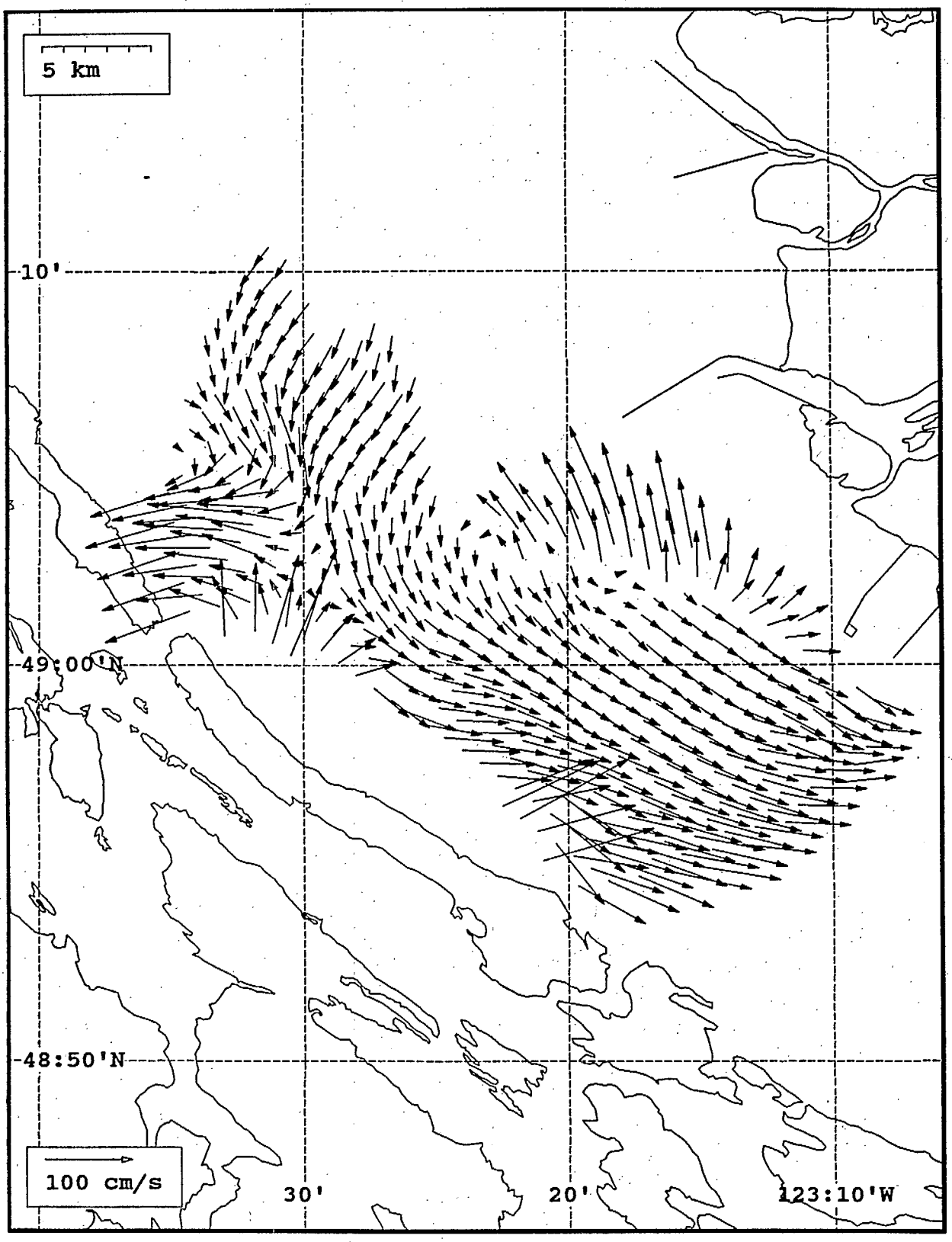

SeaSonde current field from the Strait of Georgia, off the mouth of the Fraser River, for 12:00 Z, July 27, 1993.

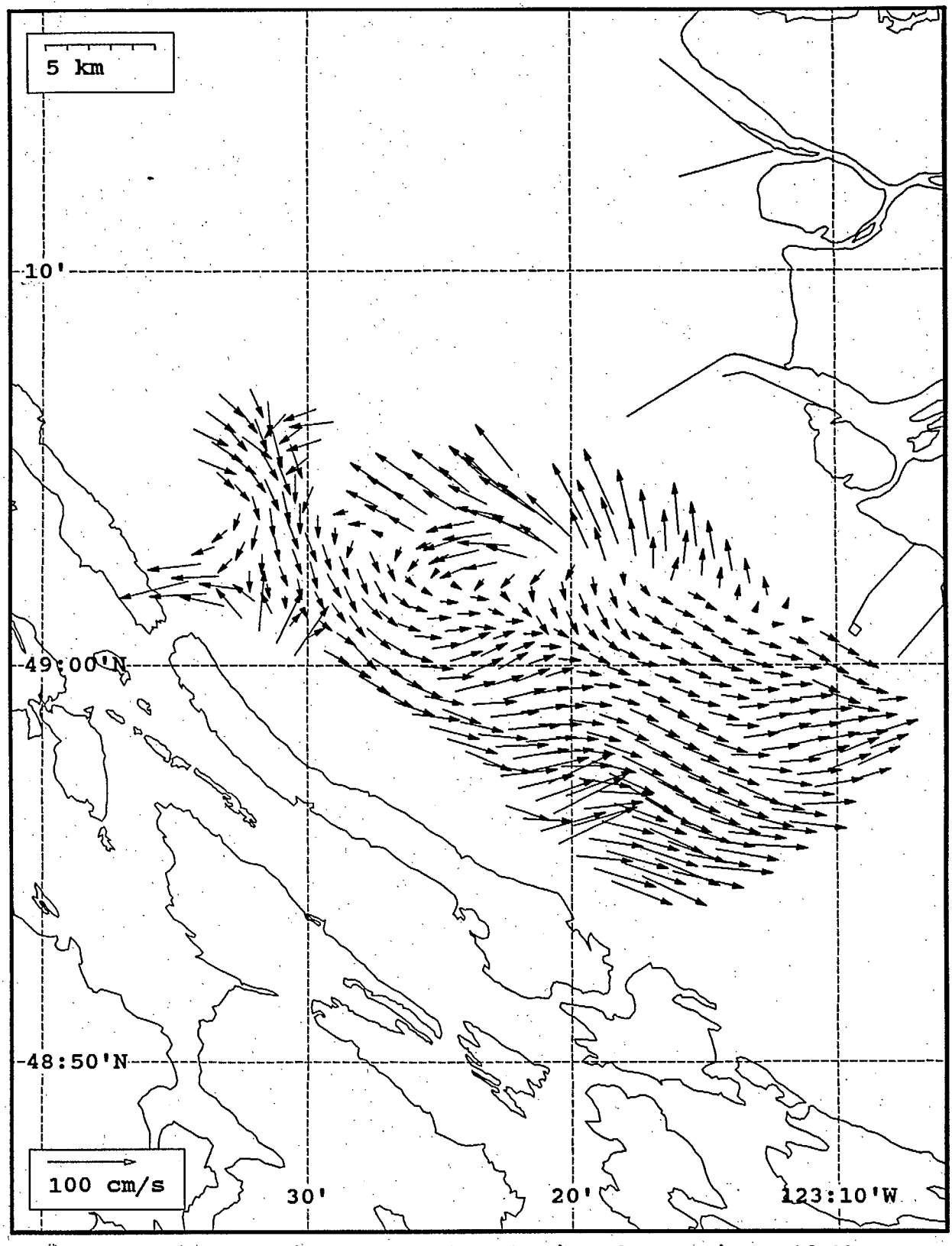

SeaSonde current field from the Strait of Georgia, off the mouth of the Fraser River, for 13:00 Z, July 27, 1993.

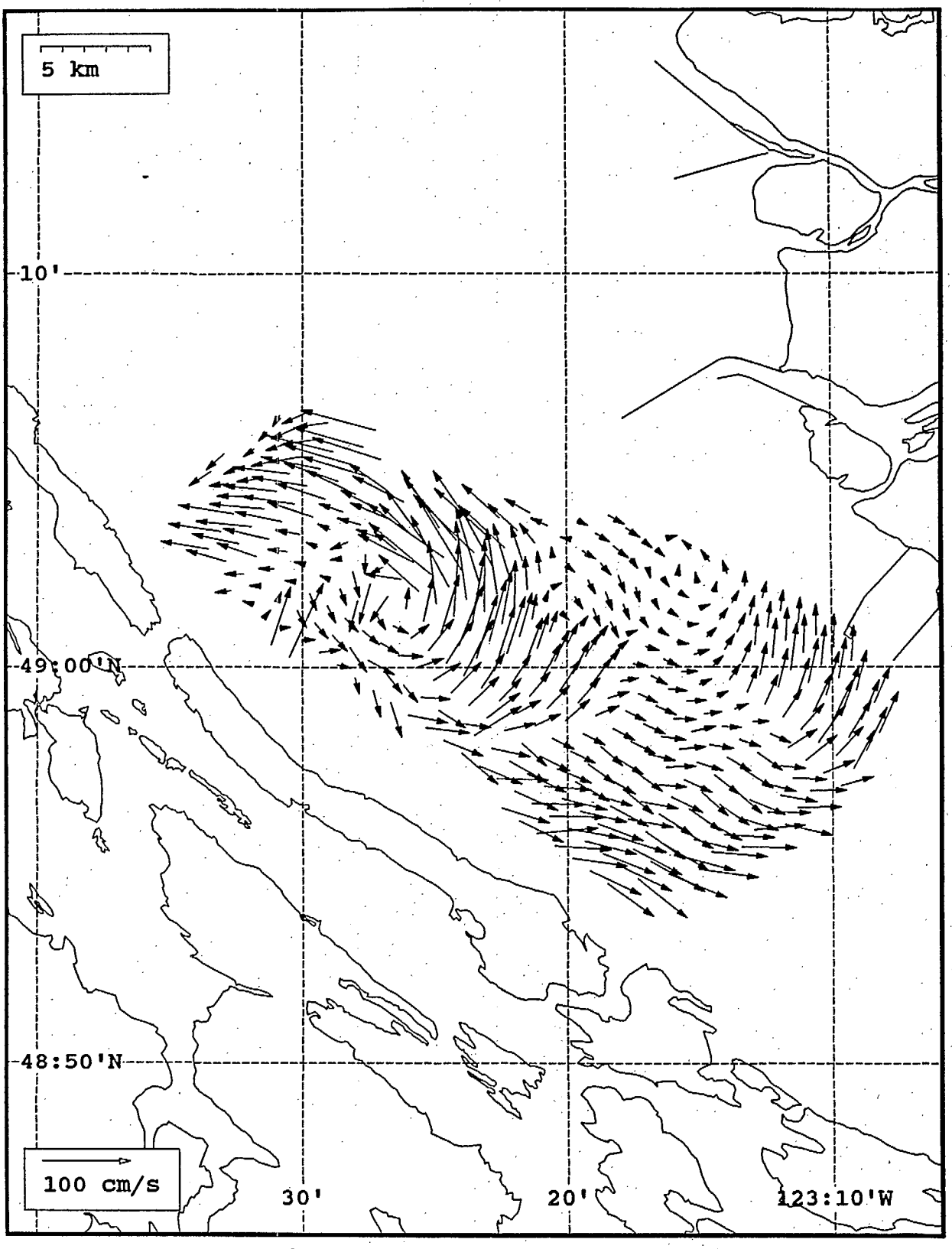

SeaSonde current field from the Strait of Georgia, off the mouth of the Fraser River, for 14:00 Z, July 27, 1993.

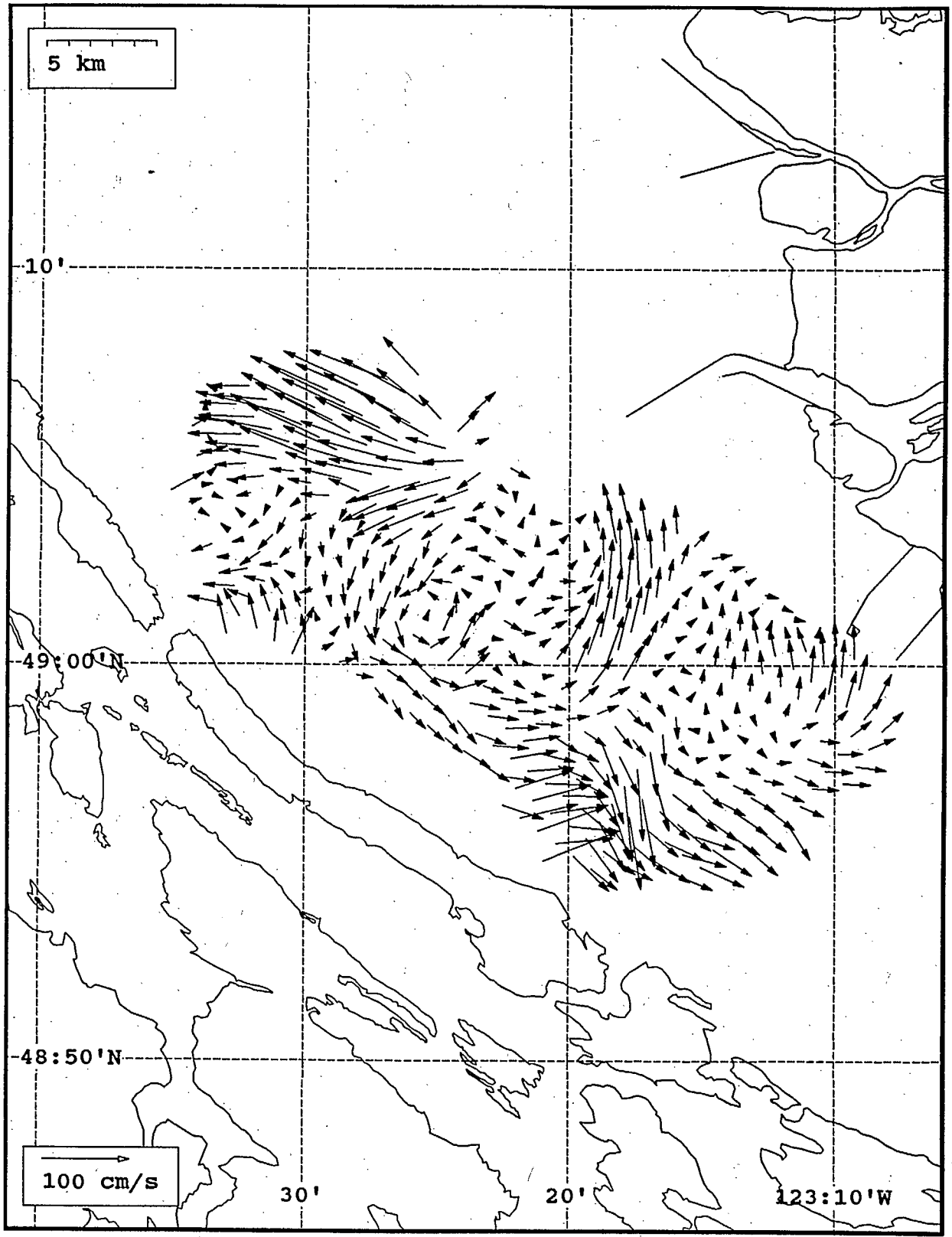

SeaSonde current field from the Strait of Georgia, off the mouth of the Fraser River, for 15:00 Z, July 27, 1993.

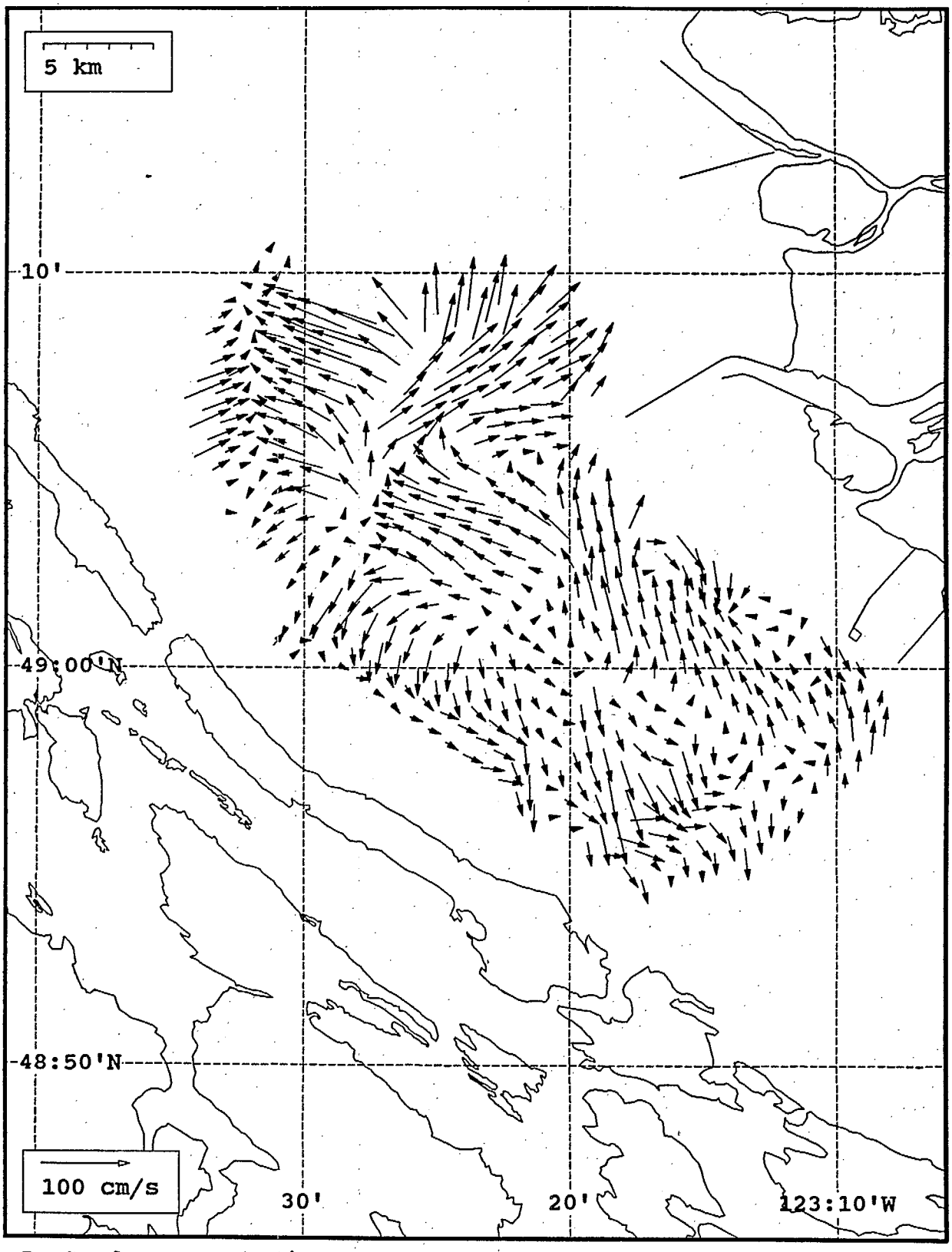

SeaSonde current field from the Strait of Georgia, off the mouth of the Fraser River, for 16:00 Z, July 27, 1993.

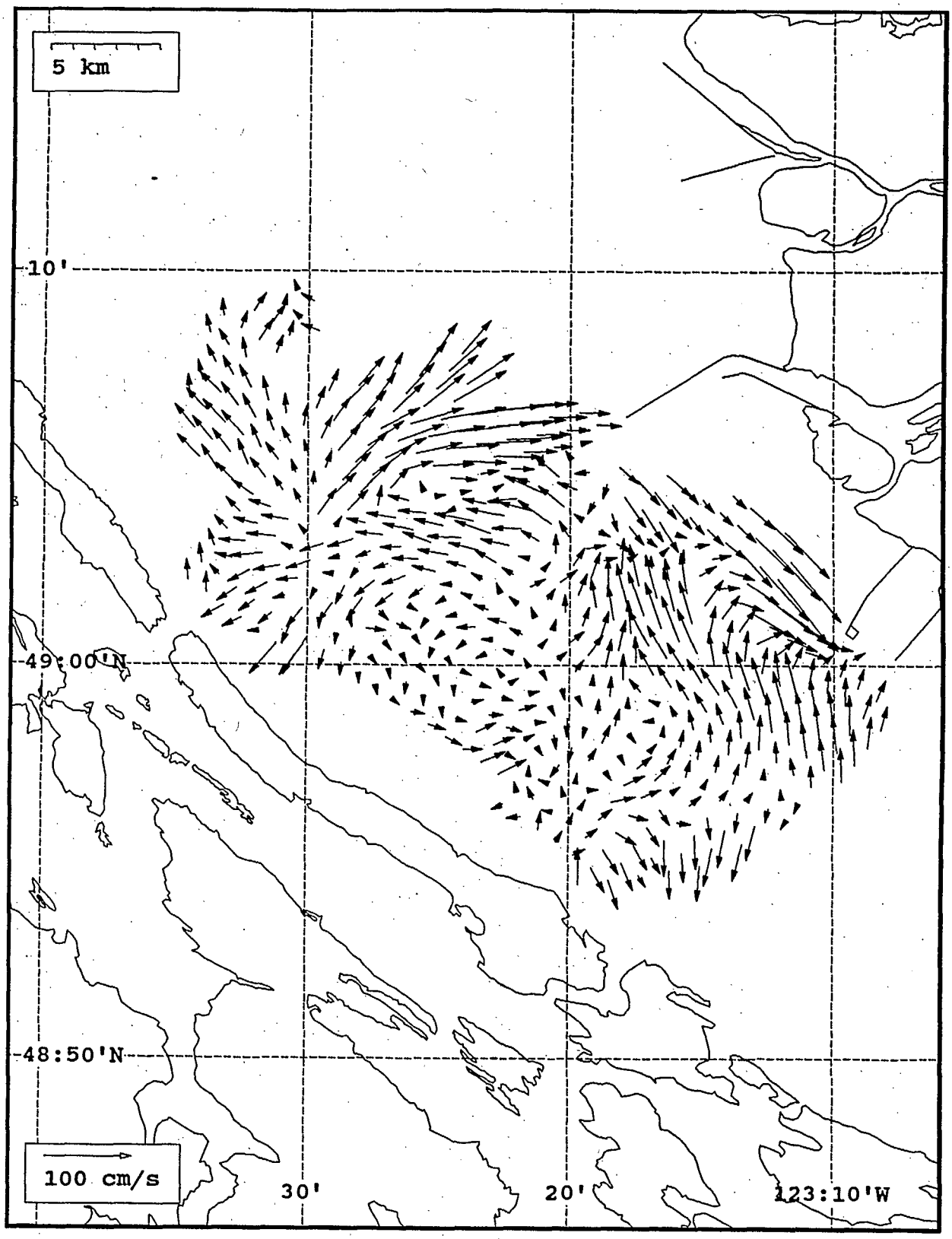

SeaSonde current field from the Strait of Georgia, off the mouth of the Fraser River, for 17:00 Z, July 27, 1993.

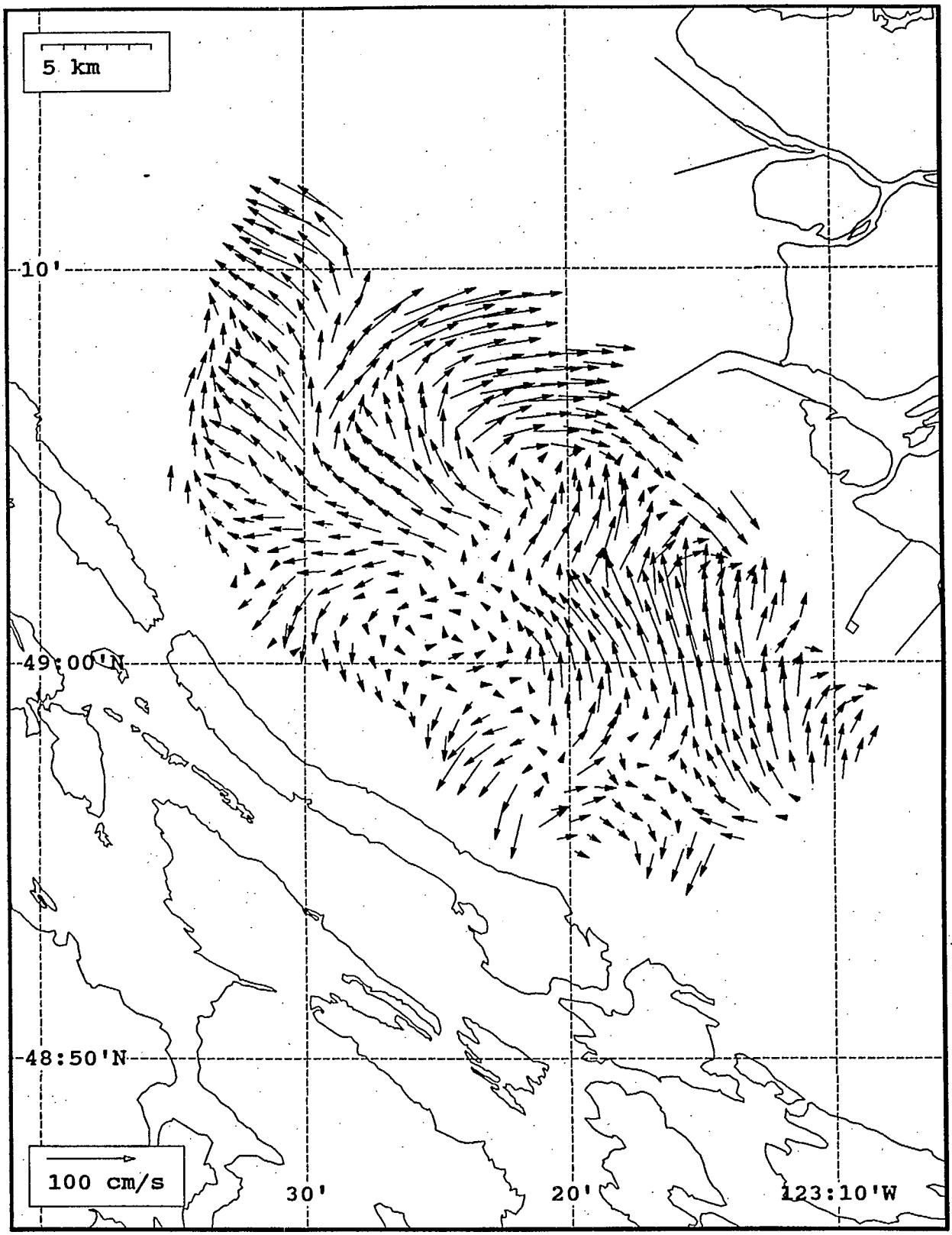

SeaSonde current field from the Strait of Georgia, off the mouth of the Fraser River, for 18:00 Z, July 27, 1993.

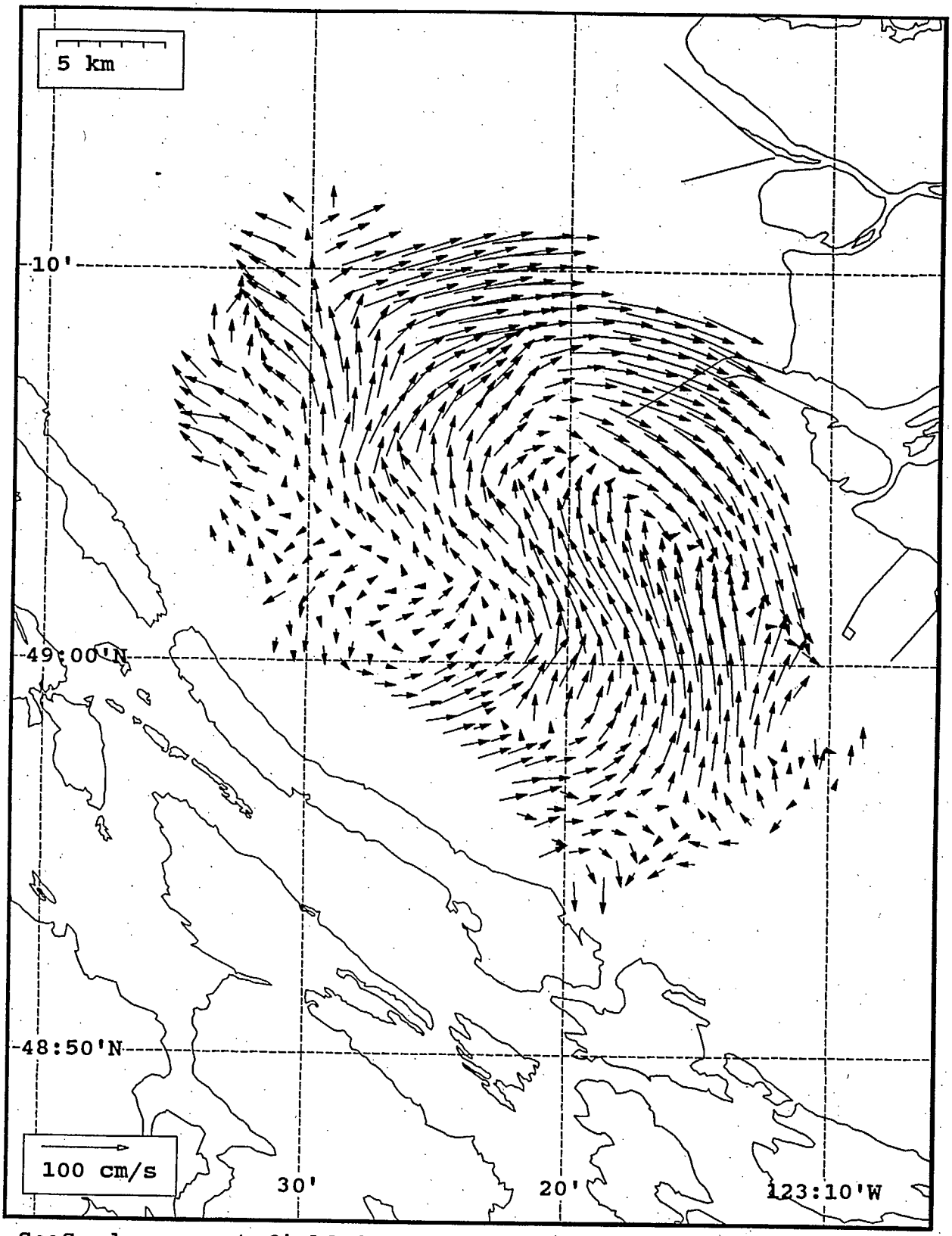

SeaSonde current field from the Strait of Georgia, off the mouth of the Fraser River, for 19:00 Z, July 27, 1993.

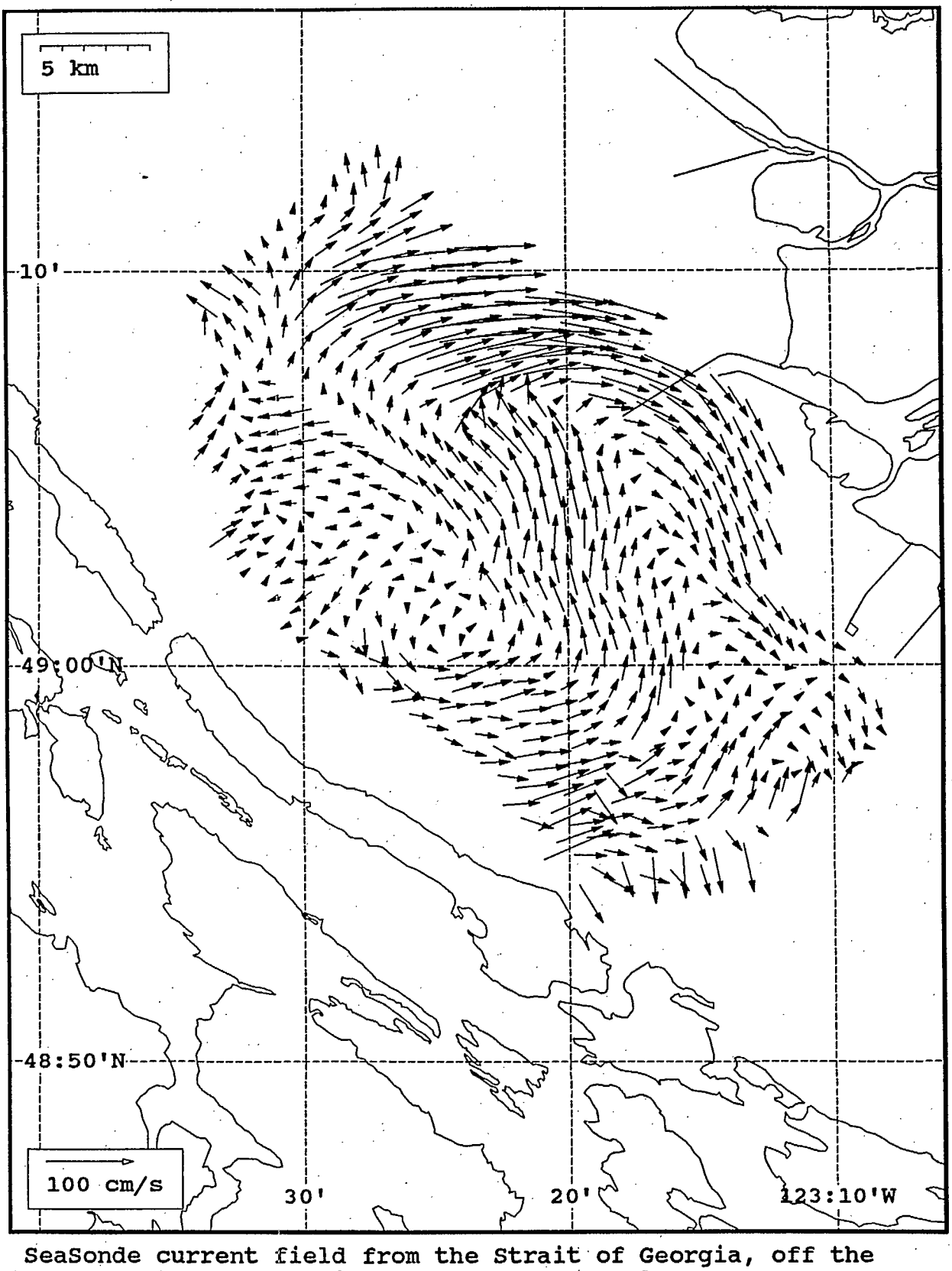

SeaSonde current field from the Strait of Georgia, off the mouth of the Fraser River, for 20:00 Z, July 27, 1993.

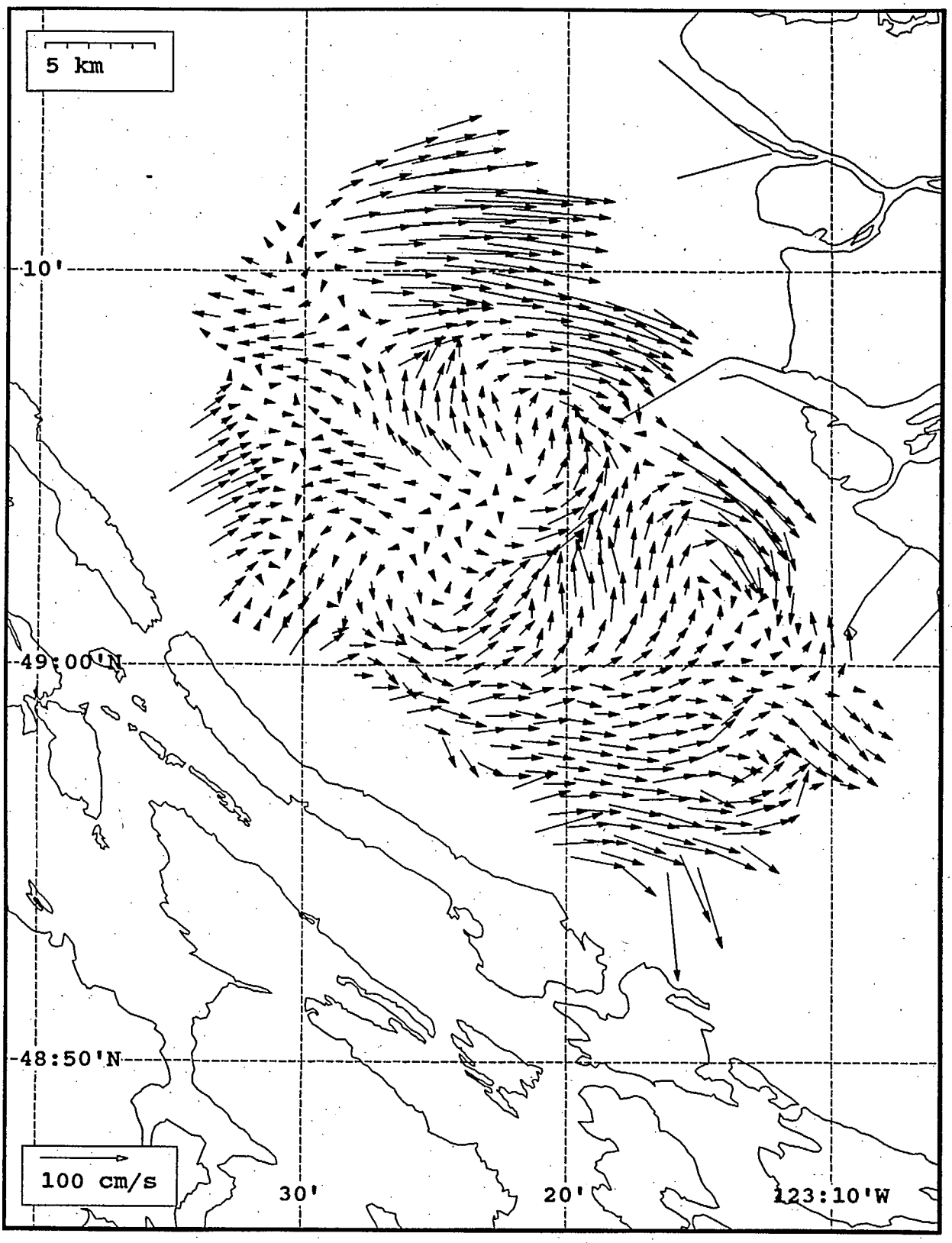

SeaSonde current field from the Strait of Georgia, off the mouth of the Fraser River, for 21:00 Z, July 27, 1993.

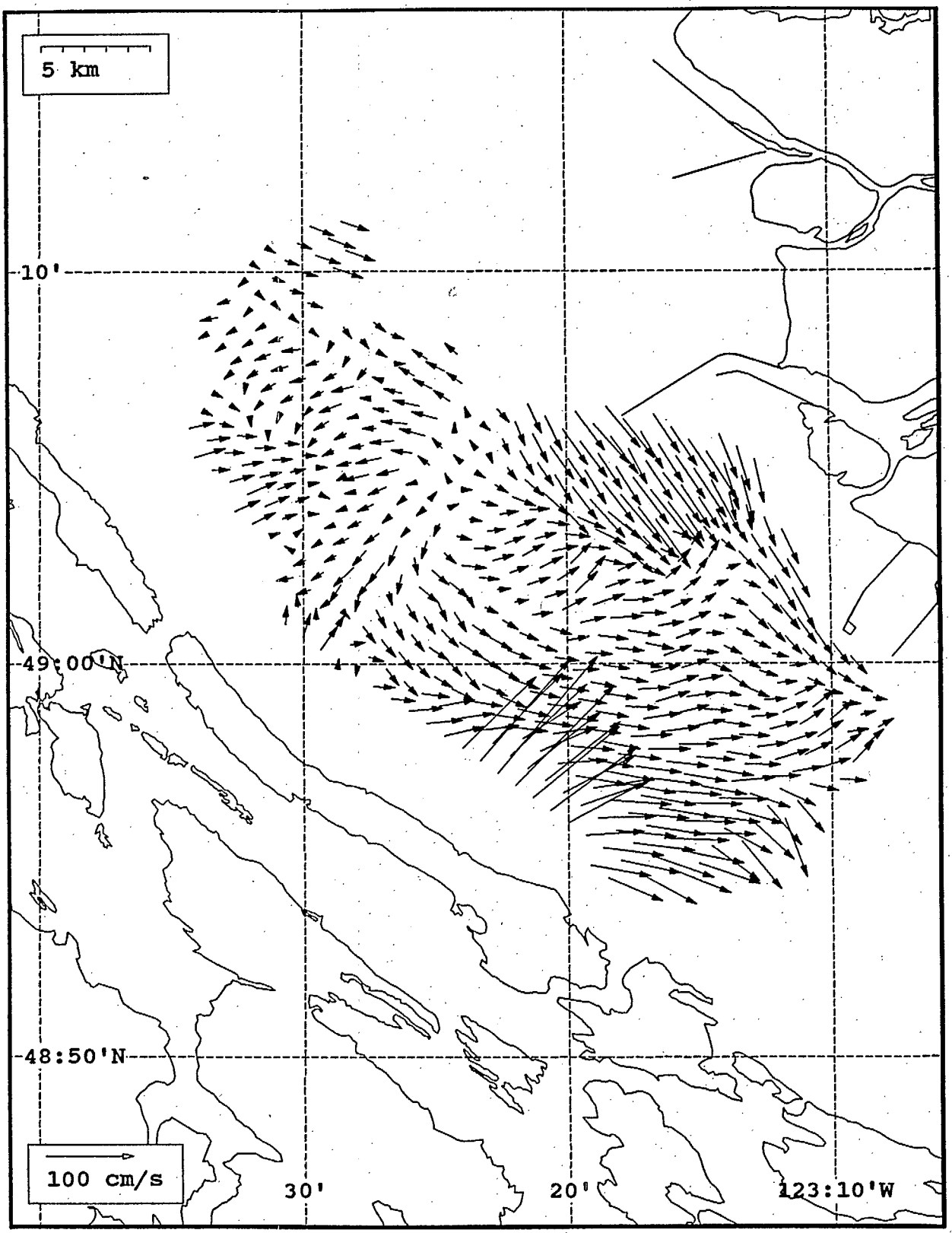

SeaSonde current field from the Strait of Georgia, off the mouth of the Fraser River, for 22:00 Z, July 27, 1993.

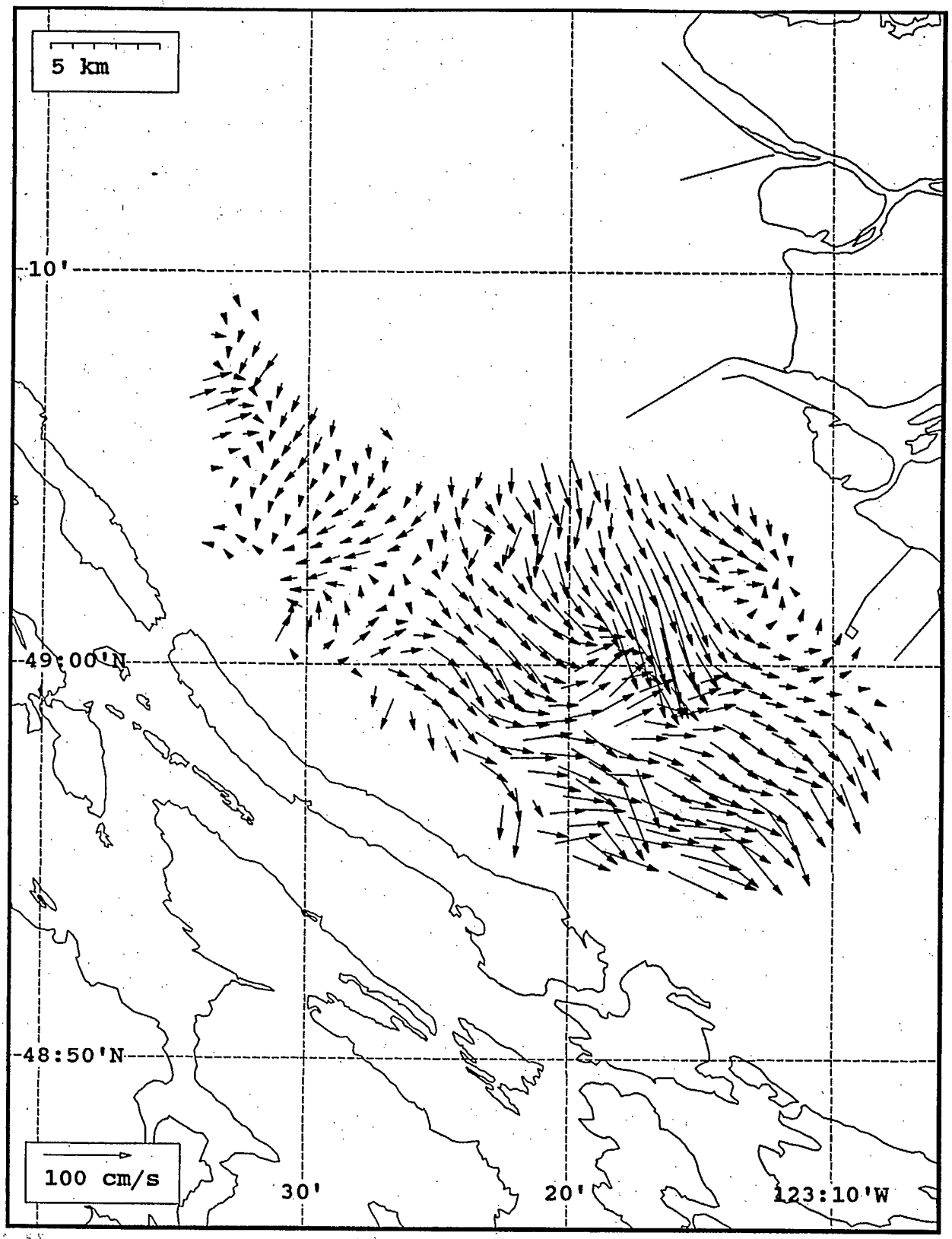

SeaSonde current field from the Strait of Georgia, off the mouth of the Fraser River, for 23:00 Z, July 27, 1993.

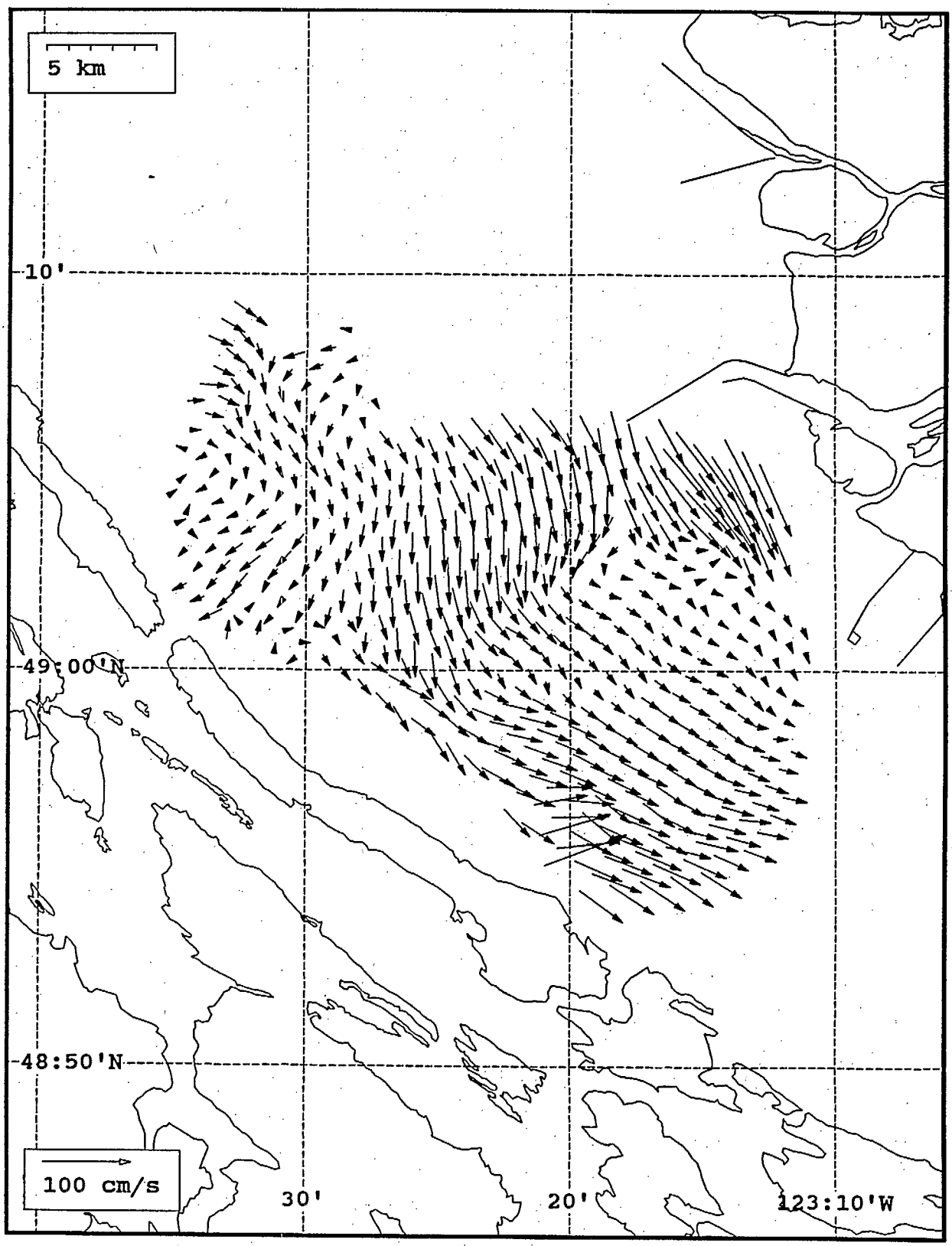

SeaSonde current field from the Strait of Georgia, off the mouth of the Fraser River, for 00:00 Z, July 28, 1993.

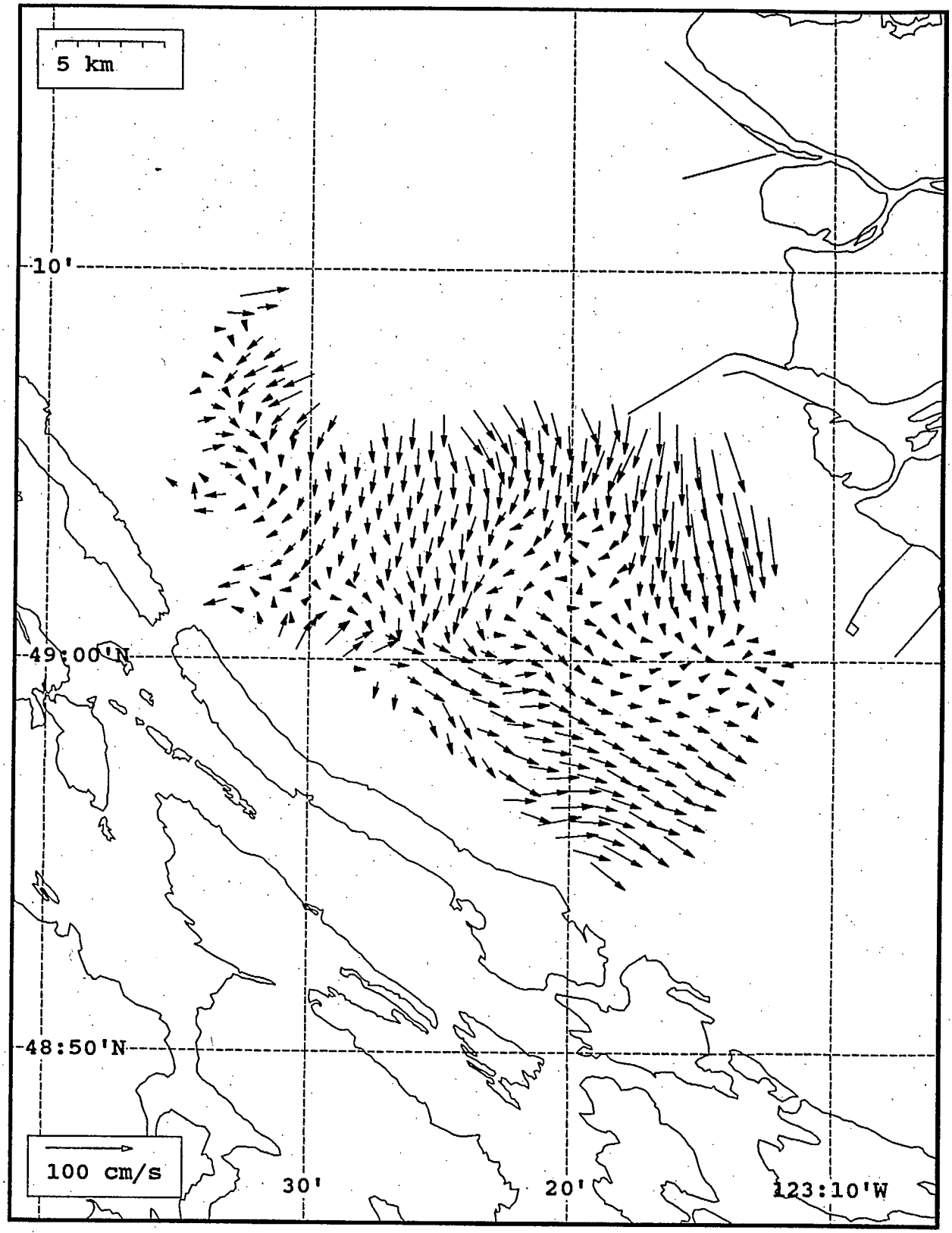

SeaSonde current field from the Strait of Georgia, off the mouth of the Fraser River, for 01:00 Z, July 28, 1993.

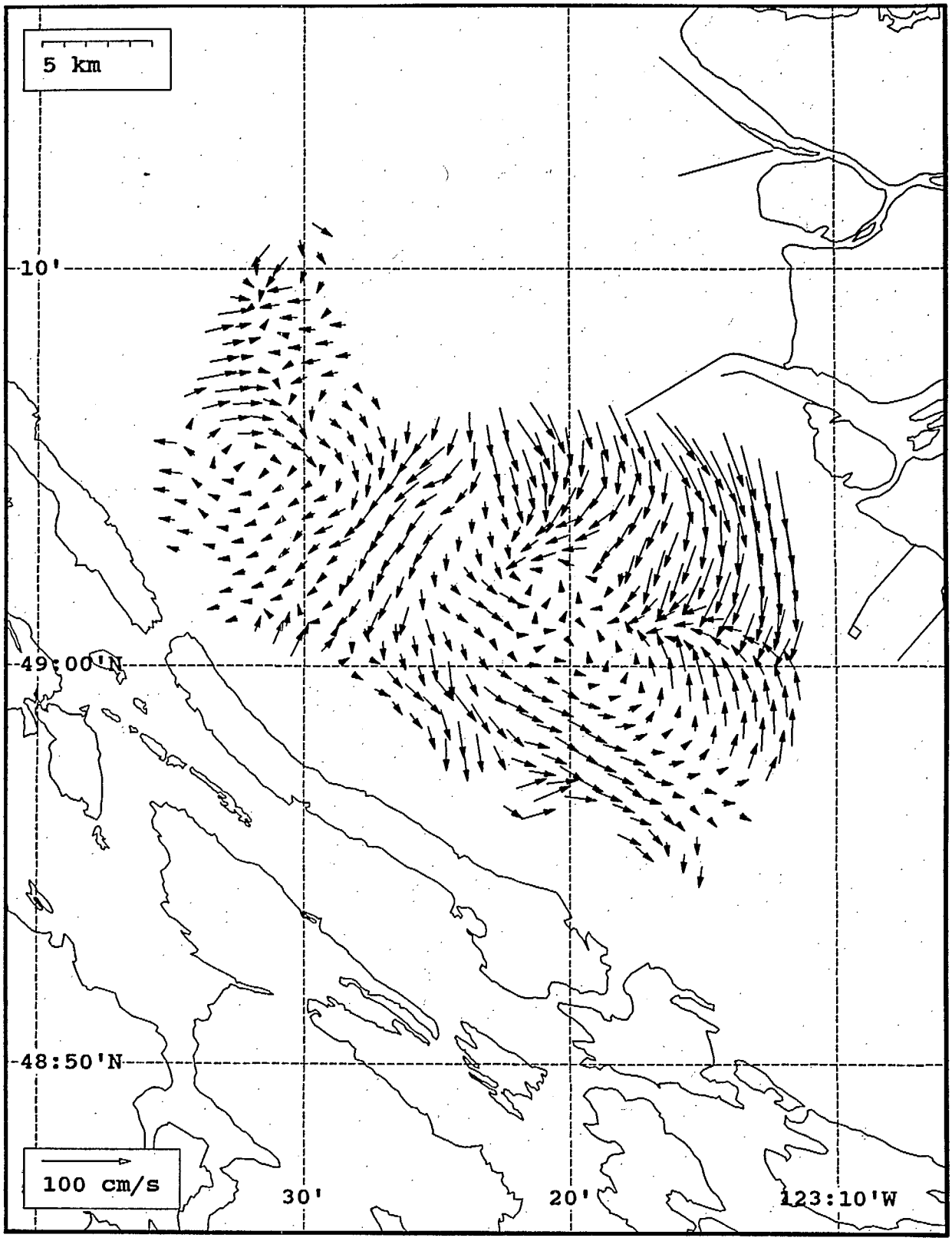

SeaSonde current field from the Strait of Georgia, off the mouth of the Fraser River, for 02:00 Z, July 28, 1993.

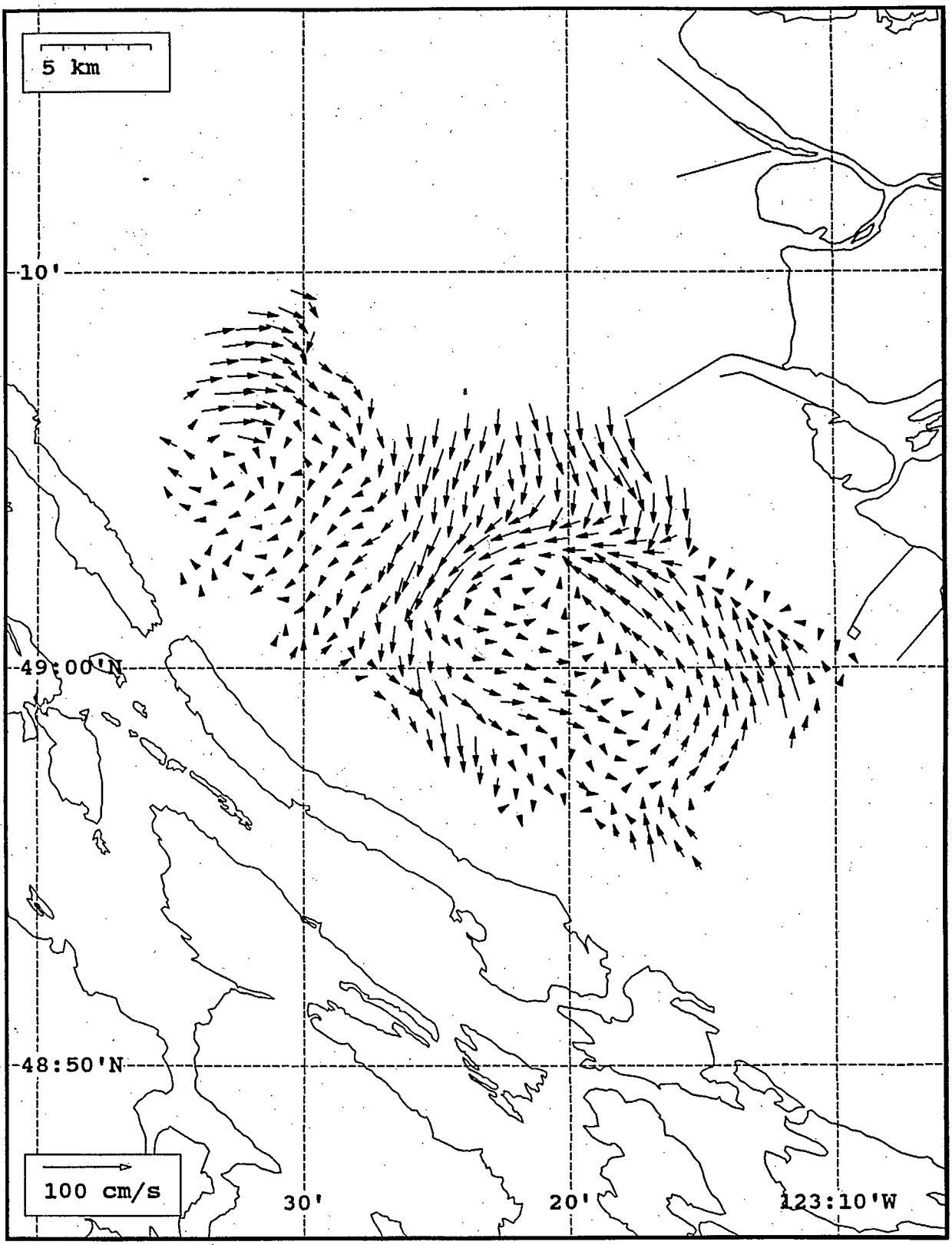

SeaSonde current field from the Strait of Georgia, off the mouth of the Fraser River, for 03:00 Z, July 28, 1993.

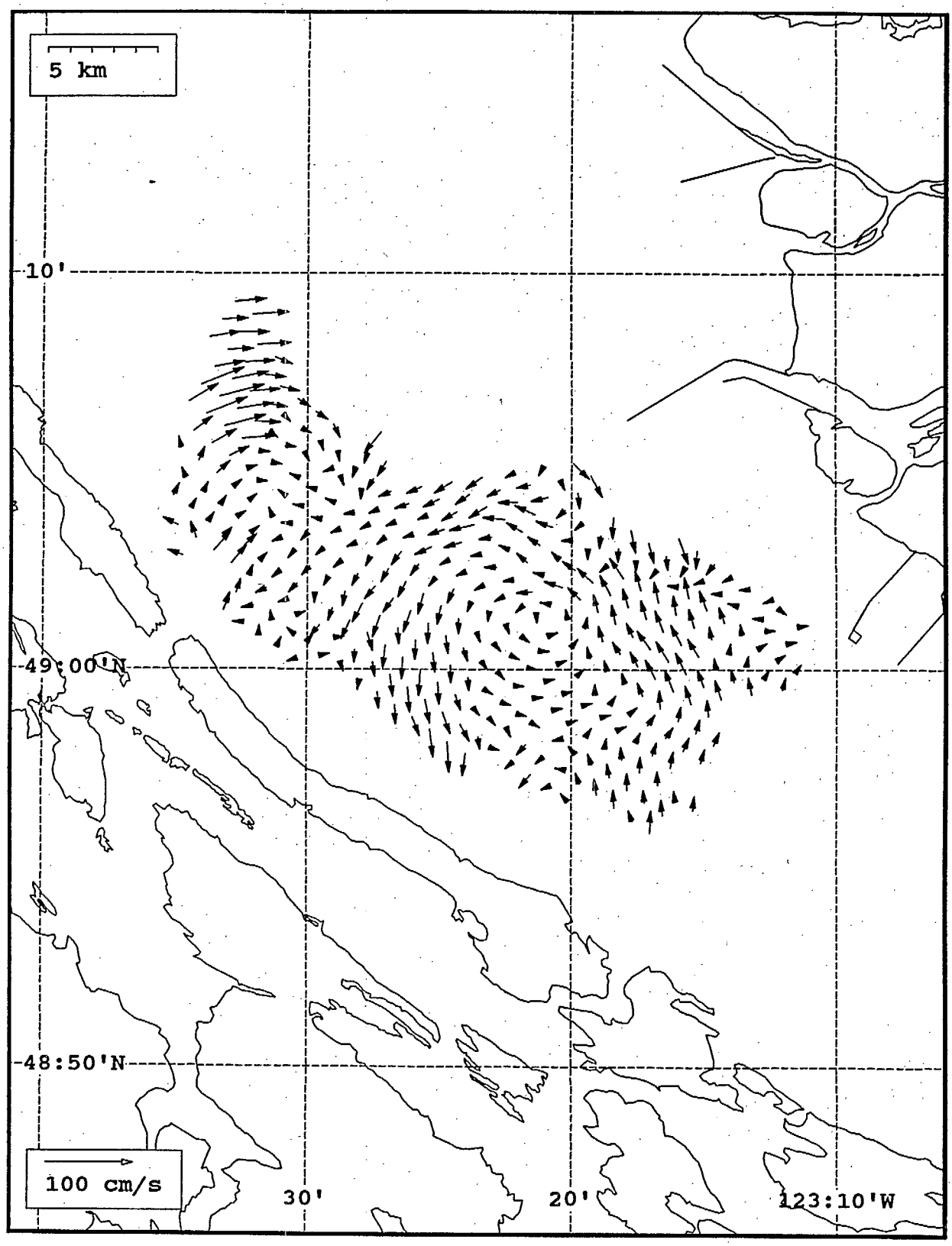

SeaSonde current field from the Strait of Georgia, off the mouth of the Fraser River, for 04:00 Z, July 28, 1993.

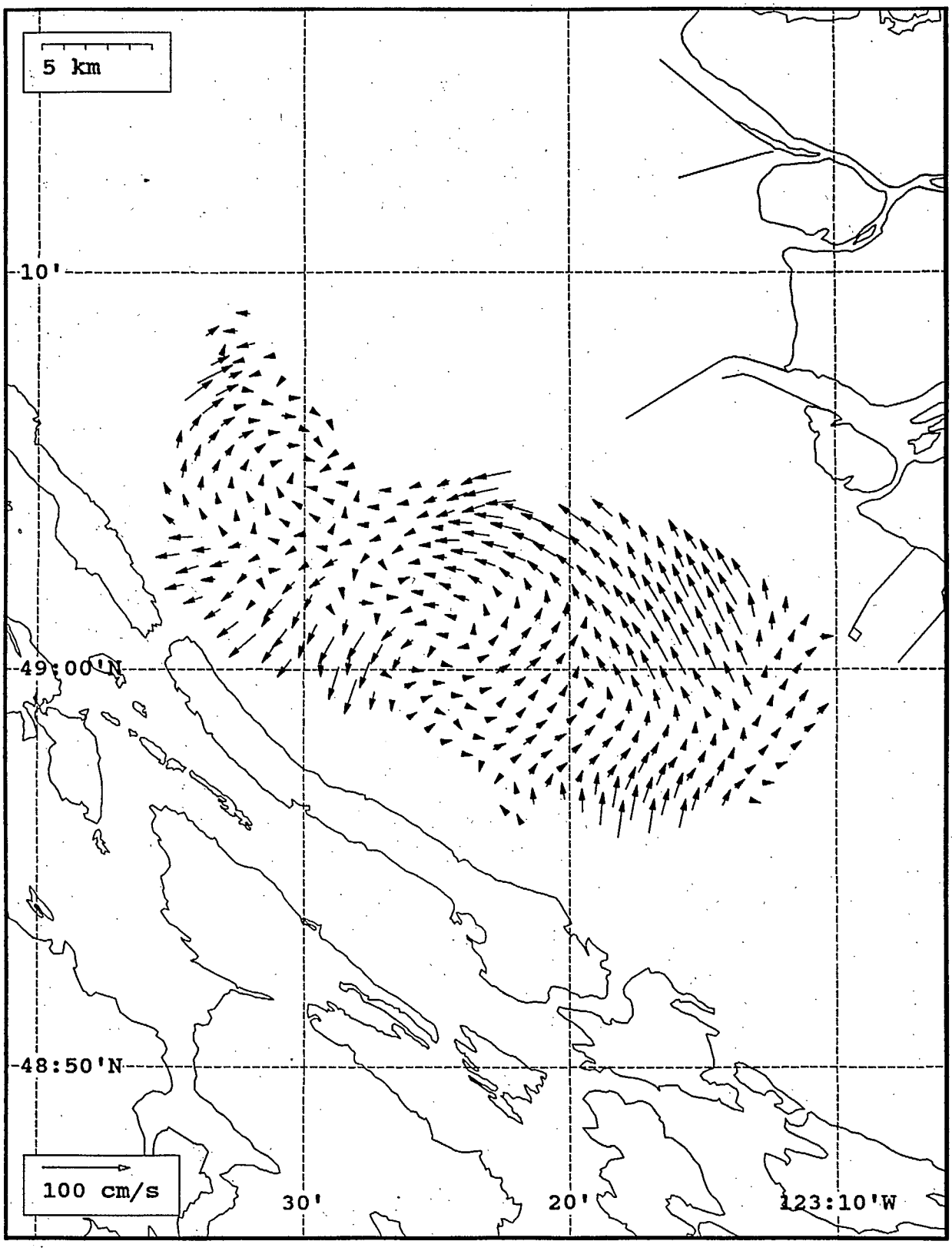

SeaSonde current field from the Strait of Georgia, off the mouth of the Fraser River, for 05:00 Z, July 28, 1993.

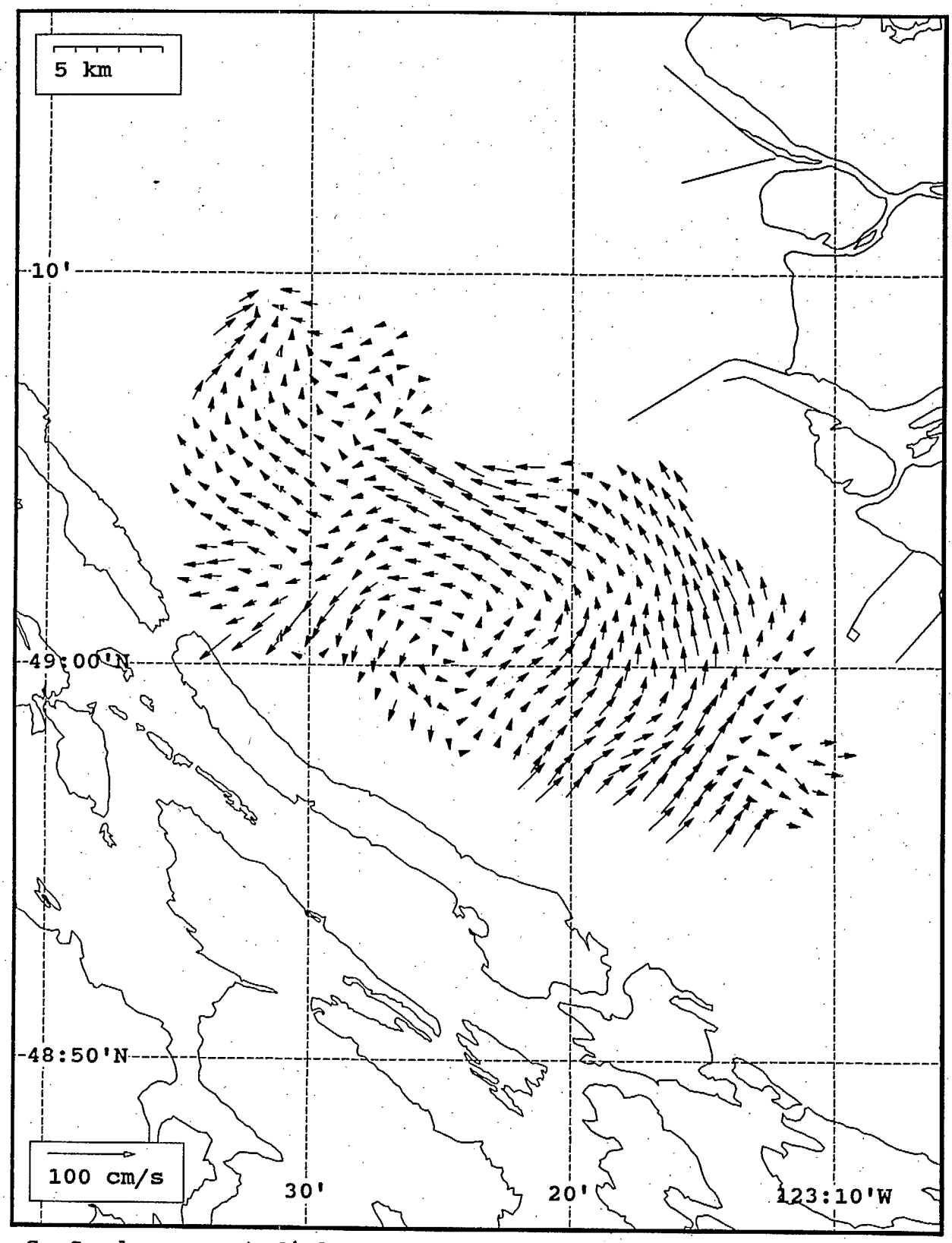

SeaSonde current field from the Strait of Georgia, off the mouth of the Fraser River, for 06:00 Z, July 28, 1993.

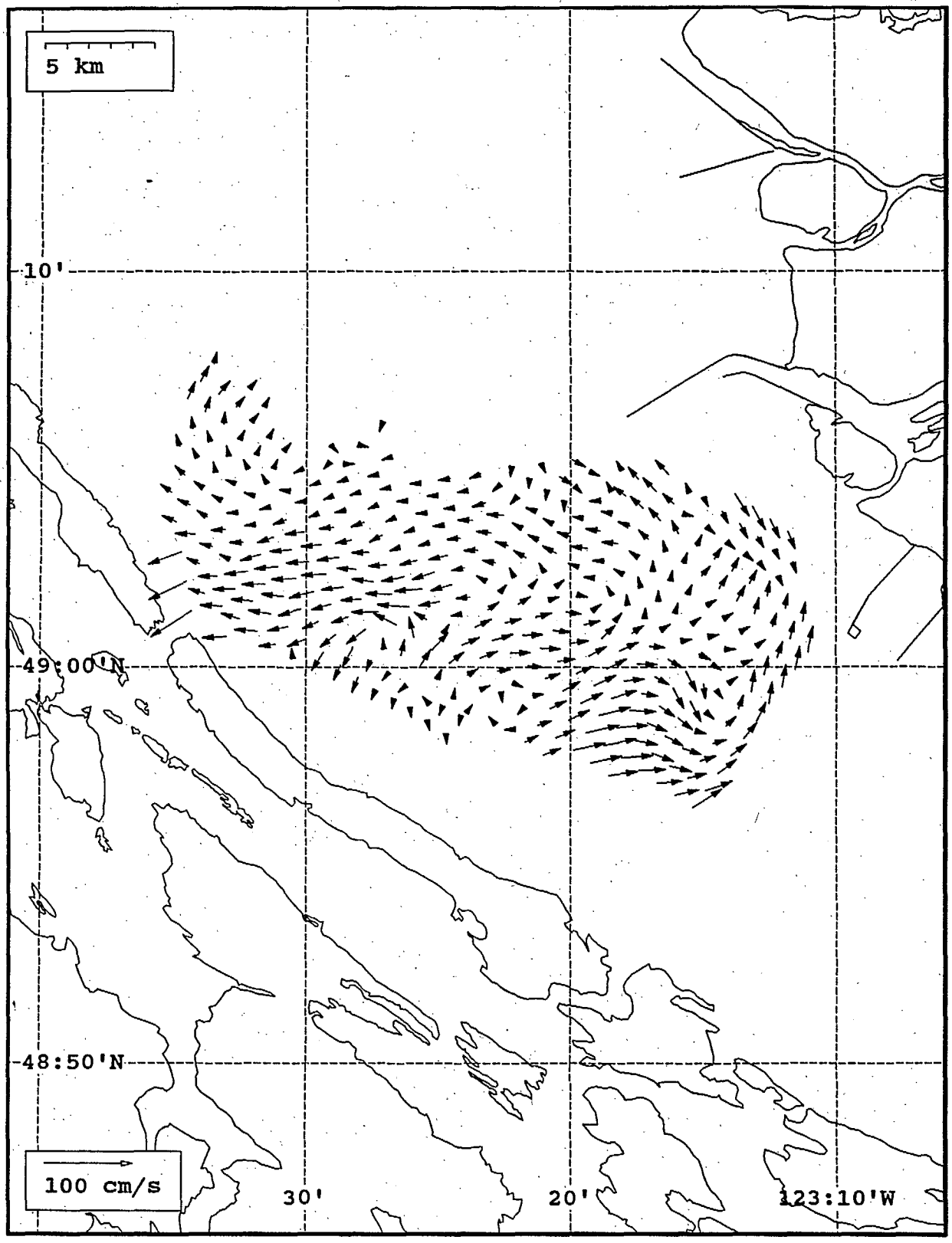

SeaSonde current field from the Strait of Georgia, off the mouth of the Fraser River, for 07:00 Z, July 28, 1993.

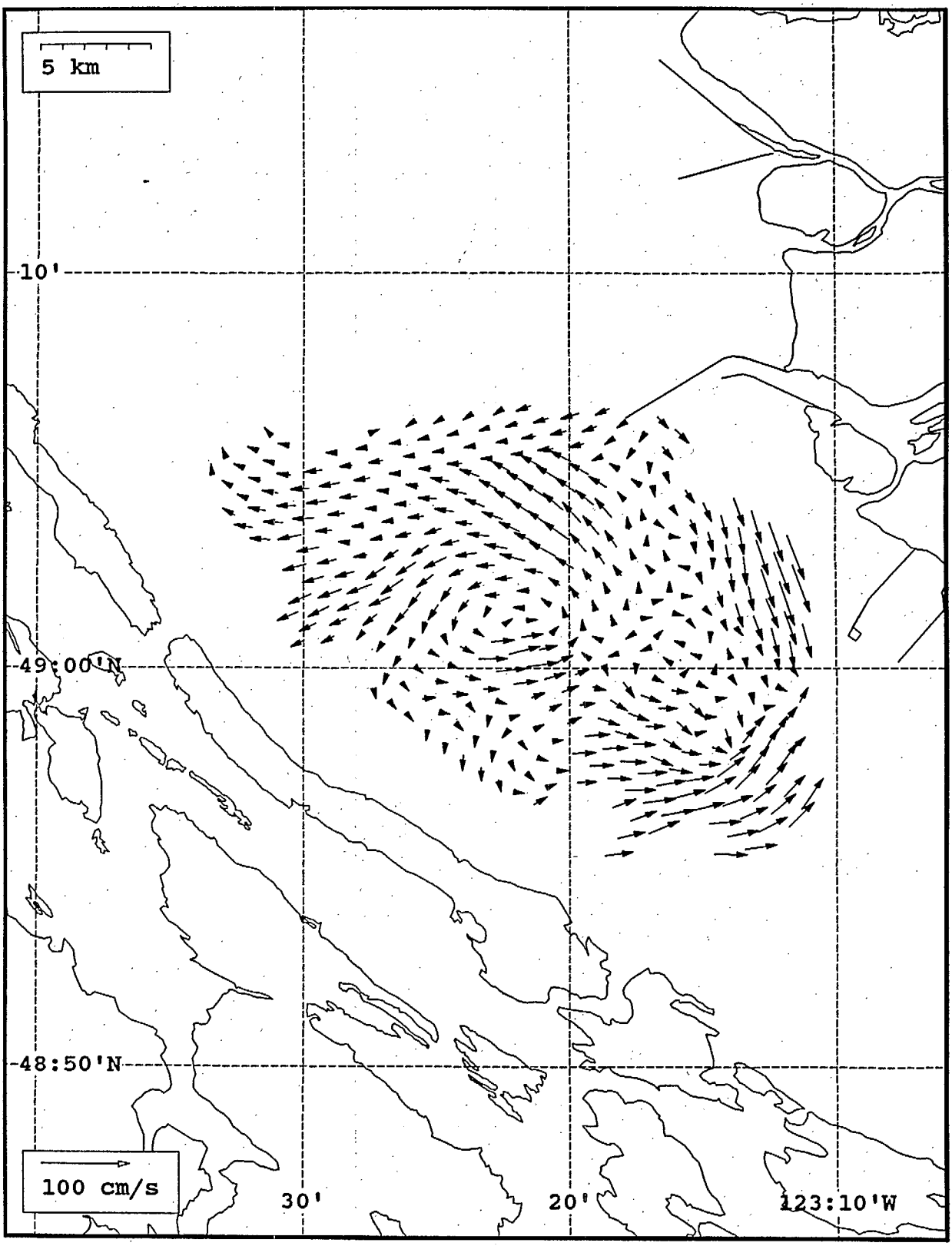

SeaSonde current field from the Strait of Georgia, off the mouth of the Fraser River, for 08:00 Z, July 28, 1993.

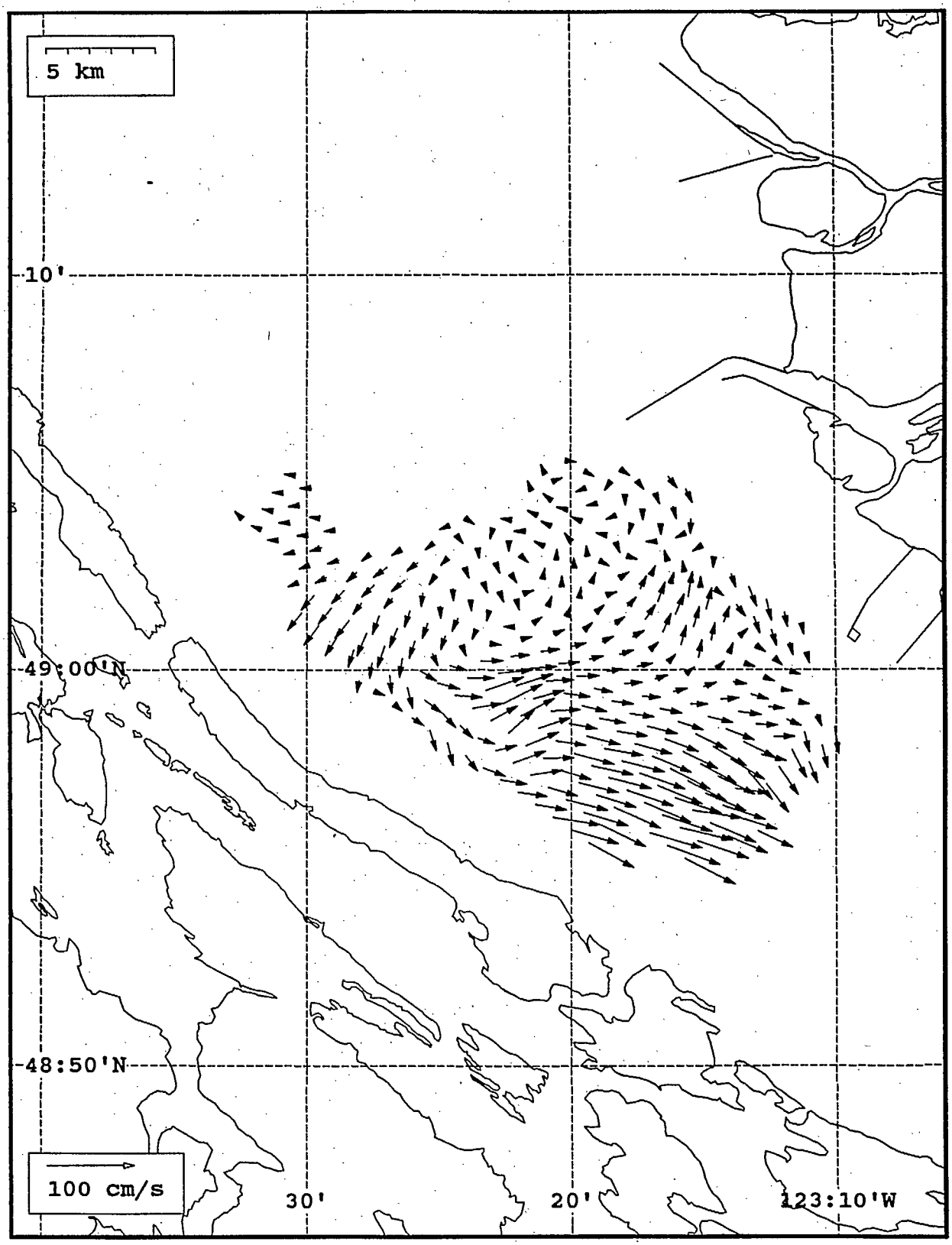

SeaSonde current field from the Strait of Georgia, off the mouth of the Fraser River, for 09:00 Z, July 28, 1993.

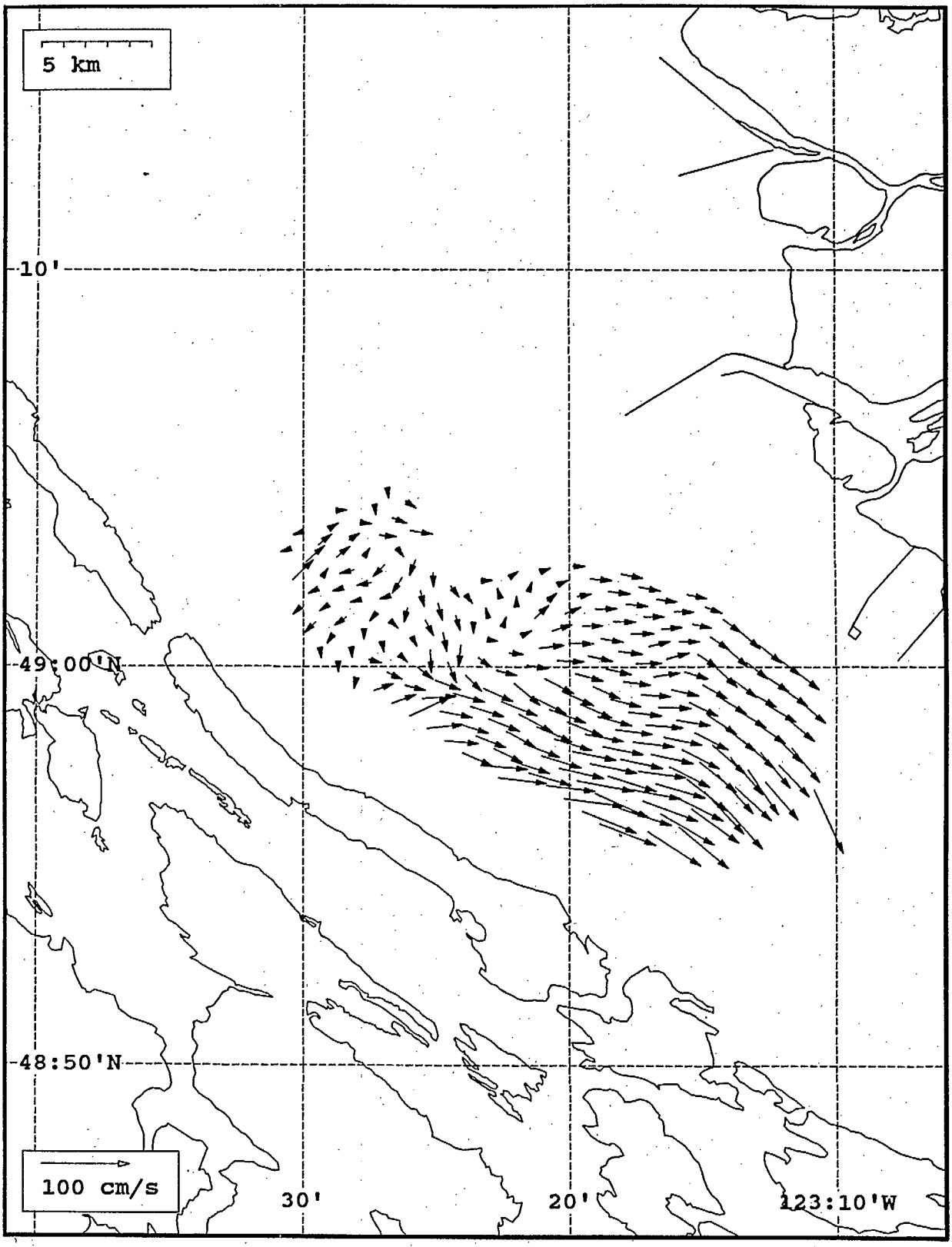

SeaSonde current field from the Strait of Georgia, off the mouth of the Fraser River, for 10:00 Z, July 28, 1993.

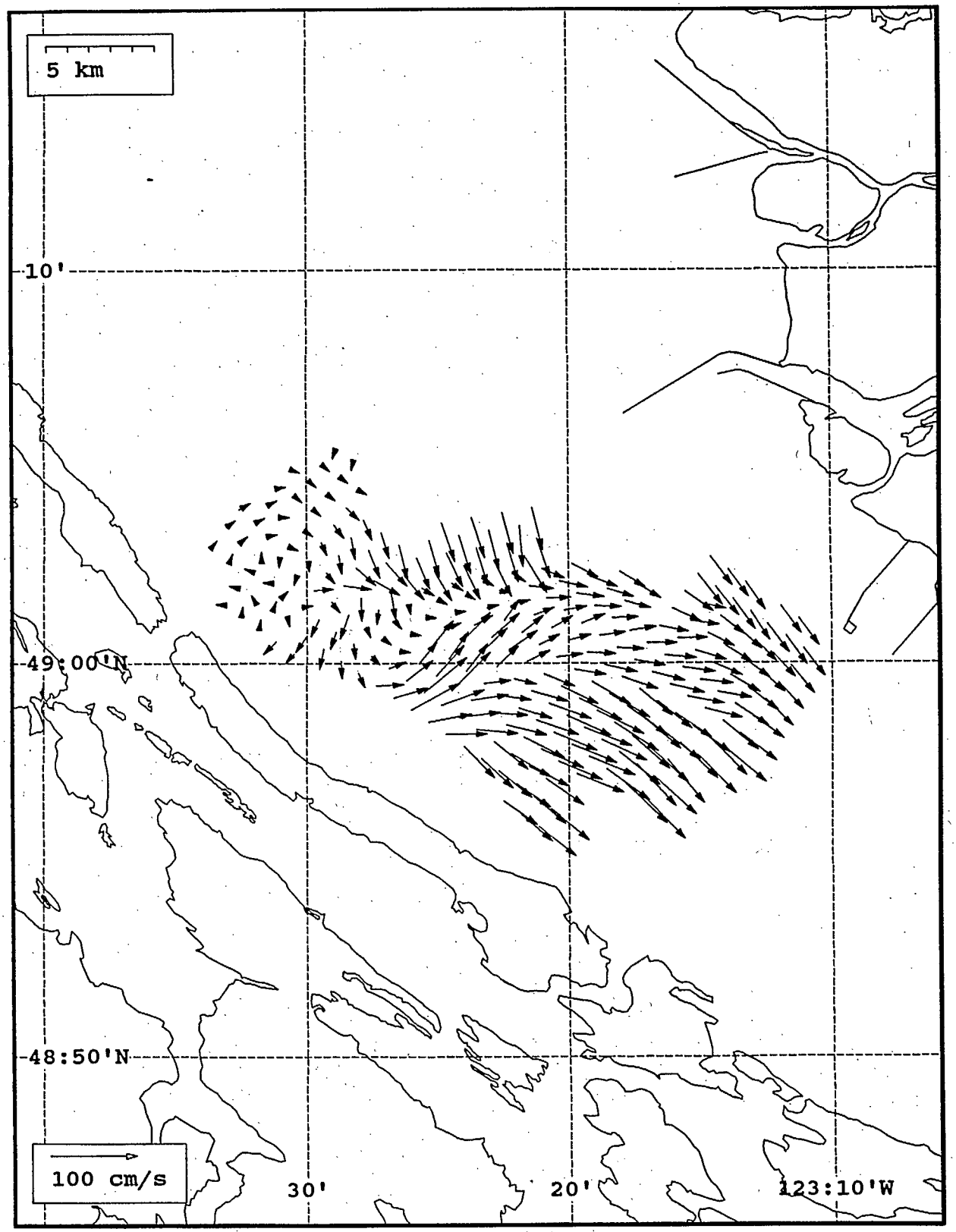

SeaSonde current field from the Strait of Georgia, off the mouth of the Fraser River, for 11:00 Z, July 28, 1993.

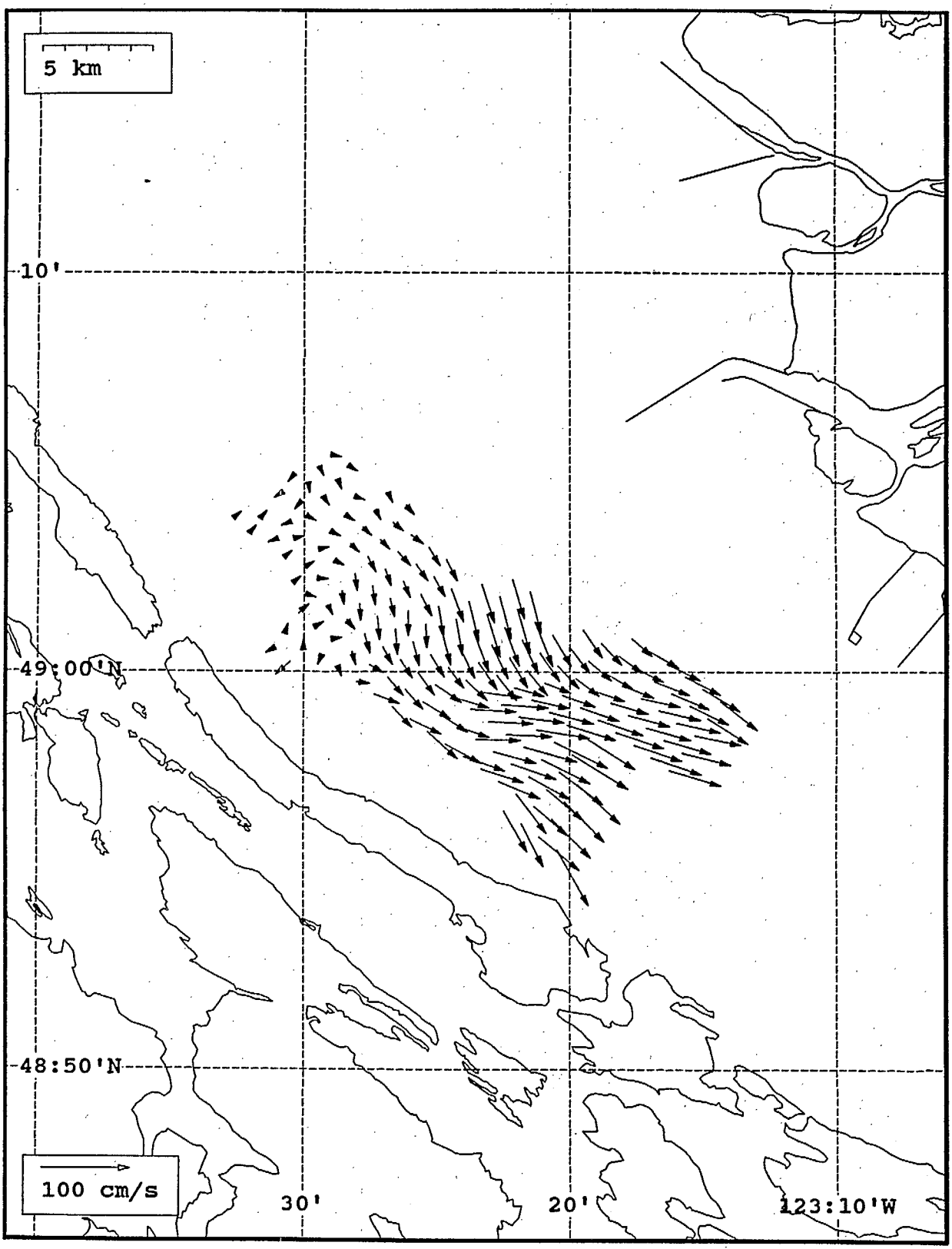

SeaSonde current field from the Strait of Georgia, off the mouth of the Fraser River, for 12:00 Z, July 28, 1993.

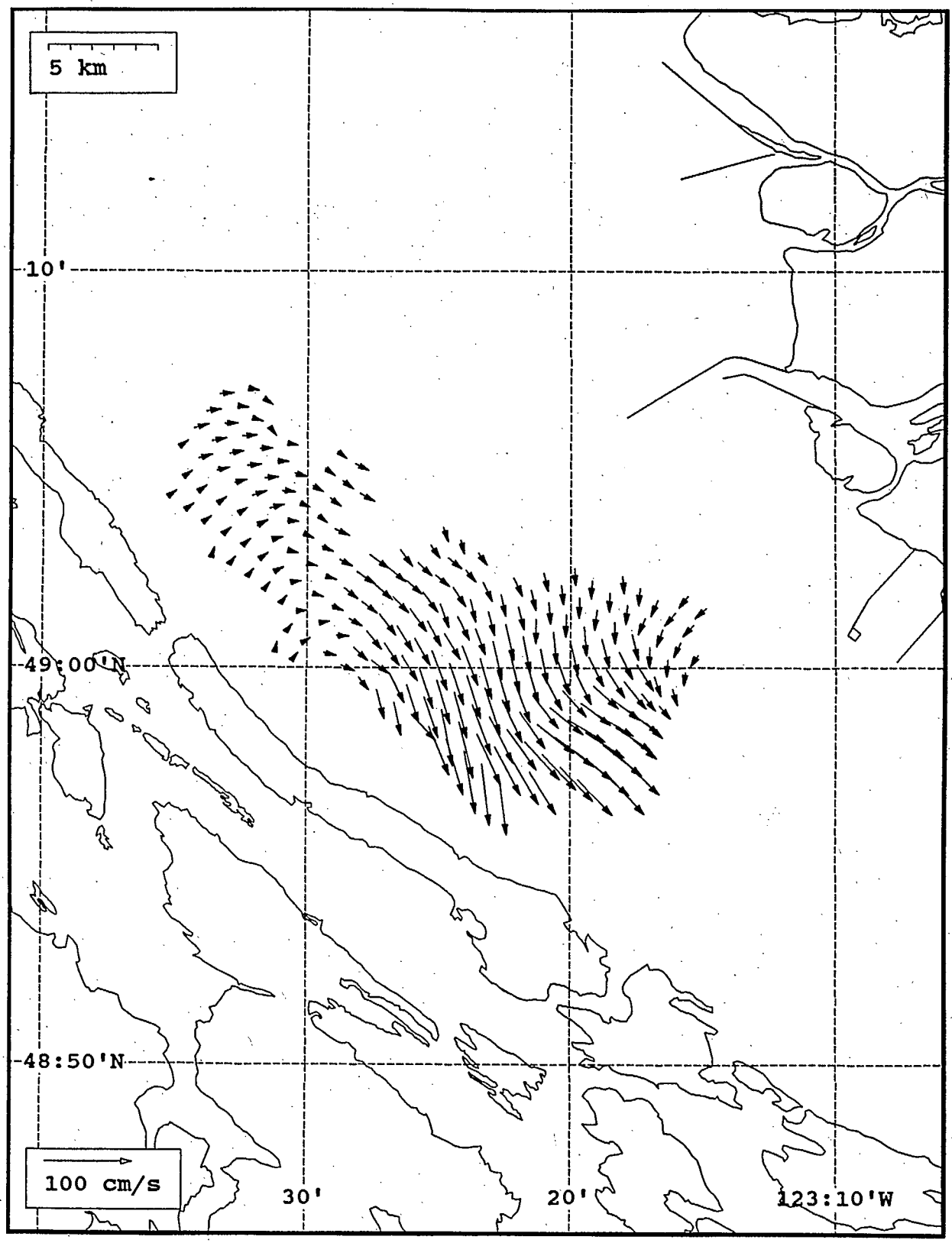

SeaSonde current field from the Strait of Georgia, off the mouth of the Fraser River, for 13:00 Z, July 28, 1993.

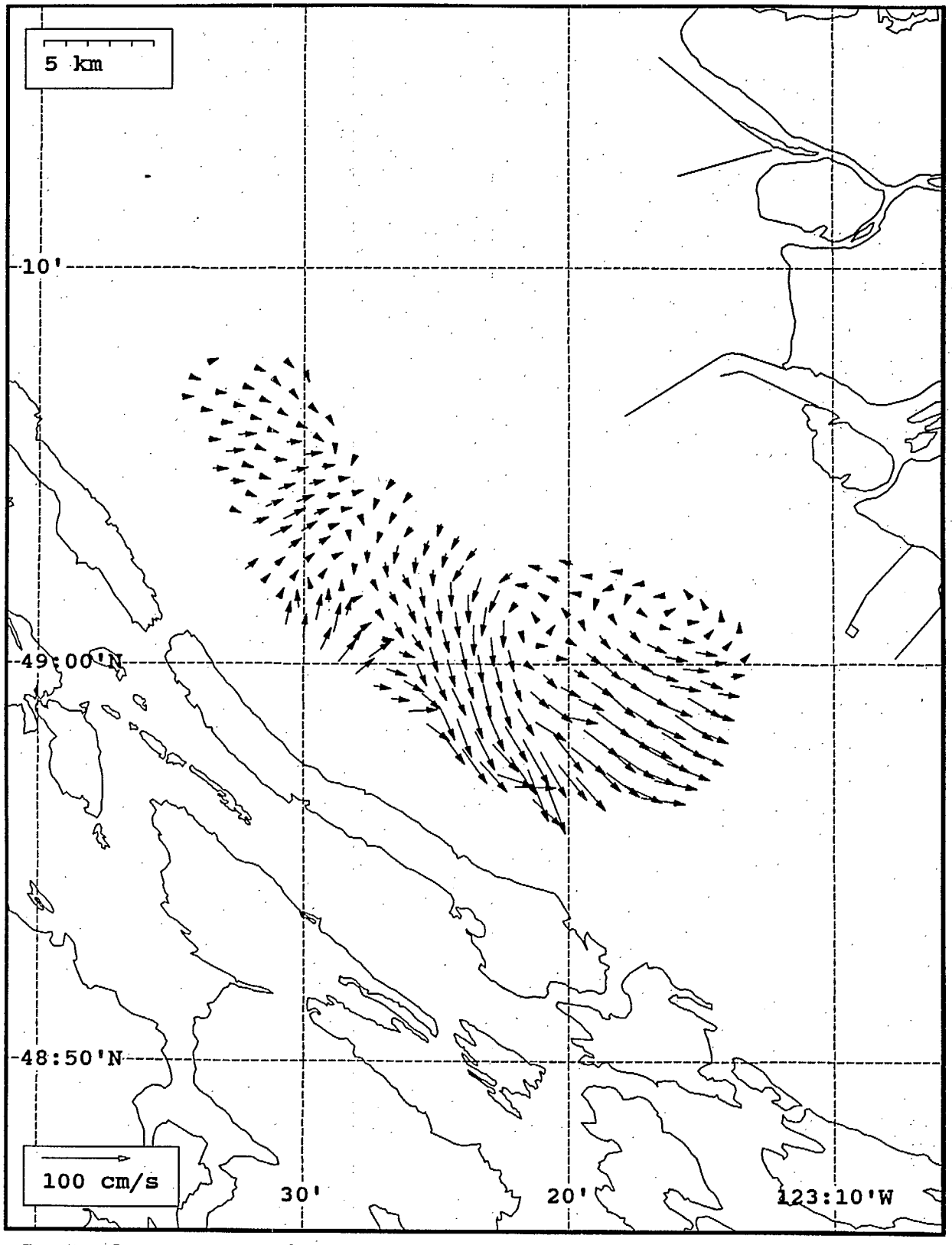

SeaSonde current field from the Strait of Georgia, off the mouth of the Fraser River, for 14:00 Z, July 28, 1993.

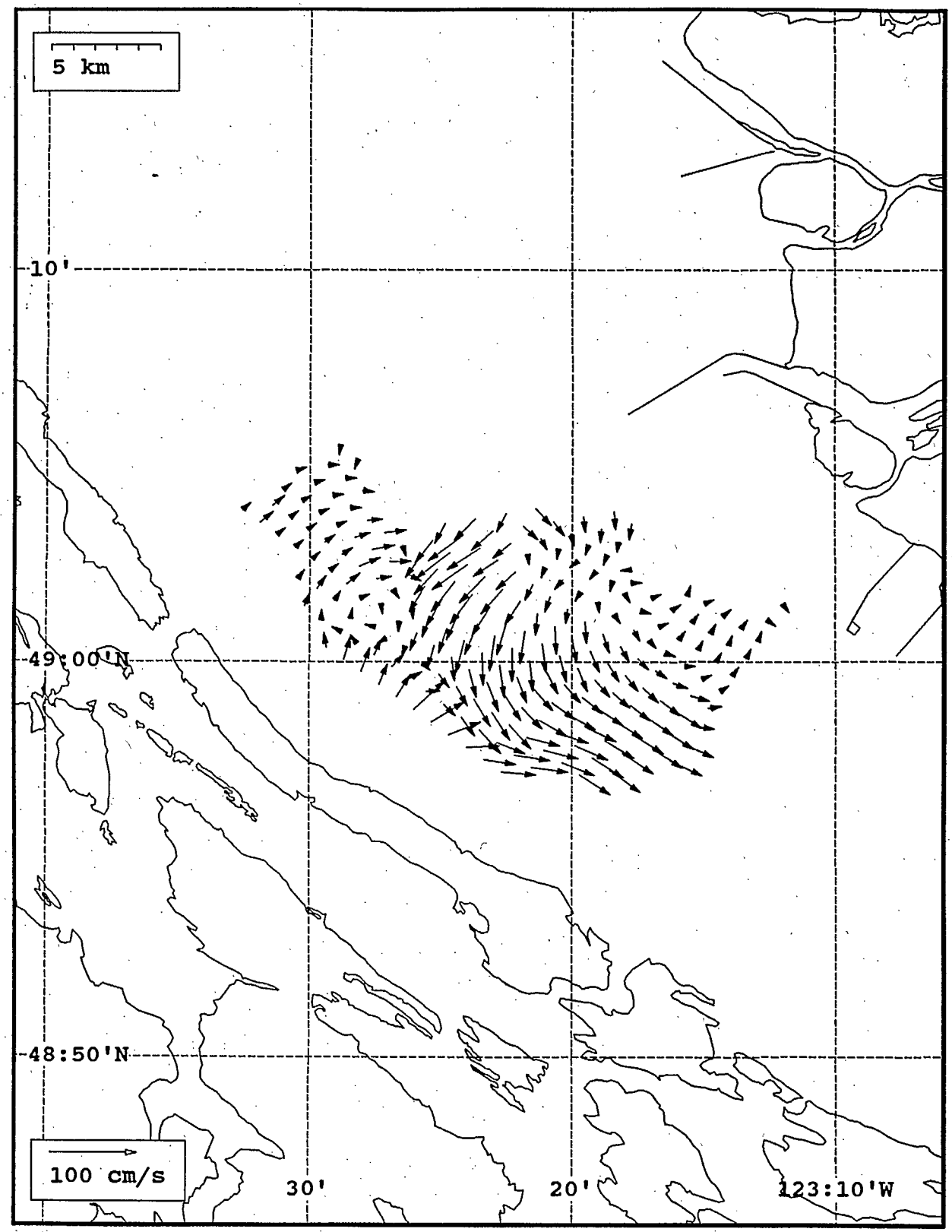

SeaSonde current field from the Strait of Georgia, off the mouth of the Fraser River, for 15:00 Z, July 28, 1993.

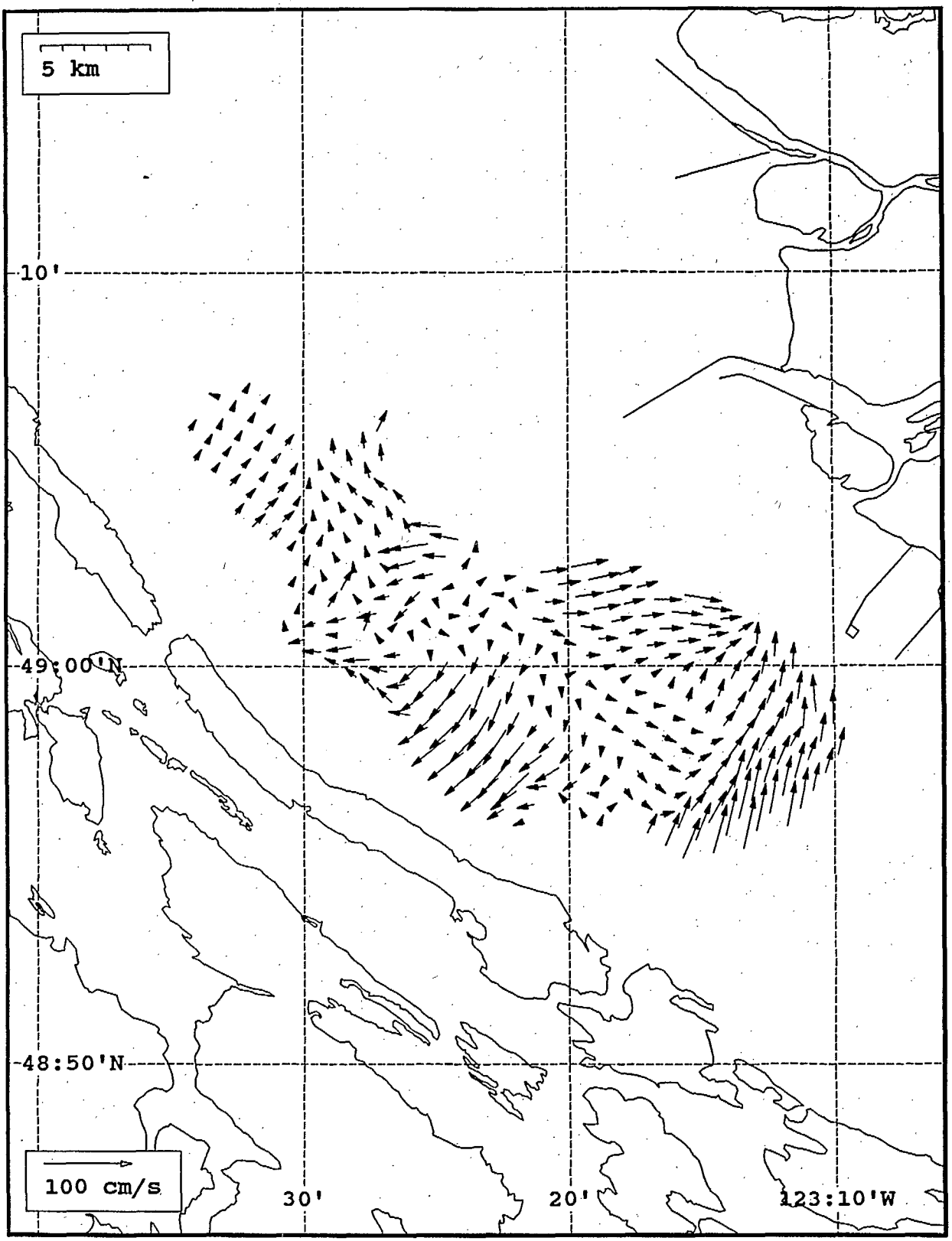

SeaSonde current field from the Strait of Georgia, off the mouth of the Fraser River, for 16:00 Z, July 28, 1993.

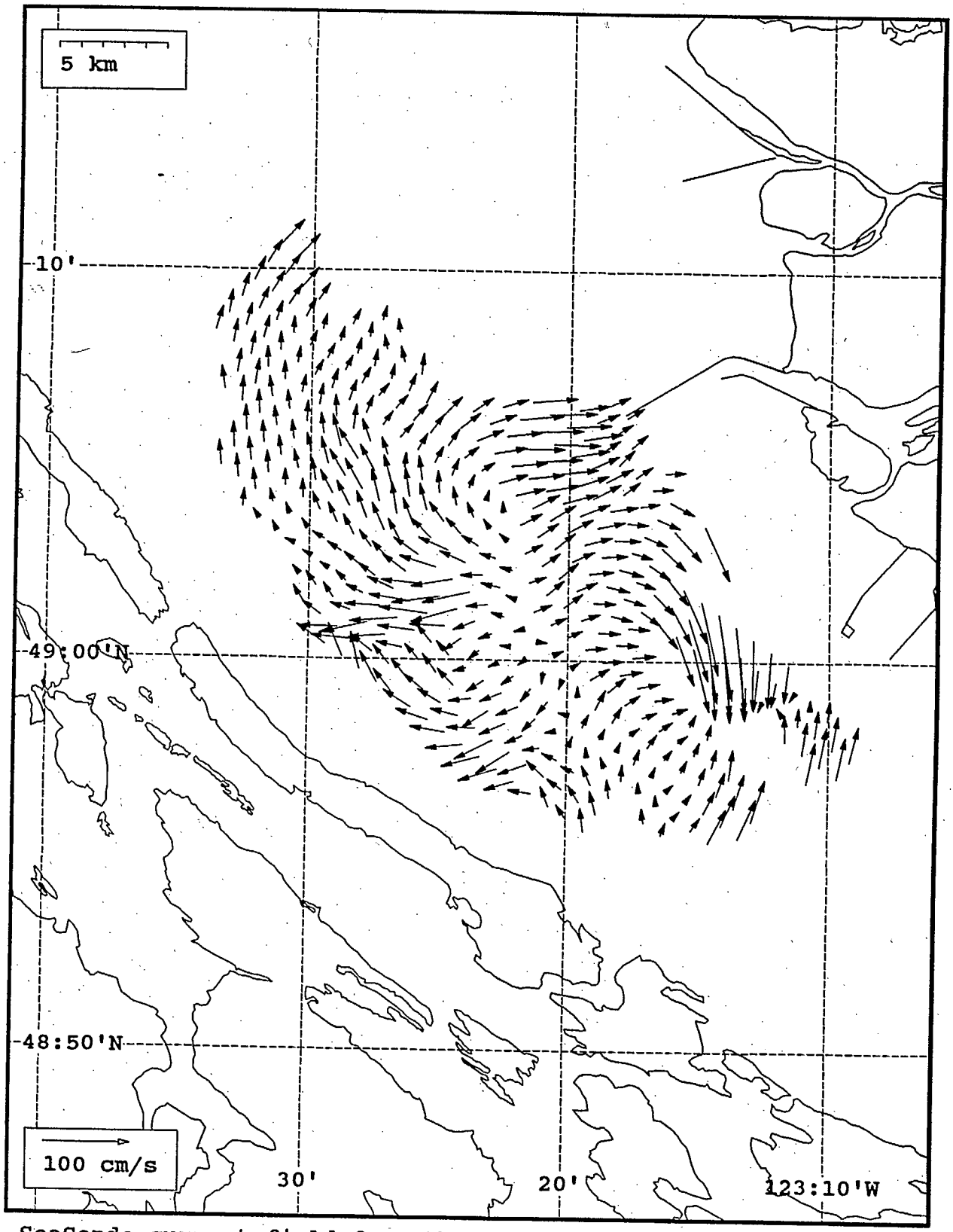

SeaSonde current field from the Strait of Georgia, off the mouth of the Fraser River, for 17:00 Z, July 28, 1993.

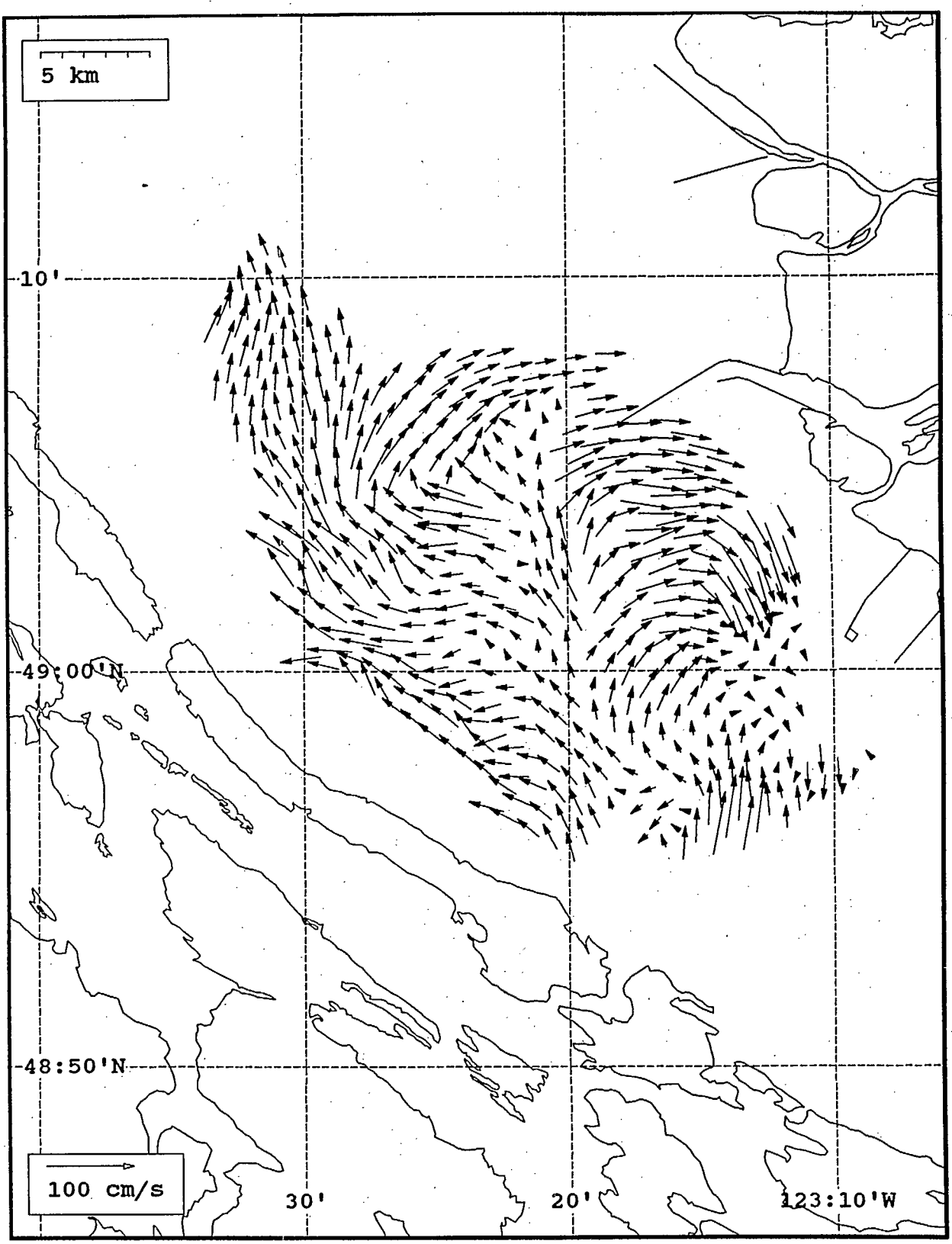

SeaSonde current field from the Strait of Georgia, off the mouth of the Fraser River, for 18:00 Z, July 28, 1993.

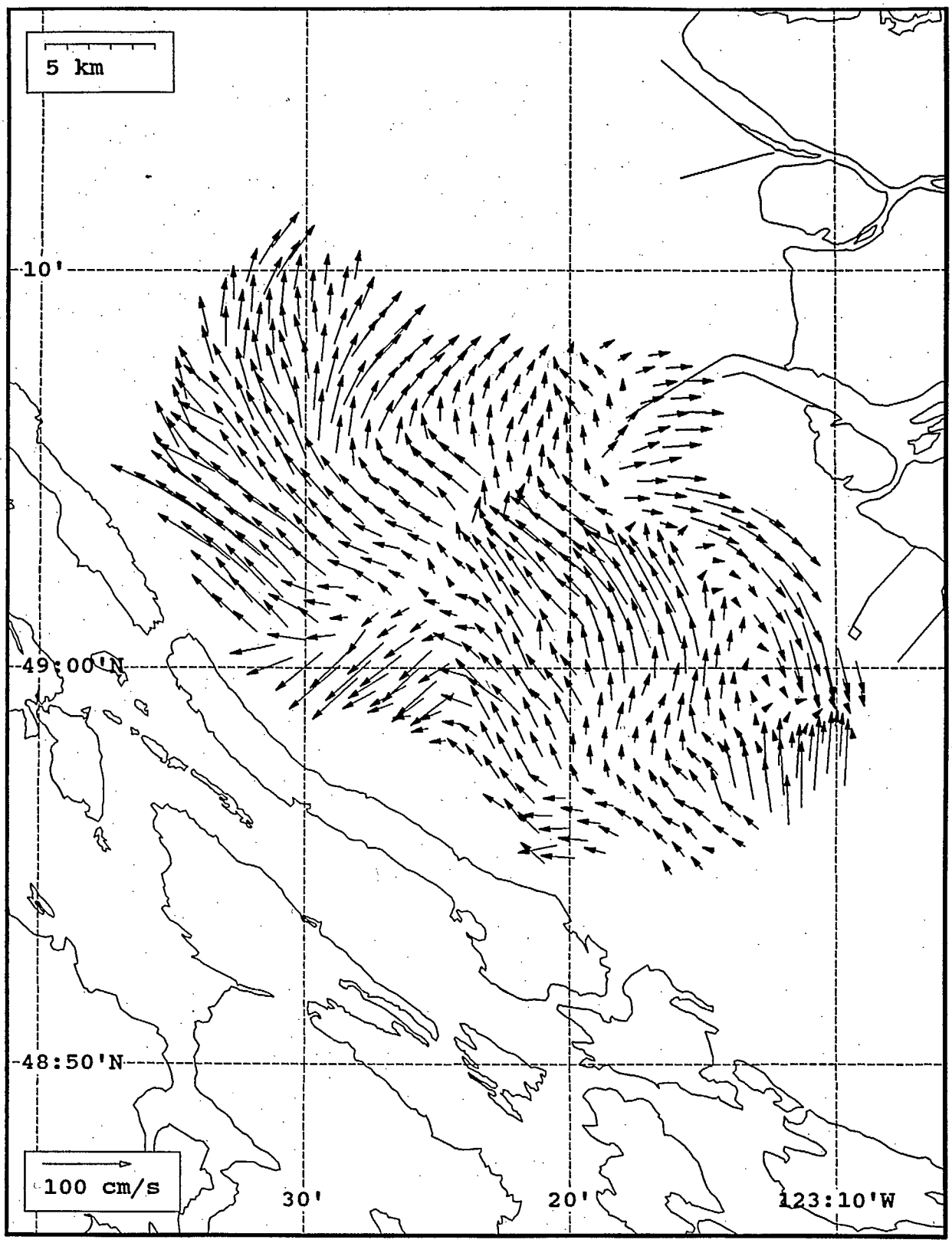

SeaSonde current field from the Strait of Georgia, off the mouth of the Fraser River, for 19:00 Z, July 28, 1993.

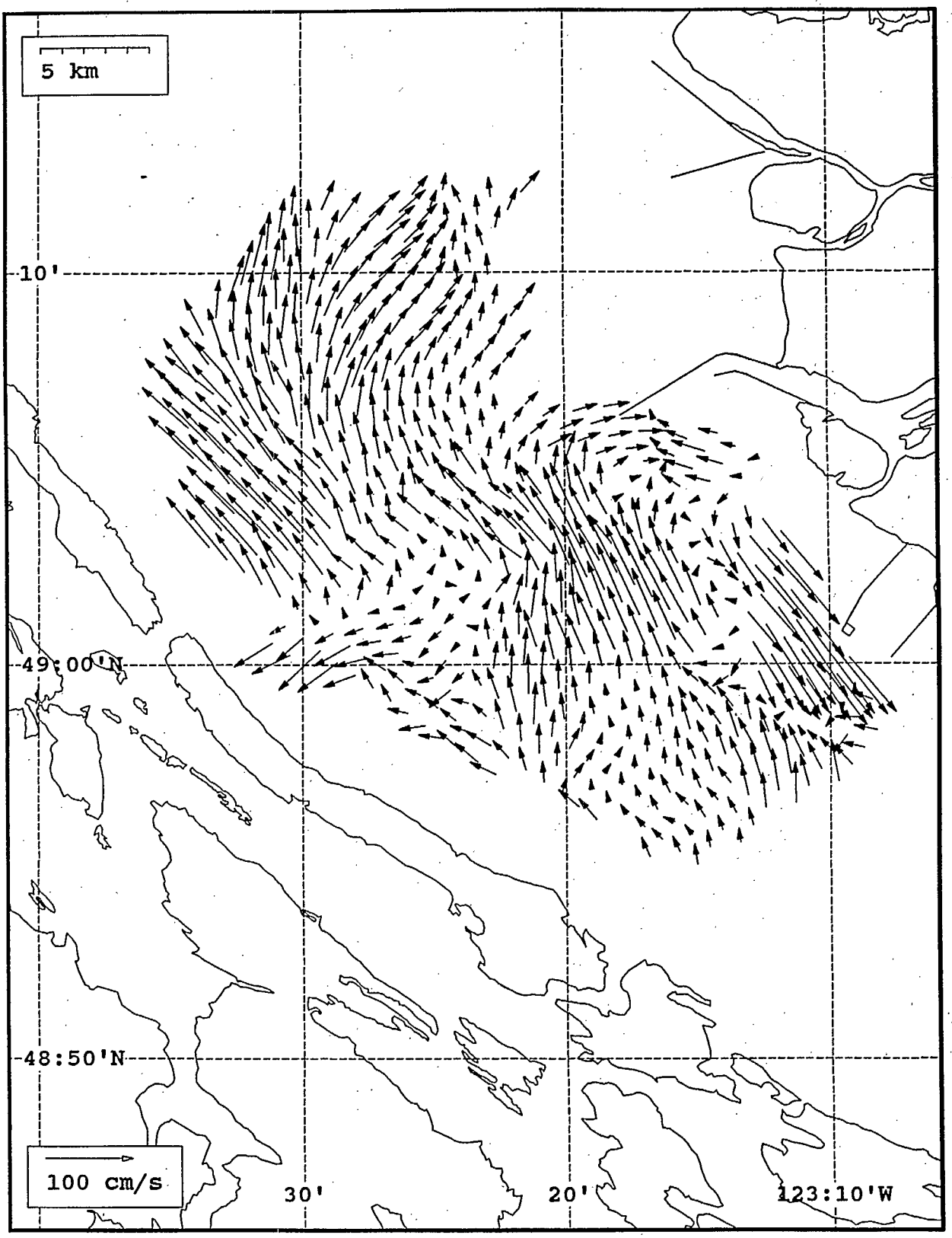

SeaSonde current field from the Strait of Georgia, off the mouth of the Fraser River, for 20:00 Z, July 28, 1993.

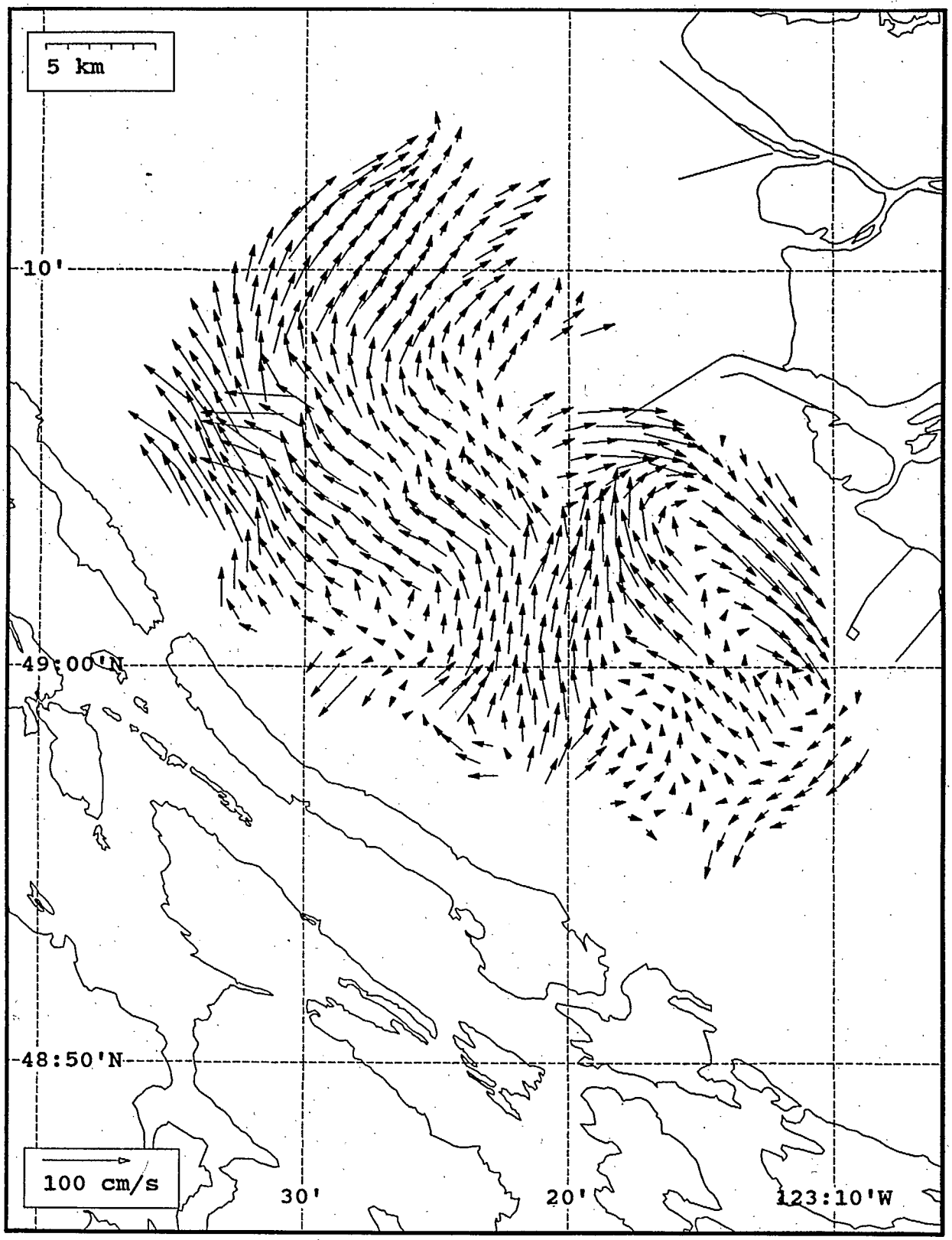

SeaSonde current field from the Strait of Georgia, off the mouth of the Fraser River, for 21:00 Z, July 28, 1993.

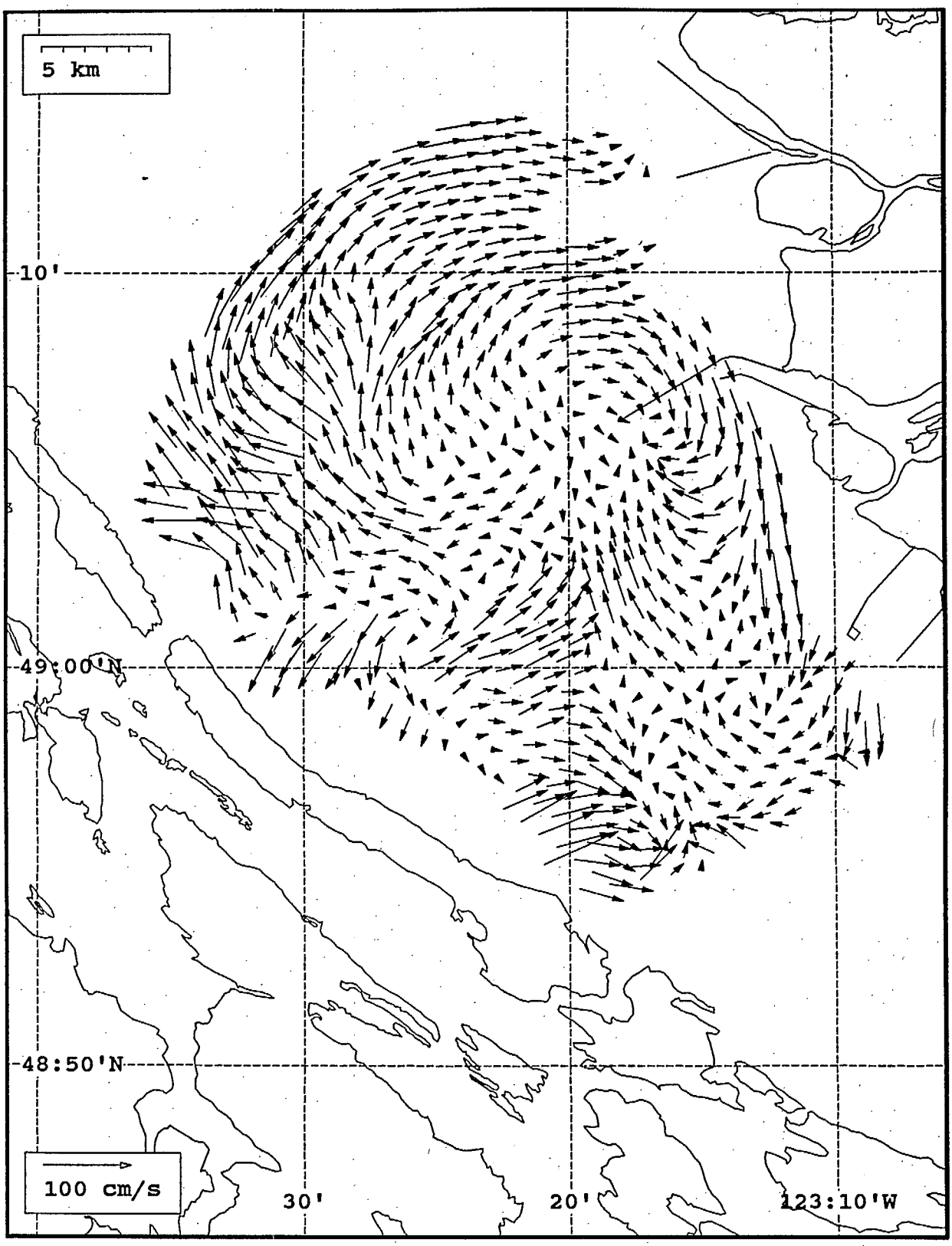

SeaSonde current field from the Strait of Georgia, off the mouth of the Fraser River, for 23:00 Z, July 28, 1993.

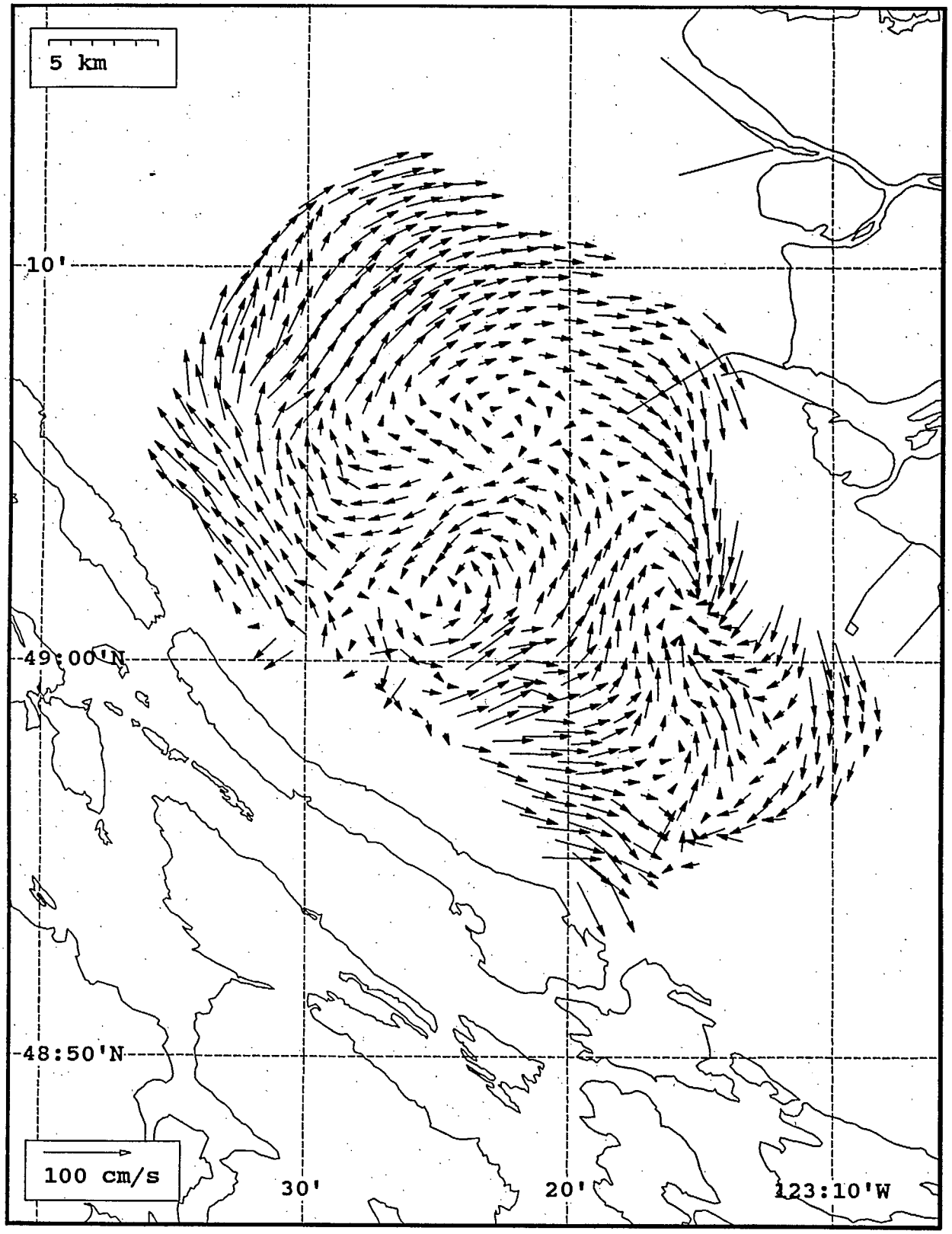

SeaSonde current field from the Strait of Georgia, off the mouth of the Fraser River, for 00:00 Z, July 29, 1993.

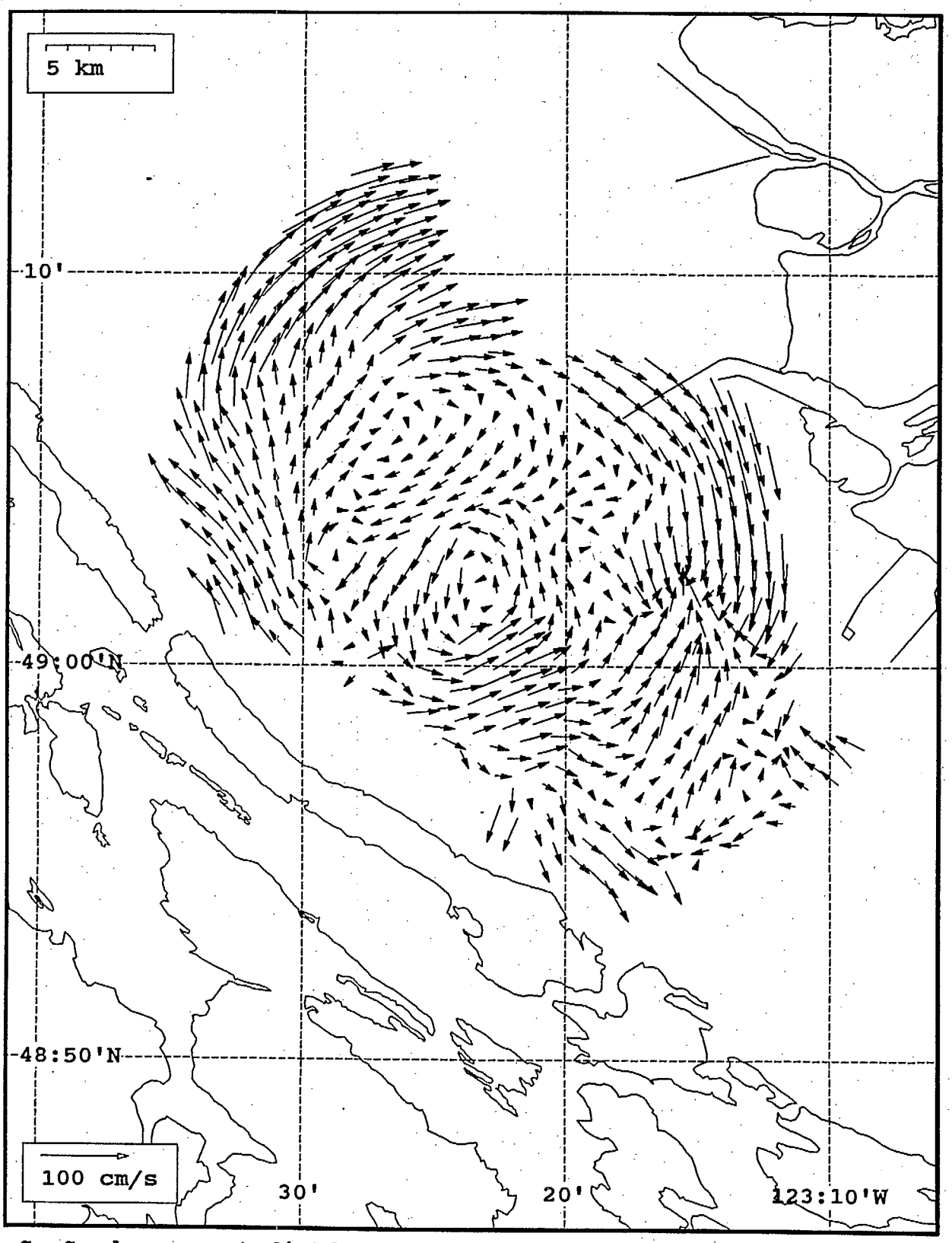

SeaSonde current field from the Strait of Georgia, off the mouth of the Fraser River, for 01:00 Z, July 29, 1993.

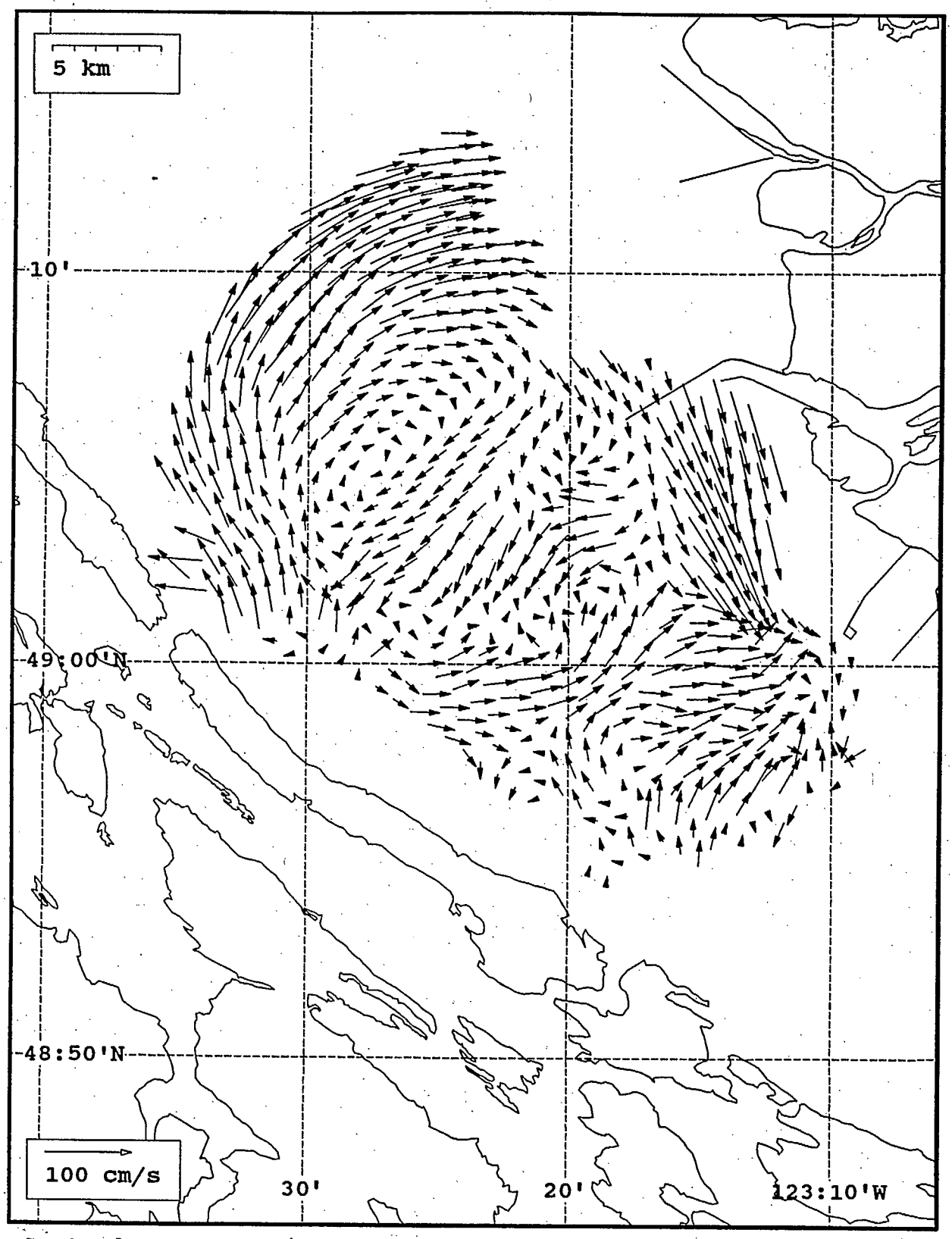

SeaSonde current field from the Strait of Georgia, off the mouth of the Fraser River, for 02:00 Z, July 29, 1993.

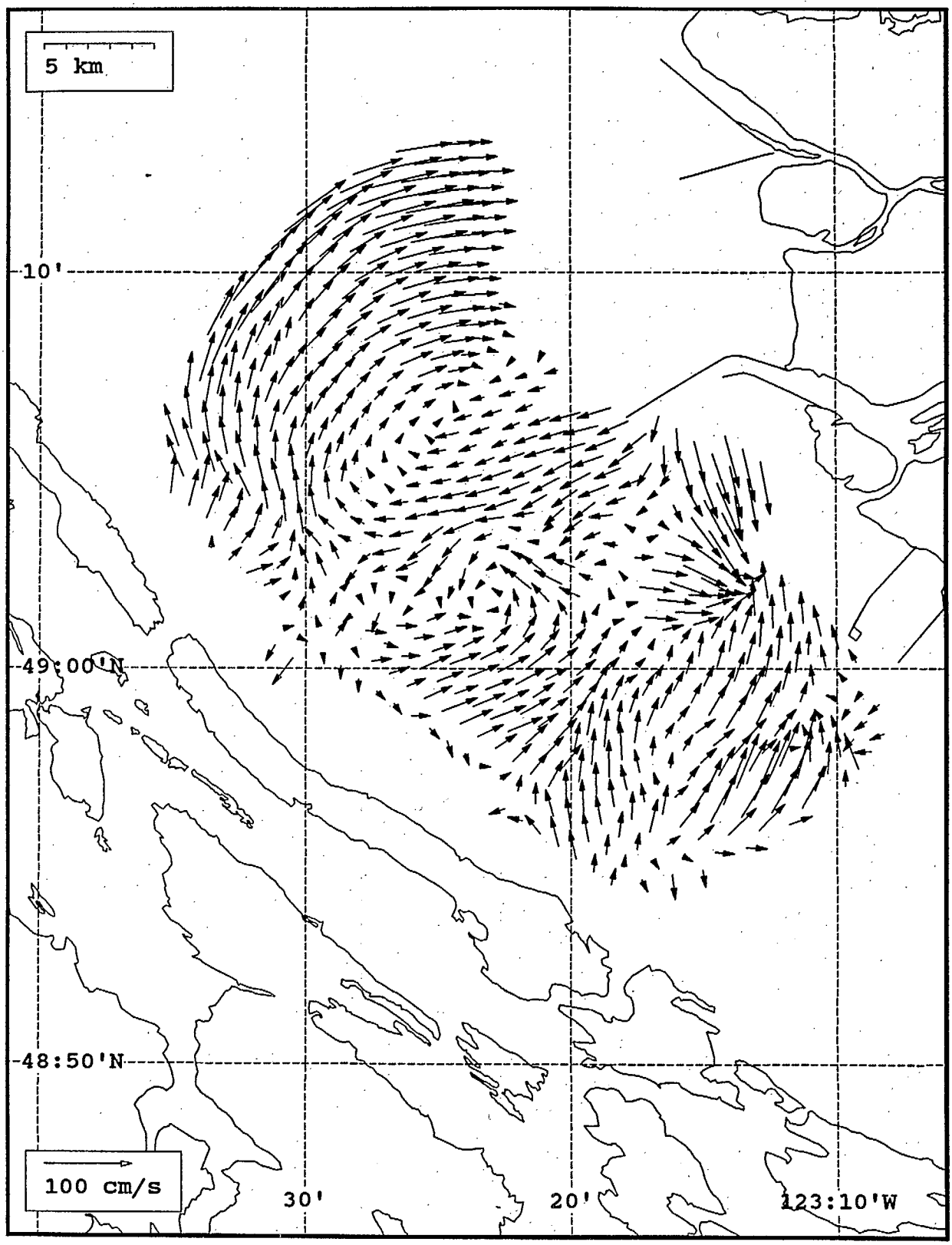

SeaSonde current field from the Strait of Georgia, off the mouth of the Fraser River, for 03:00 Z, July 29, 1993.

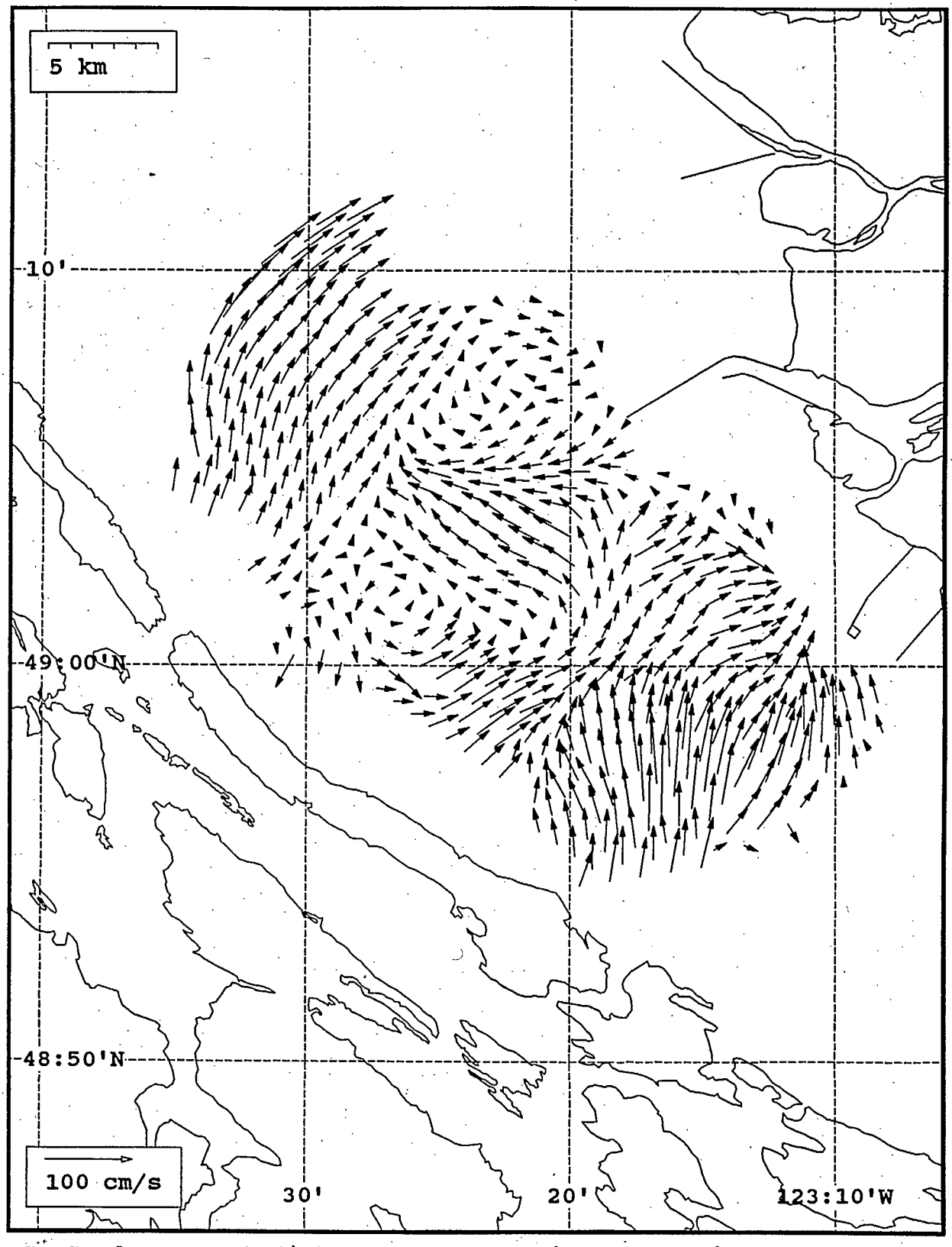

SeaSonde current field from the Strait of Georgia, off the mouth of the Fraser River, for 04:00 Z, July 29, 1993.

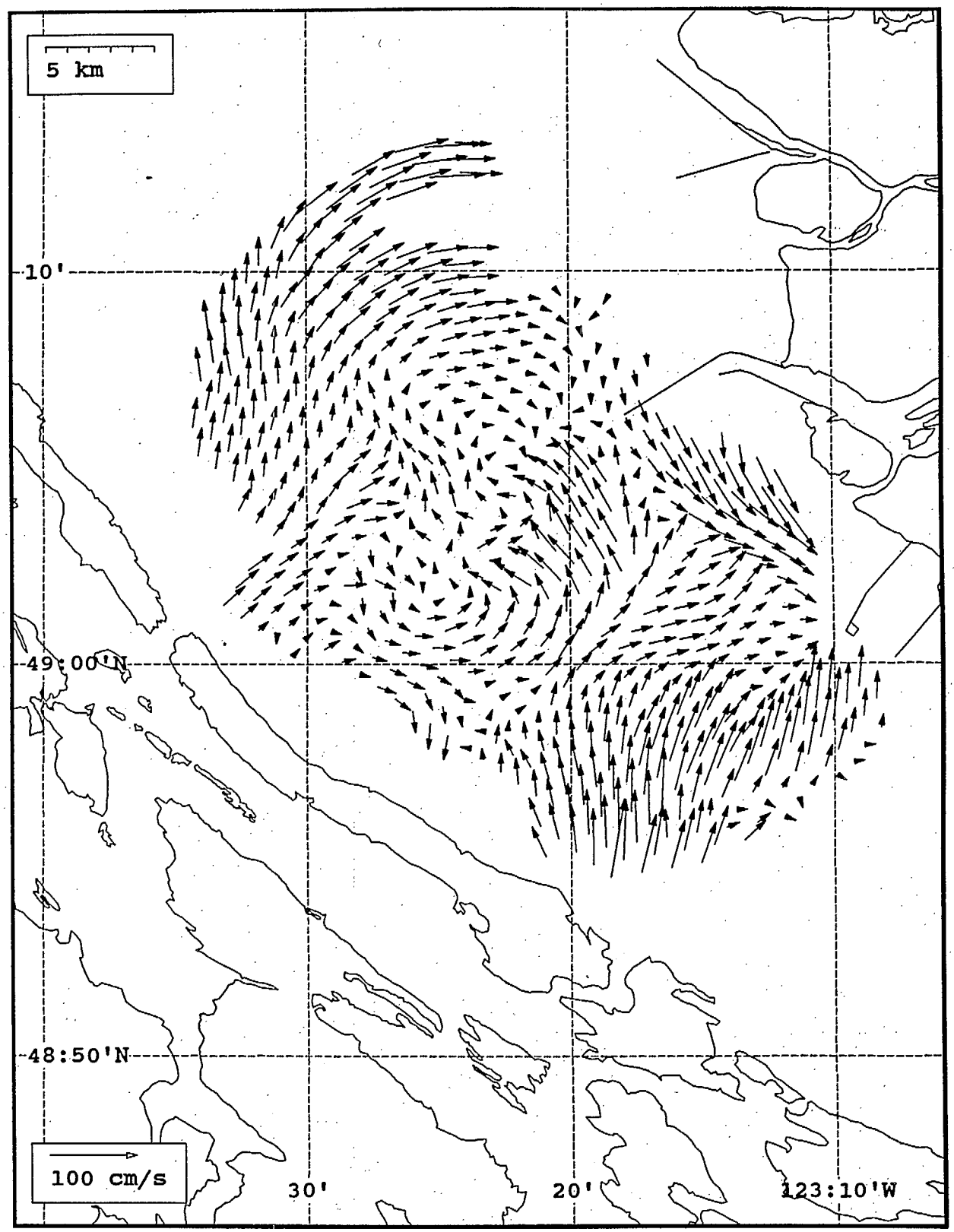

SeaSonde current field from the Strait of Georgia, off the mouth of the Fraser River, for 05:00 Z, July 29, 1993.

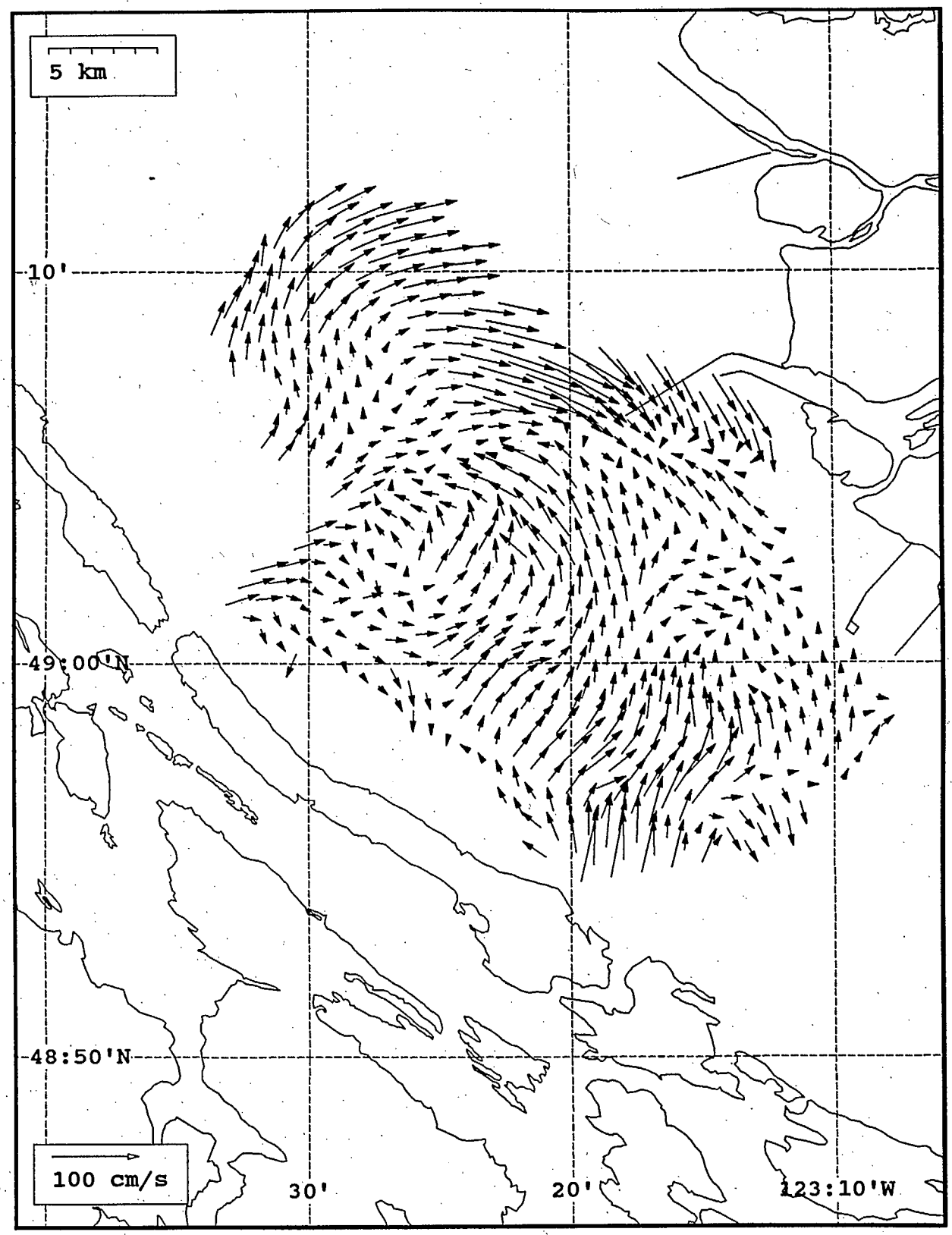

SeaSonde current field from the Strait of Georgia, off the mouth of the Fraser River, for 06:00 Z, July 29, 1993.

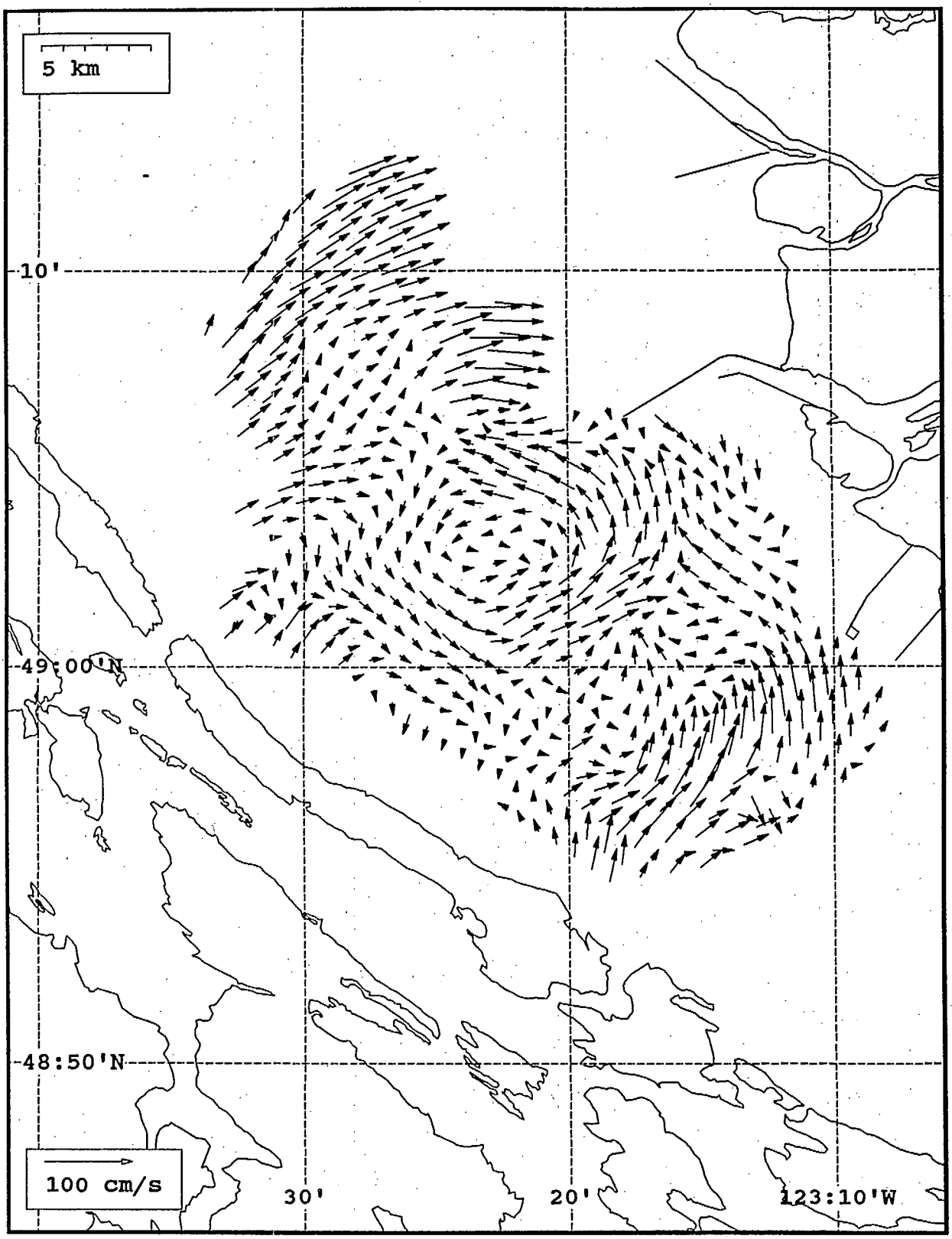

SeaSonde current field from the Strait of Georgia, off the mouth of the Fraser River, for 07:00 Z, July 29, 1993.

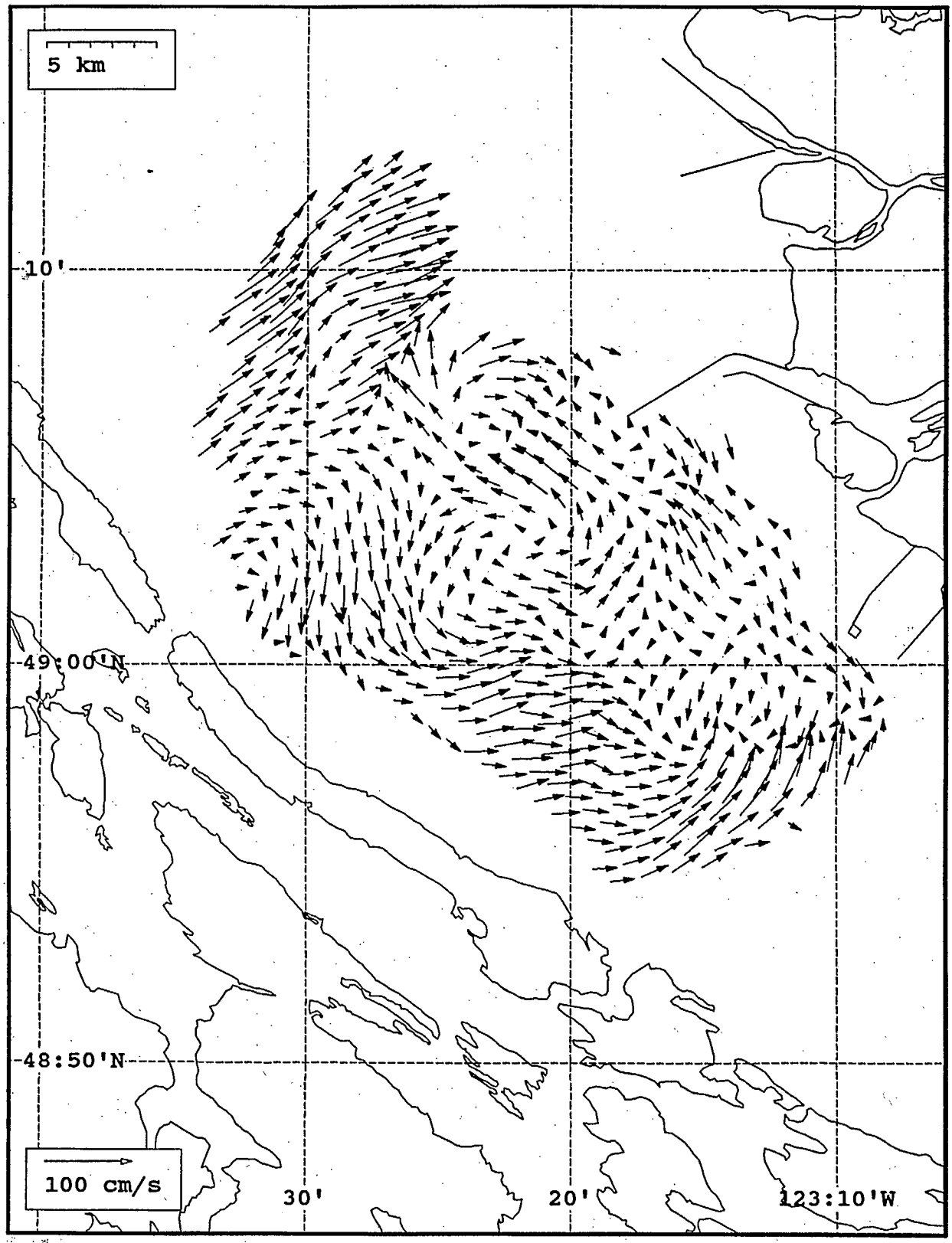

SeaSonde current field from the Strait of Georgia, off the mouth of the Fraser River, for 08:00 Z, July 29, 1993.

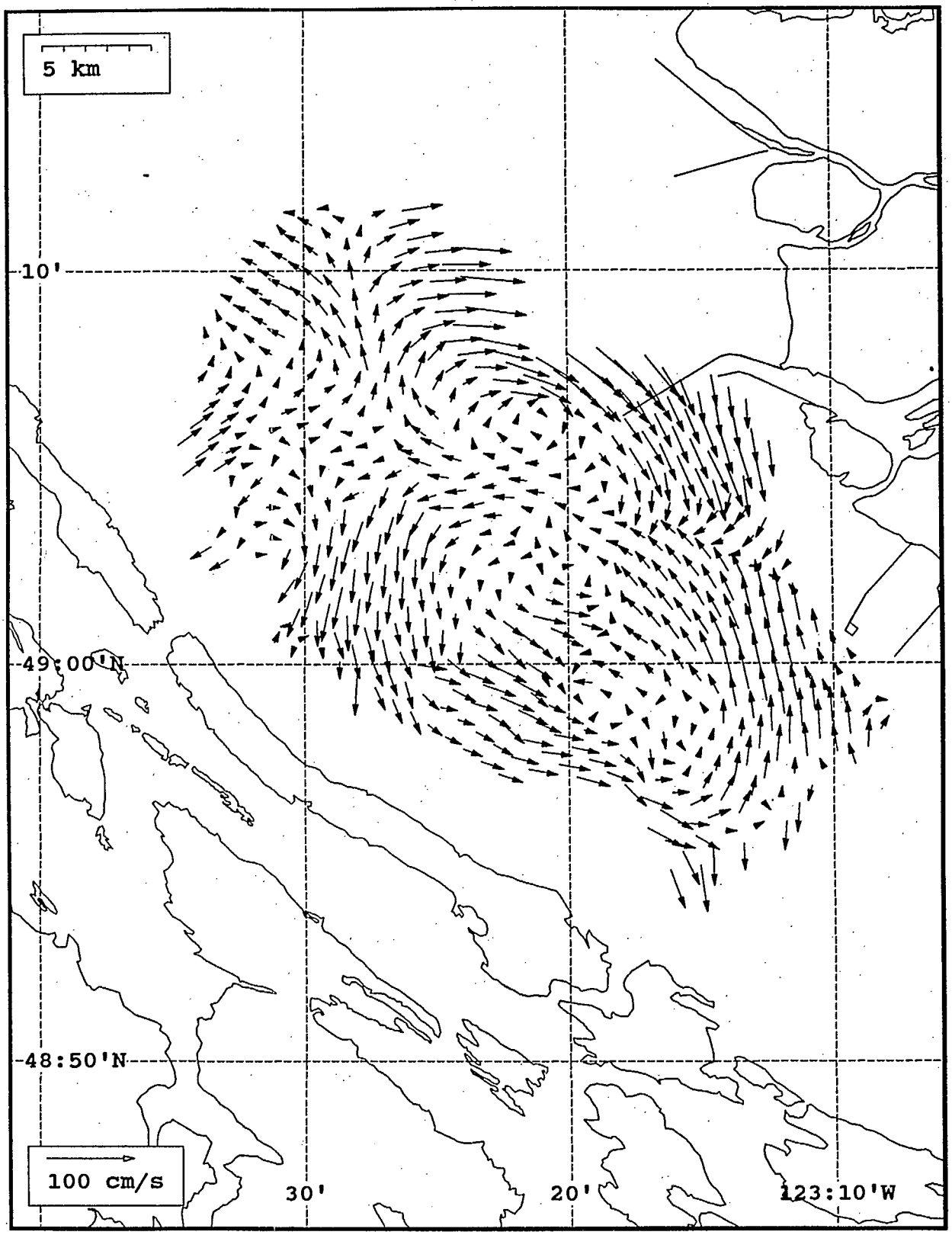

SeaSonde current field from the Strait of Georgia, off the mouth of the Fraser River, for 09:00 Z, July 29, 1993.

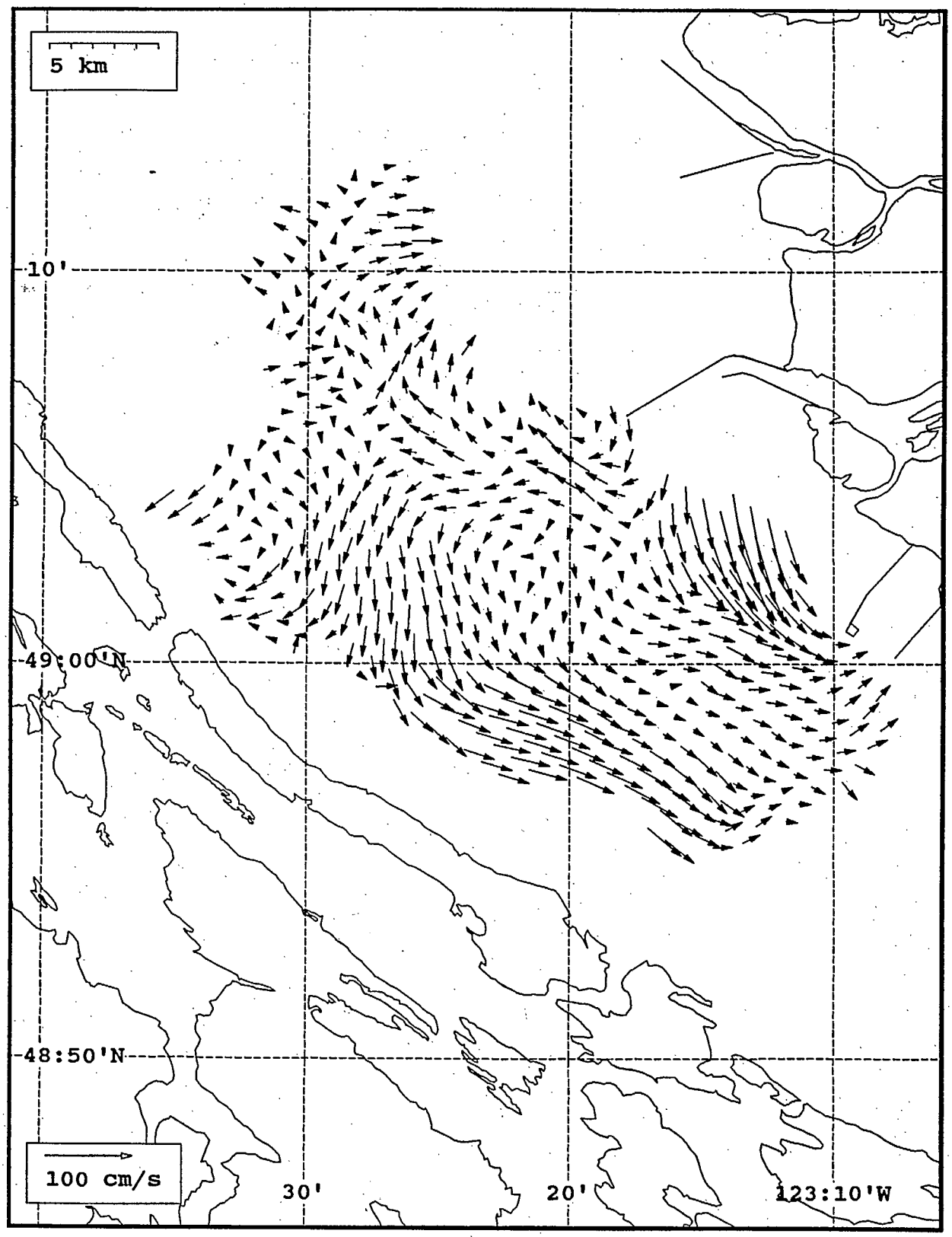

SeaSonde current field from the Strait of Georgia, off the mouth of the Fraser River, for 10:00 Z, July 29, 1993.

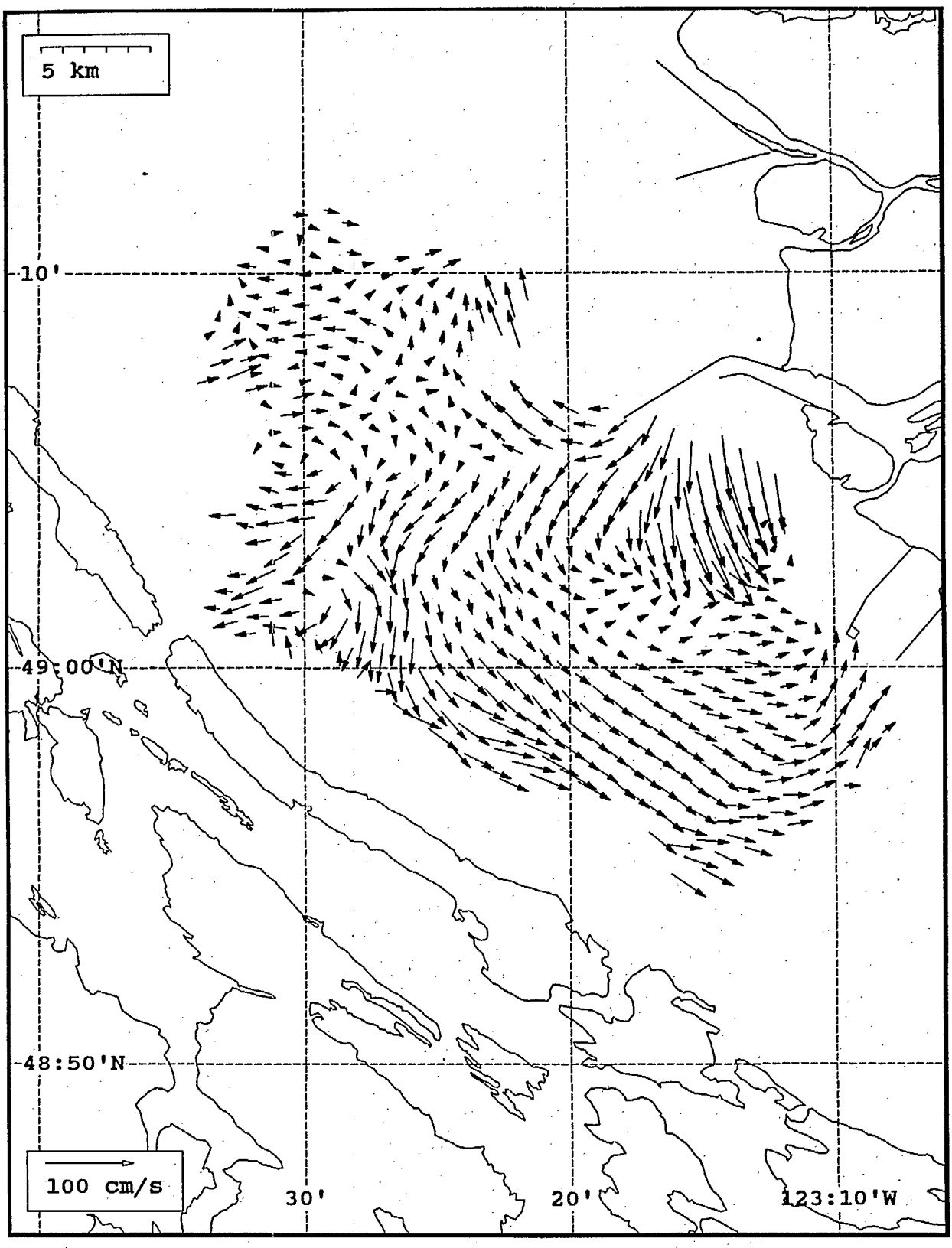

SeaSonde current field from the Strait of Georgia, off the mouth of the Fraser River, for 11:00 Z, July 29, 1993.

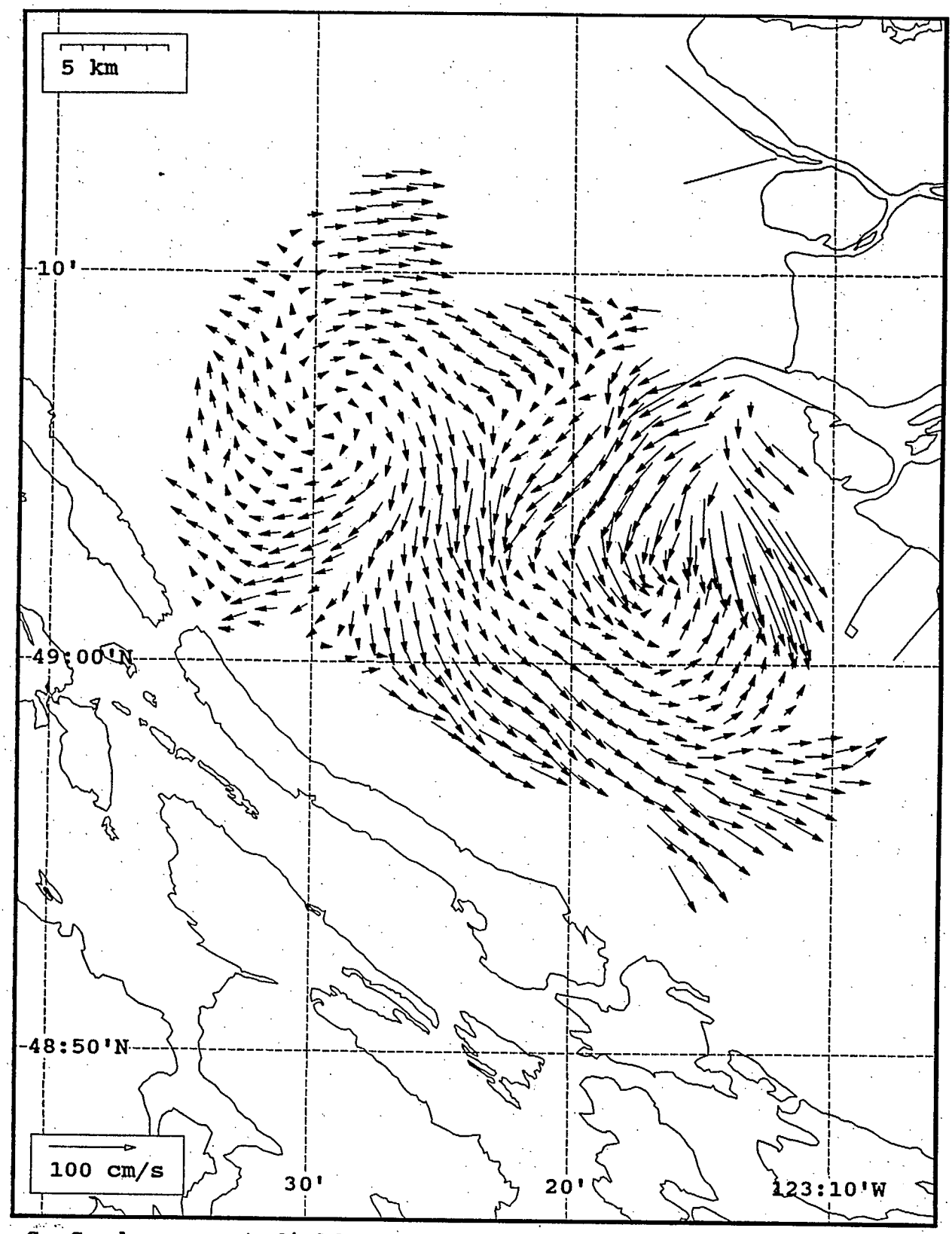

SeaSonde current field from the Strait of Georgia, off the mouth of the Fraser River, for 12:00 Z, July 29, 1993.

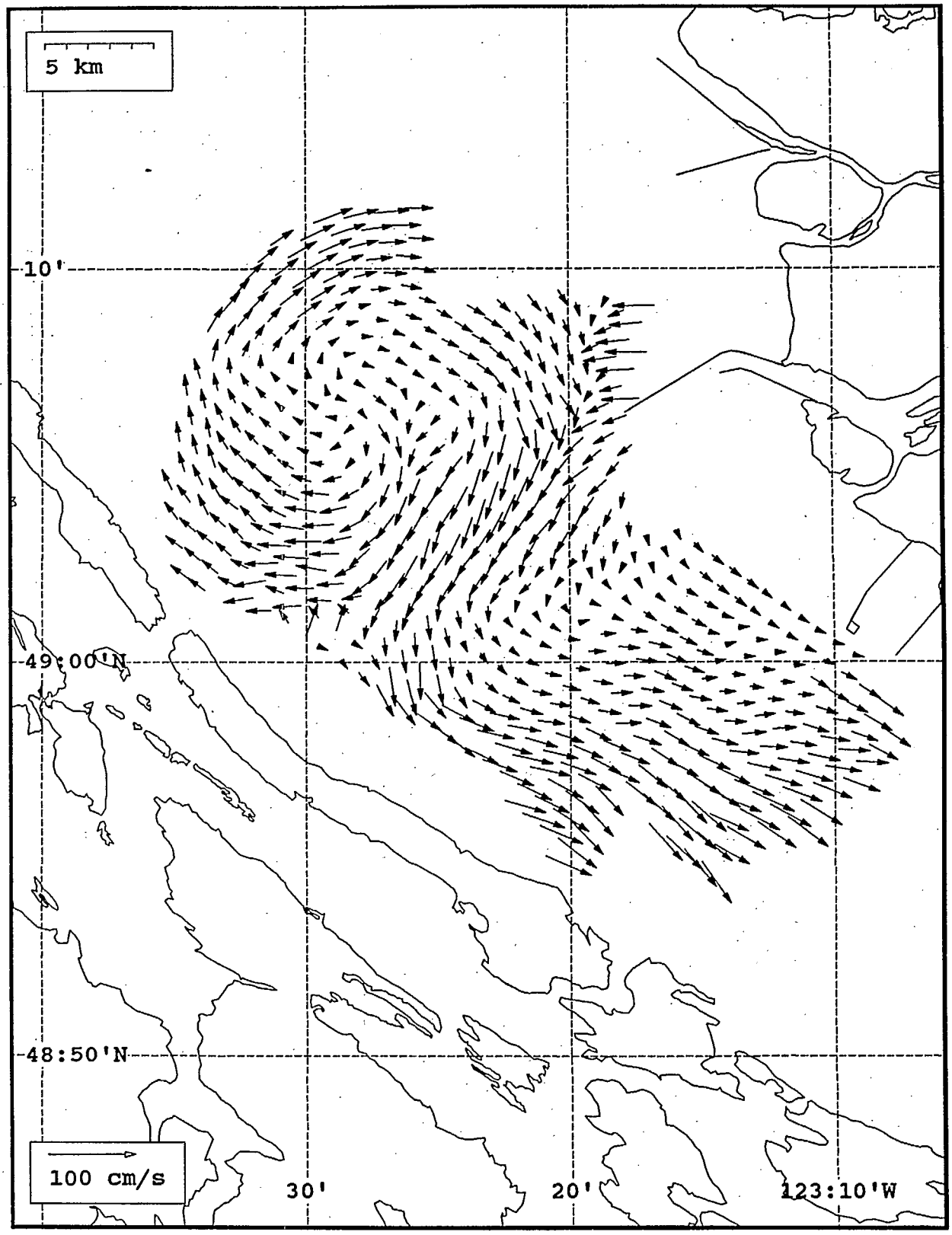

SeaSonde current field from the Strait of Georgia, off the mouth of the Fraser River, for 13:00 Z, July 29, 1993.

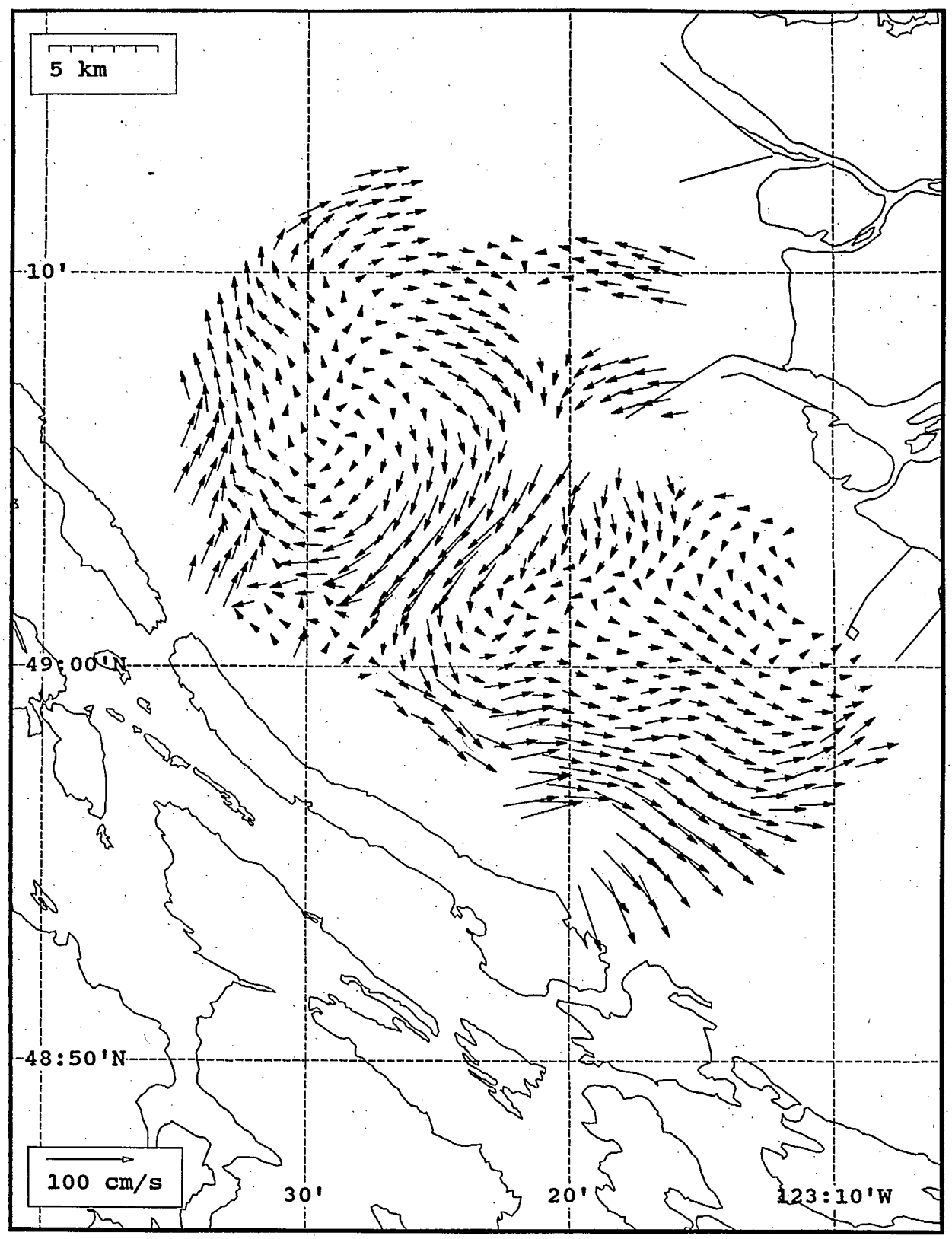

SeaSonde current field from the Strait of Georgia, off the mouth of the Fraser River, for 14:00 Z, July 29, 1993.

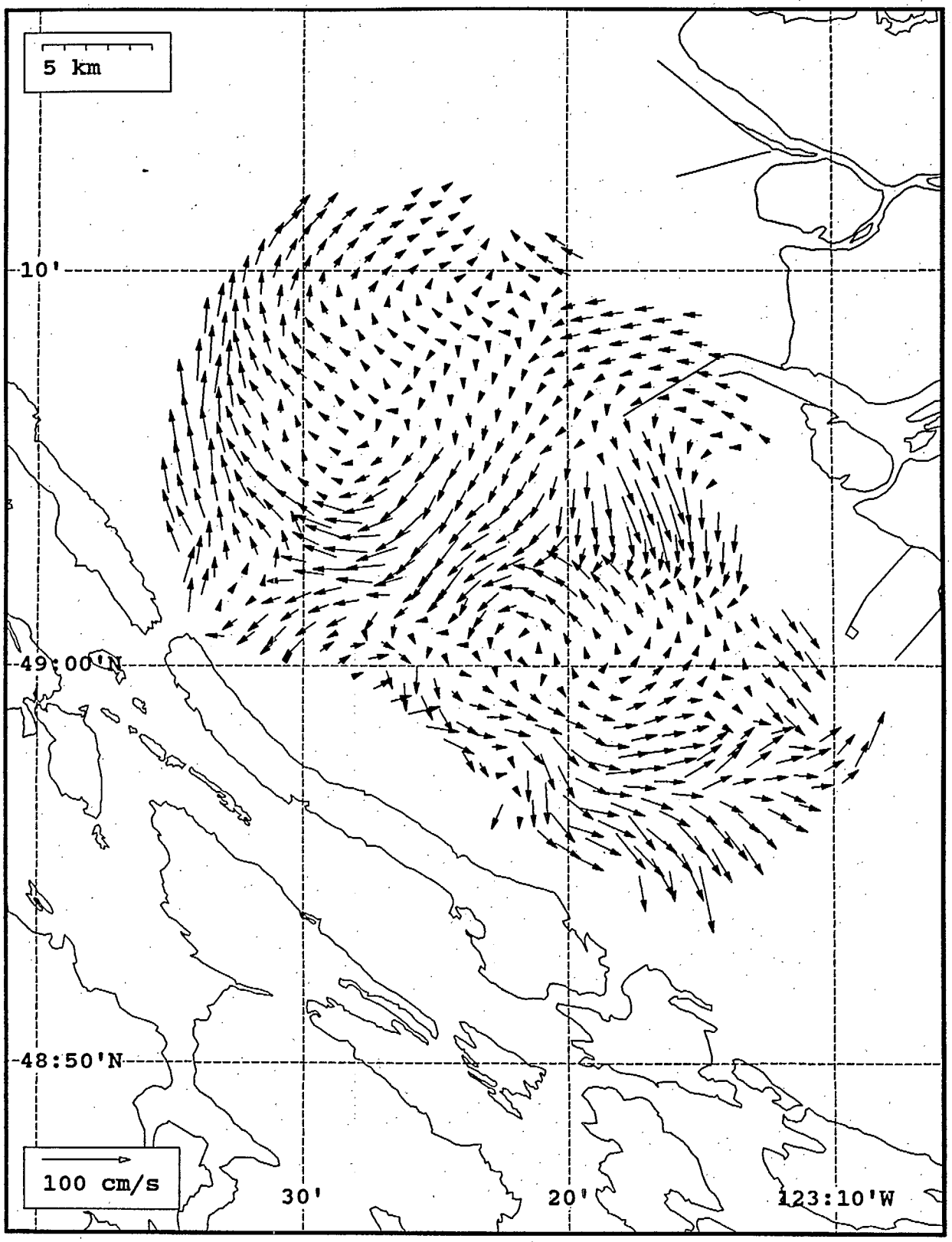

SeaSonde current field from the Strait of Georgia, off the mouth of the Fraser River, for 15:00 Z, July 29, 1993.

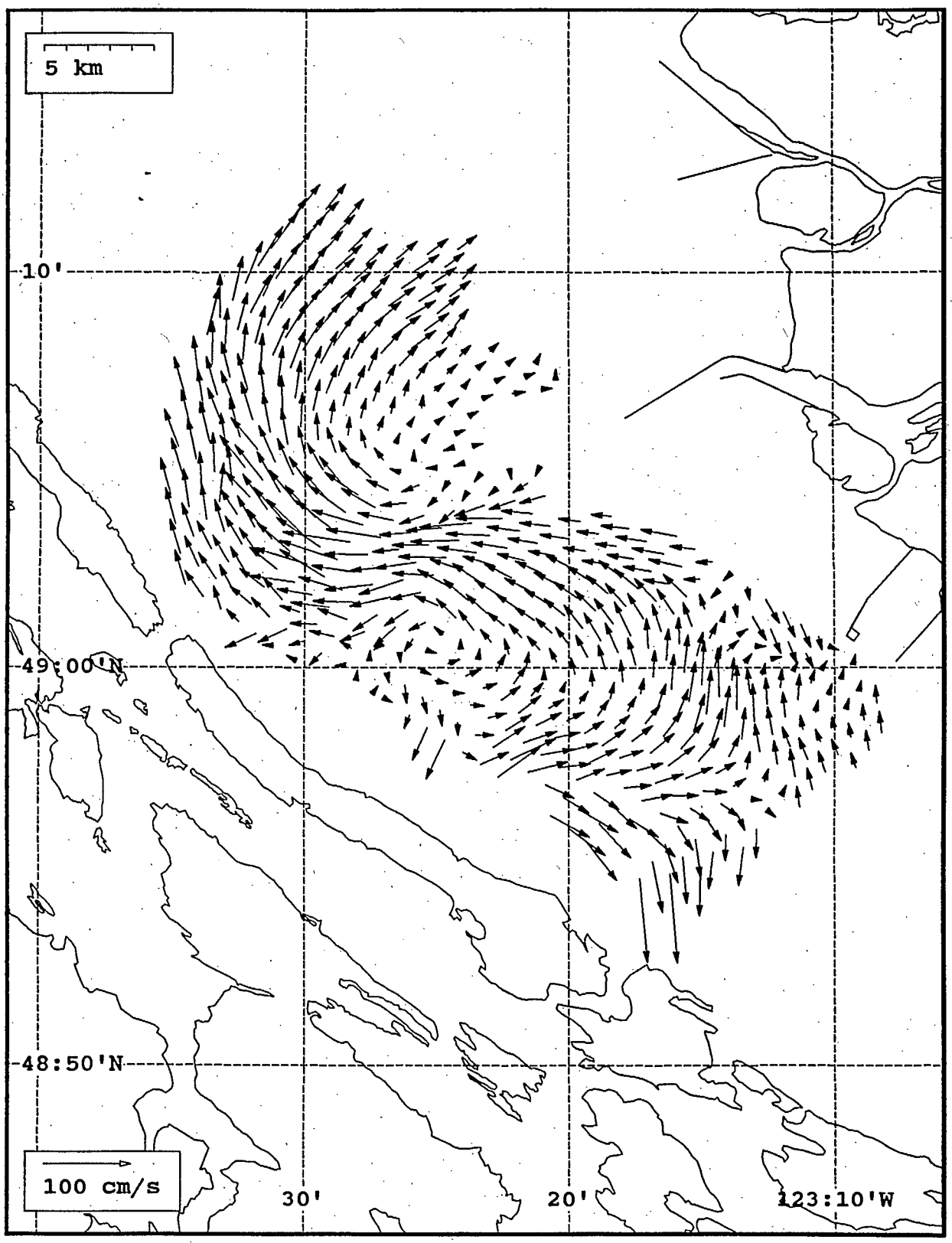

SeaSonde current field from the Strait of Georgia, off the mouth of the Fraser River, for 16:00 Z, July 29, 1993.

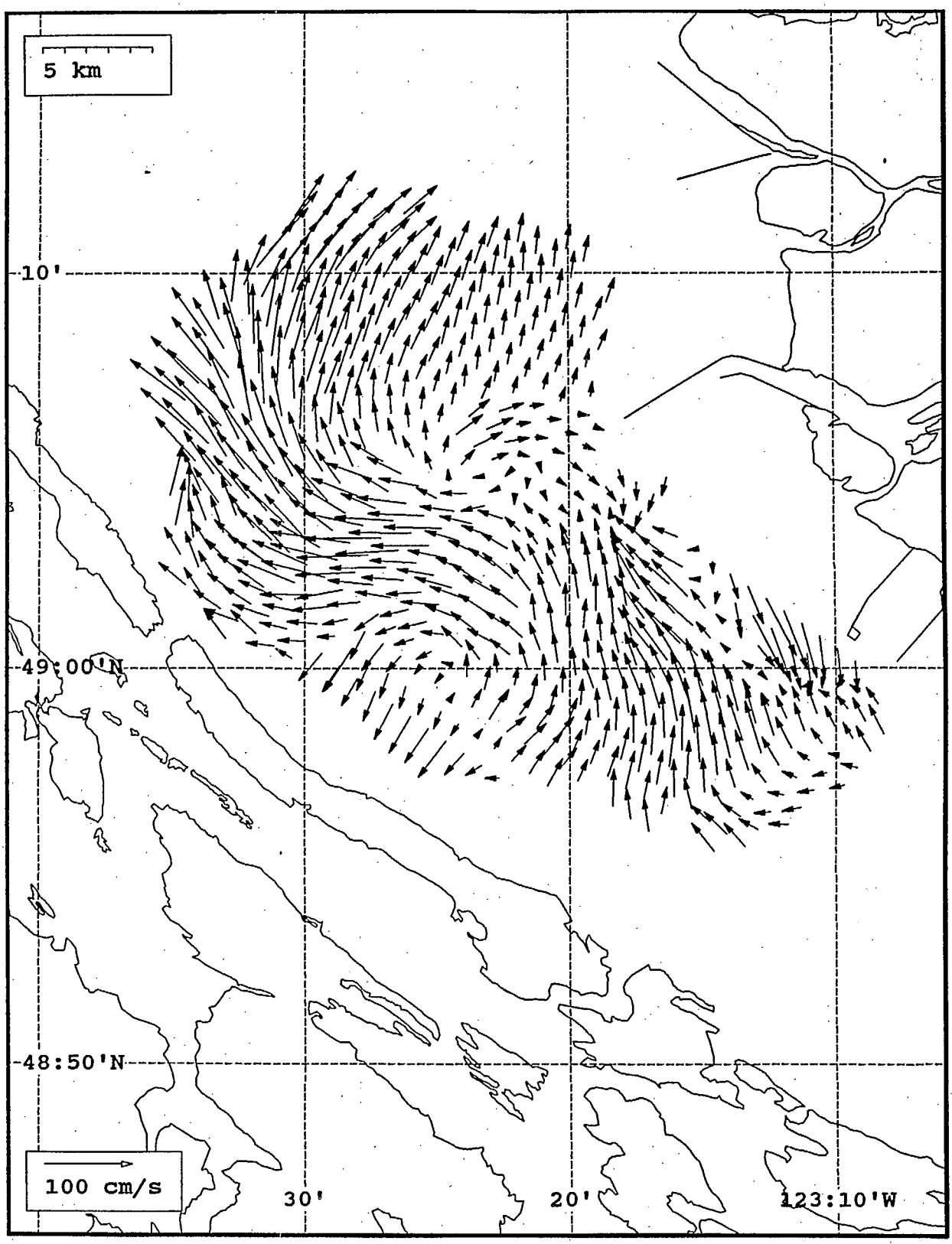

SeaSonde current field from the Strait of Georgia, off the mouth of the Fraser River, for 17:00 Z, July 29, 1993.

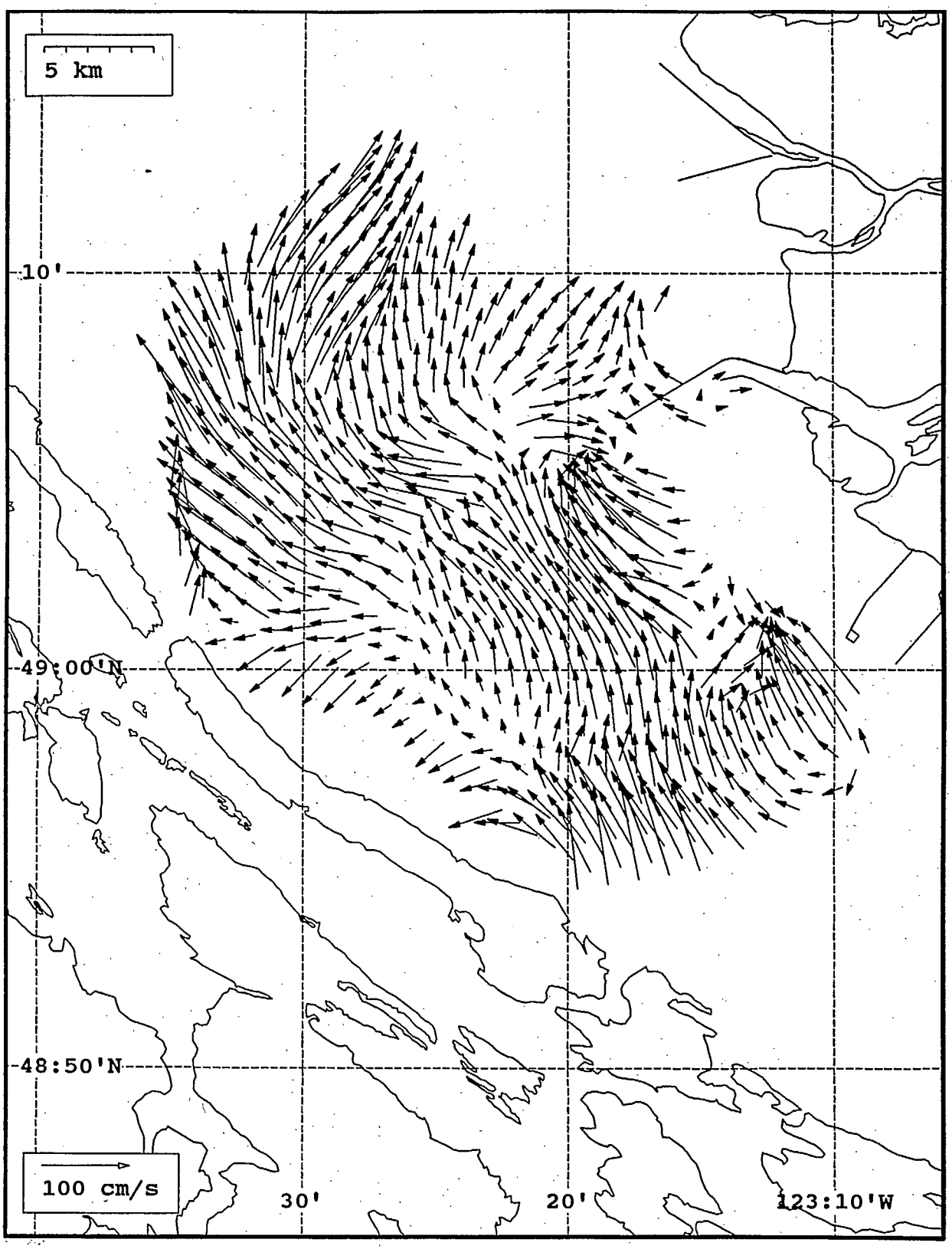

SeaSonde current field from the Strait of Georgia, off the mouth of the Fraser River, for 18:00 Z, July 29, 1993.

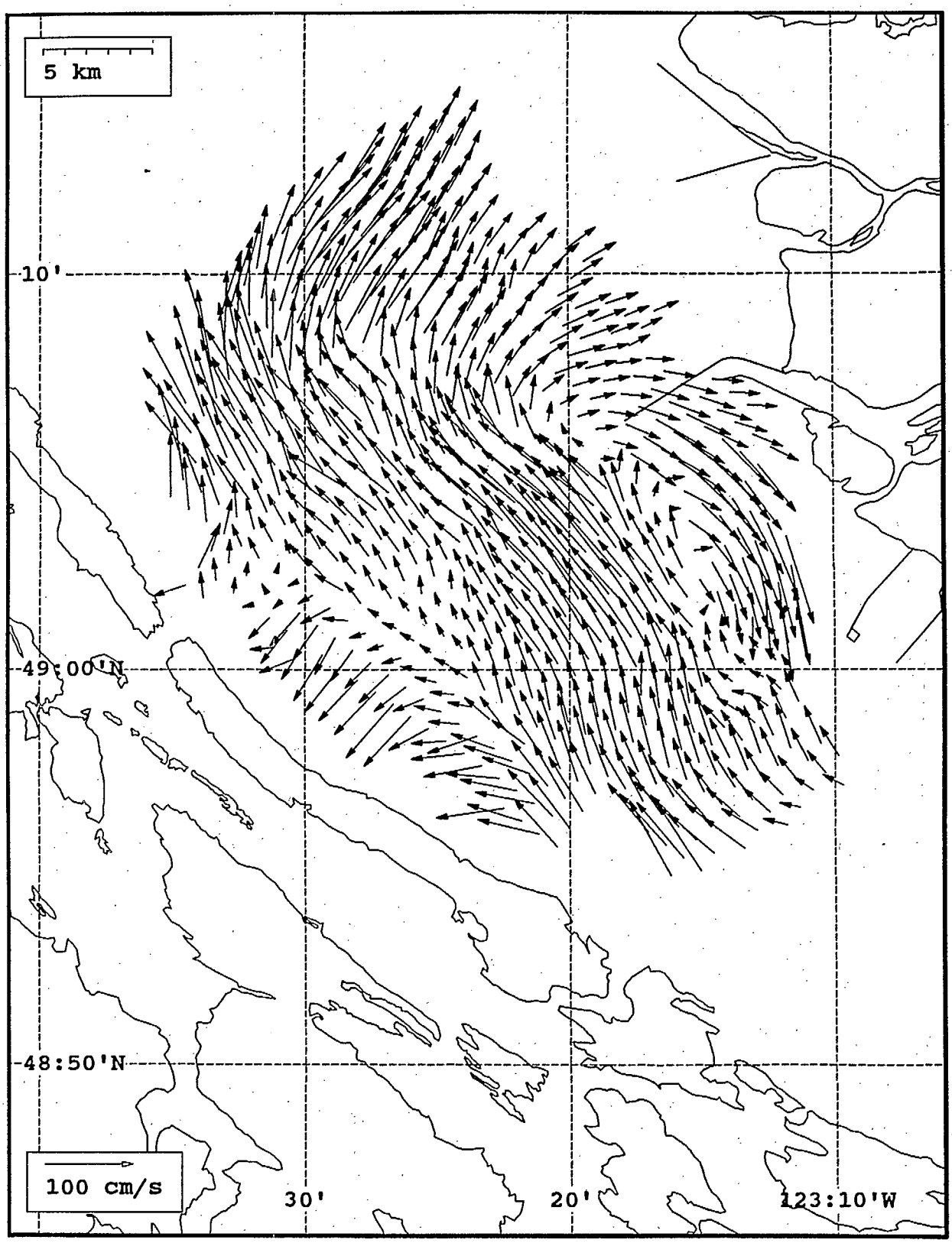

SeaSonde current field from the Strait of Georgia, off the mouth of the Fraser River, for 19:00 Z, July 29, 1993.

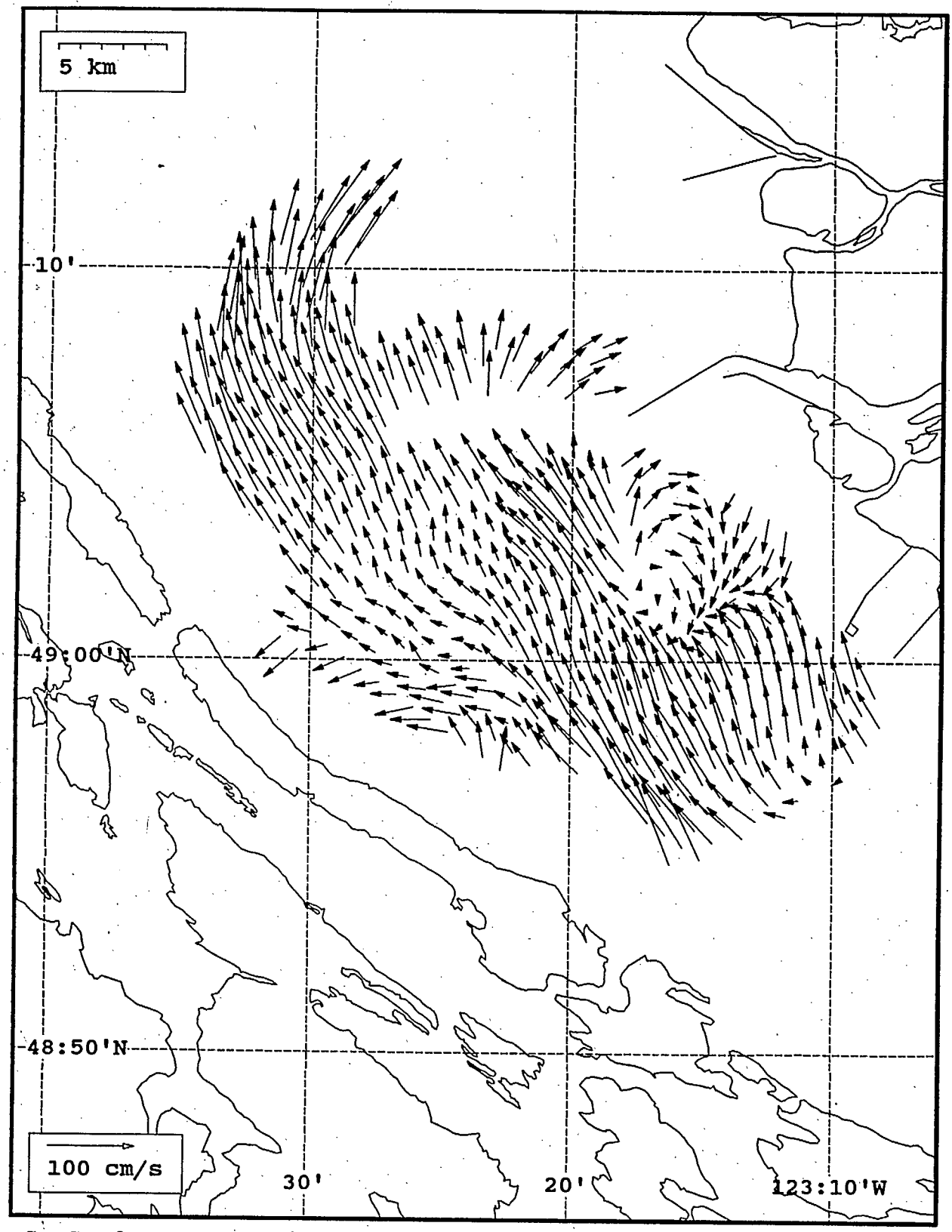

SeaSonde current field from the Strait of Georgia, off the mouth of the Fraser River, for 20:00 Z, July 29, 1993.

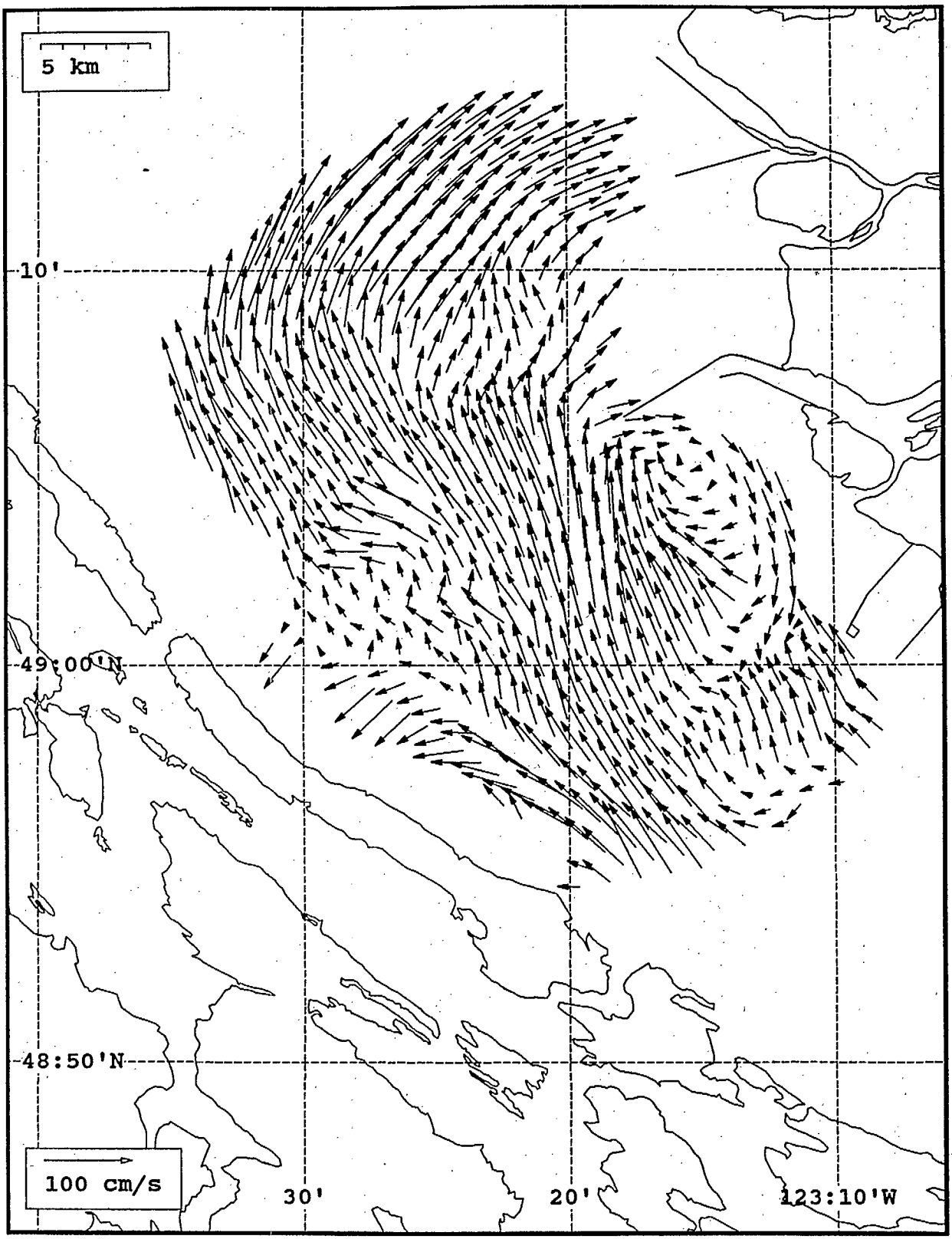

SeaSonde current field from the Strait of Georgia, off the mouth of the Fraser River, for 21:00 Z, July 29, 1993.

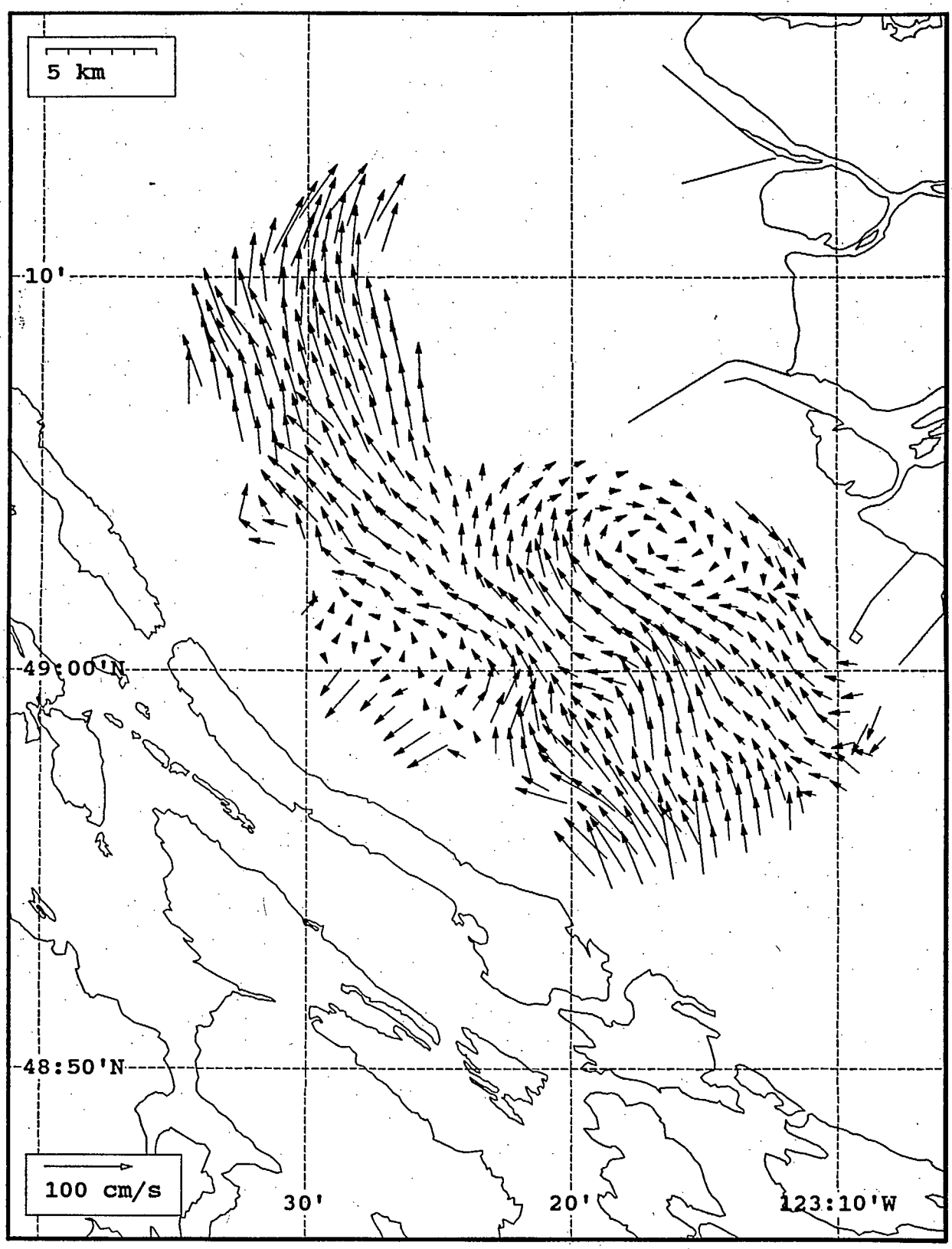

SeaSonde current field from the Strait of Georgia, off the mouth of the Fraser River, for 22:00 Z, July 29, 1993.

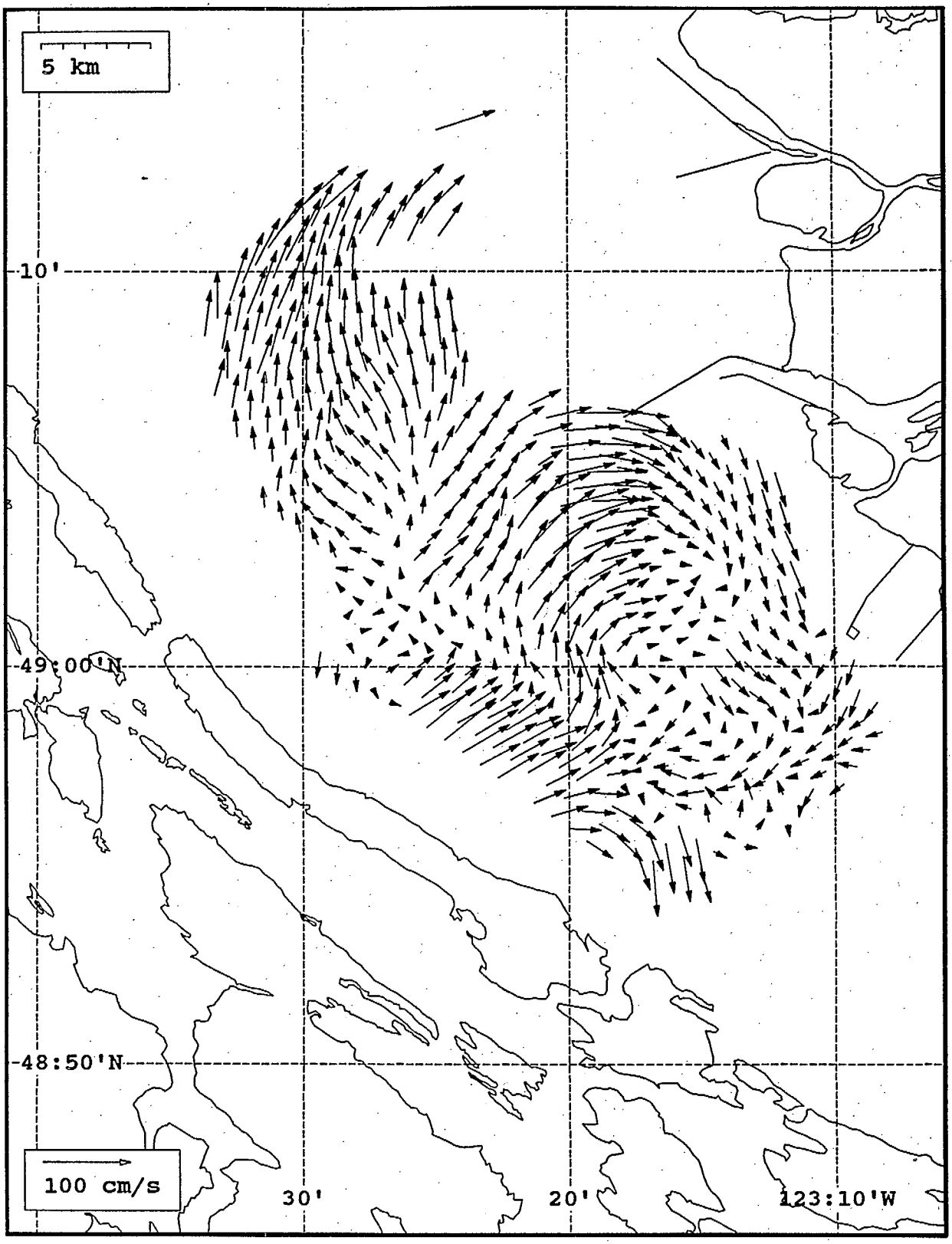

SeaSonde current field from the Strait of Georgia, off the mouth of the Fraser River, for 23:00 Z, July 29, 1993.

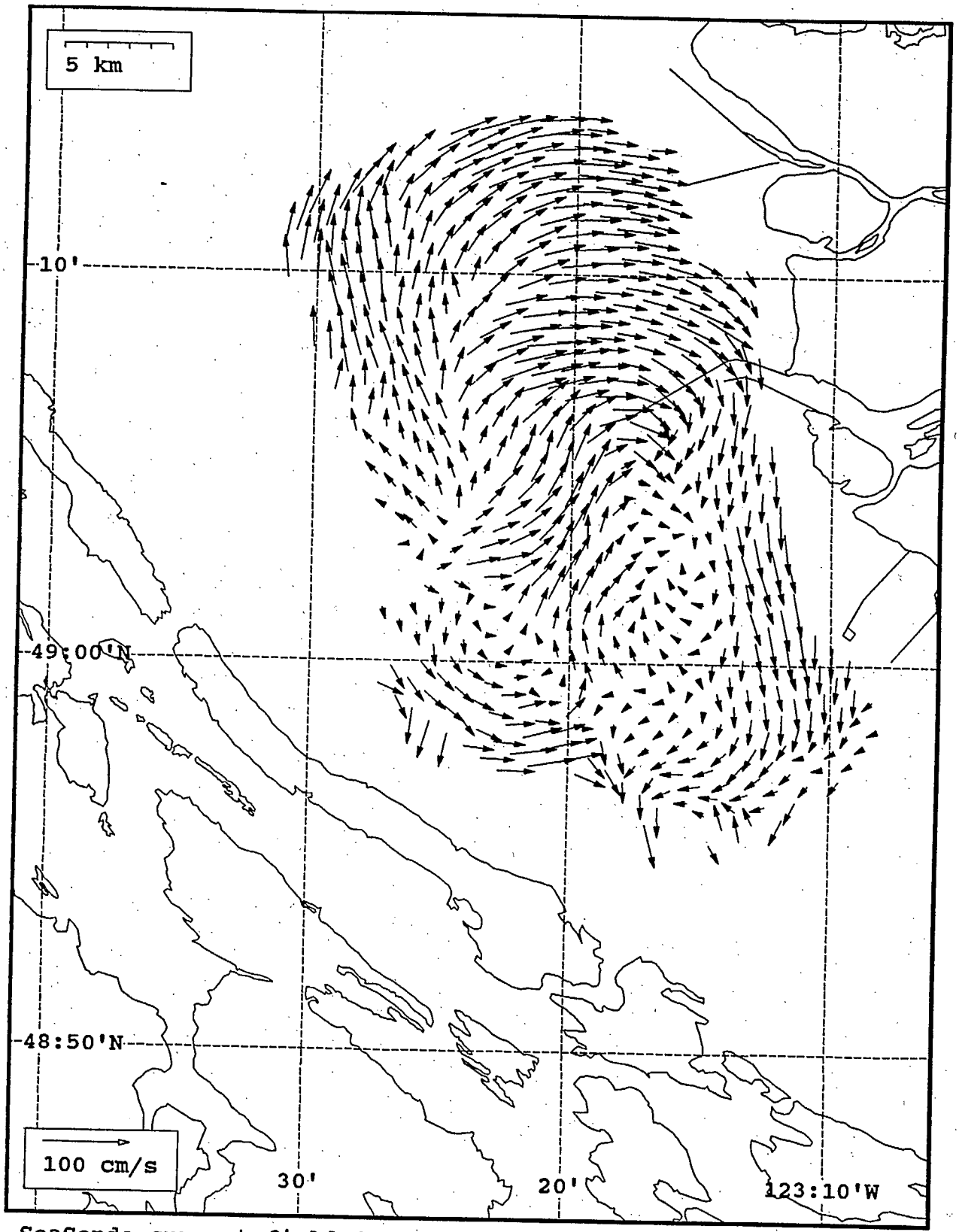

SeaSonde current field from the Strait of Georgia, off the mouth of the Fraser River, for 00:00 Z, July 30, 1993.

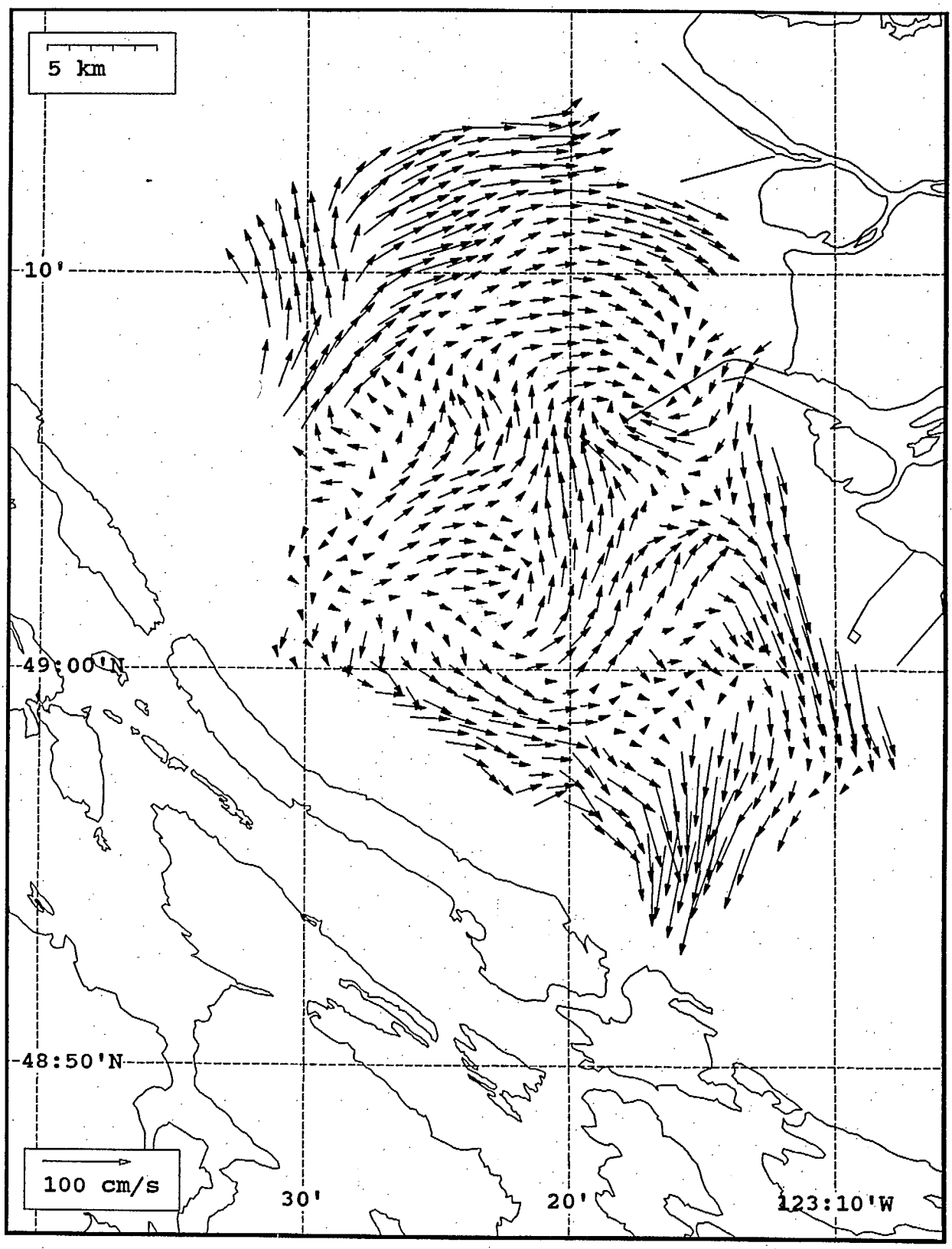

SeaSonde current field from the Strait of Georgia, off the mouth of the Fraser River, for 01:00 Z, July 30, 1993.

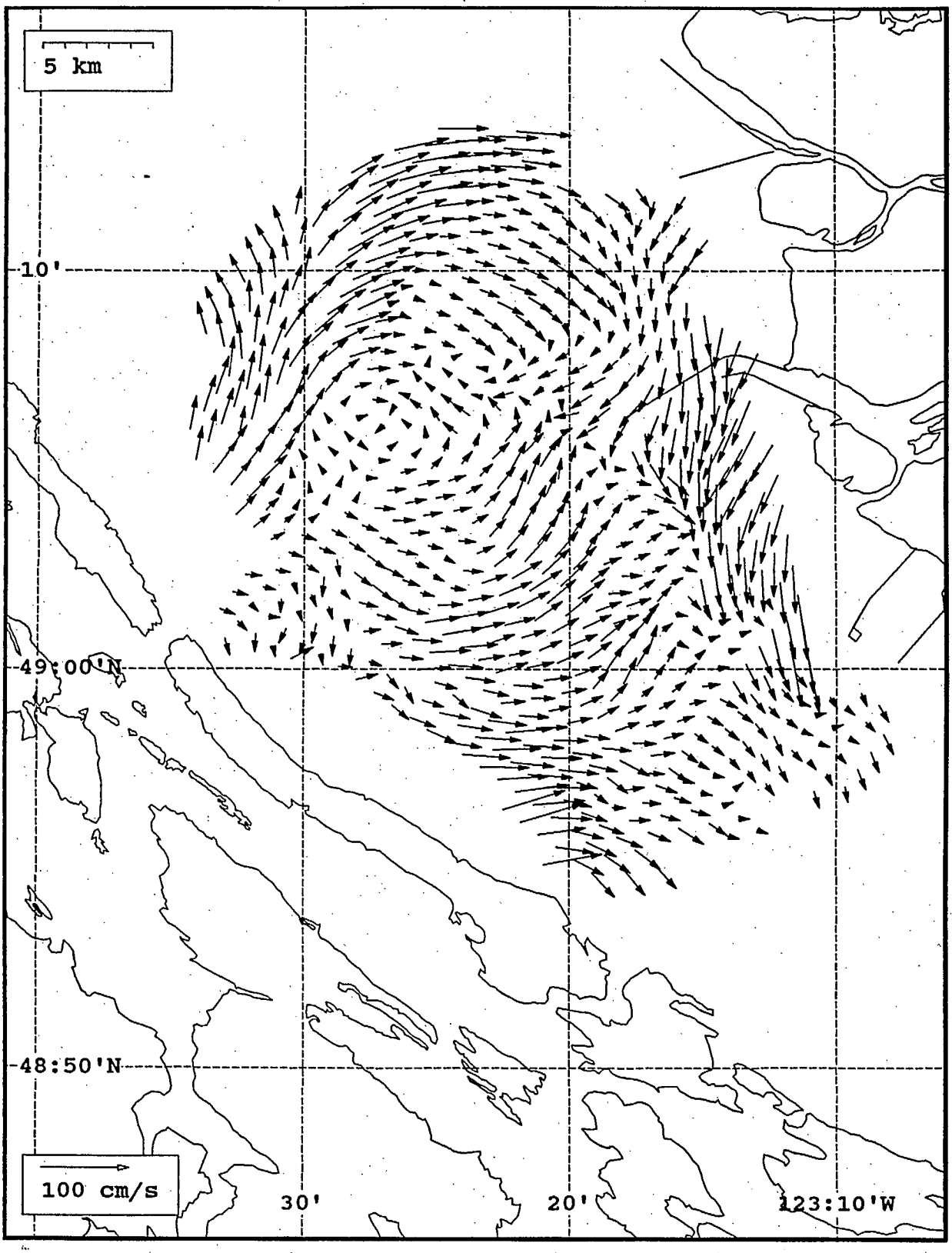

SeaSonde current field from the Strait of Georgia, off the mouth of the Fraser River, for 02:00 Z, July 30, 1993.

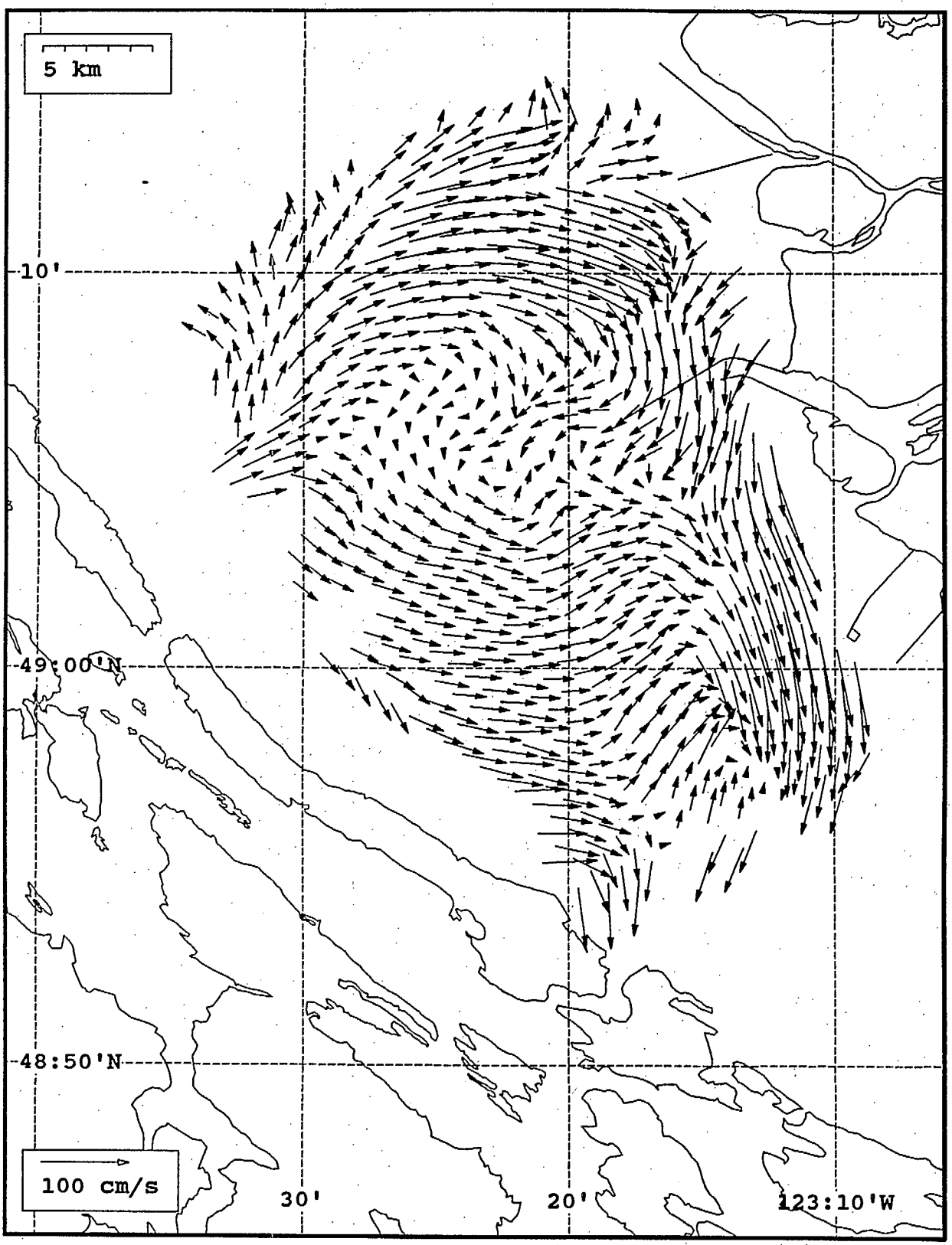

SeaSonde current field from the Strait of Georgia, off the mouth of the Fraser River, for 03:00 Z, July 30, 1993.

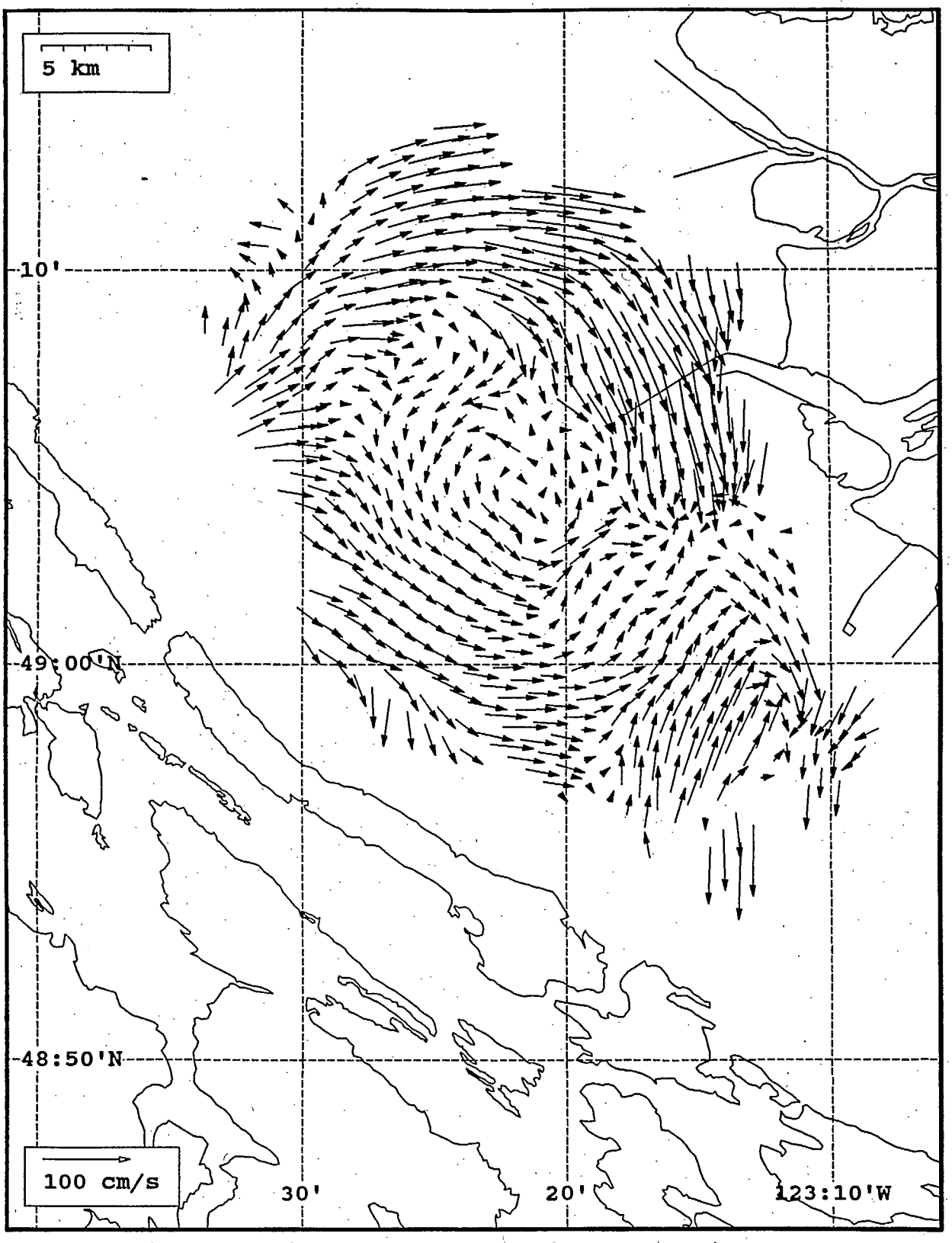

SeaSonde current field from the Strait of Georgia, off the mouth of the Fraser River, for 04:00 Z, July 30, 1993.

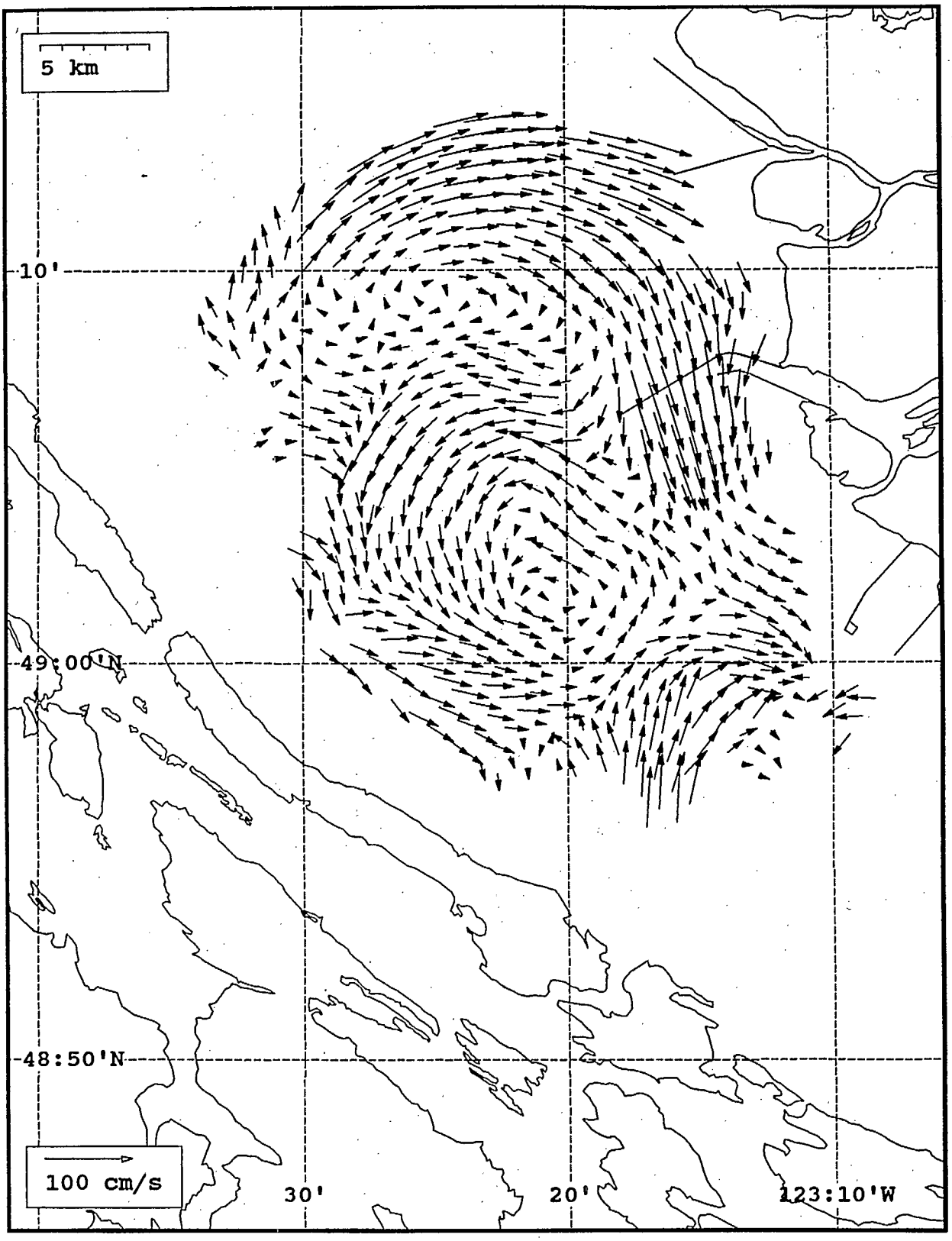

SeaSonde current field from the Strait of Georgia, off the mouth of the Fraser River, for 05:00 Z, July 30, 1993.

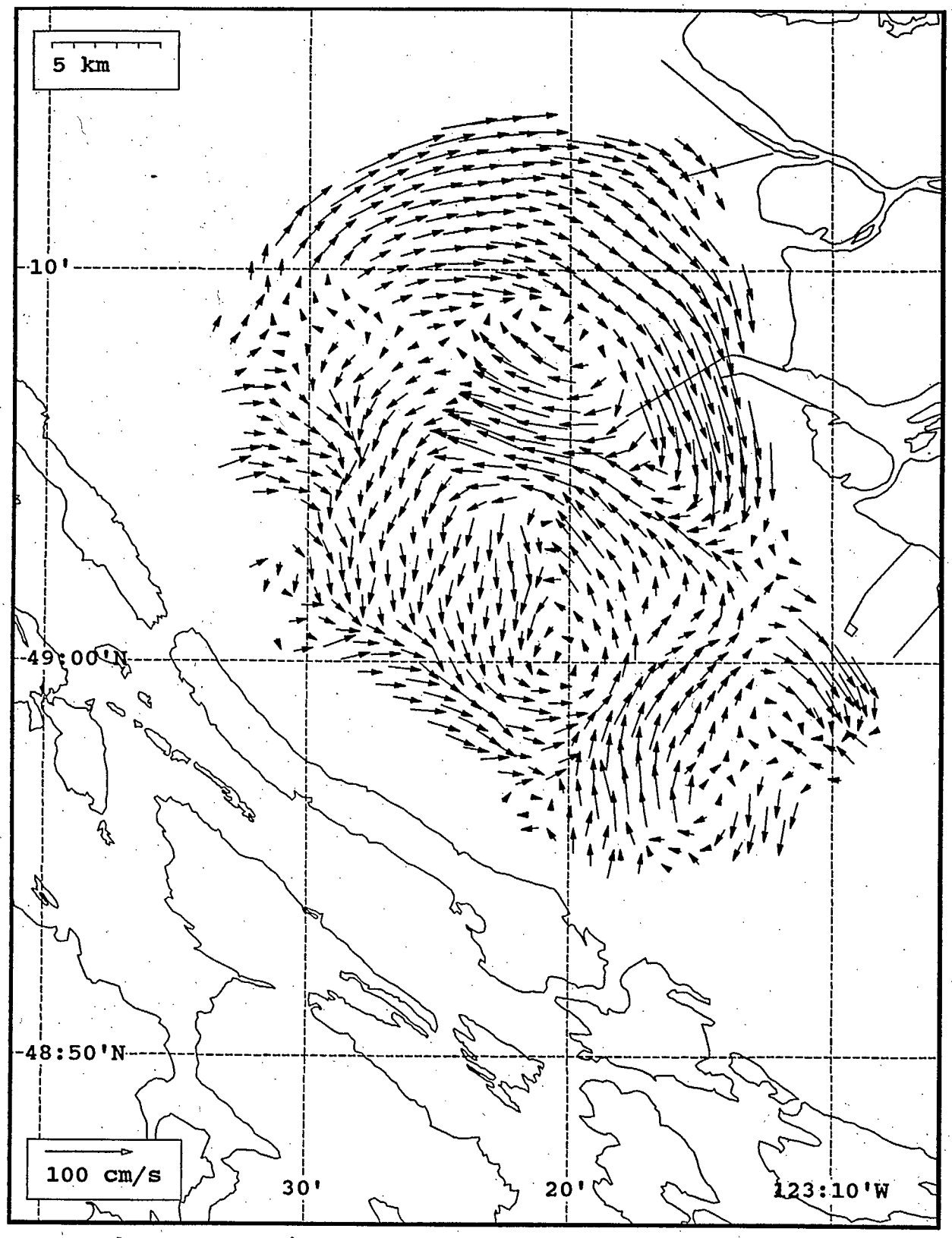

SeaSonde current field from the Strait of Georgia, off the mouth of the Fraser River, for 06:00 Z, July 30, 1993.

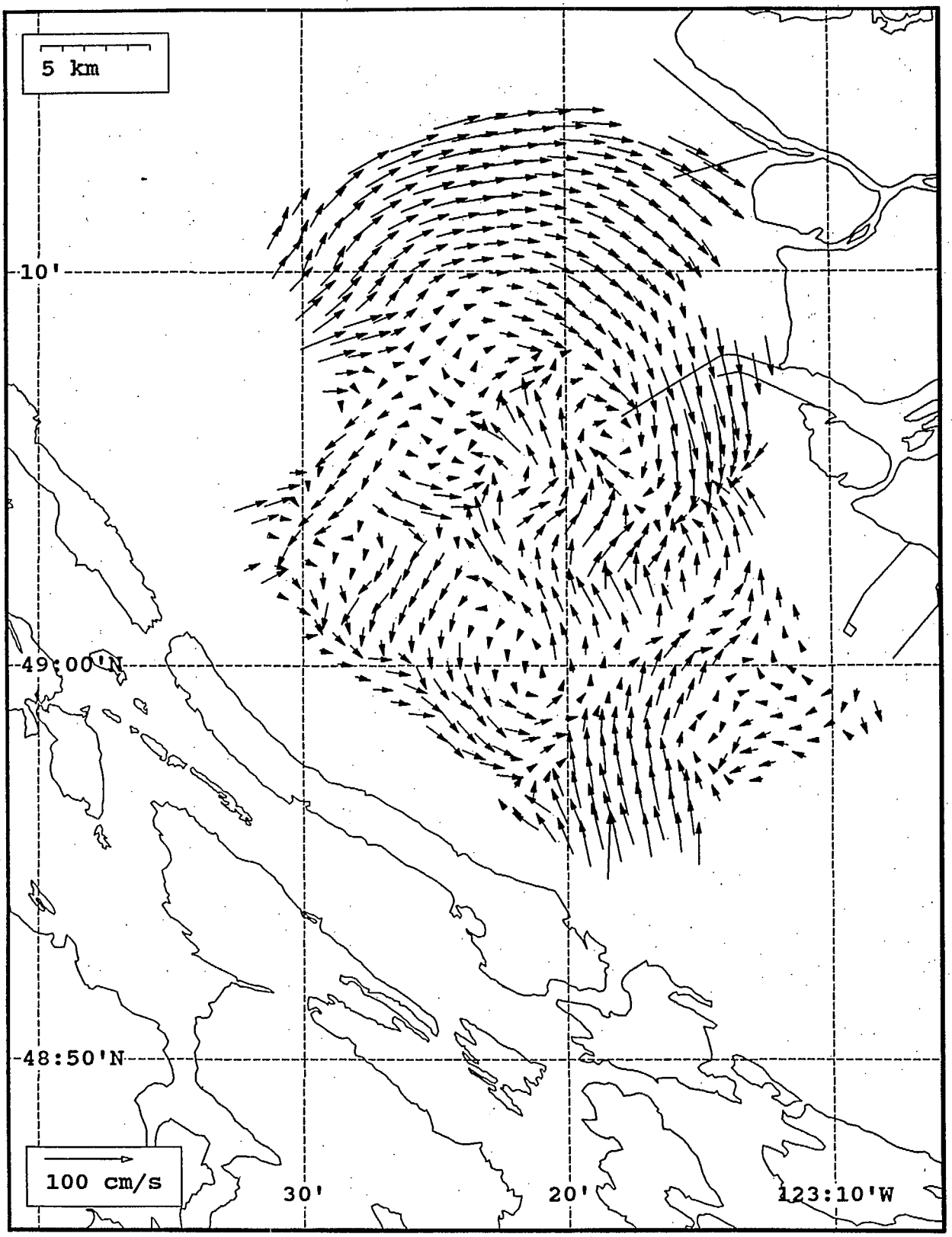

SeaSonde current field from the Strait of Georgia, off the mouth of the Fraser River, for 07:00 Z, July 30, 1993.

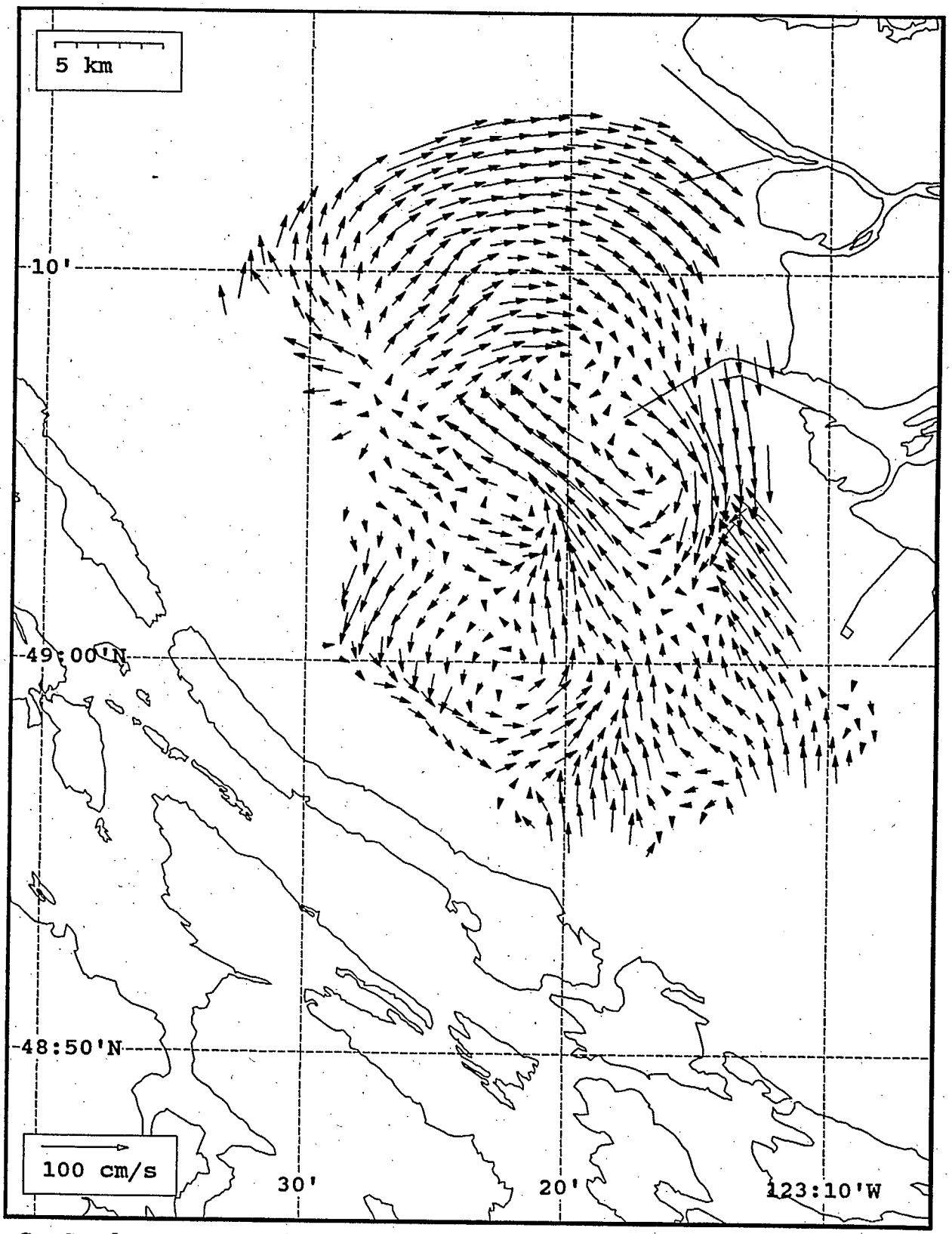

SeaSonde current field from the Strait of Georgia, off the mouth of the Fraser River, for 08:00 Z, July 30, 1993.

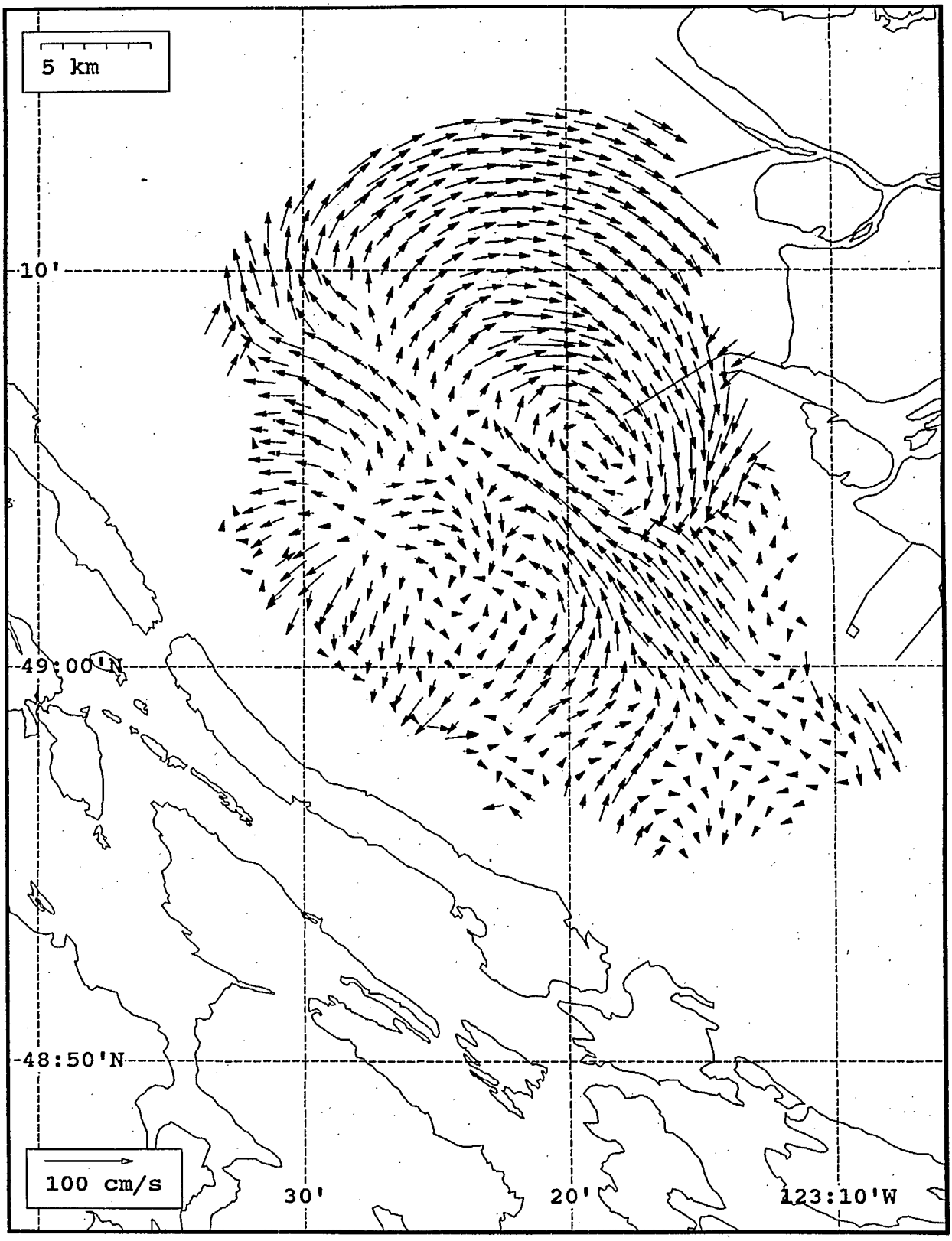

SeaSonde current field from the Strait of Georgia, off the mouth of the Fraser River, for 09:00 Z, July 30, 1993.

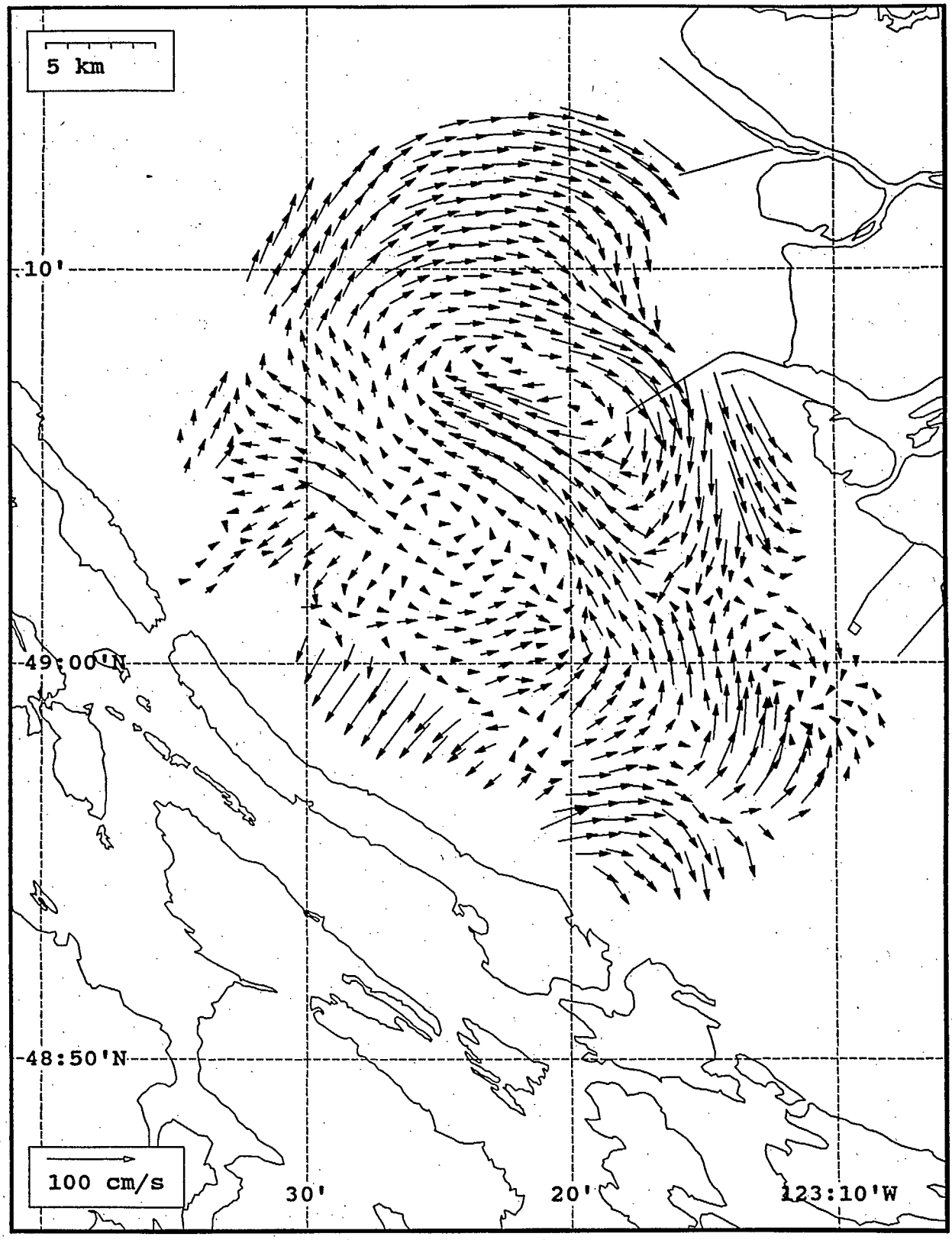

SeaSonde current field from the Strait of Georgia, off the mouth of the Fraser River, for 10:00 Z, July 30, 1993.

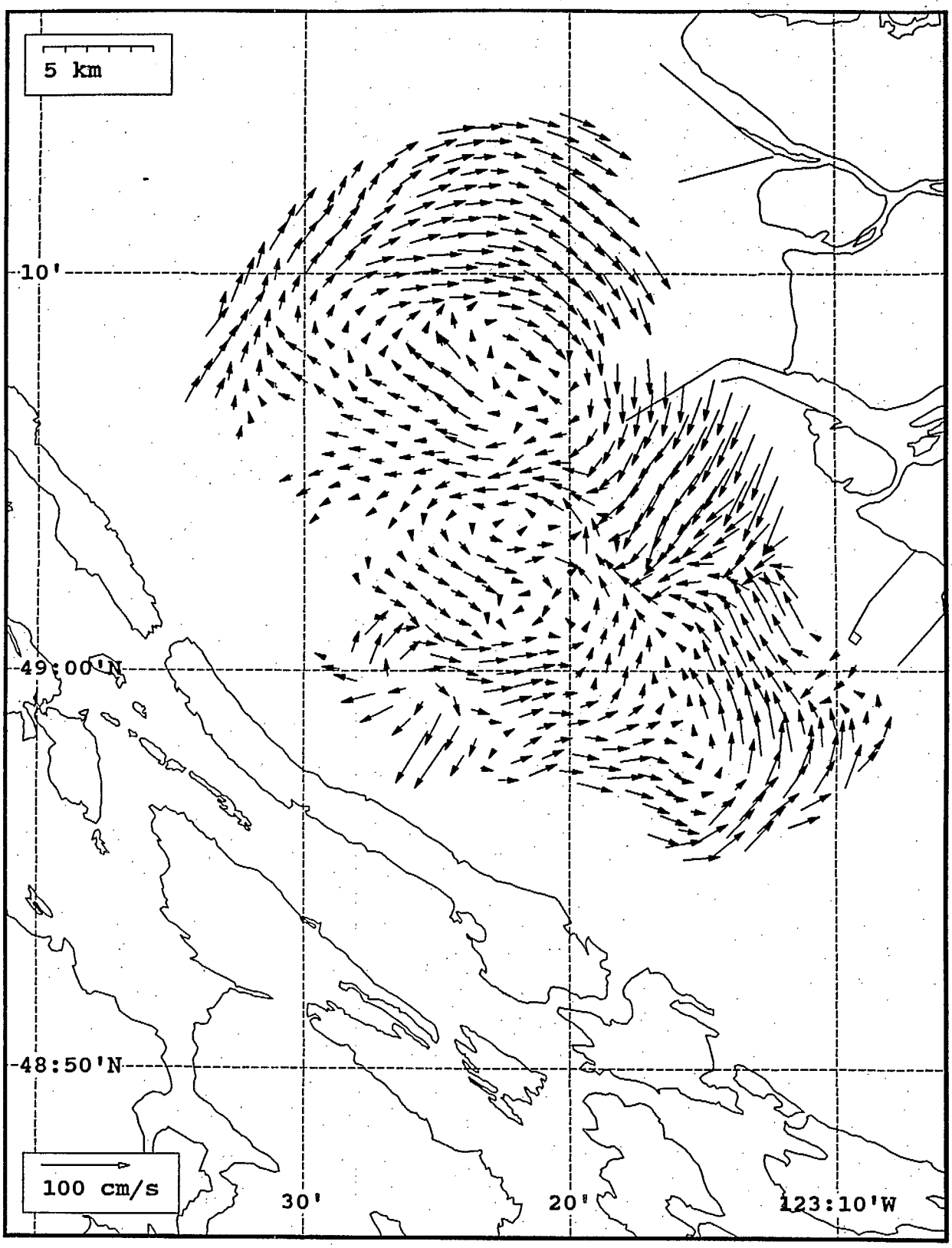

SeaSonde current field from the Strait of Georgia, off the mouth of the Fraser River, for 11:00 Z, July 30, 1993.

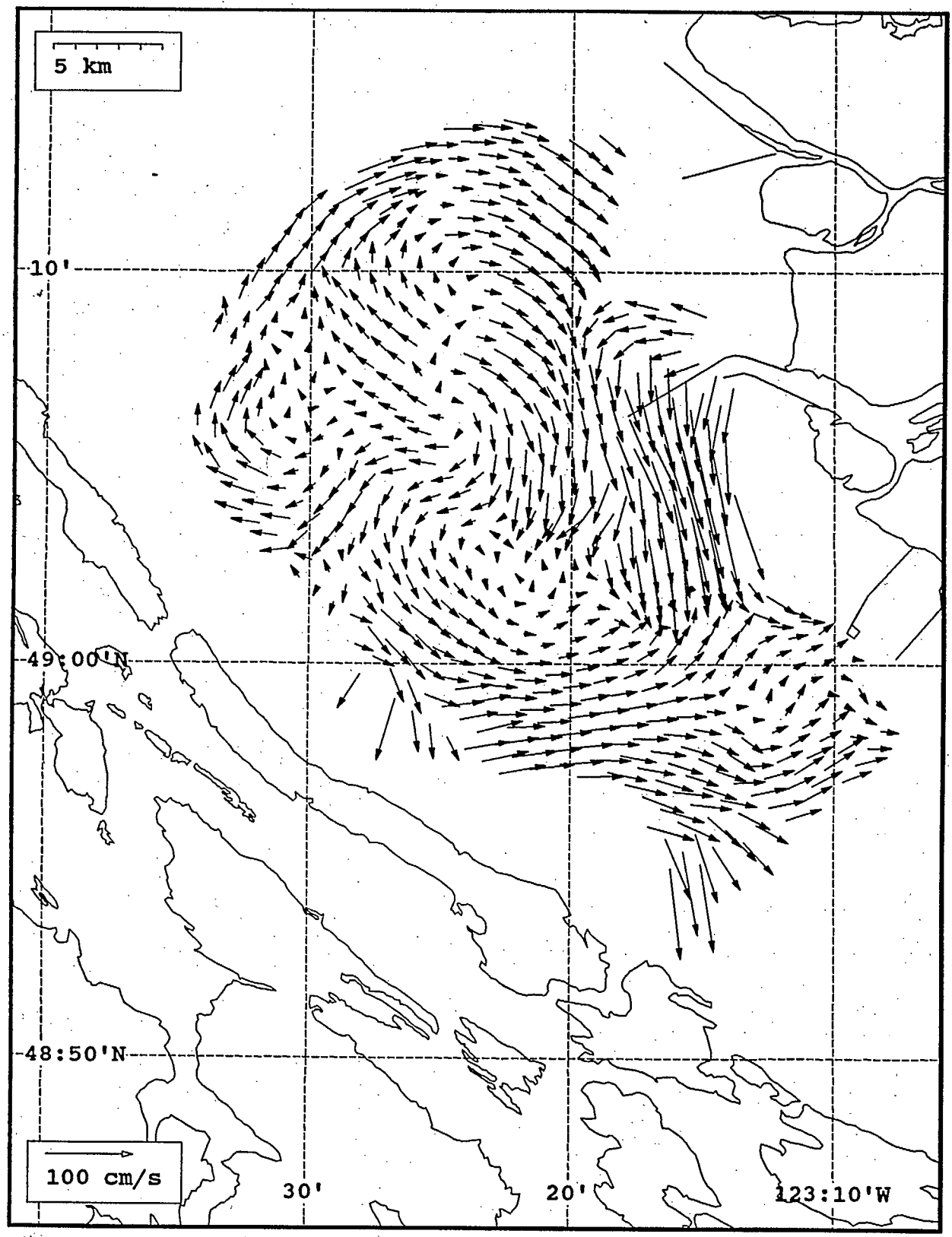

SeaSonde current field from the Strait of Georgia, off the mouth of the Fraser River, for 12:00 Z, July 30, 1993.

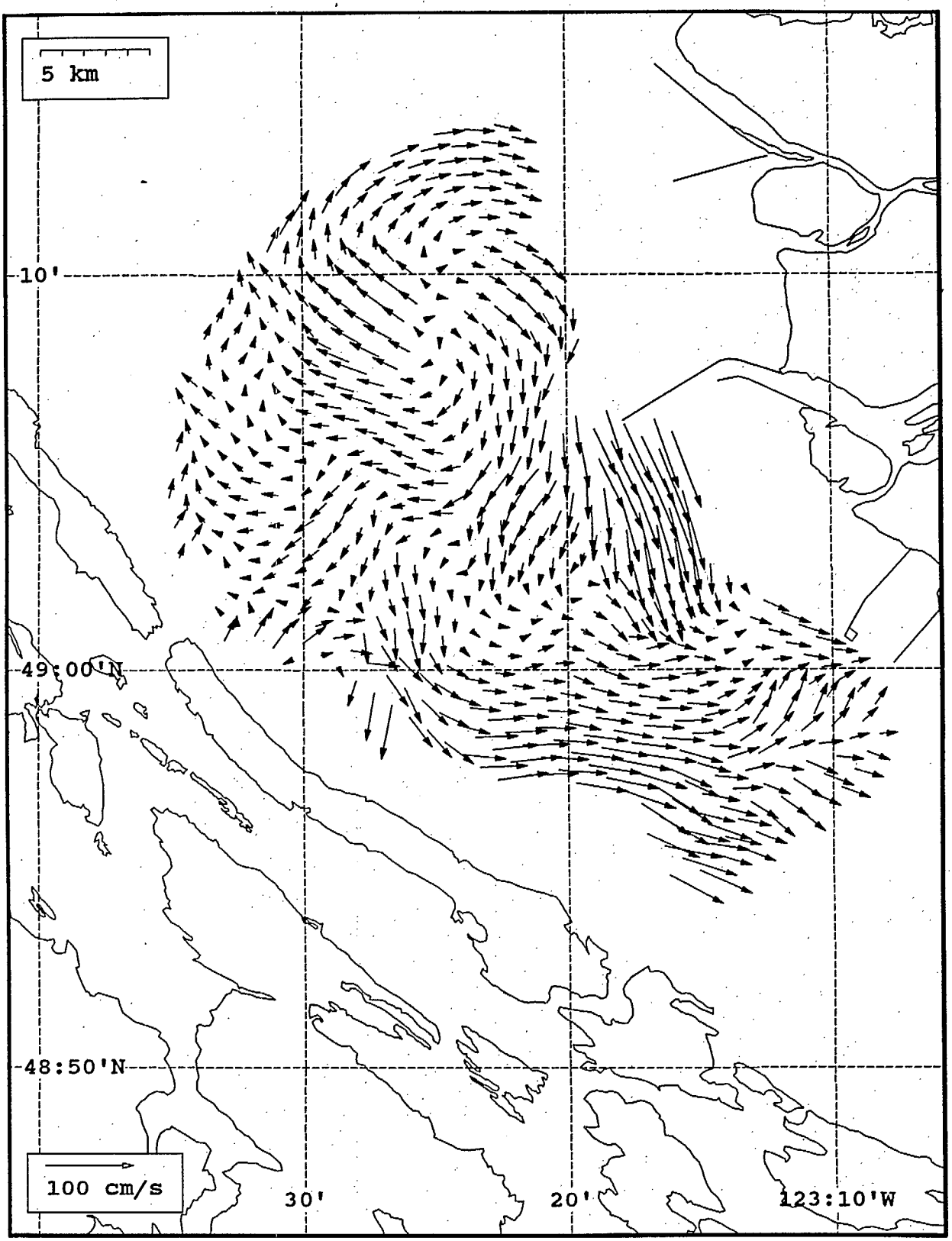

SeaSonde current field from the Strait of Georgia, off the mouth of the Fraser River, for 13:00 Z, July 30, 1993.

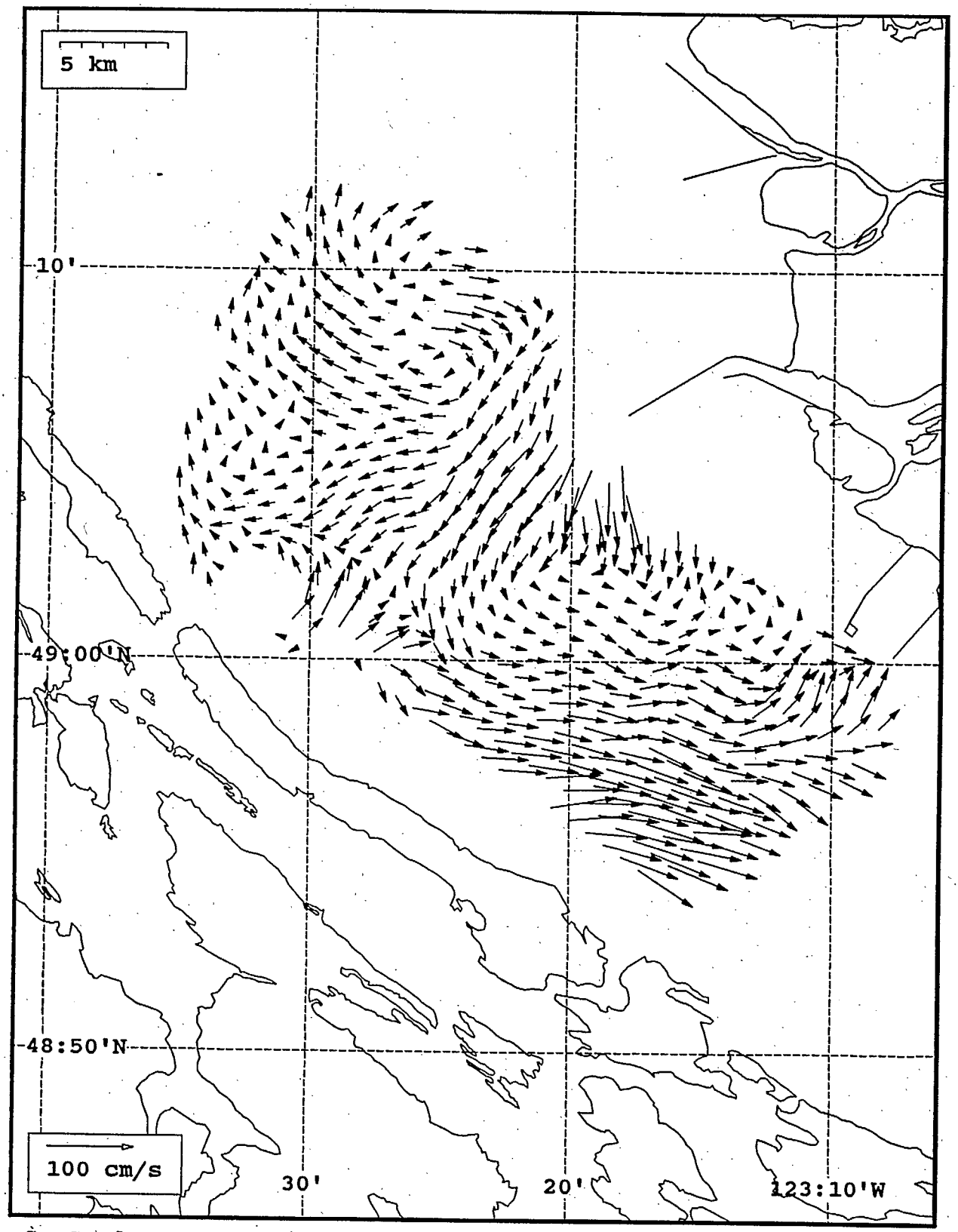

SeaSonde current field from the Strait of Georgia, off the mouth of the Fraser River, for 14:00 Z, July 30, 1993.

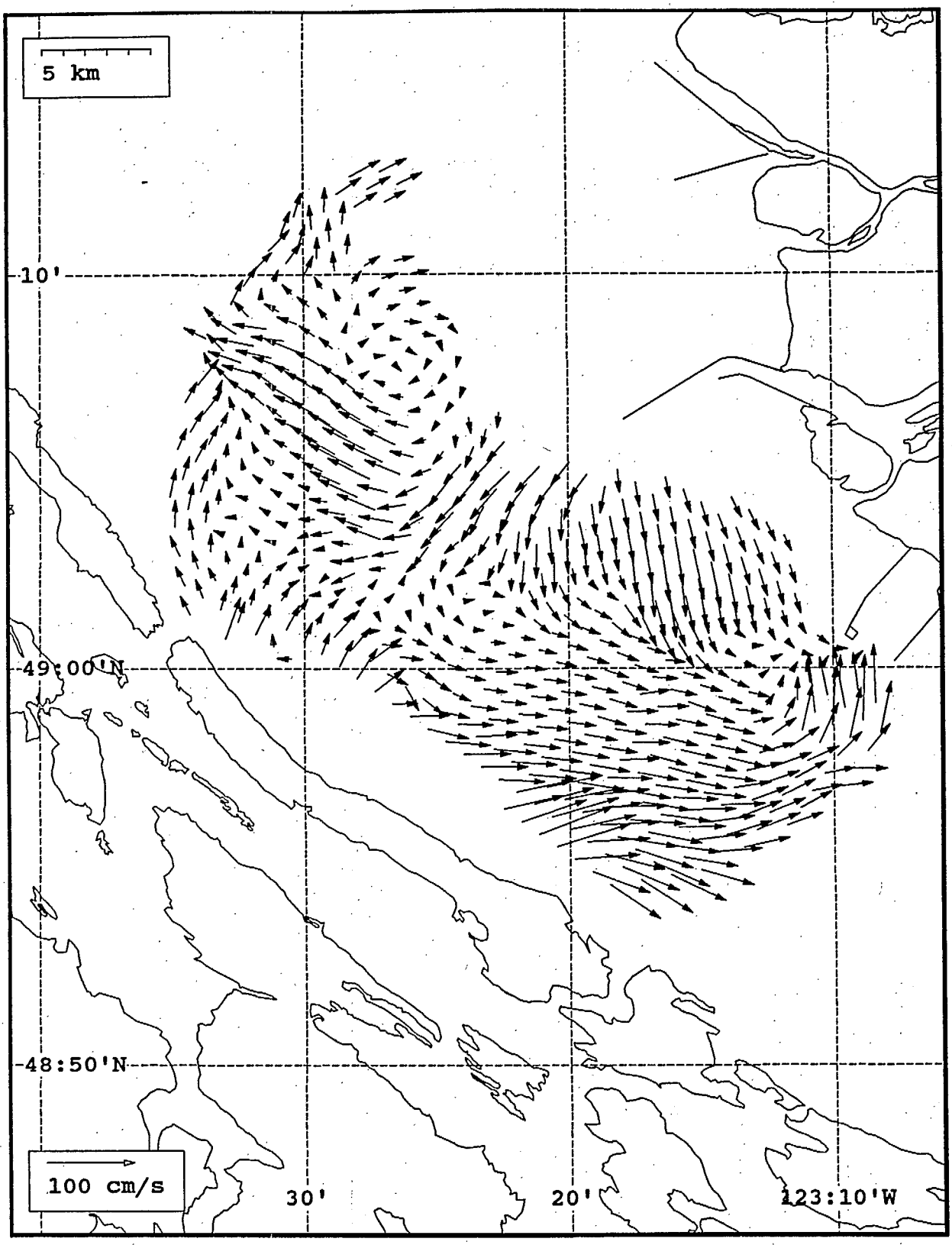

SeaSonde current field from the Strait of Georgia, off the mouth of the Fraser River, for 15:00 Z, July 30, 1993.

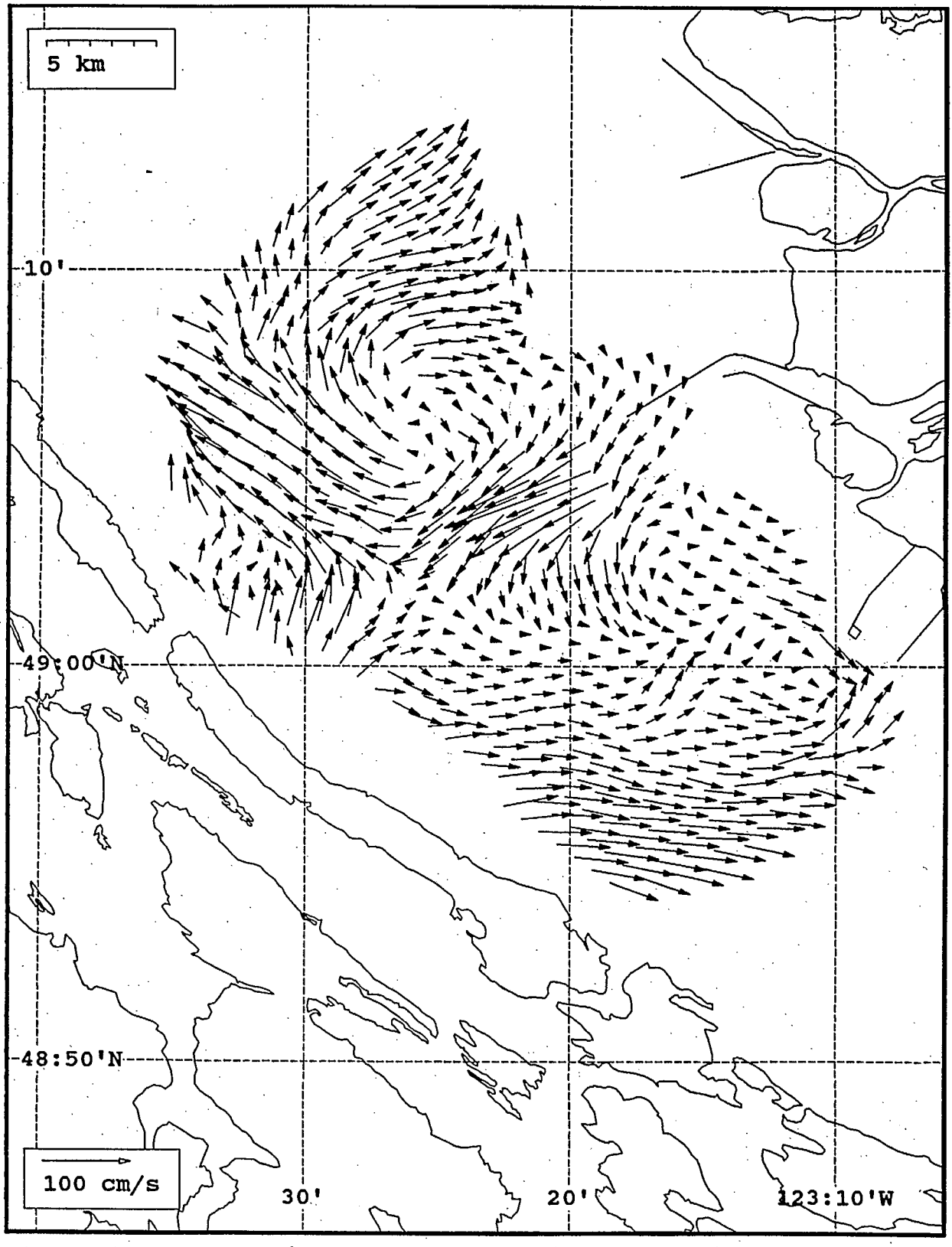

SeaSonde current field from the Strait of Georgia, off the mouth of the Fraser River, for 16:00 Z, July 30, 1993.

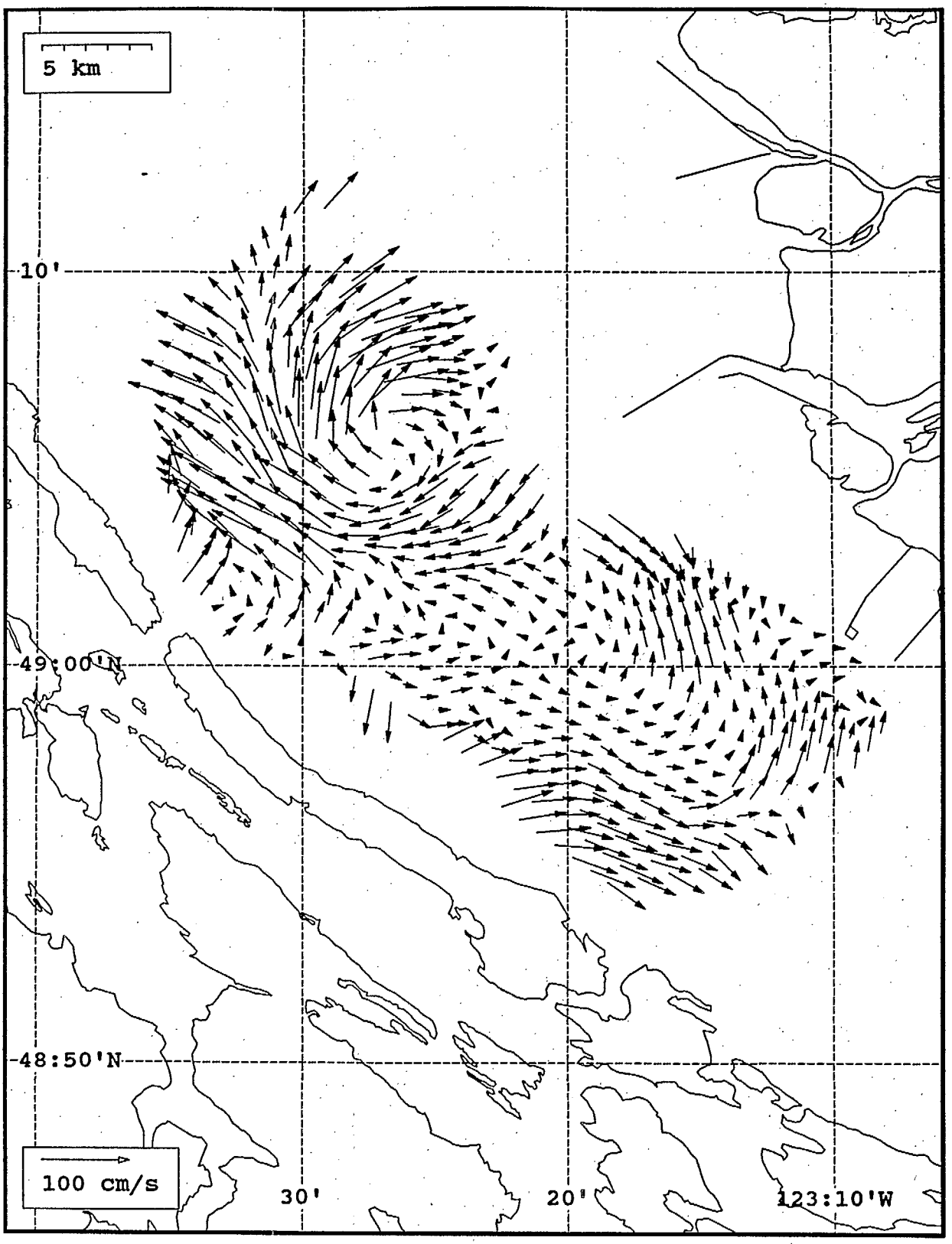

SeaSonde current field from the Strait of Georgia, off the mouth of the Fraser River, for 17:00 Z, July 30, 1993.

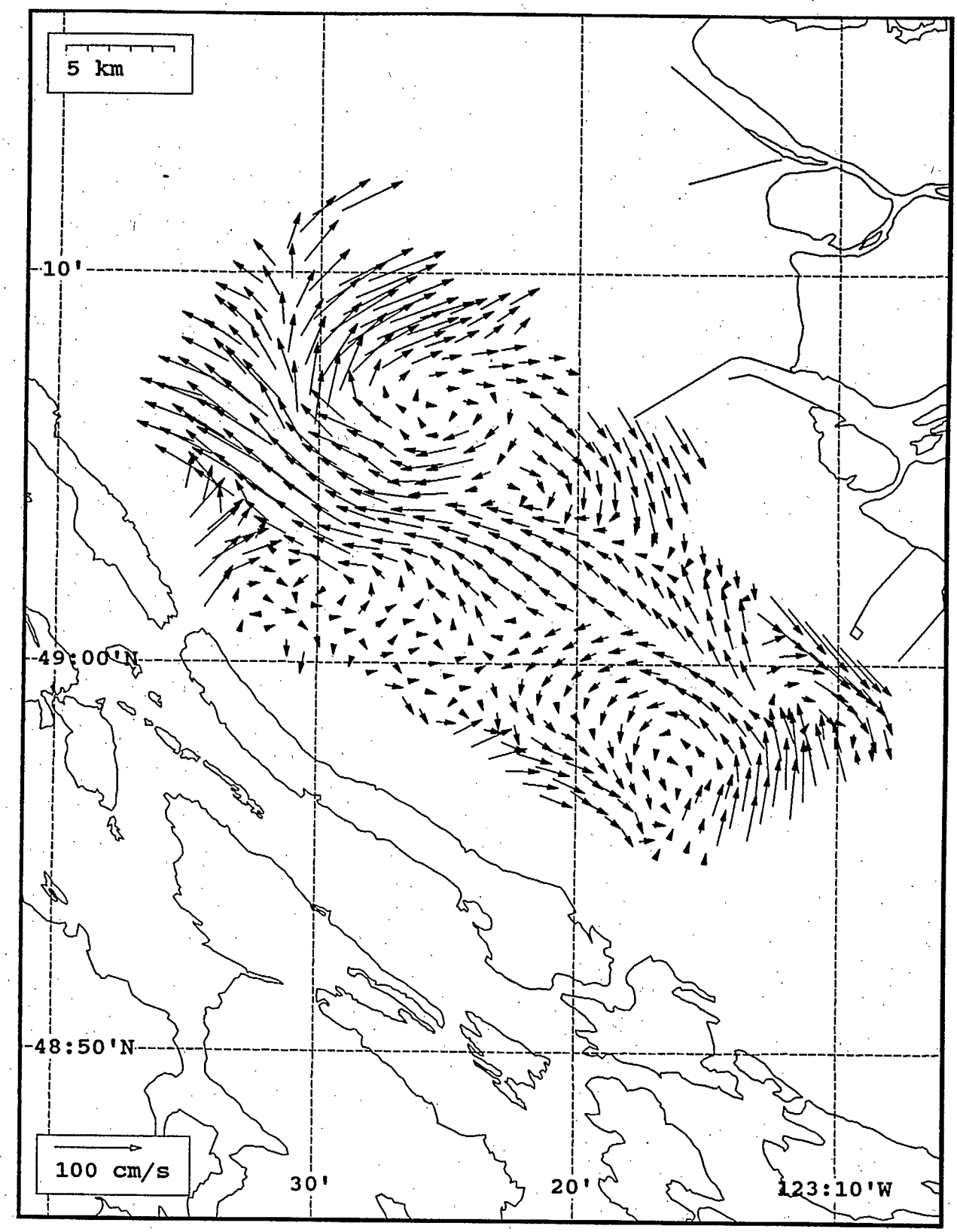

SeaSonde current field from the Strait of Georgia, off the mouth of the Fraser River, for 18:00 Z, July 30, 1993.

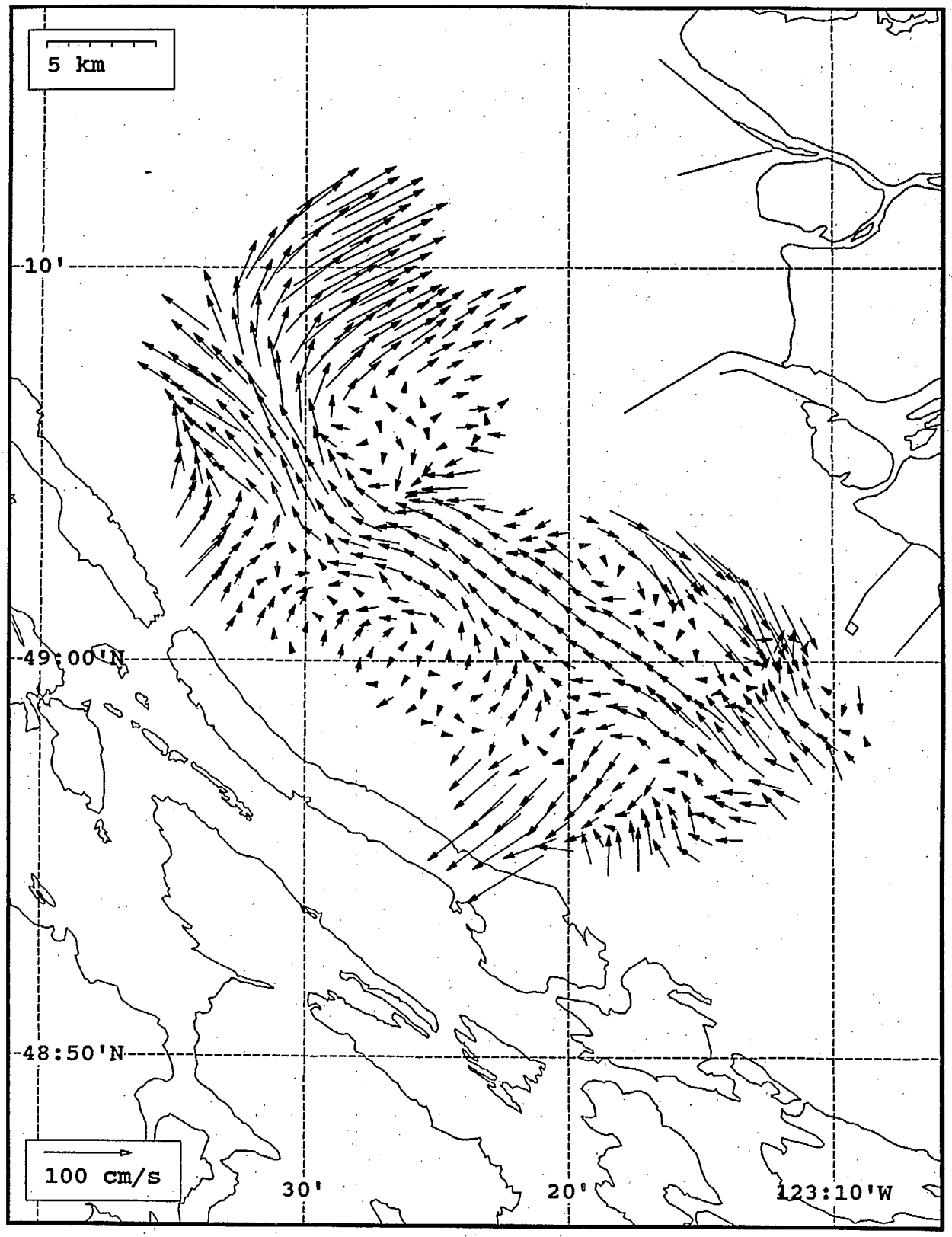

SeaSonde current field from the Strait of Georgia, off the mouth of the Fraser River, for 19:00 Z, July 30, 1993.

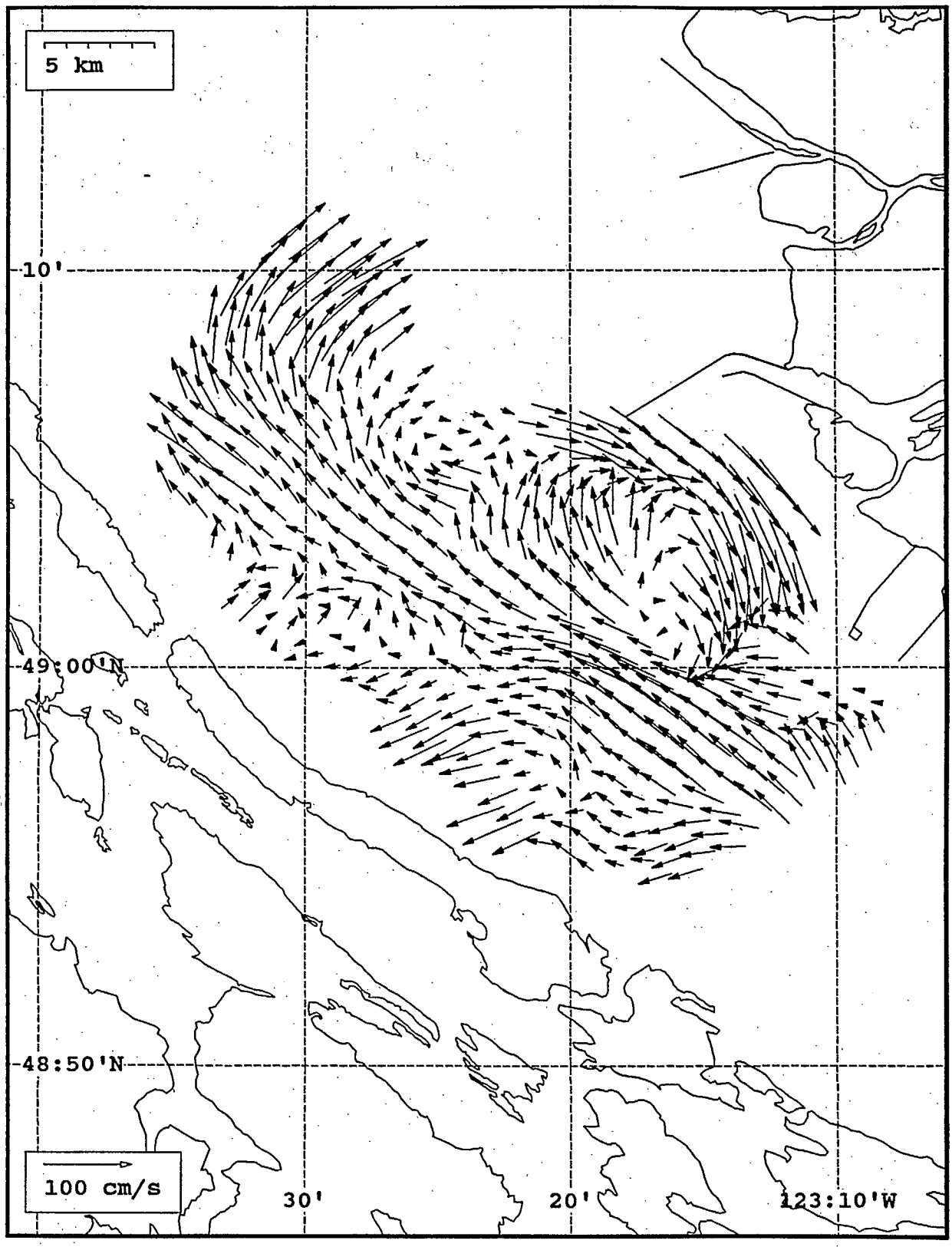

SeaSonde current field from the Strait of Georgia, off the mouth of the Fraser River, for 20:00 Z, July 30, 1993.

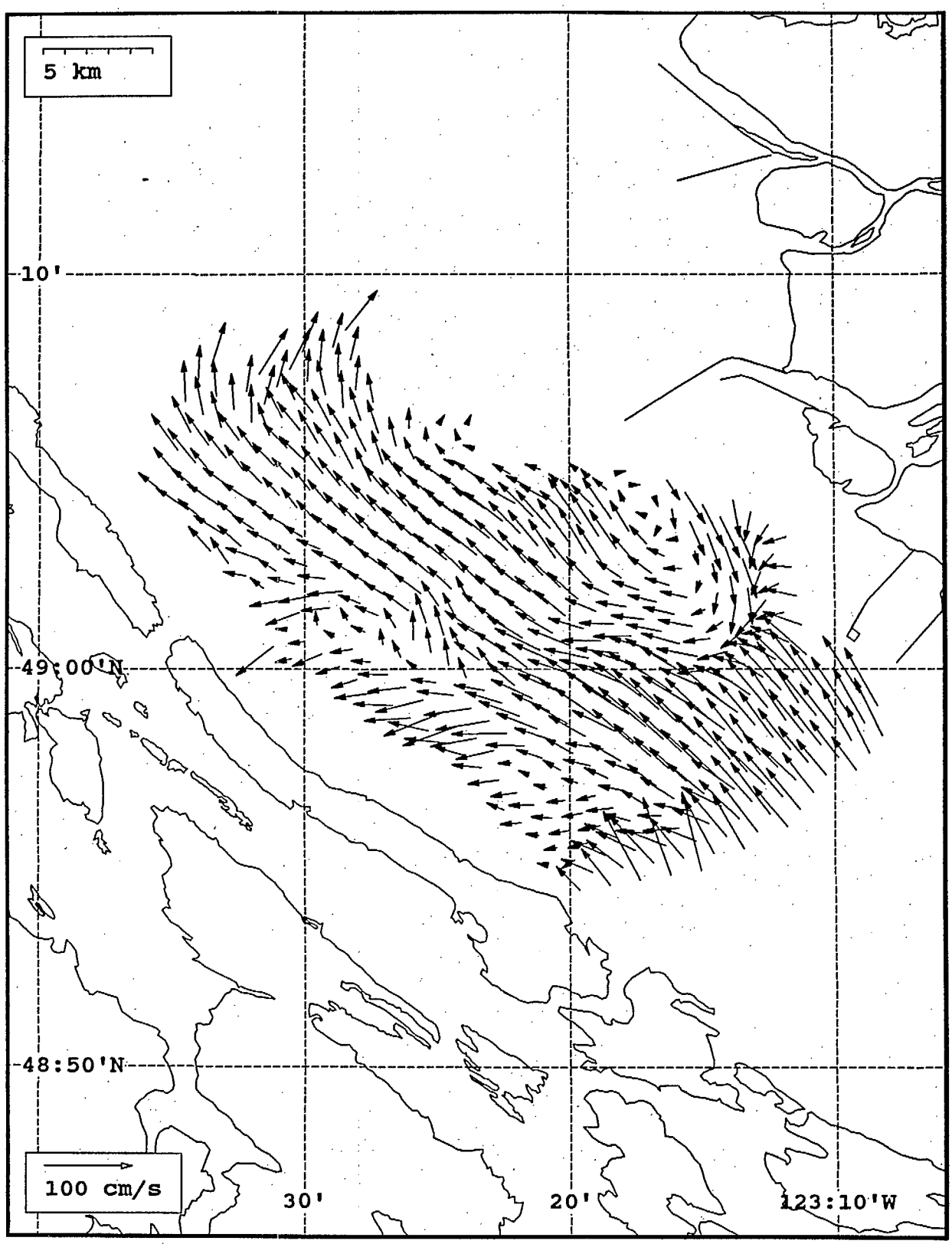

SeaSonde current field from the Strait of Georgia, off the mouth of the Fraser River, for 21:00 Z, July 30, 1993.

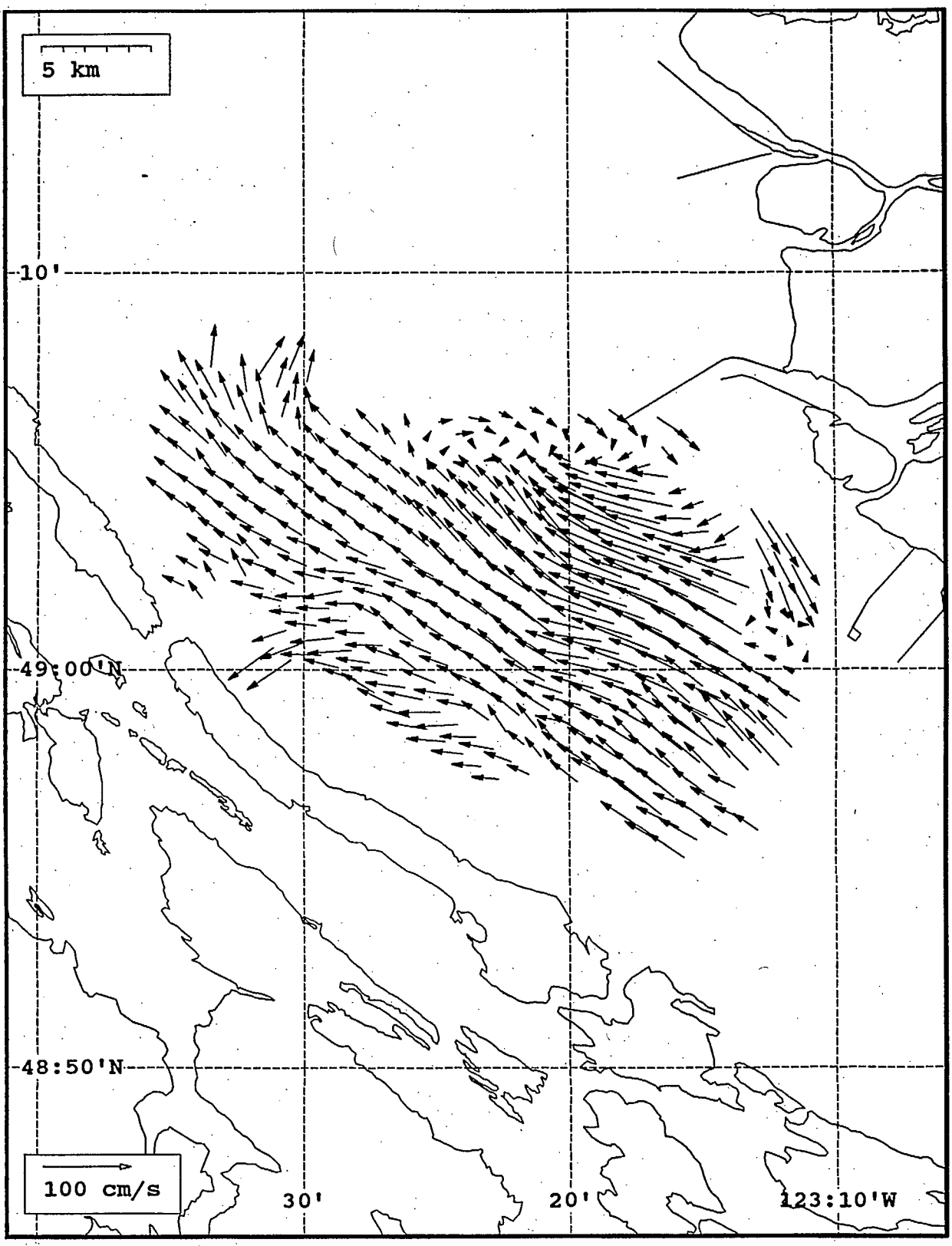

SeaSonde current field from the Strait of Georgia, off the mouth of the Fraser River, for 22:00 Z, July 30, 1993.

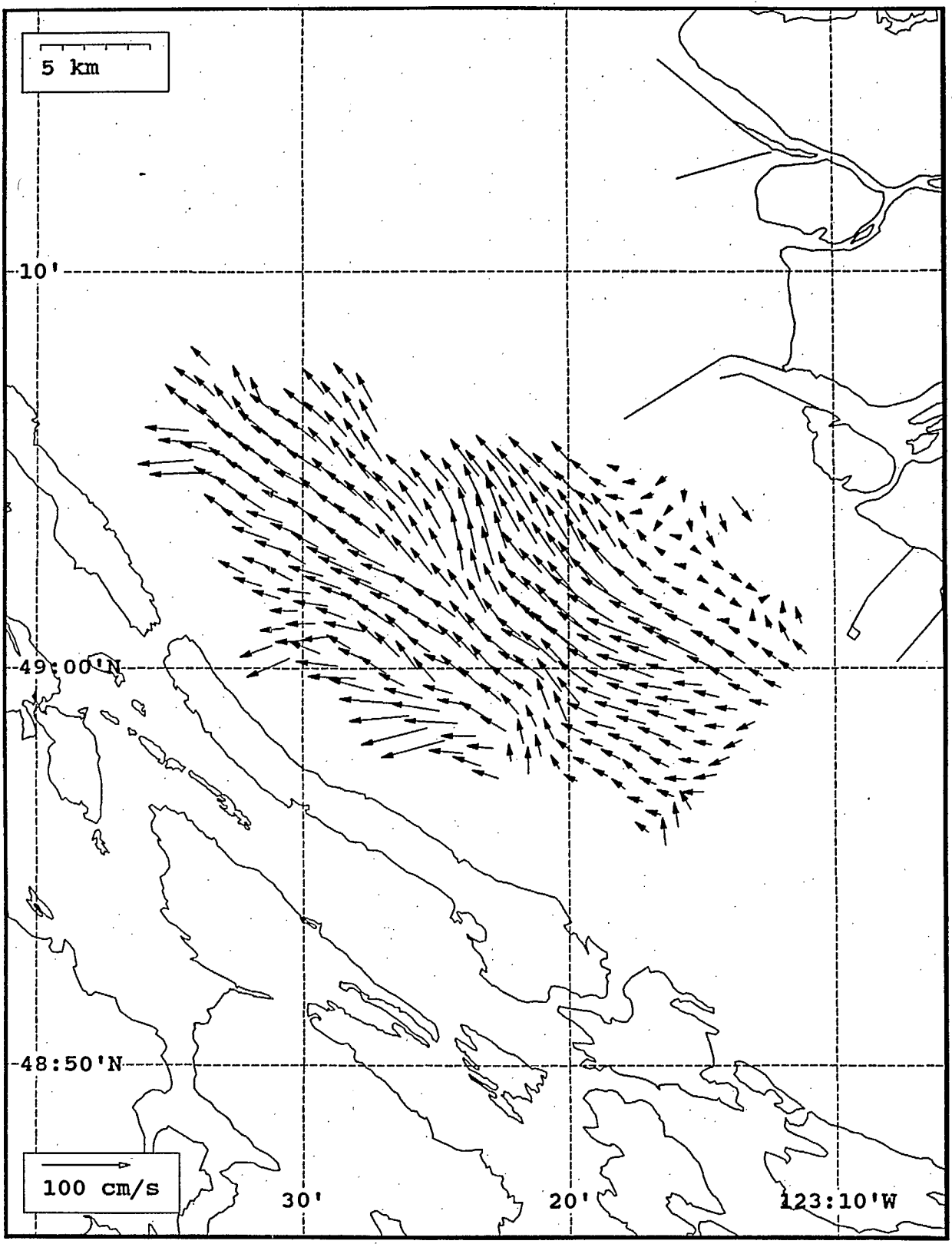

SeaSonde current field from the Strait of Georgia, off the mouth of the Fraser River, for 23:00 Z, July 30, 1993.

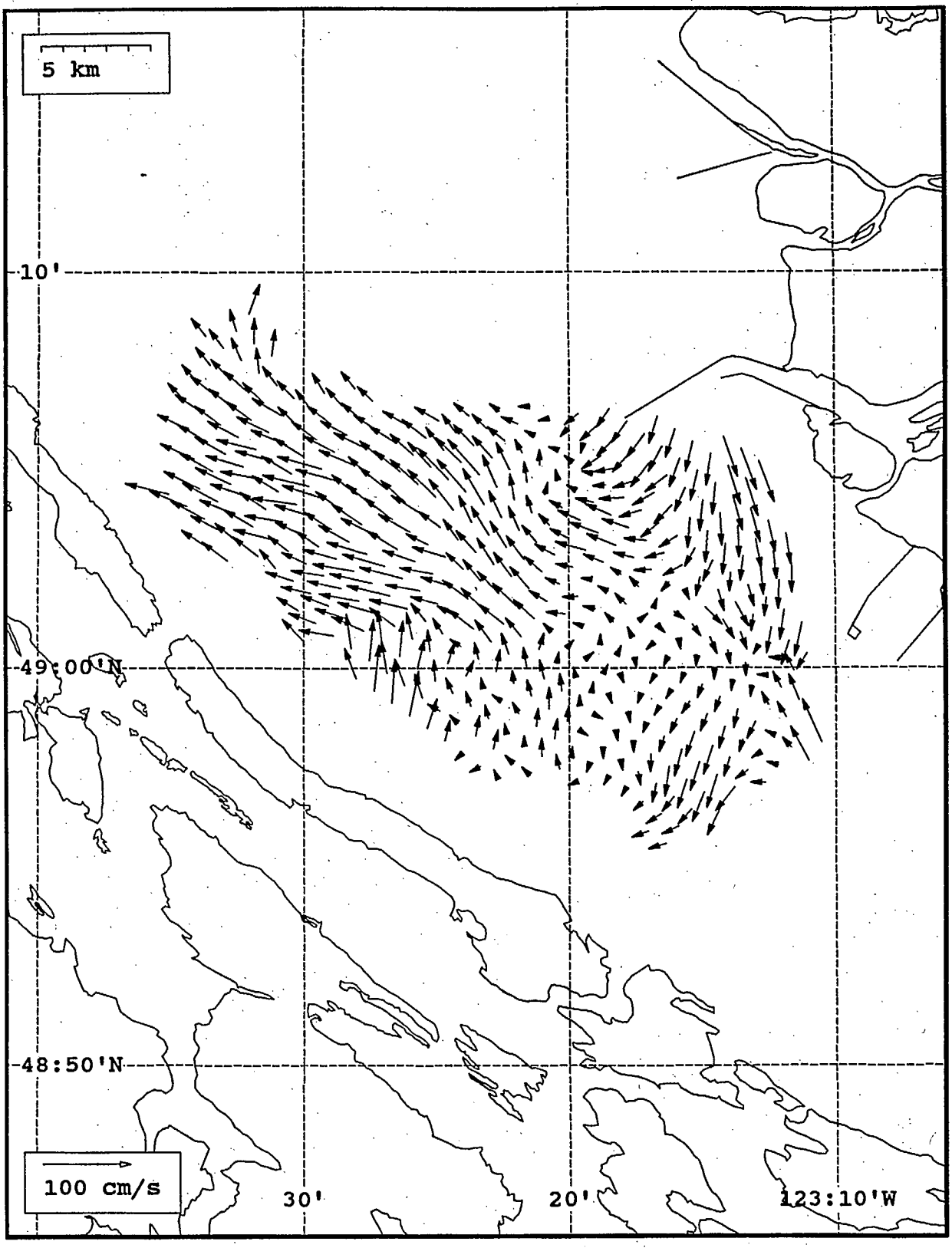

SeaSonde current field from the Strait of Georgia, off the mouth of the Fraser River, for 00:00 Z, July 31, 1993.

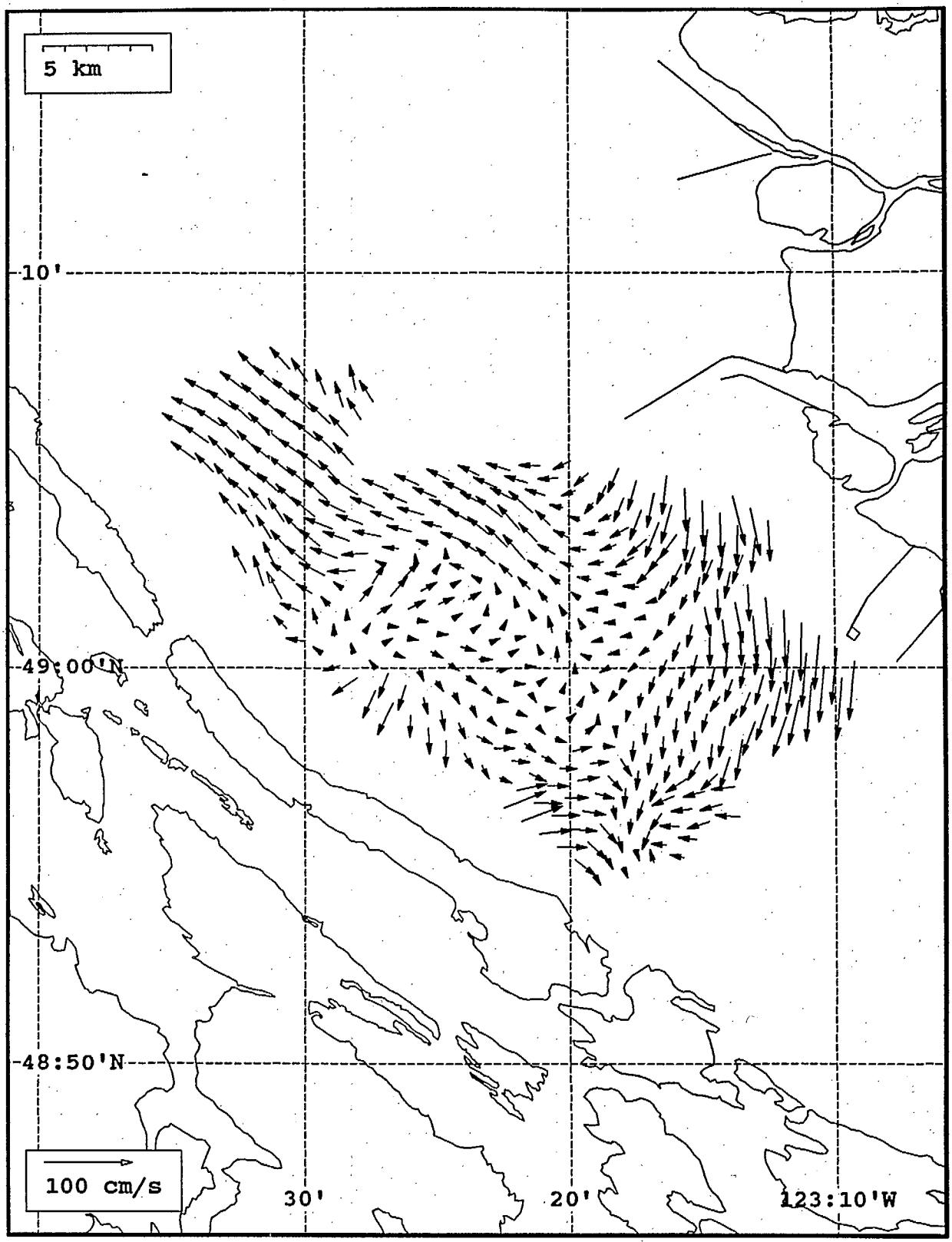

SeaSonde current field from the Strait of Georgia, off the mouth of the Fraser River, for 01:00 Z, July 31, 1993.

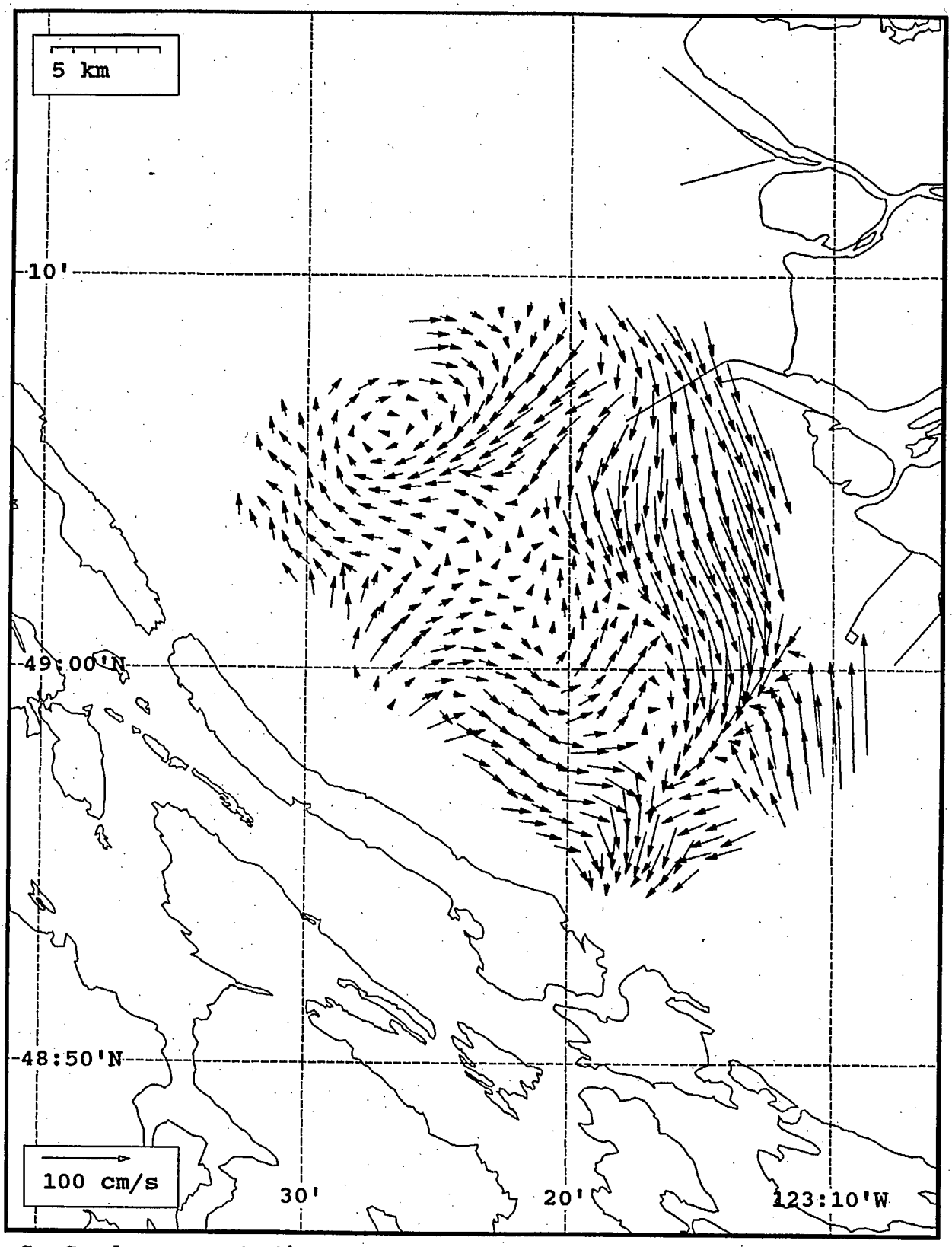

SeaSonde current field from the Strait of Georgia, off the mouth of the Fraser River, for 02:00 Z, July 31, 1993.

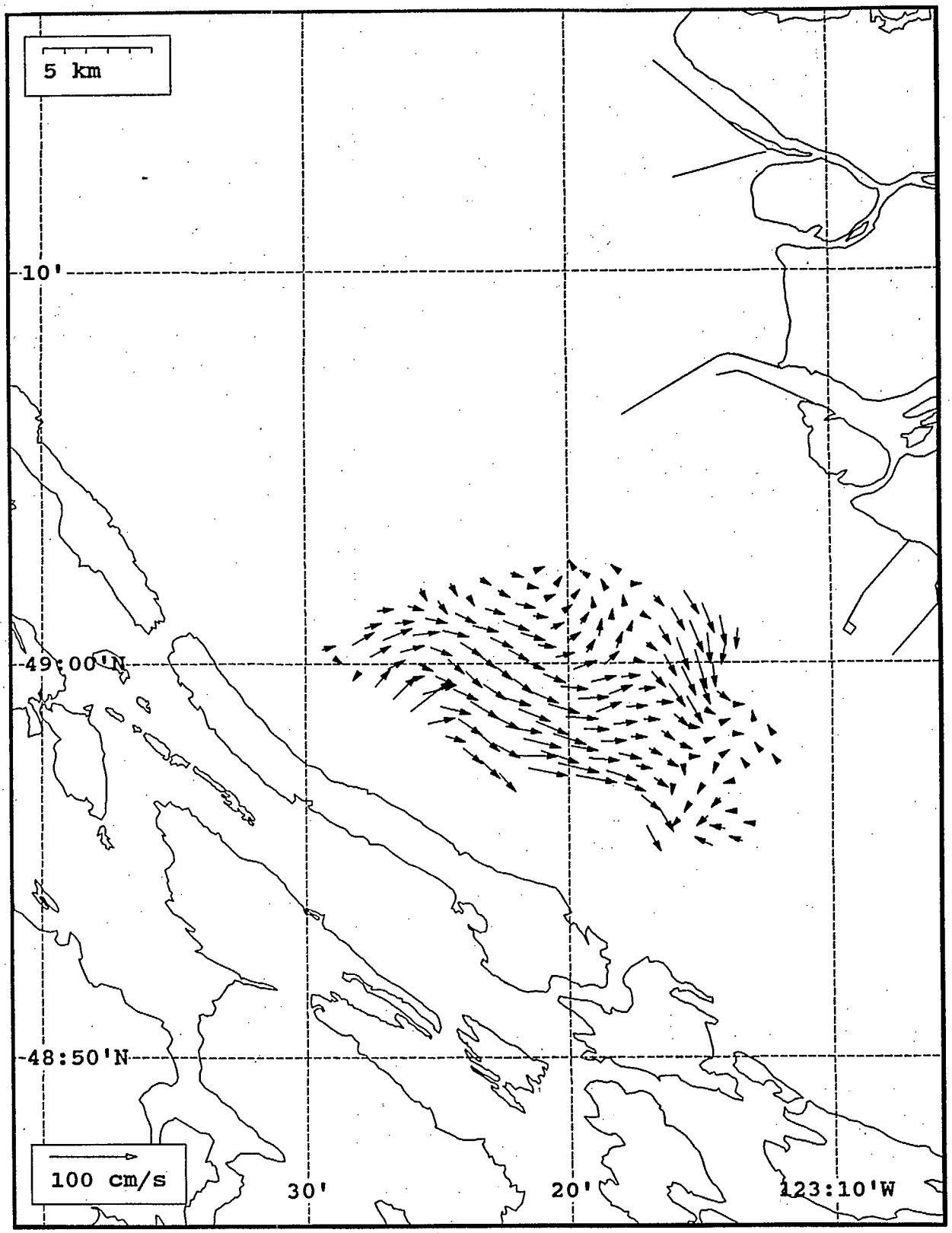

SeaSonde current field from the Strait of Georgia, off the mouth of the Fraser River, for 03:00 Z, July 31, 1993.

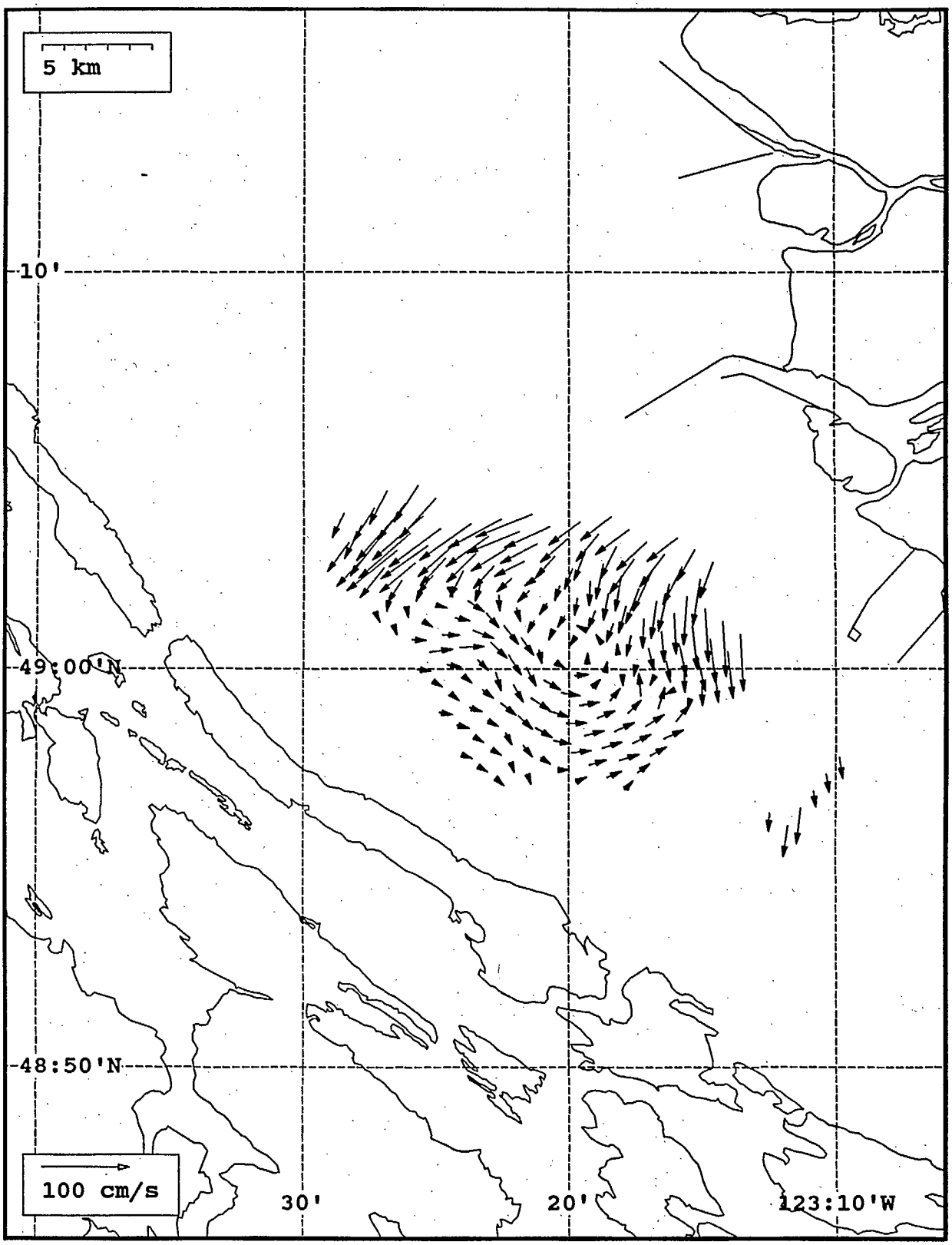

SeaSonde current field from the Strait of Georgia, off the mouth of the Fraser River, for 05:00 Z, July 31, 1993.

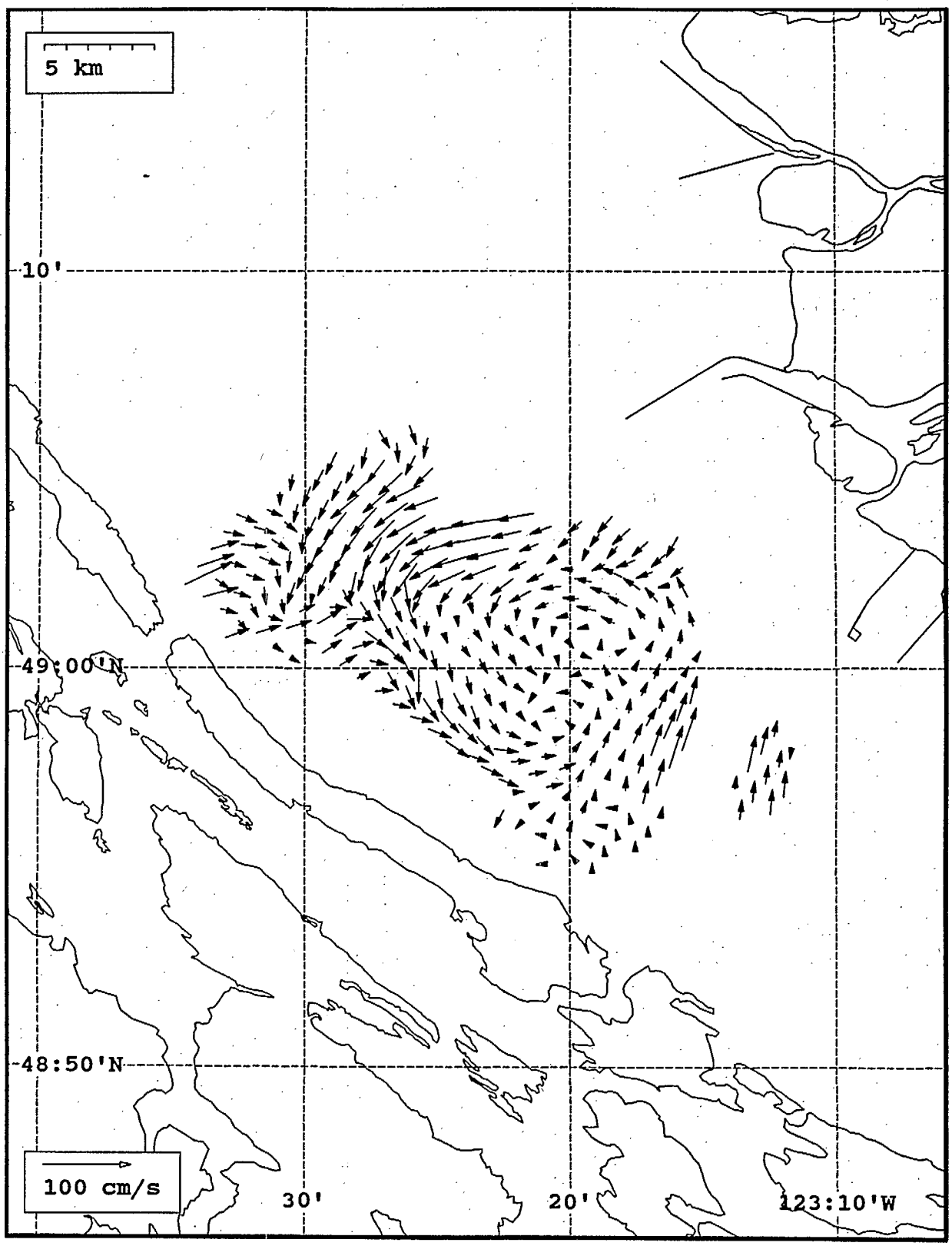

SeaSonde current field from the Strait of Georgia, off the mouth of the Fraser River, for 06:00 Z, July 31, 1993.

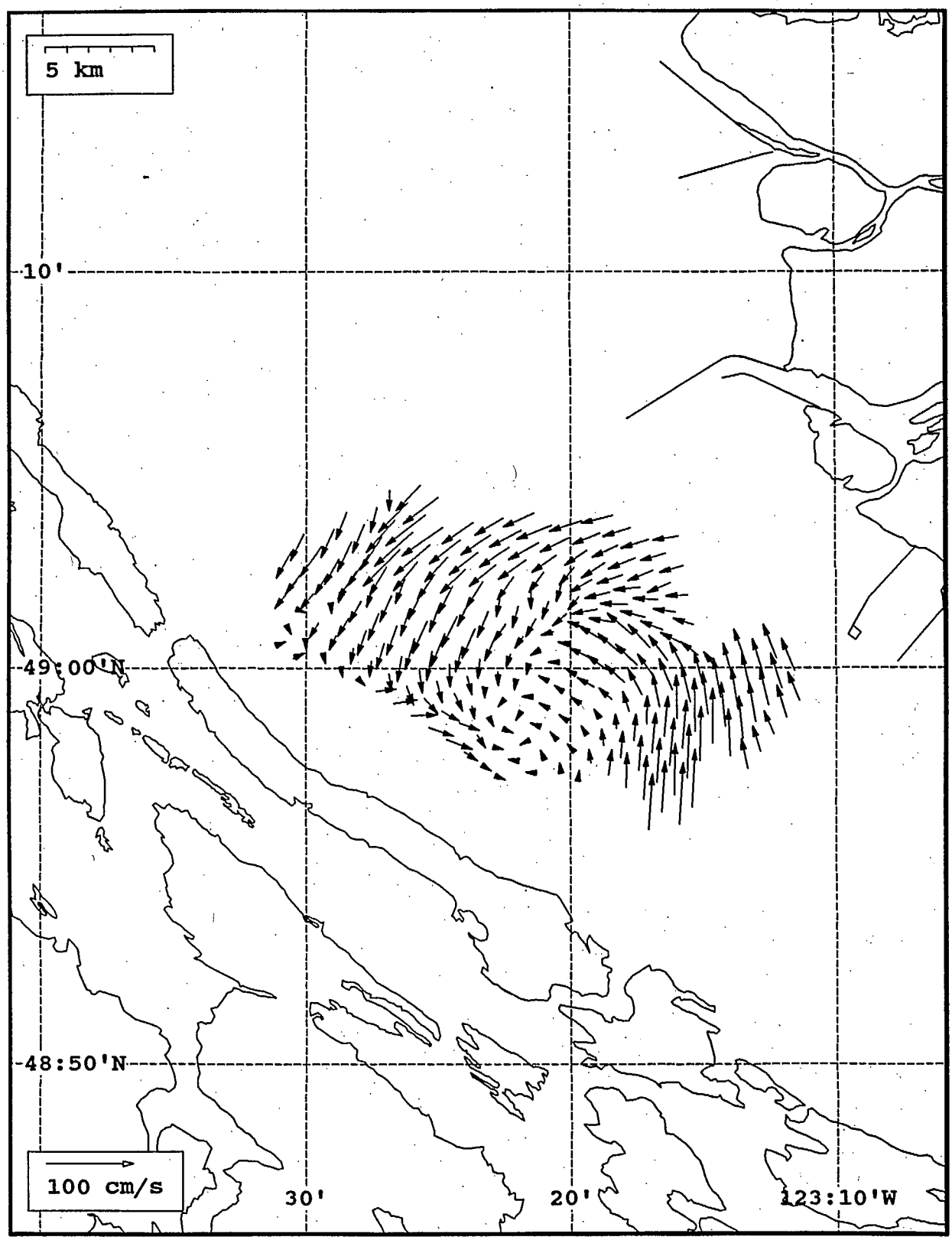

SeaSonde current field from the Strait of Georgia, off the mouth of the Fraser River, for 07:00 Z, July 31, 1993.

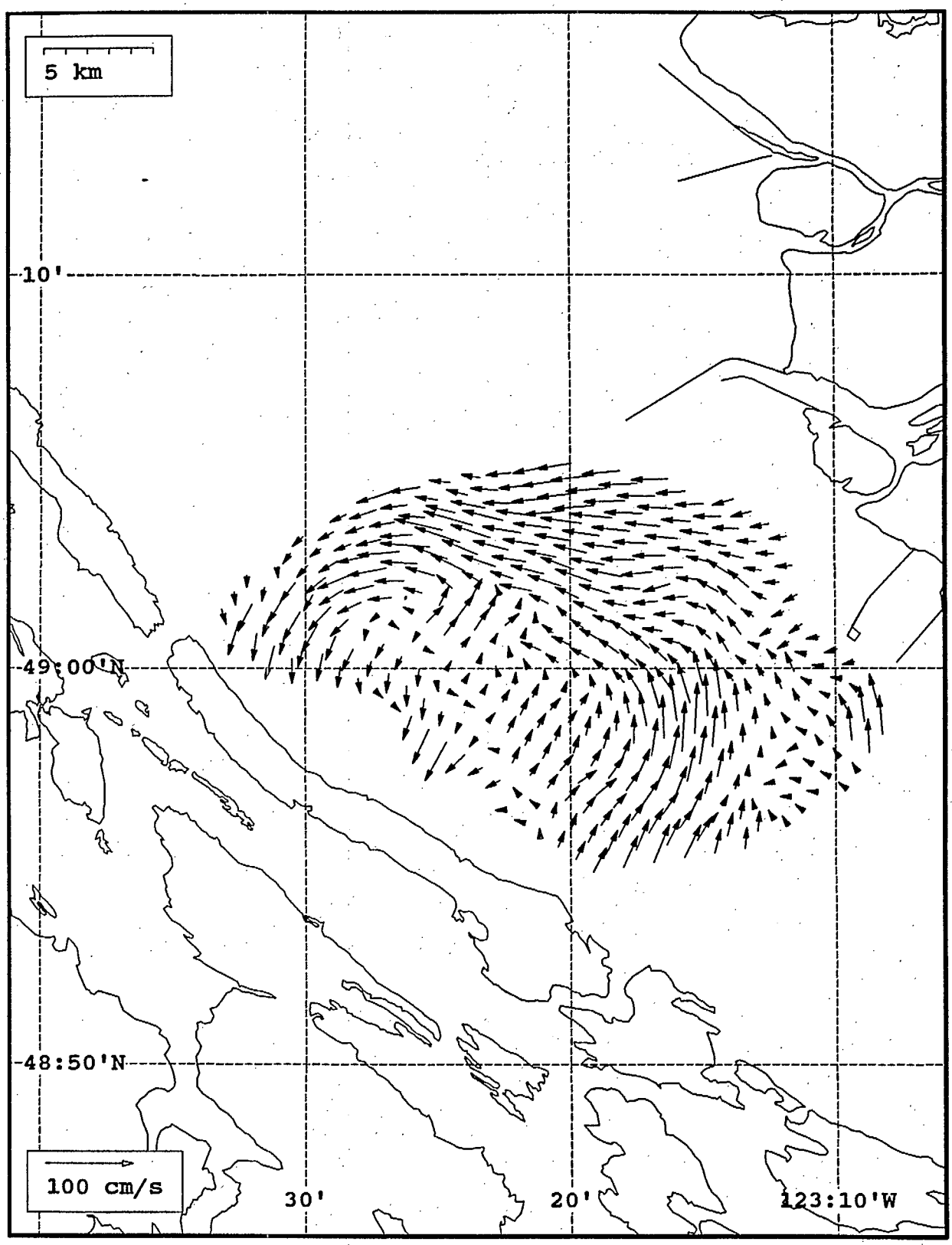

SeaSonde current field from the Strait of Georgia, off the mouth of the Fraser River, for 08:00 Z, July 31, 1993.

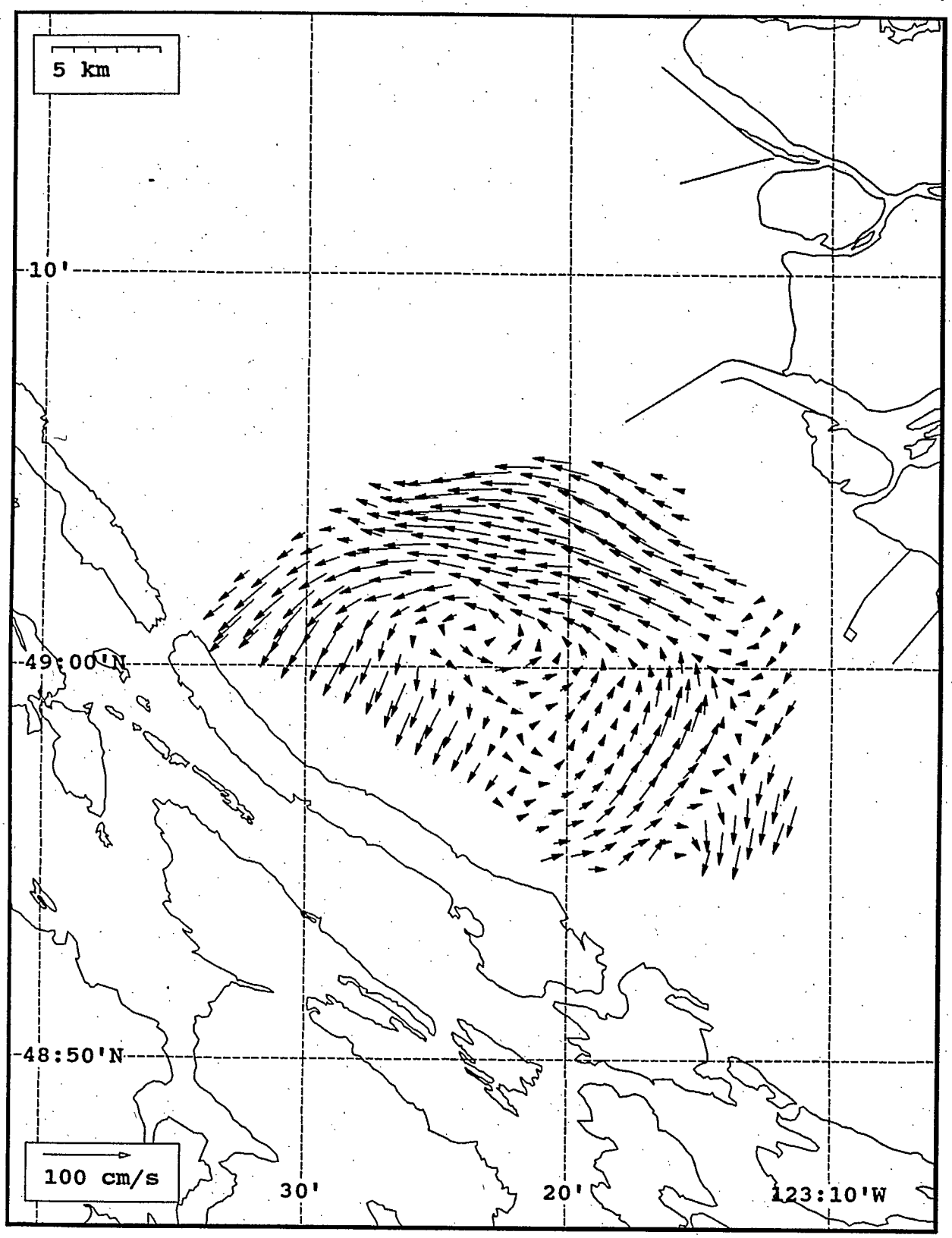

SeaSonde current field from the Strait of Georgia, off the mouth of the Fraser River, for 09:00 Z, July 31, 1993.

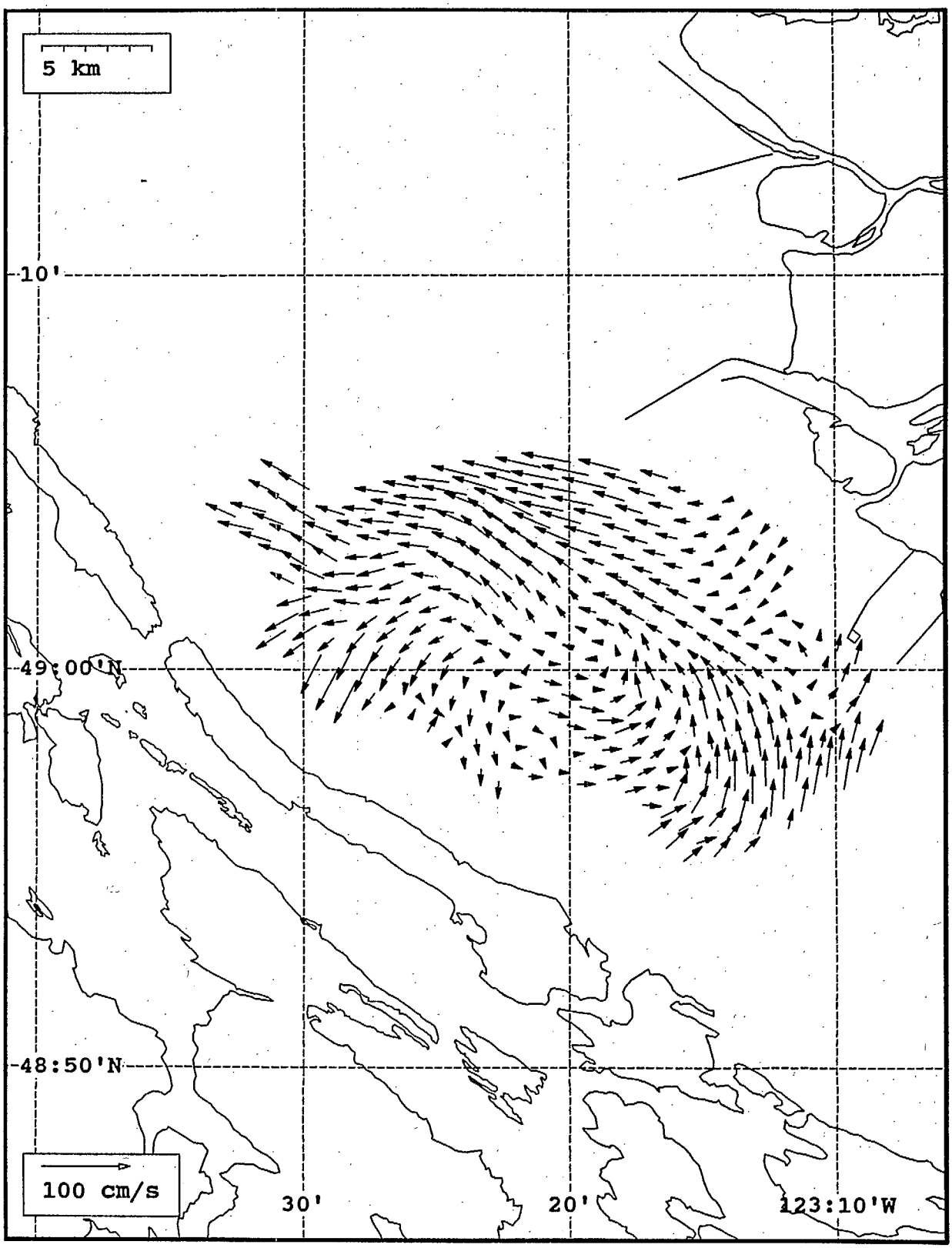

SeaSonde current field from the Strait of Georgia, off the mouth of the Fraser River, for 10:00 Z, July 31, 1993.

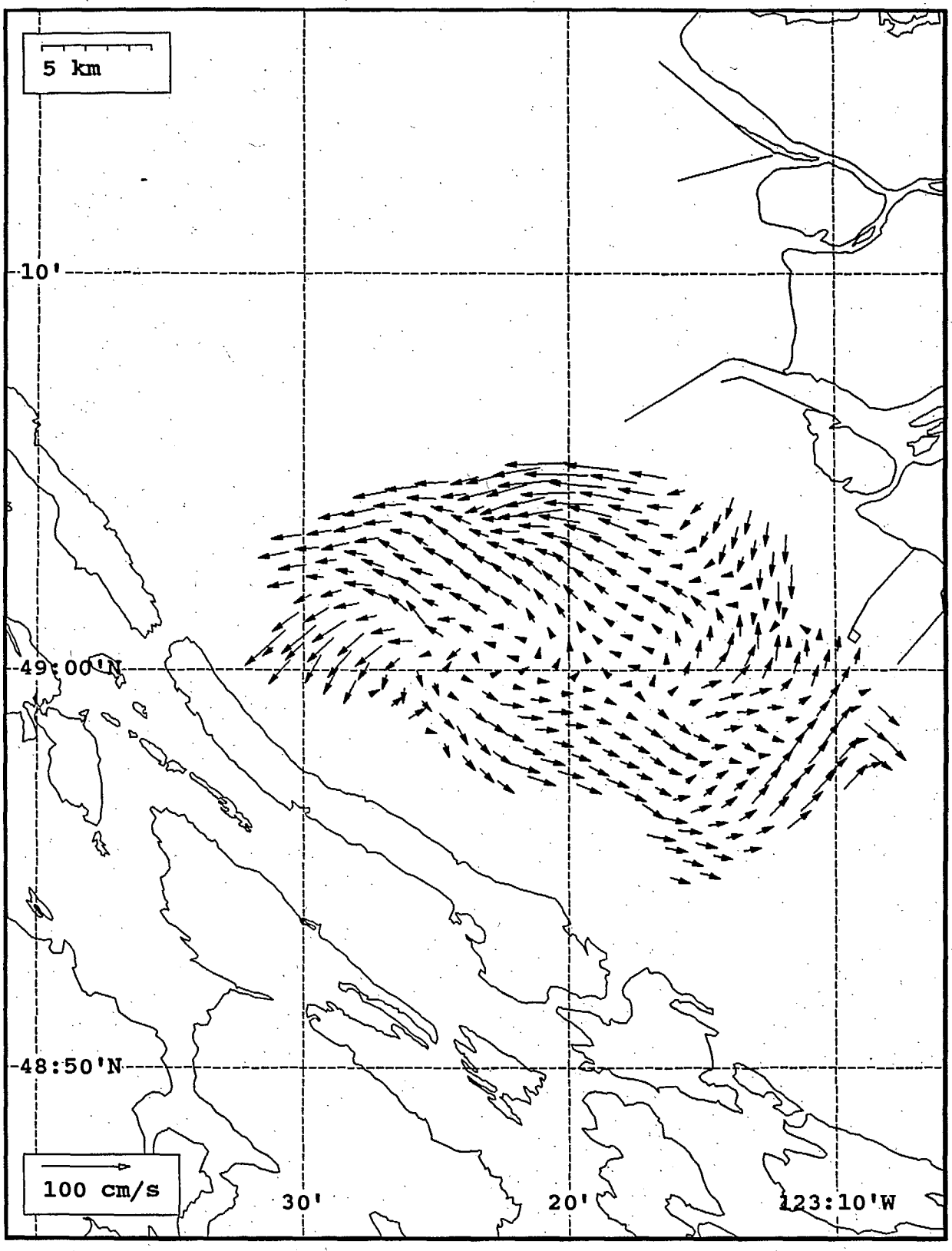

SeaSonde current field from the Strait of Georgia, off the mouth of the Fraser River, for 11:00 Z, July 31, 1993.

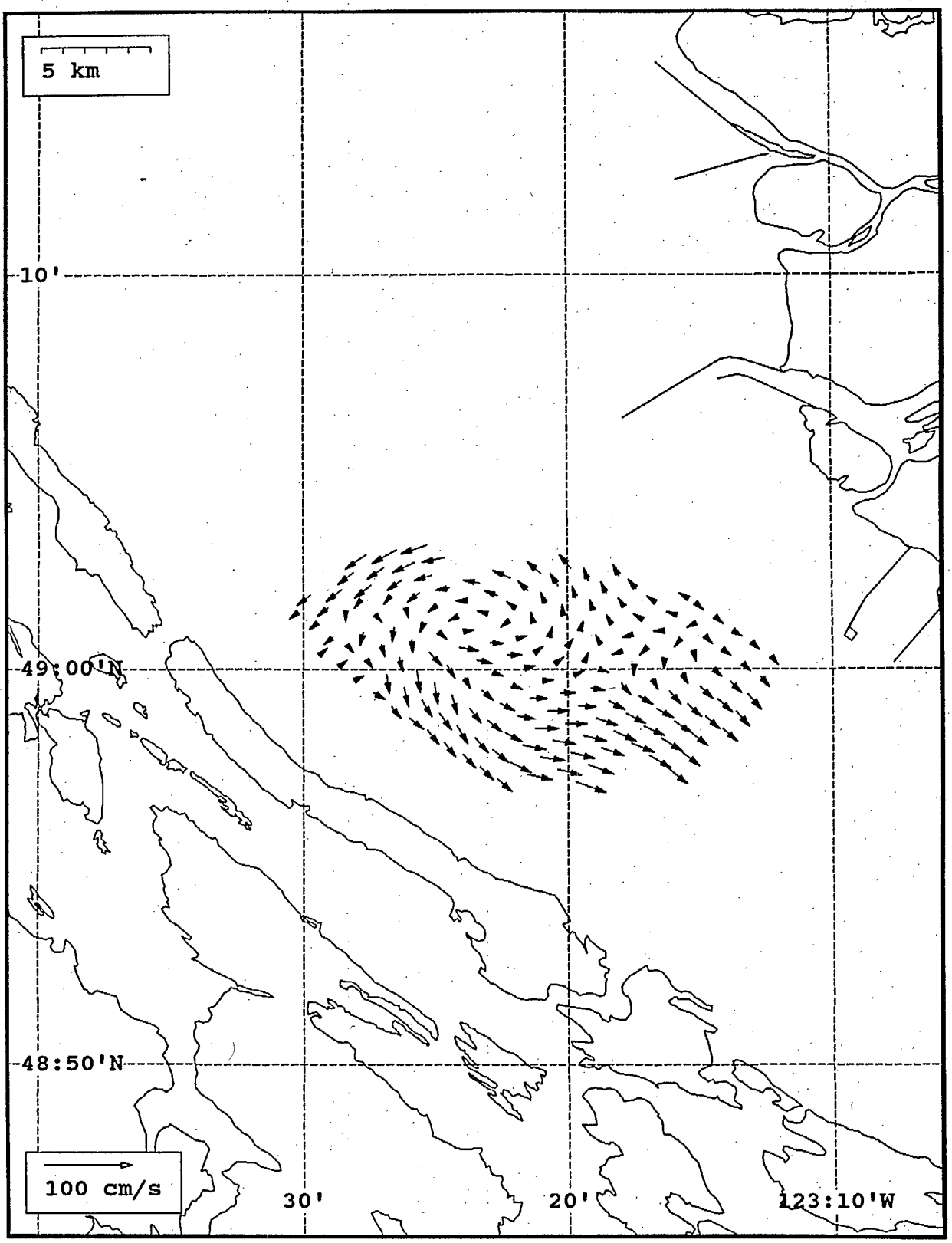

SeaSonde current field from the Strait of Georgia, off the mouth of the Fraser River, for 12:00 Z, July 31, 1993.

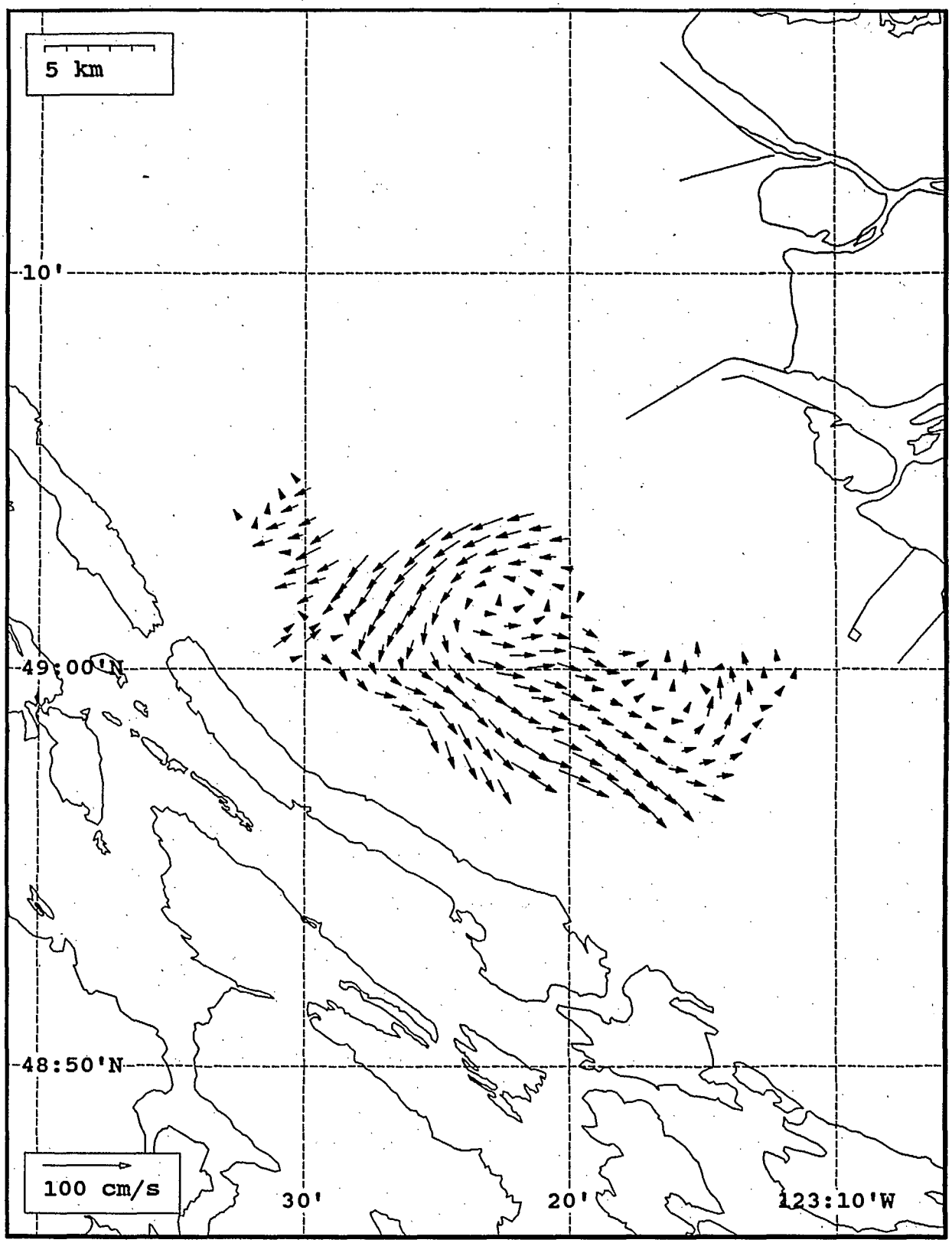

SeaSonde current field from the Strait of Georgia, off the mouth of the Fraser River, for 13:00 Z, July 31, 1993.

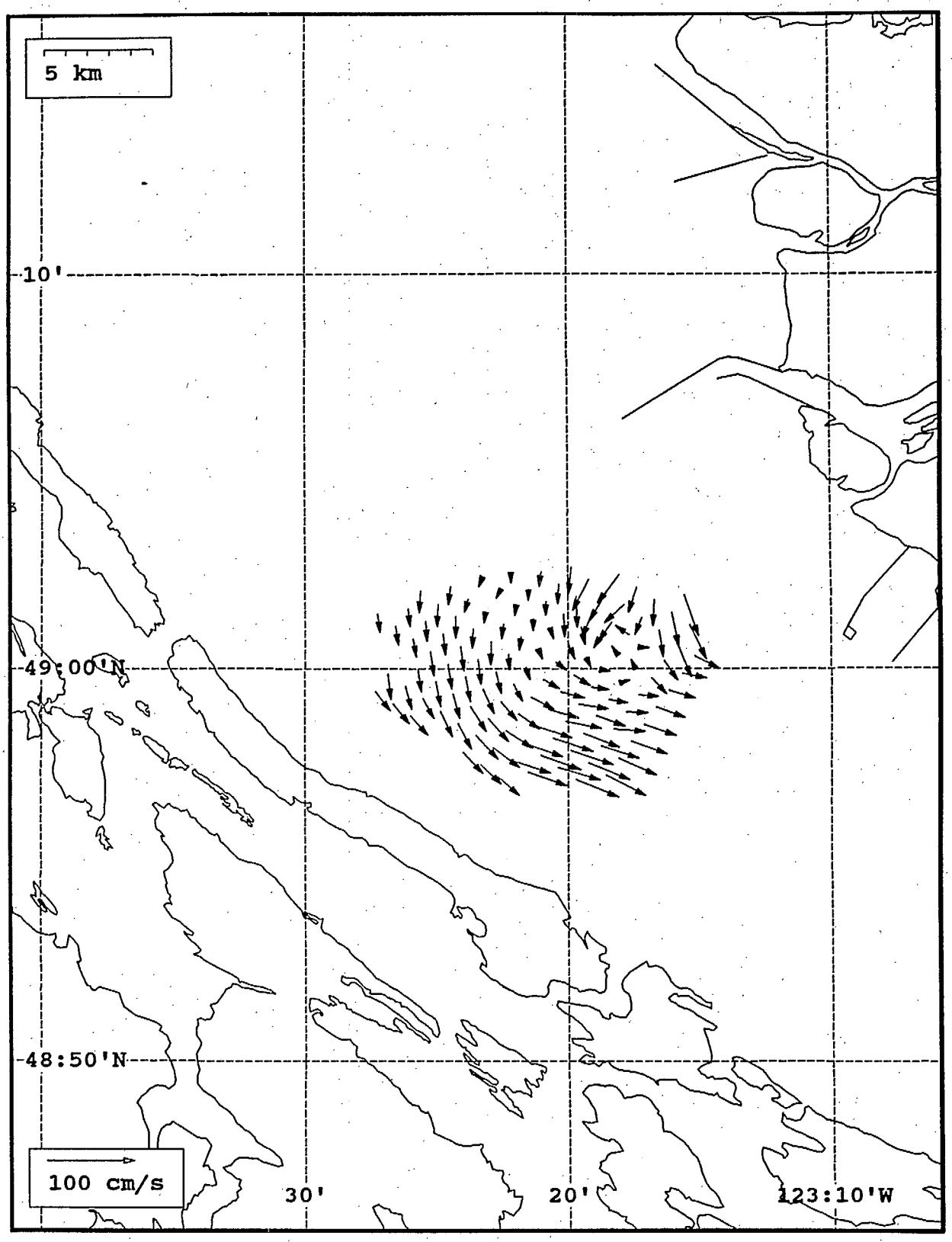

SeaSonde current field from the Strait of Georgia, off the mouth of the Fraser River, for 14:00 Z, July 31, 1993.

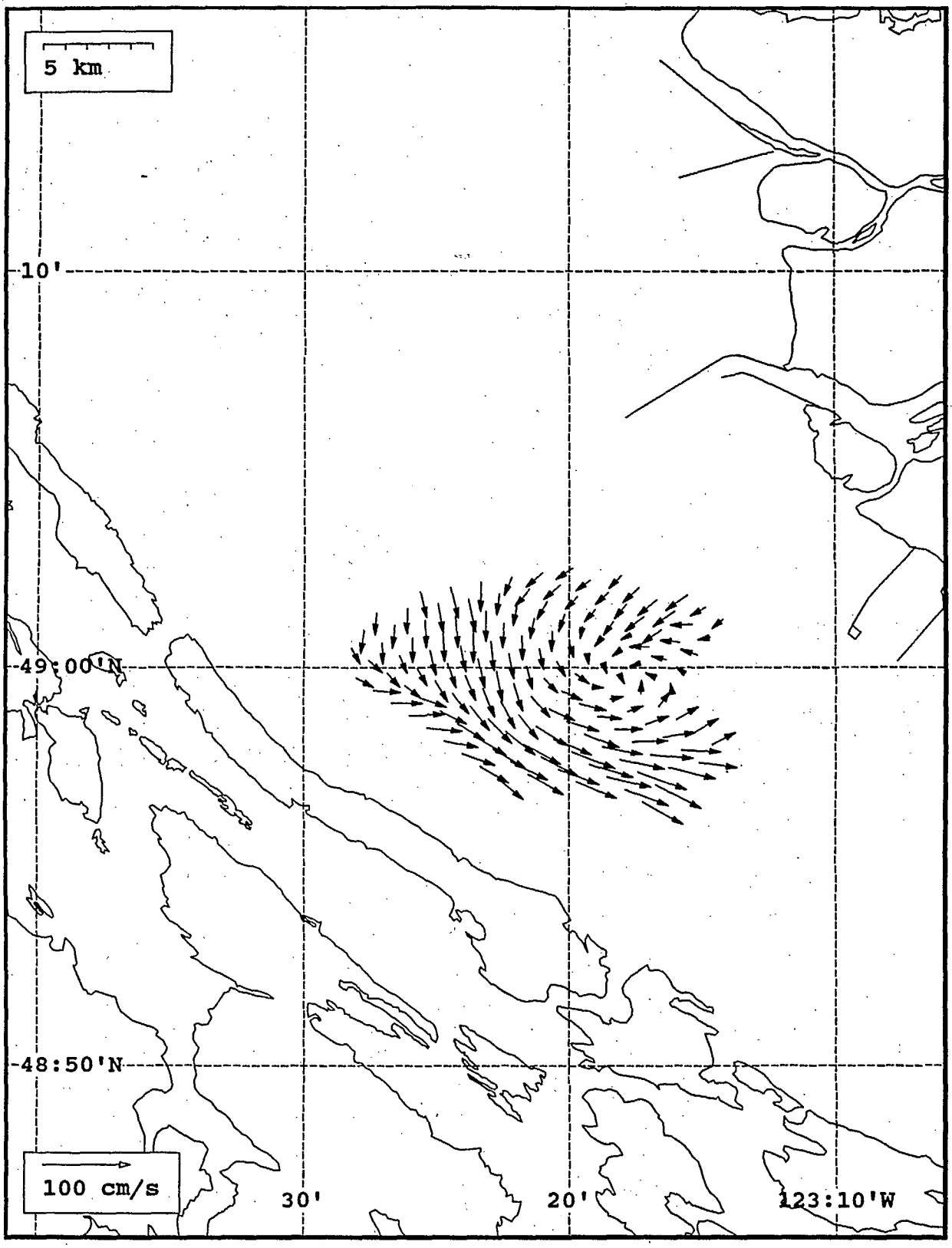

SeaSonde current field from the Strait of Georgia, off the mouth of the Fraser River, for 15:00 Z, July 31, 1993.

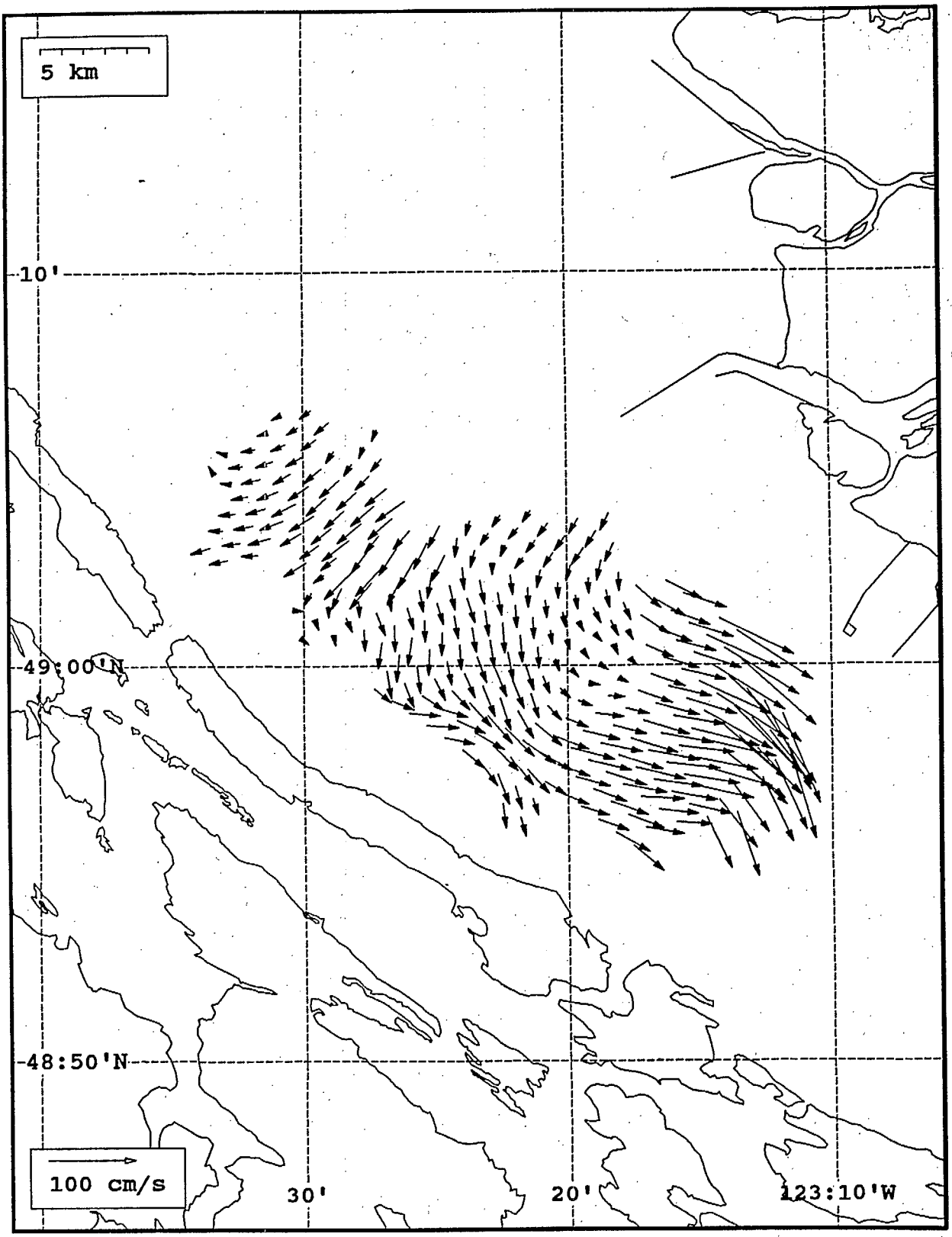

SeaSonde current field from the Strait of Georgia, off the mouth of the Fraser River, for 16:00 Z, July 31, 1993.

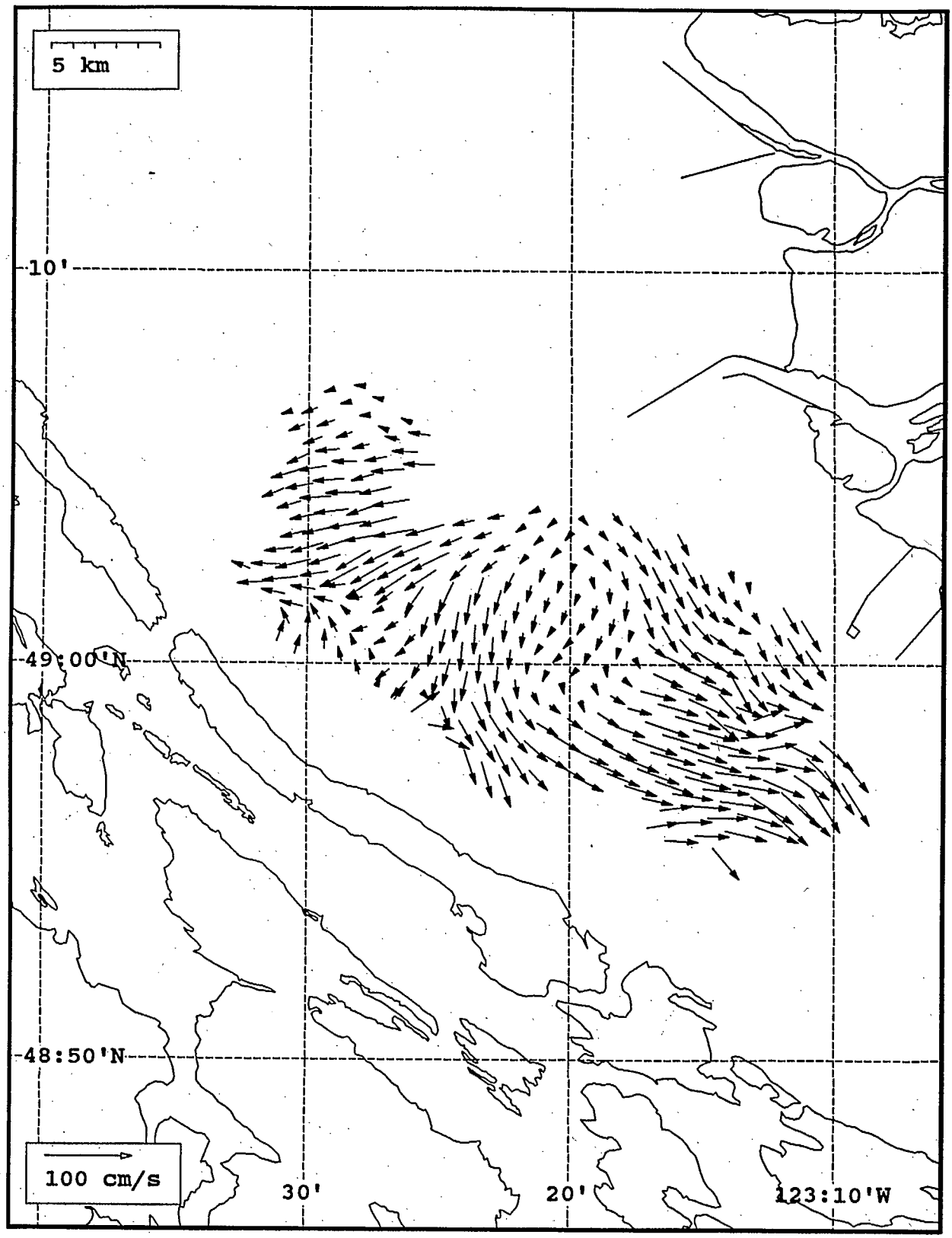

SeaSonde current field from the Strait of Georgia, off the mouth of the Fraser River, for 17:00 Z, July 31, 1993.

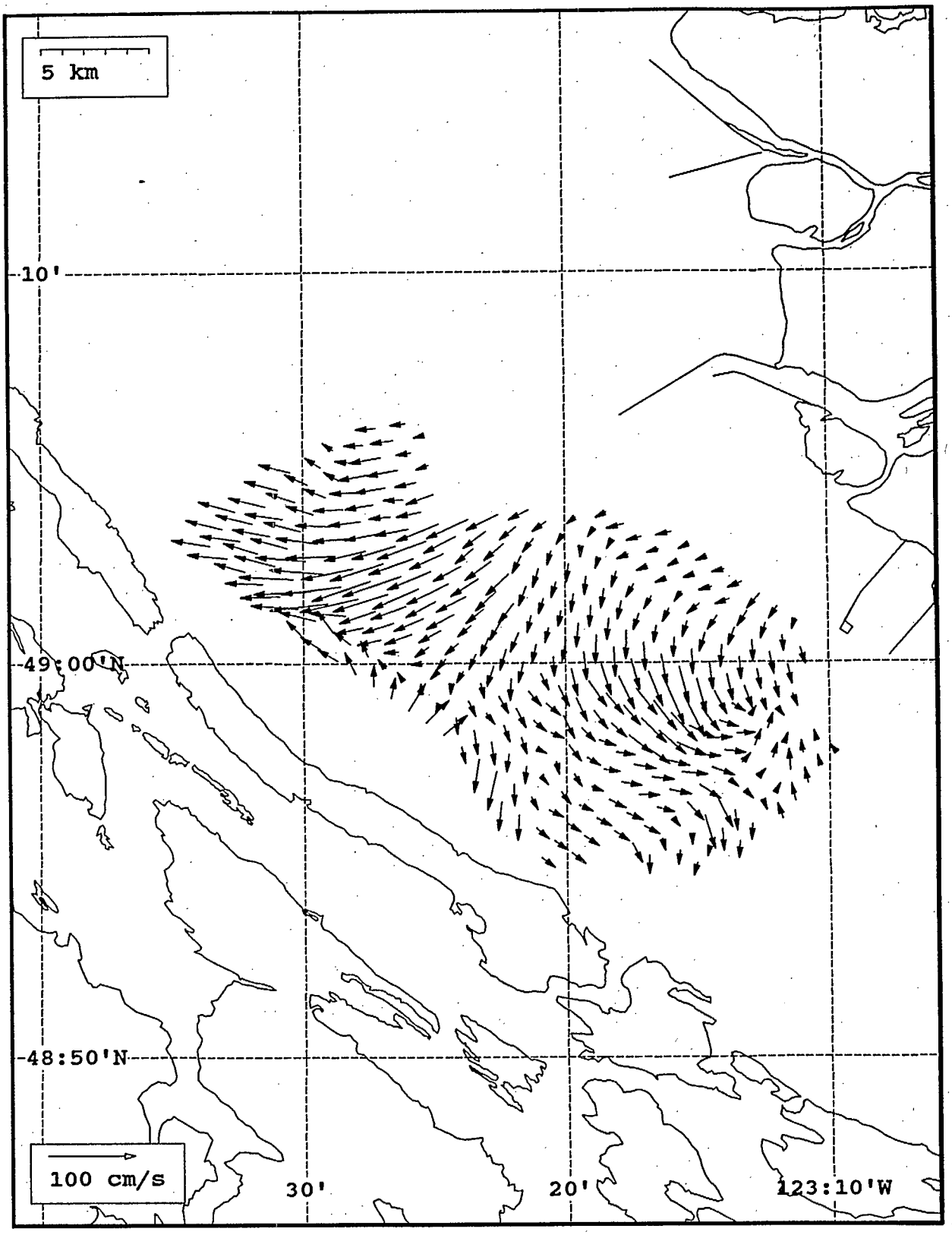

SeaSonde current field from the Strait of Georgia, off the mouth of the Fraser River, for 18:00 Z, July 31, 1993.

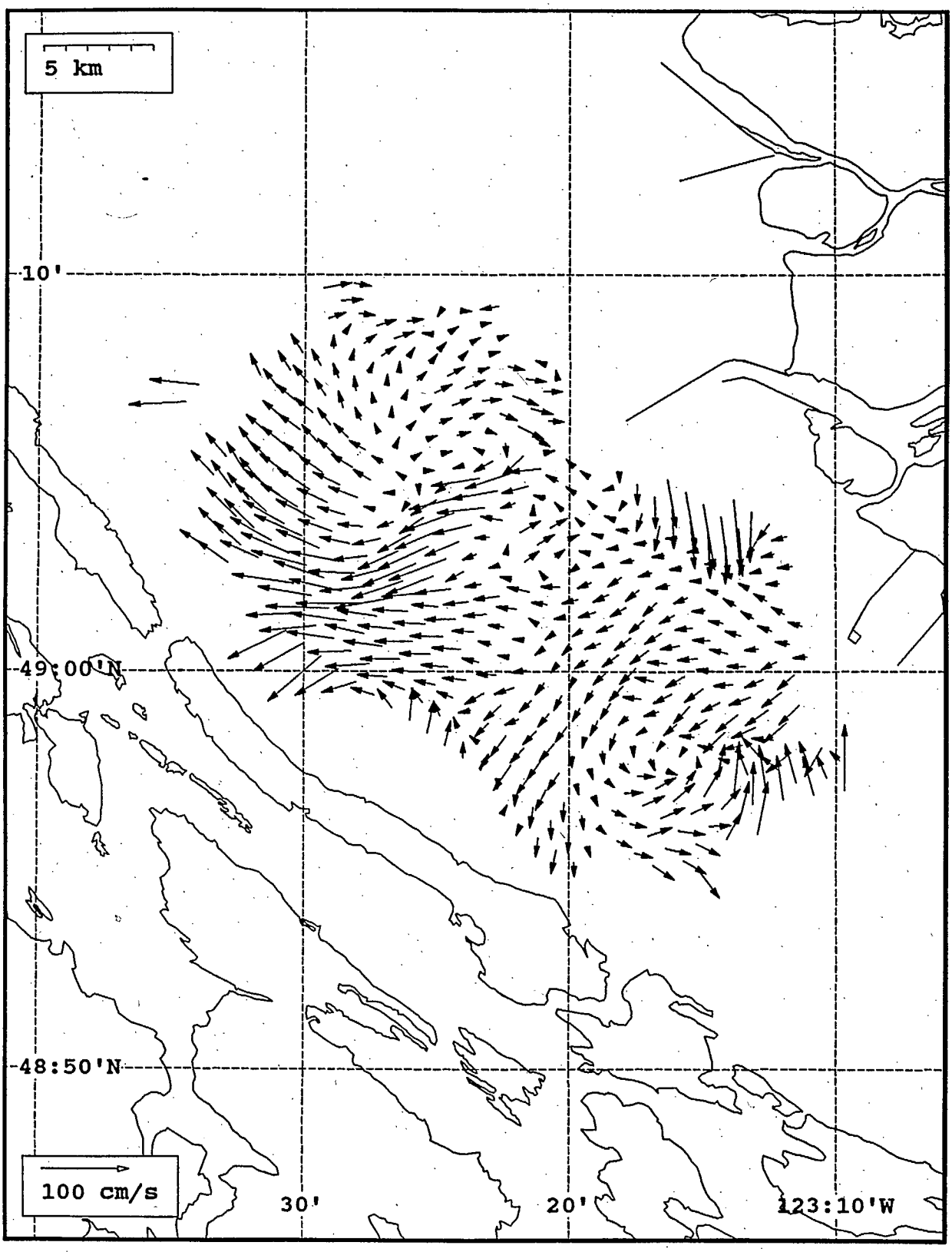

SeaSonde current field from the Strait of Georgia, off the mouth of the Fraser River, for 19:00 Z, July 31, 1993.

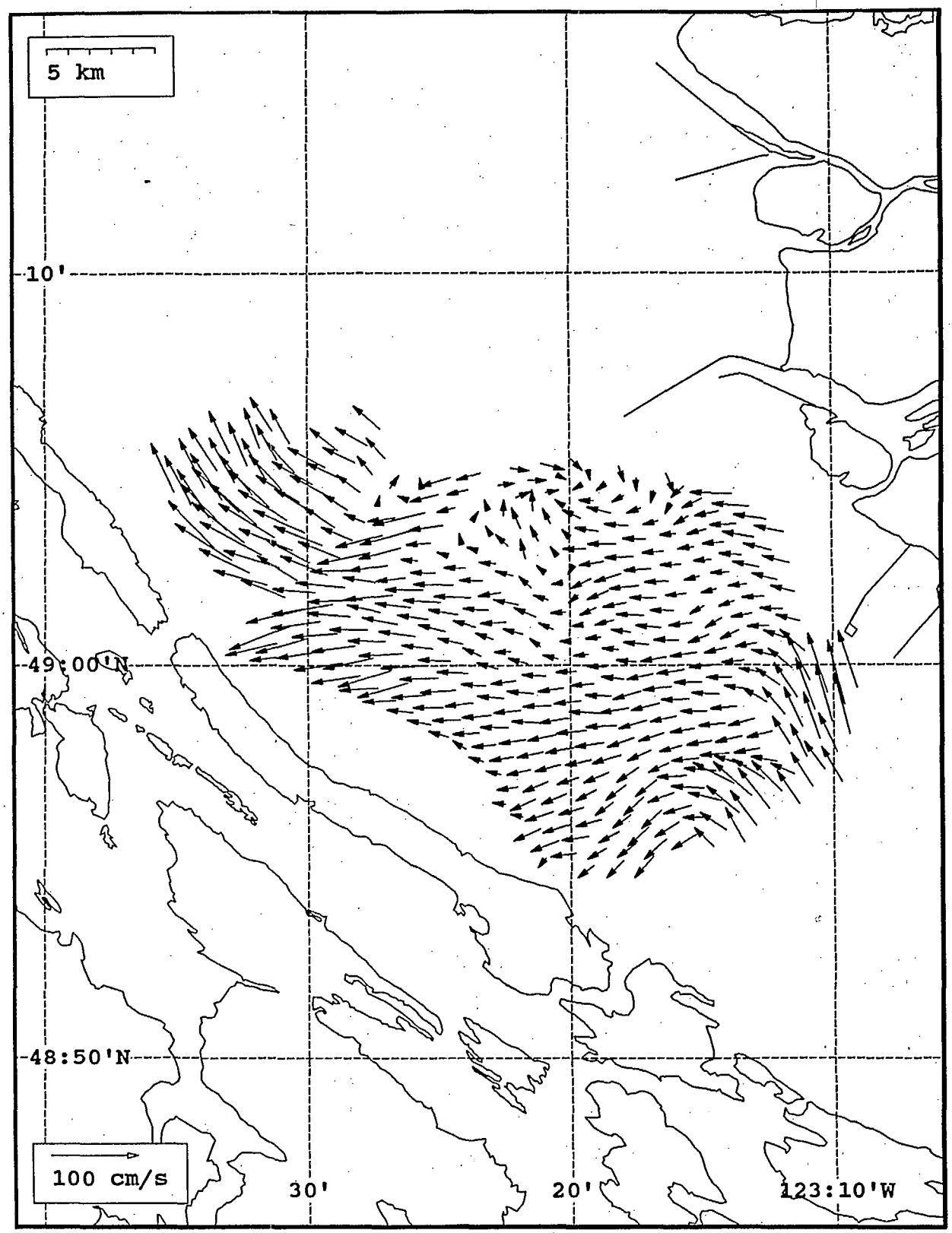

SeaSonde current field from the Strait of Georgia, off the mouth of the Fraser River, for 20:00 Z, July 31, 1993.

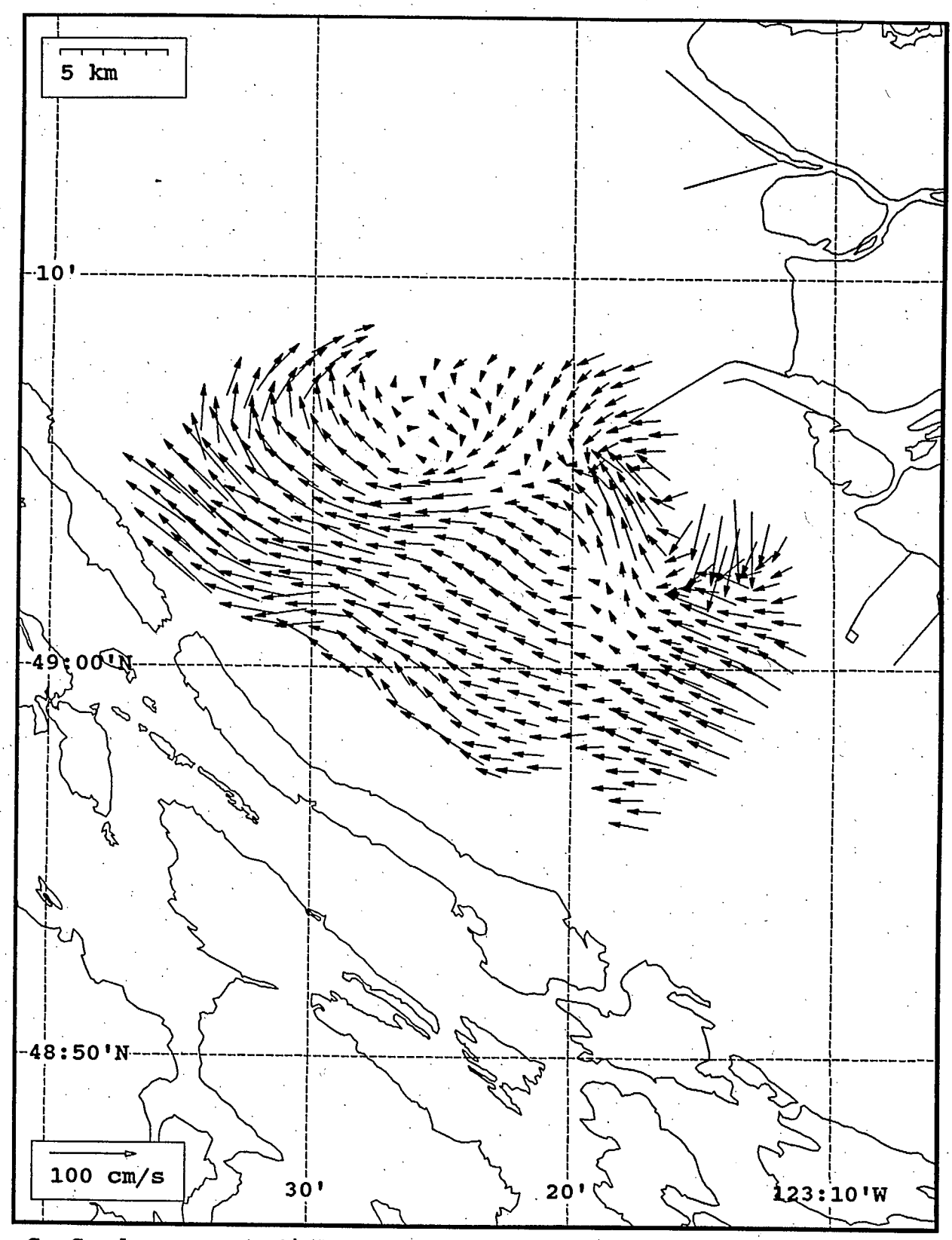

SeaSonde current field from the Strait of Georgia, off the mouth of the Fraser River, for 21:00 Z, July 31, 1993.

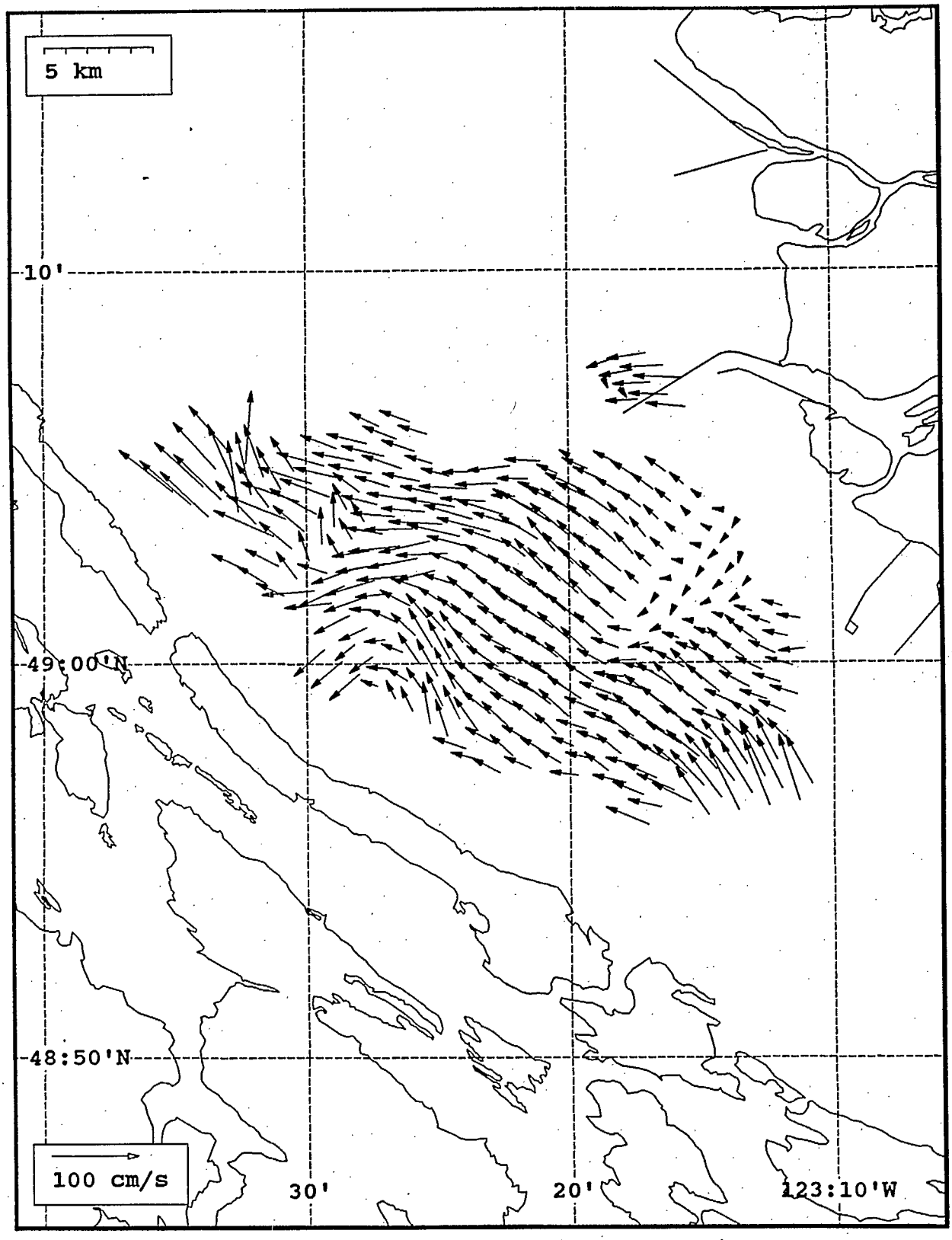

SeaSonde current field from the Strait of Georgia, off the mouth of the Fraser River, for 22:00 Z, July 31, 1993.

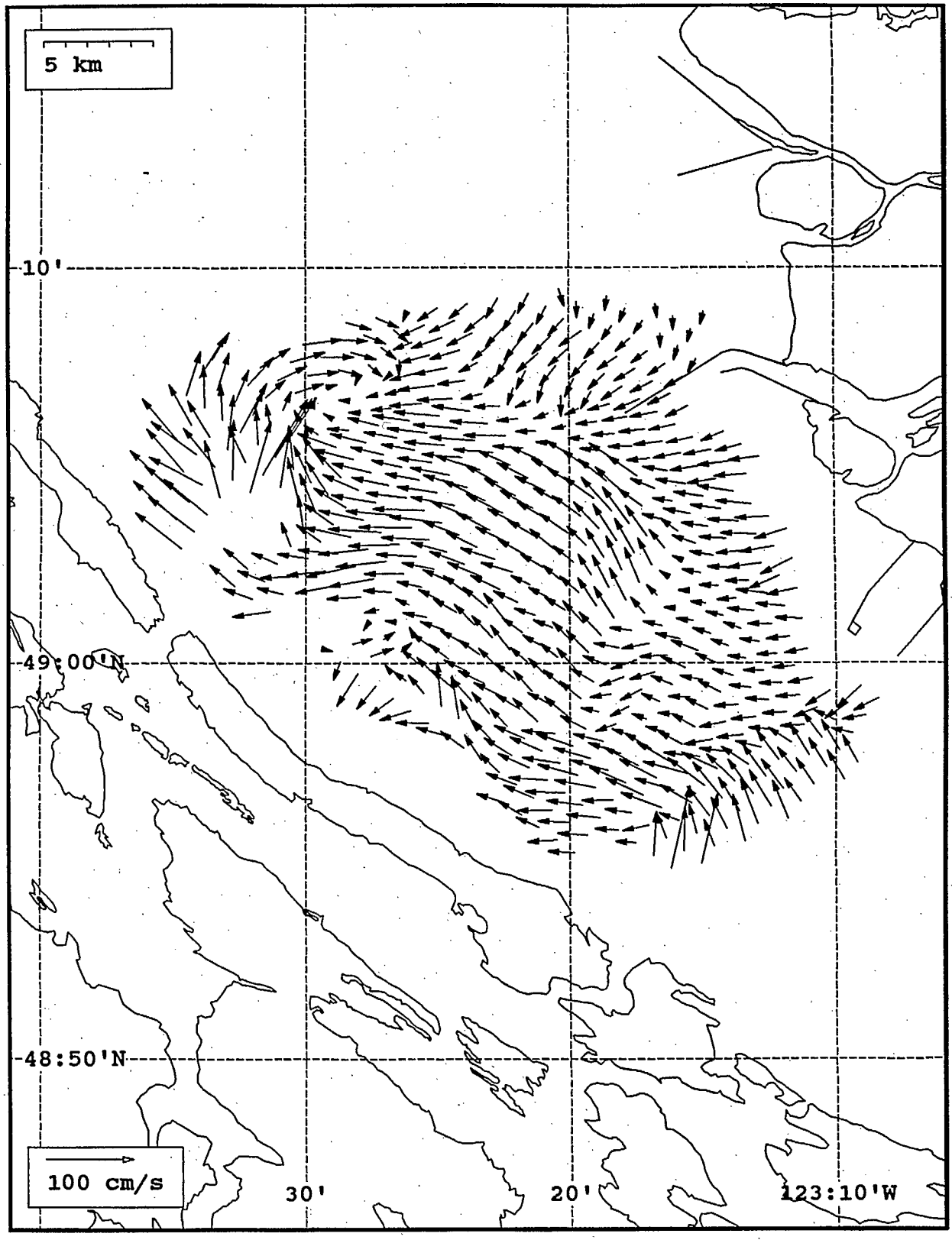

SeaSonde current field from the Strait of Georgia, off the mouth of the Fraser River, for 23:00 Z, July 31, 1993.

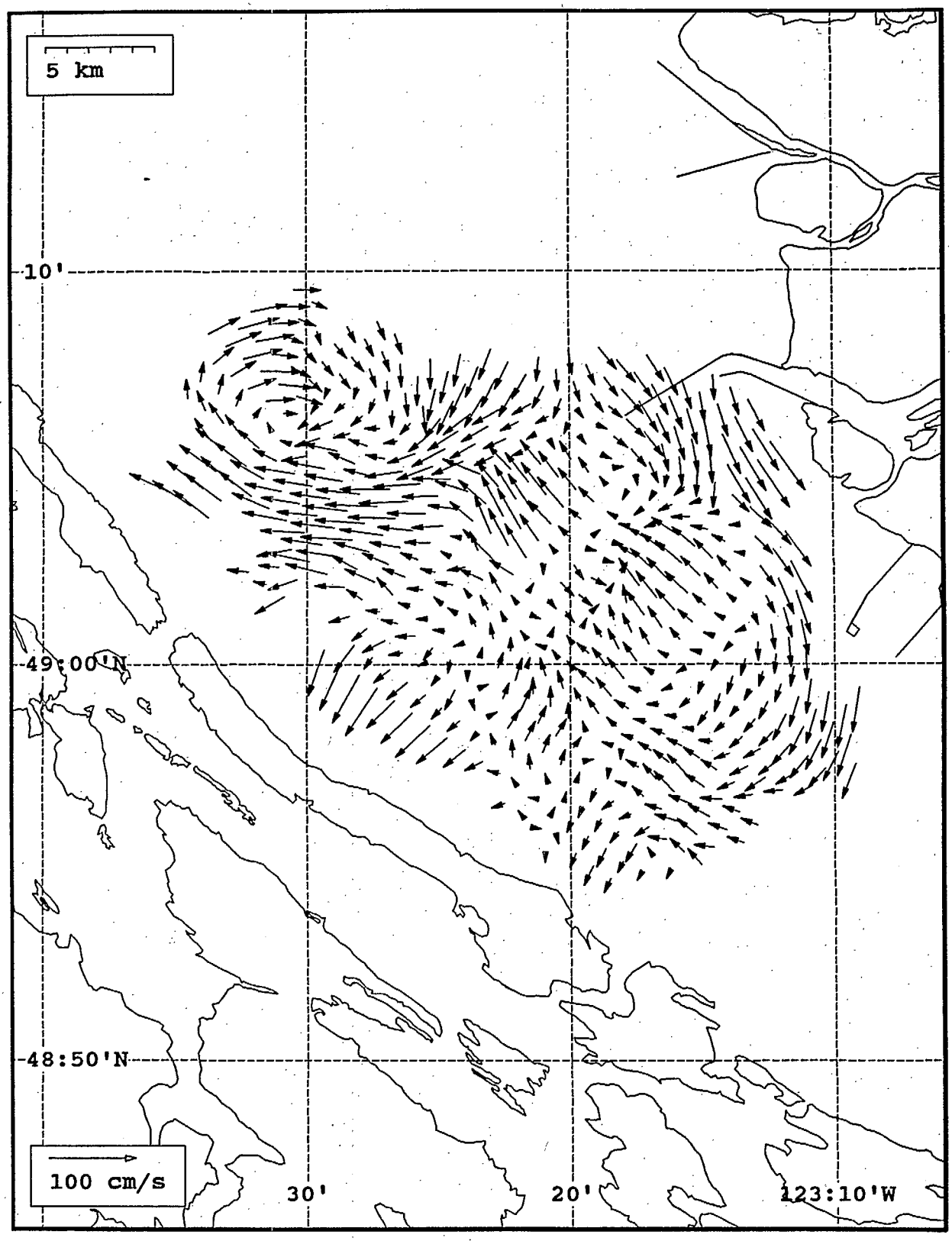

SeaSonde current field from the Strait of Georgia, off the mouth of the Fraser River, for 00:00 Z, August 1, 1993.

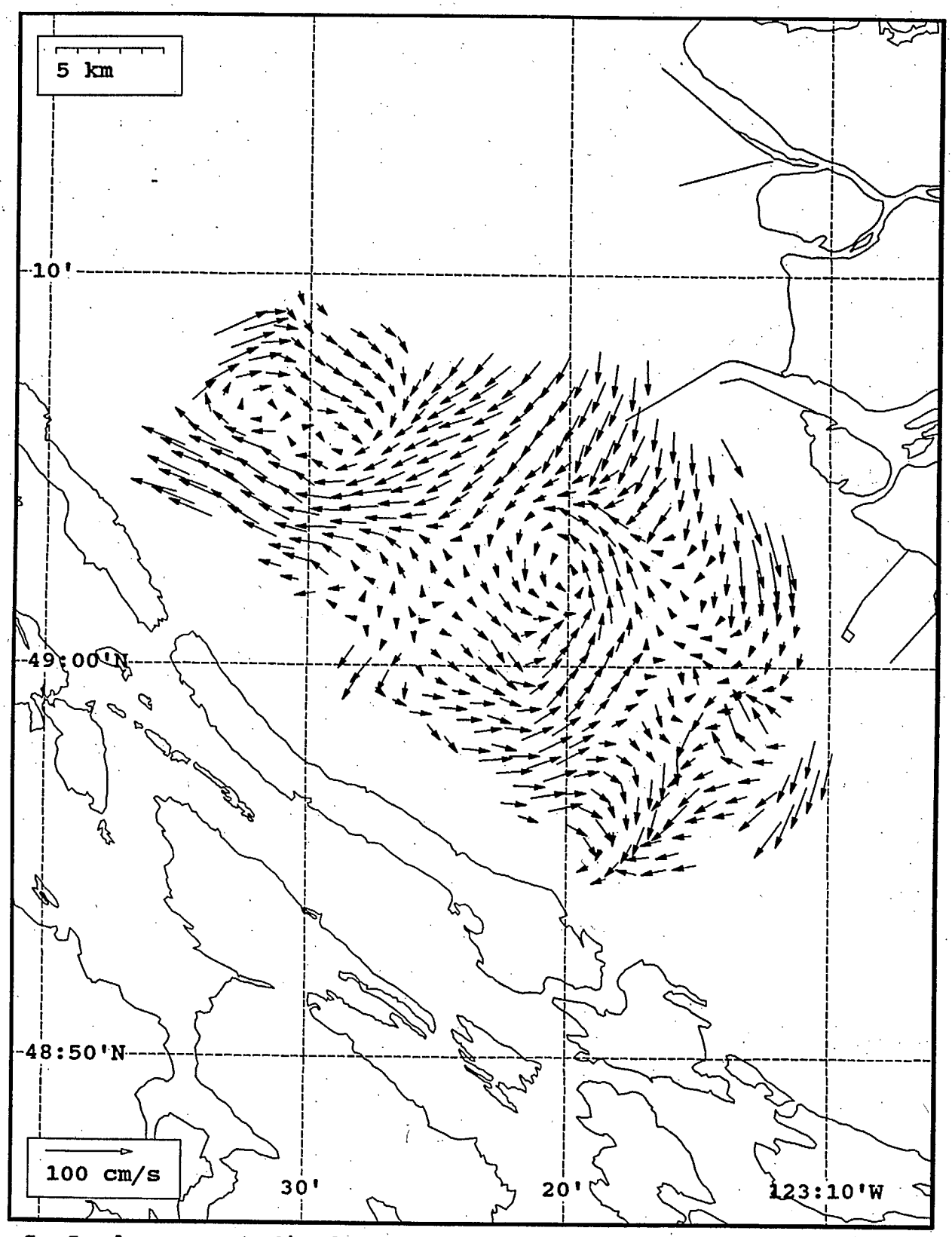

SeaSonde current field from the Strait of Georgia, off the mouth of the Fraser River, for 01:00 Z, August 1, 1993.

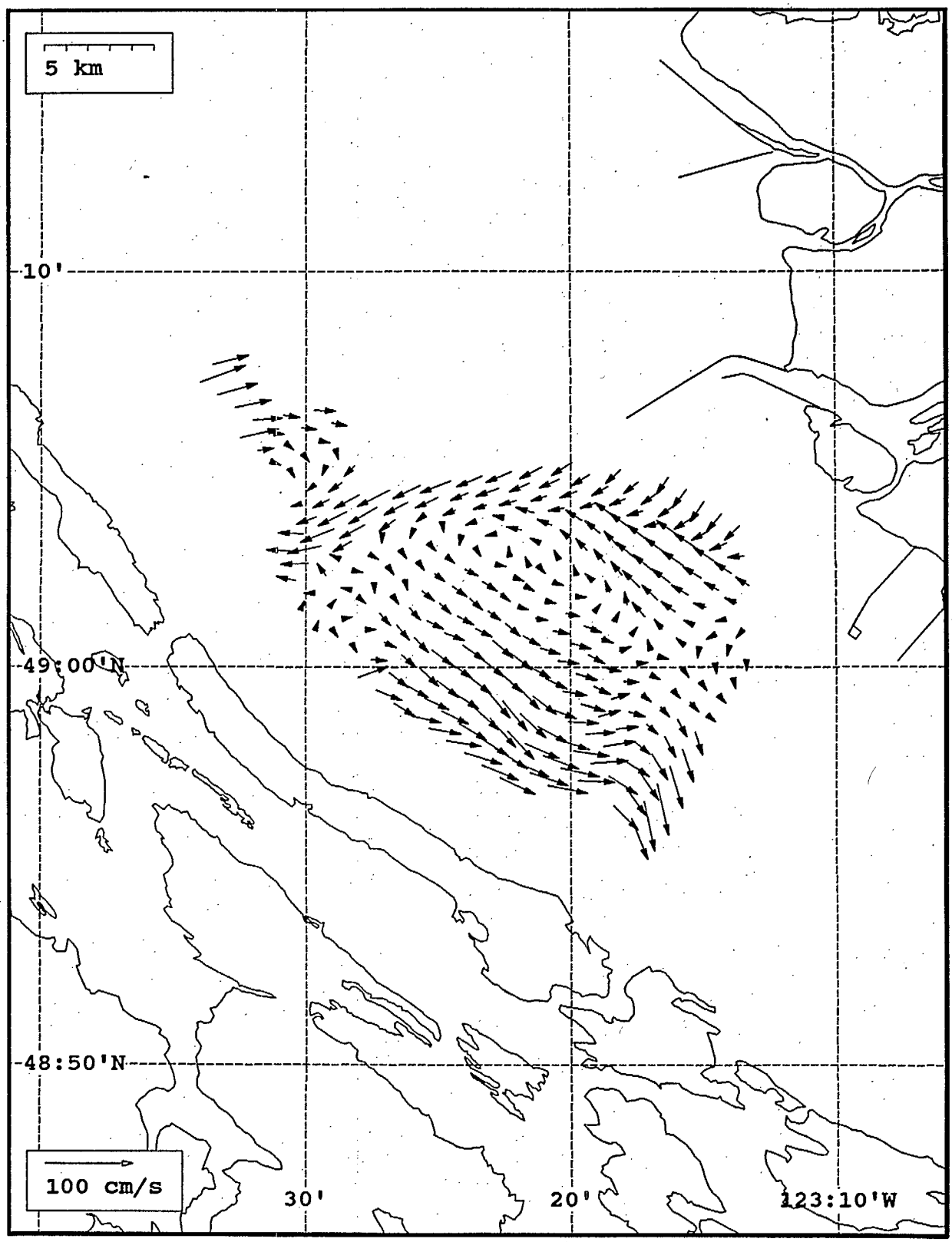

SeaSonde current field from the Strait of Georgia, off the mouth of the Fraser River, for 02:00 Z, August 1, 1993.

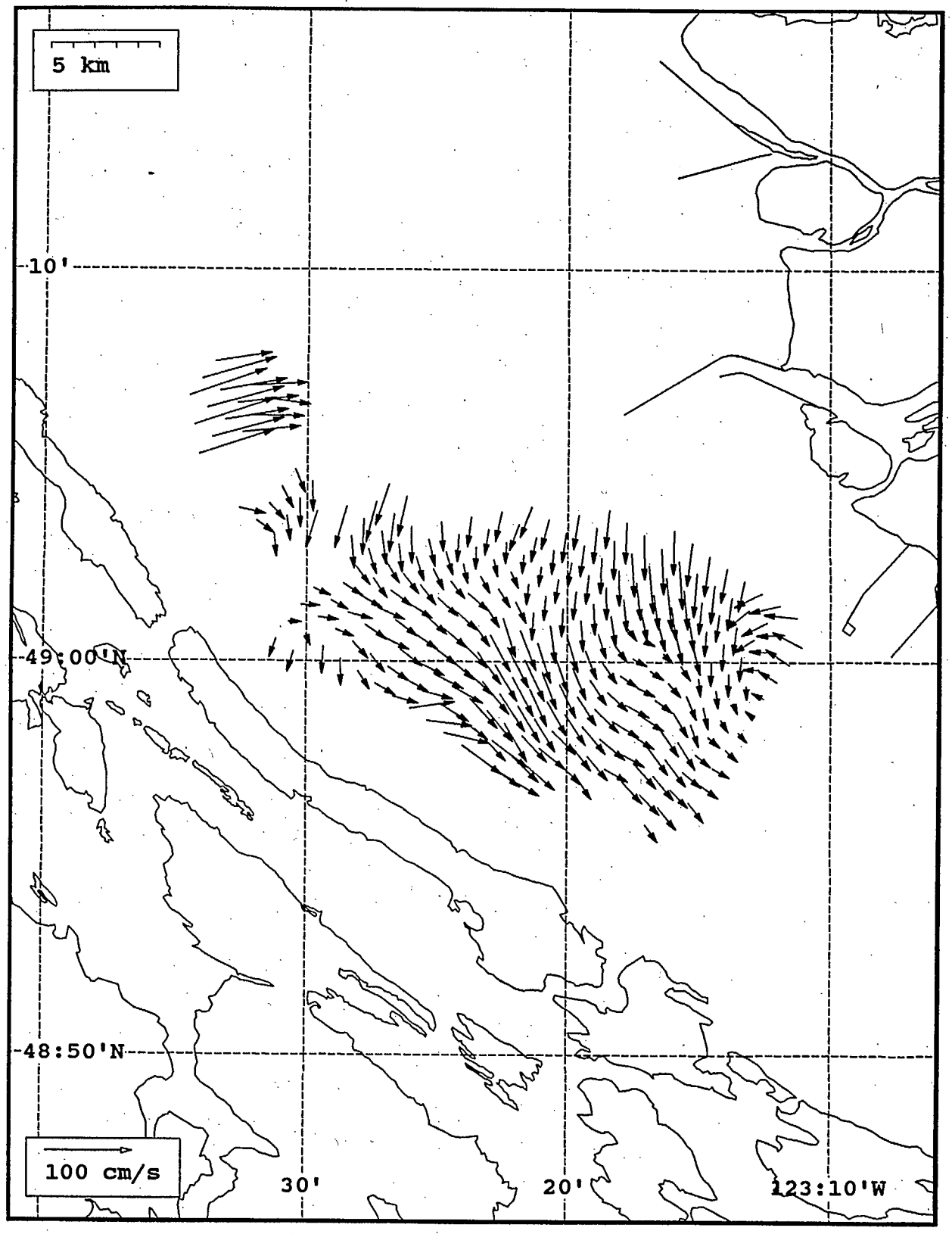

SeaSonde current field from the Strait of Georgia, off the mouth of the Fraser River, for 03:00 Z, August 1, 1993.

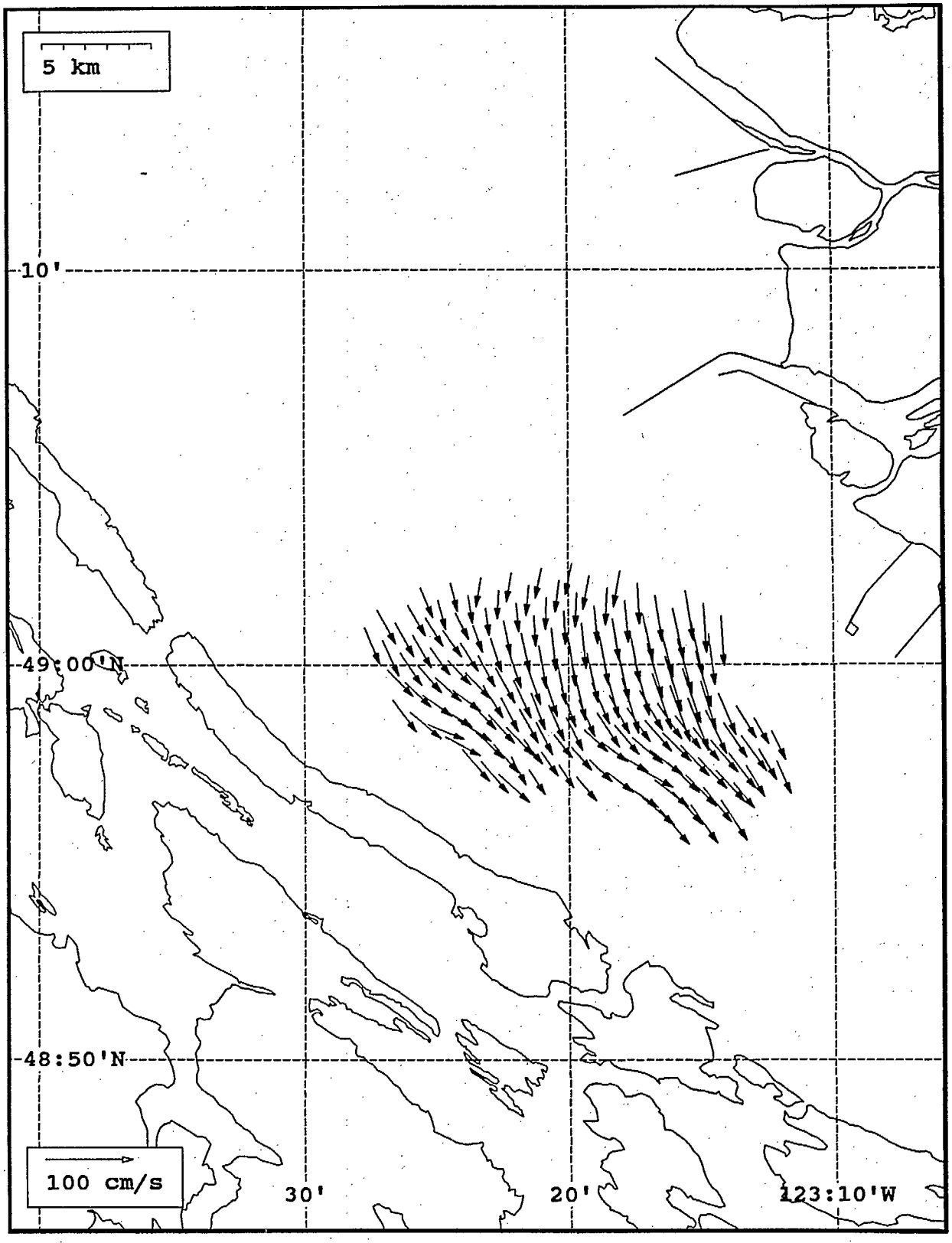

SeaSonde current field from the Strait of Georgia, off the mouth of the Fraser River, for 04:00 Z, August 1, 1993.

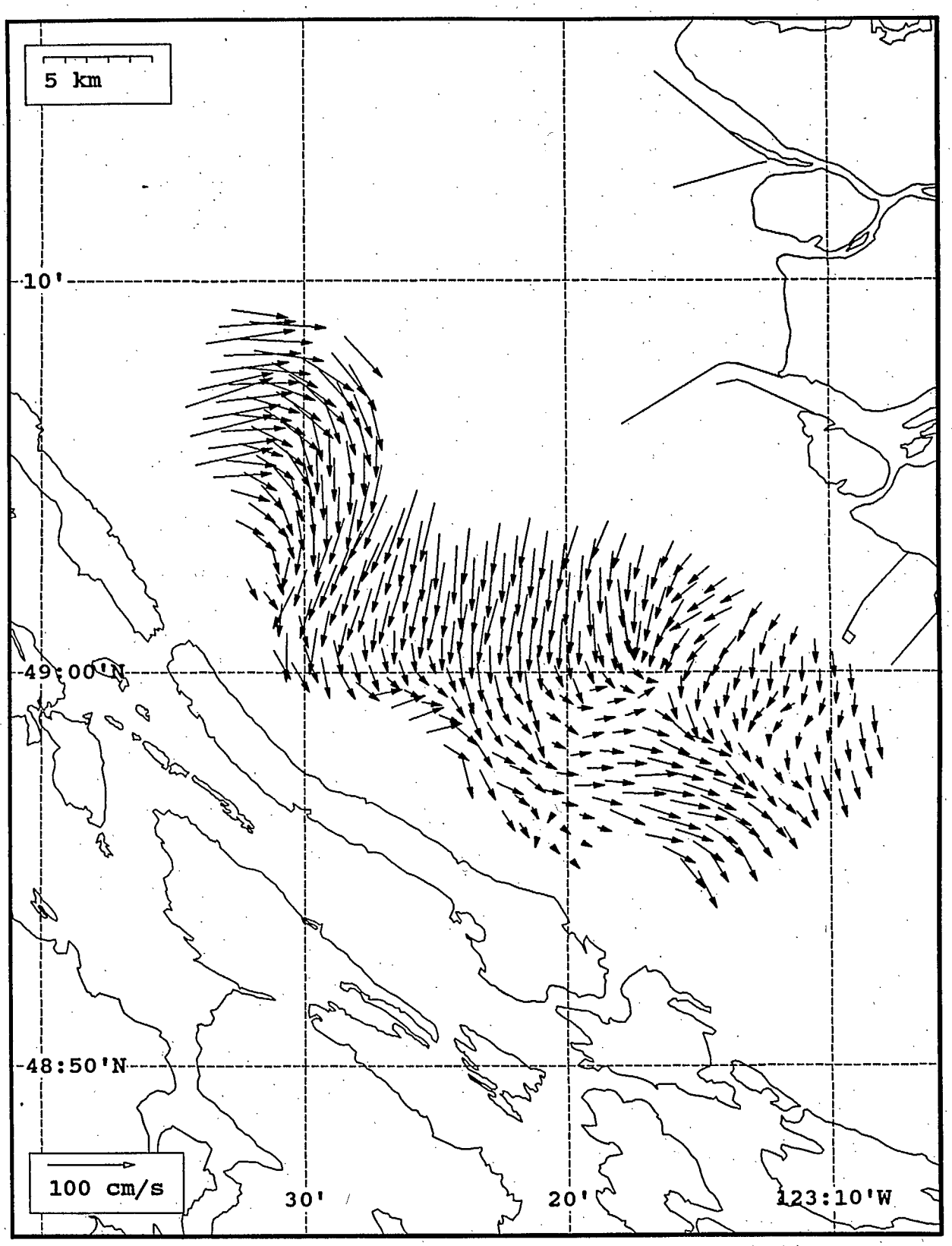

SeaSonde current field from the Strait of Georgia, off the mouth of the Fraser River, for 05:00 Z, August 1, 1993.

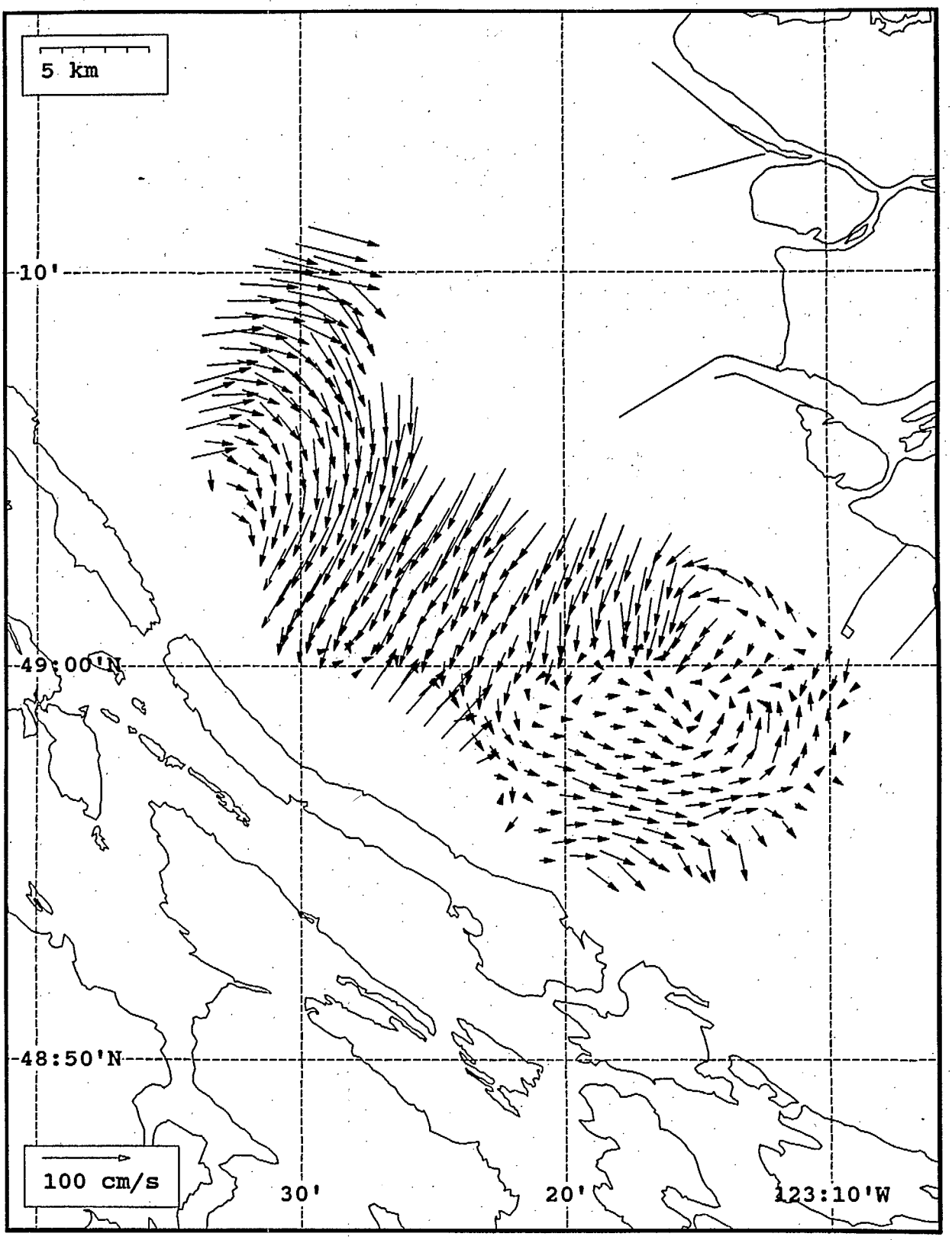

SeaSonde current field from the Strait of Georgia, off the mouth of the Fraser River, for 06:00 Z, August 1, 1993.

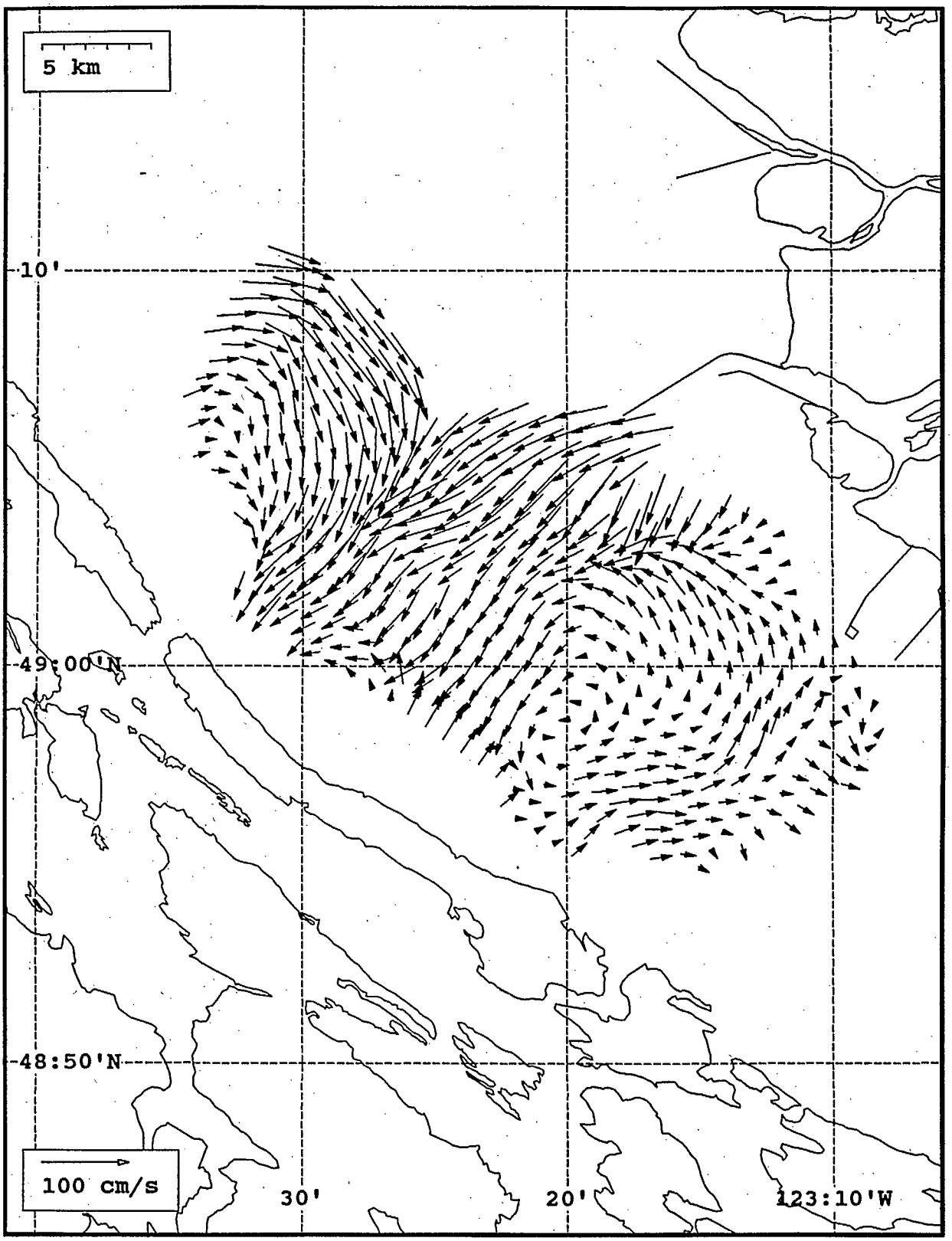

SeaSonde current field from the Strait of Georgia, off the mouth of the Fraser River, for 07:00 Z, August 1, 1993.

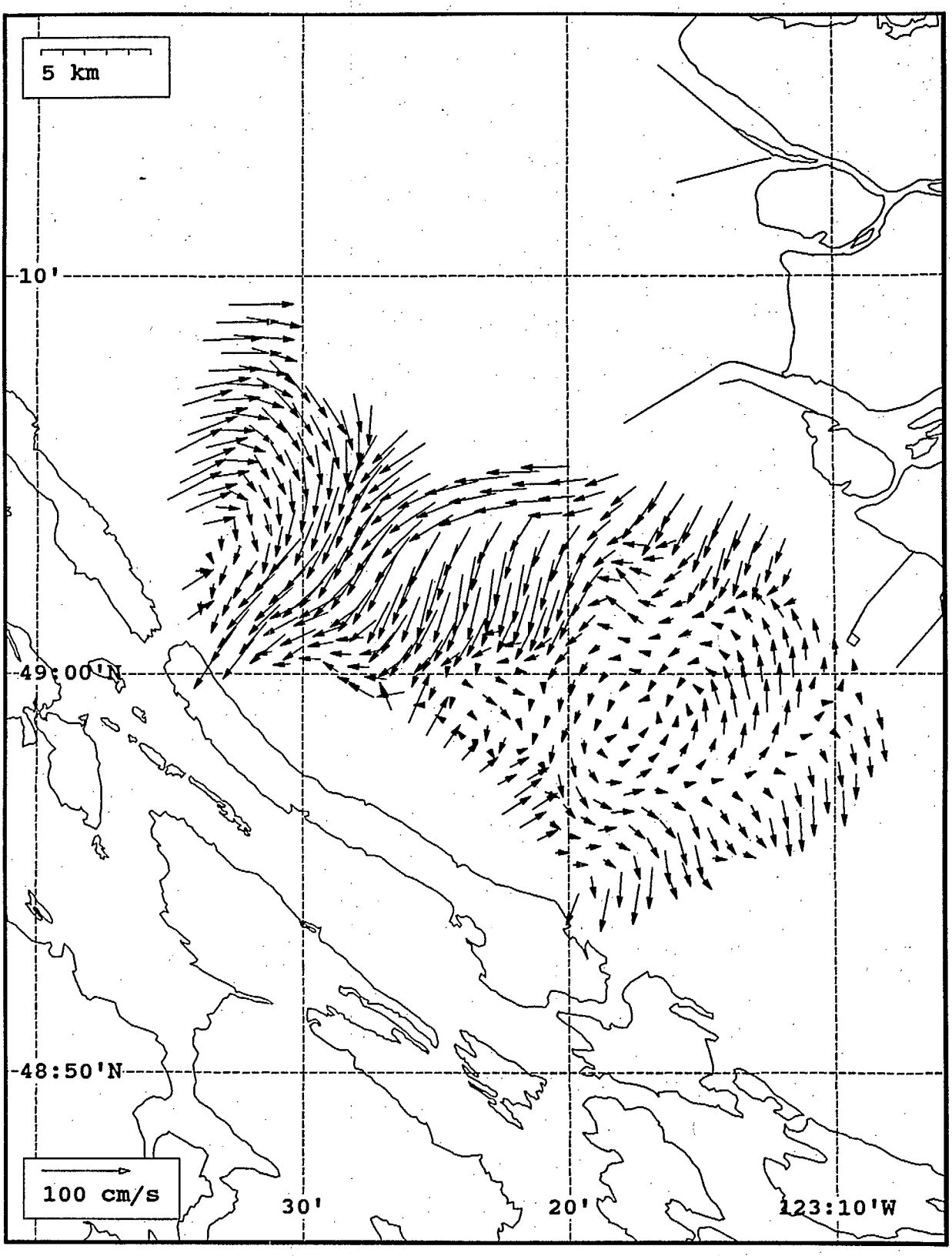

SeaSonde current field from the Strait of Georgia, off the mouth of the Fraser River, for 08:00 Z, August 1, 1993.

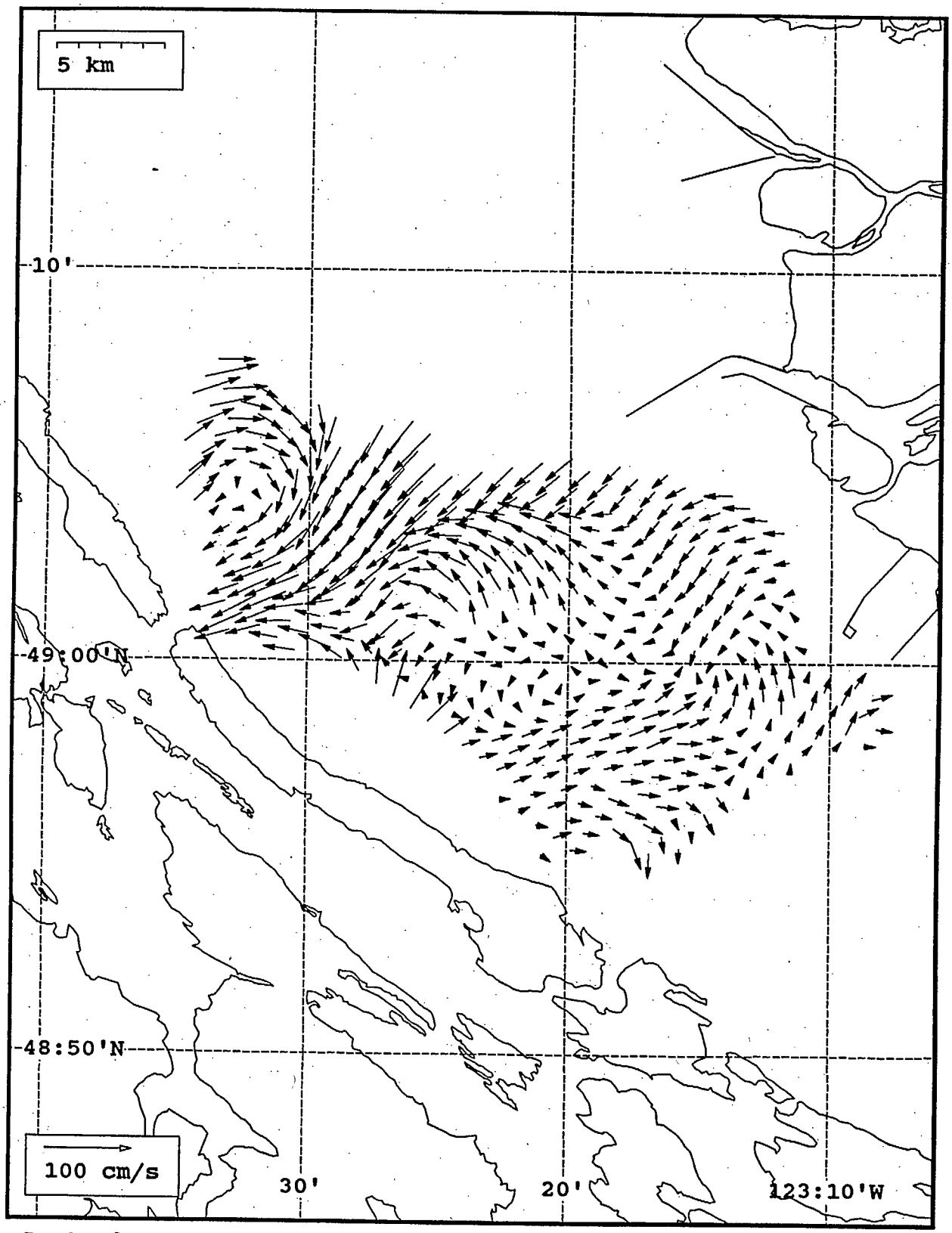

SeaSonde current field from the Strait of Georgia, off the mouth of the Fraser River, for 09:00 Z, August 1, 1993.

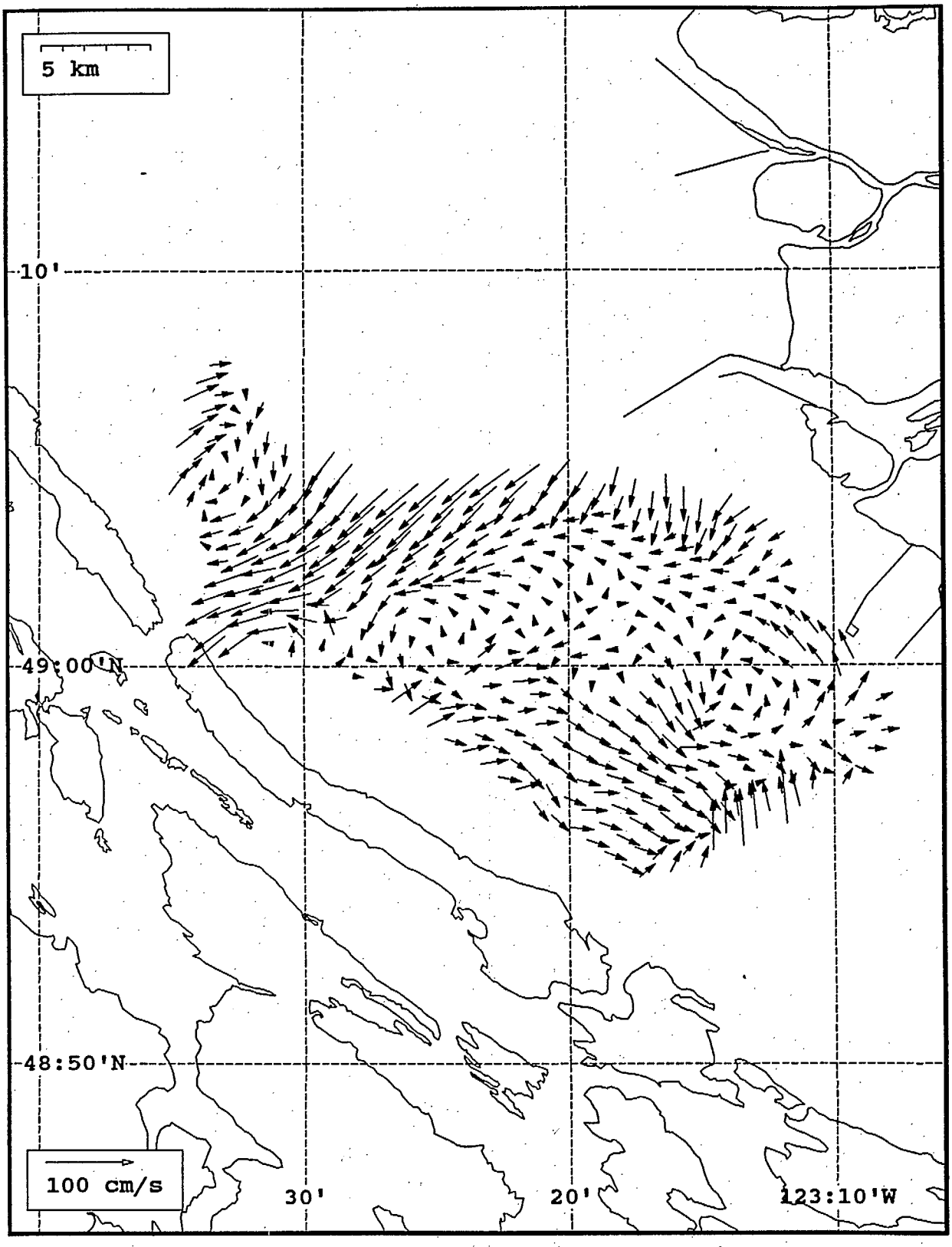

SeaSonde current field from the Strait of Georgia, off the mouth of the Fraser River, for 10:00 Z, August 1, 1993.

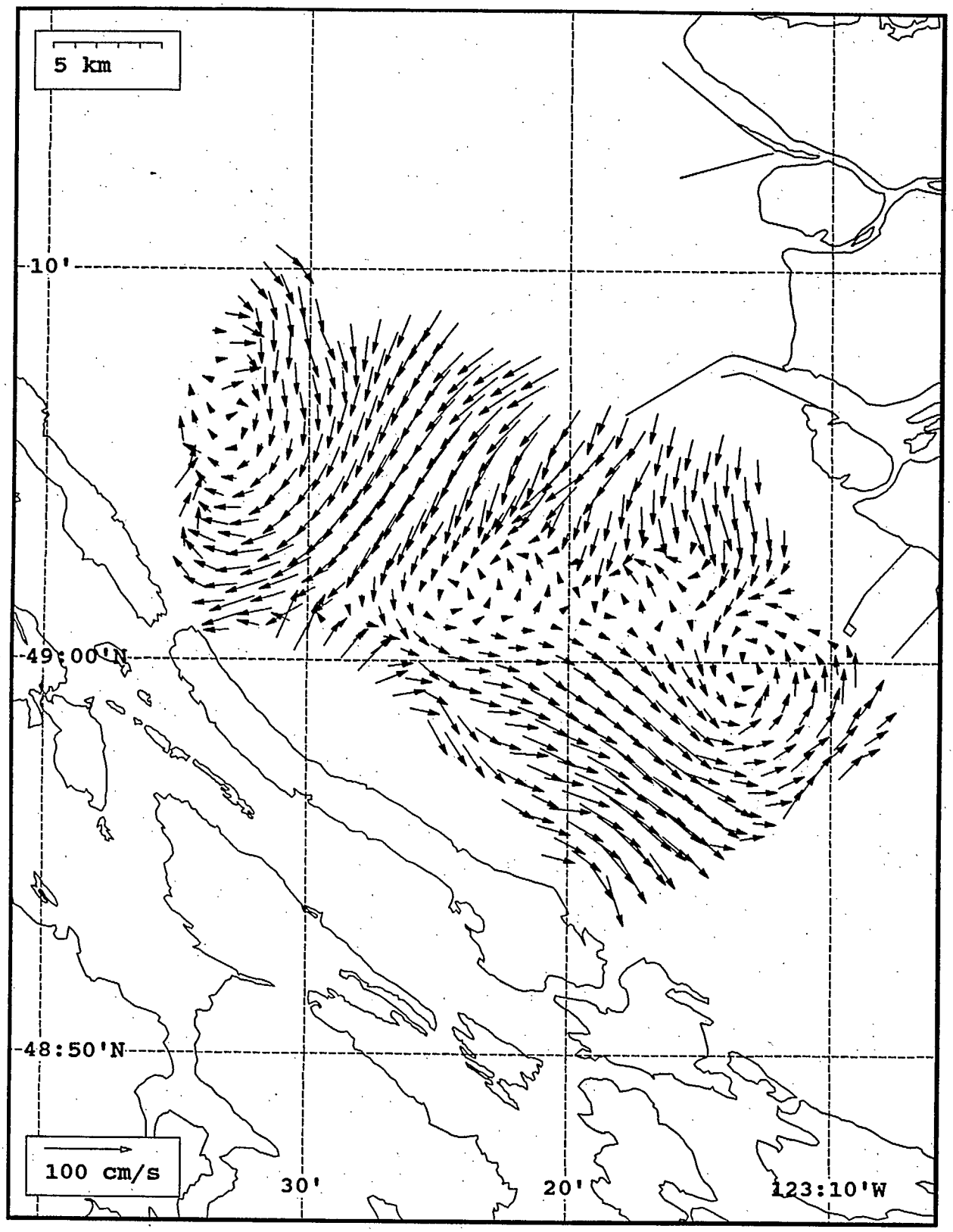

SeaSonde current field from the Strait of Georgia, off the mouth of the Fraser River, for 11:00 Z, August 1, 1993.

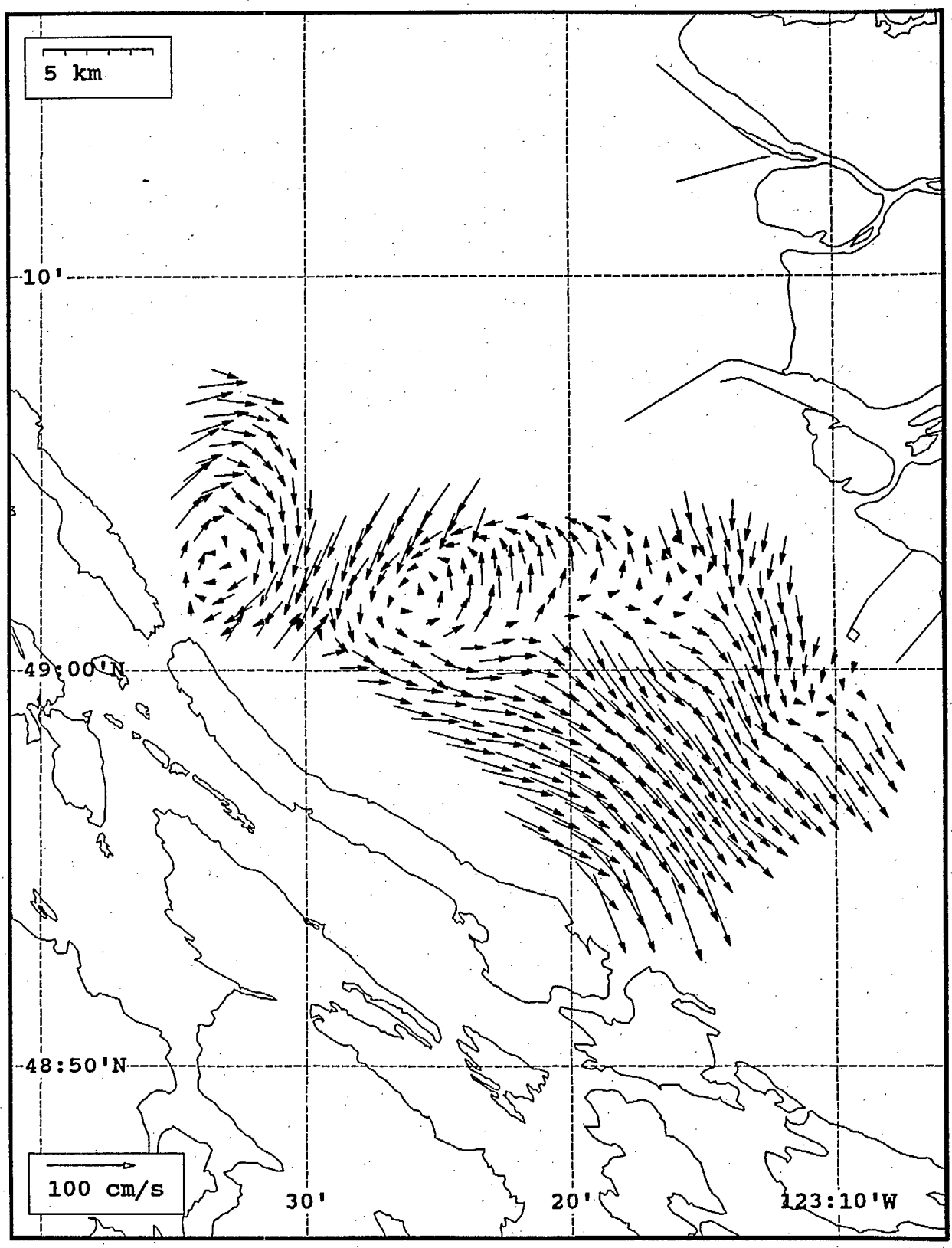

SeaSonde current field from the Strait of Georgia, off the mouth of the Fraser River, for 12:00 Z, August 1, 1993.

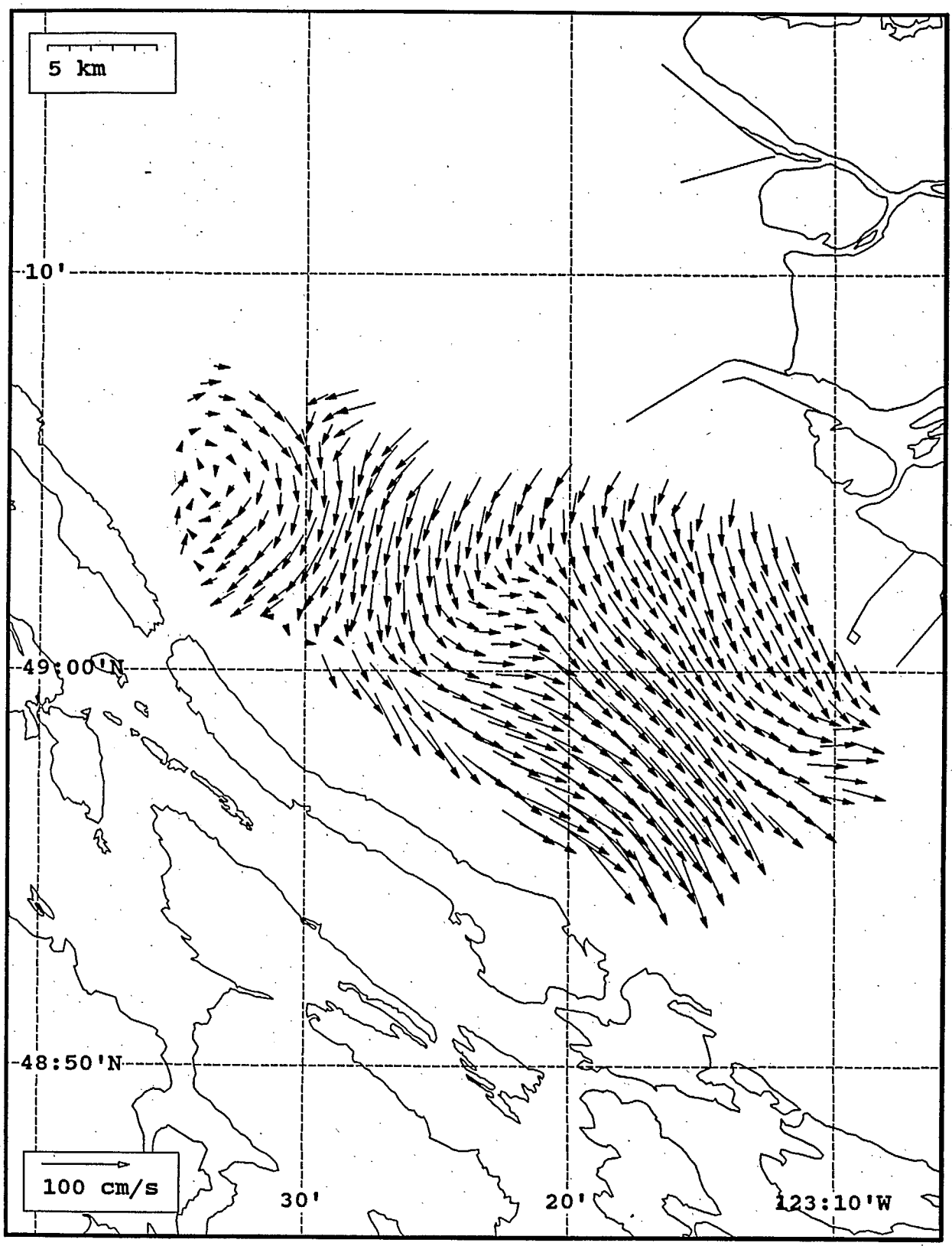

SeaSonde current field from the Strait of Georgia, off the mouth of the Fraser River, for 13:00 Z, August 1, 1993.

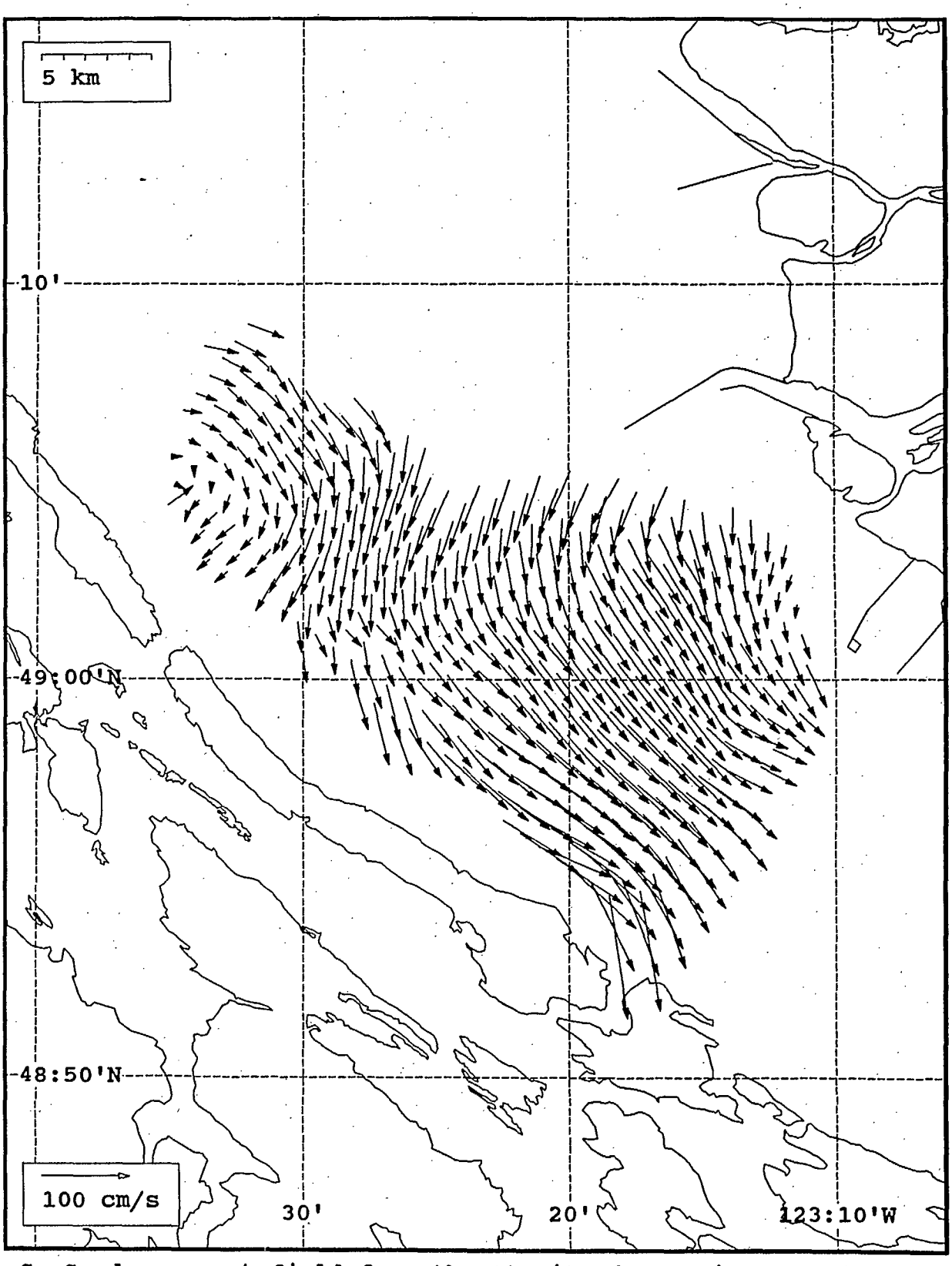

SeaSonde current field from the Strait of Georgia, off the mouth of the Fraser River, for 14:00 Z, August 1, 1993.

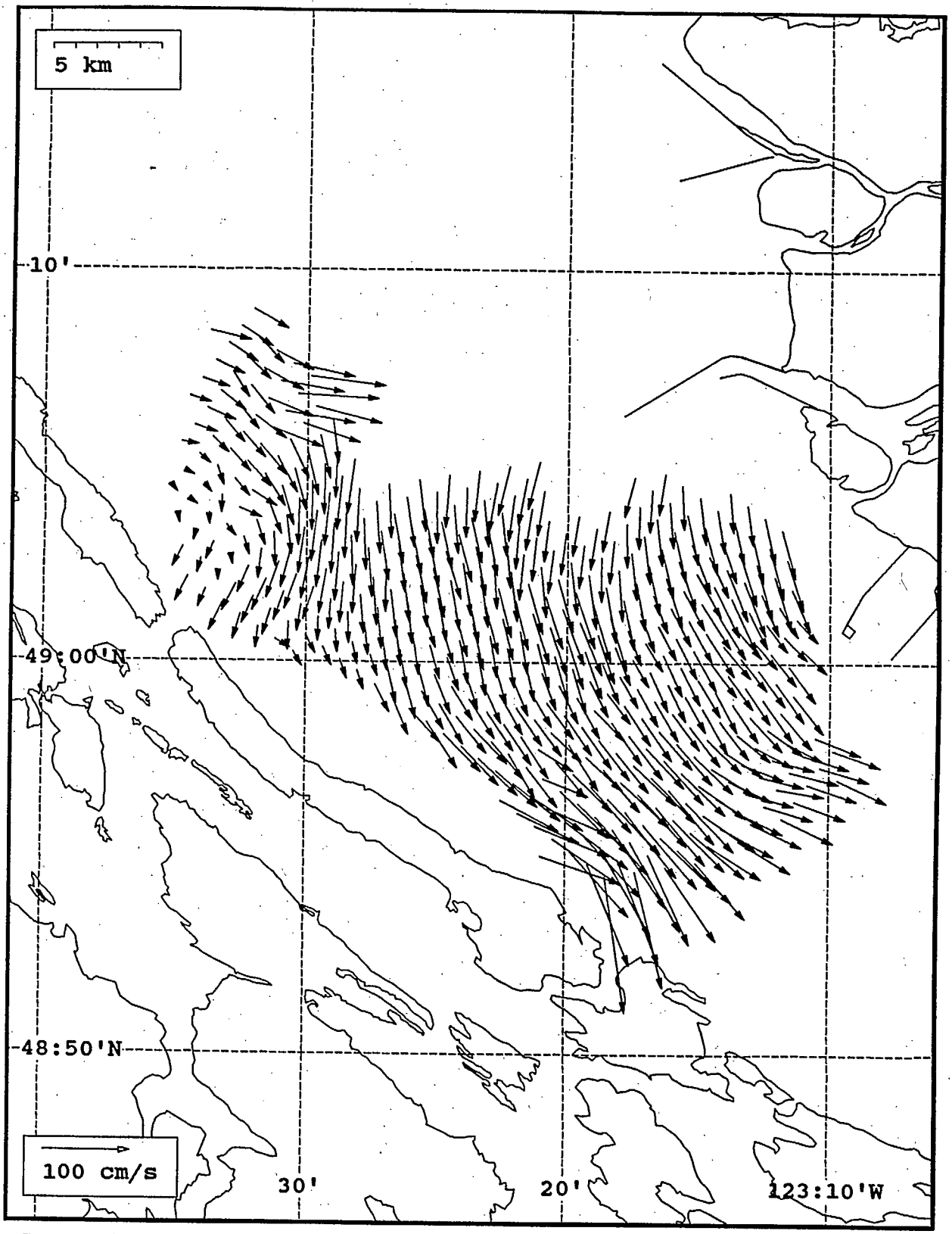

SeaSonde current field from the Strait of Georgia, off the mouth of the Fraser River, for 15:00 Z, August 1, 1993.

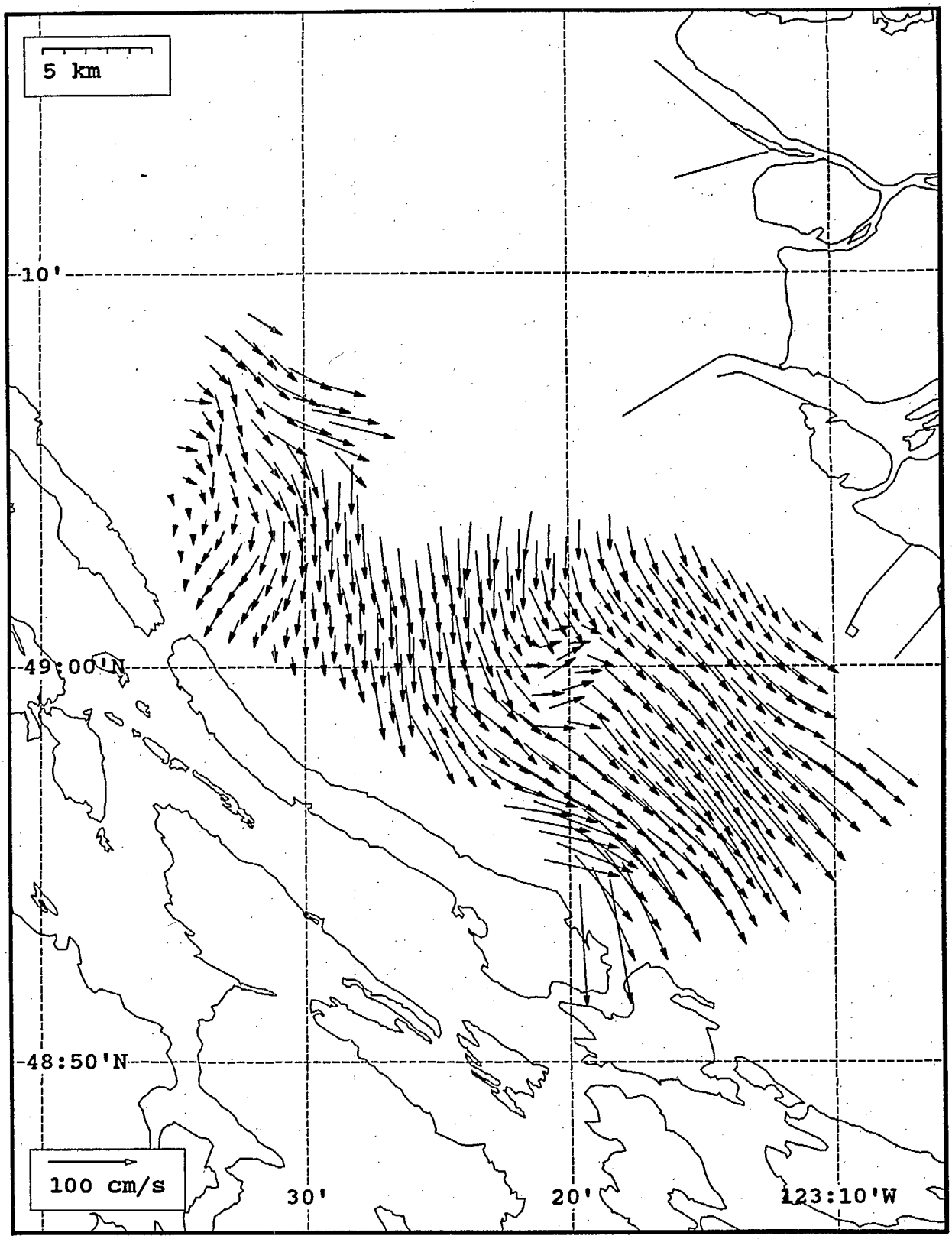

SeaSonde current field from the Strait of Georgia, off the mouth of the Fraser River, for 16:00 Z, August 1, 1993.

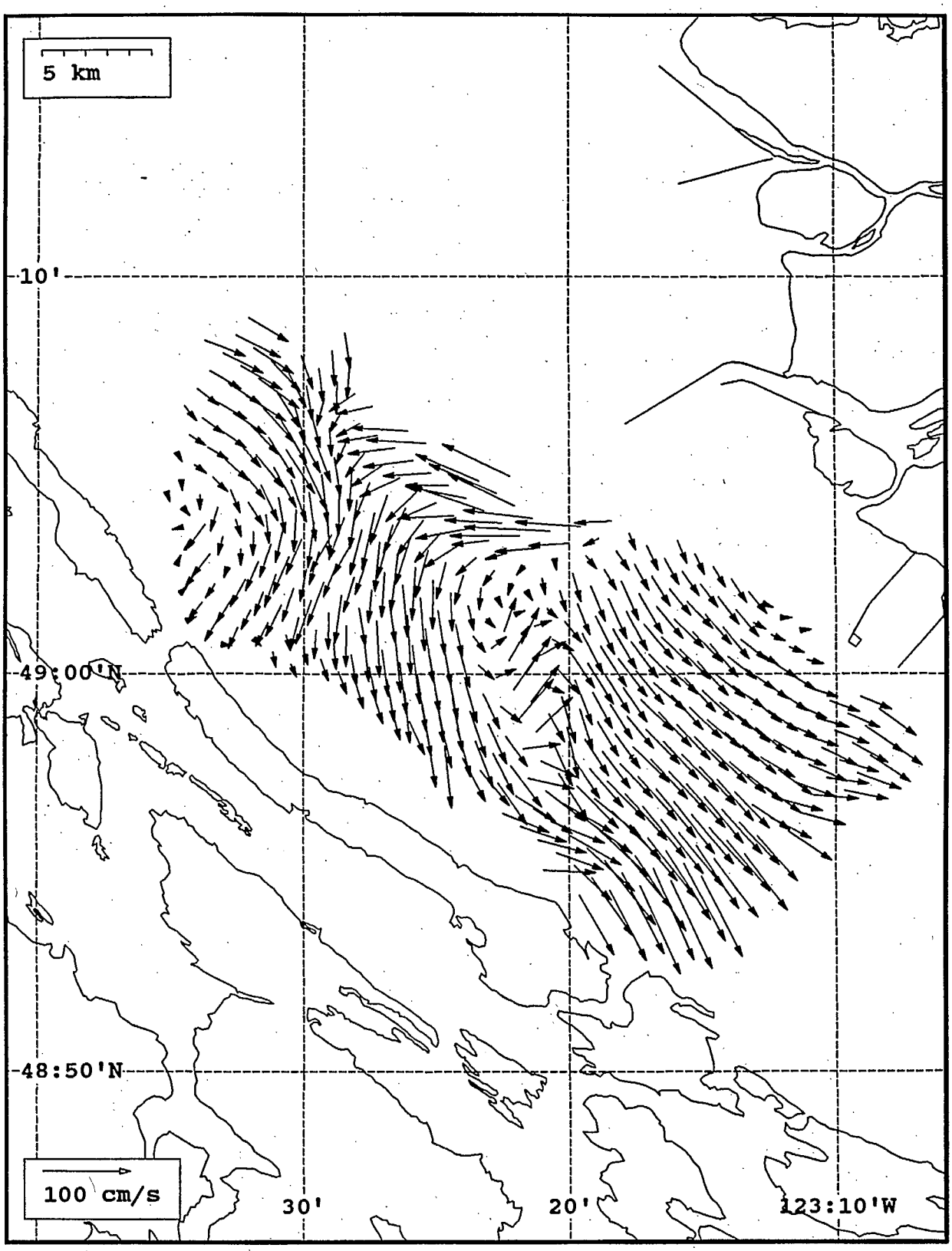

SeaSonde current field from the Strait of Georgia, off the mouth of the Fraser River, for 17:00 Z, August 1, 1993.

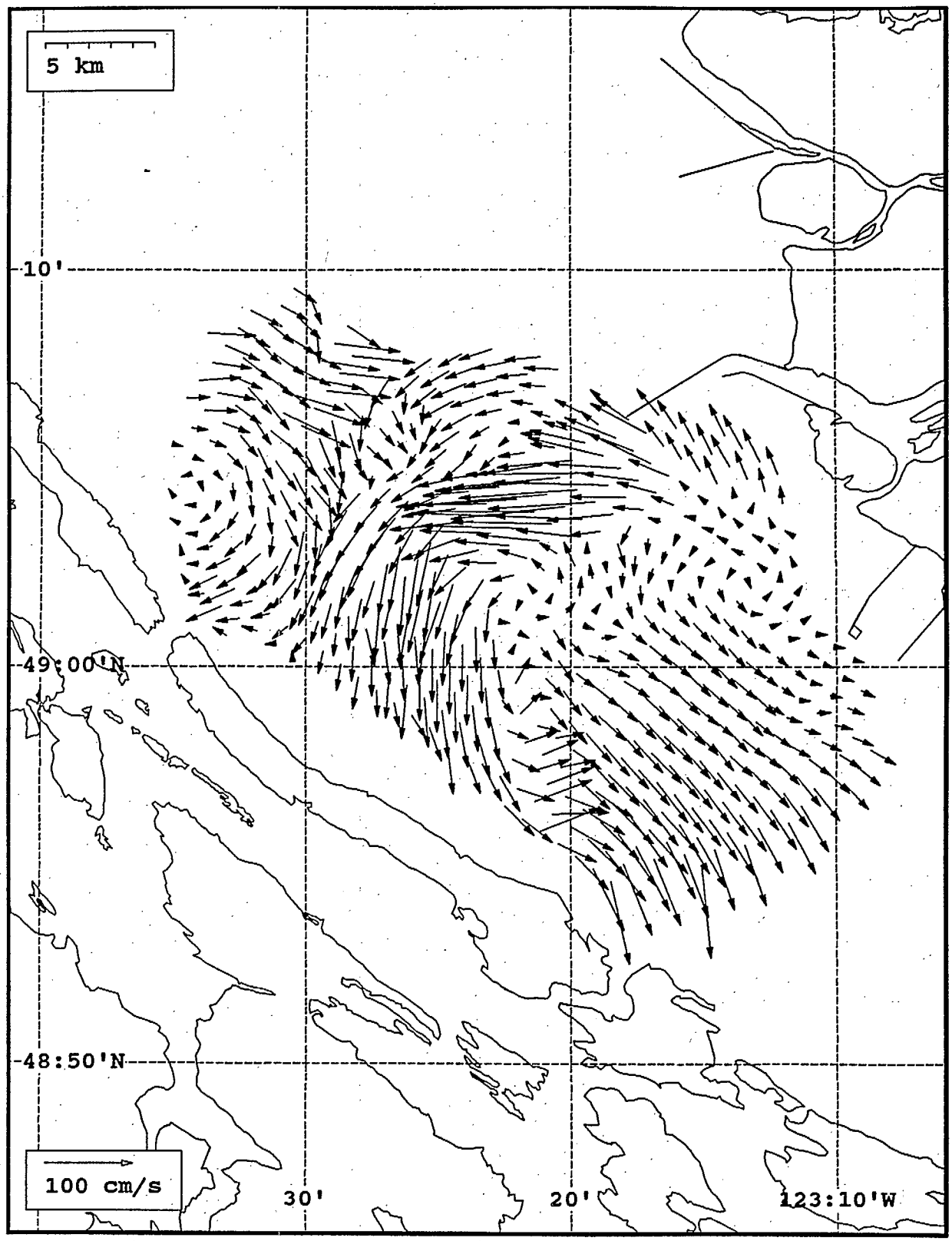

SeaSonde current field from the Strait of Georgia, off the mouth of the Fraser River, for 18:00 Z, August 1, 1993.

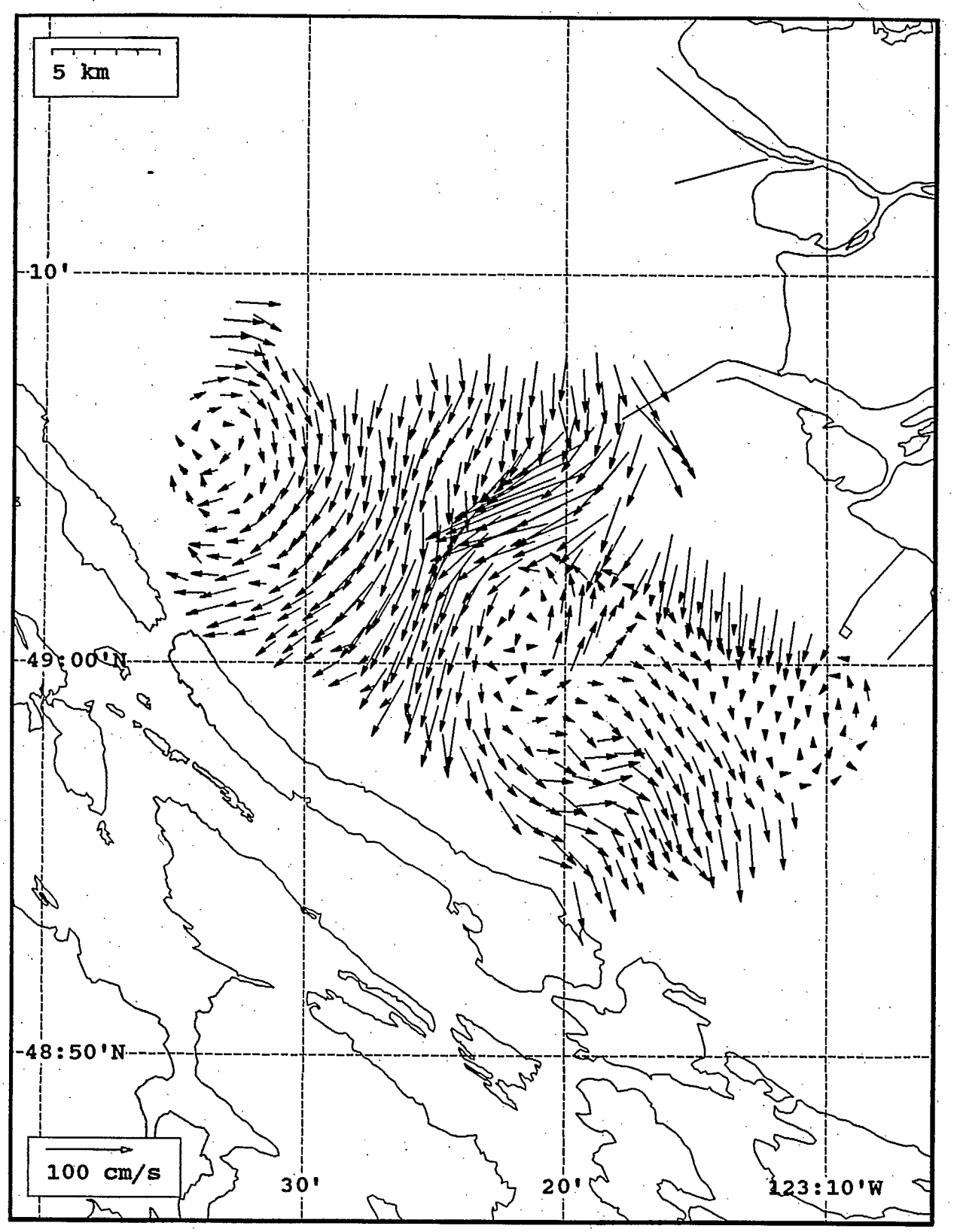

SeaSonde current field from the Strait of Georgia, off the mouth of the Fraser River, for 19:00 Z, August 1, 1993.

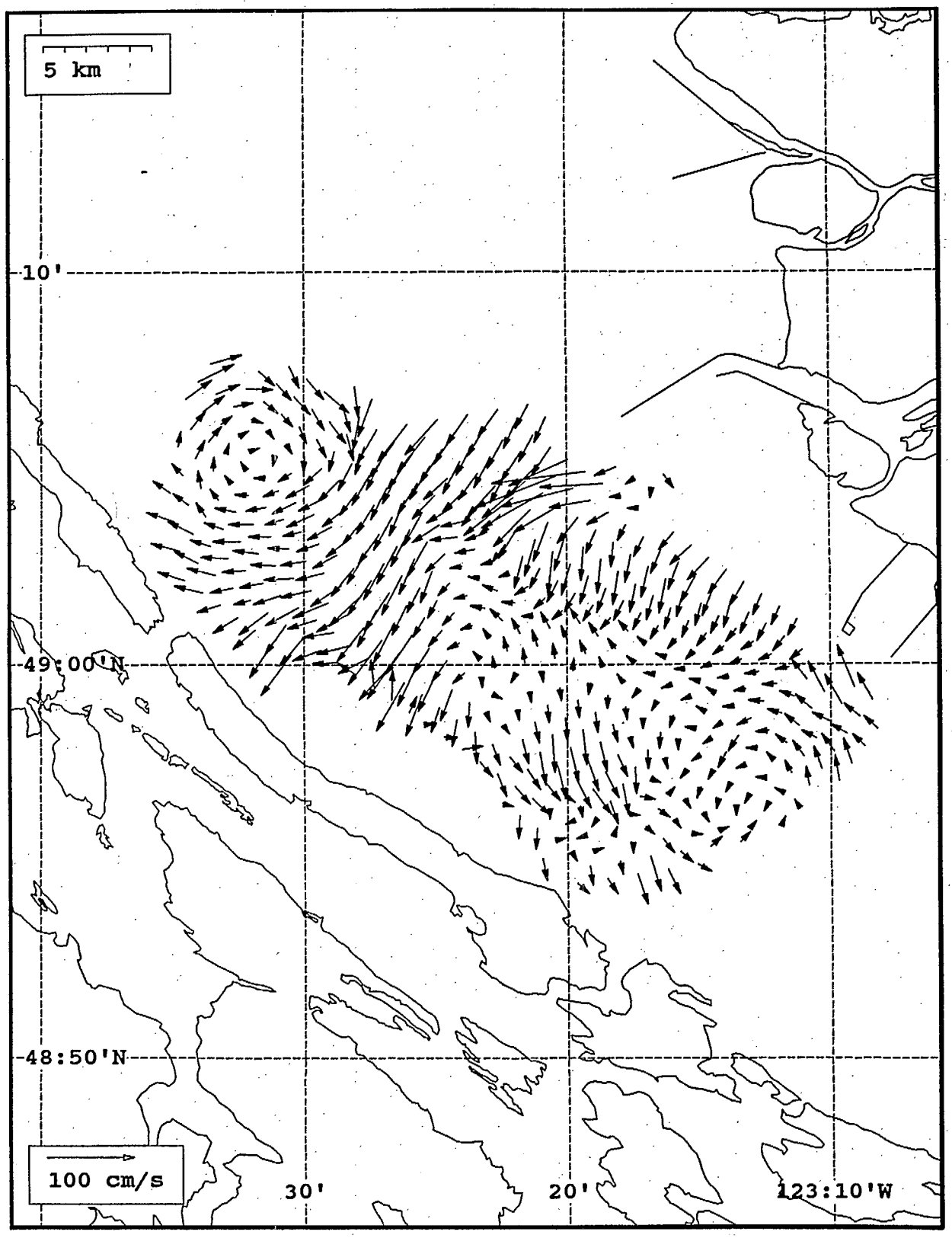

SeaSonde current field from the Strait of Georgia, off the mouth of the Fraser River, for 20:00 Z, August 1, 1993.

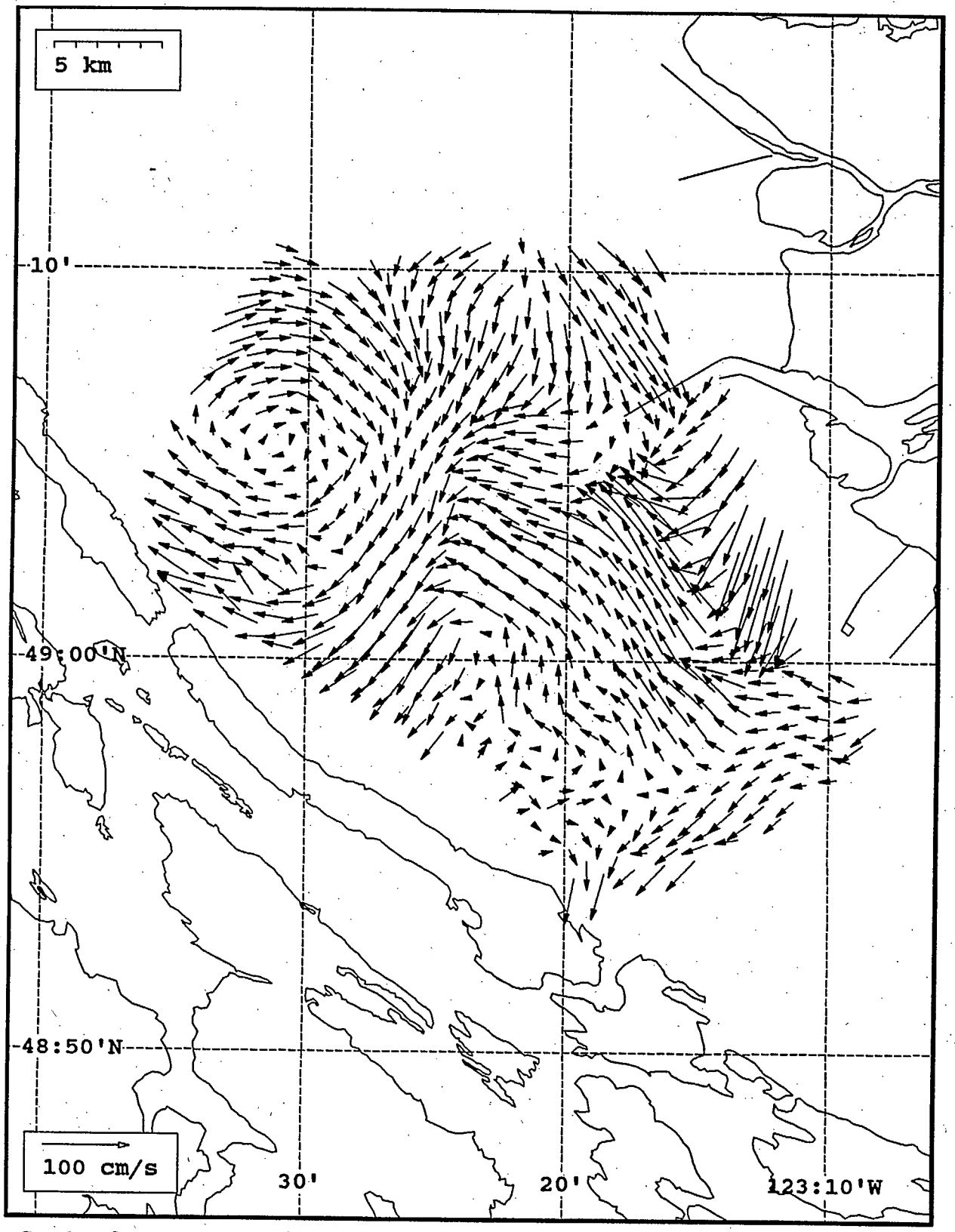

SeaSonde current field from the Strait of Georgia, off the mouth of the Fraser River, for 21:00 Z, August 1, 1993.

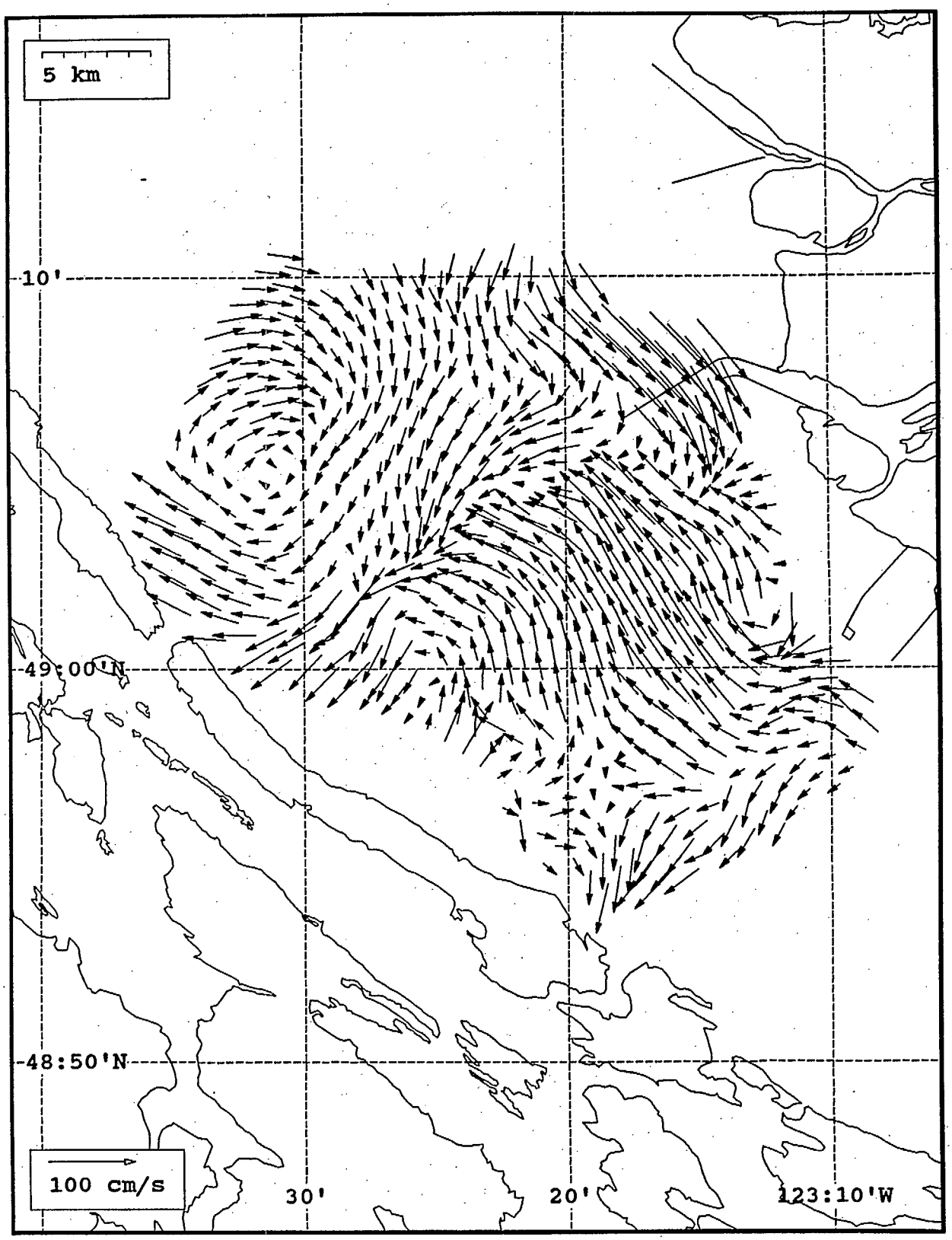

SeaSonde current field from the Strait of Georgia, off the mouth of the Fraser River, for 22:00 Z, August 1, 1993.

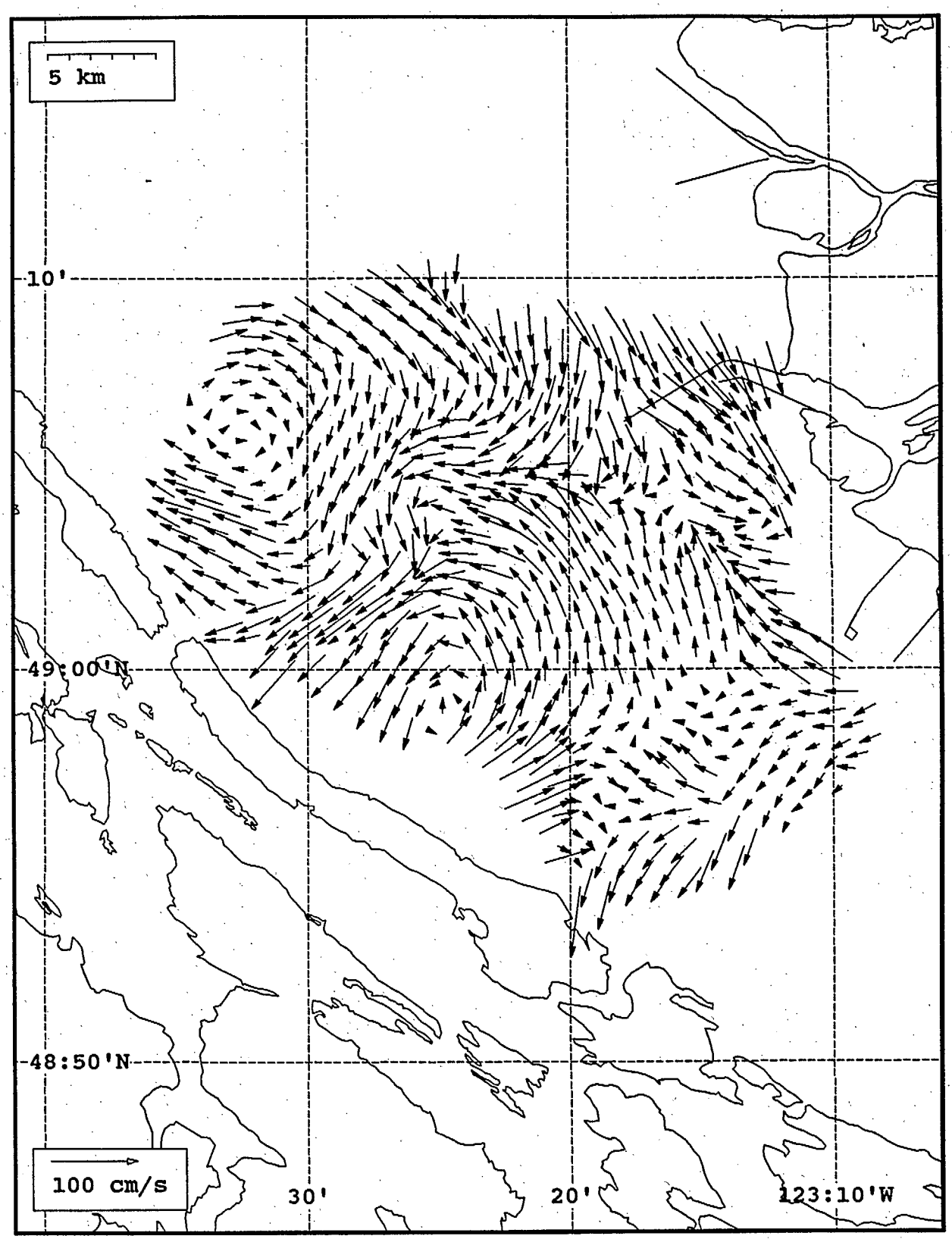

SeaSonde current field from the Strait of Georgia, off the mouth of the Fraser River, for 23:00 Z, August 1, 1993.

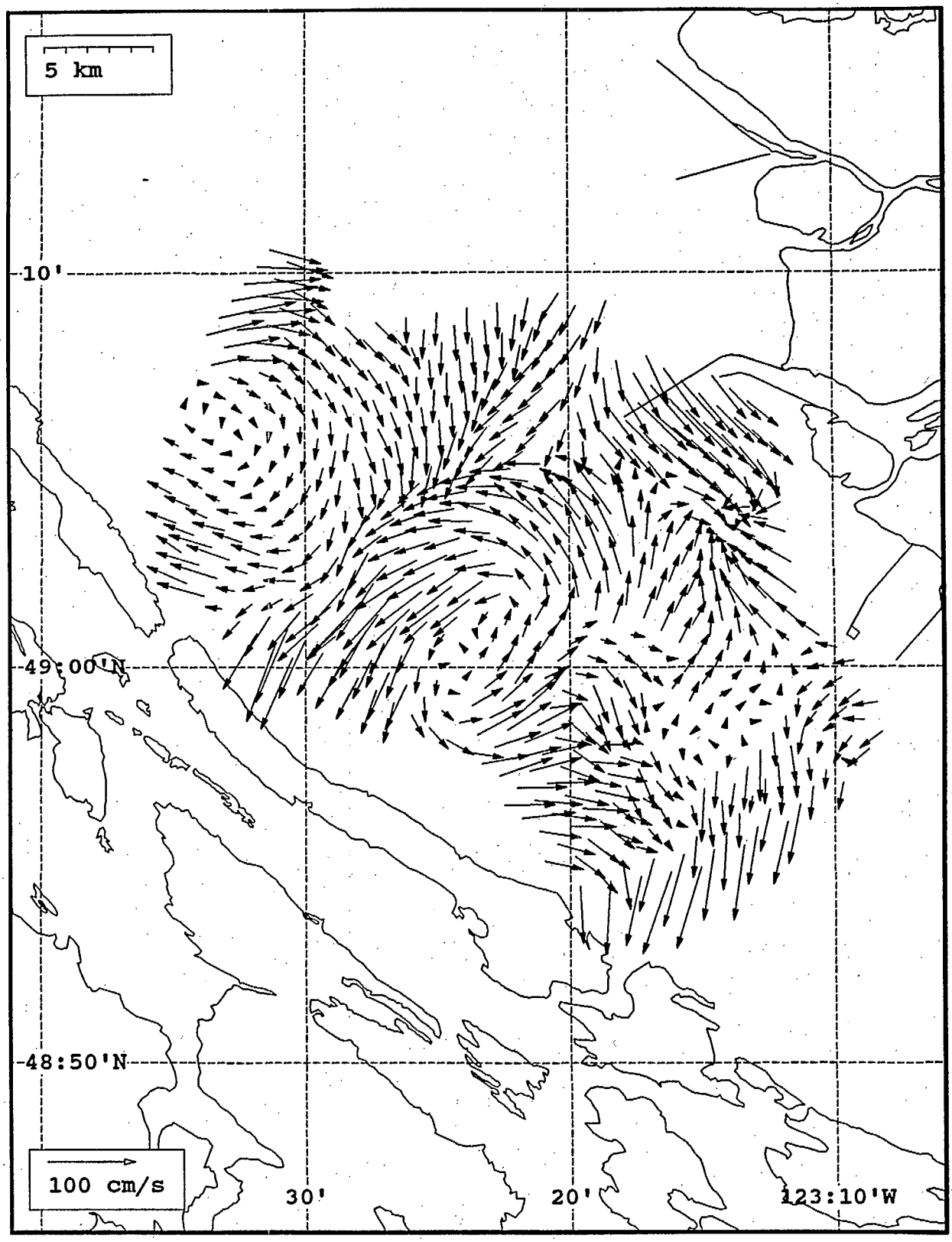

SeaSonde current field from the Strait of Georgia, off the mouth of the Fraser River, for 00:00 Z, August 2, 1993.

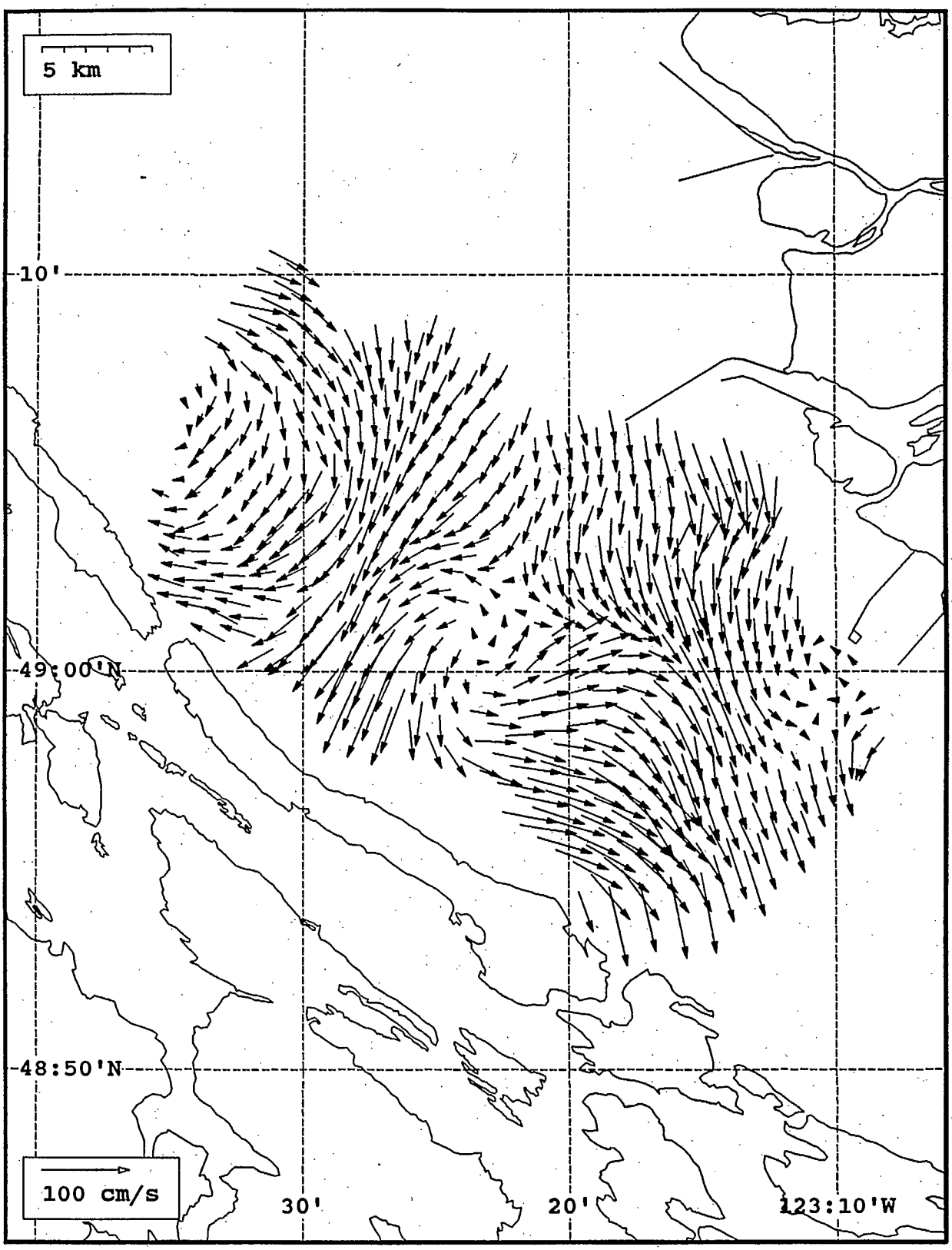

SeaSonde current field from the Strait of Georgia, off the mouth of the Fraser River, for 01:00 Z, August 2, 1993.

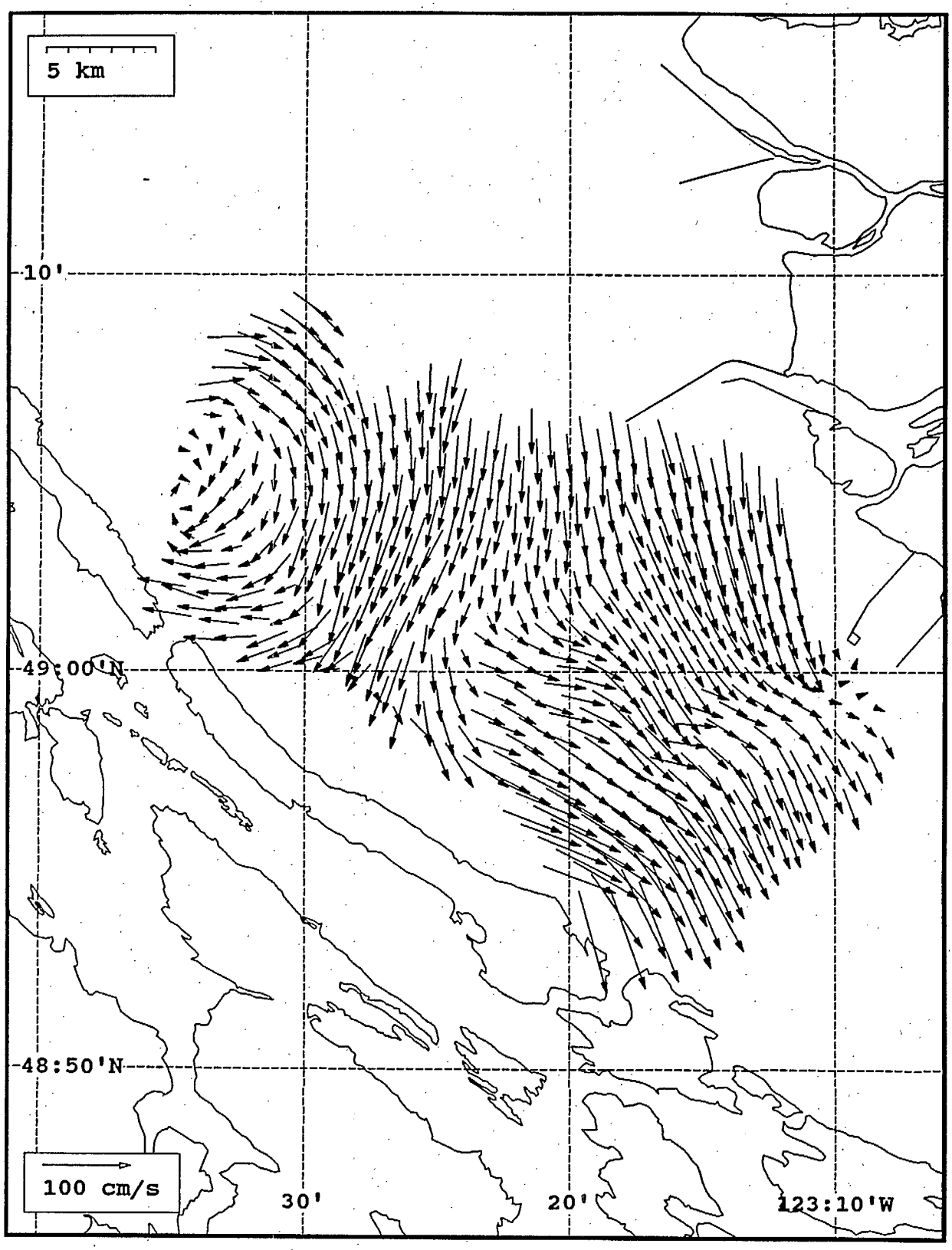

SeaSonde current field from the Strait of Georgia, off the mouth of the Fraser River, for 02:00 Z, August 2, 1993.

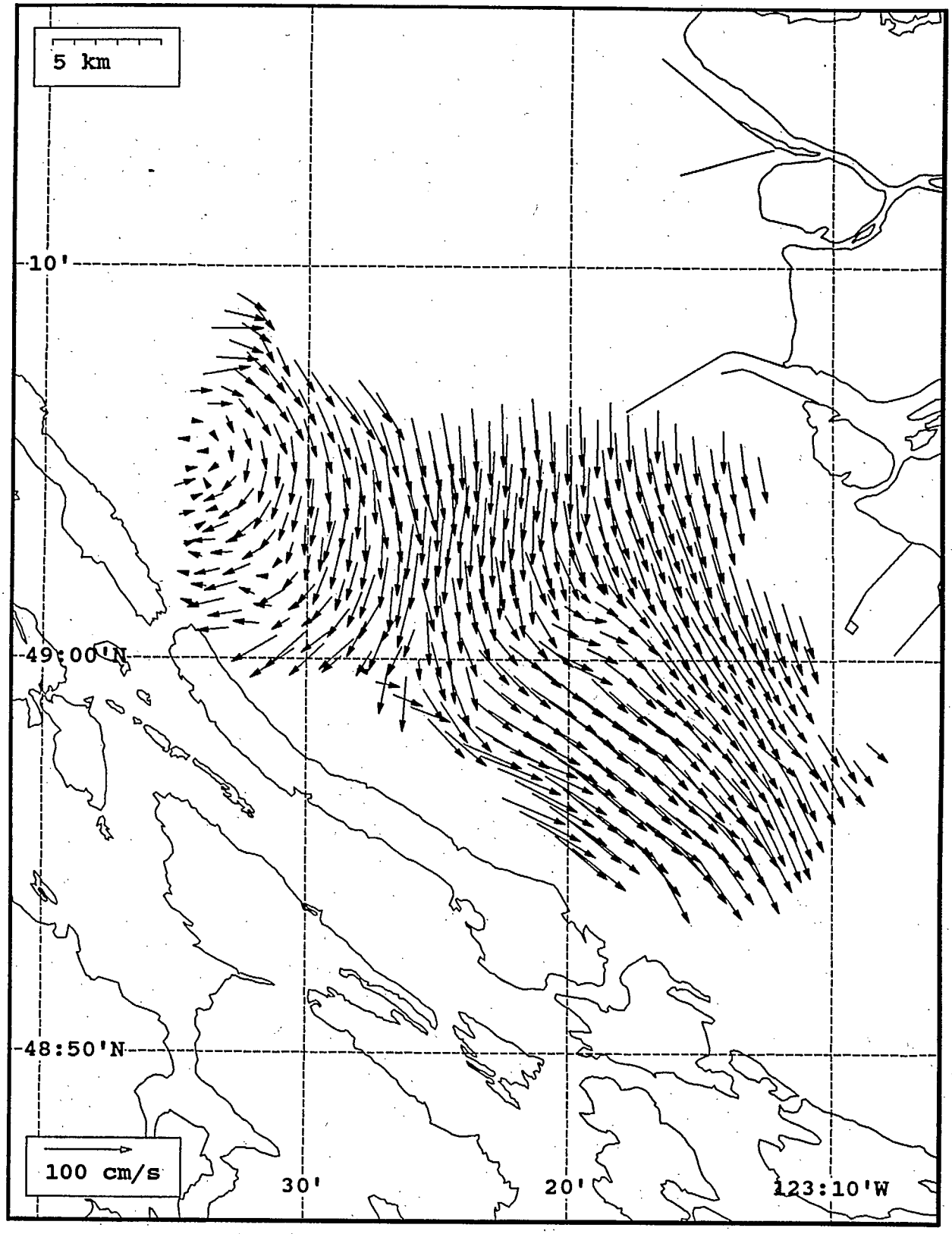

SeaSonde current field from the Strait of Georgia, off the mouth of the Fraser River, for 03:00 Z, August 2, 1993.

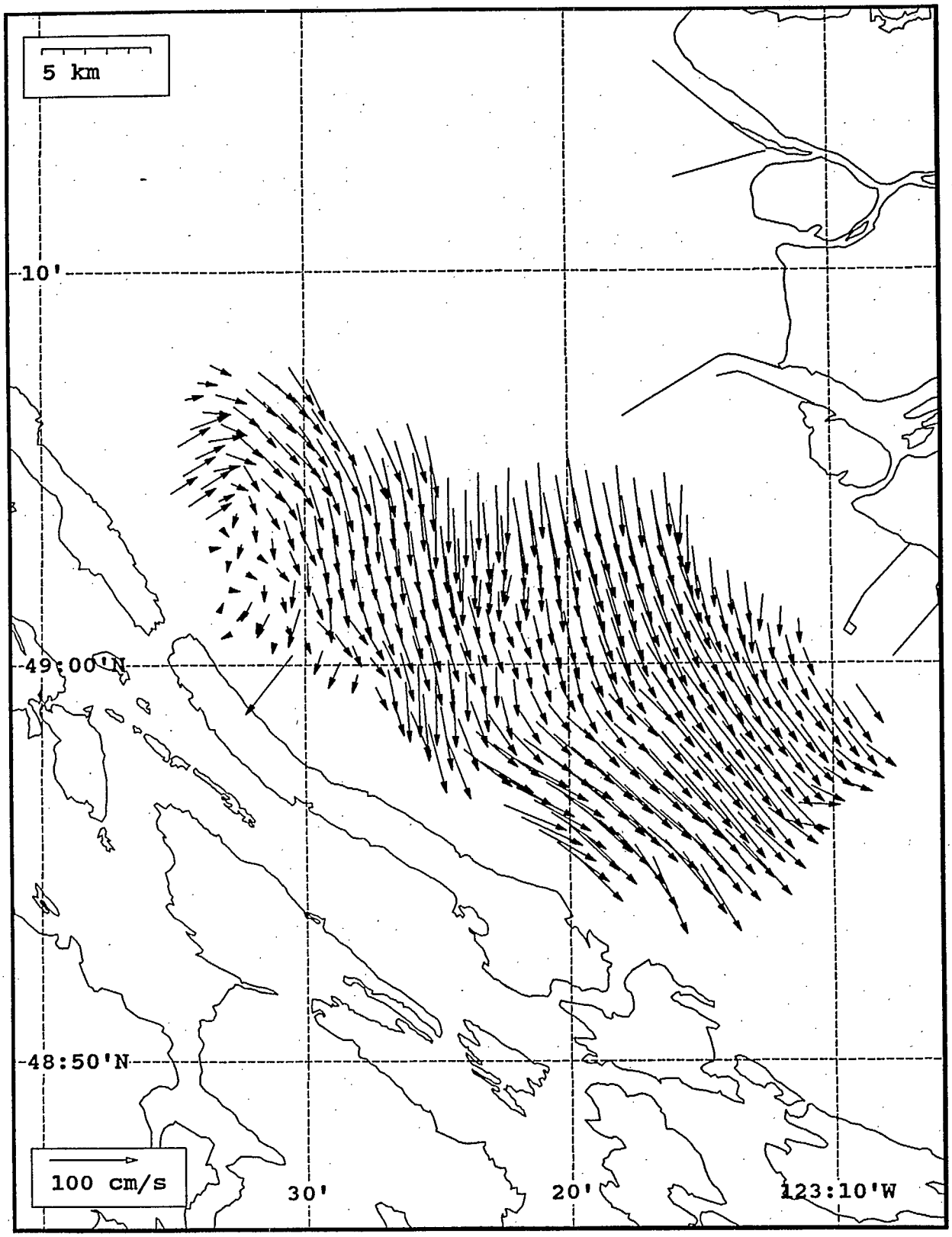

SeaSonde current field from the Strait of Georgia, off the mouth of the Fraser River, for 04:00 Z, August 2, 1993.

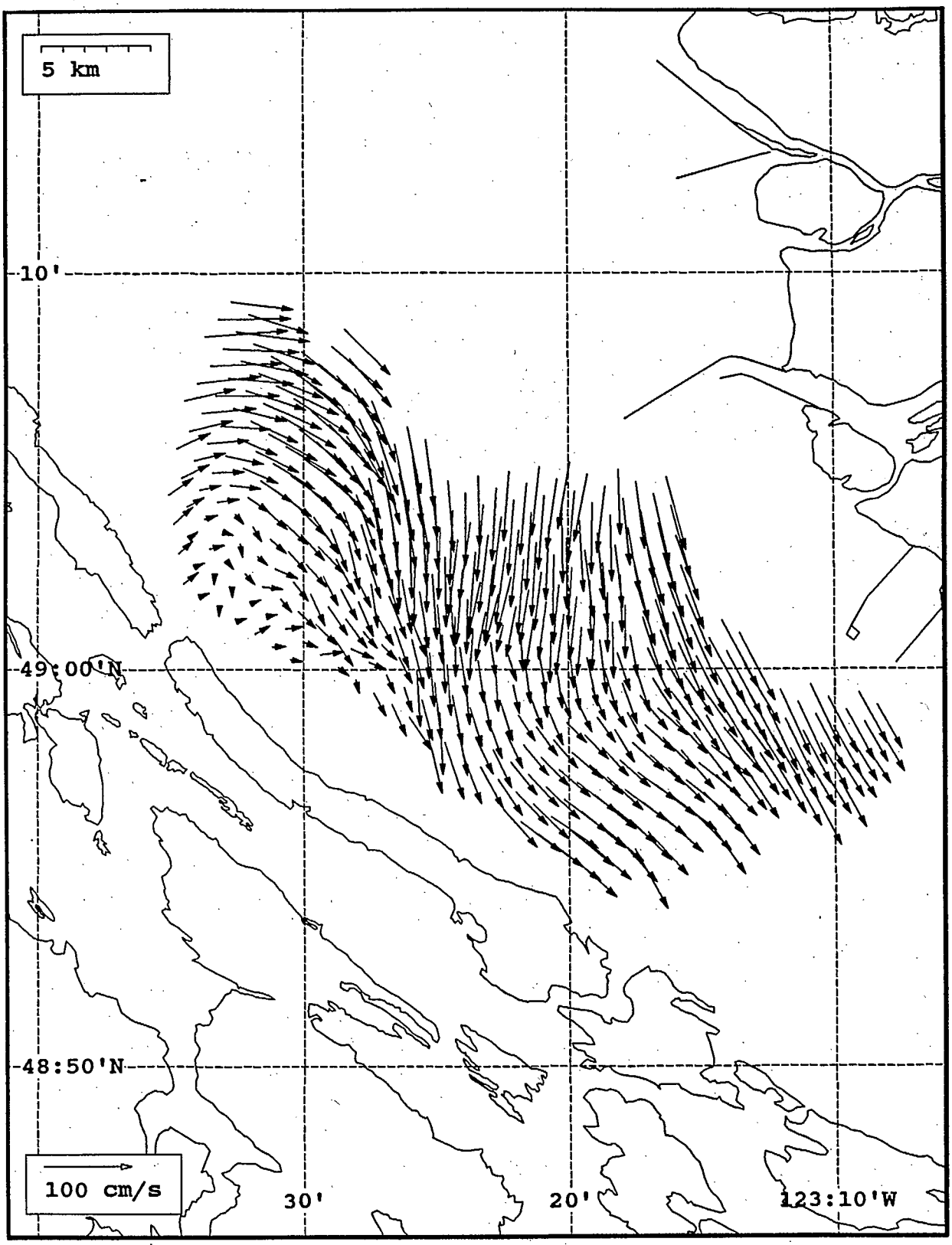

SeaSonde current field from the Strait of Georgia, off the mouth of the Fraser River, for 05:00 Z, August 2, 1993.

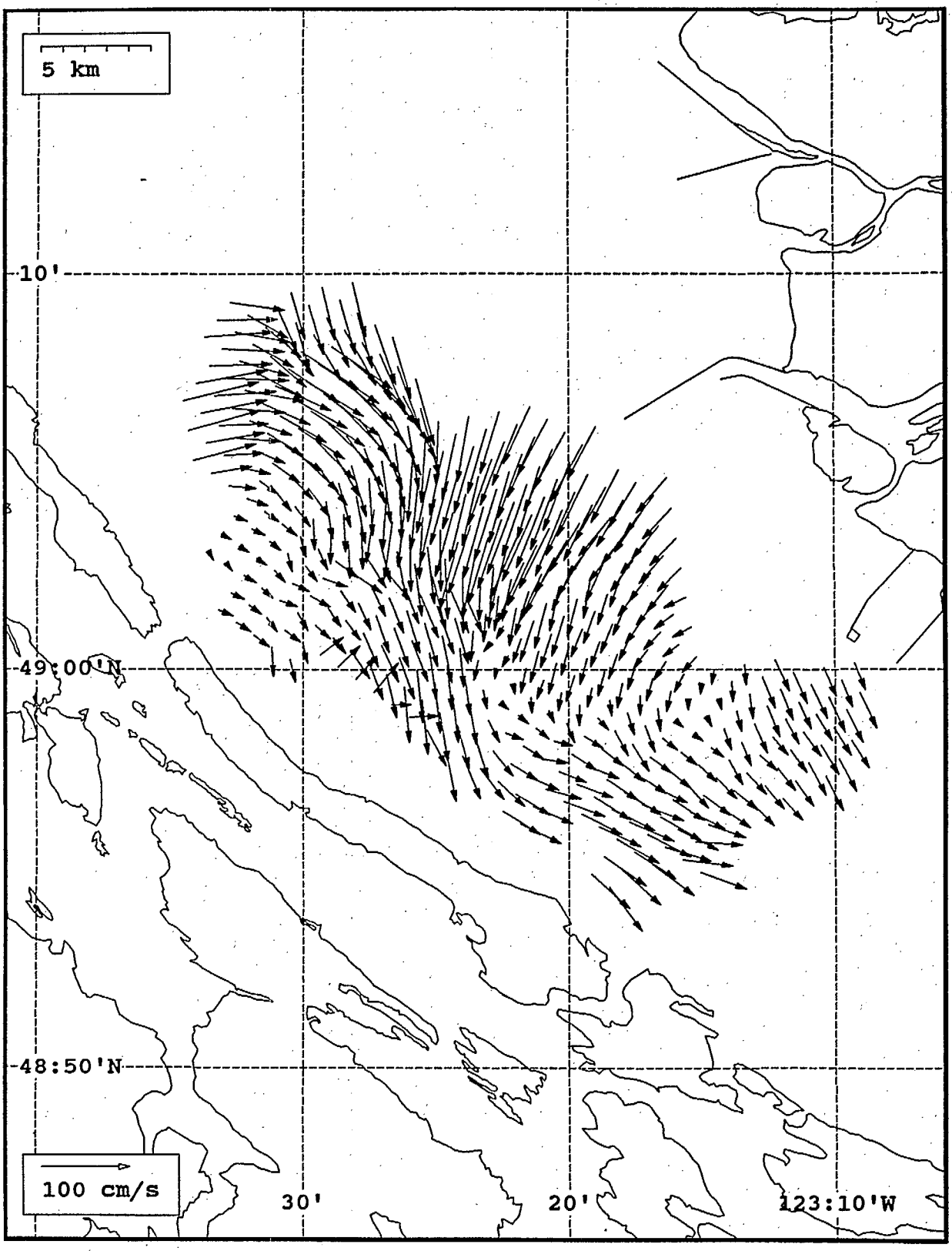

SeaSonde current field from the Strait of Georgia, off the mouth of the Fraser River, for 06:00 Z, August 2, 1993.

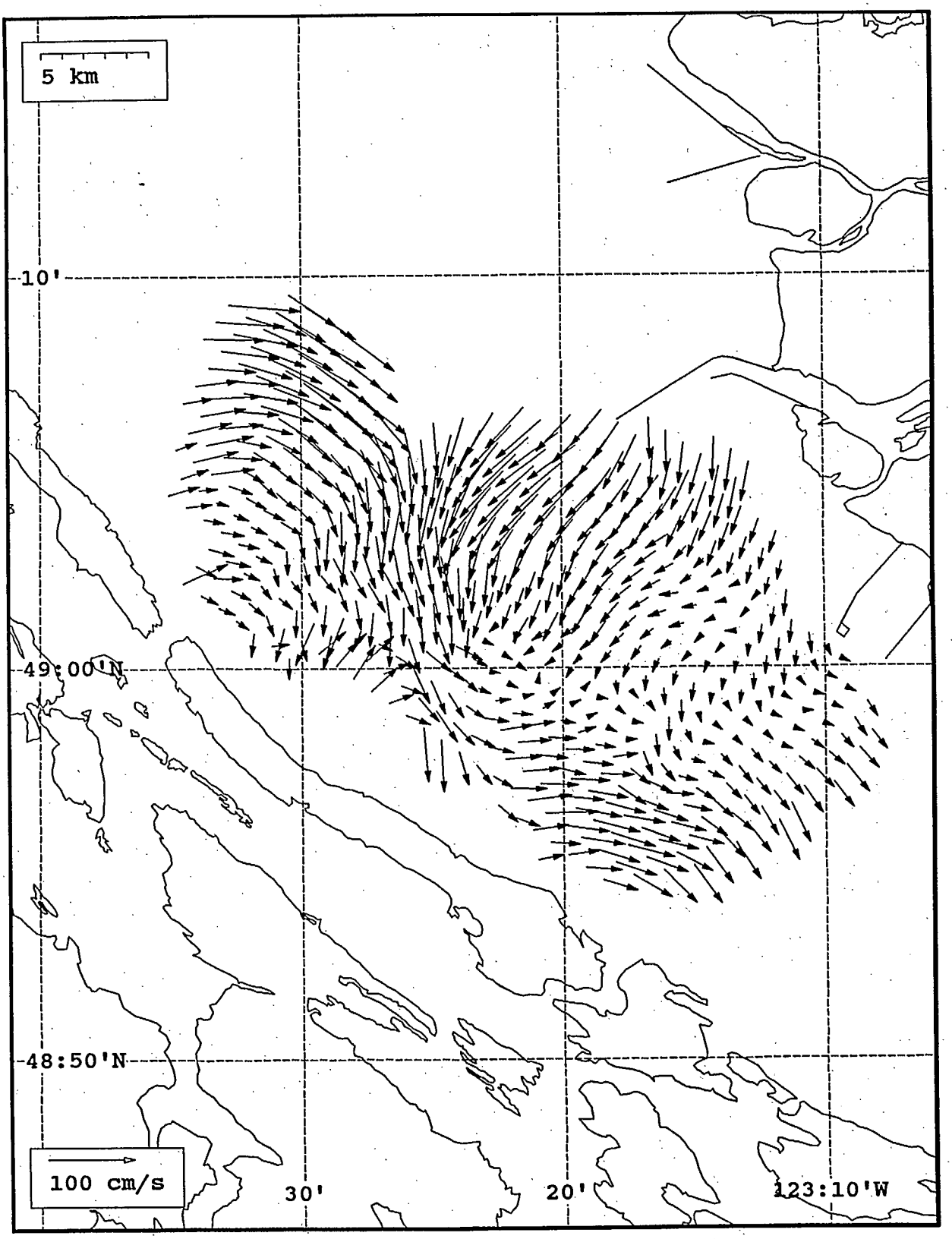

SeaSonde current field from the Strait of Georgia, off the mouth of the Fraser River, for 07:00 Z, August 2, 1993.

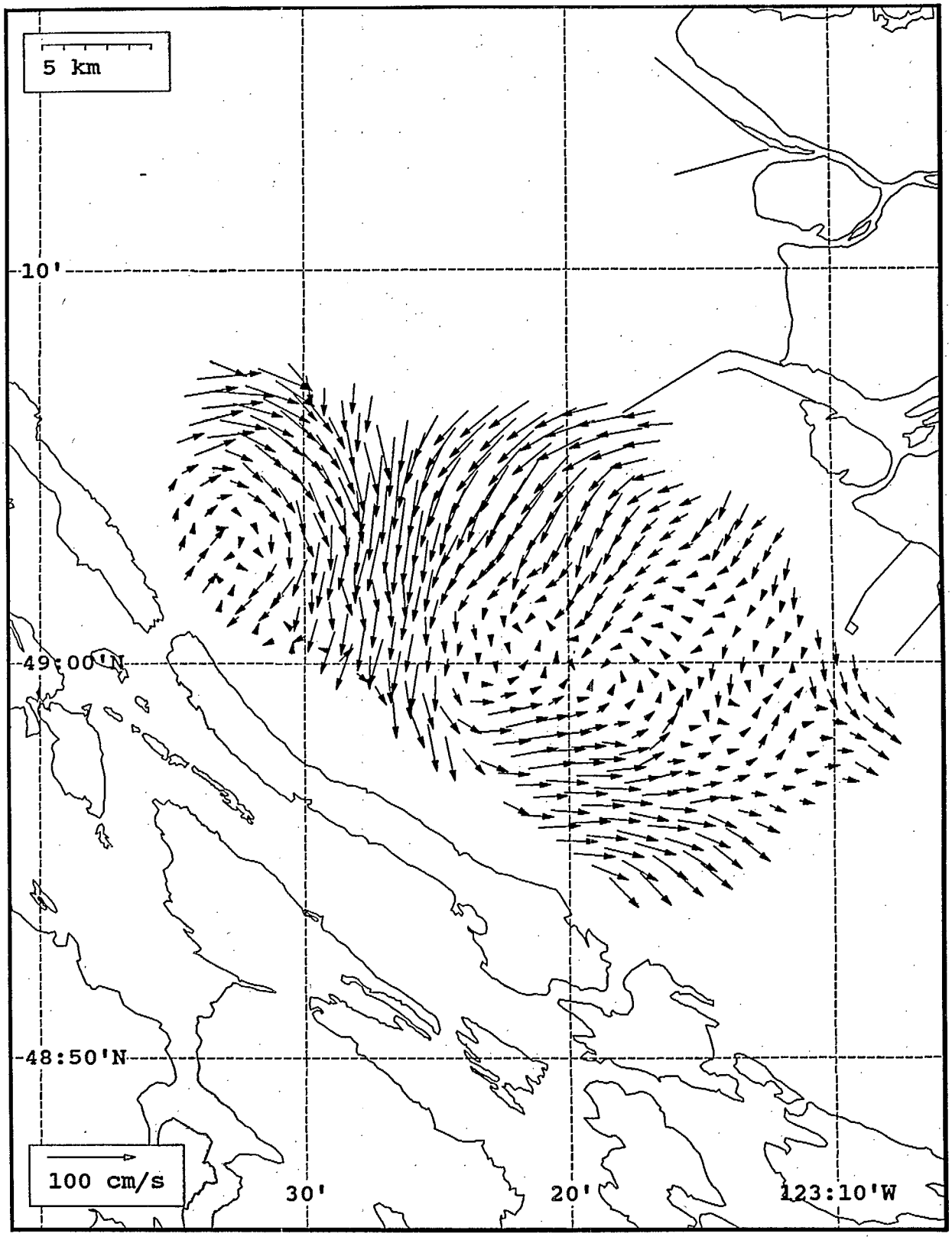

SeaSonde current field from the Strait of Georgia, off the mouth of the Fraser River, for 08:00 Z, August 2, 1993.

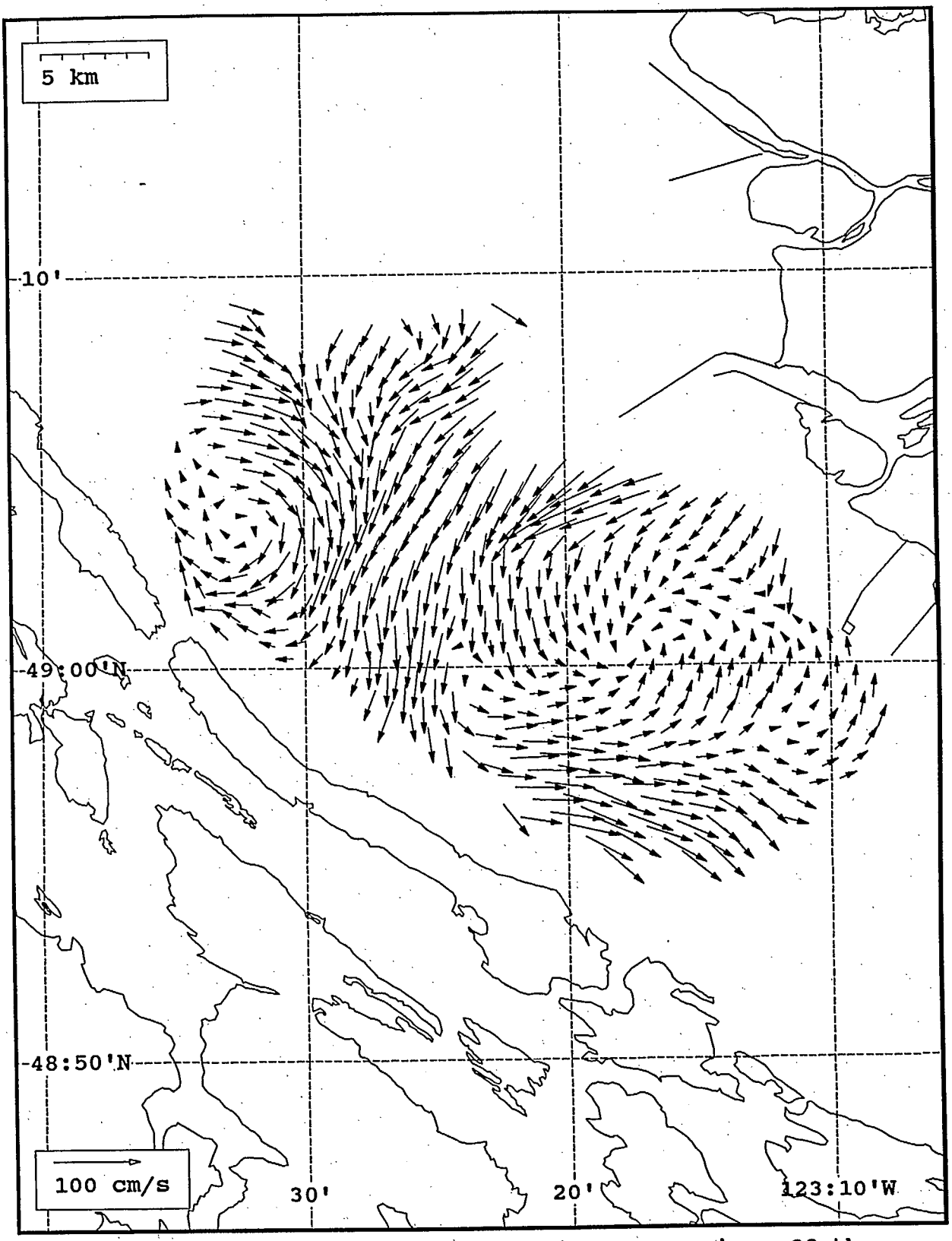

SeaSonde current field from the Strait of Georgia, off the mouth of the Fraser River, for 09:00 Z, August 2, 1993.

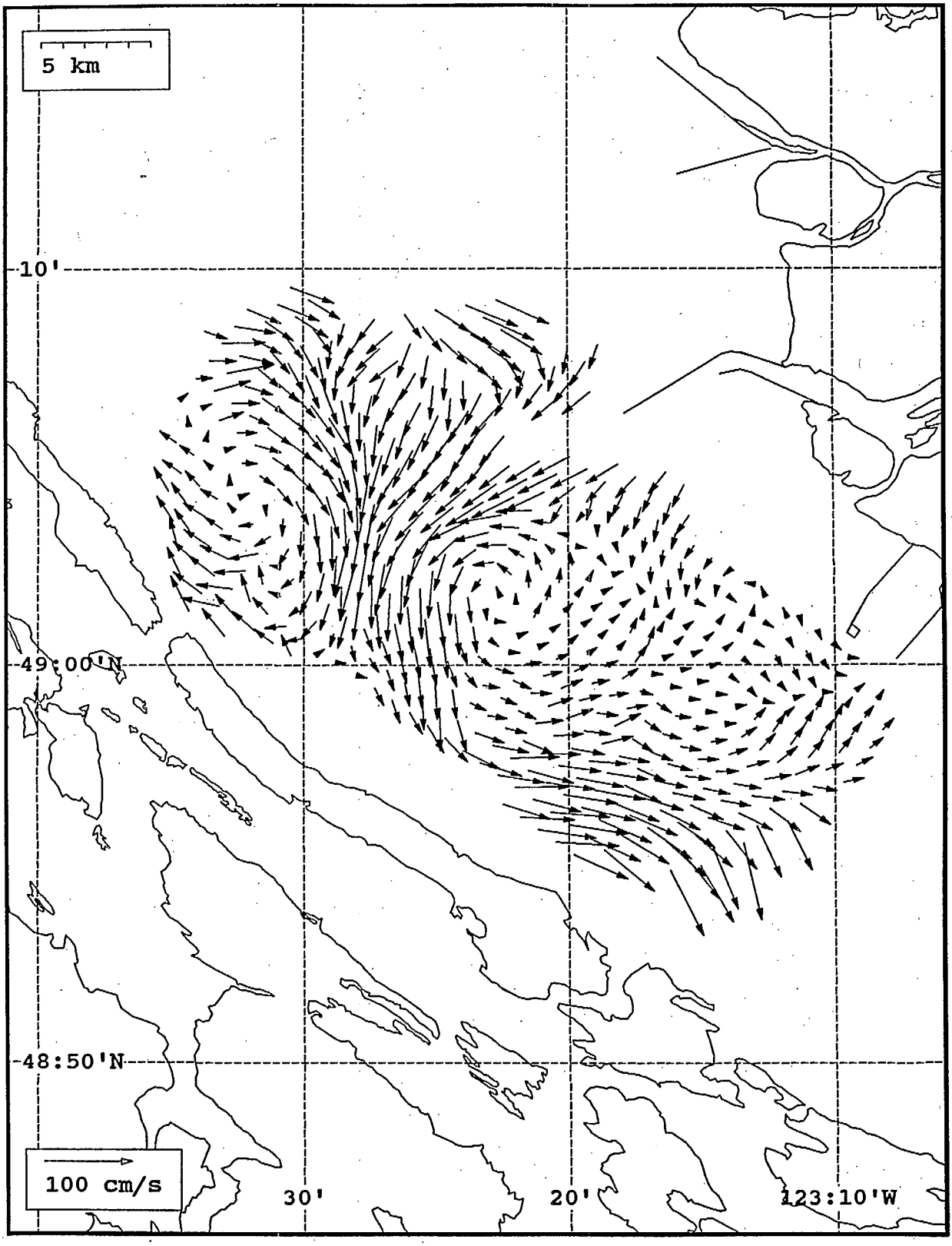

SeaSonde current field from the Strait of Georgia, off the mouth of the Fraser River, for 10:00 Z, August 2, 1993.

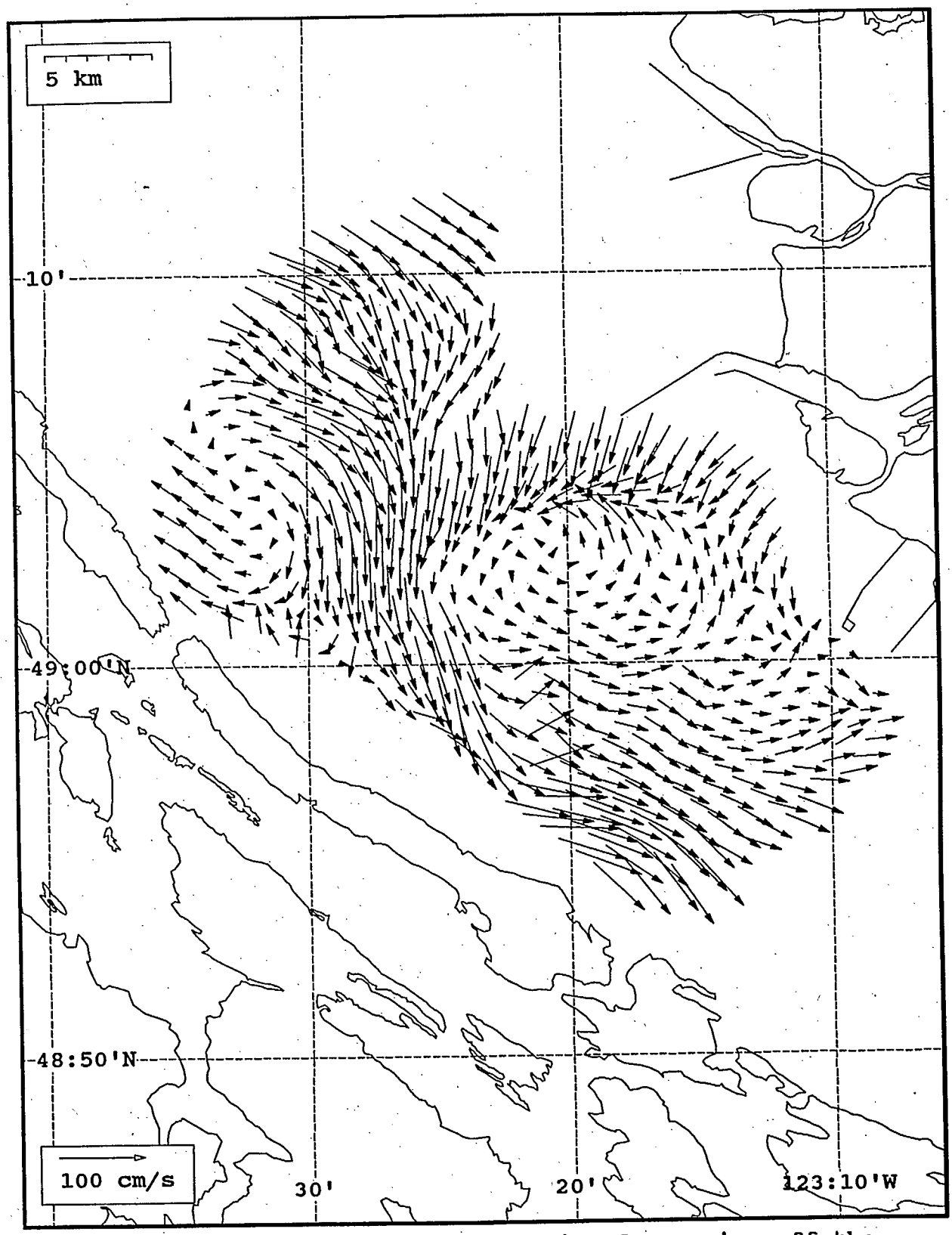

SeaSonde current field from the Strait of Georgia, off the mouth of the Fraser River, for 11:00 Z, August 2, 1993.

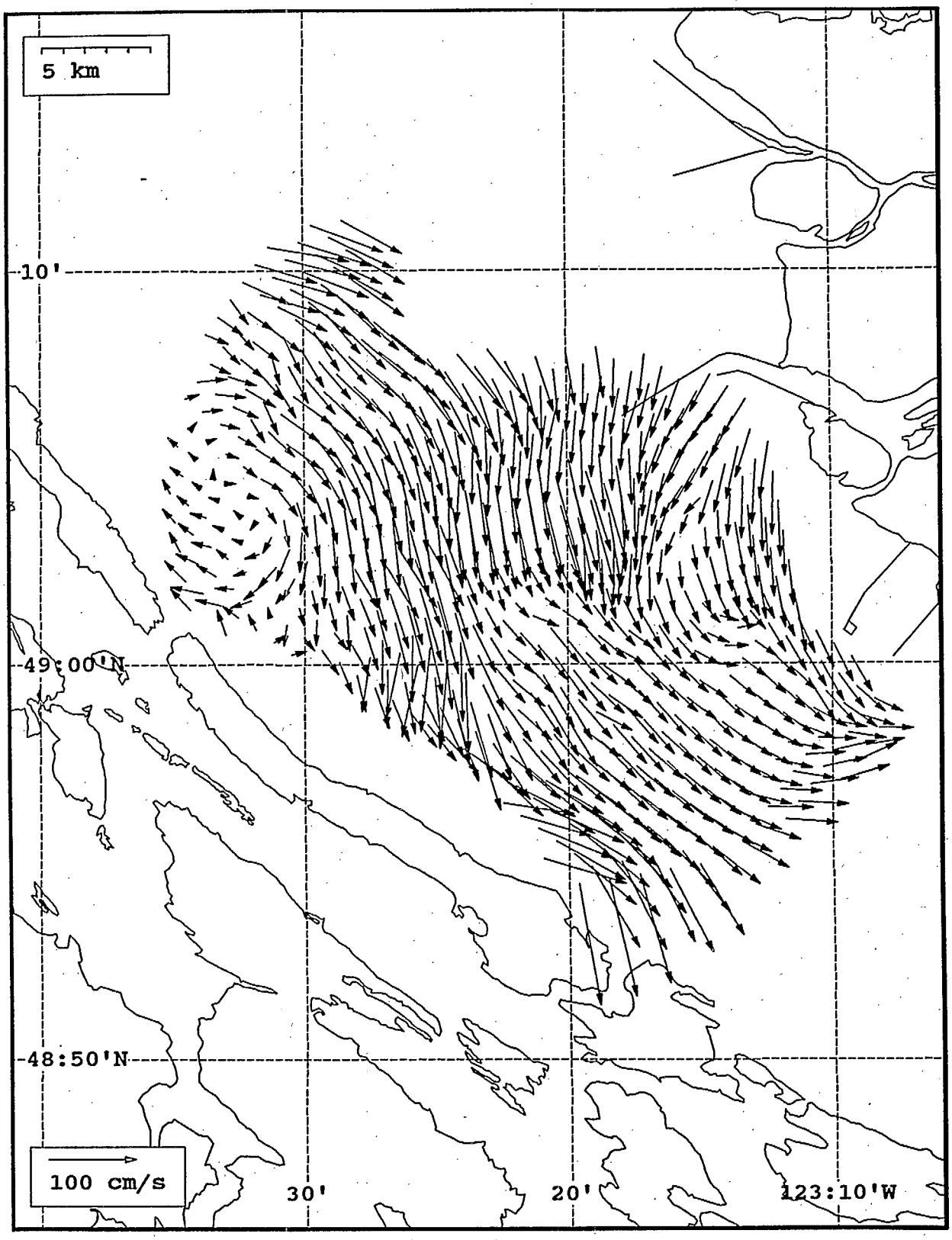

SeaSonde current field from the Strait of Georgia, off the mouth of the Fraser River, for 12:00 Z, August 2, 1993.

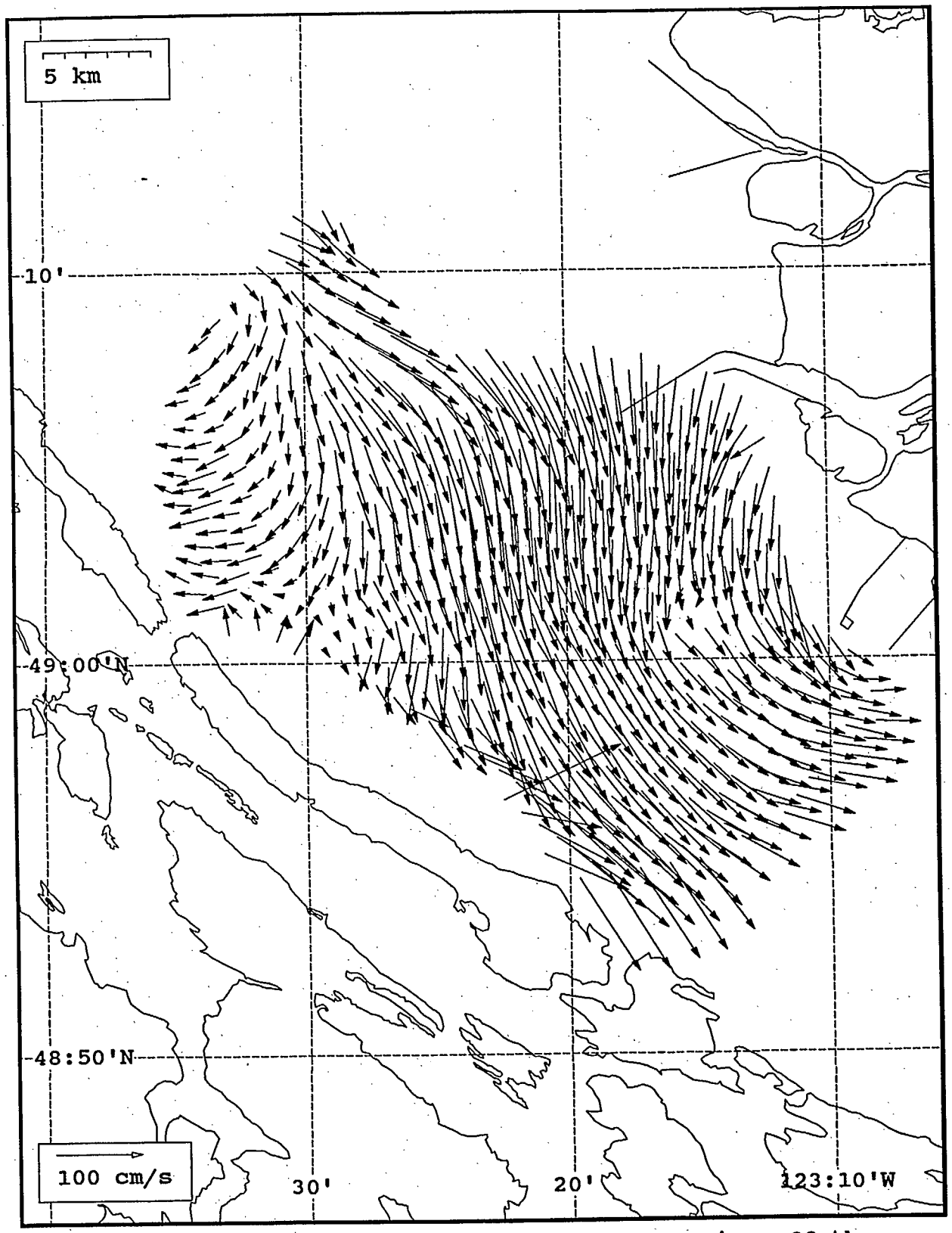

SeaSonde current field from the Strait of Georgia, off the mouth of the Fraser River, for 13:00 Z, August 2, 1993.

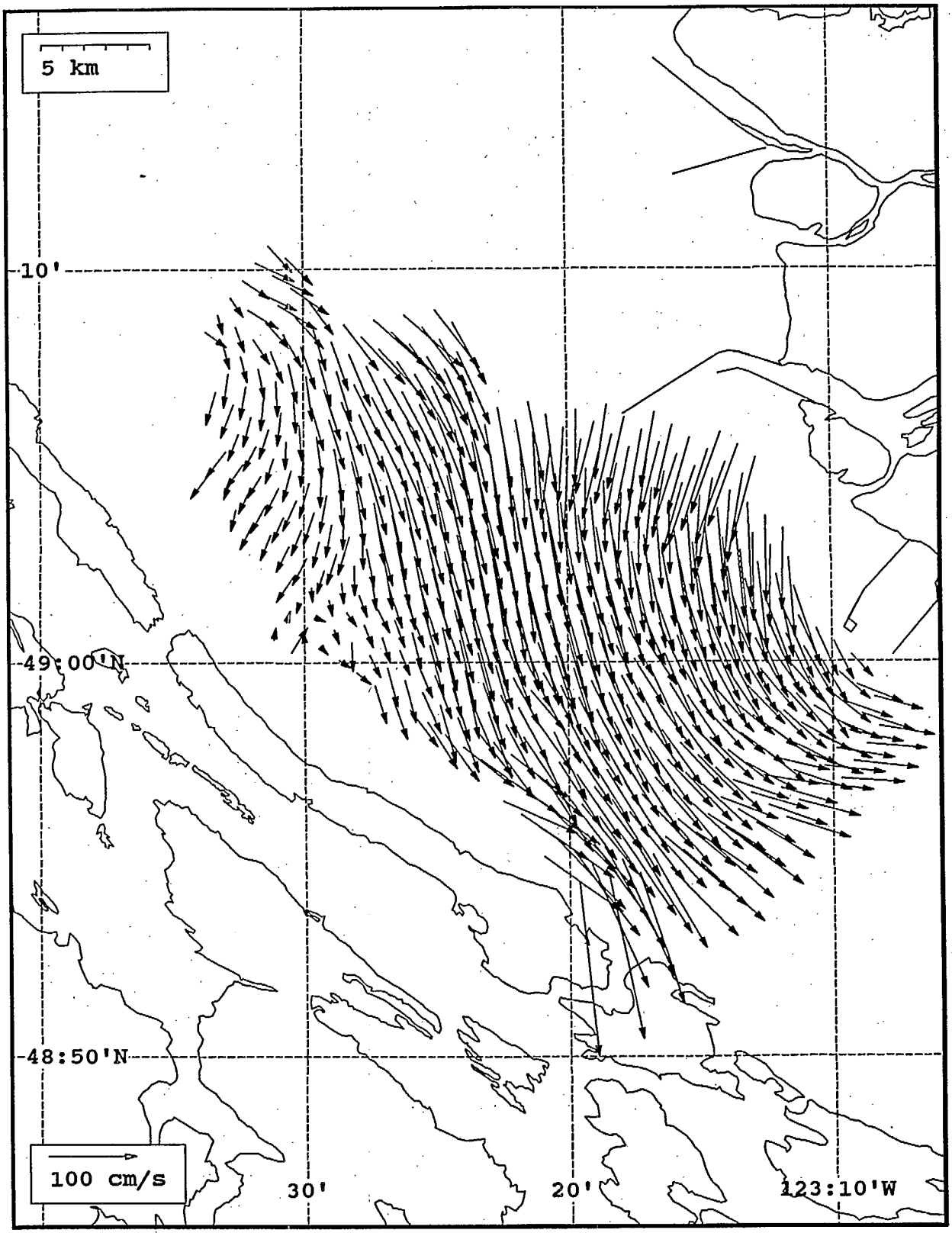

SeaSonde current field from the Strait of Georgia, off the mouth of the Fraser River, for 14:00 Z, August 2, 1993.

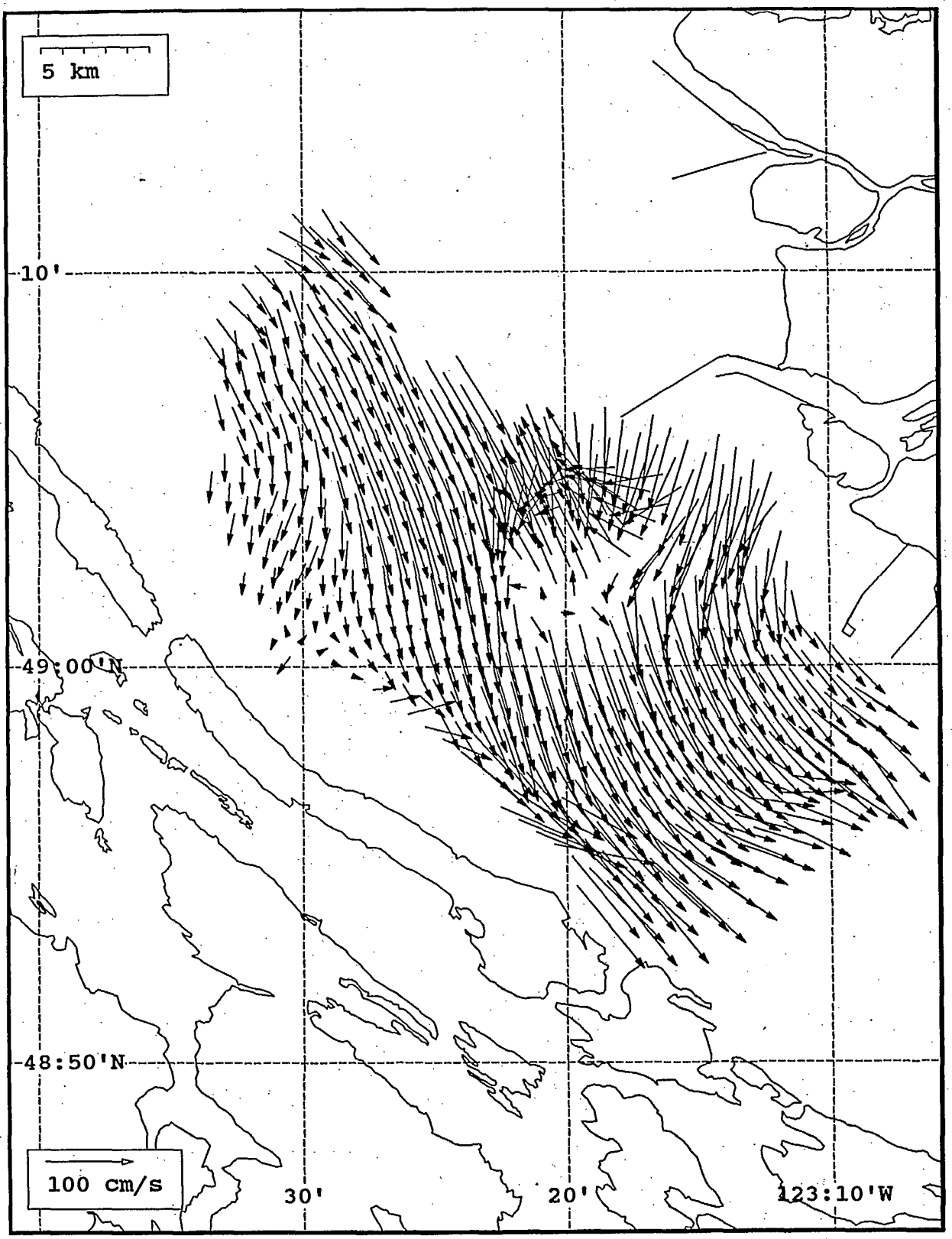

SeaSonde current field from the Strait of Georgia, off the mouth of the Fraser River, for 15:00 Z, August 2, 1993.

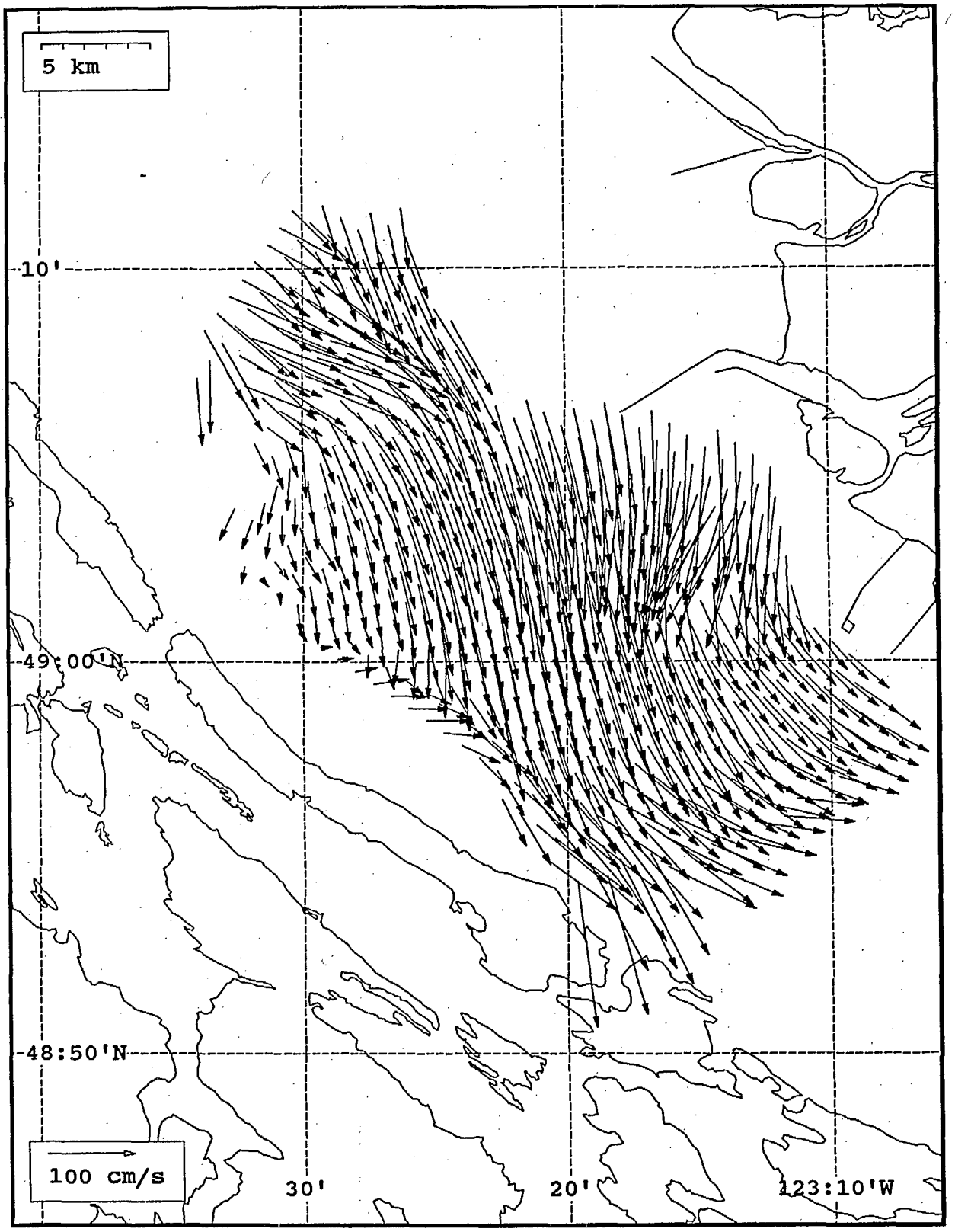

SeaSonde current field from the Strait of Georgia, off the mouth of the Fraser River, for 16:00 Z, August 2, 1993.

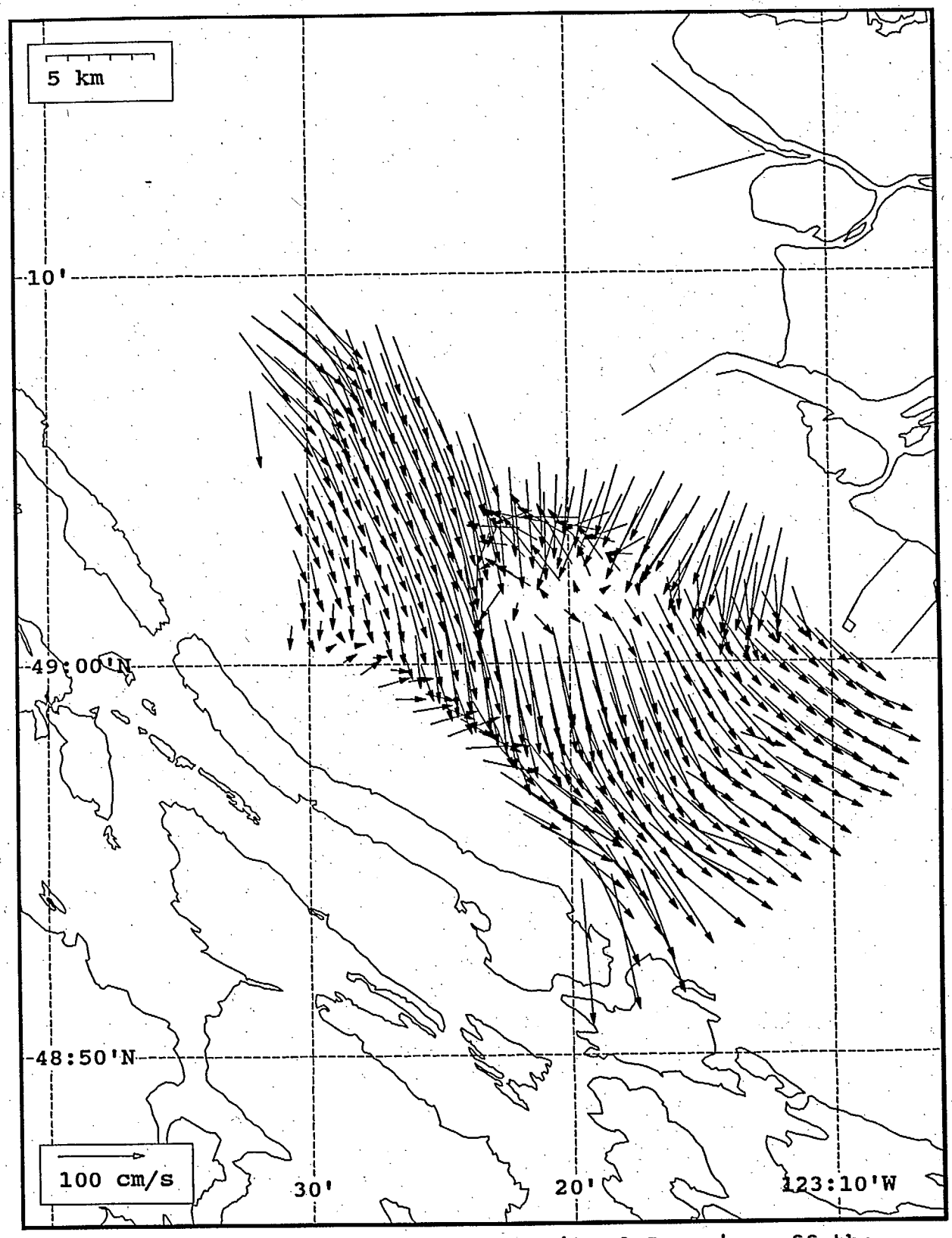

SeaSonde current field from the Strait of Georgia, off the mouth of the Fraser River, for 17:00 Z, August 2, 1993.

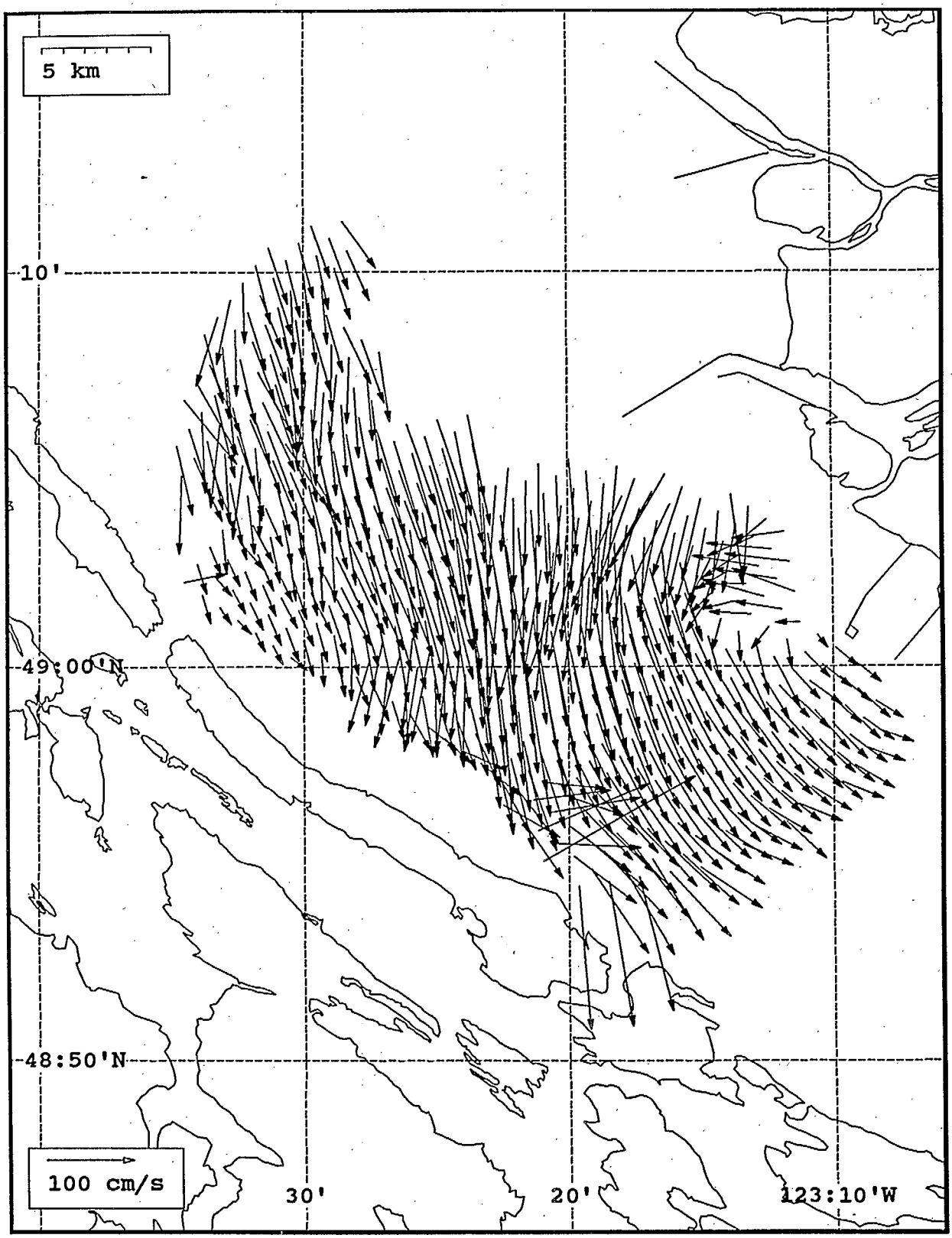

SeaSonde current field from the Strait of Georgia, off the mouth of the Fraser River, for 18:00 Z, August 2, 1993.

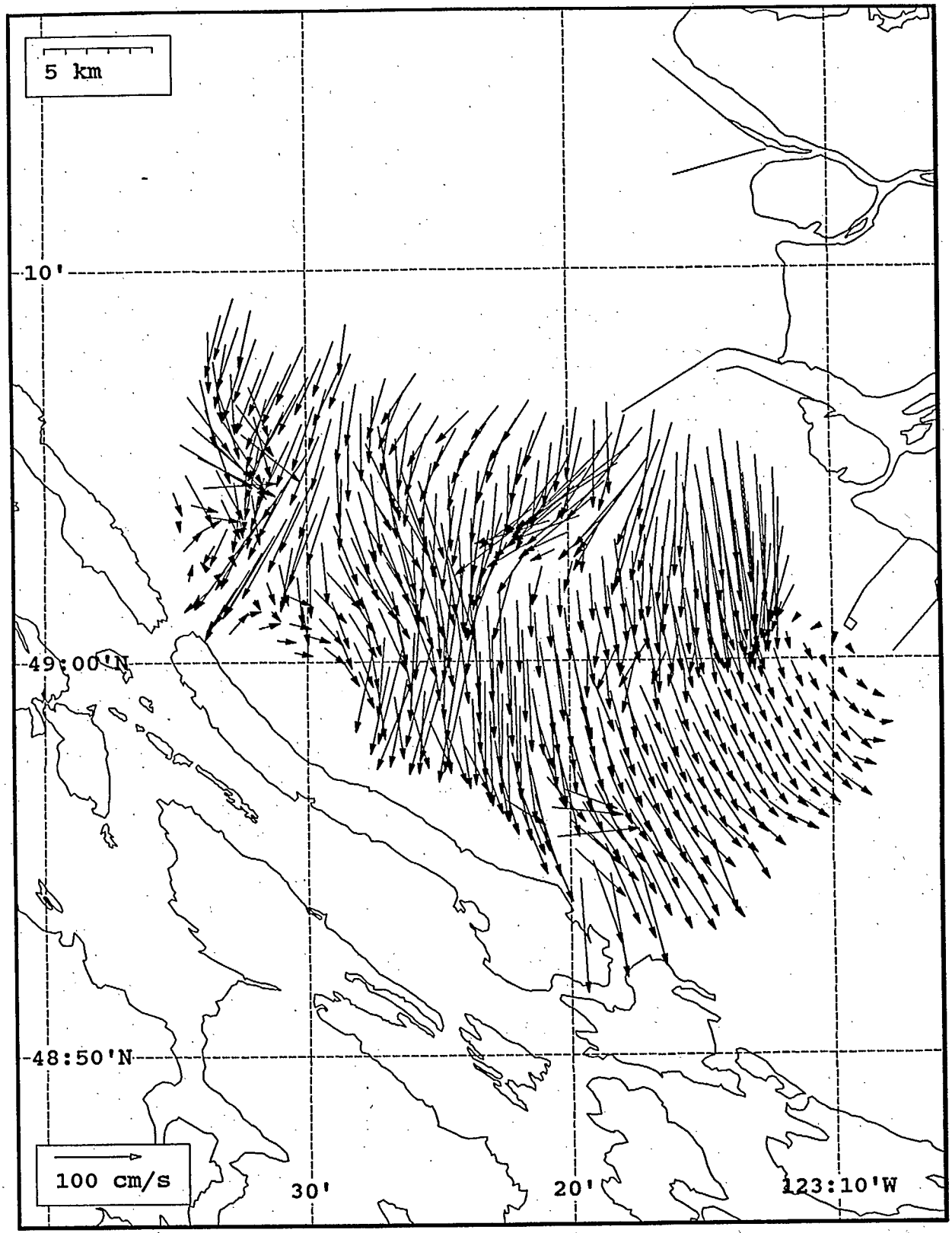

SeaSonde current field from the Strait of Georgia, off the mouth of the Fraser River, for 19:00 Z, August 2, 1993.

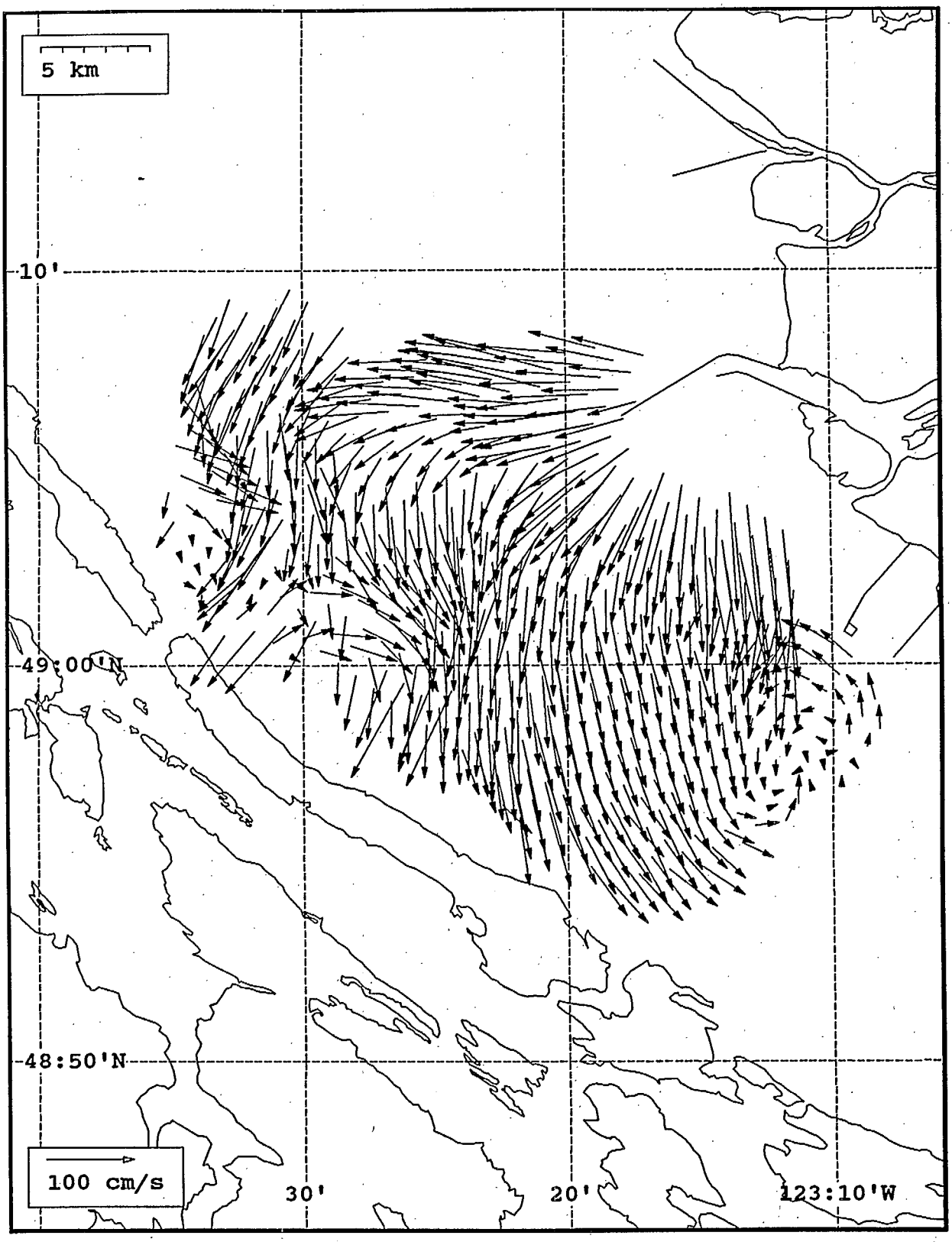

SeaSonde current field from the Strait of Georgia, off the mouth of the Fraser River, for 20:00 Z, August 2, 1993.

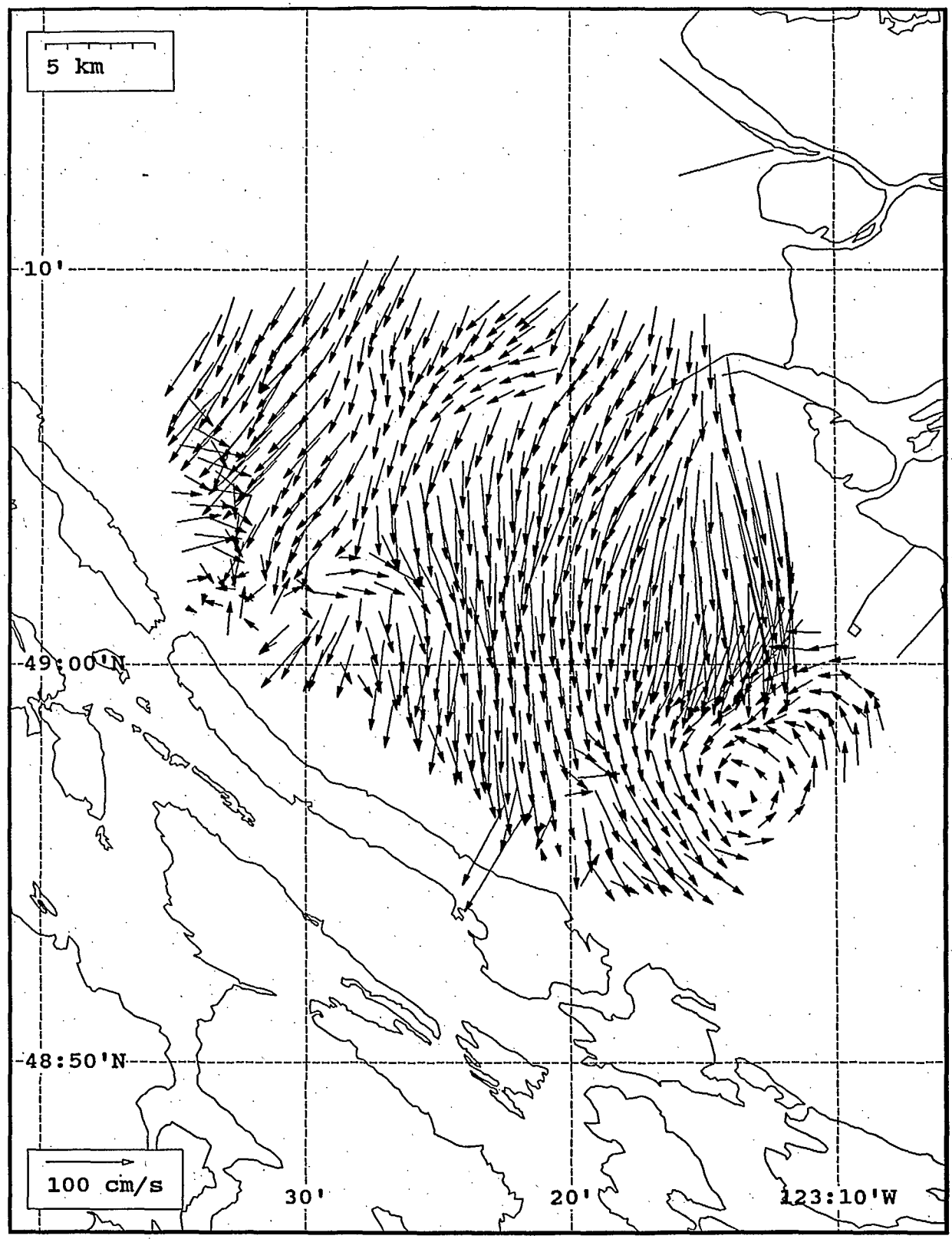

SeaSonde current field from the Strait of Georgia, off the mouth of the Fraser River, for 21:00 Z, August 2, 1993.

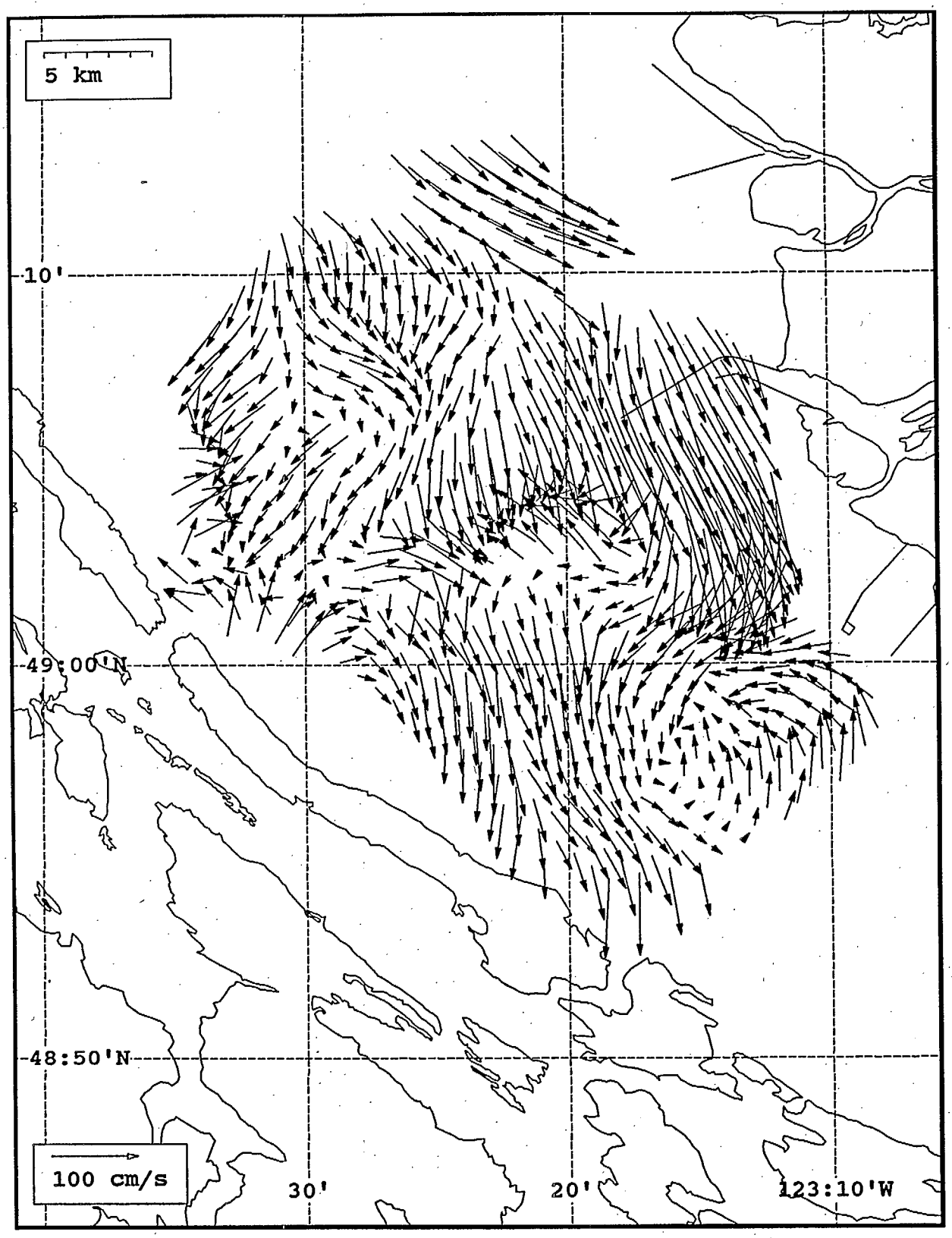

SeaSonde current field from the Strait of Georgia, off the mouth of the Fraser River, for 22:00 Z, August 2, 1993.

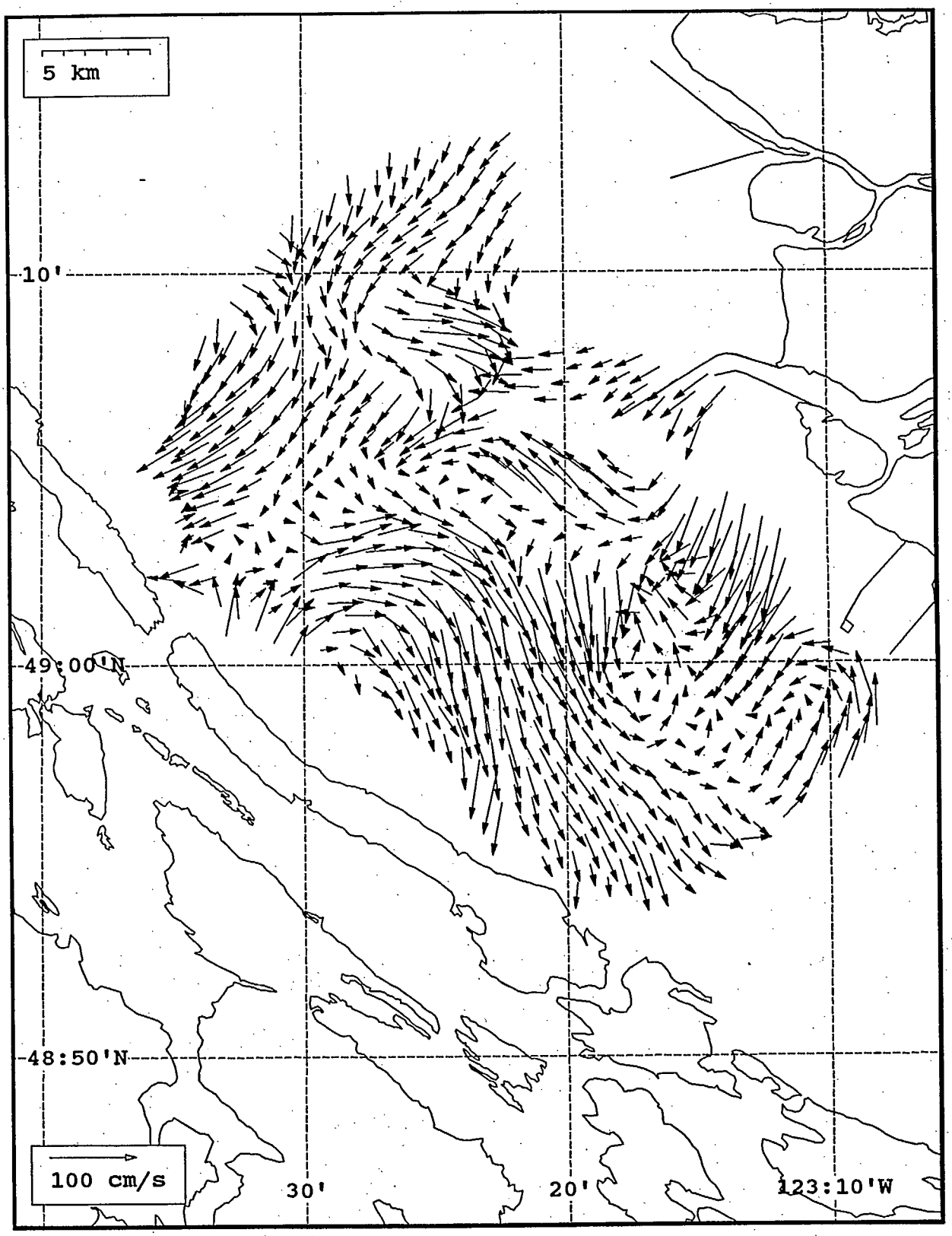

SeaSonde current field from the Strait of Georgia, off the mouth of the Fraser River, for 23:00 Z, August 2, 1993.

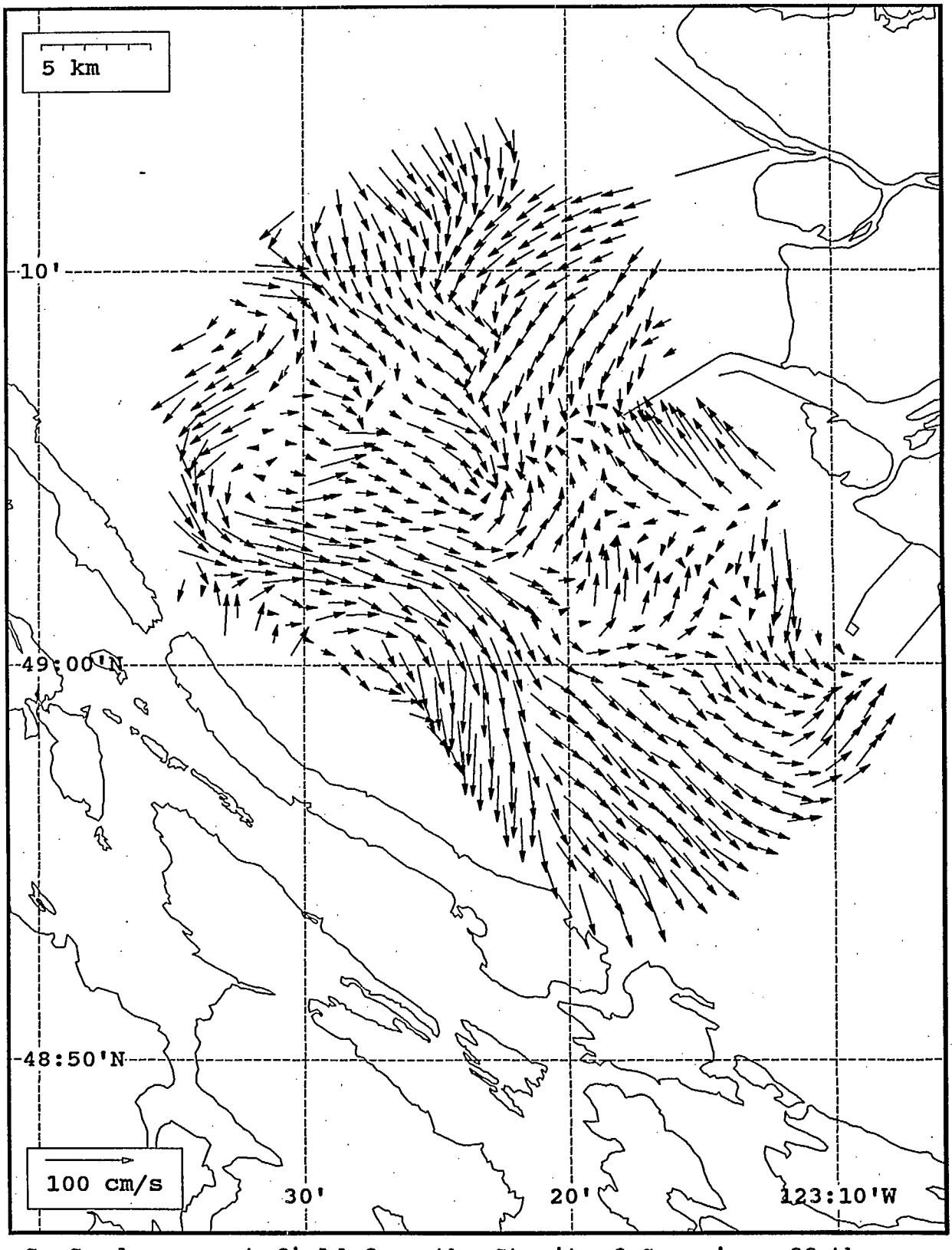

SeaSonde current field from the Strait of Georgia, off the mouth of the Fraser River, for 00:00 Z, August 3, 1993.

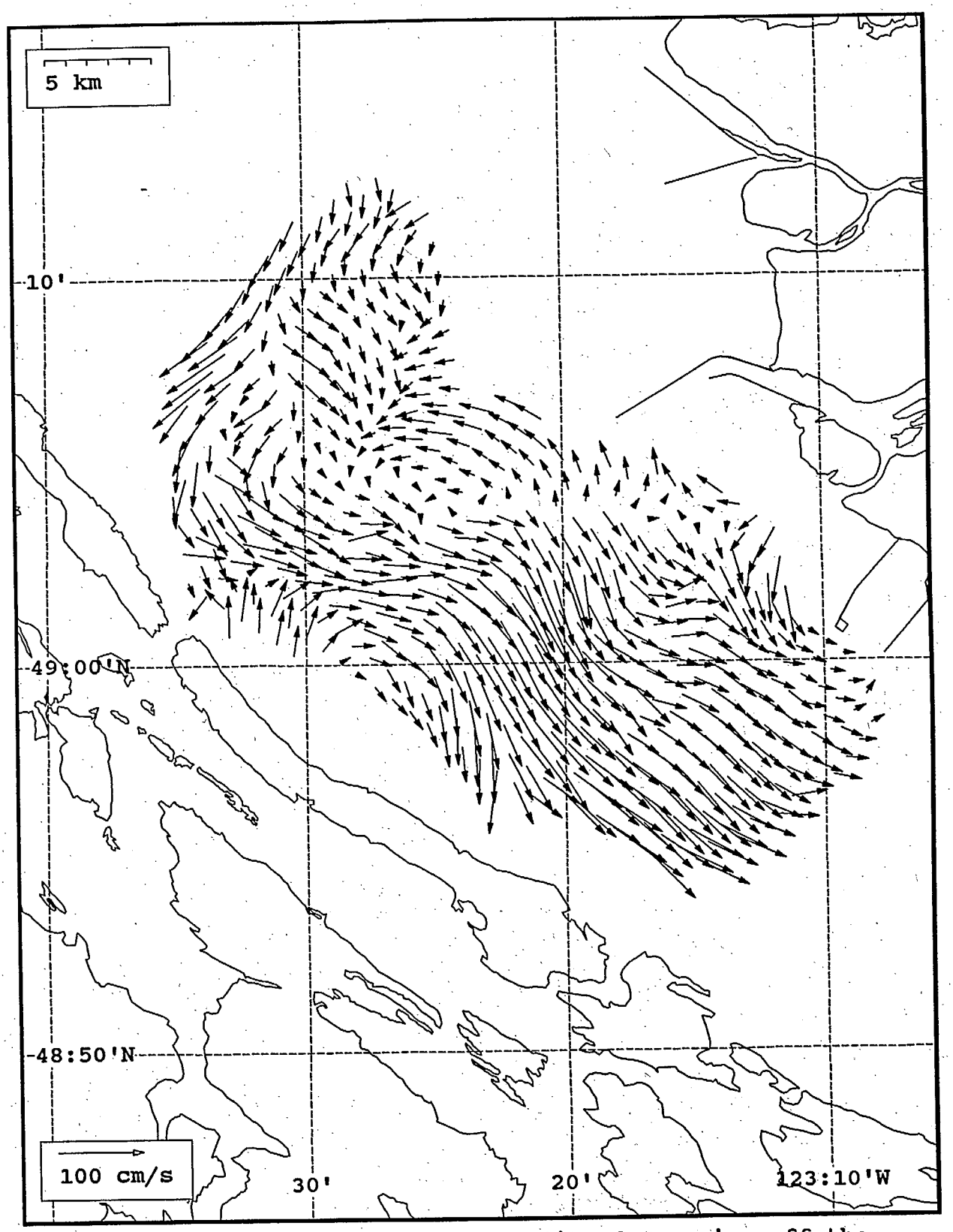

SeaSonde current field from the Strait of Georgia, off the mouth of the Fraser River, for 01:00 Z, August 3, 1993.

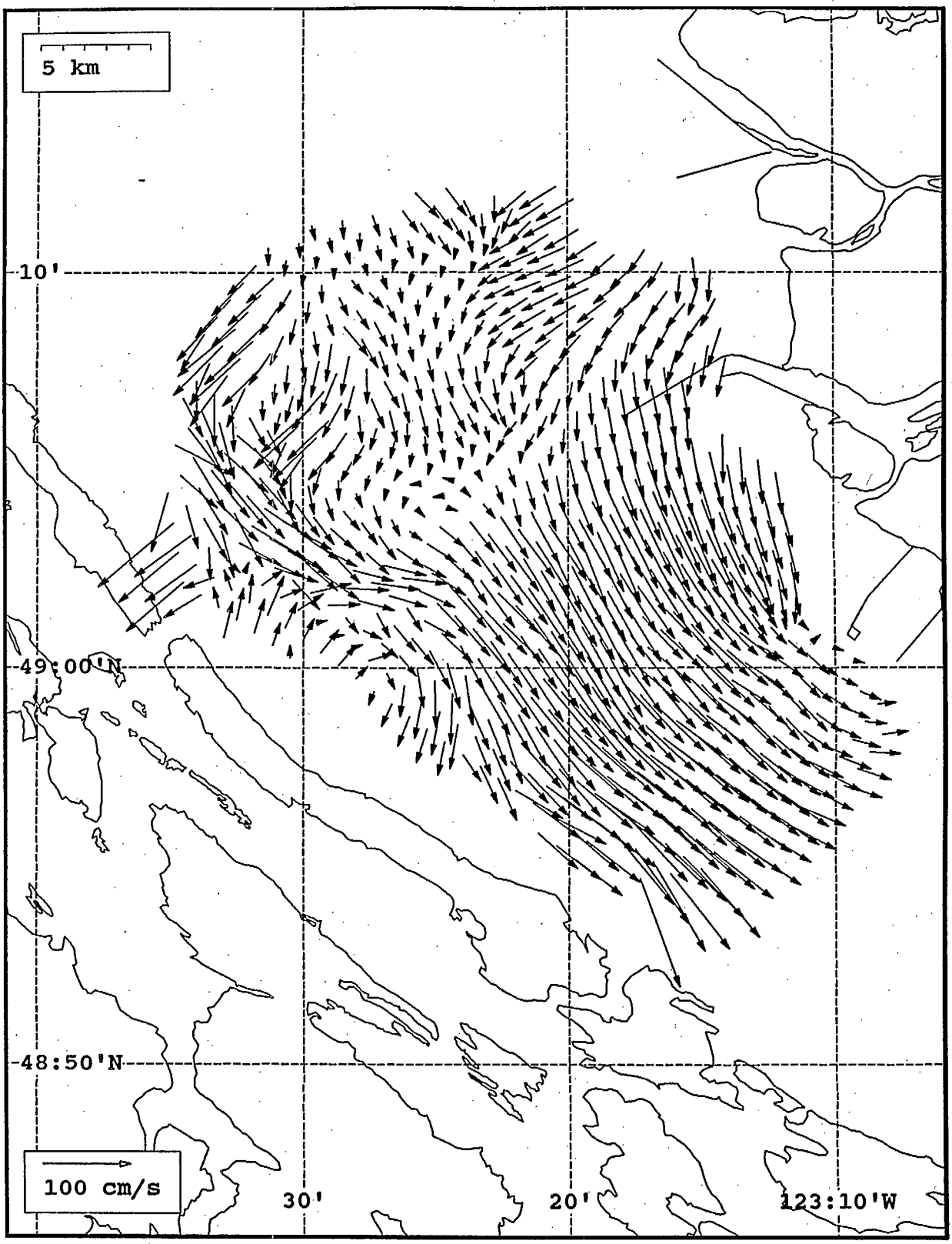

SeaSonde current field from the Strait of Georgia, off the mouth of the Fraser River, for 02:00 Z, August 3, 1993.

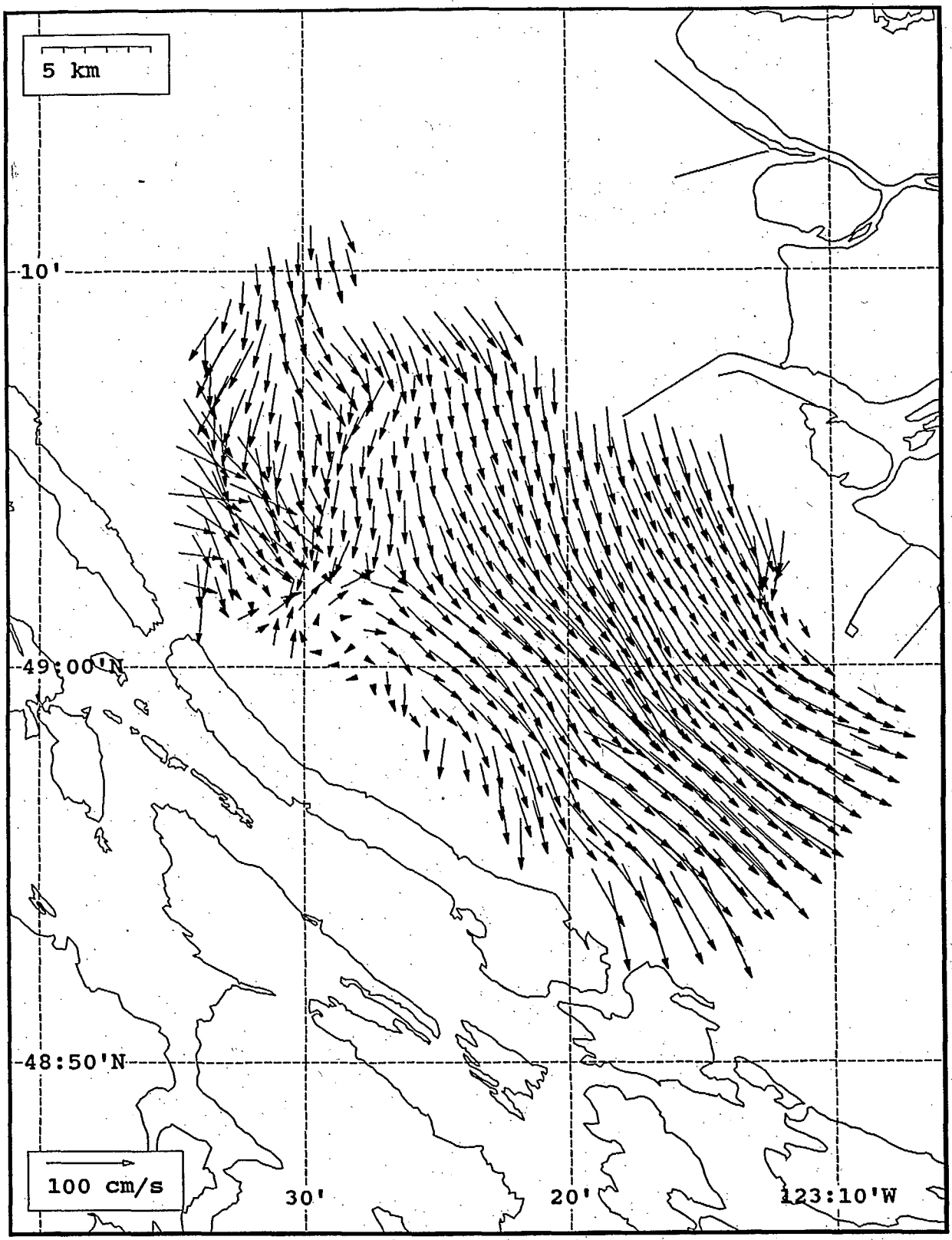

SeaSonde current field from the Strait of Georgia, off the mouth of the Fraser River, for 03:00 Z, August 3, 1993.

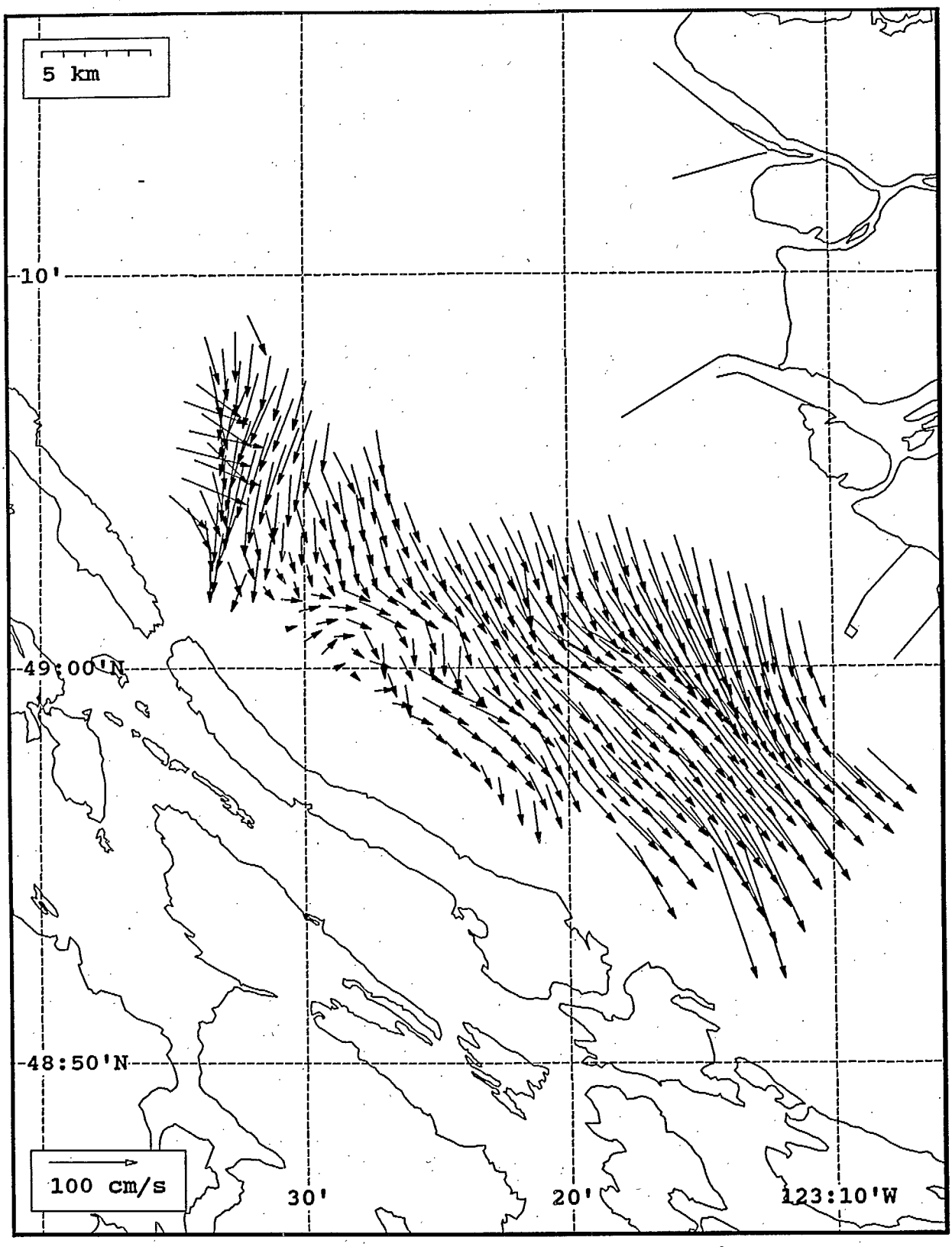

SeaSonde current field from the Strait of Georgia, off the mouth of the Fraser River, for 04:00 Z, August 3, 1993.

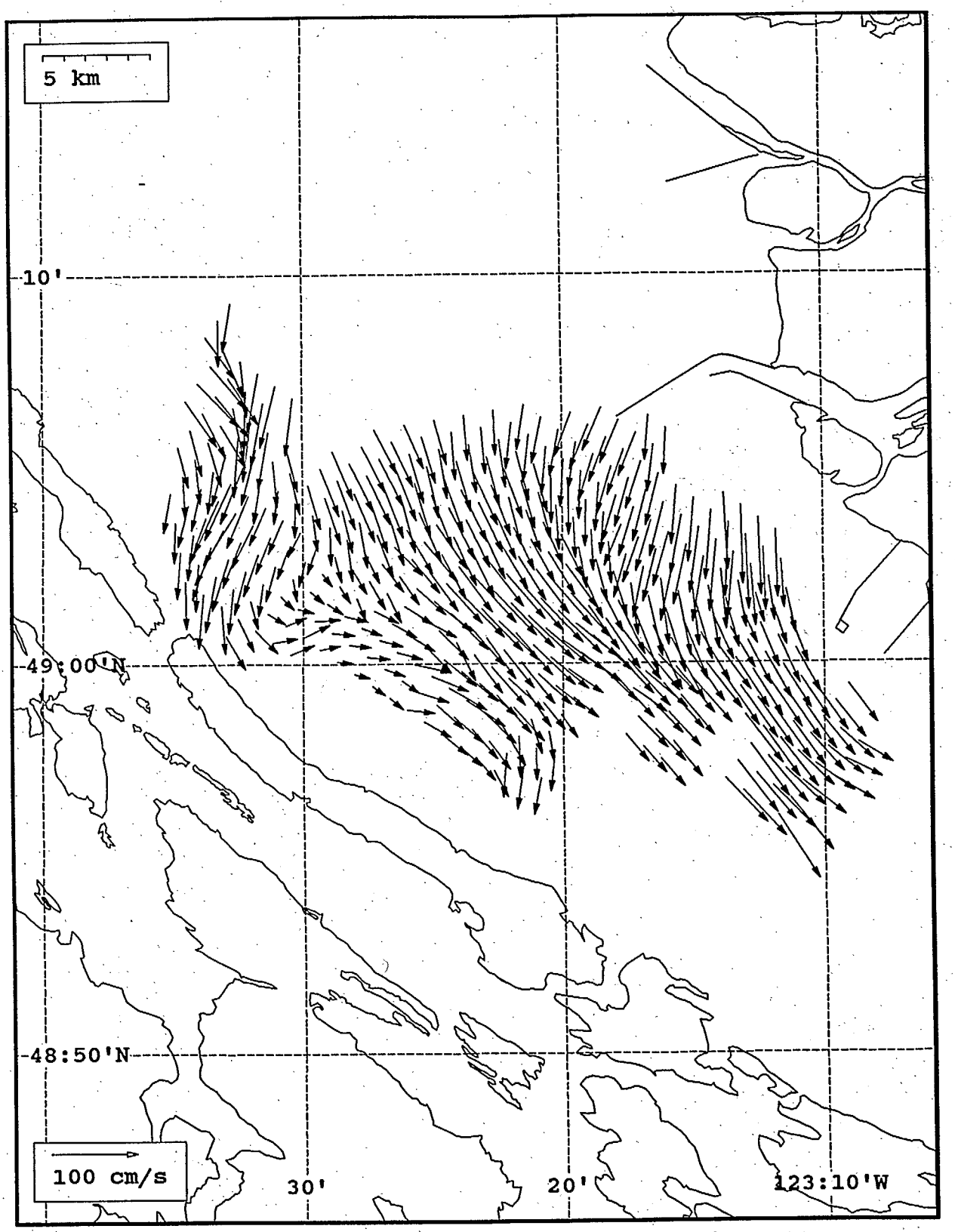

SeaSonde current field from the Strait of Georgia, off the mouth of the Fraser River, for 05:00 Z, August 3, 1993.

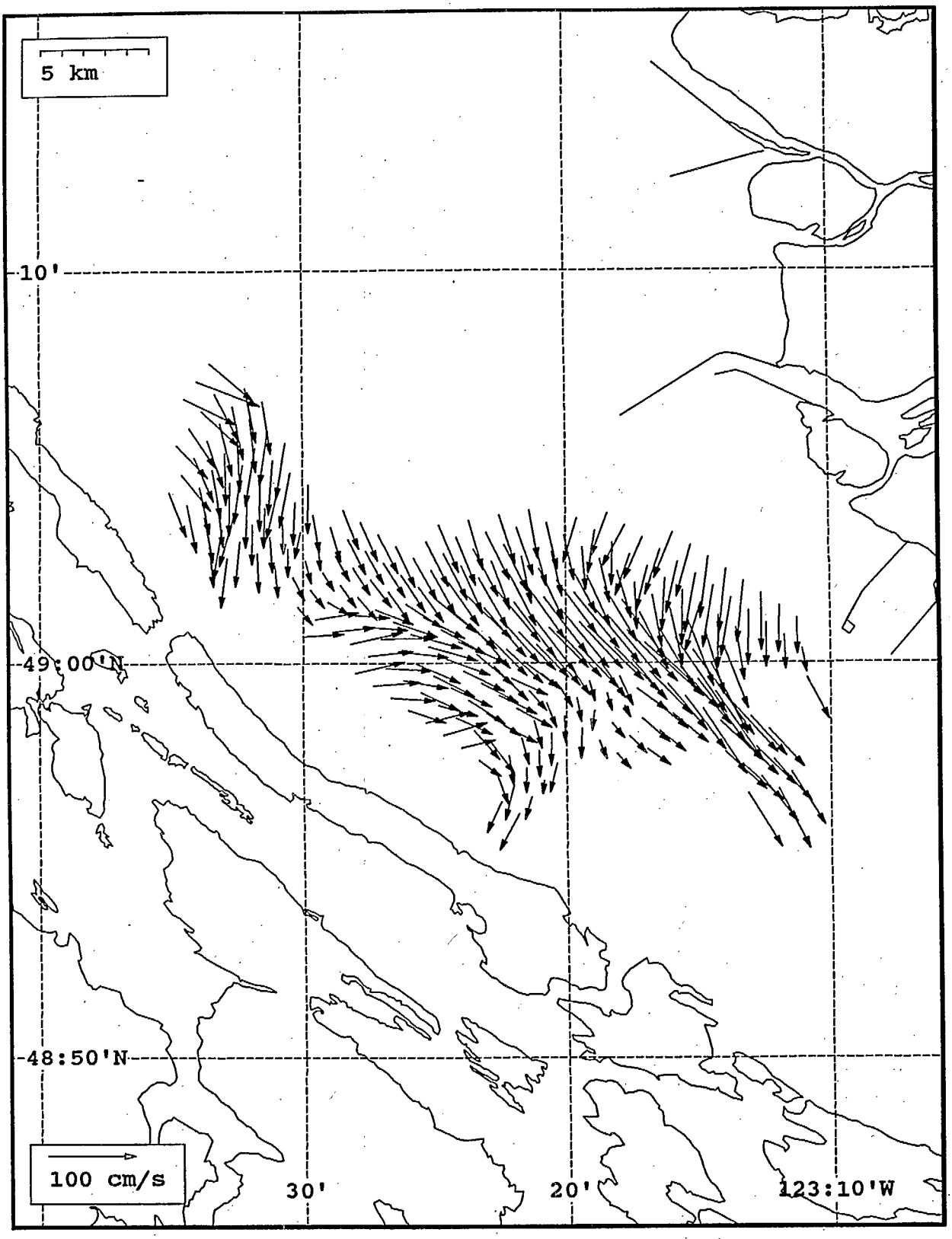

SeaSonde current field from the Strait of Georgia, off the mouth of the Fraser River, for 06:00 Z, August 3, 1993.

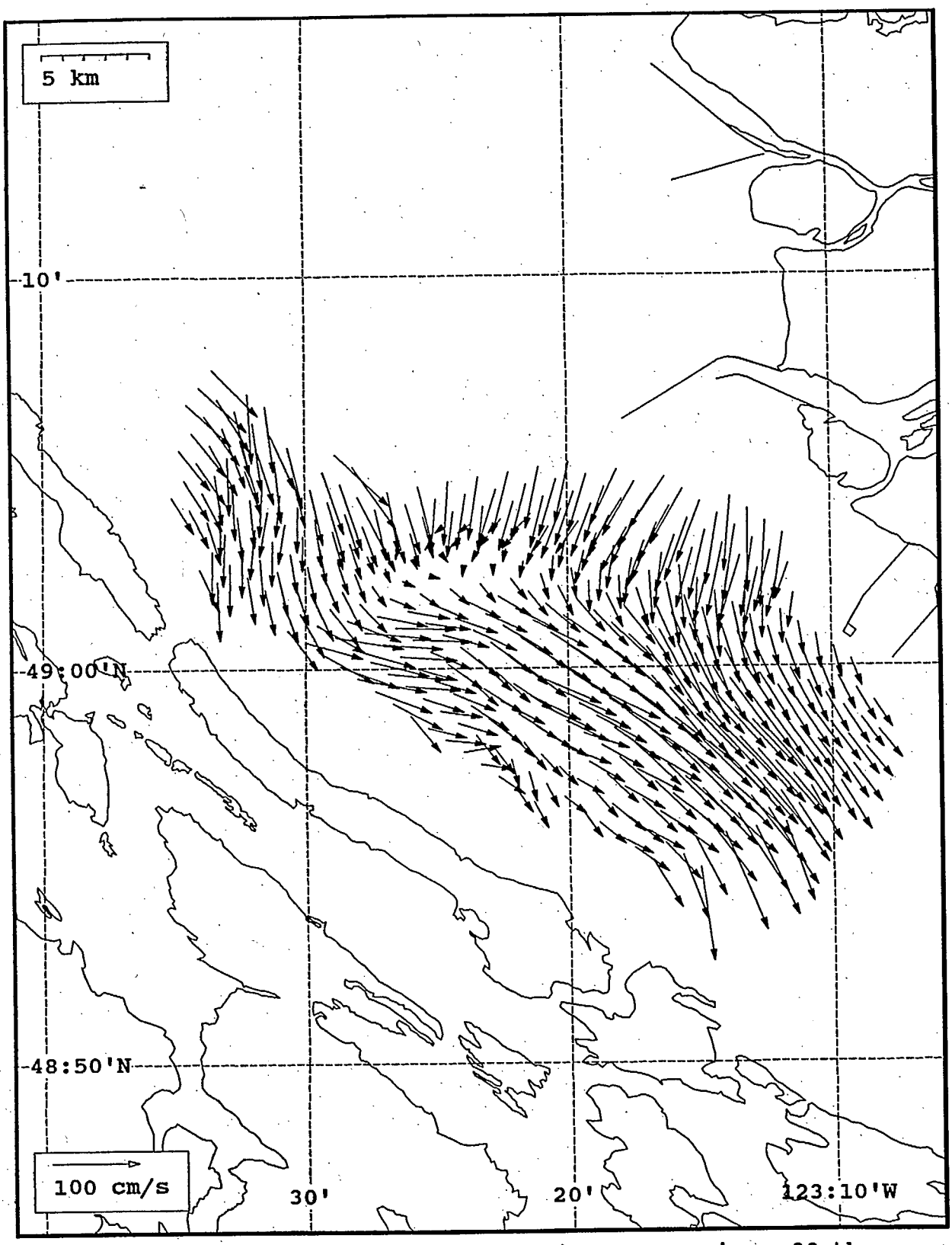

SeaSonde current field from the Strait of Georgia, off the mouth of the Fraser River, for 07:00 Z, August 3, 1993.

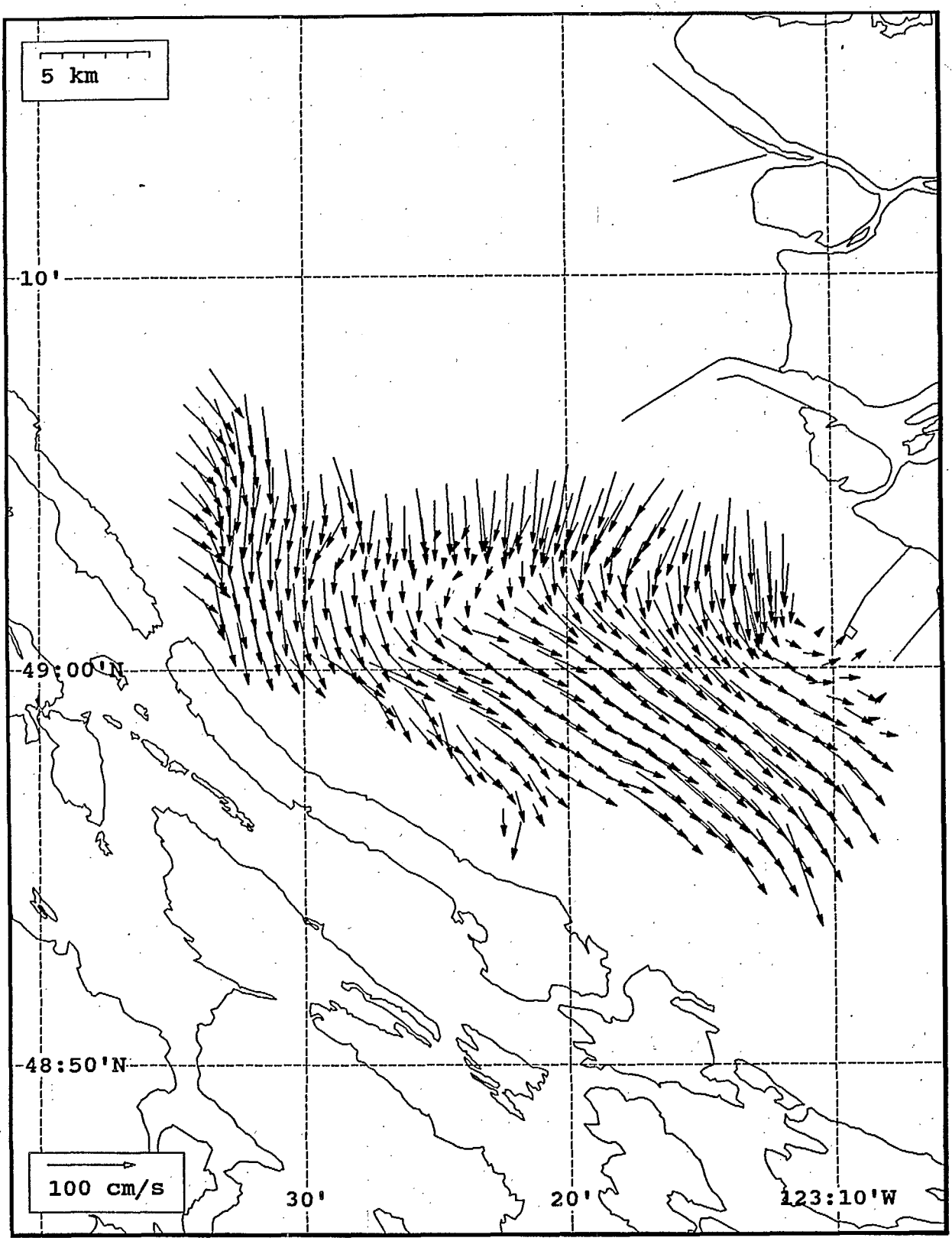

SeaSonde current field from the Strait of Georgia, off the mouth of the Fraser River, for 08:00 Z, August 3, 1993.

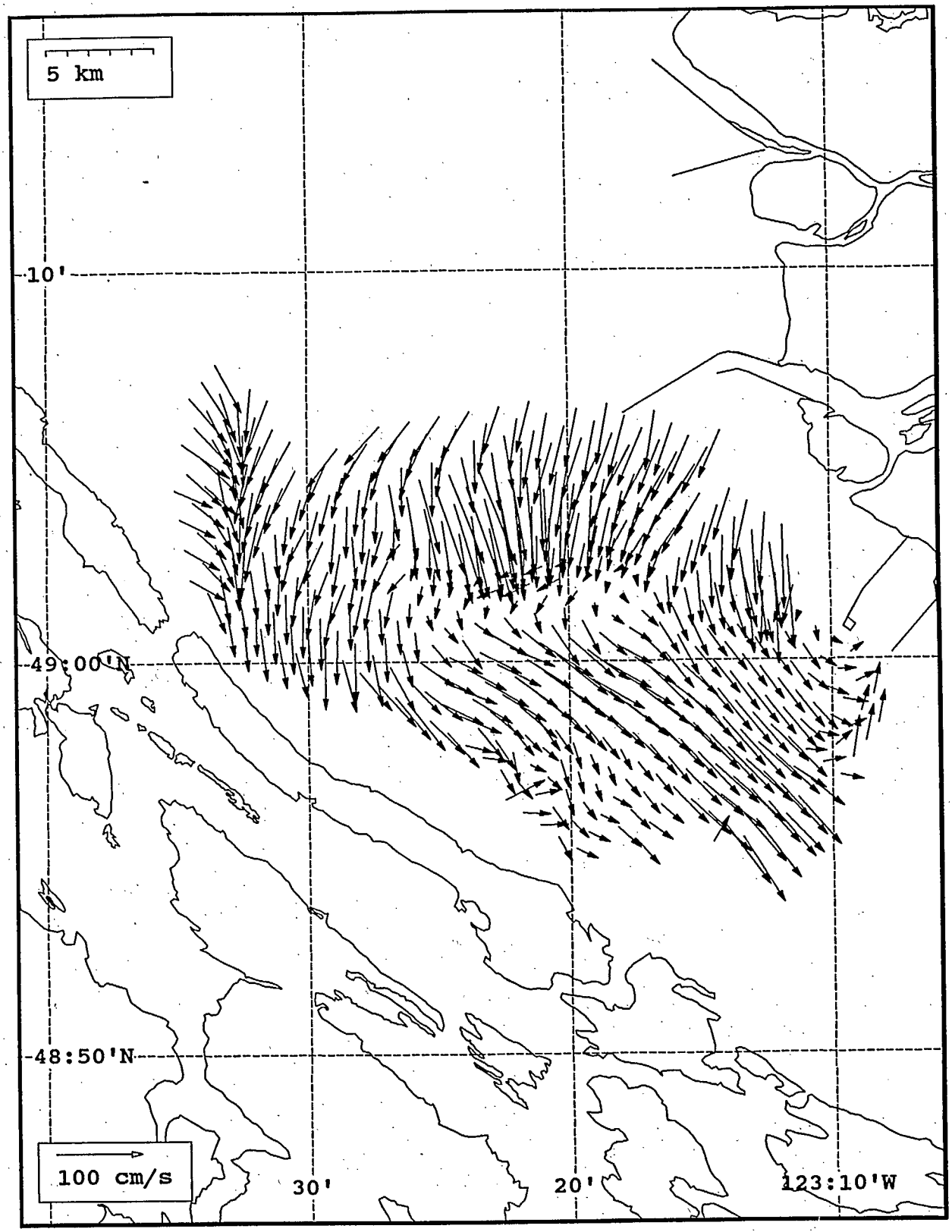

SeaSonde current field from the Strait of Georgia, off the mouth of the Fraser River, for 09:00 Z, August 3, 1993.

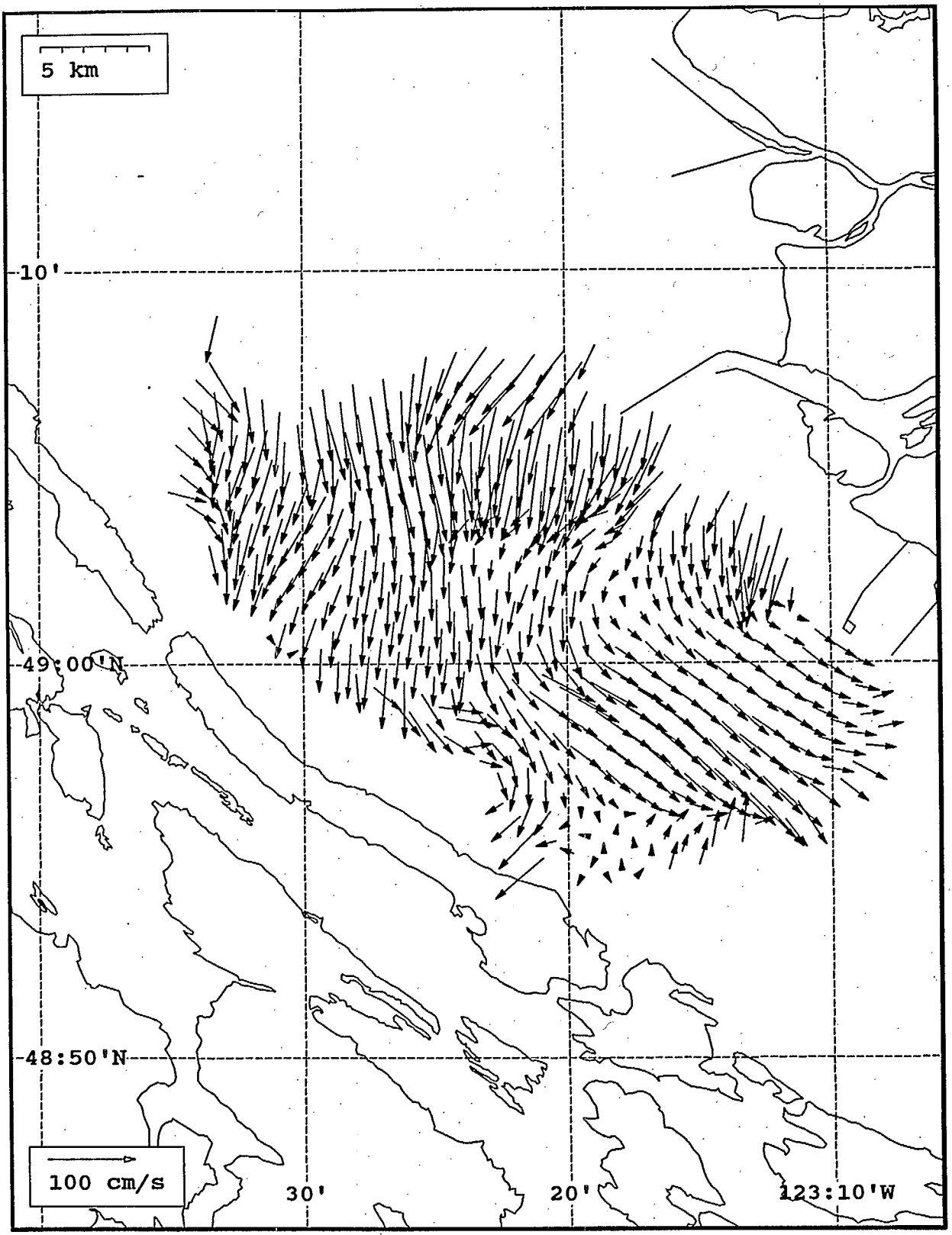

SeaSonde current field from the Strait of Georgia, off the mouth of the Fraser River, for 10:00 Z, August 3, 1993.

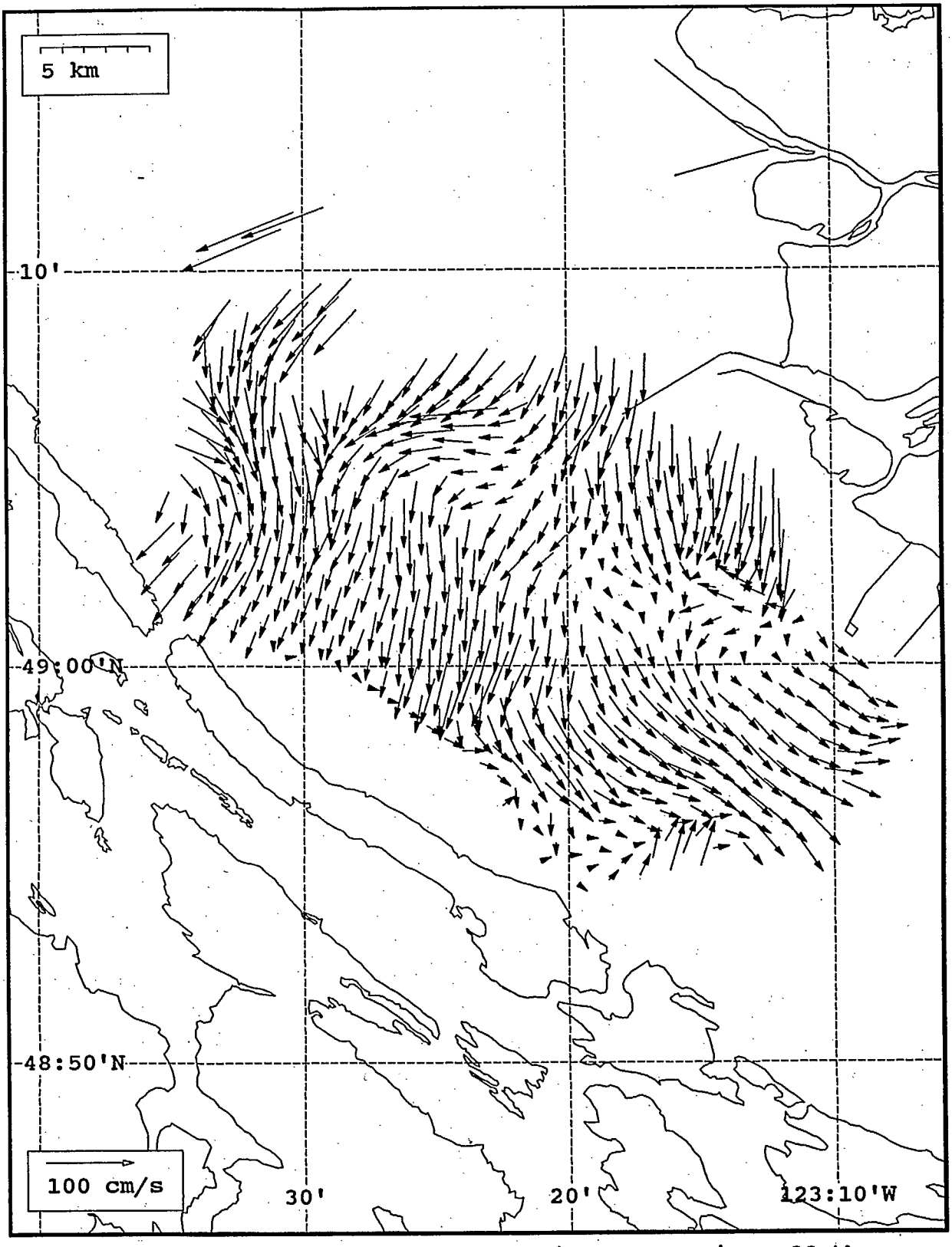

SeaSonde current field from the Strait of Georgia, off the mouth of the Fraser River, for 11:00 Z, August 3, 1993.

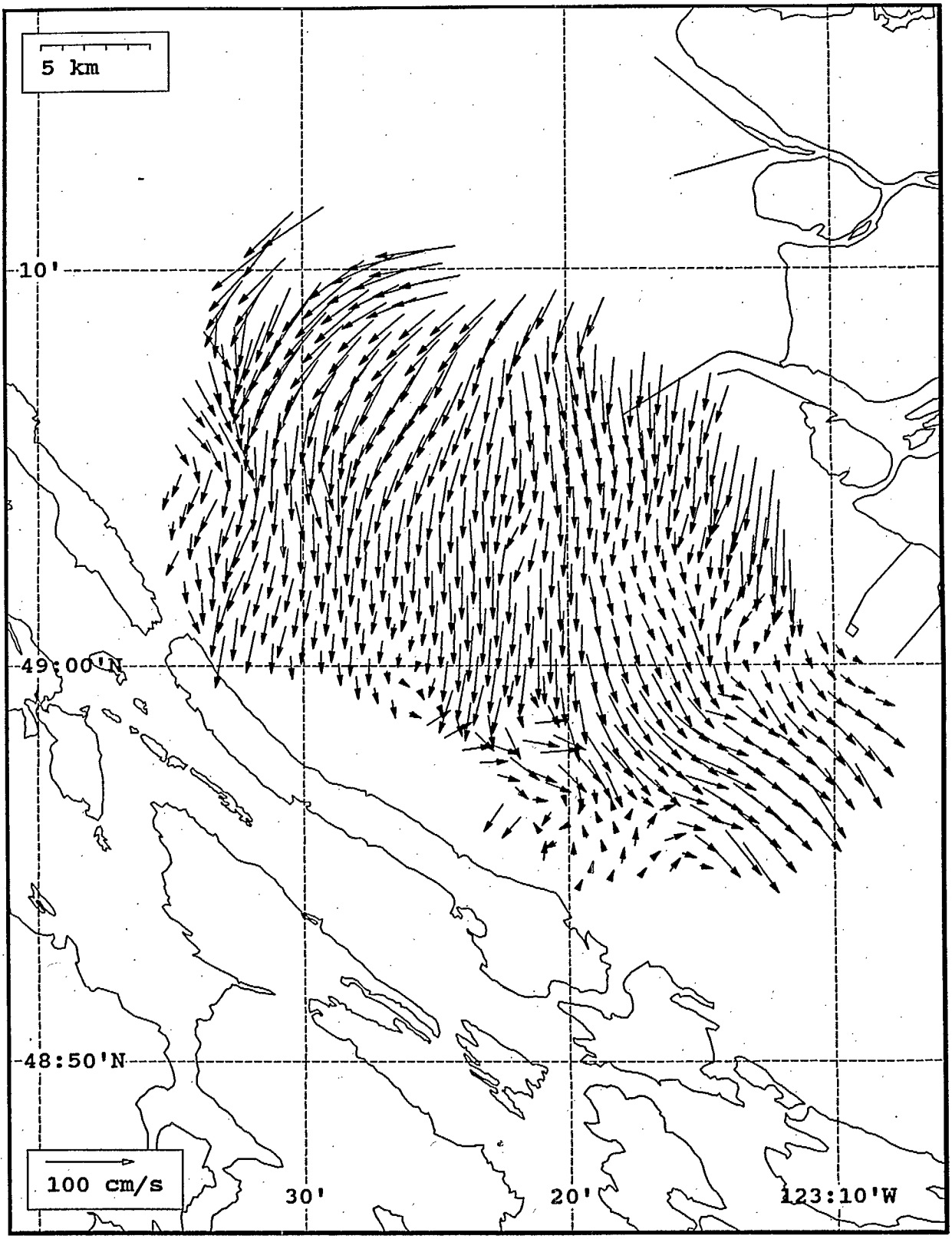

SeaSonde current field from the Strait of Georgia, off the mouth of the Fraser River, for 12:00 Z, August 3, 1993.

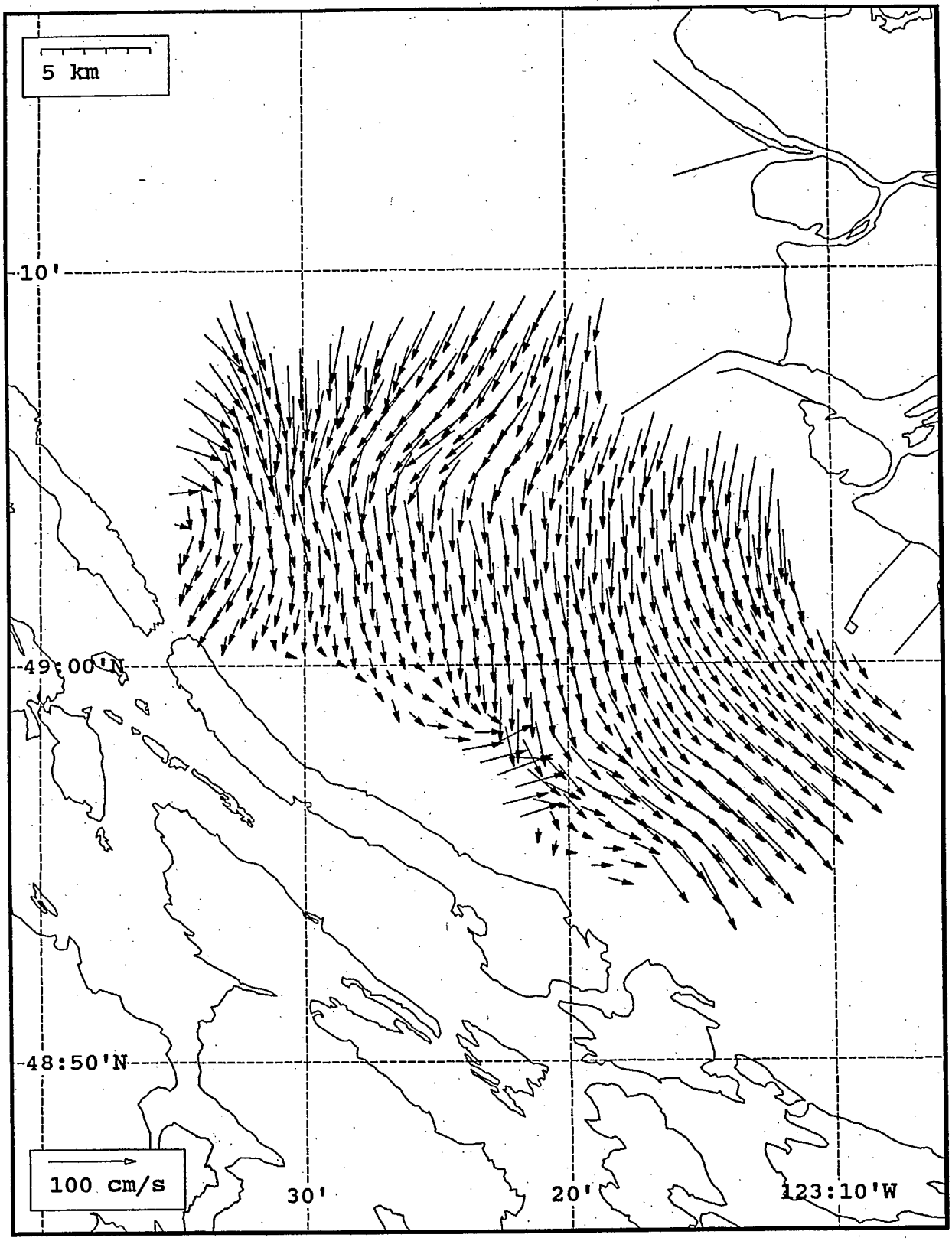

SeaSonde current field from the Strait of Georgia, off the mouth of the Fraser River, for 13:00 Z, August 3, 1993.

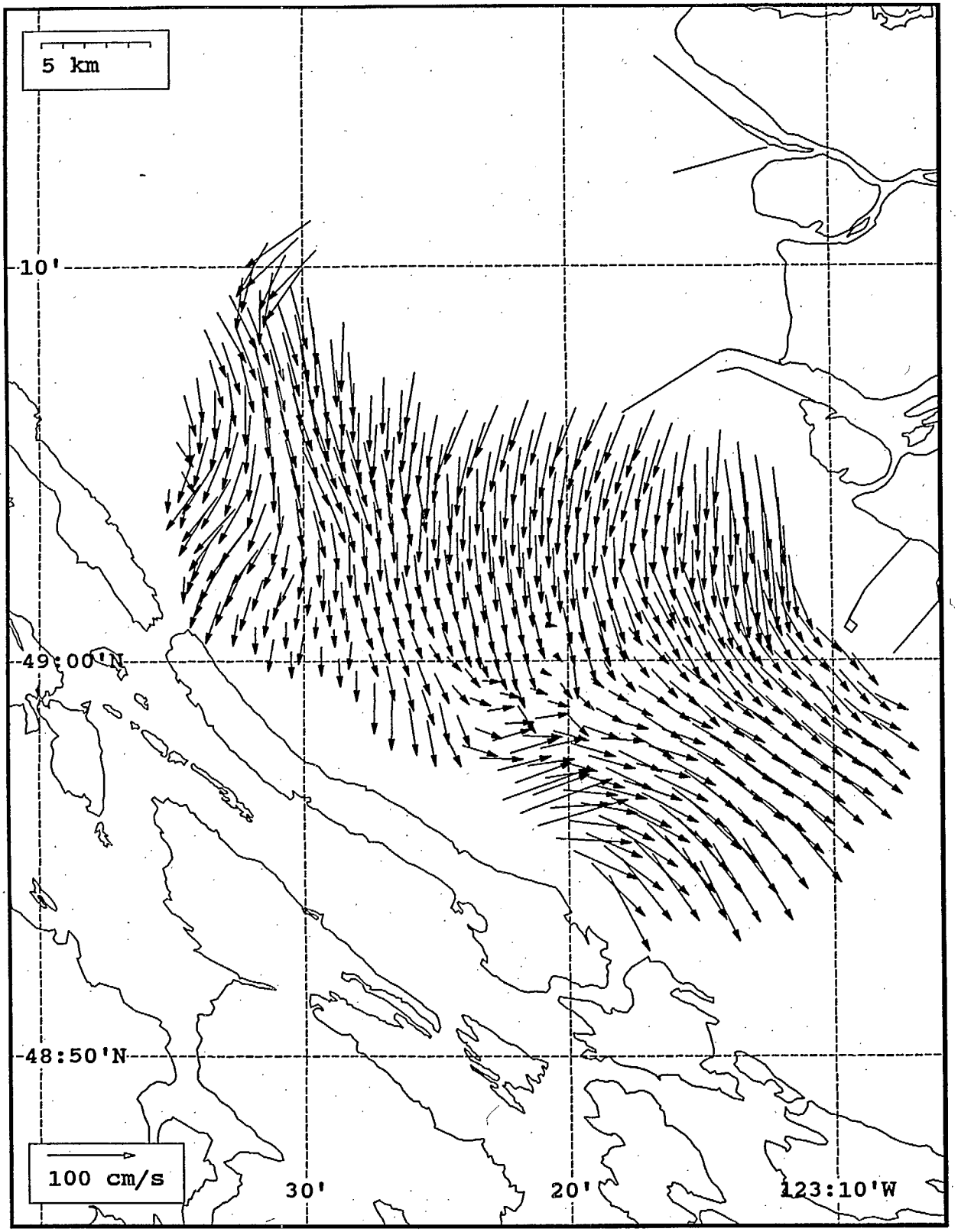

SeaSonde current field from the Strait of Georgia, off the mouth of the Fraser River, for 14:00 Z, August 3, 1993.

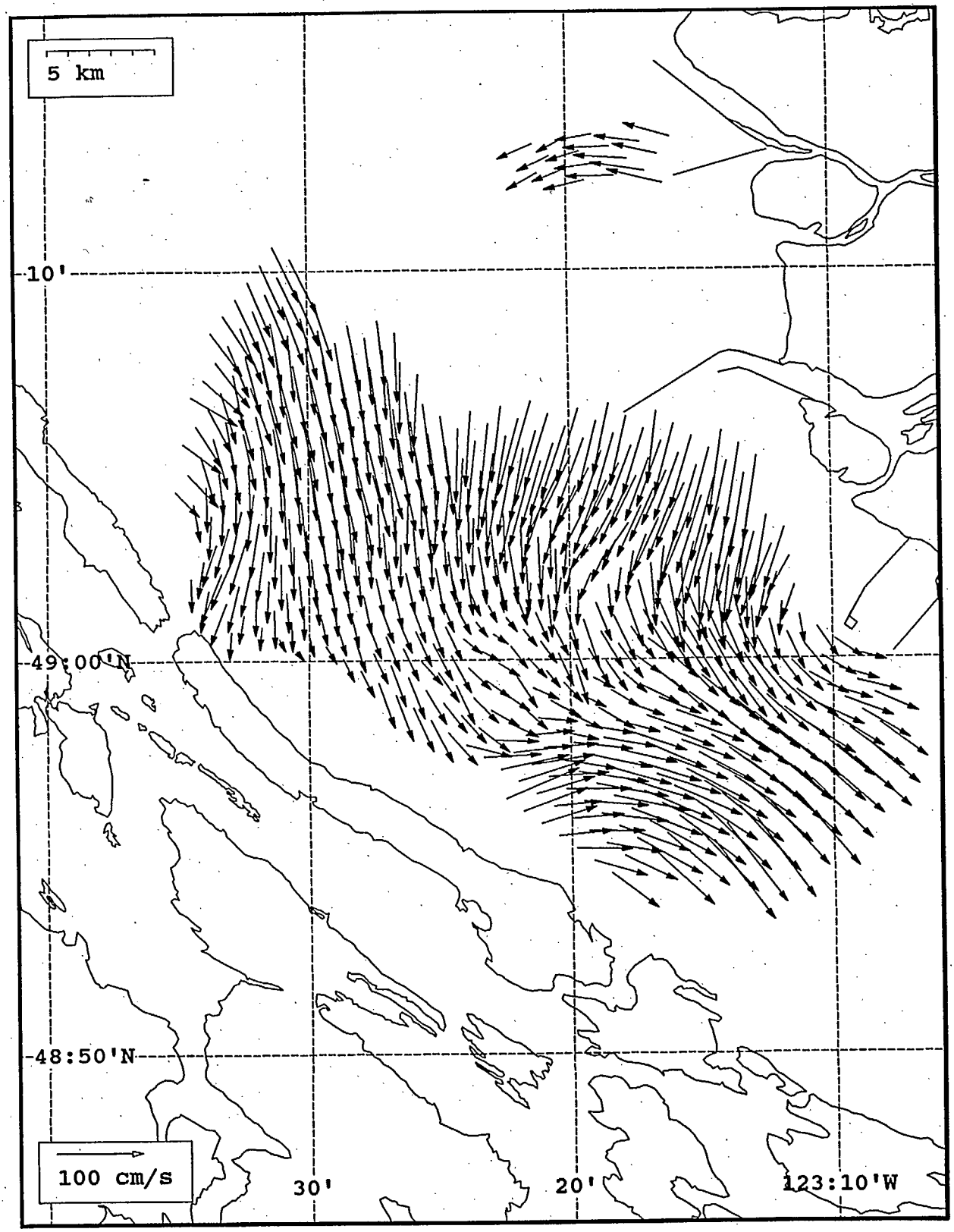

SeaSonde current field from the Strait of Georgia, off the mouth of the Fraser River, for 15:00 Z, August 3, 1993.

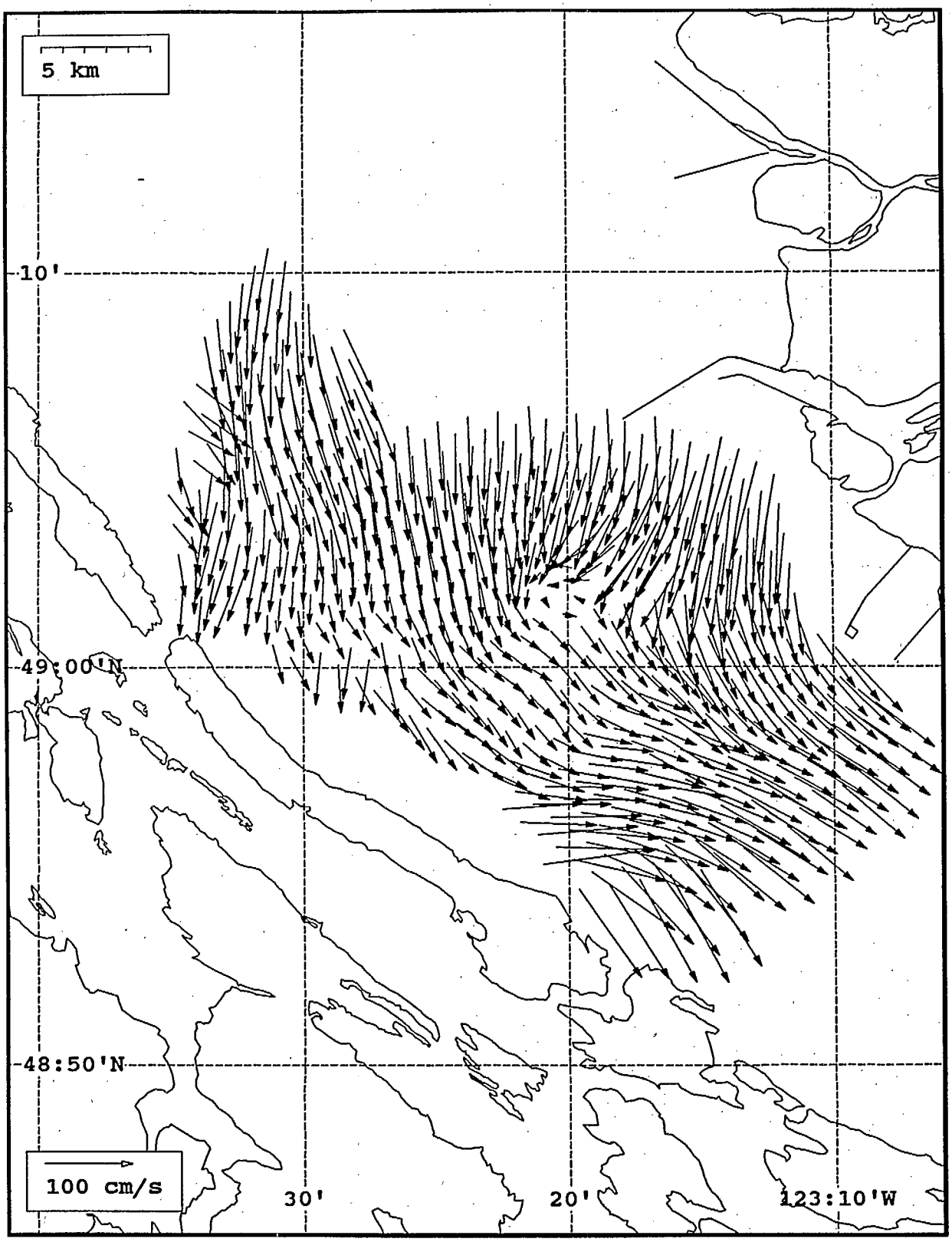

SeaSonde current field from the Strait of Georgia, off the mouth of the Fraser River, for 16:00 Z, August 3, 1993.

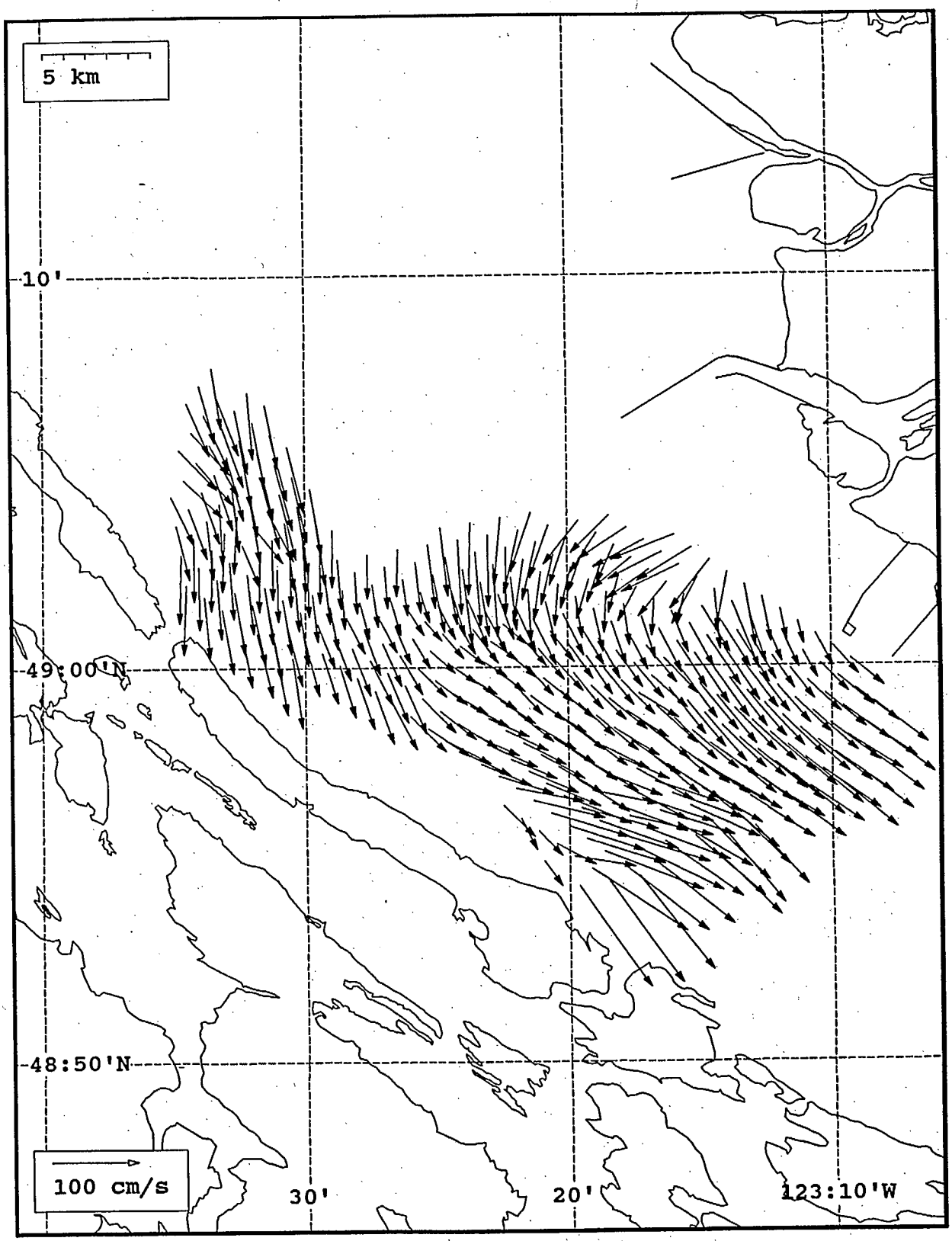

SeaSonde current field from the Strait of Georgia, off the mouth of the Fraser River, for 17:00 Z, August 3, 1993.

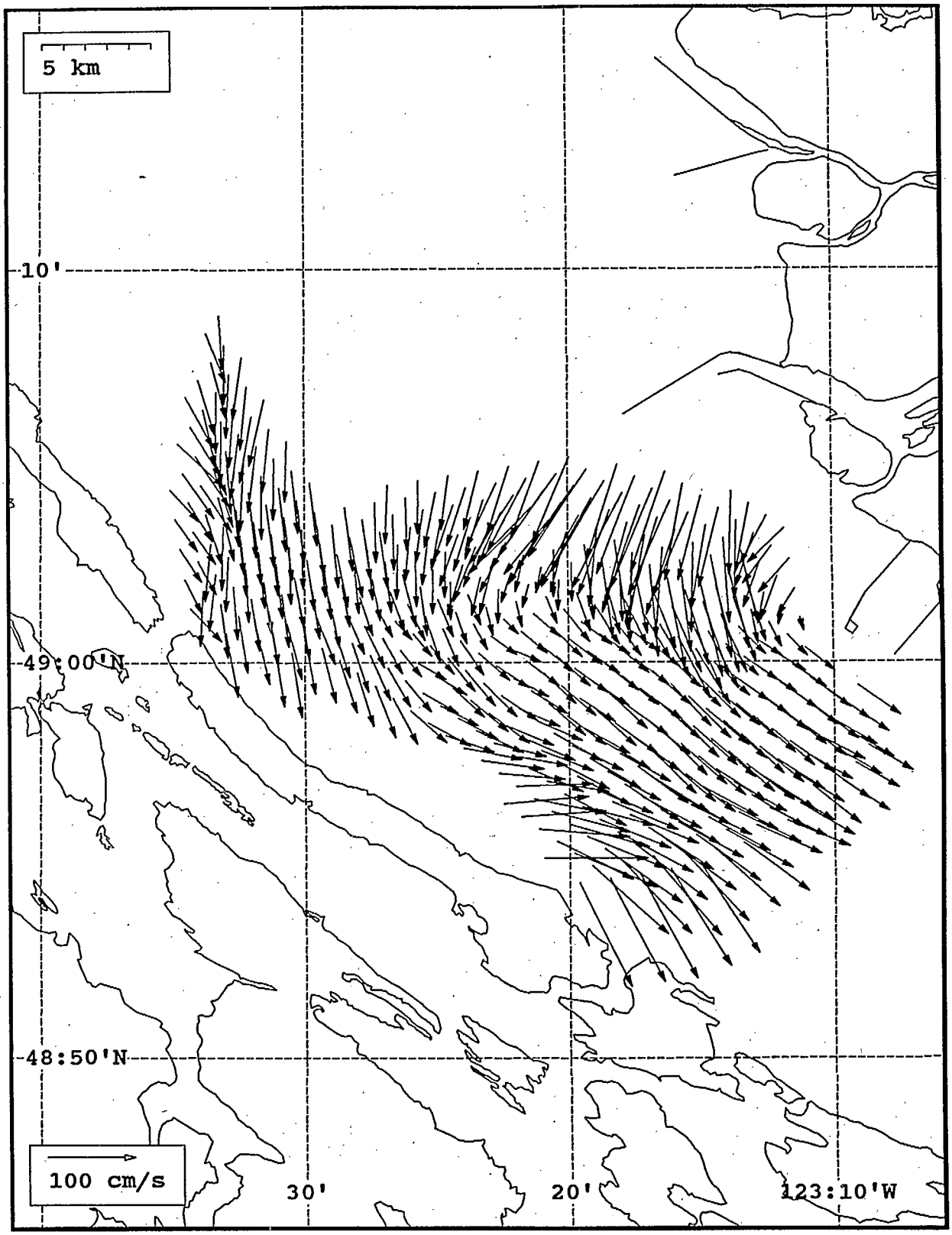

SeaSonde current field from the Strait of Georgia, off the mouth of the Fraser River, for 18:00 Z, August 3, 1993.

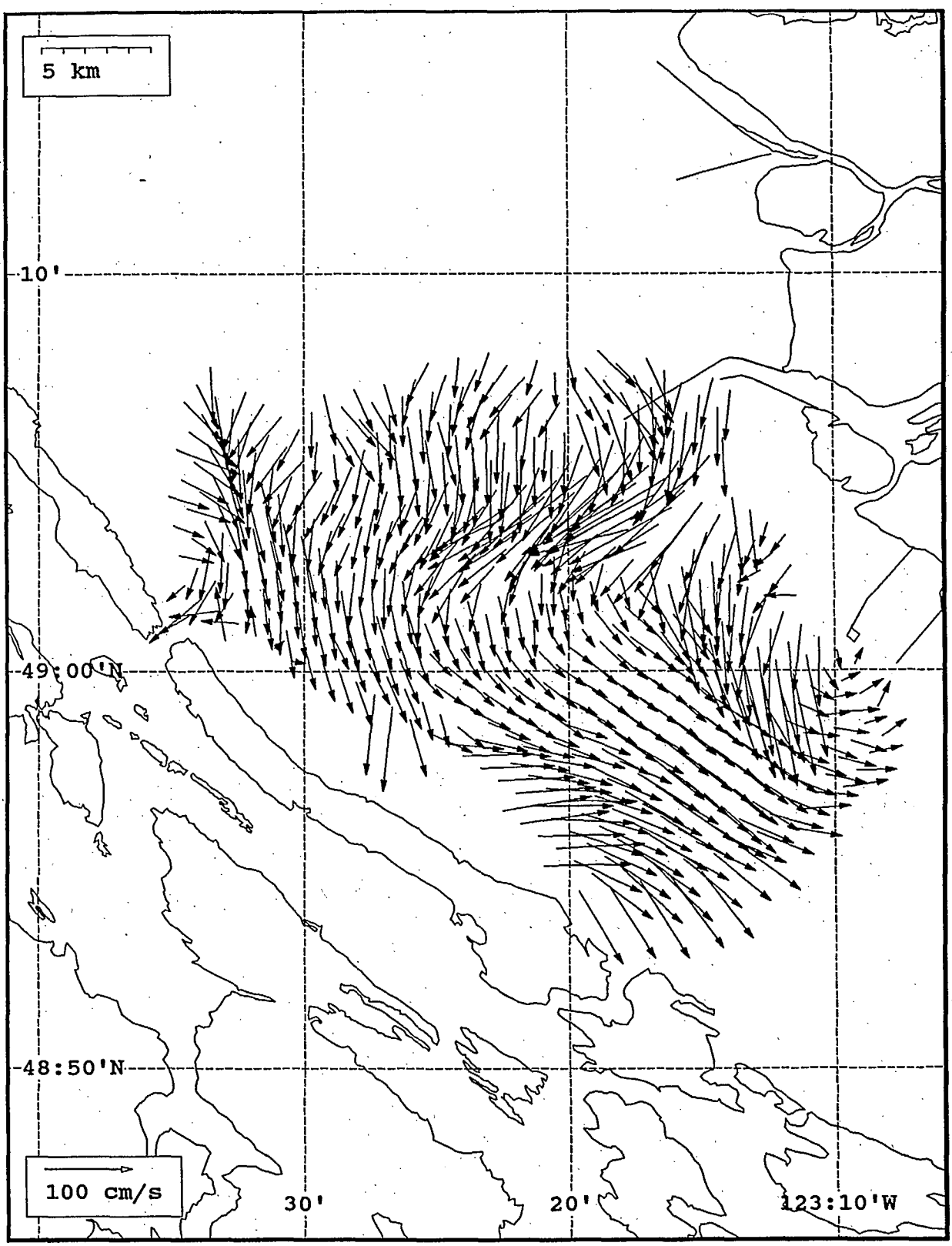

SeaSonde current field from the Strait of Georgia, off the mouth of the Fraser River, for 19:00 Z, August 3, 1993.

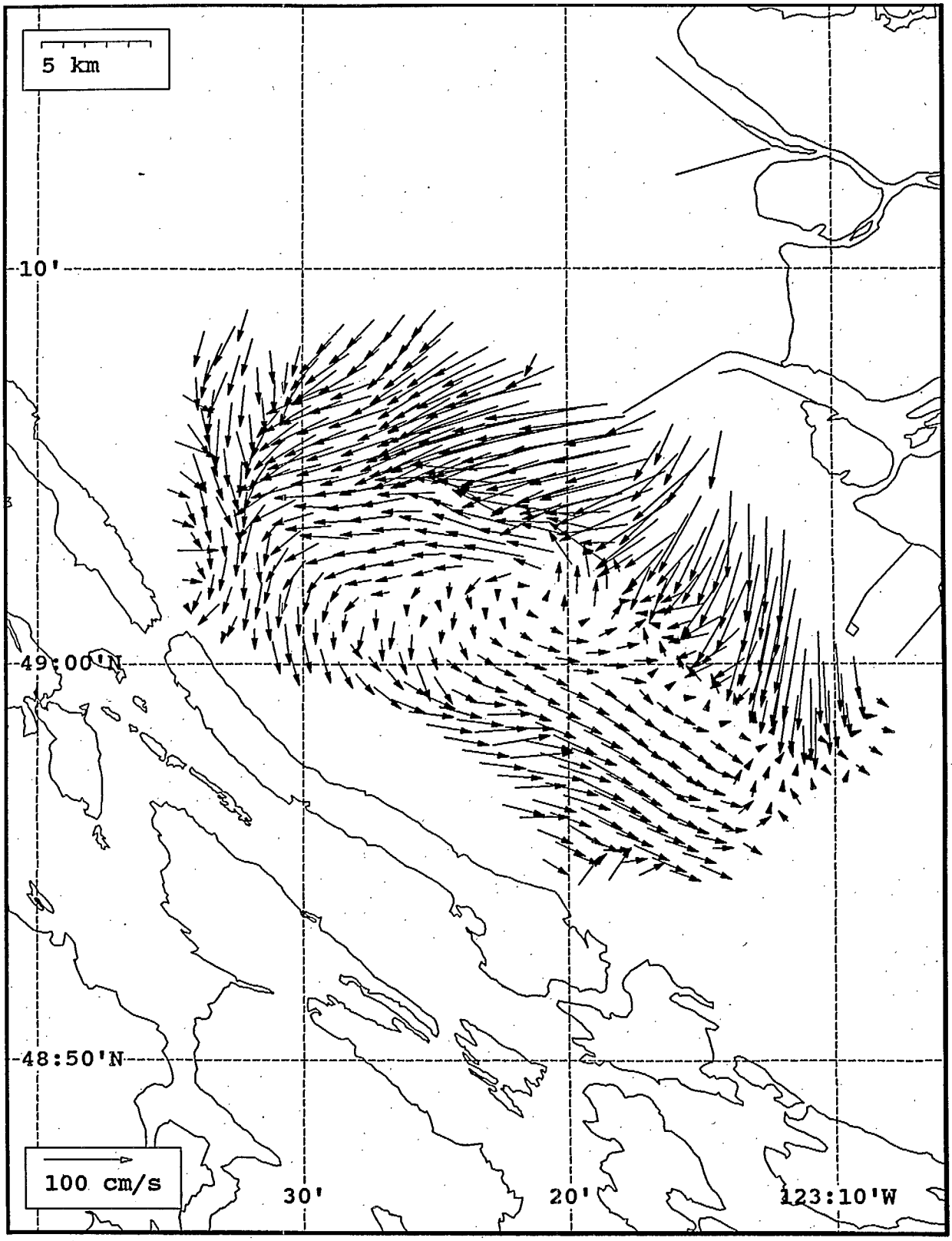

SeaSonde current field from the Strait of Georgia, off the mouth of the Fraser River, for 21:00 Z, August 3, 1993.

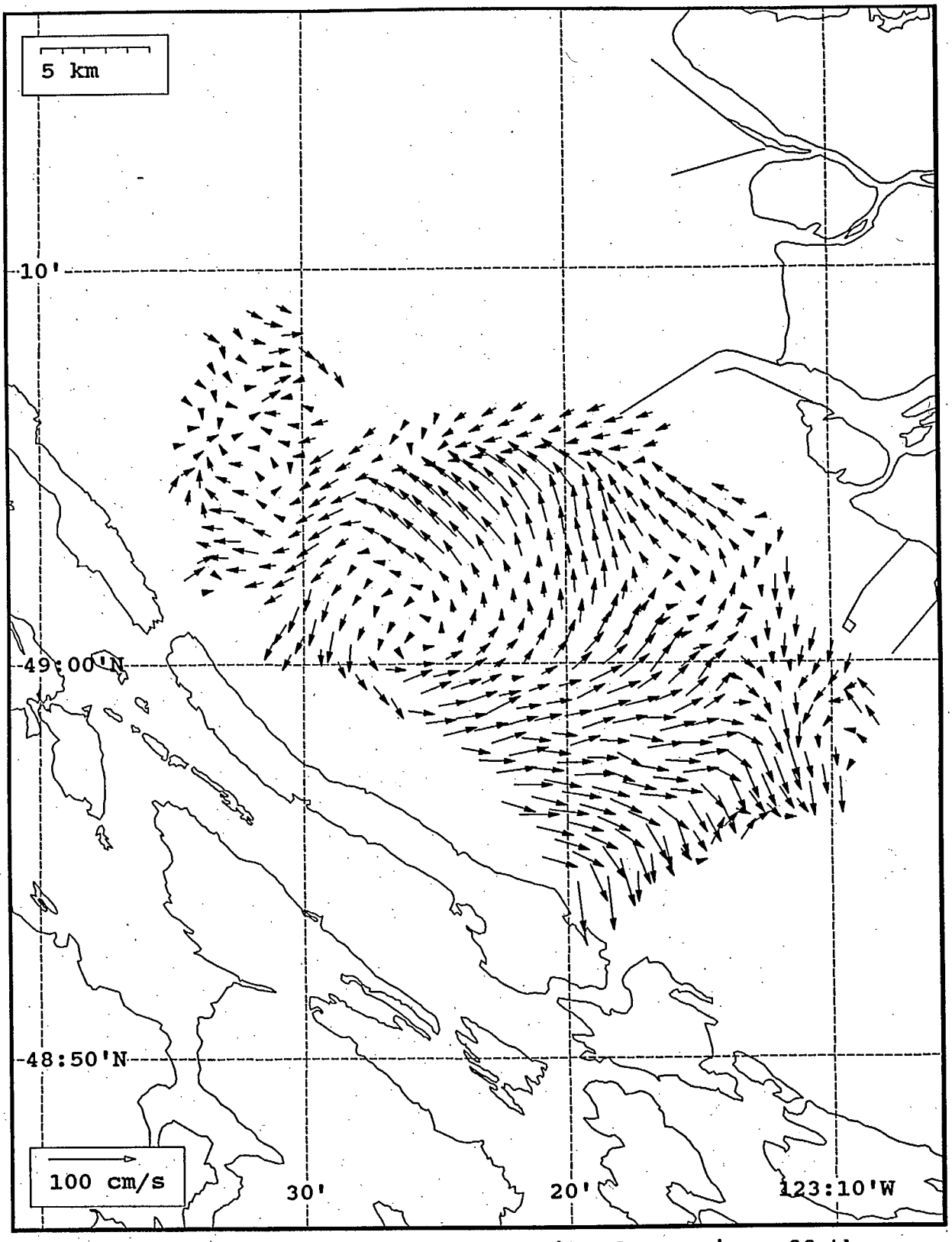

SeaSonde current field from the Strait of Georgia, off the mouth of the Fraser River, for 01:00 Z, August 5, 1993.

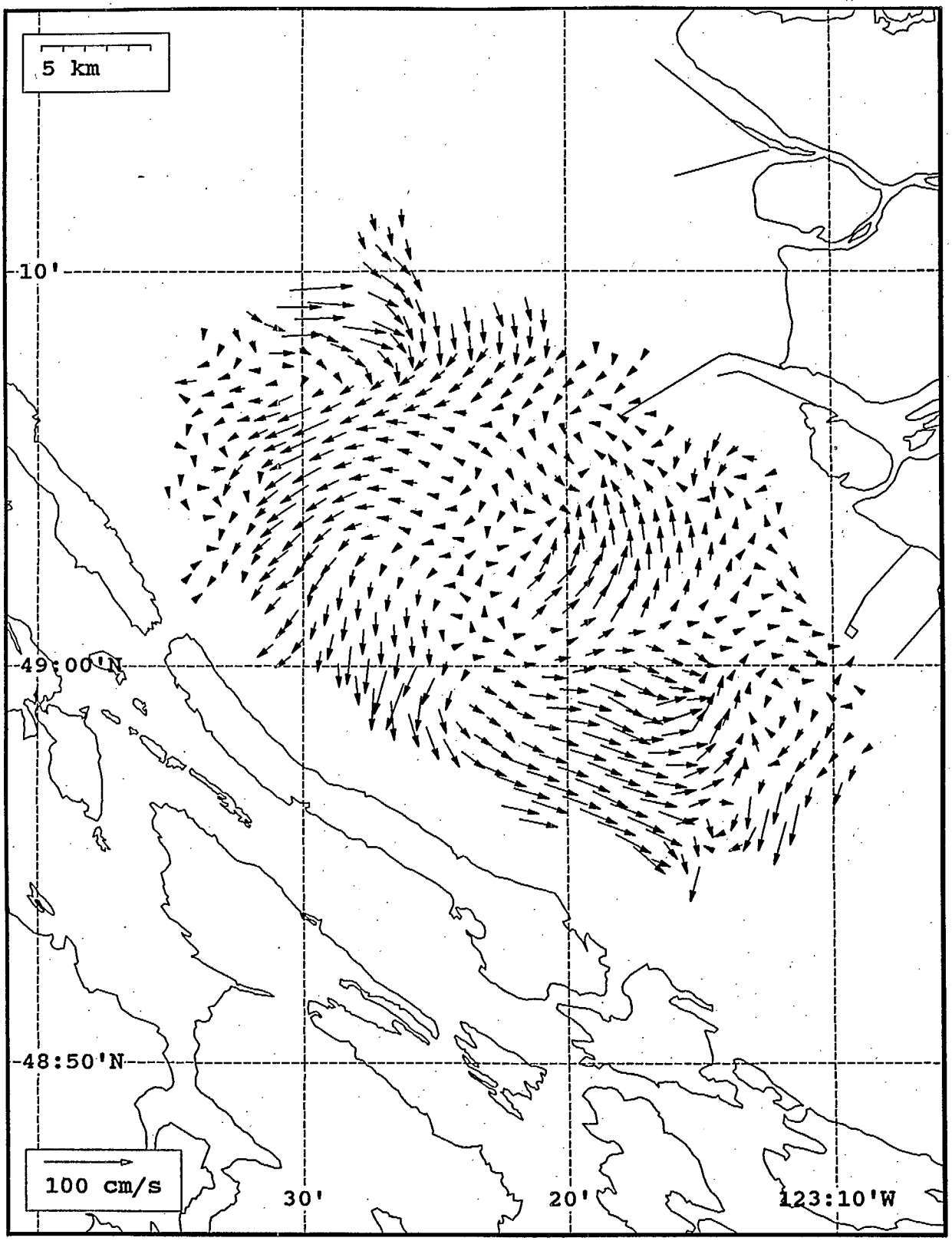

SeaSonde current field from the Strait of Georgia, off the mouth of the Fraser River, for 02:00 Z, August 5, 1993.

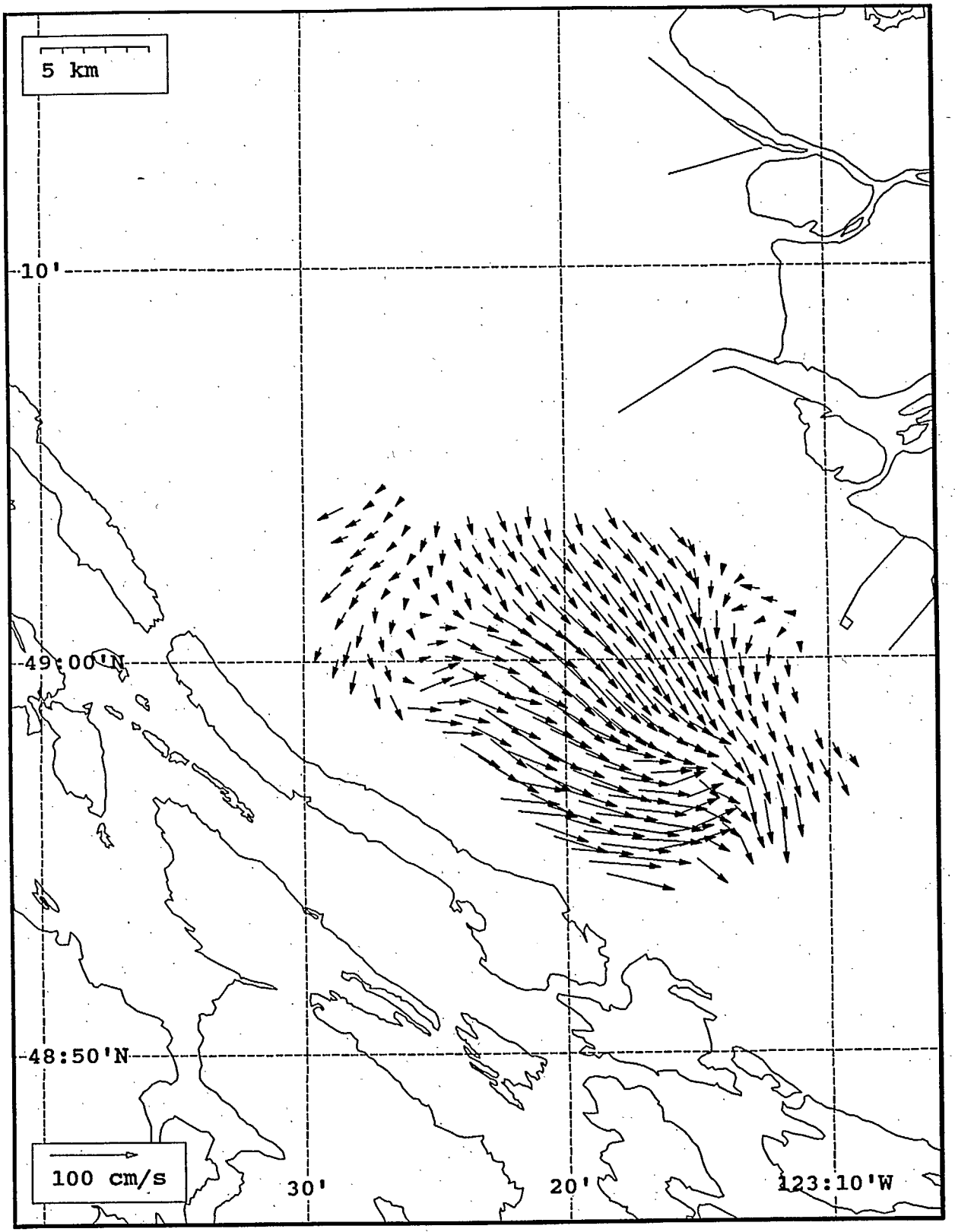

SeaSonde current field from the Strait of Georgia, off the mouth of the Fraser River, for 04:00 Z, August 5, 1993.

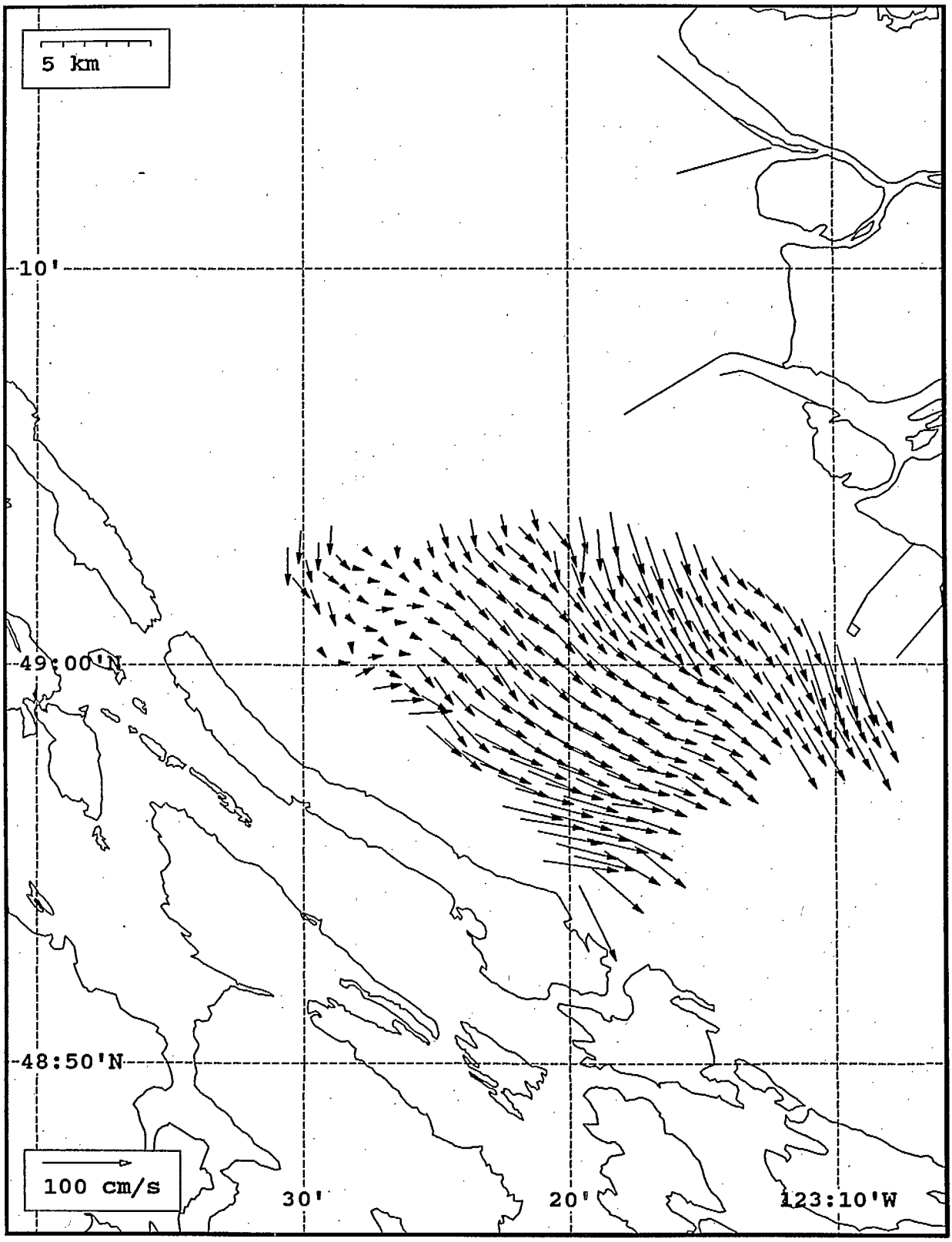

SeaSonde current field from the Strait of Georgia, off the mouth of the Fraser River, for 05:00 Z, August 5, 1993.

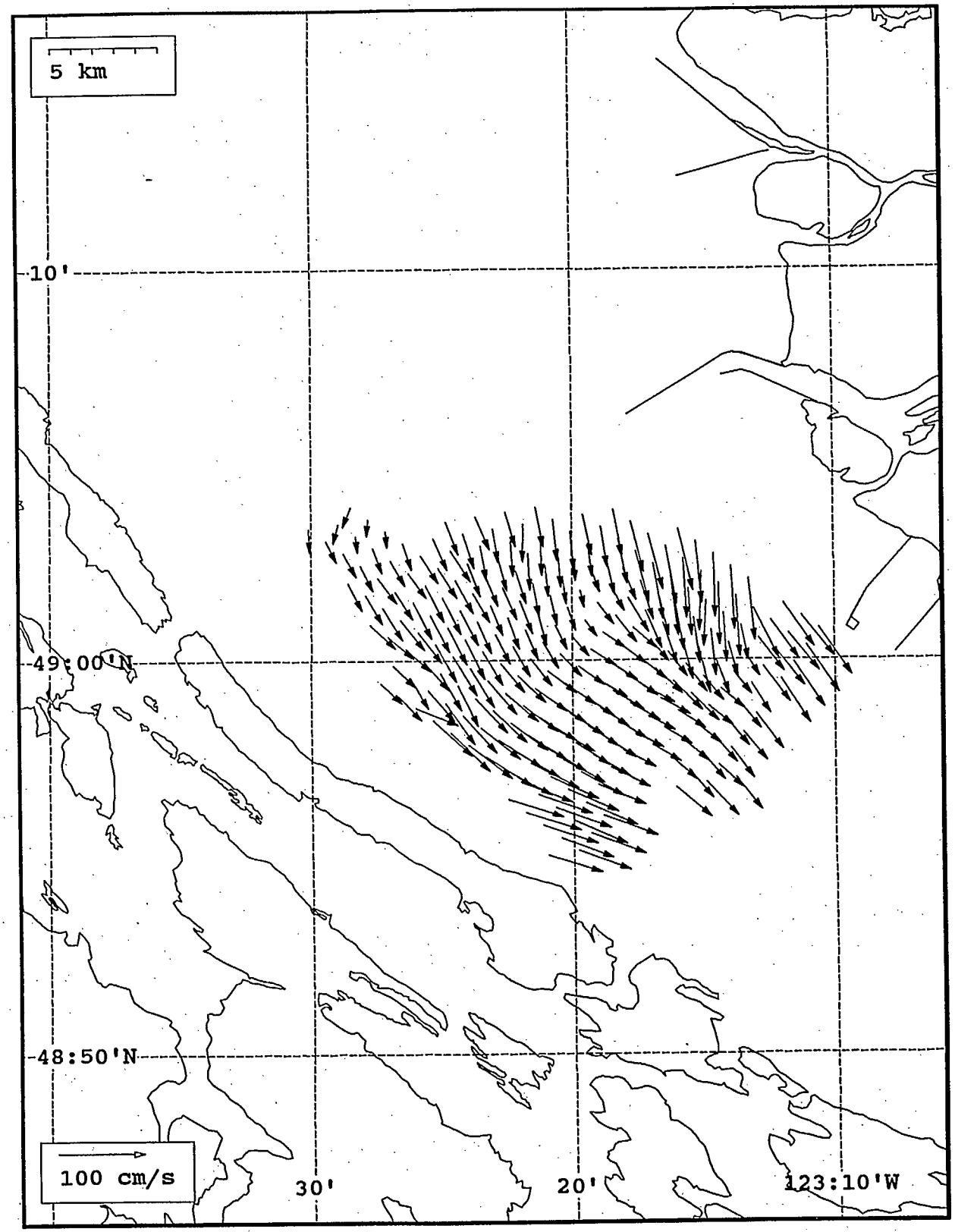

SeaSonde current field from the Strait of Georgia, off the mouth of the Fraser River, for 06:00 Z, August 5, 1993.

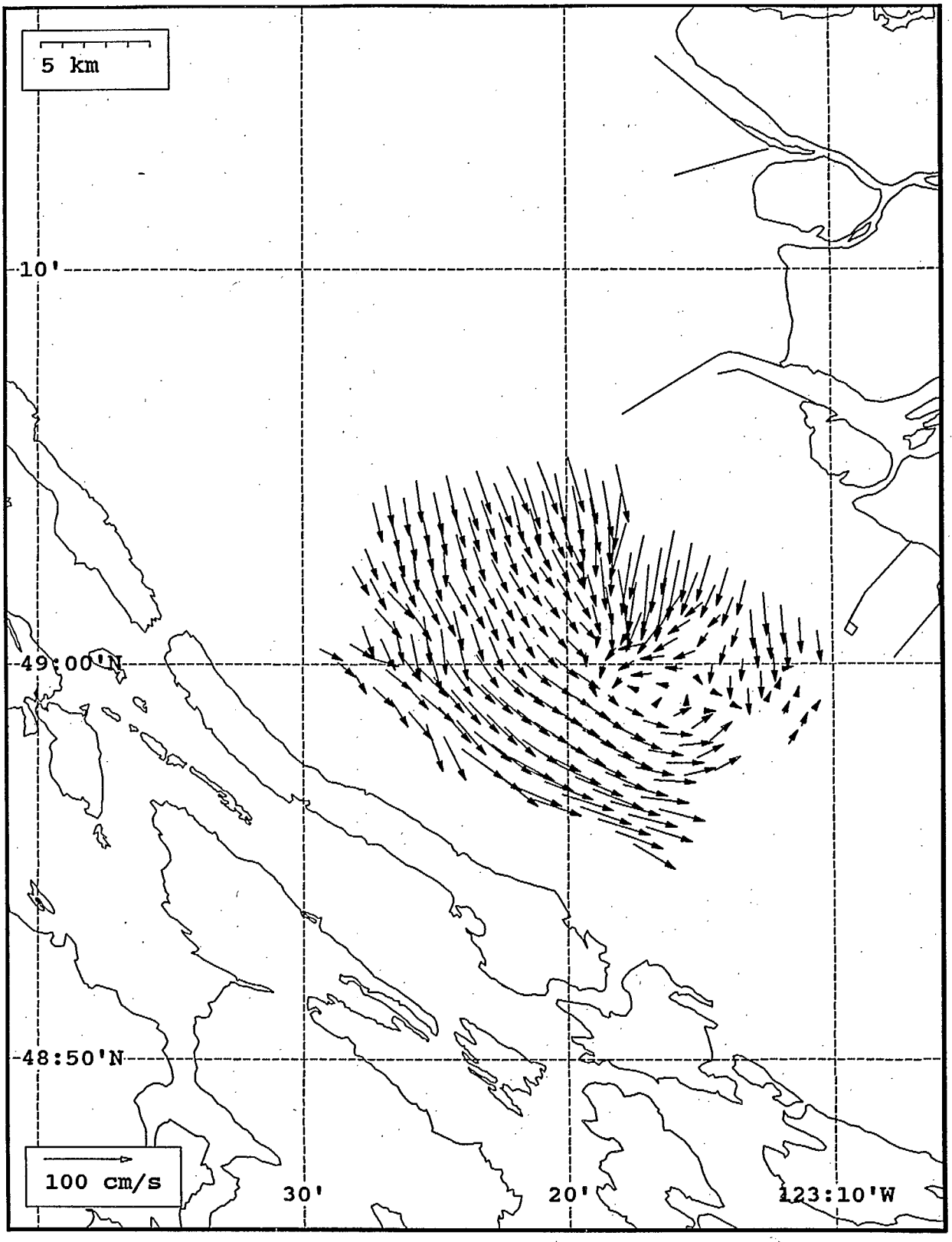

SeaSonde current field from the Strait of Georgia, off the mouth of the Fraser River, for 07:00 Z, August 5, 1993.

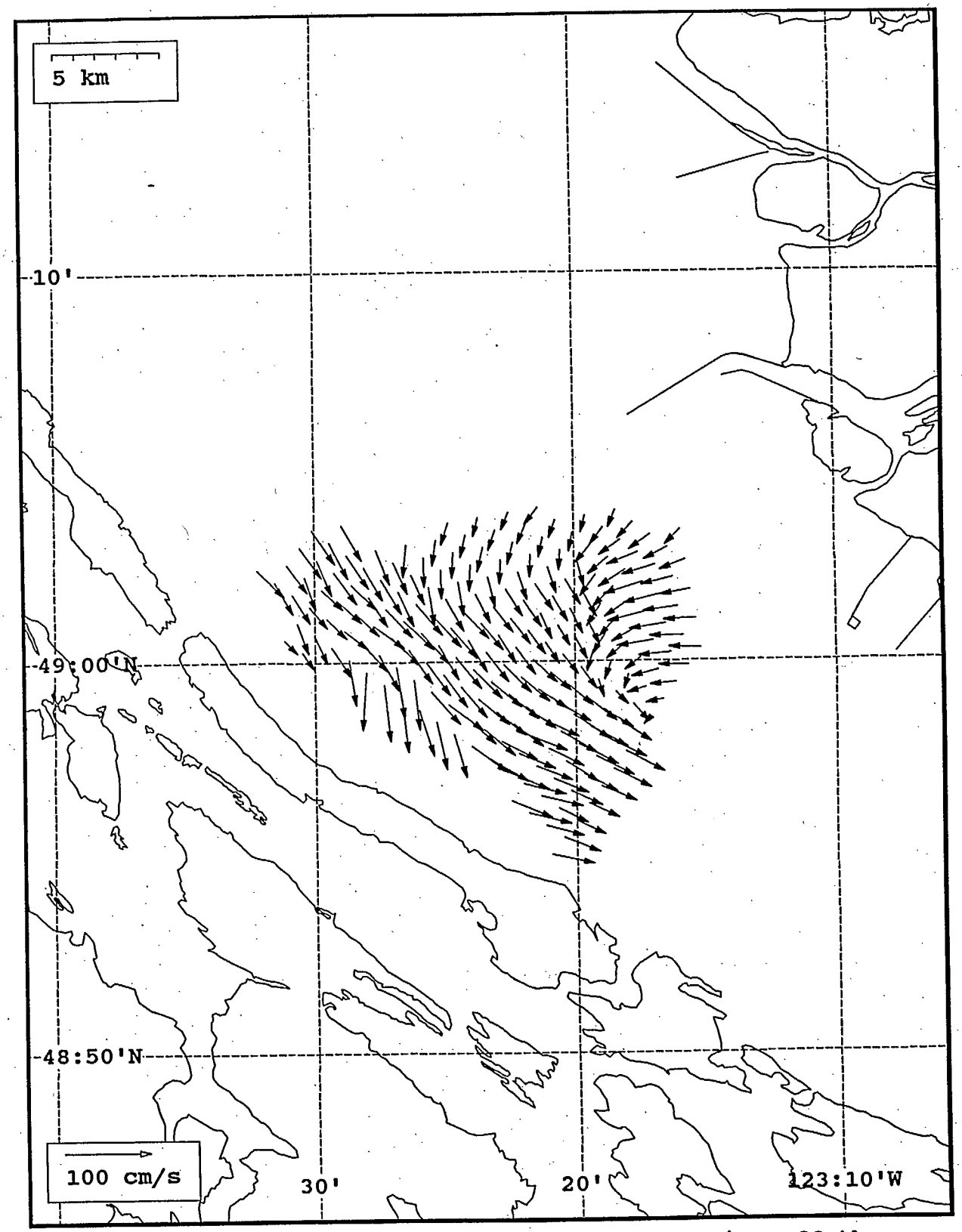

SeaSonde current field from the Strait of Georgia, off the mouth of the Fraser River, for 08:00 Z, August 5, 1993.

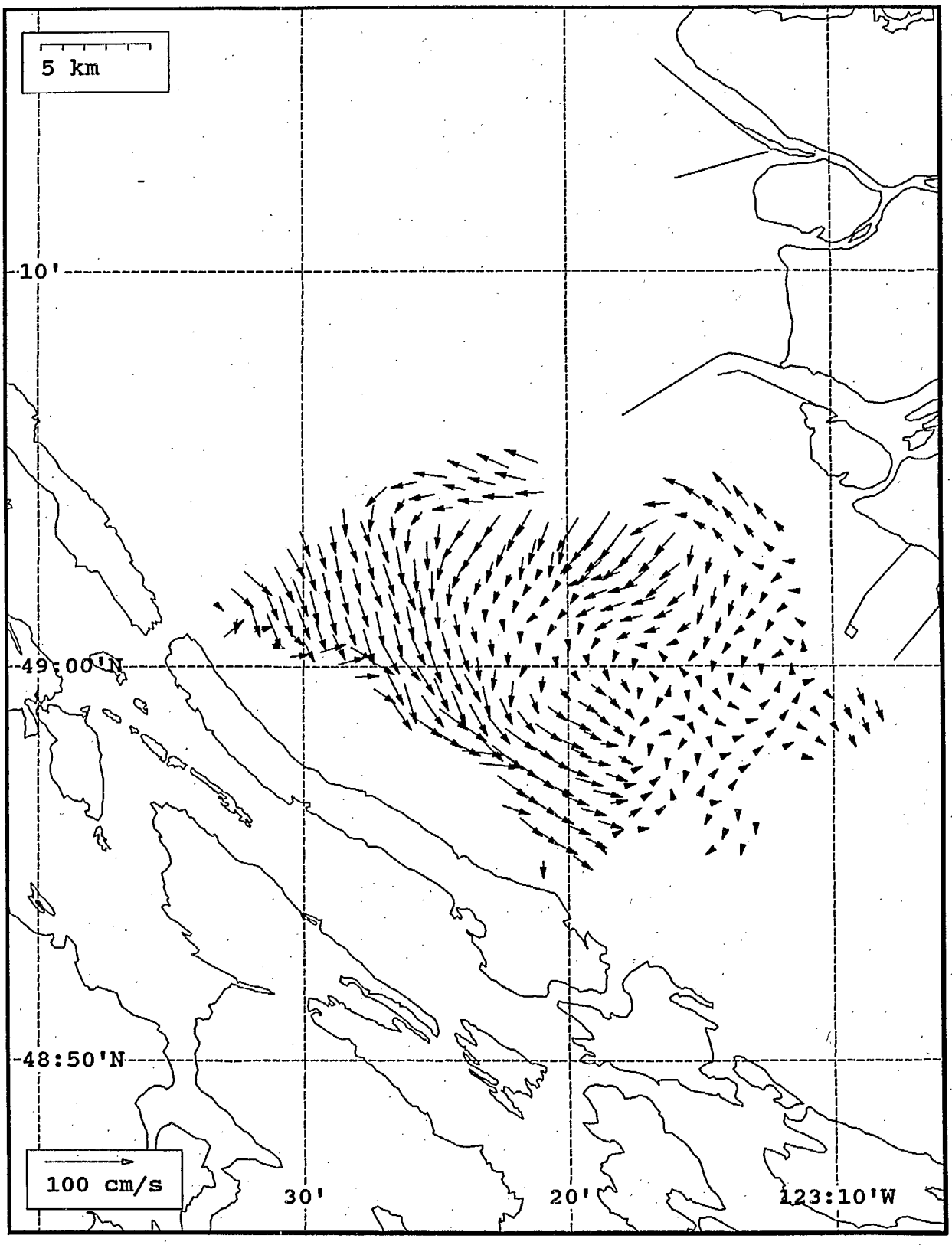

SeaSonde current field from the Strait of Georgia, off the mouth of the Fraser River, for 09:00 Z, August 5, 1993.

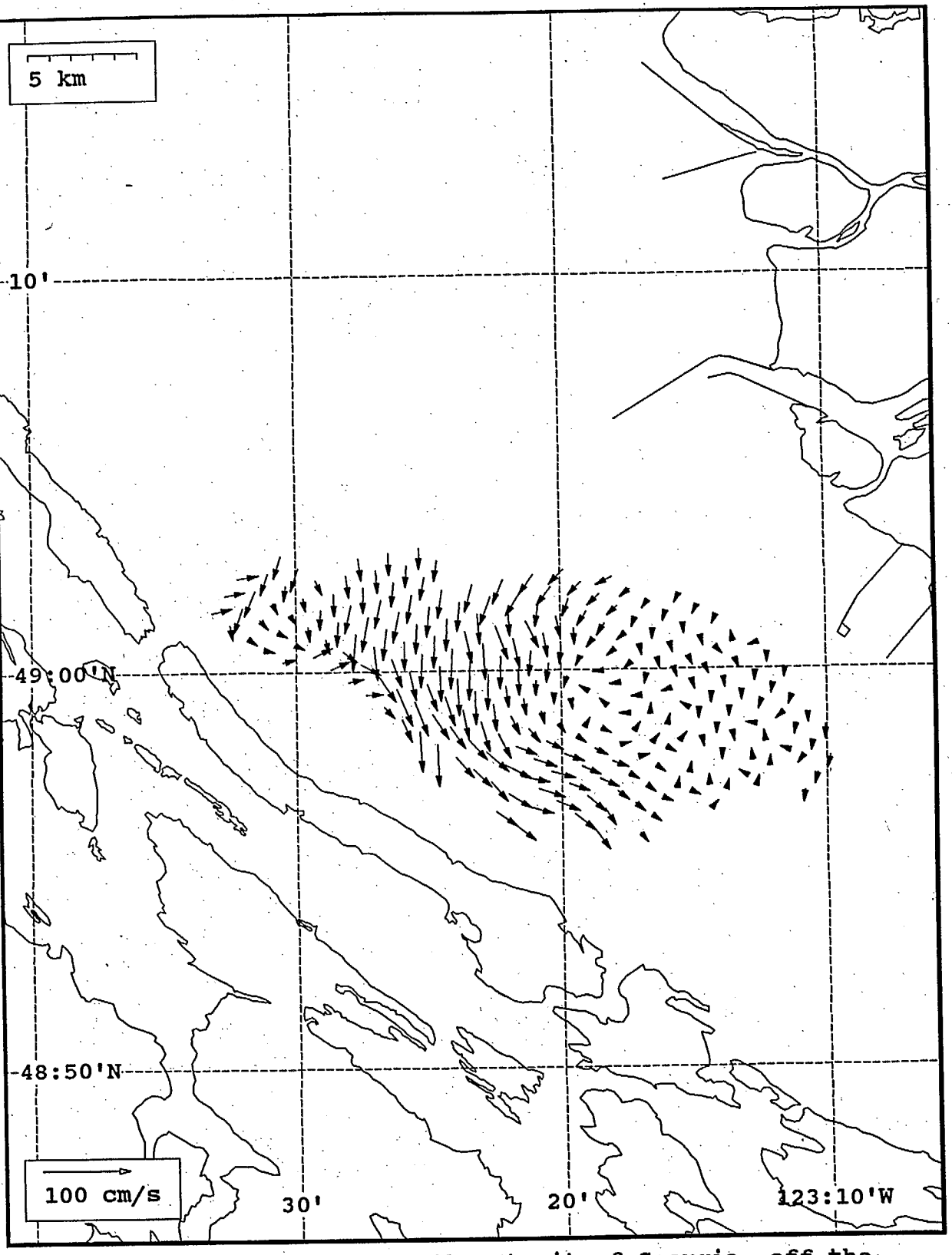

SeaSonde current field from the Strait of Georgia, off the mouth of the Fraser River, for 10:00 Z, August 5, 1993.

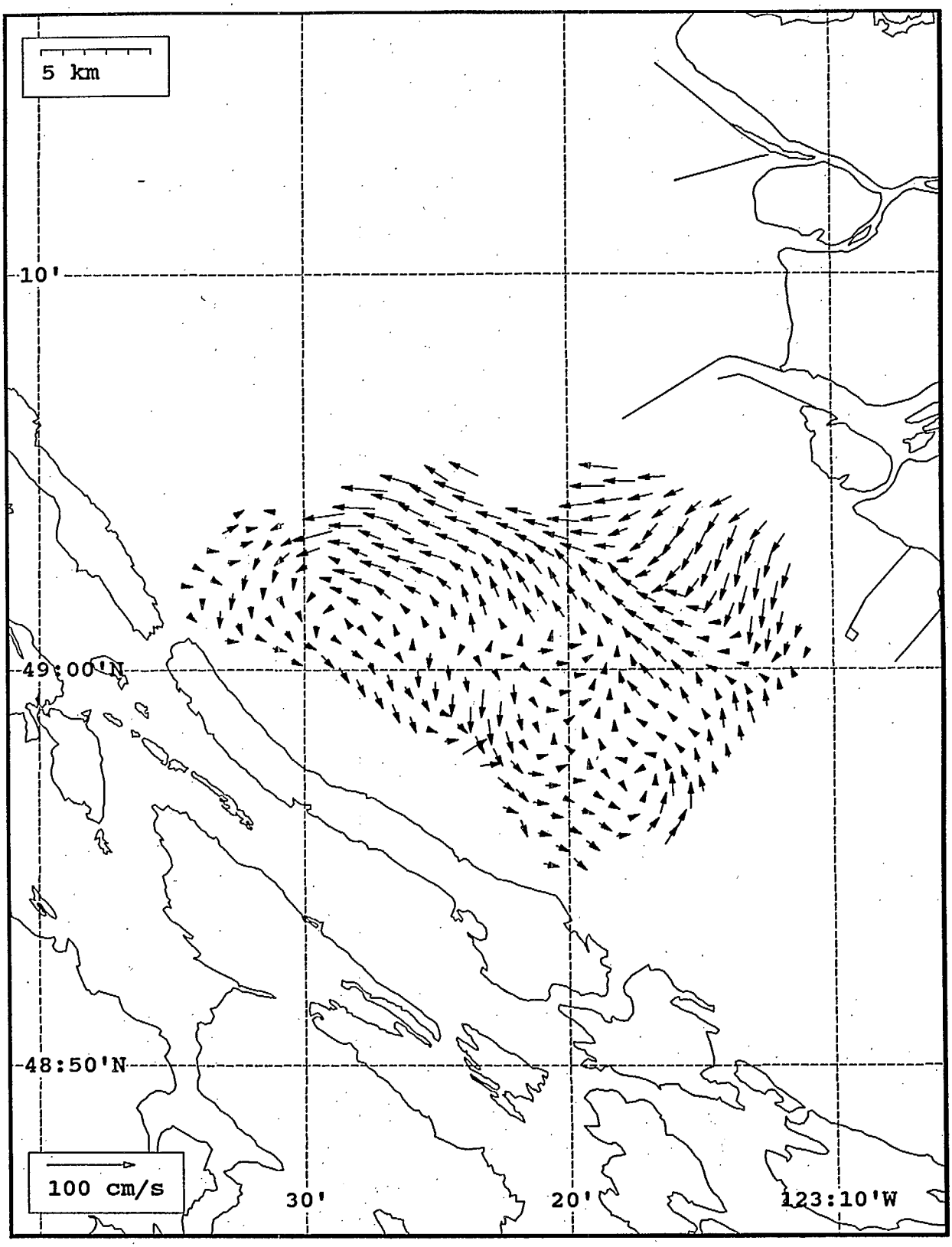

SeaSonde current field from the Strait of Georgia, off the mouth of the Fraser River, for 11:00 Z, August 5, 1993.

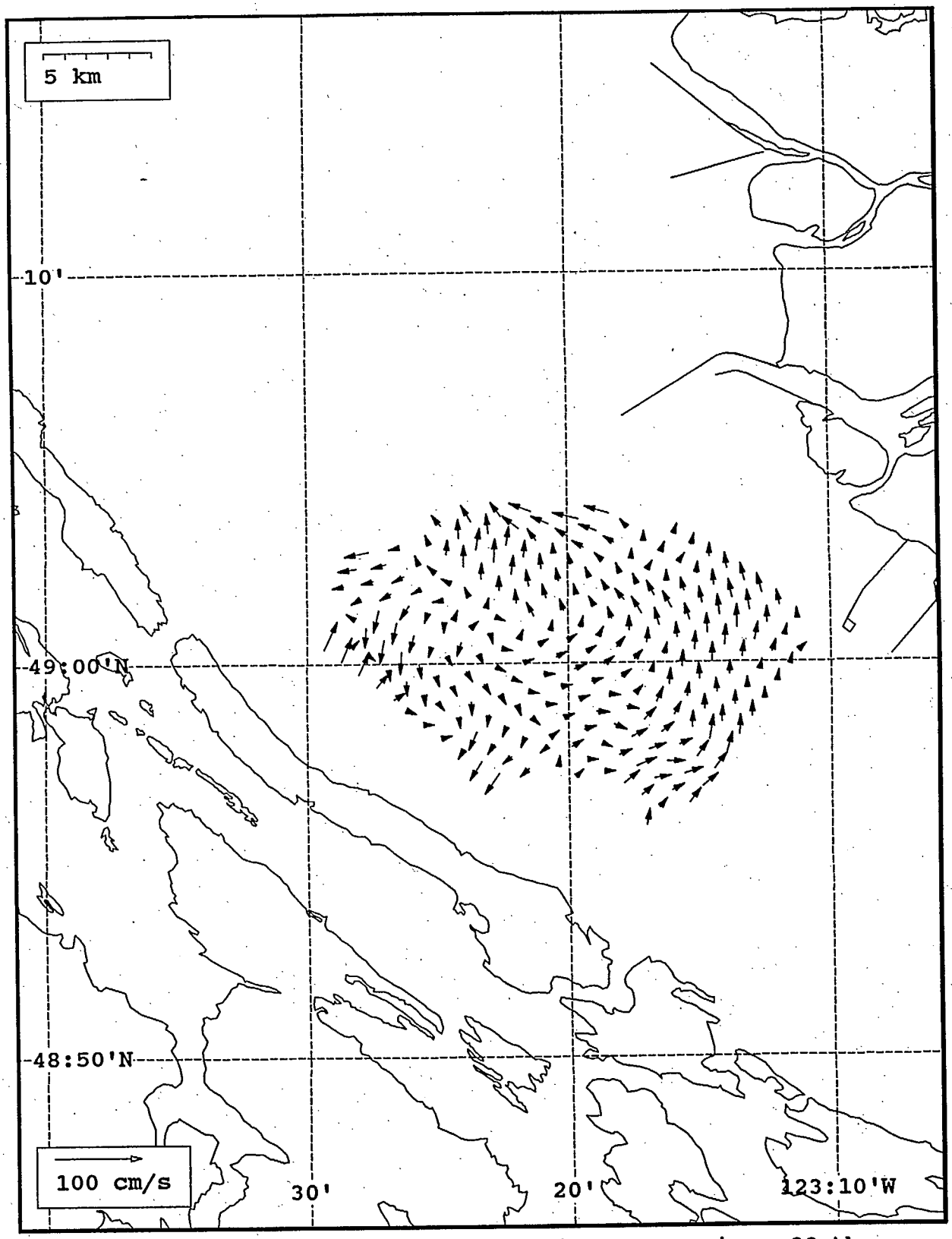

SeaSonde current field from the Strait of Georgia, off the mouth of the Fraser River, for 12:00 Z, August 5, 1993.

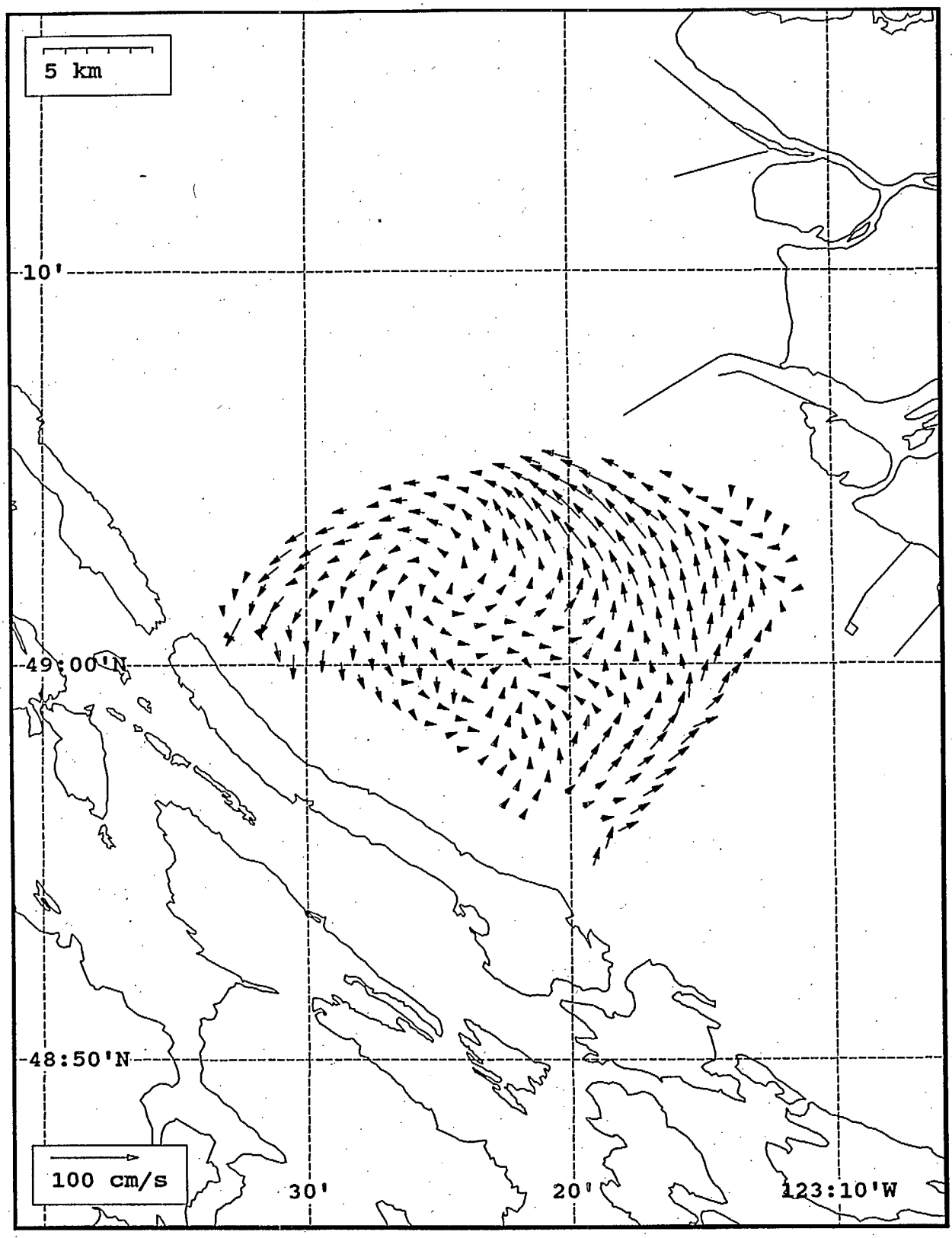

SeaSonde current field from the Strait of Georgia, off the mouth of the Fraser River, for 13:00 Z, August 5, 1993.

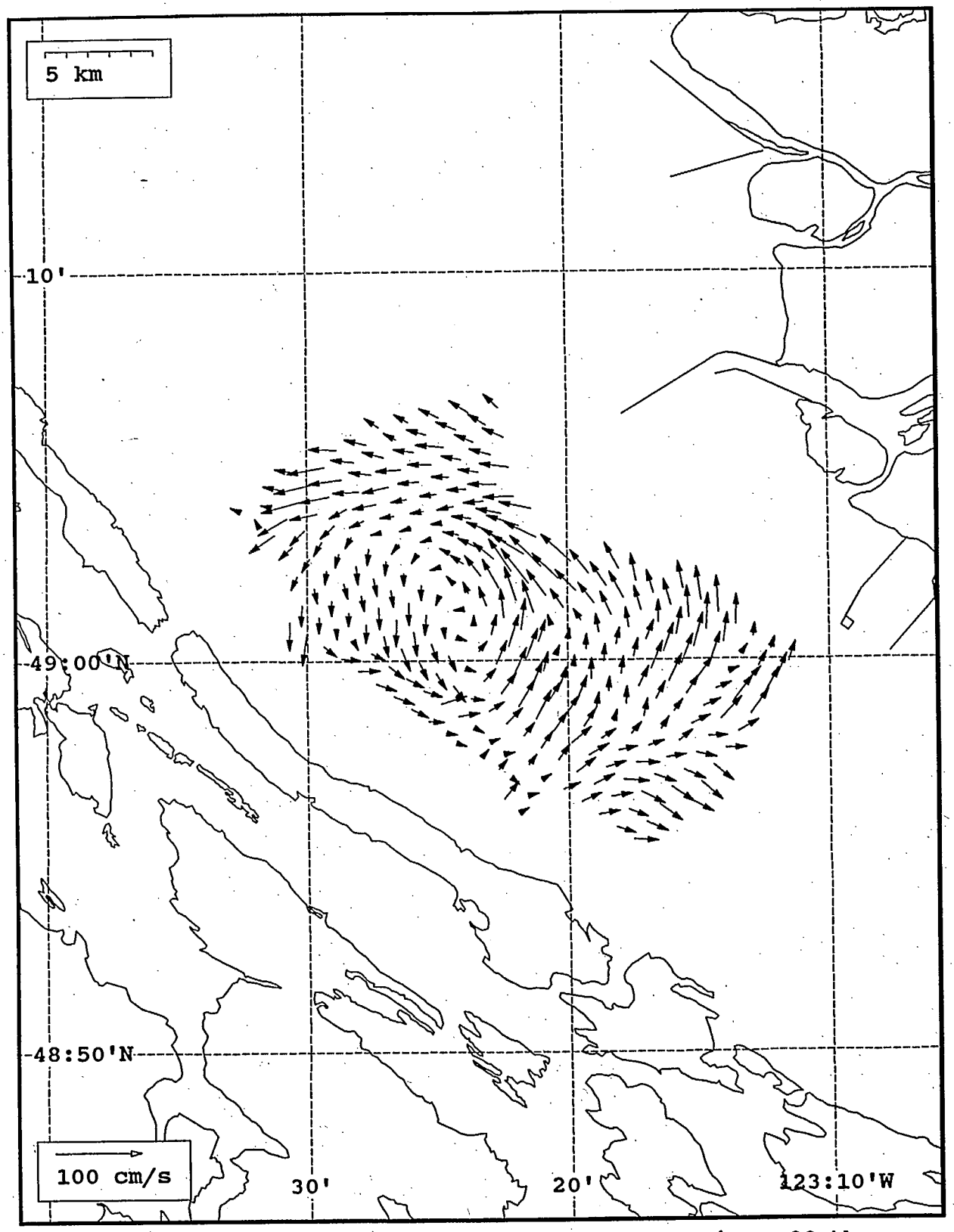

SeaSonde current field from the Strait of Georgia, off the mouth of the Fraser River, for 14:00 Z, August 5, 1993.

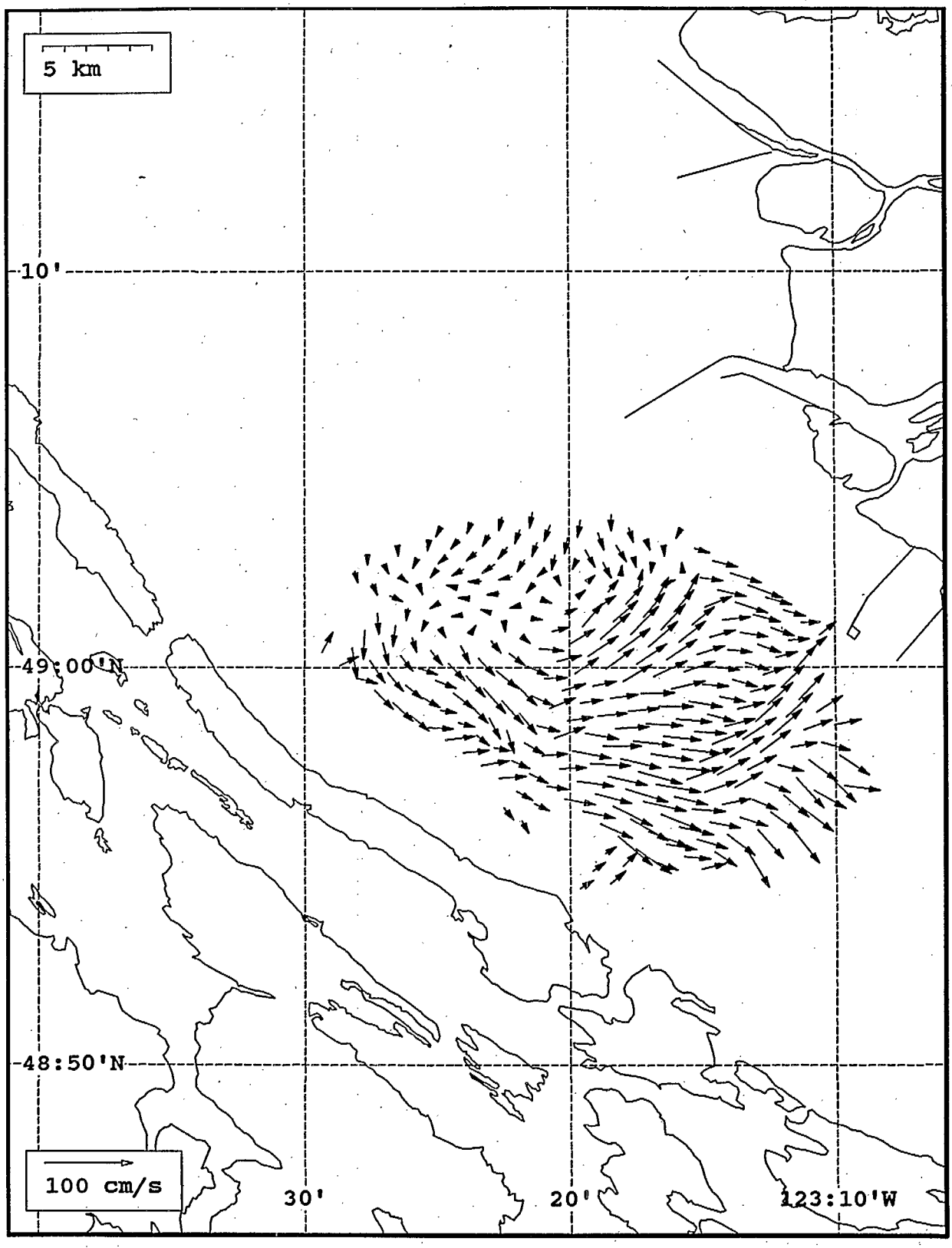

SeaSonde current field from the Strait of Georgia, off the mouth of the Fraser River, for 15:00 Z, August 5, 1993.

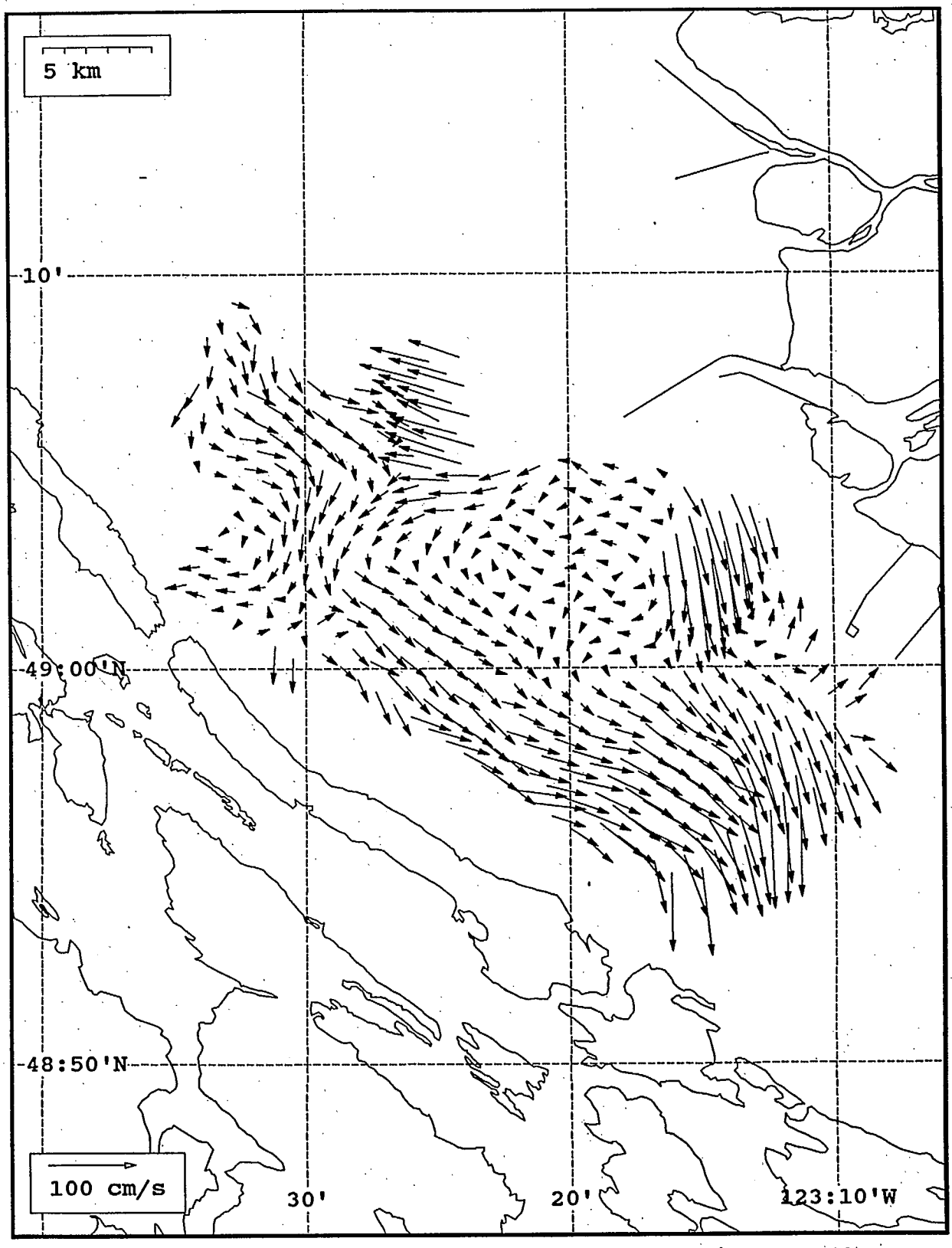

SeaSonde current field from the Strait of Georgia, off the mouth of the Fraser River, for 20:00 Z, August 5, 1993.